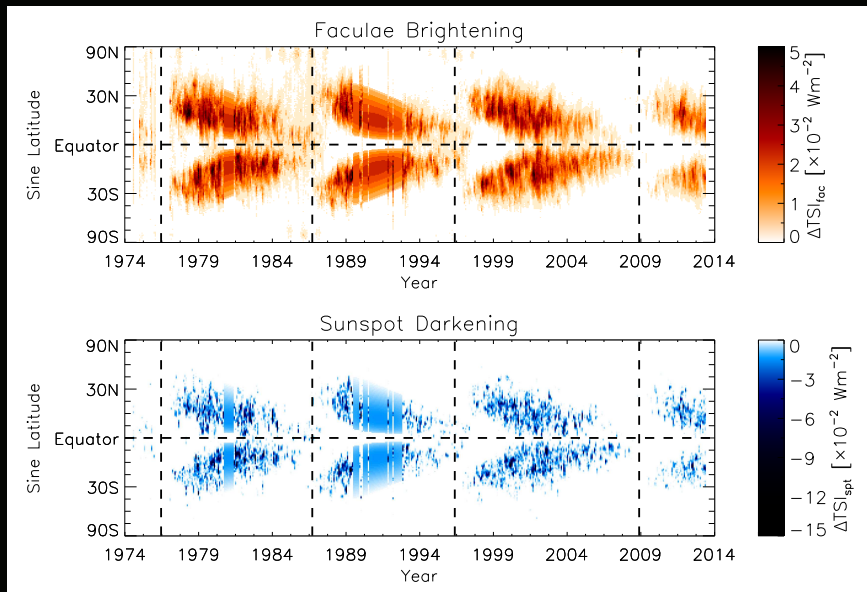


Analysis and modeling of solar irradiance variations



Kok Leng Yeo

International Max Planck Research School
for Solar System Science
at the University of Göttingen

Analysis and modeling of solar irradiance variations

Von der Fakultät für Elektrotechnik, Informationstechnik, Physik
der Technischen Universität Carolo-Wilhelmina

zu Braunschweig

zur Erlangung des Grades eines
Doktors der Naturwissenschaften

(Dr.rer.nat.)

genehmigte

Dissertation

Kumulative Arbeit

von Kok Leng Yeo

aus Singapur

1. Referentin oder Referent: Professor Dr. Sami K. Solanki
 2. Referentin oder Referent: Professor Dr. Karl-Heinz Glaßmeier
- eingereicht am: 22 April 2014
mündliche Prüfung (Disputation) am: 11 Juli 2014
(2014)

Vorveröffentlichung der Dissertation

Teilergebnisse aus dieser Arbeit wurden mit Genehmigung der Fakultät für Elektrotechnik, Informationstechnik, Physik, vertreten durch den Mentor der Arbeit, in folgenden Beiträgen vorab veröffentlicht:

Publikationen

- Yeo, K. L., Krivova, N. A., Solanki, S. K., Glassmeier, K. H., 2014, Reconstruction of total and spectral solar irradiance since 1974 based on KPVT, SoHO/MDI and SDO/HMI observations, *Astron. Astrophys.*, 570, A85
- Thuillier, G., Schmidtke, G., Erhardt, C., Nikutowski, B., Shapiro, A. I., Bolduc, C., Lean, J., Krivova, N. A., Charbonneau, P., Cessateur, G., Haberleiter, M., Melo, S., Delouille, V., Mampaey, B., Yeo, K. L., Schmutz, W., 2014, Solar spectral irradiance variability in November/December 2012: comparison of observations by instruments on the International Space Station and models, *Sol. Phys.*, online
- Yeo, K. L., Krivova, N. A., Solanki, S. K., 2014, Solar cycle variation in solar irradiance, *Space Sci. Rev.*, online
- Yeo, K. L., Feller, A., Solanki, S. K., Couvidat, S., Danilovic, S., Krivova, N. A., 2014, Point spread function of SDO/HMI and the effects of stray light correction on the apparent properties of solar surface phenomena, *Astron. Astrophys.*, 561, A22
- Yeo, K. L., Solanki, S. K., Krivova, N. A., 2013, Intensity contrast of network and faculae, *Astron. Astrophys.*, 550, A95

Tagungsbeiträge

- Yeo, K. L., Solanki, S. K., Krivova, N. A., Solar irradiance variability and the Earth's climate, SCOSTEP's 13th Quadrennial Solar-Terrestrial Physics Symposium, Xi'an, China, 13 to 18 October 2014 (invited talk)
- Yeo, K. L., Solanki, S. K., Krivova, N. A., Model reconstruction of total and spectral solar irradiance since 1974, AOGS 11th Annual Meeting, Sapporo, Japan, 28 July to 1 August 2014 (poster)
- Yeo, K. L., Krivova, N. A., Solanki, S. K., Reconstruction of TSI and SSI in the satellite era. EGU General Assembly 2014, Vienna, Austria, 27 April to 2 May 2014 (invited talk)

- Krivova, N. A., Yeo, K. L., Solanki, S. K., Dasi-Espuig, M., Ball, W., Modelling solar irradiance with SATIRE, 2014 SORCE Science Meeting, Cocoa Beach, Florida, USA, 28 to 31 January 2014 (invited talk)
- Yeo, K. L., Solanki, S. K., Krivova, N. A., SATIRE-S reconstruction of total and spectral solar irradiance from 1974 to 2013, International CAWSES-II Symposium, 18 to 22 November 2013, Nagoya, Japan (poster)
- Yeo, K. L., Krivova, N. A., Solanki, S. K., Cyclic variation in solar irradiance, ‘The Solar Activity Cycle: Physical Causes And Consequences’ Workshop, Bern, Switzerland, 11 to 15 November 2013 (invited talk)
- Yeo, K. L., Solanki, S. K., Krivova, N. A., Network & facular contribution to solar irradiance variation, Space Climate 5, Oulu, Finland, 15 to 19 June 2013 (poster)
- Yeo, K. L., Solanki, S. K., Krivova, N. A., Comparing irradiance reconstructions from HMI magnetograms with SORCE observations, 2011 SORCE Science Meeting, Sedona, Arizona, USA, 13 to 16 September 2011 (poster)
- Yeo, K. L., Solanki, S. K., Krivova, N. A., Reconstructing total solar irradiance from HMI/SDO observations, LWS/SDO-1 Workshop, Squaw Creek, California, USA, 1 to 5 May 2011 (poster)

Contents

Summary	9
1 Introduction	11
1.1 Measurements and models of solar irradiance	11
1.2 SDO/HMI	15
1.3 SATIRE-S	17
1.4 Thesis outline	20
2 Background	23
2.1 Physical origin of solar radiation	23
2.1.1 Energy transport in the solar interior	23
2.1.2 Formation of the solar spectrum	24
2.2 The 11-year activity cycle of the Sun and solar magnetism	26
2.2.1 Solar cycle variation in solar magnetism	27
2.2.2 The solar dynamo	31
2.3 Solar model atmospheres and intensity spectra	33
2.3.1 The radiative transfer equation	34
2.3.2 Local thermodynamic equilibrium	35
2.3.3 Line blanketing and opacity	36
2.3.4 Three-dimensional model atmospheres	38
3 Intensity contrast of solar network and faculae	
<i>(The contents of this chapter are identical to the printed version of Yeo, K. L., Solanki, S. K., Krivova, N. A., 2013, Intensity contrast of network and faculae, Astron. Astrophys., 550, A95.)</i>	41
3.1 Introduction	42
3.2 Method	44
3.2.1 SDO/HMI data	44
3.2.2 Data reduction	45
3.2.2.1 Magnetogram noise level	45
3.2.2.2 Quiet Sun intensity	46
3.2.2.3 Identification of network and faculae	48
3.2.2.4 Definition of intensity contrast	52
3.3 Results	53
3.3.1 Variation with position and magnetogram signal	53
3.3.2 Surface fits	56
3.3.3 Intrinsic contrast	58

3.4	Discussion	61
3.4.1	Comparison with Ortiz et al. (2002)	61
3.4.2	Continuum intensity contrast about disc centre	66
3.4.3	Line core intensity contrast	69
3.4.4	Facular contribution to variation in solar irradiance	72
3.5	Conclusion	75
4	Point spread function of SDO/HMI and the effects of stray light correction on the apparent properties of solar surface phenomena	
	<i>(The contents of this chapter are identical to the printed version of Yeo, K. L., Feller, A., Solanki, S. K., Couvidat, S., Danilovic, S., Krivova, N. A., 2014, Point spread function of SDO/HMI and the effects of stray light correction on the apparent properties of solar surface phenomena, Astron. Astrophys., 561, A22.)</i>	77
4.1	Introduction	78
4.2	PSF derivation	80
4.2.1	Data selection	80
4.2.2	PSF derivation method	84
4.2.3	Image restoration method	91
4.2.4	Interaction between solar radiation and the venusian atmosphere	92
4.2.4.1	Diffusion and scattering of solar radiation in the venusian atmosphere	92
4.2.4.2	Refraction of solar radiation in the venusian atmosphere	94
4.2.4.3	Final estimate of the PSF	99
4.2.5	Partial lunar eclipse and solar limb observations	100
4.3	Application of the derived PSF to HMI observations	101
4.3.1	Granulation contrast	101
4.3.2	Effect of image restoration on the Dopplergram, longitudinal magnetogram, continuum intensity and line depth data products	107
4.3.2.1	Intensity contrast and magnetogram signal of small-scale magnetic concentrations	108
4.3.2.2	Intensity and magnetogram signal of sunspots and pores	111
4.3.2.3	Amount of magnetic flux on the solar surface	111
4.3.2.4	Line-of-sight velocity	116
4.4	Variation of the PSF within the FOV, between the HMI CCDs and with time	119
4.4.1	Variation of the PSF with FOV position	119
4.4.2	Variation of the PSF between the HMI CCDs and with time	122
4.5	Summary	124
5	Reconstruction of total and spectral solar irradiance from 1974 to 2013 based on KPVT, SoHO/MDI and SDO/HMI observations	
	<i>(The contents of this chapter are identical to the submitted version of Yeo, K. L., Krivova, N. A., Solanki, S. K., Glassmeier, K. H., 2014, Reconstruction of total and spectral solar irradiance from 1974 to 2013 based on KPVT, SoHO/MDI and SDO/HMI observations, Astron. Astrophys., 570, A85.)</i>	127
5.1	Introduction	128
5.2	The SATIRE-S model	130

5.3	Data selection and preparation	131
5.3.1	Daily full-disc continuum intensity images and longitudinal magnetograms	131
5.3.1.1	HMI	132
5.3.1.2	MDI	132
5.3.1.3	KPVT	134
5.3.2	TSI measurements	136
5.4	Solar irradiance reconstruction	137
5.4.1	Harmonizing the model input from multiple instruments	137
5.4.1.1	Umbra and penumbra	137
5.4.1.2	Faculae	138
5.4.2	The free parameter	144
5.4.3	Ultraviolet solar irradiance	148
5.4.4	Data gaps	153
5.4.5	Error analysis	155
5.5	Discussion	156
5.5.1	Comparison with observations	156
5.5.1.1	TSI composites	156
5.5.1.2	Solar Lyman- α irradiance and Mg II index composites	160
5.5.1.3	UARS and SORCE ultraviolet solar irradiance	162
5.5.1.4	SORCE/SIM SSI	166
5.5.2	Facular and sunspot contribution to variation in TSI	171
5.6	Summary	173
6	Solar cycle variation in solar irradiance	
	<i>(The contents of this chapter are identical to the submitted version of Yeo, K. L., Krivova, N. A., Solanki, S. K., 2014, Solar cycle variation in solar irradiance, Space Sci. Rev., online.)</i>	179
6.1	Introduction	179
6.2	Measurements	180
6.2.1	Total solar irradiance, TSI	180
6.2.2	Spectral solar irradiance, SSI	183
6.3	Models	188
6.3.1	Solar surface magnetism	188
6.3.2	Model architectures	192
6.3.3	SSI models capable of returning the full solar spectrum	194
6.3.3.1	SATIRE-S	194
6.3.3.2	Other present-day models	197
6.4	Reconciling measurements and models	200
6.4.1	Proxy models	200
6.4.2	Semi-empirical models	201
6.5	Summary	202
7	Summary and outlook	207

A Appendix	215
A.1 Yeo, K. L., Solanki, S. K., Krivova, N. A., 2013, Intensity contrast of network and faculae, <i>Astron. Astrophys.</i> , 550, A95	215
A.2 Yeo, K. L., Feller, A., Solanki, S. K., Couvidat, S., Danilovic, S., Krivova, N. A., 2014, Point spread function of SDO/HMI and the effects of stray light correction on the apparent properties of solar surface phenomena, <i>Astron. Astrophys.</i> , 561, A22	235
A.3 Yeo, K. L., Krivova, N. A., Solanki, S. K., Glassmeier, K. H., 2014, Reconstruction of total and spectral solar irradiance from 1974 to 2013 based on KPVT, SoHO/MDI and SDO/HMI observations, <i>Astron. Astrophys.</i> , 570, A85	259
A.4 Yeo, K. L., Krivova, N. A., Solanki, S. K., 2014, Solar cycle variation in solar irradiance, <i>Space Sci. Rev.</i> , online	278
Bibliography	313
Publications	335
Acknowledgements	337
Curriculum Vitae	339
Erklärung zum eigenen Beitrag	341

Summary

A prominent manifestation of the solar dynamo is the 11-year activity cycle, visible in indicators of solar activity, including the topic of this thesis, solar irradiance. Two quantities are of interest, total and spectral solar irradiance, TSI and SSI. They are defined as the total and wavelength-resolved solar radiative flux above the Earth's atmosphere, normalized to one AU. Excluding the interaction between solar radiation and the Earth's atmosphere, and changes in the Earth to Sun distance, TSI and SSI isolate the radiant property of the Earth-facing hemisphere of the Sun.

A relationship between solar activity and the brightness of the Sun had long been suspected. It was however, only directly observed when satellite measurements, free from the effects of atmospheric intensity fluctuations and stray light, became available. TSI and SSI (at least in the ultraviolet) have been measured on a regular basis by a succession of space missions, almost without interruption, since 1978. The measurement of solar irradiance from space is accompanied by the development of models aimed at describing the apparent variability in these observations by the intensity excess/deficit in the solar surface and atmosphere brought on by magnetic structures in the photosphere. While the body of satellite measurements is largely consistent at solar rotation timescales and show obvious solar cycle modulation, there is considerable scatter in the absolute radiometry, secular variation and the spectral dependence of the variation over the solar cycle, due to the challenge in accounting for instrumental influences. Consequently, models of solar irradiance serve as an important complement to direct observations, helping us understand the apparent variability and the physical processes driving them.

The more sophisticated models, termed semi-empirical, rely on the calculated intensity spectra of magnetic structures on the solar surface and in the solar atmosphere, generated with spectral synthesis codes from semi-empirical solar model atmospheres. An established example of such models is SATIRE-S (Spectral And Total Irradiance REconstruction for the Satellite era). Obviously, the robust reconstruction of solar irradiance depends on how realistic these intensity spectra are. There are two key sources of uncertainty. One, the account of departures from local thermodynamic equilibrium (LTE) in the spectral synthesis. Two, the fact that the radiant properties of network and faculae are neither fully understood nor adequately represented in current models by the use of plane-parallel model atmospheres (as opposed to three-dimensional model atmospheres). In SATIRE-S, this is responsible for the sole free parameter in the model. Semi-empirical models have achieved considerable success replicating the apparent variability in solar irradiance observations. The unambiguous account of the outstanding discrepancy between model and measurement will require however, an improvement in how non-LTE effects, and the influence of network and faculae on solar irradiance is included in semi-empirical models.

This thesis is the compilation of four publications, detailing the results of investigations aimed at setting the groundwork necessary for the eventual introduction of three-dimensional atmospheres into SATIRE-S. Also presented is an update of the SATIRE-S model, and a review of the current state of the measurement and modelling of solar irradiance.

We examined the intensity contrast of network and faculae in observations from the Helioseismic and Magnetic Imager onboard the Solar Dynamics Observatory (SDO/HMI), and estimated the point spread function (PSF) of the instrument. The derived intensity contrasts and PSF can be used, in future efforts, to constrain three-dimensional model atmospheres, key to improving the reliability of semi-empirical models. The results of these studies also offered new insights into the radiant behaviour of network and faculae (and their contribution to variation in solar irradiance), and the effects of stray light on the apparent properties of solar surface phenomena.

The SATIRE-S model had previously been applied to full-disc intensity images and magnetograms from the Kitt Peak Vacuum Telescope and the Michelson Doppler Imager (onboard the Solar and Heliospheric Observatory) to reconstruct TSI and SSI over the period of 1974 to 2009. On top of extending these preceding efforts to the present time with similar data from HMI, we made various refinements to the reconstruction method. The result is a daily reconstruction of TSI and SSI, covering 1974 to the present, that is more reliable and, in most cases, extended than similar reconstructions from contemporary models. The reconstruction is also highly consistent with observations from multiple sources, demonstrating its utility for solar irradiance and climate studies.

1 Introduction

1.1 Measurements and models of solar irradiance

The 11-year activity cycle of the Sun, a manifestation of the solar dynamo, can be seen in indicators of solar activity (Hathaway 2010). This includes, the sunspot area and number, chromospheric and coronal indices such as the 10.7 cm radio flux, Mg II index and X-ray flux, and in the topic of this thesis, solar irradiance (Fig. 1.1). Solar irradiance, the radiative output of the Sun, is described in terms of what is termed total and spectral solar irradiance, TSI and SSI. They are defined the total and wavelength-resolved solar radiative flux above the Earth's atmosphere, normalized to one AU (units of power per unit area, and power per unit area and wavelength, respectively). Excluding the interaction between solar radiation and the Earth's atmosphere, and changes in the Earth-Sun separation, TSI and SSI follows the radiant property of the hemisphere of the Sun facing the Earth.

A relationship between solar activity and the radiative output of the Sun had long been speculated (Abbot et al. 1923, Smith and Gottlieb 1975, Eddy 1976). This was however, not confirmed until satellite measurements, free from the effects of fluctuations in atmospheric transmittance, became available. TSI and SSI (at least in the ultraviolet) have been monitored regularly by a succession of space missions, almost without interruption, since 1978 (Hickey et al. 1980, Willson and Hudson 1988, Fröhlich 2006, DeLand and Cebula 2008, Kopp et al. 2012). The early TSI observations quickly revealed a correlation between the apparent variability and the passage of active regions across the solar disc (Willson et al. 1981a, Hudson et al. 1982, Oster et al. 1982, Foukal and Lean 1986). Consequently, the measurement of solar irradiance from space is accompanied by the development of models aimed at describing the apparent variability in these observations by the intensity excess/deficit in the solar surface and atmosphere brought about by photospheric magnetism.

The action of magnetic concentrations in the photosphere on the thermal structure and therefore the radiant property of the solar surface/atmosphere is not the only mechanism mooted to explain the observed variability in solar irradiance, but it is by far the most established. Models relating variations in solar irradiance to the emergence and evolution of photospheric magnetism have achieved considerable success in replicating observations (Domingo et al. 2009). Other mechanisms, related to physical processes in the solar interior, have been proposed (Wolff and Hickey 1987, Kuhn et al. 1988, Cossette et al. 2013) but there is as yet little direct evidence.

While the measurements from the succession of solar irradiance monitors sent into orbit are largely consistent at solar rotation timescales and show obvious solar cycle modulation (though not without exception), there is considerable scatter in the absolute ra-

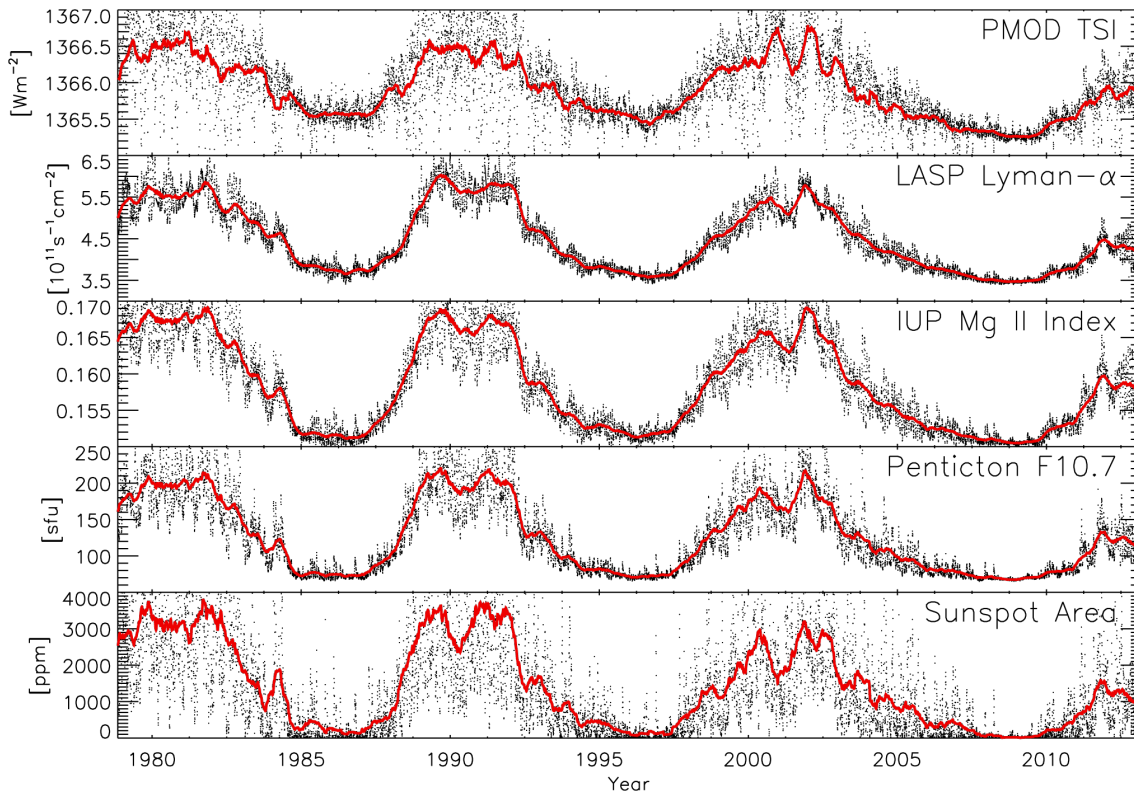


Figure 1.1: Indices of solar activity. From top to bottom; the PMOD total solar irradiance composite (version d41_62_1302, Fröhlich 2000), the LASP Lyman- α irradiance composite (Woods et al. 2000), the IUP Mg II index composite (version 4, Viereck and Puga 1999, Skupin et al. 2005b,c), the Ottawa and Penticton adjusted 10.7 cm radio flux record (Tapping 1987, 2013) and the projected sunspot area composite by Balmaceda et al. 2009 (version 0613). The red curves follow the 181-day moving mean.

diometry, secular variation and the spectral dependence of the variation over the solar cycle (see Figs. 1.2 and 1.3, and Ermolli et al. 2013, Solanki et al. 2013). This is primarily due to the significant challenge in accounting for changes in instrument response from ageing and exposure (Hoyt et al. 1992, Lee et al. 1995, Dewitte et al. 2004a, Fröhlich 2006, DeLand and Cebula 2008). Due to the uncertainties afflicting the direct observation of solar irradiance, models of solar irradiance based on photospheric magnetism have emerged as an important tool for understanding the apparent variability in these measurements and the associated physical processes.

The most straightforward way to model solar irradiance (adopted since the earliest models) is to reconstruct it by the regression of indices of solar activity, acting as proxies of the radiant effects of photospheric magnetism, to measurements.

The influence of sunspots and pores is typically represented by sunspot area or what is termed the photometric sunspot index (PSI, Hudson et al. 1982, Fröhlich et al. 1994), and network and faculae by chromospheric indices. (The PSI is the proportional deficit in solar irradiance, from the magnetically quiet Sun level, due to sunspot darkening. This can be calculated from the sunspot number, sunspot area or from full-disc intensity images.)

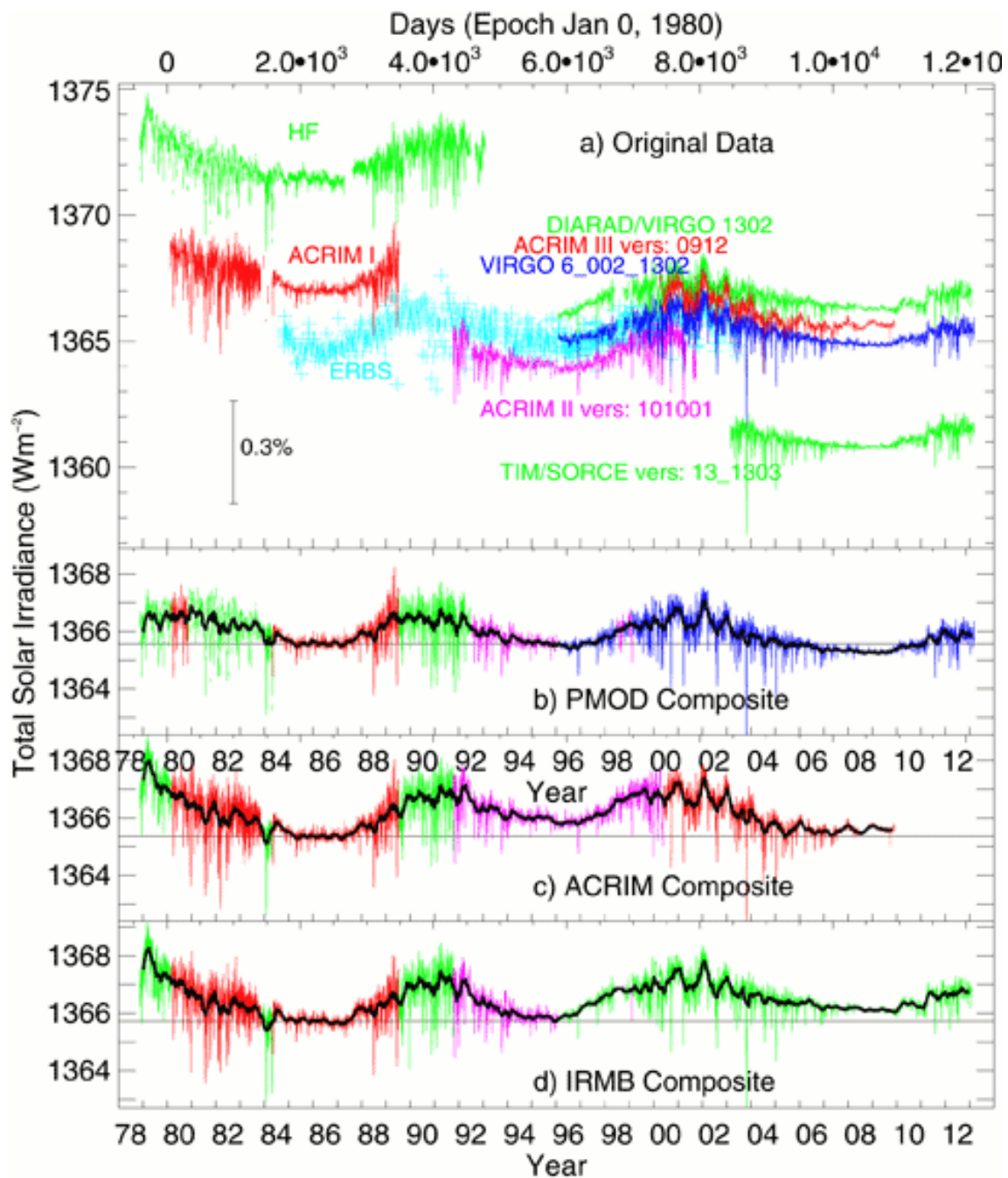


Figure 1.2: a) The published TSI measurements from the various radiometers sent into orbit since 1978 and the competing composite records of TSI by b) PMOD, c) ACRIM and d) IRMB. These observations and composites are introduced in detail in Chap. 6.2.1. Courtesy of C. Fröhlich (<http://www.pmodwrc.ch/pmod.php?topic=tsi/composite/SolarConstant>).

While straightforward, such models depend on and are therefore limited by the availability of reliable measurements. They are also limited by uncertainties in the solar activity index data employed and offer little physical insight into the underlying relationship between

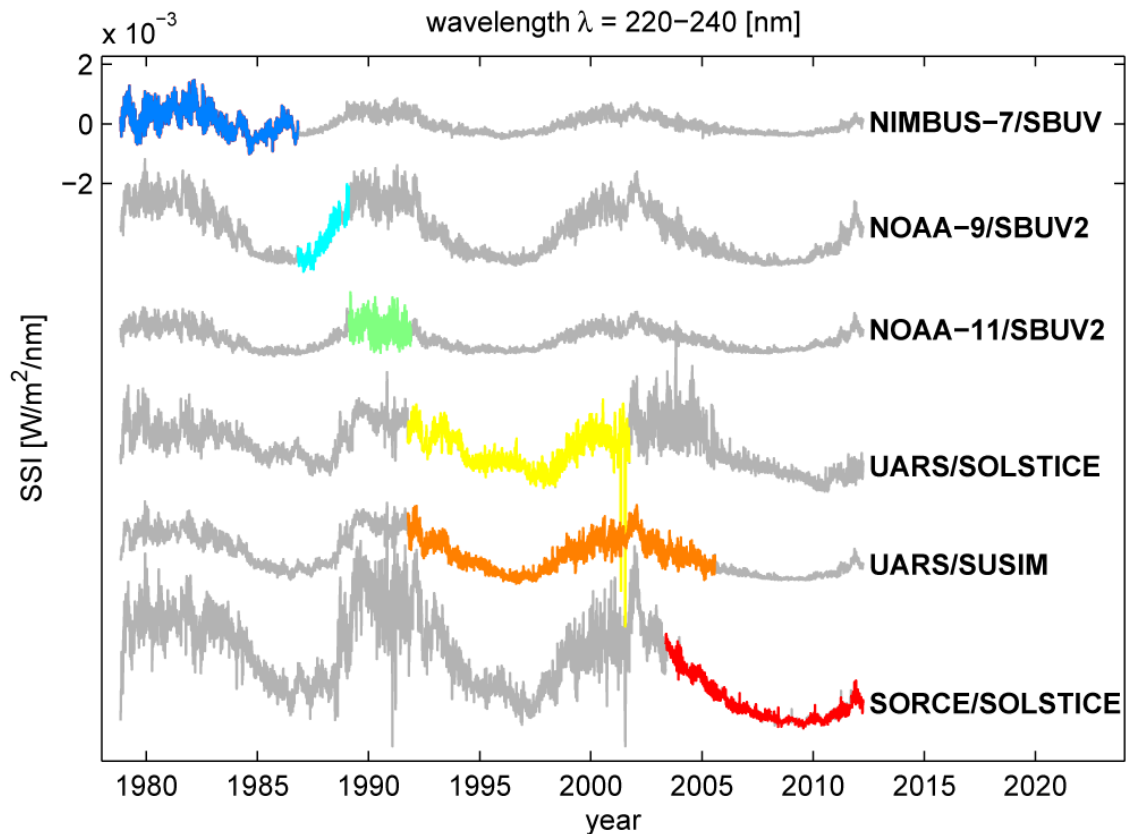


Figure 1.3: Integrated solar irradiance between 220 and 240 nm from six instruments, offset from one another for the purpose of illustration. Each record is extrapolated backwards and forwards in time by the method set out in Dudok de Wit (2011), drawn in grey. Taken from Ermolli et al. (2013).

solar irradiance and photospheric magnetism. Critically, these models usually assume a linear relationship between the proxies and solar irradiance, which is not true in the case of chromospheric indices (Solanki and Krivova 2004, Foukal et al. 2011). Variation in solar irradiance is the sum effect of the influence of photospheric magnetism on the solar surface and enclosed atmosphere (Mitchell and Livingston 1991, Unruh et al. 1999, Preminger et al. 2002). This would obviously not be entirely captured in chromospheric indices, highlighting another fundamental limit of the approach.

A more physics-based approach has been in development by various groups over the past two decades (Fontenla et al. 1999, Fligge et al. 2000, Krivova et al. 2003, Penza et al. 2003, Haberreiter et al. 2005). The overall architecture of these models, referred to as semi-empirical, is similar. The solar disc is segmented by surface magnetic feature type. The intensity spectrum of each feature type is calculated from spectral synthesis codes with the respective semi-empirical model atmosphere¹ as input. The solar spectrum is then recreated from the sum of these intensity spectra, weighted by the apparent

¹The model atmospheres describe the temperature and density within each feature type as a function of height. They are described as semi-empirical from the fact that they are constrained by observations.

surface coverage of each feature type. An established example of semi-empirical models is SATIRE-S (Spectral And Total Irradiance REconstruction for the Satellite era, Fligge et al. 2000, Krivova et al. 2003, 2011b). Prior to this thesis, it had been applied to full-disc observations from the Kitt Peak Vacuum Telescope (KPVT, Livingston et al. 1976, Jones et al. 1992) and the Michelson Doppler Imager onboard the Solar and Heliospheric Observatory (SoHO/MDI, Scherrer et al. 1995) to reconstruct TSI and SSI between 1974 and 2009 (Krivova et al. 2003, 2006, 2009b, 2011a, Wenzler et al. 2005, 2006, 2009, Unruh et al. 2008, Ball et al. 2011, 2012, 2014).

Evidently, the robust reconstruction of solar irradiance by the semi-empirical approach depends on how reliable/realistic are the intensity spectra of solar surface features utilized. A major source of uncertainty is the fact that the radiant behaviour of quiet Sun network and active region faculae is neither fully understood nor adequately represented in current models by the use of plane-parallel model atmospheres (as opposed to three-dimensional model atmospheres). The small-scale magnetic concentrations that make up network and faculae are, at present, still largely unresolved in available observations. The effect of atmospheric and instrumental scattered light on the apparent properties of these surface features is also not completely known. In spite of the current insufficiencies, semi-empirical models such as the SATIRE-S have been very successful in reproducing most of the apparent variability in solar irradiance observations. The unambiguous account of the outstanding discrepancy between model and measurement will require, amongst other things, an improvement in how the effects of network and faculae on solar irradiance is included in semi-empirical models.

This thesis is the compilation of four publications, detailing the results of investigations aimed at addressing the present limits of semi-empirical models (discussed above) and updating the SATIRE-S model, and also includes a review of the current state of the measurement and modelling of solar irradiance. These studies made use of full-disc observations from the Helioseismic and Magnetic Imager onboard the Solar Dynamics Observatory (launched in 2010, Schou et al. 2012b). In the following, we give a brief introduction to the HMI instrument (Sect. 1.2) and the SATIRE-S model (Sect. 1.3), before providing an outline of this thesis (Sect. 1.4).

1.2 SDO/HMI

SDO/HMI Schou et al. (2012b) is the follow-up to the highly successful SoHO/MDI (Scherrer et al. 1995), the first ever spaceborne magnetograph. HMI is designed to return continuous full-disc measurements of intensity, magnetic field vector and line-of-sight velocity from spectropolarimetry of the Fe I 6173 Å line.

The instrument comprises of two 4096×4096 pixel CCD cameras, which share a common optical path, referred to as the side and front CCDs (Fig. 1.4). The optical assembly includes a Lyot filter and two Michelson interferometers (both tunable), and a series of waveplates, which set the bandpass and polarization, respectively. The pixel scale is 0.505 arcsec and the diffraction-limited spatial resolution is 0.91 arcsec. Narrow (FWHM of 76 mÅ) bandpass images or filtergrams of the full solar disc are collected continuously, at 1.875 second intervals, on the two CCDs in turn. The observation sequence cycles through six positions within the Fe I 6173 Å line (spaced 69 mÅ apart) and six

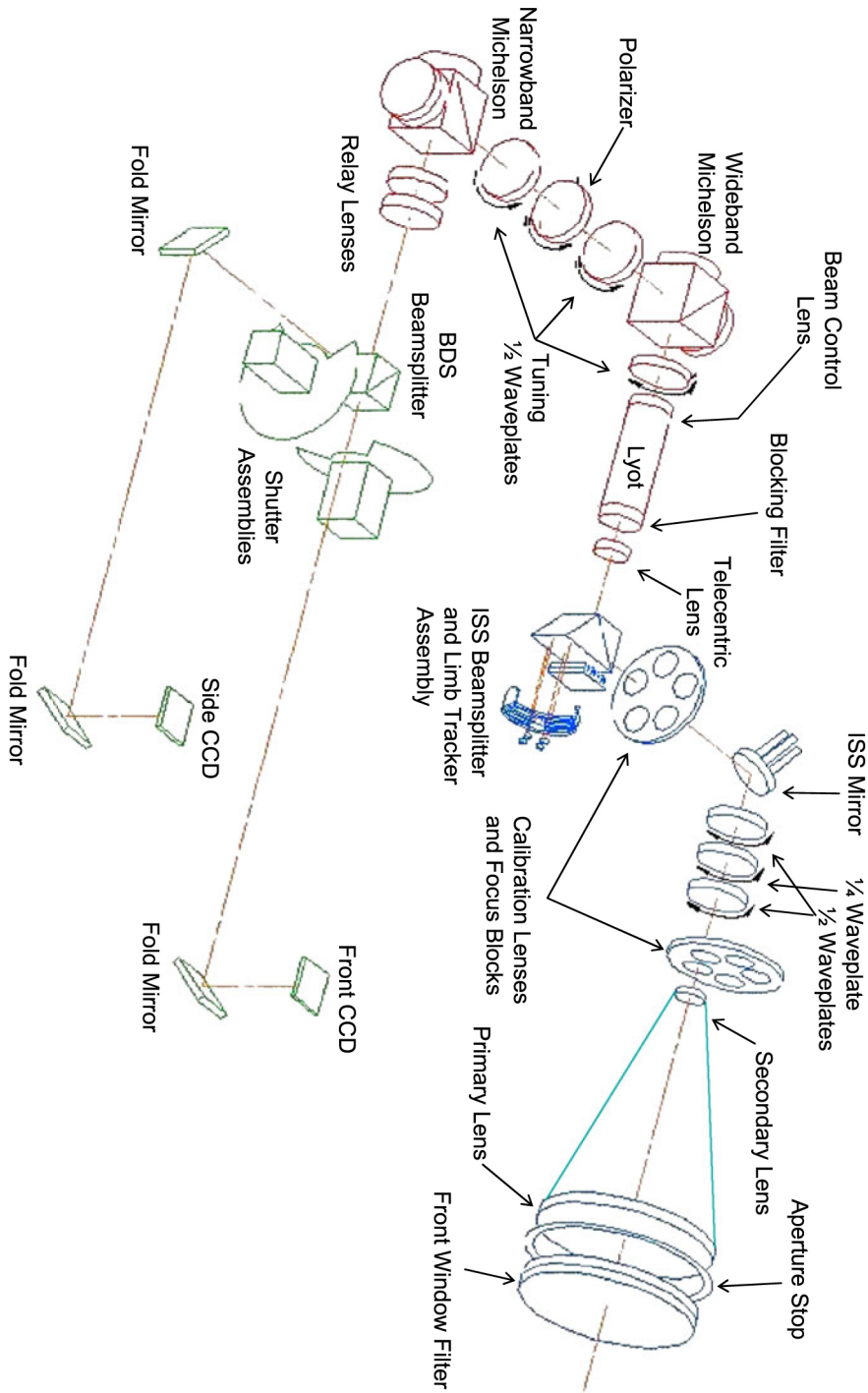


Figure 1.4: HMI optical assembly (not to scale). Taken from Schou et al. (2012b).

polarizations (Stokes $I \pm Q$, $I \pm U$ and $I \pm V$).

A set of 12 filtergrams, covering the $I+V$ and $I-V$ polarizations at each line position is collected on the front CCD every 45 seconds. A set of 36 filtergrams, of each combination of polarization and line position, is registered on the side CCD every 135 seconds. The sequence of filtergrams from the front and from the side CCD are combined to yield longitudinal magnetograms, Dopplergrams and intensity images (continuum intensity, line depth and line width) at 45 and 720-second cadence, respectively. Full-Stokes parameters (i.e., the Stokes I, Q, U and V images) are also generated from the side CCD filtergram sequence, again at intervals of 720 seconds. These are inverted using the VFISV (Very Fast Inversion of Stokes Vector) Milne-Eddington inversion scheme by Borrero et al. (2011), the primary output of which is the vector magnetogram (giving both magnetic flux density and pointing). For the work detailed in this thesis we preferred the longitudinal magnetogram data product over the vector magnetogram, even though it gives just the line-of-sight component of the magnetic flux density. Due to the significant noise level in the Stokes Q and U parameters, the VFISV algorithm produces artificial magnetic fields (order of 100 G in strength, largely horizontal and random in pointing) in the quiet Sun.

The temporal and spatial resolution of HMI is the highest of any full-disc spectromagnetograph. Being spaceborne, it is also free from the detrimental effects of atmospheric seeing. The noise level of HMI longitudinal magnetograms has been demonstrated to be much lower than in similar observations from MDI (Liu et al. 2012). This is, in all likelihood, also true of the other data products. The unprecedented quality of HMI magnetograms permits the resolution of small and/or weak magnetic features that would otherwise be hidden in similar data from other instruments. This grants us the ability to characterize the prevailing photospheric magnetism at never before accuracy, a boon for solar irradiance studies.

Also, while MDI intensity images, and magnetograms and Dopplergrams are generated from different filtergrams², these observables are generated from the exact same filtergrams in HMI, allowing perfectly co-spatial and co-temporal observations of intensity, magnetic field and line-of-sight velocity. This, together with the superior image quality, made HMI observations particularly suitable for the investigations detailed in this thesis.

1.3 SATIRE-S

The SATIRE-S semi-empirical model of solar irradiance is one version of the SATIRE model (Fligge et al. 2000, Krivova et al. 2003, 2011b). The key assumption of the model is that variations in solar irradiance, on timescales greater than a day, arise from photospheric magnetism alone. At timescales shorter than a day, fluctuations from flares, granulation and p -modes (i.e., acoustic oscillations) become significant (Hudson 1988, Woods et al. 2006, Seleznyov et al. 2011). Variations in solar luminosity from thermal relaxation of the convection zone of the Sun and changes in the chemistry of the core occur at timescales exceeding 10^5 years (Solanki et al. 2013) and can therefore be safely ignored when considering variations over the 11-year activity cycle.

²The MDI data processing pipeline is different from that implemented in HMI, requiring unpolarized filtergrams for the intensity observables, and circularly polarized filtergrams for the line-of-sight magnetograms and Dopplergrams.

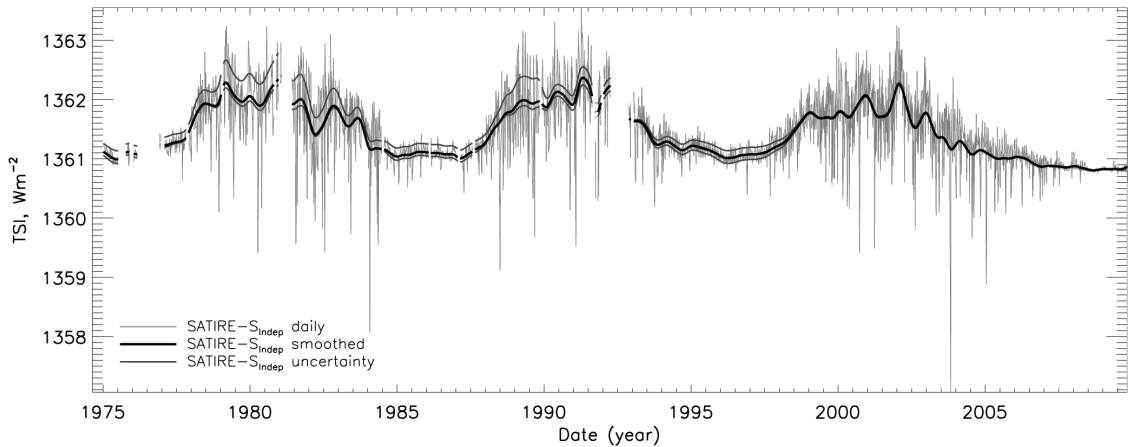


Figure 1.5: SATIRE-S reconstruction of TSI based on KPVT and MDI full-disc longitudinal magnetograms and continuum intensity images. Taken from Ball et al. (2012).

The solar disc is modelled as comprising of four components, quiet Sun, faculae, sunspot umbra and sunspot penumbra. The difference between SATIRE-S and the other variants of the model is the data used to determine the surface coverage by faculae and sunspots. SATIRE-T uses the sunspot number to reconstruct solar irradiance back to the 17th century (Krivova et al. 2007), and SATIRE-M³ cosmogenic isotope data covering the Holocene (Vieira et al. 2011). The SATIRE-S is the most accurate, employing spatially resolved full-disc observations of intensity and magnetic flux. Such observations allow the prevailing magnetism, including the disc position, to be determined with much greater precision than from sunspot number or cosmogenic isotope records. Apart from offering no information on the position of magnetic structures on the solar disc, the sunspot number is modulated by active region activity and cosmogenic isotope concentrations by the open magnetic flux alone. Neither index of solar magnetism constitutes a complete measure of prevailing magnetism. The only drawback with full-disc magnetograms is that they are only available for the last four decades. However, for the purpose of aiding the interpretation of satellite measurements of solar irradiance, which span a similar period, this is sufficient.

As stated in Sect. 1.1, the model has previously been applied to longitudinal magnetograms and continuum intensity images from the KPVT and MDI. The TSI and SSI reconstructions from these studies extend over various periods between 1974 and 2009 (see example in Fig. 1.5). The KPVT ceased observations in 2003, and MDI in 2011. One of the objectives of this thesis was to extend the model to the present with similar observations from HMI.

Sunspots are identified from the continuum intensity, and faculae by the longitudinal magnetogram signal. Points on the solar disc below threshold intensity levels representing the umbra-to-penumbra and penumbra-to-granulation boundaries are taken to correspond to umbra and penumbra, respectively. Image pixels above a threshold magnetogram sig-

³The suffixes denote their application to reconstructing solar irradiance over the period Telescopes (and therefore sunspot number records) are available, and over Millennial timescales.

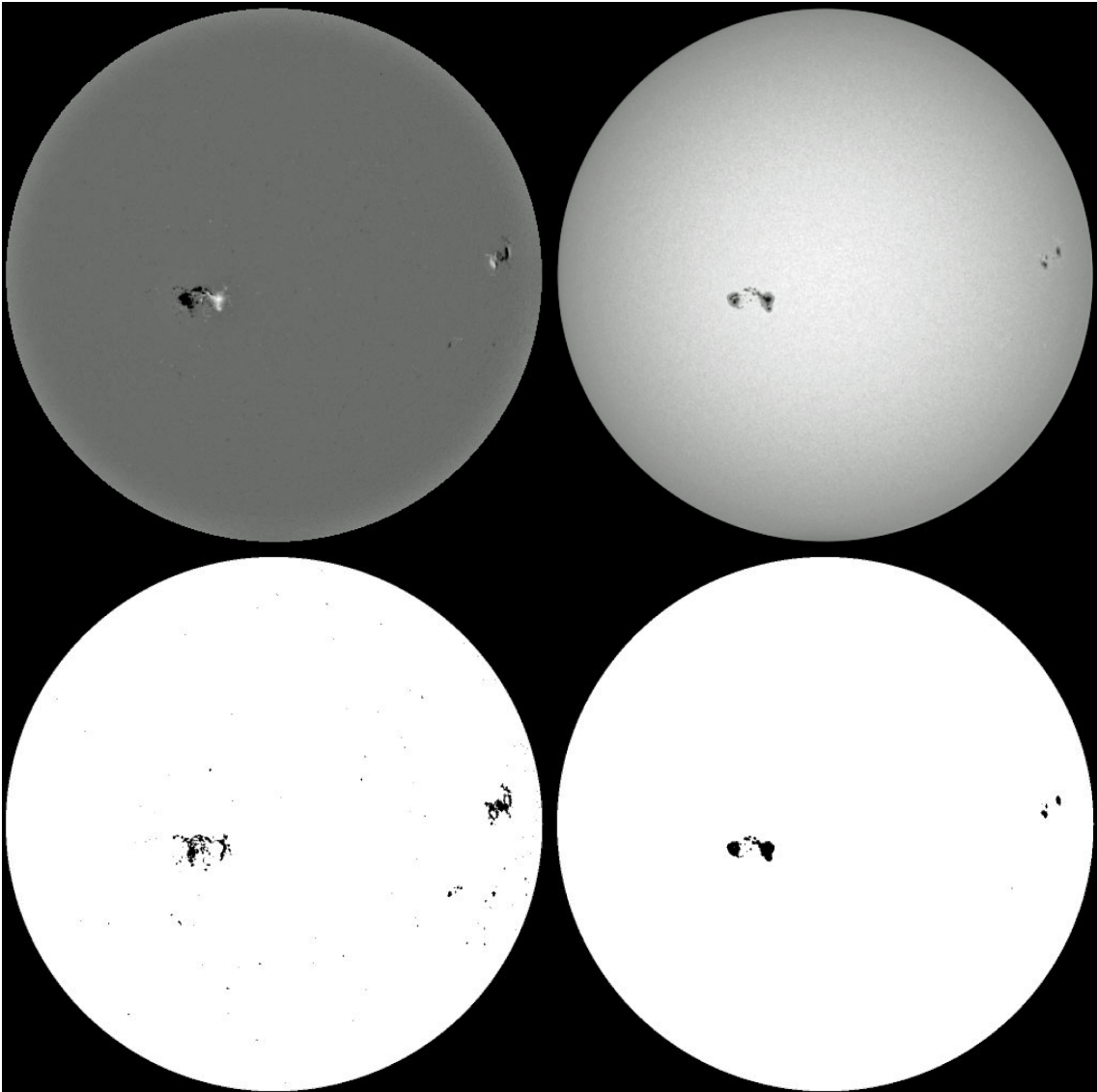


Figure 1.6: Top: MDI longitudinal magnetogram (left) and continuum intensity image (right) from November 25, 1996. Bottom: Corresponding map indicating (in black) the pixels identified as corresponding to faculae (left) and to sunspots (right) by the image segmentation method employed in the SATIRE-S model. Taken from Fligge et al. (2000).

nal (determined by the noise level) and not already classed as sunspots are identified as faculae. (This encompasses all bright magnetic features detectable by such an analysis, which includes both active region faculae and quiet Sun network.) An example is given in Fig. 1.6.

The small-scale magnetic concentrations that make up network and faculae are not fully resolved in available full-disc observations. This is roughly accounted for by scaling the faculae filling factor, the effective proportion of a given resolution element covered by faculae, with the magnetogram signal. The filling factor of each facular pixel is scaled linearly with $\langle B_l \rangle / \mu$, the ratio of the longitudinal magnetogram signal and the cosine of

the heliocentric angle⁴, saturating at unity at what is termed $(\langle B_l \rangle / \mu)_{\text{sat}}$. The $\langle B_l \rangle / \mu$ level at which the faculae filling factor saturates, $(\langle B_l \rangle / \mu)_{\text{sat}}$, is the only free parameter in the model, determined by comparing the reconstruction to measured TSI.

The apparent surface coverage by faculae and sunspots is converted to solar irradiance by means of the intensity spectra of quiet Sun, faculae, umbra and penumbra by Unruh et al. (1999). The quiet Sun model atmosphere is given by the ATLAS9 standard solar model (Kurucz 1993), and the sunspot penumbra and umbra model atmospheres by the standard stellar models corresponding to effective temperatures of 5450 K and 4500 K from the ATLAS9 grid of stellar models. The faculae model atmosphere, introduced by Unruh et al. (1999), is a modification of the FAL P model by Fontenla et al. (1993).

The intensity spectrum of each surface component at varying heliocentric angles was generated with the ATLAS9 spectral synthesis code. The code assumes local thermodynamic equilibrium, LTE (see Chap. 2.3.2). This assumption breaks down in the ultraviolet, formed in the upper photosphere and lower chromosphere, due to the increasingly collisionless condition. As a result, the output from the code is too weak below approximately 300 nm. Prior to the work of this thesis, this was accounted for by rescaling the 115 to 270 nm segment of reconstructed solar irradiance to the measurements from UARS/SUSIM⁵ (Krivova et al. 2006). We introduced an updated correction, described in Chap. 5.4.3.

SSI is reconstructed by assigning to each image pixel on the solar disc the appropriate surface component intensity spectrum, and summing the result over the entire solar disc. The wavelength range of the reconstructed solar spectra is 115 to 160000 nm, basically given by the ATLAS9 spectral synthesis code and the wavelength range of the spectroscopic data used to correct the ultraviolet segment. TSI is derived taking the integral under the reconstructed solar spectra.

1.4 Thesis outline

The main body of this thesis comprises of four publications, presented as individual chapters in chronological order (Chaps. 3 to 6). Before that, we will first discuss background knowledge relevant to the investigations detailed in these publications in Chap. 2.

In Chap. 3, we examined the intensity contrast of quiet Sun network and active region faculae in HMI data. The aim was to gain insights into the complex radiant behaviour of these magnetic features and their contribution to variation in solar irradiance. In Chap. 4, we derived an estimate of the point spread function, PSF of the HMI instrument. We also investigated the effect of correcting HMI observations for stray light (using this PSF), including the apparent surface coverage and magnetic field strength of network and faculae (relevant to the use of such data in semi-empirical models of solar irradiance). An overarching objective with these two studies is the derivation of information that can be used, in future efforts, to constrain three-dimensional model atmospheres, key to improving the

⁴The longitudinal magnetogram signal, $\langle B_l \rangle$, represents the pixel-averaged line-of-sight magnetic flux density. Small-scale magnetic concentrations are largely orientated normal to the solar surface due to magnetic buoyancy. The ratio with μ , $\langle B_l \rangle / \mu$ is therefore an approximation of the pixel-averaged magnetic flux density.

⁵The Solar Ultraviolet Spectral Irradiance Monitor onboard the Upper Atmosphere Research Satellite (Brueckner et al. 1993, Floyd et al. 2003).

reliability of semi-empirical models of solar irradiance. Specifically, the relationship between intensity contrast, and disc position and magnetic field strength in HMI data from the first study, and the PSF of the instrument from the second will allow a precise quantitative comparison of the intensity contrast in HMI observations with that in artificial solar images synthesized from three-dimensional model atmospheres (based on magnetohydrodynamics or MHD simulations, see Chap. 2.3.4).

In Chap. 5, we present a daily reconstruction of TSI and SSI, with the SATIRE-S model, based on full-disc observations from the KPVT, MDI and HMI. The reconstruction spans 1974 to 2013. On top of extending earlier efforts with the model based on KPVT and MDI data to the present time with HMI observations, we made various refinements to the reconstruction method. The most important improvement being how the model output based on observations from the various instruments are combined into a single, consistent time series. The aim was to provide a reliable, extended daily reconstruction of TSI/SSI for solar irradiance and climate studies (climate models require solar irradiance input). Then, in Chap. 6, we have a review of the current state of solar irradiance measurements and models, including a discussion of the key challenges in reconciling the outstanding discrepancies between the two. This review also sets the results presented in Chaps. 3 and 5 in the wider context of the field of study.

Finally, a summary of Chaps. 3 to 6, including an outlook of future work based on the results presented, is provided in Chap. 7.

2 Background

2.1 Physical origin of solar radiation

In classical theory, the Sun is treated as a radially stratified body. In this convention, it is described as a succession of spherical layers, which track the graduation in physical property. Going out from the centre, we have the core, radiative zone, convective zone, photosphere, chromosphere, transition region and corona, the general properties of which are summarized in Figs. 2.1 and 2.2.

2.1.1 Energy transport in the solar interior

The energy flux radiated by the Sun, comprising of both corpuscular and electromagnetic radiation (the focus of this thesis), originates in the thermonuclear core. Nuclear fusion in the core is dominated by the proton-proton chain reaction, which releases neutrinos and gamma photons. Neutrinos, being weakly interacting, pass out of the Sun largely unhindered. Photons, on the other hand, are repeatedly scattered in the dense plasma medium. Estimates vary, but according to Mitalas and Sills (1992), the overall mean free path in the core and radiative zone is 9×10^{-4} m and the diffusion timescale, the time it takes for a photon to reach the top of the radiative zone, is 1.7×10^5 years.

From the top of the convective zone to the bottom, hydrogen is increasingly ionized, with the effect of enhancing the opacity (and therefore the extent to which the plasma medium is absorbing radiation and heating up) with depth. This enhanced opacity gradient pushes the temperature gradient above what is termed the adiabatic temperature gradient (c.f., Schwarzschild's criterion for convective stability). Under such conditions, a vertically displaced parcel of fluid will keep ascending/descending until it reaches the top/bottom of the convective zone (or is dissipated by diffusive processes). In the convective zone, energy is no longer transported by radiation but by convection¹. This is a far more efficient process; again estimates vary but the time it takes for a parcel of fluid to travel from the bottom of the convective zone to the top is in the order of about a month (Eggleton 2011). The upwelling of heated plasma from deeper layers and the cool down-flow produces the convection cell pattern visible on the solar surface (defined below).

¹Hydrogen opacity is the dominant but not sole effect driving the convection. The partial ionization also introduces latent heat. Let us assume that rising plasma behaves adiabatically (i.e., no heat exchange with its environment). To remain in pressure balance with its increasingly less dense and cooler surroundings, it must expand and cool. Since the latent heat makes it harder for the plasma to cool, it must instead expand more, enhancing the buoyancy. The partial ionization of helium in the convective zone also plays a similar albeit smaller role (being far less abundant).

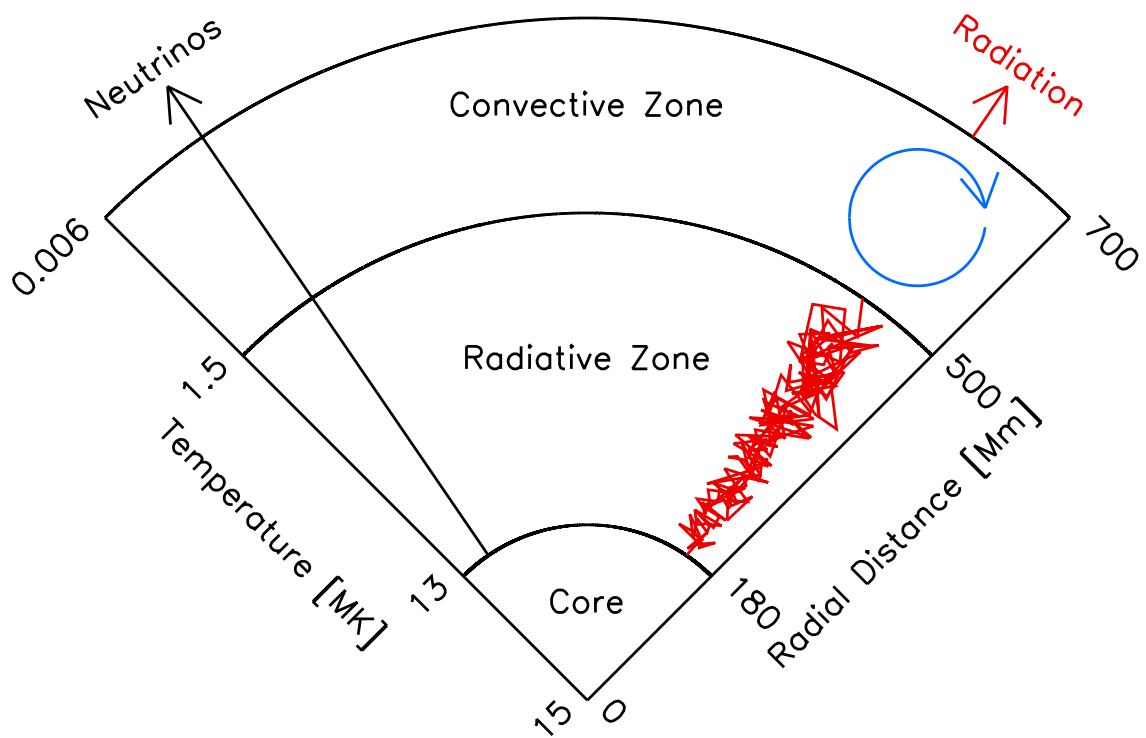


Figure 2.1: Schematic of the solar interior. Neutrinos produced in the core pass largely unhindered out of the Sun. The bulk of the energy generated is transported by radiation (red) and then by convection (blue) to the solar surface.

They show up at two distinct spatial scales, what is termed granulation (around 1 Mm in diameter) and supergranulation (10 to 30 Mm, Hirzberger et al. 2008).

2.1.2 Formation of the solar spectrum

Above the convective zone, the density is low enough that photons can escape unhindered. The opacity of the plasma medium and therefore the height where this occurs varies with wavelength. The bulk of solar radiative flux is released in the photosphere, where the continuum is formed. The position of optical depth unity (in other words, where the plasma goes from being opaque to transparent) is deepest in the visible and near-infrared, at the lower photosphere. As this is the deepest into the Sun one can observe directly, the lower photosphere is a natural candidate for the solar surface (being a plasma body, the Sun has no ‘bona fide’ surface in the conventional sense), marking the boundary between the solar interior and atmosphere.

The solar atmosphere is by no means spherically symmetrical. The symmetry is broken by the combined influence of the Sun’s rotation and magnetism (see Sect. 2.2). A plane-parallel description of the solar atmosphere, while not strictly correct, is nonetheless convenient and still informative. The temperature and density stratification of the solar atmosphere, from such a consideration (Reeves et al. 1977, Vernazza et al. 1981, Avrett and Loeser 1992), is depicted in Fig. 2.2. While density decreases monotonically with height, temperature declines from around 6000 to 4000 K across the photosphere,

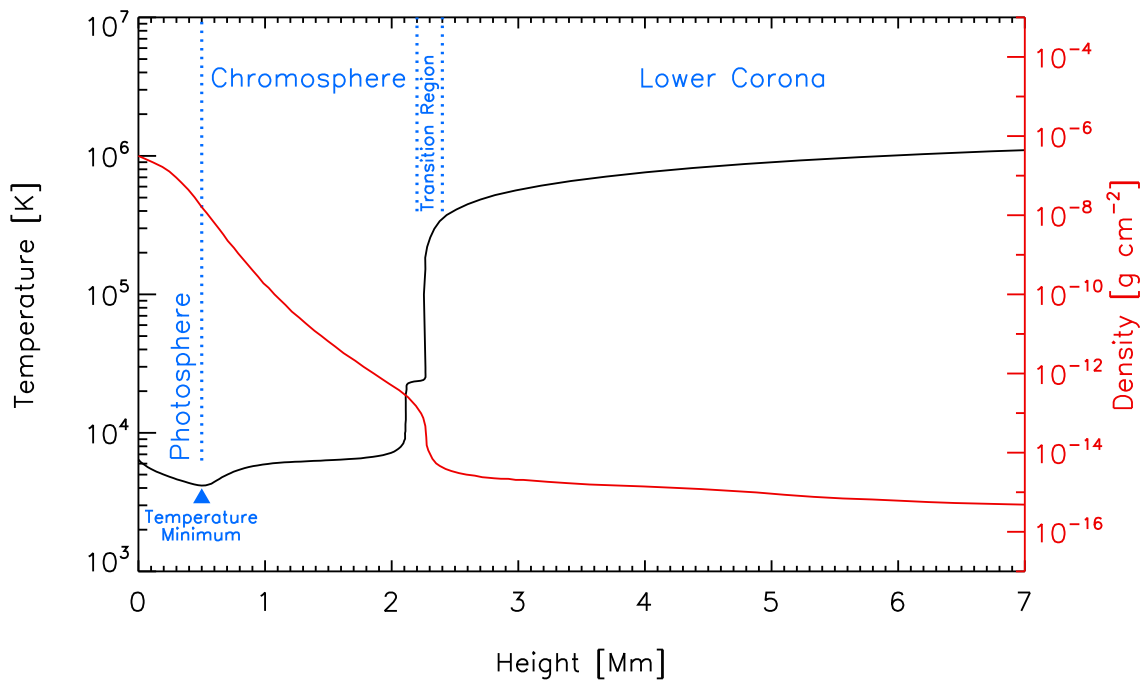


Figure 2.2: Temperature (black, left axis) and density (red, right axis) profile of the solar atmosphere (based on Reeves et al. 1977, Vernazza et al. 1981, Avrett and Loeser 1992). Here, as typically done, geometric height of zero is defined as at where the optical depth at 5000 \AA is unity. Adapted from Jafarzadeh (2013).

before increasing again, eventually to several 10^6 K in the corona, most of the gain coming in the transition region. Due to efficient thermal conductivity, the decline in coronal temperature with radial distance is slow enough that the plasma eventually overcomes gravity and escape as solar wind (largely electrons and photons).

Up to the photosphere, the plasma is collision-dominated, such that it behaves approximately like a blackbody emitter. For this reason, the solar spectrum broadly resembles that of a blackbody at its effective temperature, which is about 5800 K (Fig. 2.3). The departures from the blackbody spectrum arises mainly from the combined action of the wavelength dependence of the opacity and the vertical temperature gradient (Fig. 2.2); the radiation at different wavelengths is formed at varying heights and therefore temperatures.

Continuum radiation is formed by free-free and bound-free interactions, and spectral lines by bound-bound interactions². At a given wavelength, the solar atmosphere is, above the continuum formation height, too sparse for free-free and bound-free interactions to take hold but bound-bound interactions (if there are present at that wavelength) are still relevant. At the wavelengths corresponding to bound-bound interactions in the solar atmosphere, the plasma medium remains optically thick up to where photons no

²Free-free and bound-free interactions refer to the absorption and emission processes that move an electron between two free states, and between a bound and a free state (i.e., ionization and recombination). Since the energy of a free electron is not discrete but continuous, interactions involving free states produce the smoothly varying (with wavelength) radiation we identify as continuum. Electron transitions between the discrete energy levels in an atom/molecule (bound-bound) give rise to spectral lines.

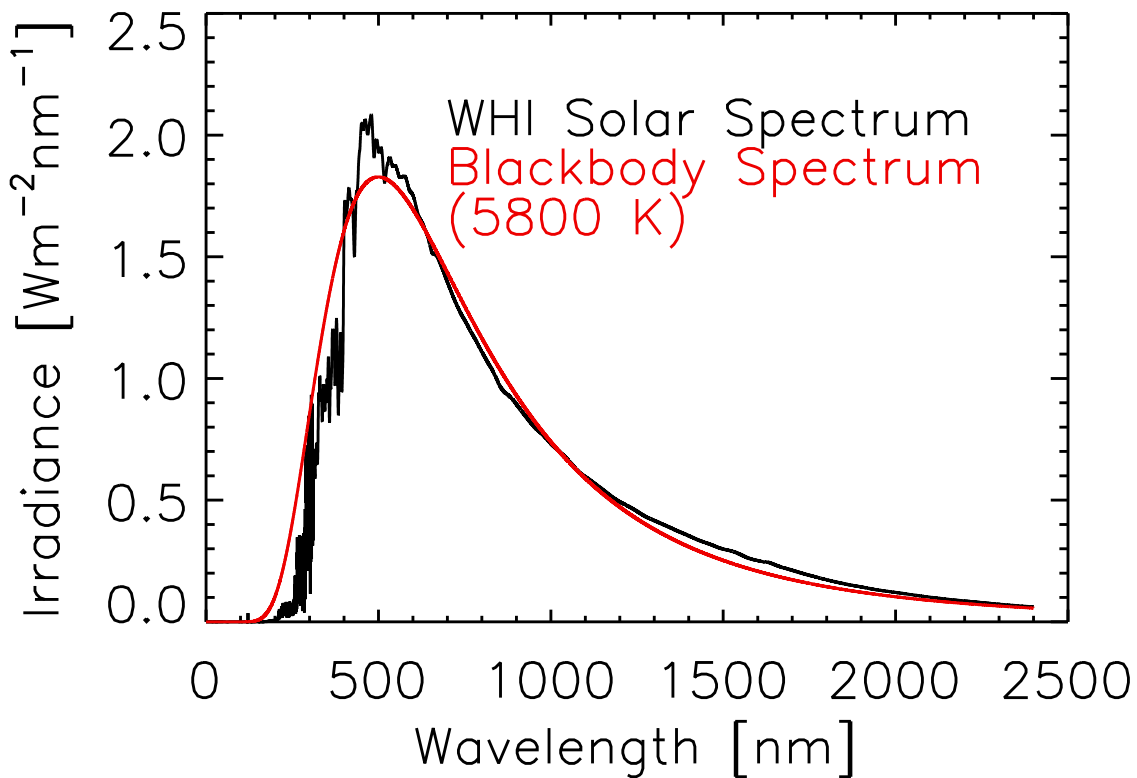


Figure 2.3: The Whole Heliospheric Interval (WHI) reference solar spectrum (for low activity conditions) by Woods et al. (2009) and the solar spectrum if the Sun were a blackbody with a temperature of 5800 K.

longer interact with the responsible species and escape. Spectral lines are formed above the continuum radiation at similar wavelengths, and at different heights, depending on the abundance and location of the respective species. Whether a particular spectral line appears as an absorption or emission feature then depends on the property of the solar atmosphere at the formation height, explained in Sect. 2.3.1. An echelle spectrum representation of the visible solar spectrum is depicted in Fig. 2.4, and a plot of the vacuum ultraviolet (<200 nm) spectrum in Fig. 2.5.

2.2 The 11-year activity cycle of the Sun and solar magnetism

As pointed out in Chap. 1.3, acoustic oscillations and convective motions on the solar surface are short-lived phenomena (lifetimes of minutes to around a day), whereas the thermal and nuclear timescale of the Sun exceeds 10^5 years. Except at these very short and very long timescales, the dynamics of the Sun is dominated by solar magnetism, the most pronounced variability of which is the 11-year cycle. As a consequence, signatures of the 11-year magnetic cycle show up in just about every measurable indication of solar activity, including solar irradiance.

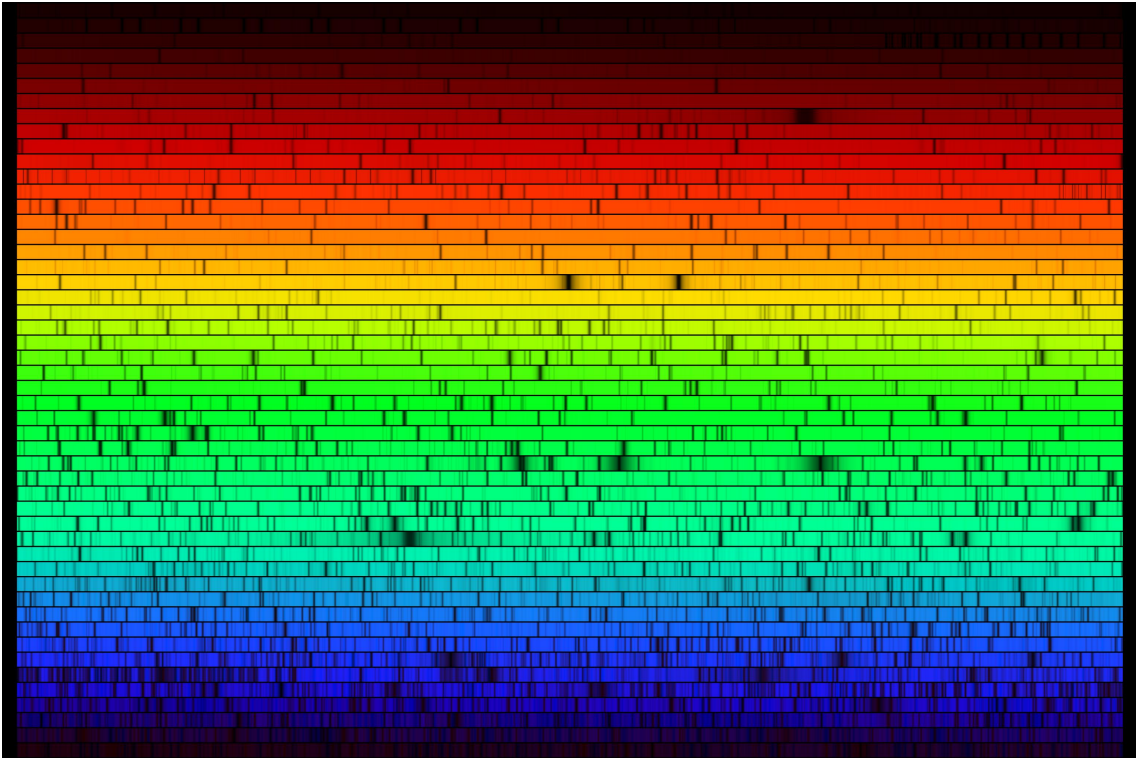


Figure 2.4: Echelle spectrum constructed from the digital atlas of the solar spectrum by the National Optical Astronomy Observatory. From bottom to top, each row corresponds to 6 nm, covering 400 to 700 nm (i.e., the visible spectral range). The dark features correspond to absorption lines, formed dominantly in the photosphere. Courtesy of N. A. Sharp, NOAO/NSO/Kitt Peak FTS/AURA/NSF.

2.2.1 Solar cycle variation in solar magnetism

The most prominent configuration of emergent magnetic flux on the solar surface is the formation of bipolar active regions. A bipolar active region is a region of intense magnetic activity with two distinct zones of opposite magnetic polarity. There are active regions with more complex morphologies, the result of bipolar active regions forming near or within an existing active region (Bumba and Howard 1965). At full development, the larger active regions feature sunspots, pores and faculae.

The 11-year activity cycle of the Sun was first discovered by Heinrich Schwabe in 1843, in the daily number of sunspot groups, and in the number of spotless days over an 18-year period. A few years after, Rudolf Wolf devised what is now termed the international sunspot number, R , given by

$$R = k(10g + n), \quad (2.1)$$

where g and n denotes the number of sunspot groups and individual sunspots visible on the solar disc, respectively. Systematic differences between the measurements made by different observers are accounted for by the correction factor, k . He also incorporated earlier observations, extending the record back in time to 1749. Still tabulated today, the

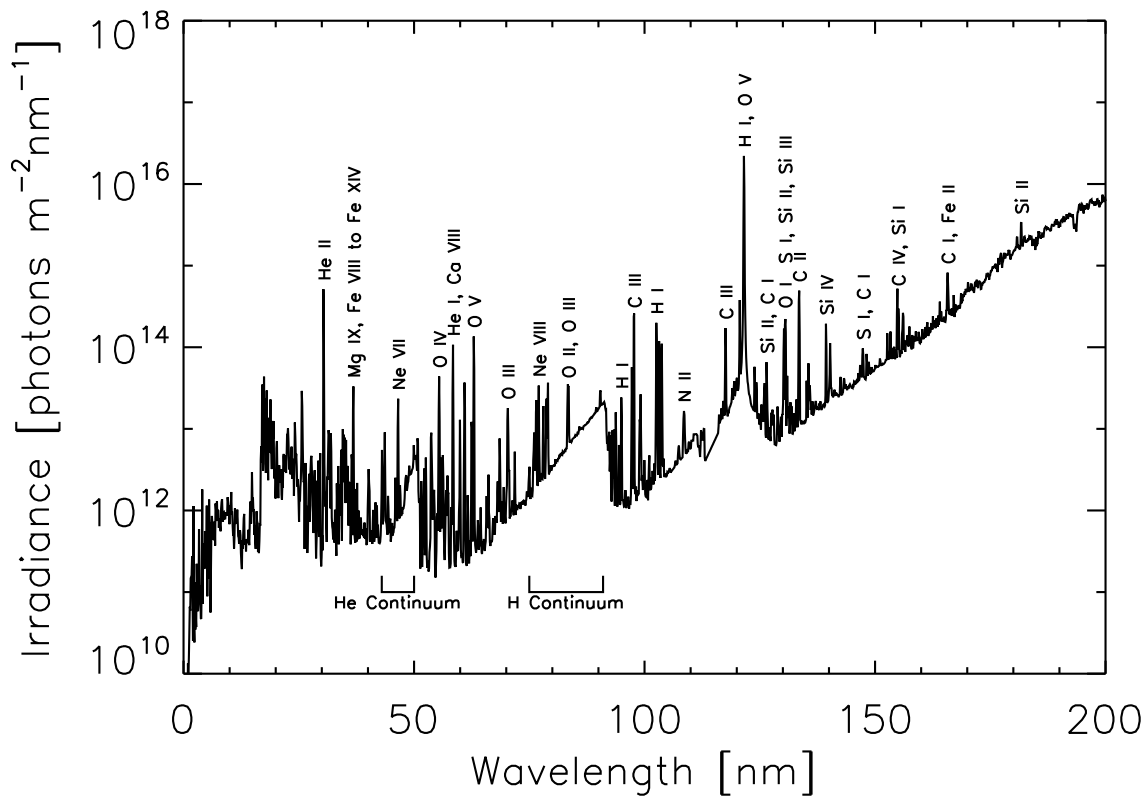


Figure 2.5: Solar vacuum ultraviolet spectrum (from the WHI reference spectrum for low activity conditions, Fig. 2.3). The emission lines are formed in the chromosphere, transition region and corona. The wedge shaped continua correspond to emission from hydrogen and helium bound-free recombination. The vertical edge correspond to the minimum energy from such an interaction, the ionization potential.

international sunspot number is one of the longest daily record of solar activity available³. While the definition of the international sunspot number is somewhat arbitrary, it turns out to be highly correlated and so a good proxy of sunspot area, which has a more readily appreciable physical meaning (see Figs. 6 and 7 in Hathaway 2010). The minimum in 1755 (Fig. 2.6) is designated as the start of solar cycle 1, and each successive minimum marks the start of the following cycle. Also apparent in the figure, solar cycle amplitude and length (10.9 ± 1.2 years, Hathaway et al. 2002) fluctuates considerably.

Apart from the 11-year periodicity in overall emergence apparent in the sunspot number (and similar measures), solar magnetism also exhibits the following large-scale behaviour.

- Spörer's law of zones: Near the onset of each solar cycle, active regions emerge between around 15° and 30° latitude, in both the northern and southern hemispheres. Over the course of the cycle, they appear at lower and lower latitudes, eventually close to the equator. This migration produces the 'butterfly wings' pattern in time

³Only the sunspot group number record compiled by Hoyt and Schatten (1997), which extends from 1610 to 1995, is longer.

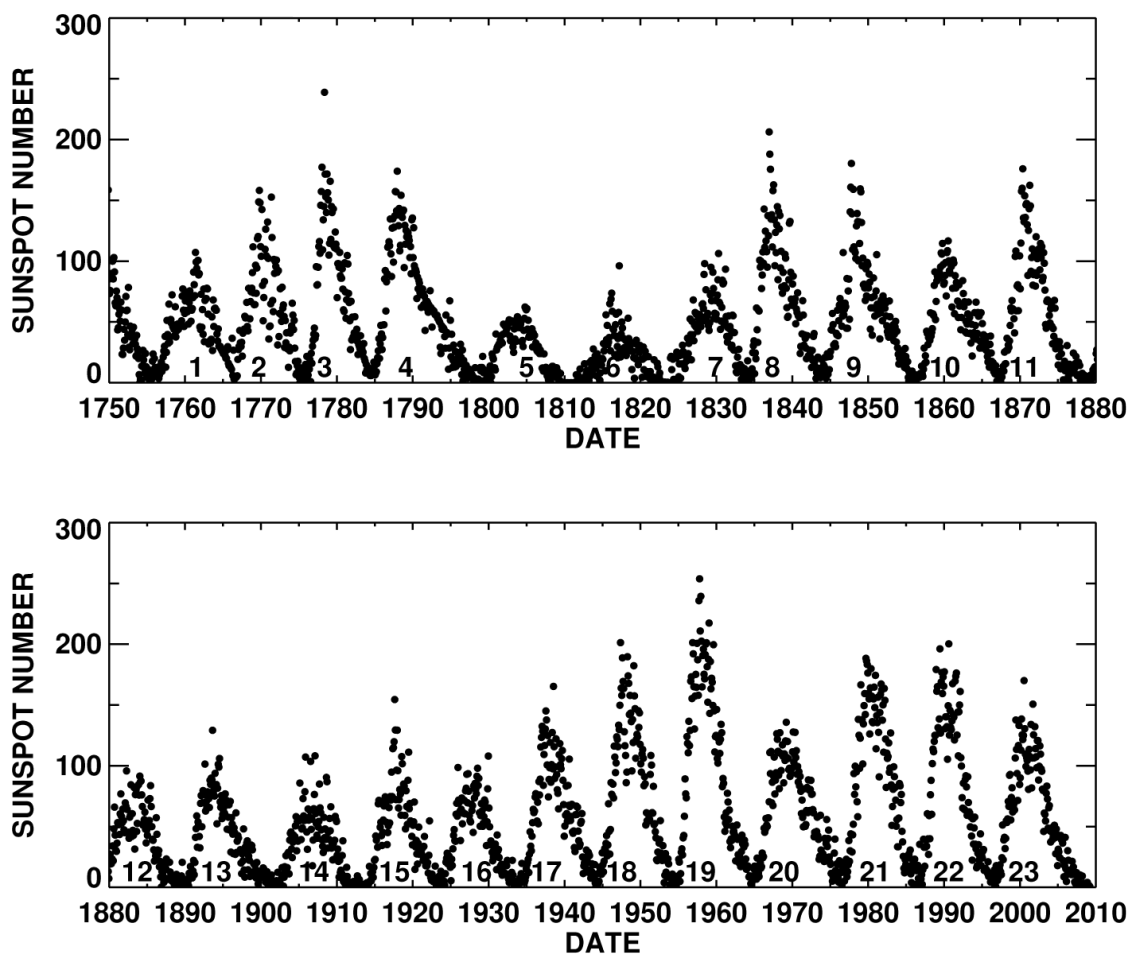


Figure 2.6: Monthly mean of the international sunspot number. Solar cycle number is indicated. Taken from Hathaway (2010).

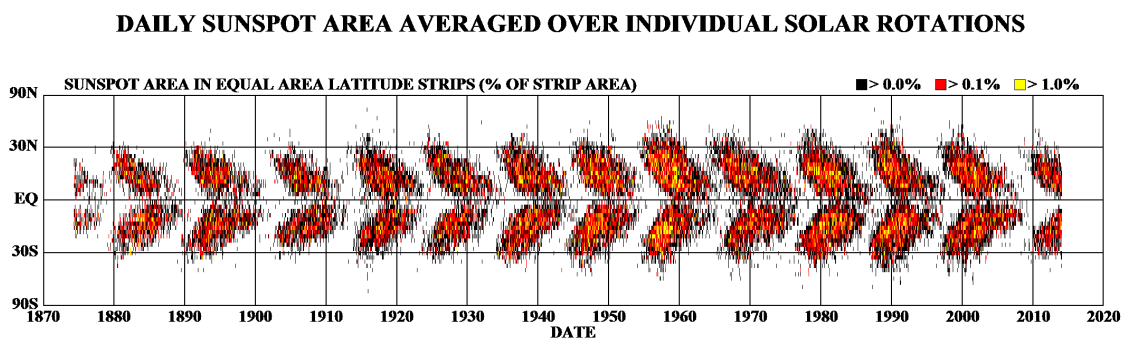


Figure 2.7: The variation in sunspot area with time and latitude. Courtesy of D. H. Hathaway, NASA/MSFC.

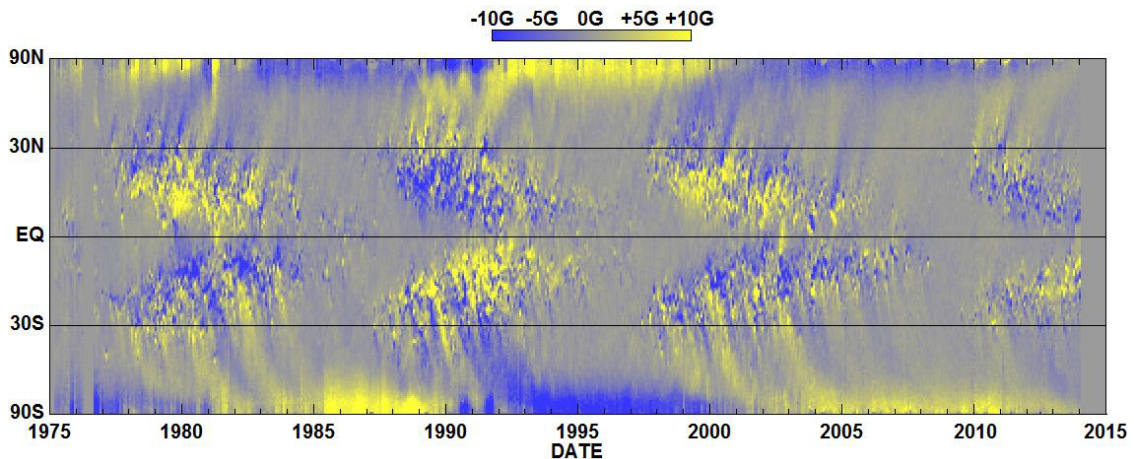


Figure 2.8: Longitudinally-averaged signed magnetic flux density as a function of time and latitude. Courtesy of D. H. Hathaway, NASA/MSFC.

series representations of the latitudinal distribution of magnetic activity on the solar disc (not surprisingly, these are termed butterfly diagrams, two examples of which are given in Figs. 2.7 and 2.8).

- Joy’s law (Hale et al. 1919): Bipolar active regions are orientated such that the leading (in the direction of the Sun’s rotation) polarity is closer to the equator. Overall, the higher the latitude, the more pronounced this tilt between the lagging and leading polarity. Taken together with Spörer’s law, it indicates that tilt angles decline over the solar cycle.
- Hale’s polarity law (Hale and Nicholson 1925): The broad orientation of bipolar active regions (which polarity is leading/lagging) within either the northern or southern hemisphere over a given cycle is constant but opposite between the two hemispheres and alternates from cycle-to-cycle. So, while there is an 11-year modulation in the emergence of solar magnetism, the magnetic cycle is really 22-years.
- Polar flux: The cyclic variation in active region activity at low and mid-latitudes is accompanied by an apparent anti-phase fluctuation (i.e., strongest/weakest around cycle minima/maxima) in the amount of magnetic flux near the poles. Polar flux in the northern and southern hemispheres have opposite dominant polarities which reverses mid-cycle.

Most of these large-scale features of solar magnetism are visible in the butterfly diagram of the longitudinally-averaged signed magnetic flux density (Fig. 2.8). The magnetic polarity of the inner and outer edge of each ‘butterfly wing’ arises from the combination of Joy’s law and Hale’s polarity law. As suggested by the ‘streams’ leading from the wings towards higher latitudes, polar flux correspond to magnetic flux from since decayed active regions transported polewards by meridional flows⁴. Therefore, the mid-cycle reversal in the polarity of polar flux is ultimately related to the cycle-to-cycle alternation in the

⁴This is the more commonly accepted, but not only, interpretation of the apparent poleward drift. It has

magnetic orientation of bipolar active regions (see next section). Meridional flows are slow (few 10 ms^{-1}), giving the half-cycle lag or apparent anti-phase relation between the solar cycle and the variation in the amount of polar flux.

2.2.2 The solar dynamo

The 11-year/22-year magnetic cycle, discussed above, is believed to be driven by dynamo processes⁵ in the convective zone and photosphere. Under the assumption that the plasma here is highly-conducting and flows are non-relativistic, Maxwell's equations can be combined into a single equation, which is termed the induction equation,

$$\frac{\partial \vec{B}}{\partial t} = \nabla \times (\vec{v} \times \vec{B}) + \eta \Delta \vec{B}, \quad (2.2)$$

which describes the time evolution of the magnetic field, \vec{B} . The first term on the right hand side gives the change from advection or bulk motion (\vec{v} represents velocity), and the second term the change from diffusion (η is the magnetic diffusivity, given by $\eta = 1/\mu_0\sigma$, where μ_0 and σ denote the magnetic constant and electrical conductivity). Due to the high electrical conductivity, except at extremely small spatial scales ($< 1 \text{ km}$, well below the present limits of observation), the advection term is dominant in the convective zone and photosphere (c.f., magnetic Reynolds number). In other words, diffusion is inefficient here. (For example, it will take sunspots on the order of a few thousand years to dissipate by diffusion alone, far greater than the observed lifetime of days to weeks.) This also means that magnetic flux is effectively frozen into the plasma, such that advecting plasma will carry the enclosed magnetic field along with it. The apparent variation in solar magnetism must, as stated earlier, involve the induction effect of bulk motion in the convective zone and photosphere (i.e., a dynamo).

The high electrical conductivity of the plasma medium is also the reason why the magnetic concentrations that make up network and faculae are mostly nested inside intergranular lanes, the cool dark downflows on the boundary of convection cells. Emergent magnetic field, frozen into the plasma, is expelled by convection flows towards the intergranular lanes (Parker 1963, Weiss 1966, Tao et al. 1998).

While the exact workings of the solar dynamo is still debated (see the review by Charbonneau 2010), there is some degree of consensus over certain key features, illustrated in Fig. 2.9.

- Omega-effect (Figs. 2.9a and 2.9b): In the radiative zone, the Sun is largely a rigid rotator. In the convective zone however, the rotational frequency varies significantly with latitude and radial distance (differential rotation). As a result, poloidal magnetic field in the convective zone is stretched and wound as the plasma it encloses rotates around the Sun at different speeds, producing toroidal magnetic field of opposite magnetic orientation in the northern and southern hemispheres (c.f., Hale's polarity law).

been suggested that this could indicate the presence of high latitude dynamo processes that somehow do not result in the formation of active regions (Gilman et al. 1989, Petrovay and Szakály 1999).

⁵The processes by which the magnetic field of an astrophysical object is sustained by the inductive action of the motion of electrically conducting fluids.

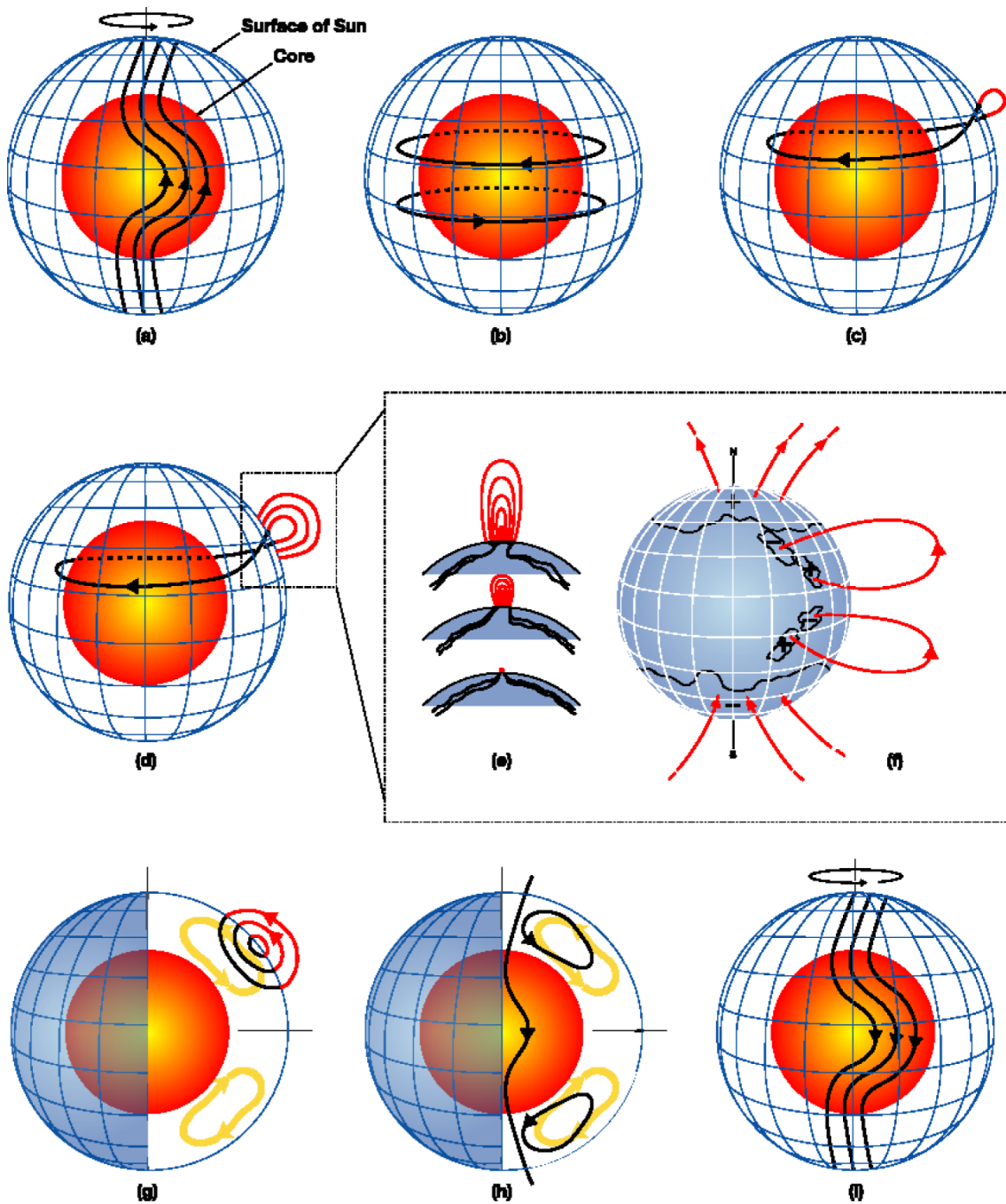


Figure 2.9: Schematic of a ‘typical’ surface flux transport model (see text for explanation). Taken from Dikpati and Gilman (2009).

- Alpha-effect (Figs. 2.9c to 2.9f): For the magnetic ($B^2/2\mu_0$) and gas pressure within magnetic flux tubes to balance external gas pressure, the enclosed plasma must have a lower density. Magnetic flux tubes are therefore buoyant. Due to the action of the Coriolis force, magnetic loops (from the toroidal magnetic field) twist as they emerge, producing the tilt between the leading and lagging polarity of the resulting active regions (c.f., Joy’s law).

- Meridional flow (Figs. 2.9g to 2.9i): As noted earlier in this section, this brings the decay products of active regions polewards, eventually reversing the polarity around mid-cycle. (Since the leading polarities from the two hemispheres have a greater tendency to meet and annihilate due to the equator-ward tilt, polar flux is dominated by the lagging polarity.) The return flow brings polar flux down into the convective zone, forming poloidal magnetic field with an opposite magnetic orientation to that at the beginning of the sequence (Fig. 2.9a).
- The solar dynamo is believed to be situated near the bottom of the convective zone. Due to the convective instability, the convective zone cannot store magnetic fields long enough for the omega-effect to take hold or sustain 11-year cycles. The radiative zone, lacking differential rotation, cannot support the omega-effect. Also, magnetic flux tubes here will not be able to rise to the surface for the same reasons that convection cannot take place (lack of a strong temperature gradient). It is proposed that magnetic flux is transported and confined to the layers just below the convective zone by convective downflows (Brandenburg et al. 1996, Tobias et al. 1998, Dorch and Nordlund 2001). Here, in the interface between the radiative and convective zones, rotational shear is still present, permitting the omega-effect, and toroidal magnetic fields can, when sufficiently amplified, still rise up the convective zone.

These features are incorporated into the class of dynamo models termed surface flux transport models, which have found reasonable success reproducing the main features of the magnetic cycle summarized earlier in Sect. 2.2 (Dikpati and Gilman 2009).

The presence of magnetic concentrations on the solar surface has a profound effect on the temperature structure and consequently the radiant properties of the solar atmosphere, reviewed in Chap. 6.3.1. This is believed to be the main driver of variations in solar irradiance, supported by the success of models of solar irradiance based on this mechanism (Domingo et al. 2009). Other mechanisms have been proposed to explain the observed solar cycle modulation in solar irradiance. For instance, slow decaying global oscillations driven by the Coriolis force (Wolff and Hickey 1987), thermal shadowing related to the toroidal magnetic field (Kuhn et al. 1988) and magnetic modulation of convective flow patterns (Cossette et al. 2013). However, as stated in Chap. 1.1, direct evidence is still wanting.

2.3 Solar model atmospheres and intensity spectra

As we will review in Chap. 6, semi-empirical models of solar irradiance are the most sophisticated available. The robust reconstruction of solar irradiance through such models relies on two things. One, an accurate estimation of the prevailing solar magnetism at the sampled points in time. Two, realistic intensity spectra of the solar surface components. The latter is provided by numerical models aimed at returning the stratification of the solar atmosphere (what is usually termed ‘model atmospheres’) and the emergent intensity spectrum through the solution to the radiative transfer equation, RTE (introduced next). The ATLAS9 code by Kurucz (1993) is one such model. As noted in Chap. 1.3, in SATIRE-S, the sunspot and quiet Sun model atmospheres are based on ATLAS9 model

atmospheres, and the intensity spectra of solar surface components are generated from the respective model atmospheres using the ATLAS9 code.

2.3.1 The radiative transfer equation

The specific intensity, $I_\nu(\vec{r}, \vec{n}, t)$ at frequency ν , position \vec{r} , in direction \vec{n} at time t is defined the energy transported as radiation dE_ν , per unit frequency, solid angle $d\omega$ and time passing through a unit area normal to \vec{n} . The energy passing through an area dA is given by

$$dE_\nu = I_\nu(\vec{r}, \vec{n}, t) d\nu d\omega dt \mu dA, \quad (2.3)$$

where μ is the cosine of the angle between the normal to dA and \vec{n} . A useful property of the specific intensity is that, in the absence of sources (emission) and sinks (absorption), it is invariant along a pencil of light. This allows us to describe the change in specific intensity in a pencil of light from emission and absorption by

$$\mu dI_\nu(s) = j_\nu(s) ds - \alpha_\nu(s) I_\nu(s) ds, \quad (2.4)$$

where s denotes path length, $j_\nu(s)$ the emission coefficient and $\alpha_\nu(s)$ the absorption coefficient. The quantity $1/\alpha_\nu(s)$ is also the local photon mean free path. A more natural way to describe distance than is by the optical distance, τ_ν where $d\tau_\nu = \alpha_\nu(s) ds$. This allows us to rewrite equation 2.4 as

$$\mu \frac{dI_\nu}{d\tau_\nu} = S_\nu - I_\nu, \quad (2.5)$$

what is termed the radiative transfer equation (RTE), where S_ν is the source function, given by

$$S_\nu = \frac{j_\nu}{\alpha_\nu}. \quad (2.6)$$

The source function characterizes the combined action of emission and absorption on the radiation field. Whether a given spectral line manifests as an absorption or emission feature depends on the source function at that wavelength. As noted in Sect. 2.1.2, spectral lines are formed above the continuum at similar wavelengths. If the source function is weaker at the line formation height than at where the continuum at adjacent wavelengths is formed (i.e., absorption is dominant), the intensity here is weaker than in the nearby continuum, producing what we see as an absorption feature in the spectrum. Conversely, if the source function is stronger at the line formation height, an emission feature is formed.

It can be shown that, under conditions of local thermodynamic equilibrium, LTE (explained in Sect. 2.3.2) and in the absence of scattering, the source function at a given height is given by Planck's function at the local temperature. The LTE assumption is largely valid in the photosphere. As the temperature in the photosphere declines with height up to the temperature minimum (Fig. 2.2), so does the source function, explaining why photospheric lines are, with few exceptions, absorption lines (Fig. 2.4).

Apart from the frequency/wavelength dependence, the emission and absorption coefficients, and therefore the optical distance and source function, depend on temperature, pressure, atomic/molecular abundances and the corresponding occupation numbers⁶. The

⁶For a given species, the distribution between the various bound and ionized states.

goal then is to solve the RTE for the emergent intensity from a solar atmosphere, retrieving along the way the temperature and pressure stratification of said atmosphere. The problem is intractable without any simplifications. Classical radiative transfer models such as ATLAS9 are set up with the following assumptions.

- Plane-parallel atmosphere: The thickness of the solar atmosphere is small enough compared to the radius of the Sun that we can treat it as a series of homogenous plane-parallel layers, reducing the problem down to one dimension. The limitations of this assumption are discussed in Chap. 7. In this geometry, μ is equivalent to the cosine of the heliocentric angle.
- Semi-infinite atmosphere: The solar atmosphere is sufficiently thick that the optical distance (zero at the observer's end, increasing with depth into the atmosphere) can be taken to extend to infinity.
- Radiative equilibrium: All energy transport is by radiation. This is valid since hydrogen ionization (and therefore convection) in the Sun occurs below the solar surface (Sect. 2.1.1). It can be shown that under this condition, total flux is constant with depth.
- Local thermodynamic equilibrium: The infinitesimal slab of material at any given depth (i.e., between τ_ν and $\tau_\nu + d\tau_\nu$), is taken to be in a state of thermodynamic equilibrium, therefore behaving like a blackbody at the local temperature. This allows one to calculate the occupation numbers from temperature and electron density (see next section).
- Steady state: The solar atmosphere does not vary with time. This requires that the occupation numbers are constant, a condition that is satisfied by the LTE assumption.
- Hydrostatic equilibrium: There are no velocity fields. The pressure stratification is given by the balance between gas pressure and gravity.

From an initial guess of the temperature stratification, the pressure and electron density profile can be calculated, and from that the optical distance and the source function. This is iterated, adjusting the temperature stratification until the solution to the RTE satisfies the radiative equilibrium condition (i.e., total flux is invariant with depth).

2.3.2 Local thermodynamic equilibrium

Occupation numbers are governed by radiative and collisional bound-bound and bound-free processes. In this context, by the term 'radiative' we refer to transitions that are spontaneous or triggered by radiation, and by 'collisional' transitions effected by collisions. Local thermodynamic equilibrium refers to the condition where the plasma is collision-dominated enough for the radiation field to relax to the blackbody radiation at the local temperature. The specific intensity of a blackbody at temperature T , $B_\nu(T)$, given by Planck's law, is

$$B_\nu(T) = \frac{2h\nu^2}{c^2} \frac{1}{\exp\left(\frac{h\nu}{k_B T}\right) - 1}, \quad (2.7)$$

where h is Planck's constant, c the speed of light and k_B Boltzmann's constant. Let n represent number density and E the energy at a given level, the distribution of atoms with electrons in either of two bound states (denoted i and j) follow Boltzmann's distribution,

$$\frac{n_i}{n_j} = \frac{g_i}{g_j} \exp\left(-\frac{E_i - E_j}{k_B T}\right), \quad (2.8)$$

where $g = 2J + 1$, a statistical weight to account for degenerate sub-levels (J is the angular momentum quantum number). The analogue for atoms in either of two ionized state is given by the Saha equation,

$$\frac{n_i}{n_j} = \frac{2}{n_e} \left(\frac{2\pi m_e k_B T}{h^2}\right)^{\frac{3}{2}} \frac{g_i}{g_j} \exp\left(-\frac{E_i - E_j}{k_B T}\right), \quad (2.9)$$

where n_e is the electron density and m_e the electron mass. Notice, from equations 2.8 and 2.9, that the occupation numbers are functions of temperature and electron density alone.

As stated in the last section, the assumption of steady state requires that the occupation numbers must be constant. The mathematical expression of the requirement that the rate of population change from all relevant radiative and collisional processes sum to zero is what is termed the equations of statistical equilibrium. In the case collisional processes are not sufficiently dominant that we can assume LTE, occupation numbers must instead come from the solution to the equations of statistical equilibrium. This is difficult, as the rate of radiative processes is, by definition, influenced by the prevailing radiation field. Assuming LTE allows us to express occupation numbers as a function of temperature and electron density alone, which reduces the problem down to that of optimizing the temperature stratification to satisfy radiative equilibrium. If LTE cannot be assumed, one would have to solve the equations of statistical equilibrium for all depths and the RTE simultaneously in a self-consistent manner, a far more tedious problem. (Particularly as this would require complete knowledge of the rates of all relevant radiative and collisional processes.)

In the solar atmosphere, the plasma medium is increasingly sparse and therefore collisionless with height. LTE, while a convenient simplification, is not entirely realistic. The disparity between intensity spectra from ATLAS9 and measured solar spectra arising from the assumption of LTE is discussed in Chap. 5.4.3.

2.3.3 Line blanketing and opacity

The solar spectrum, especially in the visible and ultraviolet, is dense with spectral lines (Figs. 2.4 and 2.5). Formed above the continuum at similar wavelengths (Sect. 2.1.2), spectral lines block radiation from below, which in turn warms up the deeper layers, causing it to radiate at higher temperatures ('backwarming'). Consequently, the emergent intensity, not just at the spectral lines but also at continuum wavelengths, is spectrally redistributed. The formation of spectral lines in the higher layers of the solar atmosphere, by facilitating radiation, also causes it cool, an effect referred to as surface cooling. This, together with backwarming, enhances the vertical temperature gradient. These effects of spectral lines on stellar atmospheres and the emergent intensity spectra are collectively termed line blanketing. The inclusion of line blanketing is crucial to recovering accurate

solutions of the solar atmosphere and intensity spectra. Ideally, this would be achieved by performing the computation described in Sect. 2.3.1 at every frequency with a spectral line. However, the spectral lines in the solar spectrum number in the millions, making this computationally unfeasible.

Spectral lines are represented in the RTE by their contribution to the absorption coefficient. The challenge is to include the opacity⁷ of the immense number of spectral lines present as completely as possible while solving the RTE at a manageable number of frequencies. There are various ways around this problem, each with its advantages and disadvantages.

- **Mean opacities:** The idea here is to assume that the atmosphere is what is termed ‘grey’, that is to say, the opacity does not vary with frequency. The problem is then reduced to calculating a suitably weighted mean opacity. One key advantage is that the RTE can be solved exactly for a grey atmosphere. However, the spectral distribution in the emergent intensity spectra turns out to be far from realistic. As line opacities are averaged out, the spectra will be missing spectral lines. The continuum will be affected as well as the decline in temperature with height will also be underestimated. In recent years, this approach has been used more to provide an initial estimate of the temperature stratification than as a solution in itself. Although, due to the computational simplicity, it is sometimes employed in MHD simulations to describe the action of radiative energy transfer.
- **Opacity distribution function (ODF):** This is the approach taken by the ATLAS9 code. The frequency range is divided into intervals. Within each interval, the absorption coefficient, $\alpha_\nu(s)$ is evaluated at narrow frequency steps to capture the rapid variation with frequency from the presence of multiple spectral lines. Following that, the opacity distribution function, describing the proportion of the interval where $\alpha_\nu(s) \geq \alpha$ as a function of α , is constructed. When solving the RTE, the ODF within each interval is sampled at a few α points to estimate a representative opacity⁸. ODFs are computationally expensive to build but it is a one-off task. They allow line blanketing to be included efficiently with reasonable accuracy by greatly limiting the number of frequency points that need to be sampled. The use of ODFs however, implicitly assumes that spectral lines do not move in/out of a given interval and relative line strengths do not change with depth and temperature (Mihalas 1978).
- **Opacity sampling (OS):** The principle of opacity sampling, first proposed by Peytremann (1974), is to restrict the RTE computation to the optimal set of frequency points necessary to capture most of the underlying physics. Various sampling schemes have been reported in the literature. For example, sampling at regularly spaced intervals (Snedden et al. 1976, Jørgensen 1992), sampling randomly selected frequencies (Carbon et al. 1984) and adopting a Planck function weighted sampling point distribution (Peytremann 1974, Ekberg et al. 1986). Generally, the ef-

⁷There are varying definitions. For this discussion, by opacity we refer to the product of the absorption coefficient and the number density.

⁸As compared to sampling $\alpha_\nu(s)$ directly, very few sampling points are needed since ODFs are smooth, monotonic functions.

fect of introducing more sampling points on the output model atmosphere diminishes with the total number of sampling points, eventually making negligible different to the outcome (i.e., ‘saturation’). Taking this to imply that OS-based models approaches the ‘ideal’ model atmosphere from complete sampling asymptotically with increased sampling, the output model atmosphere at saturation is the closest to the ideal solution practically achievable. Opacity sampling is computationally more expensive than using ODFs⁹ but has the advantage that it makes no assumptions about the stability of the distribution of $\alpha_\nu(s)$ with depth and temperature.

2.3.4 Three-dimensional model atmospheres

One of the limitations of present-day semi-empirical models of solar irradiance is the use of intensity spectra generated from plane-parallel model atmospheres. They do not capture all the complexities of the radiant behaviour of small-scale magnetic concentrations (reviewed in Chap. 6.4.2). Magnetic flux tubes are not isotropic structures; the apparent intensity and its centre-to-limb variation is not just a function of the vertical stratification of the confined atmosphere but also of the viewing geometry (c.f., flux tube model, Chap. 6.3.1).

As stated in Chap. 1.4, one of the objectives of the investigations presented in Chaps. 3 and 4 is to set some of the groundwork necessary for the incorporation of intensity spectra of solar surface components from three-dimensional model atmospheres into SATIRE-S. One of our future plans (see Chap. 7) is to employ the results from these studies as observational constraints on three-dimensional model atmospheres based on MHD simulations.

Central to this aspiration are the three dimensional MHD simulations of the upper convective zone and solar atmosphere from the MURaM¹⁰ code (Vögler 2003, 2005, Vögler et al. 2005), briefly introduced here for information. The MURaM code describes the time variation of the density ρ , momentum density $\rho\vec{v}$, energy density $e = e_{\text{int}} + \rho|\vec{v}|^2/2 + |\vec{B}|^2/8\pi$ (sum of the internal, kinetic and magnetic energy) and magnetic field strength in a three-dimensional Cartesian grid. This is achieved by solving the following non-ideal MHD equations; the continuity equation (representing mass conservation),

$$\frac{\partial\rho}{\partial t} + \nabla \cdot (\rho\vec{v}) = 0, \quad (2.10)$$

the equation of motion,

$$\frac{\partial\rho\vec{v}}{\partial t} + \nabla \cdot \left[\rho\vec{v}\vec{v} + \left(p + \frac{|\vec{B}|^2}{8\pi} \right) \underline{I} - \frac{\vec{B}\vec{B}}{4\pi} \right] = \rho\vec{g} + \nabla \cdot \underline{\tau} \quad (2.11)$$

(p represents pressure, \underline{I} the 3×3 identity matrix and $\underline{\tau}$ the viscous stress tensor), the

⁹For example, the ATLAS12 code, which is identical to ATLAS9 but for adopting the OS instead of the ODF approach, requires one to two orders of magnitude more computing time (Castelli 2005).

¹⁰In full, the Max-Planck Institute for Solar System Research/University of Chicago Radiative MHD code.

energy equation,

$$\frac{\partial e}{\partial t} + \nabla \cdot \left[\vec{v} \left(e + p + \frac{|\vec{B}|^2}{8\pi} \right) - \frac{\vec{B}(\vec{u} \cdot \vec{B})}{4\pi} \right] = \frac{\nabla \cdot (\vec{B} \times \eta \nabla \times \vec{B})}{4\pi} + \nabla \cdot (\vec{u} \cdot \underline{\tau}) + \nabla \cdot (K \nabla T) + \rho(\vec{g} \cdot \vec{v}) + Q_{\text{rad}} \quad (2.12)$$

(K denotes thermal conductivity and Q_{rad} the radiative heating rate) and the induction equation (discussed in Sect. 2.2). The solar simulation is set up by the following.

- The system of MHD equations is closed by an equation of state. This equation of state, a set of grids relating temperature and pressure to density and internal energy, is constructed taking in the solution to Saha's equation (equation 2.9) for the first ionization state of the 11 most abundant elements in the solar photosphere.
- Radiative energy transport, dominant above the convective zone, is included through the radiative heating rate term (Q_{rad}) in the energy equation (equation 2.12). This is calculated from the solution to the RTE (assuming LTE). Line opacities are included in an approximate manner by rearranging the entire frequency range into four subsets, grouping frequencies with similar opacities together, which are then each represented by a bin-averaged opacity (Vögler et al. 2004). This is a very crude implementation of the ODF approach, forced by the requirement to solve the RTE in multiple directions at each gridpoint and simulation timestep.

As demonstrated by Unruh et al. (2009) and Afram et al. (2011), one can use the run of parameters along a line through a given MURaM simulation cube as a model atmosphere for generating intensity spectra with radiative transfer codes such as the ATLAS9. Afram et al. (2011) noted that the artificial solar images so generated from MURaM simulations match the observations from Hinode (Kosugi et al. 2007) well at certain wavelengths (visible continuum) but less so others (CN and G-band). This prompted our interest to derive observational constraints on MURaM simulations from HMI data. As we will explain in Chap. 7, reconciling the intensity contrast of small-scale magnetic concentrations in HMI and MURaM will also allow us to relate the intensity spectra generated from MURaM-based model atmospheres to HMI magnetogram signal directly. This will obviate the empirical faculae filling factor and magnetogram signal relationship in SATIRE-S, described in Chap. 1.3, and the free parameter it introduces to the model.

3 Intensity contrast of solar network and faculae

Yeo, K. L., Solanki, S. K., Krivova, N. A.
Astron. Astrophys., 550, A95 (2013)*

Abstract

Aims. This study aims at setting observational constraints on the continuum and line core intensity contrast of network and faculae, specifically, their relationship with magnetic field and disc position.

Methods. Full-disc magnetograms and intensity images by the Helioseismic and Magnetic Imager (HMI) on-board the Solar Dynamics Observatory (SDO) were employed. Bright magnetic features, representing network and faculae, were identified and the relationship between their intensity contrast at continuum and line core with magnetogram signal and heliocentric angle examined. Care was taken to minimize the inclusion of the magnetic canopy and straylight from sunspots and pores as network and faculae.

Results. In line with earlier studies, network features, on a per unit magnetic flux basis, appeared brighter than facular features. Intensity contrasts in the continuum and line core differ considerably, most notably, they exhibit opposite centre-to-limb variations. We found this difference in behaviour to likely be due to the different mechanisms of the formation of the two spectral components. From a simple model based on bivariate polynomial fits to the measured contrasts we confirmed spectral line changes to be a significant driver of facular contribution to variation in solar irradiance. The discrepancy between the continuum contrast reported here and in the literature was shown to arise mainly from differences in spatial resolution and treatment of magnetic signals adjacent to sunspots and pores.

Conclusions. HMI is a source of accurate contrasts and low-noise magnetograms covering the full solar disc. For irradiance studies it is important to consider not just the contribution from the continuum but also from the spectral lines. In order not to underestimate long-term variations in solar irradiance, irradiance models should take the greater contrast per unit magnetic flux associated with magnetic features with low magnetic flux into account.

*The contents of this chapter are identical to the printed version of Yeo, K. L., Solanki, S. K., Krivova, N. A., 2013, Intensity contrast of network and faculae, *Astron. Astrophys.*, 550, A95, reproduced with permission from Astronomy & Astrophysics, © ESO.

3.1 Introduction

Photospheric magnetic activity is the dominant driver of variation in solar irradiance on rotational and cyclical timescales (Domingo et al. 2009). Magnetic flux in the photosphere is partly confined to discrete concentrations of kilogauss strengths, generally described in terms of flux tubes (Stenflo 1973, Spruit and Roberts 1983). The brightness excess, or contrast relative to the Quiet Sun, of flux tubes is strongly modulated by their size and position on the solar disc (see Solanki 1993, for a review). Within these magnetic concentrations, pressure balance dictates an evacuation of the interior and consequent depression of the optical depth unity surface (Spruit 1976). The horizontal extent influences the effect of radiative heating from the surroundings through the side walls on the temperature structure and contrast (Spruit and Zwaan 1981, Grossmann-Doerth et al. 1994). The position on the solar disc changes the viewing geometry, and therefore the degree to which the hot walls are visible and the apparent contrast (Steiner 2005). Models describing the counteracting effects on solar irradiance of dark sunspots, and bright network and faculae, characterizing the latter by the magnetic filling factor (related to number density) and position have been successful in reproducing more than 90% of observed variation over multiple solar cycles (Wenzler et al. 2006, Ball et al. 2012). Other factors, such as inclination, internal dynamics, phase of evolution and surrounding convective motions affect the brightness excess of a given flux tube, but become less important when considering the overall behaviour of an ensemble as is the case with such models (Fligge et al. 2000). The same is assumed of flux tube size, which enters these models only very indirectly, though it is known to have a significant effect on contrast.

Evidently, the robust reconstruction of solar irradiance variation from models based on photospheric magnetic activity is contingent, amongst other factors, on a firm understanding of the radiant behaviour of magnetic elements, in particular the variation with size and position on the solar disc. While the radiant behaviour of sunspots is relatively well known (Chapman et al. 1994, Mathew et al. 2007) and sufficiently described by current models (Maltby et al. 1986, Collados et al. 1994, Unruh et al. 1999), the converse is true of network and faculae, and constitutes one of the main uncertainties in current solar irradiance reconstructions. This is primarily due to the difficulty in observing such small-scale features, the detailed structure of which are only starting to be resolved (Lites et al. 2004, Lagg et al. 2010) with instruments such as the Swedish 1-m Solar Telescope, SST (Scharmer et al. 2003) and the Imaging Magnetograph eXperiment, IMaX (Martínez Pillet et al. 2011) on-board SUNRISE (Solanki et al. 2010, Barthol et al. 2011). As such, the relationship between radiance and size cannot, as yet, be studied directly. It is however appropriate and more straightforward to consider instead the relationship between apparent intensity contrast and magnetogram signal. Apart from small-scale magnetic fields observed in the quiet Sun internetwork (Khomenko et al. 2003, Lites et al. 2008, Beck and Rezaei 2009), magnetic concentrations carrying more than a minimum amount of flux exhibit similar field strengths regardless of size (Solanki and Schmidt 1993, Solanki et al. 1999). Flux tubes also tend towards vertical orientation due to magnetic buoyancy. As flux tubes exhibit a narrow range of magnetic field strengths and are largely vertical, on average the magnetogram signal at a given image pixel approximately scales with the proportion of the resolution element occupied by magnetic fields. Also, although the relationship between magnetogram signal and distribution of flux tube sizes is degenerate

(a given magnetogram signal can, for example, correspond to either a single flux tube or a concentration of numerous smaller ones), flux tube size appears, on average, to be greater where the magnetogram signal is greater (Ortiz et al. 2002).

Relatively few studies examining network and faculae contrast variation with magnetogram signal and position on the solar disc have been reported in the literature. The majority of studies from the past two decades employed high-resolution (< 0.5 arcsec) scans made with ground-based telescopes. For example, the efforts of Topka et al. (1992, 1997) and Lawrence et al. (1993) with the Swedish Vacuum Solar Telescope (SVST) and of Berger et al. (2007) with the SST. These studies suffer from variable seeing effects introduced by the Earth's atmosphere and poor representation of disc positions, a limitation imposed by the relatively narrow FOVs (field-of-view). Ortiz et al. (2002) and Kobel et al. (2011) repeated the work of Topka et al. (1992, 1997) and Lawrence et al. (1993) utilising observations from spaceborne instruments, and in so doing avoided seeing effects. Ortiz et al. (2002) employed full-disc continuum intensity images and longitudinal magnetograms from the Michelson Doppler Imager (MDI) on-board the Solar and Heliospheric Observatory (SoHO). While full-disc MDI observations presented a more complete coverage of disc positions, allowing the authors to derive an empirical relationship relating contrast to heliocentric angle and magnetogram signal, the spatial resolution is significantly poorer than in the SVST studies (4 arcsec versus $\gtrsim 0.3$ arcsec). Kobel et al. (2011) examined the relationship between contrast and magnetogram signal near disc centre using spectropolarimetric scans from the Solar Optical Telescope (SOT) on-board Hinode (Kosugi et al. 2007). In this instance, the spatial resolution (0.3 arcsec) is comparable.

In this paper we discuss continuum and line core intensity contrast of network and facular elements from full-disc observations by the Helioseismic and Magnetic Imager (HMI) on-board the Solar Dynamics Observatory (SDO) spacecraft (Schou et al. 2012b), and their relationship with heliocentric angle and magnetogram signal. The aim here is to derive stringent observational constraints on the relationship between intensity contrast, and position on the solar disc and magnetic field. This will be of utility to solar irradiance reconstructions, especially as HMI data will increasingly be used for this purpose.

This study partly echoes the similar studies discussed above, in particular that by Ortiz et al. (2002) utilising MDI observations. It presents a significant extension of the effort by Ortiz et al. (2002) in that we examined the entire solar disc not just in the continuum but also in the core of the HMI spectral line (Fe I 6173 Å). This is of particular relevance to solar irradiance variation given the observation that spectral line changes appear to have a significant influence on such variations (Mitchell and Livingston 1991, Unruh et al. 1999, Preminger et al. 2002). Both here and in the study by Ortiz et al. (2002), network and facular elements were distinguished from quiet Sun by the magnetogram signal, and sunspots and pores by the continuum intensity. HMI magnetograms are significantly less noisy than MDI magnetograms, allowing us to achieve a similar magnetogram signal threshold while averaging over a much shorter period (315 seconds versus 20 minutes). Network and facular features evolve at granular timescales (~ 10 minutes, Berger and Title 1996, Wiegmann et al. 2013). It is pertinent to keep the averaging period below this in order to avoid smearing and loss of signal. HMI also has a finer spatial resolution (1 arcsec compared to 4 arcsec), allowing weaker unresolved features to be detected at the same noise level than with MDI. The finer resolution however, also renders intensity fluc-

3 Intensity contrast of solar network and faculae

(The contents of this chapter are identical to the printed version of Yeo, K. L., Solanki, S. K., Krivova, N. A., 2013, Intensity contrast of network and faculae, Astron. Astrophys., 550, A95.)

tuations from small-scale phenomena such as granulation and filamentation more severe, which complicates the clear segmentation of sunspots and pores.

In Sect. 3.2.1 we briefly present the HMI instrument, the observables considered and the data set. The data reduction process by which we identified and derived the intensity contrast of network and facular features is detailed in Sect. 3.2.2. Following that we describe the results of our analysis of these measured contrasts (Sect. 3.3). In Sect. 3.4 we discuss our findings in the context of earlier studies and of their relevance to facular contribution to solar irradiance variation, before presenting our conclusions in Sect. 3.5.

3.2 Method

3.2.1 SDO/HMI data

SDO/HMI (Schou et al. 2012b) is designed for the continuous, full-disc observation of velocity, magnetic field and intensity on the solar surface. The instrument comprises two 4096×4096 pixel CCD cameras observing the Sun at a spatial resolution of 1 arcsec (corresponding to two pixels). By means of a tunable Lyot filter and two tunable Michelson interferometers, the instrument records 3.75-second cadence filtergrams at various polarizations and wavelengths across the Fe I absorption line at 6173 \AA . 45-second cadence Dopplergrams, longitudinal magnetograms and intensity (continuum, line depth and width) images are generated from the filtergram sequence. For this work we considered the longitudinal magnetic field, continuum intensity and line depth observables. HMI is full-Stokes capable, however, at time of study, only 720-second cadence Stokes IQUV parameters and Milne-Eddington inversions were available. As argued in Sect. 3.1, for this study it is important to keep the integration period of measurements below ~ 10 minutes. We opted to utilise the 45-second longitudinal magnetograms also to keep in line with earlier studies, which examined intensity contrast variation with line-of-sight magnetic field (e.g. Topka et al. 1992, 1997, Lawrence et al. 1993, Ortiz et al. 2002, Kobel et al. 2011). More details on the instrument can be found in Schou et al. (2012b).

The data set comprises simultaneous longitudinal magnetograms, continuum intensity and line depth images from 15 high activity days in the period May 2010 to July 2011. From each day, for each observable we took the average of the seven 45-second cadence images from a 315-second period, each rotated to the observation time of the middle image to co-register. Aside from signal-to-noise considerations, this averaging is to suppress variance from p-mode oscillations. The dates and times of the employed observations are listed in Table 3.1.

Longitudinal magnetograms describe the line-of-sight component of the average magnetic flux density over each resolution element. To first order, for a given flux tube of intrinsic magnetic field strength B , the unsigned longitudinal magnetogram signal, $\langle B_l \rangle$, is $\alpha B |\cos \gamma|$, scaled by α , the magnetic filling factor and γ , the inclination of the magnetic field from the line-of-sight. As mentioned in the introduction (Sect. 3.1), flux tubes tend towards vertical orientation. In this study we examined the overall properties of an ensemble of magnetic elements. Under this condition it is reasonable to assume that on average $\gamma \approx \theta$, the heliocentric angle, allowing us to employ the magnetogram signal as a proxy for αB via the quantity $\langle B_l \rangle / \mu$, where $\mu = \cos \theta$. This quantity also represents a

Table 3.1: Observation date and time of the data set.

Date (year.month.date)	Time (hour.minute.second)
2010.05.04	00:03:00
2010.06.11	00:00:00
2010.07.24	00:05:15
2010.08.11	00:00:00
2010.09.02	00:00:00
2010.10.25	00:00:00
2010.11.13	00:00:00
2010.12.04	00:00:00
2011.01.01	00:00:00
2011.02.14	00:00:00
2011.03.08	00:00:00
2011.04.15	00:00:00
2011.05.30	00:00:00
2011.06.02	00:00:00
2011.07.18	00:12:00

Notes. The time listed is the nominal time, in International Atomic Time (TAI), of the middle cadence in the sequence of seven considered from each day.

first-order approximation of the unsigned average magnetic flux density over each resolution element. At time of writing, HMI Dopplergrams and longitudinal magnetograms were generated from just the first Fourier component of the filtergram sequence resulting in a $\sqrt{2}$ factor increase in photon noise from the optimal level (Couvidat 2011, Couvidat et al. 2012).

Each line depth image was subtracted from the corresponding continuum intensity image to yield the line core intensity image. Hereafter we will denote the continuum and line core intensity I_C and I_L respectively. At time of writing, HMI data products are generated from the filtergram sequence assuming a Gaussian form to the Fe I 6173 Å line and delta filter transmission profiles. The effect of these approximations on Doppler velocity and longitudinal magnetic field measurements are accounted for, but not completely for the intensity observables (Couvidat 2011, Couvidat et al. 2012). The impact on this study is assumed minimal as we are only interested in contrast relative to the local mean quiet Sun level.

3.2.2 Data reduction

3.2.2.1 Magnetogram noise level

The noise level of 315-second HMI magnetograms as a function of position on the solar disc was determined. For this purpose we used 10 spot-free 315-second magnetograms recorded over a seven month period in 2010. First, we estimated the centre-to-limb vari-

3 Intensity contrast of solar network and faculae

(The contents of this chapter are identical to the printed version of Yeo, K. L., Solanki, S. K., Krivova, N. A., 2013, Intensity contrast of network and faculae, Astron. Astrophys., 550, A95.)

ation, CLV of the noise level. The pixels within each magnetogram were ordered by distance from the disc centre and sampled in successive blocks of 5000 pixels. The blocks represent concentric rings (near the limb, arcs, as the circumference of the solar disc is greater than 5000 pixels) of pixels of similar distance from the disc centre. Within each block we computed the average distance from the disc centre and the standard deviation of the magnetogram signal (iteratively, with points outside three standard deviations from the mean excluded from the succeeding iteration till convergence). A fifth-order polynomial in μ was fitted to the noise CLV; the mean of the standard deviation versus distance profiles so derived from the magnetograms. The magnetograms were then normalized by the noise CLV fit. At each disc position, the standard deviation over a 401×401 pixel window centred on the pixel of interest was computed (iteratively as above) for each normalized magnetogram and the median taken (following Ortiz et al. 2002). (Near the limb, the standard deviation was computed from just the image pixels that lie within the solar disc.) A sixth-order polynomial was fitted to the resultant surface (termed here the noise residue). This fit represents the noise level after the removal of the CLV as a function of position on the solar disc. The noise level, $\sigma_{\langle B_i \rangle}$, shown in Fig. 3.1, is then the product of the noise CLV fit and the noise residue fit. The noise level is lowest near disc centre and increases radially up to the limb (mean of 4.9 G for $\mu > 0.95$ and 8.6 G for $\mu < 0.05$). The root-mean-square, RMS difference between the noise level and the noise CLV fit is 0.4 G. The correlation with distance from disc centre and relatively small deviation from circular symmetry suggests photon noise is the dominant component. The noise level of 45-second magnetograms, derived by a like analysis, has a similar, albeit accentuated form. The ratio between the noise level, averaged over the solar disc, of 45-second and 315-second magnetograms is 2.7 (approximately $\sqrt{7}$). The noise level of 45-second magnetograms determined by Liu et al. (2012), via a vastly different method, also exhibits a similar CLV.

3.2.2.2 Quiet Sun intensity

For this part of the data reduction process, where we examined how quiet Sun intensity and the noise level of the intensity images vary with position on the solar disc, we counted all pixels with $\langle B_i \rangle / \mu \leq 10$ G as corresponding to quiet Sun (QS).

The continuum and line core intensity images were normalized by the fifth-order polynomial in μ fit to the quiet Sun pixels to correct for limb-darkening (following Neckel and Labs 1994). In the case of the line core intensity images, this was also to correct for the centre-to-limb broadening of the Fe I 6173 Å line (Norton et al. 2006). There are distortions in the intensity images such that after this normalization, the mean quiet Sun intensity is not constant at unity but varying with position on the solar disc. The mean quiet Sun intensity at the continuum and line core as a function of position on the solar disc, denoted $\langle I_{C,QS} \rangle$ and $\langle I_{L,QS} \rangle$ respectively, were determined for each of the selected days. A 401×401 pixel window was centred on each disc position and the mean continuum and line core intensity of all quiet Sun pixels inside the window computed. For each day represented in the data set, $\langle I_{C,QS} \rangle$ and $\langle I_{L,QS} \rangle$ were given by the fifth-order polynomial fits to the mean quiet Sun continuum and line core intensity surfaces so derived from the images from the day. This analysis had to be repeated for each selected day as we found the spatial distribution of $\langle I_{C,QS} \rangle$ and $\langle I_{L,QS} \rangle$ to vary significantly over the pe-

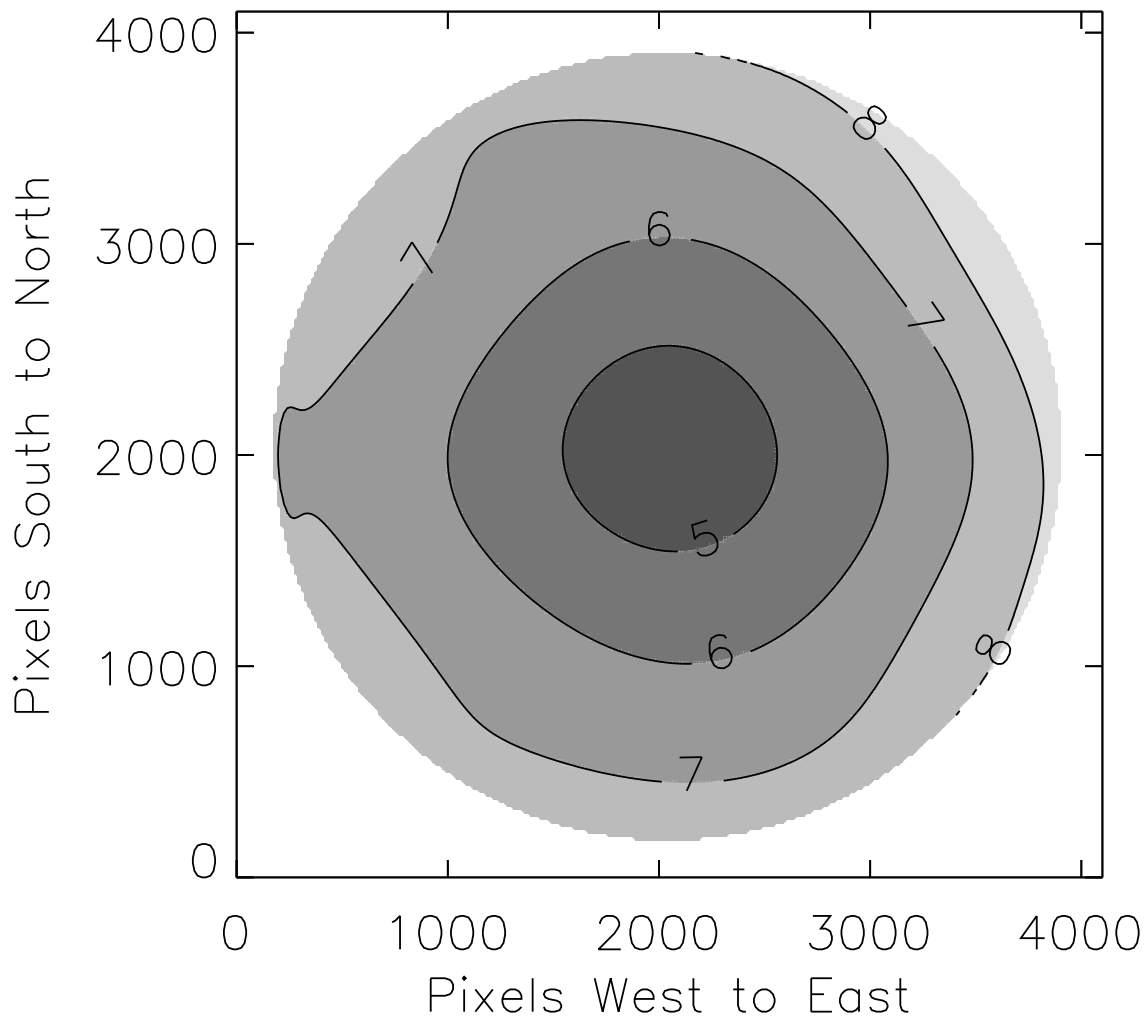


Figure 3.1: Magnetogram noise level in units of Gauss, as a function of disc position, sampled at 16-pixel intervals in either direction on the CCD.

riod of observation. The RMS value of $\langle I_{C,QS} \rangle - 1$ and $\langle I_{L,QS} \rangle - 1$, the scale of the image distortions, is on average 0.004 and 0.01 respectively.

The CLV of the standard deviation of quiet Sun intensity at continuum, $\sigma_{I_{C,QS}}$ and line core, $\sigma_{I_{L,QS}}$ were determined, from $I_C / \langle I_{C,QS} \rangle$ and $I_L / \langle I_{L,QS} \rangle$, by an analysis similar to the procedure used to derive the magnetogram noise CLV. In Fig. 3.2, we express $\sigma_{I_{C,QS}}$ and $\sigma_{I_{L,QS}}$, which carry information on the noise level of the intensity images and granulation contrast, as a function of μ . Going from disc centre, $\sigma_{I_{C,QS}}$ decreases gradually down to $\mu \sim 0.15$ before increasing rapidly towards the limb. The monotonic decline from disc centre to $\mu \sim 0.15$ resembles a similar trend in the CLV of granulation contrast reported by various authors (Sánchez Cuberes et al. 2000, 2003, and references therein). $\sigma_{I_{L,QS}}$ exhibits a similar, though less accentuated, trend. For both $\sigma_{I_{C,QS}}$ and $\sigma_{I_{L,QS}}$, the μ -dependence from disc centre to $\mu \sim 0.3$ is approximately linear, as highlighted by the linear fits (dotted lines). The elevation near limb is a direct consequence of limb-darkening; the diminishing signal-to-noise ratio translates into an escalating noise level in the normalized intensity. Given the gross scatter towards the limb, we excluded pixels outside $\mu = 0.1$, representing

3 Intensity contrast of solar network and faculae

(The contents of this chapter are identical to the printed version of Yeo, K. L., Solanki, S. K., Krivova, N. A., 2013, *Intensity contrast of network and faculae*, *Astron. Astrophys.*, 550, A95.)

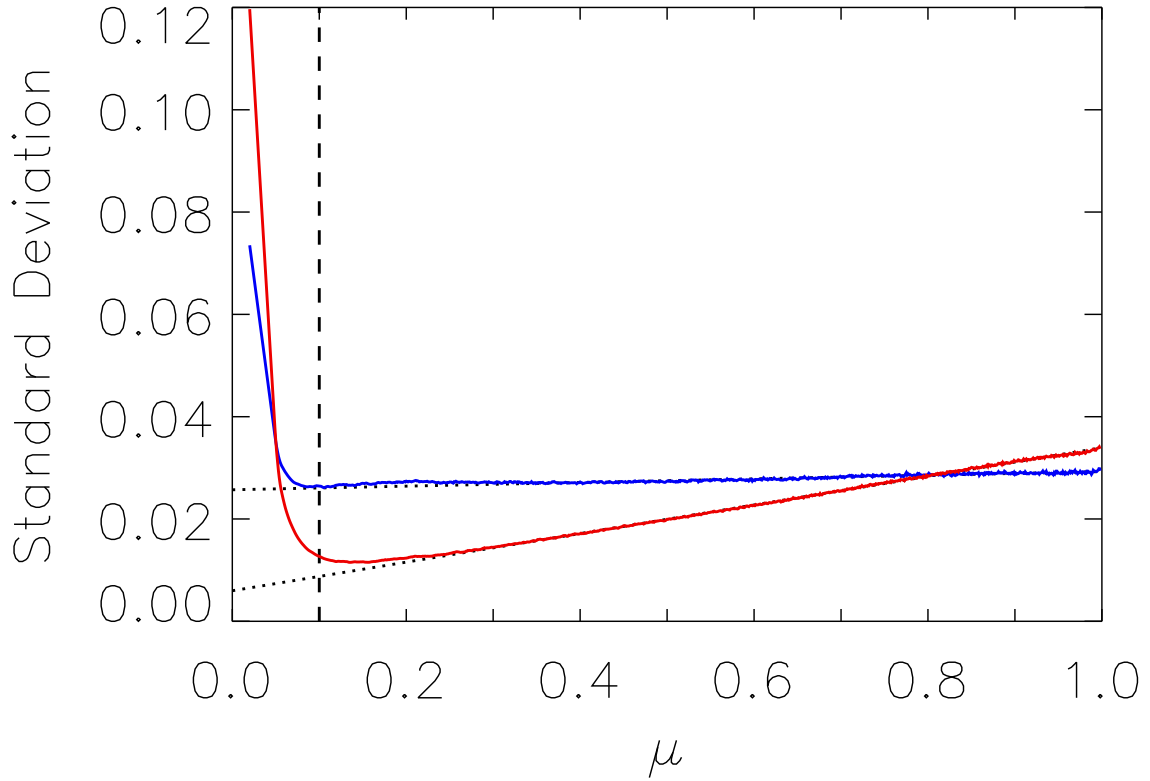


Figure 3.2: Standard deviation of quiet Sun ($\langle B_l \rangle / \mu \leq 10$ G) intensity at continuum, $\sigma_{I_{C,QS}}$ (red) and line core, $\sigma_{I_{L,QS}}$ (blue) as a function of μ . The dotted lines represents the linear fit to $\sigma_{I_{C,QS}}$ and $\sigma_{I_{L,QS}}$ over the range $0.3 \leq \mu \leq 1.0$ (largely hidden due to the close agreement), extrapolated to $\mu = 0$. The dashed line denotes the threshold ($\mu = 0.1$) below which pixels were excluded from the rest of the study in view of the scatter in measured intensity.

about 1% of the solar disc by area, from further consideration.

3.2.2.3 Identification of network and faculae

Network and facular features, the subject of this work, were identified by first distinguishing them from quiet Sun by the magnetogram signal and from sunspots and pores by the continuum intensity. Pixels with $\langle B_l \rangle / \mu > 3\sigma_{\langle B_l \rangle} / \mu$ (~ 14 G near disc centre, where $\sigma_{\langle B_l \rangle}$ is lowest) were considered to harbour substantive magnetic fields. Isolated pixels above this threshold were assumed false positives and excluded. Hereafter we will denote $3\sigma_{\langle B_l \rangle} / \mu$ as $(\langle B_l \rangle / \mu)_{TH}$. Pixels with $I_C < 0.89$ were counted as sunspots and pores. This value of the threshold is given by the mean of the minimum value of $\langle I_{C,QS} \rangle - 3\sigma_{I_{C,QS}}$ from each selected day. It was so defined to distinguish sunspots and pores with minimal wrongful inclusion of intergranular lanes and magnetic features darker than the quiet Sun in the continuum. The continuum intensity versus μ scatter plot of network and facular pixels for one of the selected days (June 2, 2011) is shown in Fig. 3.3 (top panel). The pixels identified as network and faculae lie clearly above the continuum intensity threshold.

In HMI magnetograms, magnetic signals produced by sunspots and pores extend be-

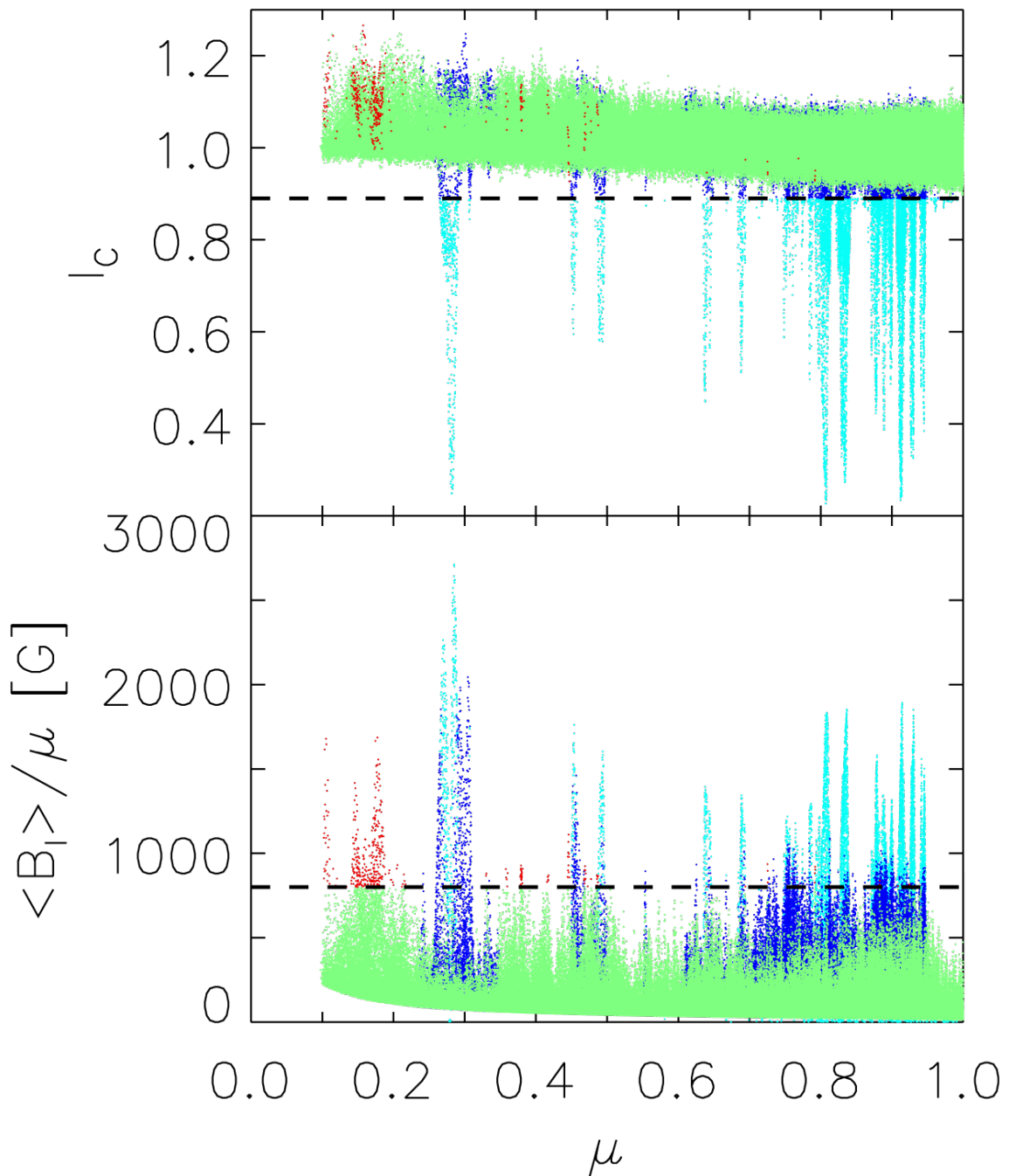


Figure 3.3: Continuum intensity, I_c versus μ (top) and $\langle B_i \rangle / \mu$ versus μ (bottom) scatter plots of pixels counted as network and faculae (green) from June 2, 2011. The pixels counted as sunspots and pores by the continuum intensity threshold and the magnetic extension removal procedure (see text) are represented by the cyan and blue dots respectively. The red dots represent network and faculae pixels that lie above the cutoff $\langle B_i \rangle / \mu$ level. The dashed lines denote the continuum intensity threshold (top) and the cutoff $\langle B_i \rangle / \mu$ level (bottom).

3 Intensity contrast of solar network and faculae

(The contents of this chapter are identical to the printed version of Yeo, K. L., Solanki, S. K., Krivova, N. A., 2013, Intensity contrast of network and faculae, Astron. Astrophys., 550, A95.)

yond their boundary (in our analysis, the $I_C = 0.89$ locus). This is illustrated for a sunspot near disc centre and another that is close to the limb on one of the selected days (July 18, 2011) in Fig. 3.4. The $I_C = 0.89$ locus is plotted over the continuum intensity image and magnetogram of both sunspots (red contours) to highlight the extension of the magnetogram signal. This arises predominantly from the lateral expansion of their magnetic field with height (i.e., magnetic canopy) and partly also from the effect of straylight from sunspots and pores on nearby pixels. Towards the limb, these magnetic features become more extensive and bipolar due to the acute orientation of the largely horizontal magnetic canopy with the line-of-sight (Giovanelli 1980), as illustrated by the near limb example (bottom panels). Figure 3.4 also highlights the presence of bright sunspot structures (such as bright penumbral filaments) that lie above the continuum intensity threshold. All of these could easily be misidentified as network and faculae by the simple application of the magnetogram signal and continuum intensity thresholds described earlier.

To account for the effects of straylight around sunspots and pores, magnetic canopies and bright sunspot structures, we expanded sunspots and pores to include adjoining magnetic signal. Pixels adjacent to sunspots and pores that lie above $(\langle B_l \rangle / \mu)_{\text{TH}}$ are reassigned to these features. This was iterated till no more pixels could be added. Here we will refer to this process as magnetic extension removal. Simply adding only adjoining pixels within a threshold distance from sunspots and pores instead is not useful as the physical extent of magnetic canopies exhibits a broad dynamic range, dependent on the position and physical properties of the associated feature. Kobel et al. (2011), in a similar study with Hinode/SOT scans, expanded pores to include adjoining pixels above a threshold magnetogram signal level of 200 G to account for their influence on surrounding pixels from telescope diffraction. While this technique appears to work for Hinode/SOT scans, here we observed that adding only adjoining pixels above a threshold magnetogram signal level results in the appearance of a knee in contrast versus $\langle B_l \rangle / \mu$ plots at this threshold level regardless of the value chosen. For these reasons we expanded sunspots and pores to include all adjoining magnetic signal, though this conservative approach inevitably assigns too many pixels, including legitimate faculae, to sunspots and pores.

All pixels identified as magnetic, and not as sunspots and pores or their extensions, were taken to correspond to network and faculae. Figure 3.3 shows the continuum intensity versus μ (top panel) and $\langle B_l \rangle / \mu$ versus μ (bottom panel) scatter plots of pixels identified as network and faculae (green), and counted as sunspots and pores by the magnetic extension removal procedure (blue) from June 2, 2011. The pixels captured by the magnetic extension removal procedure are not well distinguished from network and faculae by the continuum intensity; largely hidden by network and faculae in the continuum intensity versus μ scatter plot. It is clear from the $\langle B_l \rangle / \mu$ versus μ scatter plots however that the two classes are significantly different magnetic populations. As noted earlier, this procedure is likely too severe and results in the exclusion of some true faculae. However, for the purpose of this study it is not necessary to identify all faculae present and far more important to avoid false positives.

Finally, network and facular pixels with $\langle B_l \rangle / \mu$ above a conservative cutoff level of 800 G were excluded from the subsequent analysis (following Ball et al. 2011, 2012). They are mostly bright features concentrated near the limb (as illustrated for June 2, 2011 by the red dots in Fig. 3.3) associated with sunspots and pores. (The relatively high $\langle B_l \rangle / \mu$ values likely reflect nearly horizontal fields, for which $|\cos \gamma| \gg \mu$ towards the

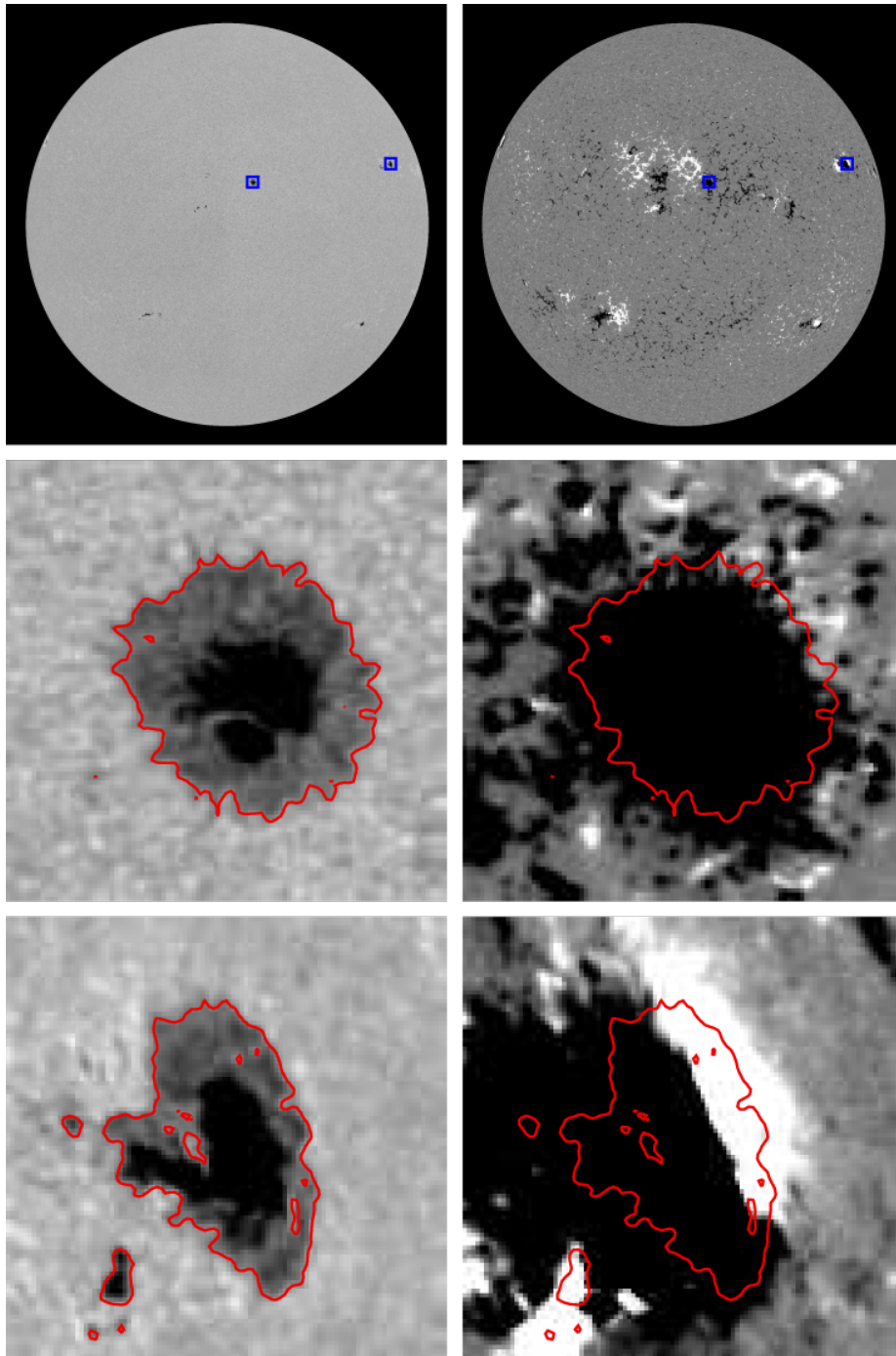


Figure 3.4: Continuum intensity image (top left) and magnetogram (top right) from July 18, 2011 and the corresponding 50×50 arcsec insets of the boxed sunspot features near disc centre (middle panels) and limb (bottom panels). The red contours represent the continuum intensity sunspot boundary (the $I_C = 0.89$ locus). The continuum intensity image is saturated at 0.6 and 1.2, and the magnetogram at $\pm 80\text{G}$ (to highlight the extension of the magnetic signal from these sunspots beyond the intensity boundary).

3 Intensity contrast of solar network and faculae

(The contents of this chapter are identical to the printed version of Yeo, K. L., Solanki, S. K., Krivova, N. A., 2013, *Intensity contrast of network and faculae*, *Astron. Astrophys.*, 550, A95.)

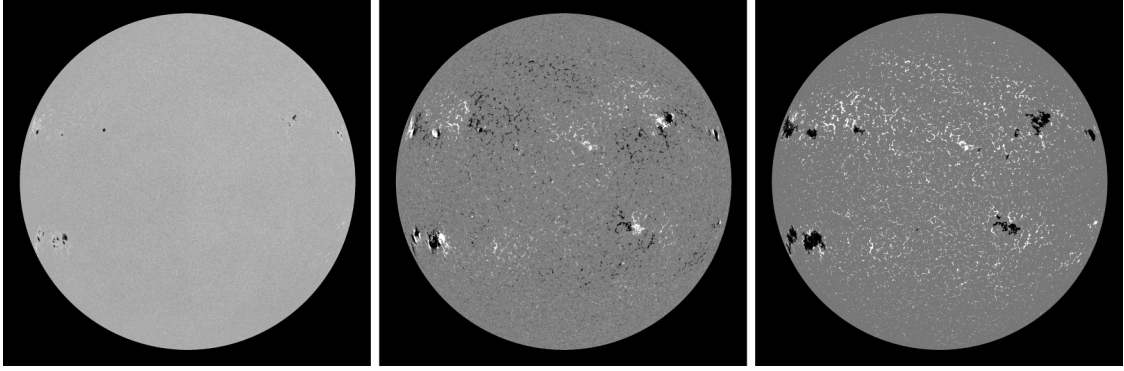


Figure 3.5: HMI continuum intensity image (left), magnetogram (middle) and classification image (right) from May 30, 2011. The classification image indicates the positions of the pixels classed as network and faculae (white), and sunspots and pores (black). The latter includes magnetic signal adjoined to sunspots and pores, counted to them to avoid counting their magnetic canopy, possible bright structures within penumbrae and straylight as network and faculae erroneously. The continuum intensity image and magnetogram are scaled between 0.6 and 1.2, and -80 G and 80 G respectively as in Fig. 3.4

limb.) This is to account for non-facular magnetic signals that might have been missed by the continuum intensity threshold and the magnetic extension removal procedure.

The classification image, indicating the positions of the pixels classed as sunspot and pores, and network and faculae for another of the selected days (May 30, 2011) is shown in Fig. 3.5. In spite of the severe measures taken to minimise the influence of sunspots and pores, a fair fraction of active region faculae remains. In total, 7.6×10^6 pixels were identified as corresponding to network and facular features from the data set (i.e. 4.5% of all solar disc pixels in the 15 continuum intensity image and magnetogram pairs examined).

3.2.2.4 Definition of intensity contrast

The average continuum and line core intensity contrast over a given resolution element, C_{I_C} and C_{I_L} were defined as:

$$C_{I_C}(x, y) = \frac{I_C(x, y) - \langle I_{C, QS} \rangle(x, y)}{\langle I_{C, QS} \rangle(x, y)} \quad (3.1)$$

and

$$C_{I_L}(x, y) = \frac{I_L(x, y) - \langle I_{L, QS} \rangle(x, y)}{\langle I_{L, QS} \rangle(x, y)} \quad (3.2)$$

respectively, where (x, y) denote position on the CCD array. These two quantities, computed for each of the pixels identified as corresponding to network and facular features, represent the normalized difference between the continuum and line core intensities at a given pixel and the local mean quiet Sun levels as given by the mean quiet Sun continuum and line core intensity surfaces, $\langle I_{C, QS} \rangle$ and $\langle I_{L, QS} \rangle$, defined earlier in Sect. 3.2.2.2.

In summary, here we extracted an ensemble of 7.6×10^6 continuum and line core intensity contrast measurements corresponding to network and facular features covering as wide a range of heliocentric angles ($0.1 \leq \mu \leq 1.0$) and magnetogram signal ($(\langle B_l \rangle / \mu)_{\text{TH}} < \langle B_l \rangle / \mu \leq 800 \text{ G}$) as reasonably possible from the data set for the succeeding analysis.

3.3 Results

3.3.1 Variation with position and magnetogram signal

The positions of pixels identified as network and faculae, classified by $\langle B_l \rangle / \mu$, in a quiet region and an active region on one of the selected days (April 15, 2011) is shown in Fig 3.6. As expected, at HMI's spatial resolution, magnetic signals with higher $\langle B_l \rangle / \mu$ are largely concentrated in active regions. Though magnetic signals with lower $\langle B_l \rangle / \mu$ are present in both quiet Sun and active regions, the fact that the solar disc is predominantly quiet Sun means these signals correspond largely to quiet Sun network and internetwork.

To elucidate the CLV of intensity contrast, we grouped the measured contrasts into eight intervals of $\langle B_l \rangle / \mu$ spanning the range $(\langle B_l \rangle / \mu)_{\text{TH}} < \langle B_l \rangle / \mu \leq 800 \text{ G}$ and within each interval into μ bins 0.05 wide. As the distribution of magnetogram signal is skewed towards the lower bound (Wenzler et al. 2004, Parnell et al. 2009), the $\langle B_l \rangle / \mu$ intervals were defined such that the widths slide from about 36 G ($(\langle B_l \rangle / \mu)_{\text{TH}} < \langle B_l \rangle / \mu \leq 50 \text{ G}$) to 160 G ($640 \text{ G} < \langle B_l \rangle / \mu \leq 800 \text{ G}$) to ensure reasonable statistics in every interval. In grouping the measured contrasts into these broad $\langle B_l \rangle / \mu$ intervals we are effectively grouping the network and facular features by αB (Sect. 3.2.1), neglecting differences in quiet Sun network and active region faculae contrast (Lawrence et al. 1993, Kobel et al. 2011). This is reasonable since the lower intervals are mainly populated by quiet Sun network and the higher intervals by active region faculae. The bin-averaged continuum and line core intensity contrast as a function of μ and the cubic polynomial fit for each of the $\langle B_l \rangle / \mu$ intervals are expressed in Figs. 3.7 and 3.8 respectively. For brevity we will refer to these bin-averaged contrasts as the contrast CLV profiles.

The truncated μ coverage in the lower $\langle B_l \rangle / \mu$ intervals is due to foreshortening. As flux tubes are mainly vertical, going from disc centre to the limb the corresponding longitudinal magnetogram signal diminishes, eventually dropping below the threshold level which itself rises towards the limb (Fig. 3.1). The fluctuations near the limb, more pronounced in the higher $\langle B_l \rangle / \mu$ intervals, is due to the inhomogeneous distribution of active regions on the solar disc, where stronger magnetic signals are concentrated on the selected days. Diminishing statistics also play a role; there are comparatively fewer pixels in the higher $\langle B_l \rangle / \mu$ intervals.

To investigate the $\langle B_l \rangle / \mu$ -dependence of intensity contrast, the measured contrasts were grouped into eight μ intervals spanning the range $0.1 \leq \mu \leq 1.0$ and within each interval into $\langle B_l \rangle / \mu$ bins 40 G wide. The μ intervals were defined such that they represent an approximately equal proportion of the solar disc by area. The bin-averaged continuum and line core intensity contrasts as a function of $\langle B_l \rangle / \mu$ and the cubic polynomial fit for each of the μ intervals are shown in Figs. 3.9 and 3.10 respectively. For brevity we will refer to these bin-averaged contrasts as the contrast versus $\langle B_l \rangle / \mu$ profiles. These

3 Intensity contrast of solar network and faculae

(The contents of this chapter are identical to the printed version of Yeo, K. L., Solanki, S. K., Krivova, N. A., 2013, *Intensity contrast of network and faculae*, *Astron. Astrophys.*, 550, A95.)

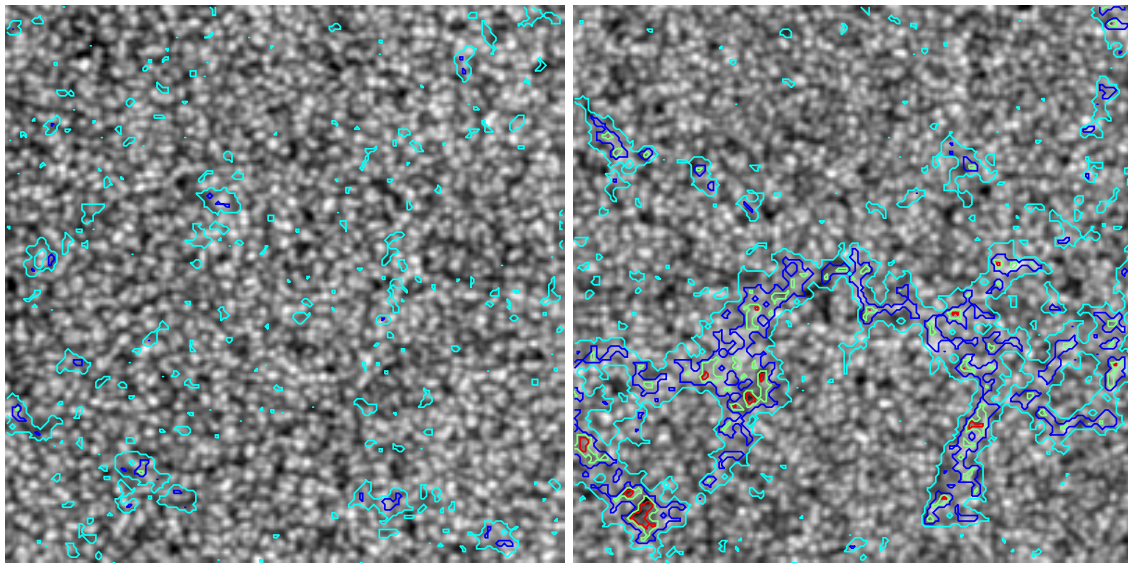


Figure 3.6: 100×100 arcsec insets of a quiet region near disc centre ($\mu > 0.99$, left) and active region NOAA 11187 ($0.82 < \mu < 0.91$, right) of the continuum intensity image from April 15, 2011. The cyan contours indicate the boundary of network and faculae. The blue, green and red contours correspond to $\langle B_l \rangle / \mu = 100$ G, 280 G and 500 G, respectively.

profiles represent the variation of continuum and line core intensity contrast ranging from internetwork and weak network to active region faculae at different distances from disc centre.

The cubic polynomial fit to each contrast versus $\langle B_l \rangle / \mu$ profile included the zeroth-degree term. This produced better fits to data at low $\langle B_l \rangle / \mu$ than constraining the fits to pass through the origin by excluding it. Approaching $\langle B_l \rangle / \mu = 0$ G, the contrast versus $\langle B_l \rangle / \mu$ profiles decline to weak, broadly negative levels. Although the cubic polynomial fits express good agreement with measurements, they are too simple to accommodate this decline well without including the unphysical zeroth-degree term. For similar considerations we included the zeroth-degree term in the cubic polynomial fits to the contrast CLV profiles, so rendering them non-zero at $\mu = 0$. These apparent offsets in the contrast CLV and contrast versus $\langle B_l \rangle / \mu$ profiles probably reflects the fact that magnetic elements are generally located in dark intergranular lanes.

In Fig. 3.11 we show a recomputation of the continuum intensity contrast versus $\langle B_l \rangle / \mu$ profile over $0.94 < \mu \leq 1.00$ from Fig. 3.9 where we included pixels below the magnetogram signal threshold and not identified as sunspots and pores (i.e., quiet Sun), and grouped the measurements by $\langle B_l \rangle / \mu$ in bins 10 G (instead of 40 G) wide. Approaching $\langle B_l \rangle / \mu = 0$ G, contrast declines gradually to below the reference level before turning back up sharply towards the origin. Similar trends were reported by Narayan and Scharmer (2010), Kobel et al. (2011) and Schnerr and Spruit (2011), who termed it the fishhook feature, based on SST and Hinode/SOT disc centre scans. Schnerr and Spruit (2011) demonstrated the resolution of granules and dark intergranular lanes, where magnetic flux concentrates, at the relatively fine spatial resolution of both instruments (0.15

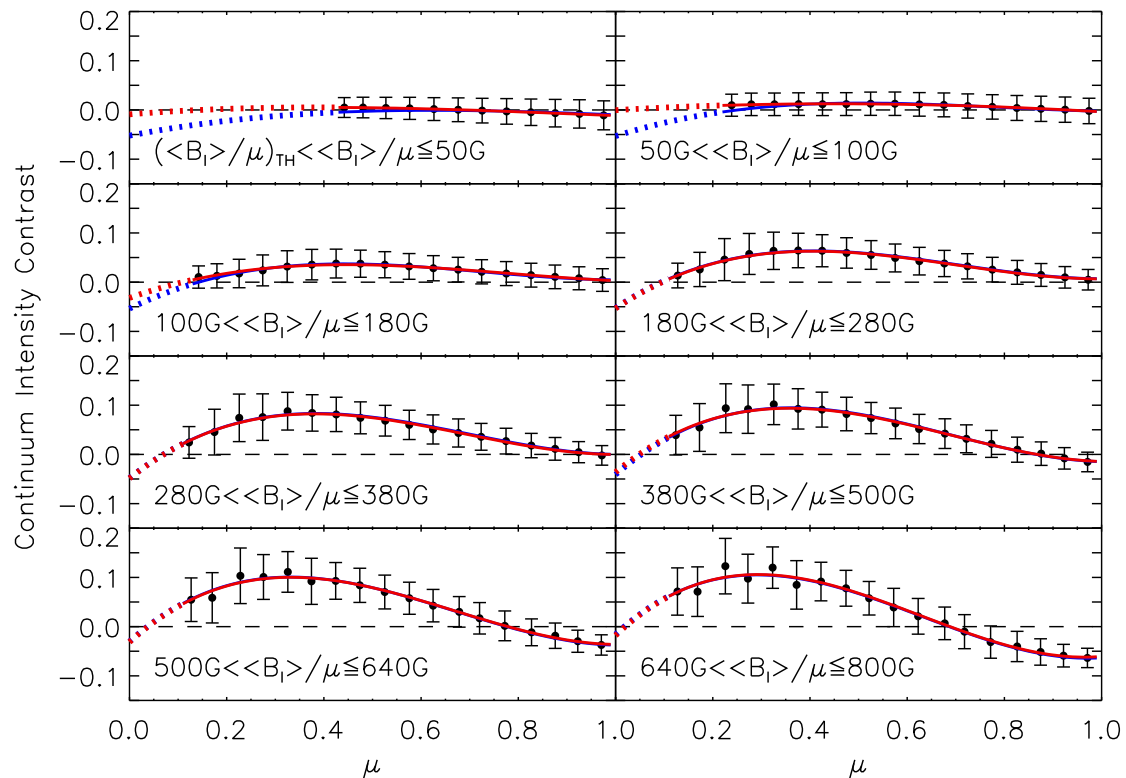


Figure 3.7: CLV of continuum intensity contrast, C_{Ic} over eight $\langle B_l \rangle / \mu$ intervals. The filled circles and error bars represent the mean and standard deviation of C_{Ic} grouped by μ in bins 0.05 wide. The red curves are third-order polynomial fits to the filled circles and the blue curves are the cross-sections of the surface fit to C_{Ic} at the mean $\langle B_l \rangle / \mu$ within each interval (largely hidden due to the close agreement), extrapolated to $\mu = 0$ (dotted segments). The horizontal dashed lines denote the mean quiet Sun level.

and 0.3 arcsec respectively) to be the cause of the fishhook feature at low magnetogram signal levels. Though HMI has a coarser resolution (1 arcsec) than either Hinode/SOT or SST, the fishhook feature near $\langle B_l \rangle / \mu = 0$ G in Fig. 3.11 indicates granulation is still sufficiently resolved to have a measurable impact on apparent contrast.

Comparing the measured intensity contrast at continuum and line core derived here, the most distinct difference is the opposite CLV. Confining this discussion to broad trends in the measurements, continuum intensity contrast is weakest near disc centre and increases up to a maximum before declining quite significantly towards the limb (Fig. 3.7). Conversely, line core intensity contrast is strongest near disc centre and declines monotonically from disc centre to limb (Fig. 3.8). Line core intensity is modulated by line strength and shape, and continuum intensity. The centre-to-limb decline exhibited by the measured line core intensity contrast arises from variation in line strength and shape (if this were absent the continuum and line core intensity contrast would vary proportionally) and would be even more acute than reflected in the CLV profiles if not partially offset by the accompanying increase in continuum intensity. This will be demonstrated, along with a closer discussion of the diverging trends exhibited by both sets of measurements in Sect 3.4.3.

3 Intensity contrast of solar network and faculae

(The contents of this chapter are identical to the printed version of Yeo, K. L., Solanki, S. K., Krivova, N. A., 2013, *Intensity contrast of network and faculae*, *Astron. Astrophys.*, 550, A95.)

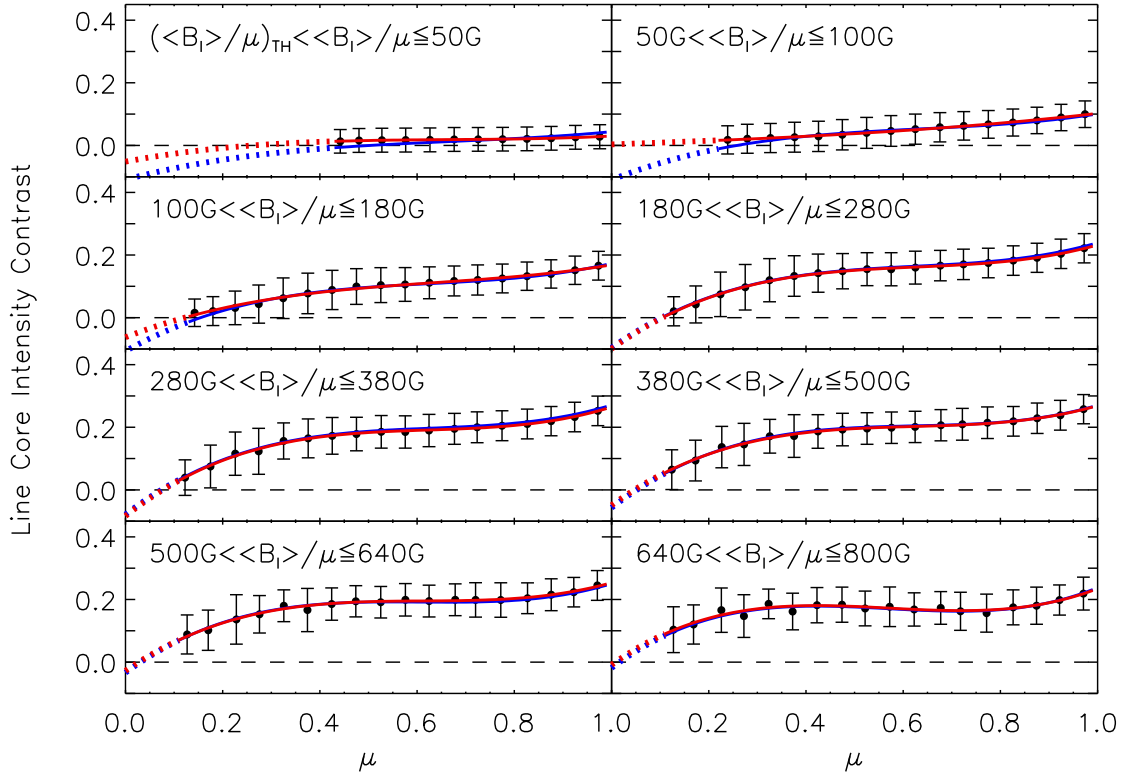


Figure 3.8: Similar to Fig. 3.7, but for line core intensity contrast.

3.3.2 Surface fits

The cubic polynomial fit to the contrast CLV and contrast versus $\langle B_l \rangle / \mu$ profiles reproduced the observations well (Figs. 3.7 to 3.10). Given this, we fit the entire set of measured network and faculae continuum and line core intensity contrast as functions of μ and $\langle B_l \rangle / \mu$ (following Ortiz et al. 2002). The measured contrasts were grouped by μ and the natural logarithm of $\langle B_l \rangle / \mu$ into a grid of 36×41 bins. The grid spans $0.1 \leq \mu \leq 1.0$ and $2.6 \leq \ln(\langle B_l \rangle / \mu) \leq 6.7$ or about 14 G to 810 G. Each bin represents an interval of 0.025 in μ and 0.1 in $\ln(\langle B_l \rangle / \mu)$. The logarithmic binning in $\langle B_l \rangle / \mu$ is to compensate for the bottom-heavy distribution of magnetogram signal, to ensure the distribution of points is not too concentrated in the lower magnetogram signal bins. At each grid element we considered the mean μ , $\langle B_l \rangle / \mu$, continuum and line core intensity contrast of the points within the bin. In accord with the cubic polynomial fits to the individual contrast CLV and contrast versus $\langle B_l \rangle / \mu$ profiles, bivariate polynomials cubic in μ and $\langle B_l \rangle / \mu$ were fitted to the bin-averaged continuum and line core intensity contrast. The zeroth μ and $\langle B_l \rangle / \mu$ orders were included based on similar considerations as with the polynomial fits to the contrast CLV and contrast versus $\langle B_l \rangle / \mu$ profiles. In linear algebra notation, the surface

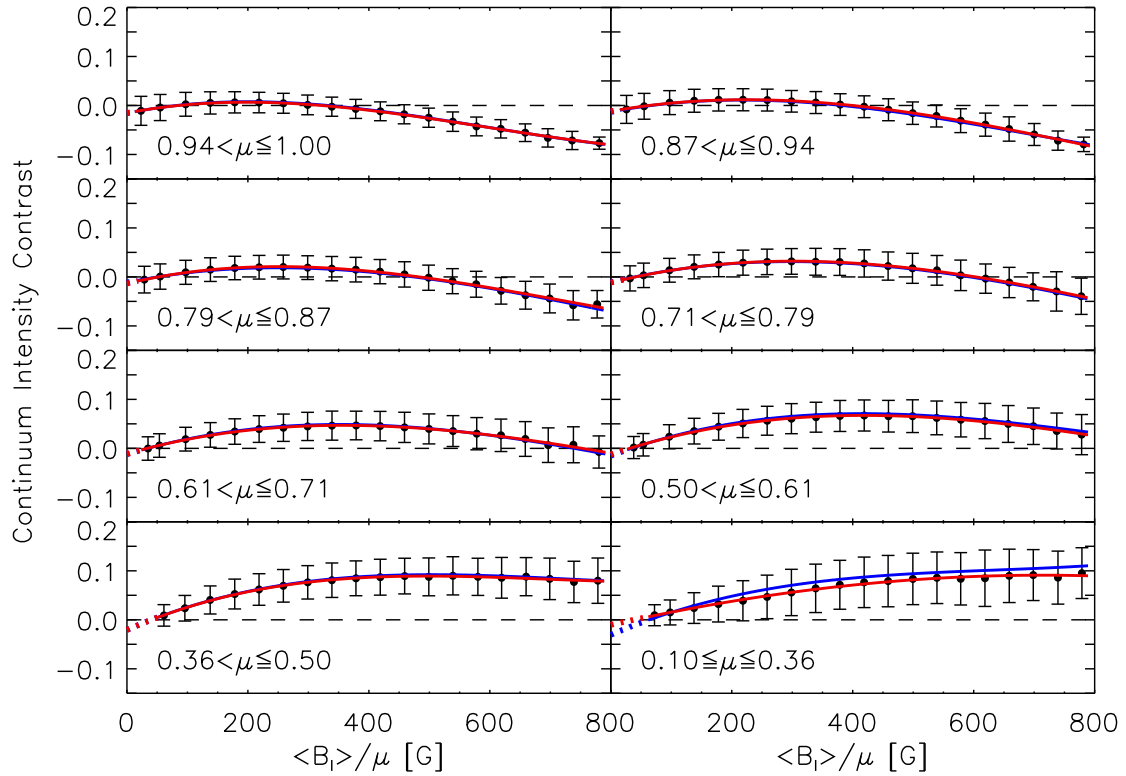


Figure 3.9: Continuum intensity contrast, C_{Ic} as a function of $\langle B_l \rangle / \mu$ over eight μ intervals. The filled circles and error bars represent the mean and standard deviation of C_{Ic} grouped by $\langle B_l \rangle / \mu$ in 40 G bins. The red and blue curves and the horizontal dashed lines have the same meanings as in Fig. 3.7.

fit to the bin-averaged continuum and line core intensity contrast are:

$$C_{Ic} \left(\mu, \frac{\langle B_l \rangle}{\mu} \right) = \begin{bmatrix} 10^{-2} \left(\frac{\langle B_l \rangle}{\mu} \right)^0 \\ 10^{-3} \left(\frac{\langle B_l \rangle}{\mu} \right)^1 \\ 10^{-6} \left(\frac{\langle B_l \rangle}{\mu} \right)^2 \\ 10^{-9} \left(\frac{\langle B_l \rangle}{\mu} \right)^3 \end{bmatrix}^T \begin{bmatrix} -5.11 & 7.74 & 0.34 & -4.72 \\ -0.04 & 3.84 & -7.42 & 3.90 \\ 0.19 & -6.27 & 12.03 & -6.78 \\ -0.08 & 3.58 & -8.04 & 5.04 \end{bmatrix} \begin{bmatrix} \mu^0 \\ \mu^1 \\ \mu^2 \\ \mu^3 \end{bmatrix} \quad (3.3)$$

and

$$C_{Il} \left(\mu, \frac{\langle B_l \rangle}{\mu} \right) = \begin{bmatrix} 10^{-1} \left(\frac{\langle B_l \rangle}{\mu} \right)^0 \\ 10^{-3} \left(\frac{\langle B_l \rangle}{\mu} \right)^1 \\ 10^{-5} \left(\frac{\langle B_l \rangle}{\mu} \right)^2 \\ 10^{-8} \left(\frac{\langle B_l \rangle}{\mu} \right)^3 \end{bmatrix}^T \begin{bmatrix} -1.08 & 2.09 & -1.78 & 0.66 \\ -0.08 & 6.84 & -11.22 & 6.34 \\ 0.07 & -1.50 & 2.52 & -1.48 \\ -0.06 & 1.03 & -1.90 & 1.18 \end{bmatrix} \begin{bmatrix} \mu^0 \\ \mu^1 \\ \mu^2 \\ \mu^3 \end{bmatrix} \quad (3.4)$$

respectively. Since contrast is wavelength dependent and bright magnetic features are largely unresolved at HMI's spatial resolution, these relationships are valid only at the instrument's operating wavelength (6173 Å) and spatial resolution (1 arcsec).

3 Intensity contrast of solar network and faculae

(The contents of this chapter are identical to the printed version of Yeo, K. L., Solanki, S. K., Krivova, N. A., 2013, *Intensity contrast of network and faculae*, *Astron. Astrophys.*, 550, A95.)

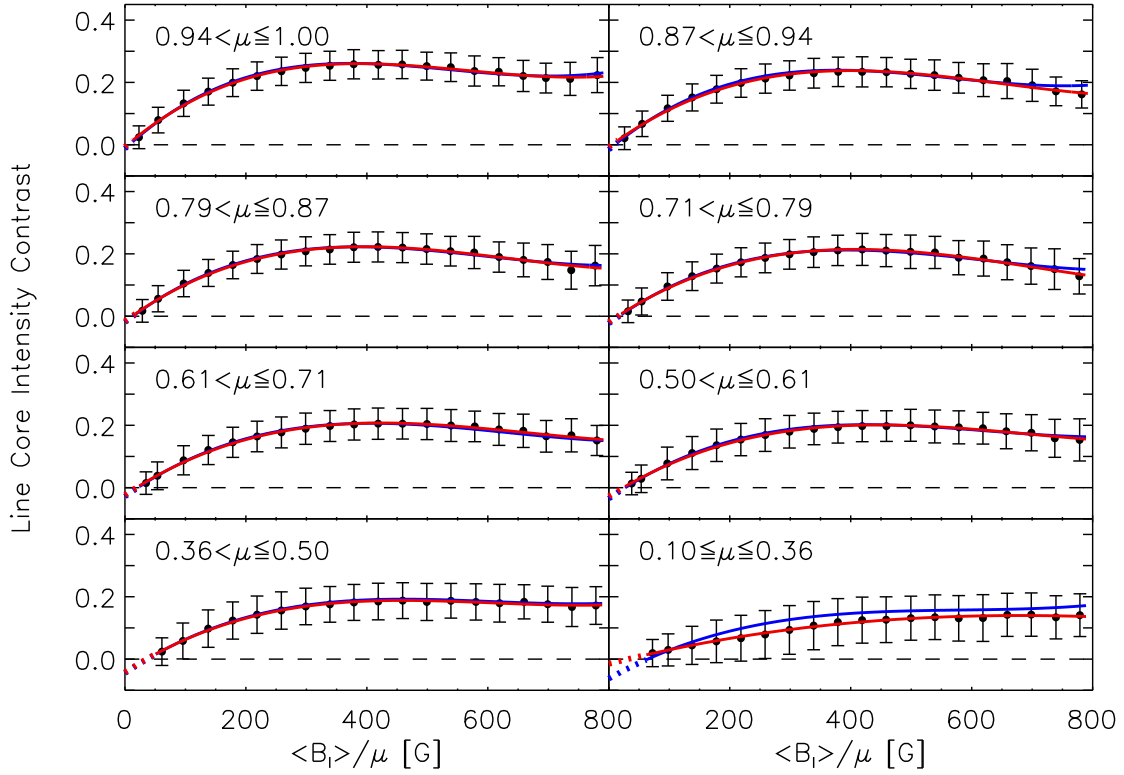


Figure 3.10: Similar to Fig. 3.9, but for line core intensity contrast.

The surface fits are illustrated as surface and grey scale plots in Figs. 3.12 and 3.13. Cross-sections to the surface fits are plotted in Figs. 3.7 to 3.10 (blue curves) along the contrast CLV and contrast versus $\langle B_l \rangle / \mu$ profiles, and the corresponding cubic polynomial fits (red curves). The surface fits are in excellent agreement with the cubic polynomial fits almost everywhere. The agreement is so close that the surface fit cross-sections are completely hidden by the cubic polynomial fits in most places. The advantage with these surface fits is that they allow us to describe how the measured contrasts vary with μ and $\langle B_l \rangle / \mu$ almost equally well and with far fewer free parameters than by the cubic polynomial fit to each individual contrast CLV and contrast versus $\langle B_l \rangle / \mu$ profile (32 versus 128 free parameters; 4 from each of 32 profiles).

3.3.3 Intrinsic contrast

At each $\langle B_l \rangle / \mu$ interval, we estimated the maximum continuum intensity contrast, $C_{Ic,max}$ and the heliocentric angle at which it is reached, μ_{max} from the cubic polynomial fit to the contrast CLV profile (Fig. 3.7). Following Ortiz et al. (2002) we term $C_{Ic,max} / (\langle B_l \rangle / \mu)$ the specific contrast; estimated here from the quotient of $C_{Ic,max}$ and $\langle \langle B_l \rangle / \mu \rangle$, the mean $\langle B_l \rangle / \mu$ of all the points within a given $\langle B_l \rangle / \mu$ interval. The values of μ_{max} , $C_{Ic,max}$ and $C_{Ic,max} / (\langle B_l \rangle / \mu)$ are shown in Fig. 3.14 as a function of $\langle B_l \rangle / \mu$ where the abscissa is given by $\langle \langle B_l \rangle / \mu \rangle$. Also plotted are the values obtained from the surface fit (Equation 3.3). The uncertainty in $C_{Ic,max}$ is given by the RMS difference between the contrast CLV profiles and their cubic polynomial fits. The uncertainty in $C_{Ic,max} / (\langle B_l \rangle / \mu)$ was

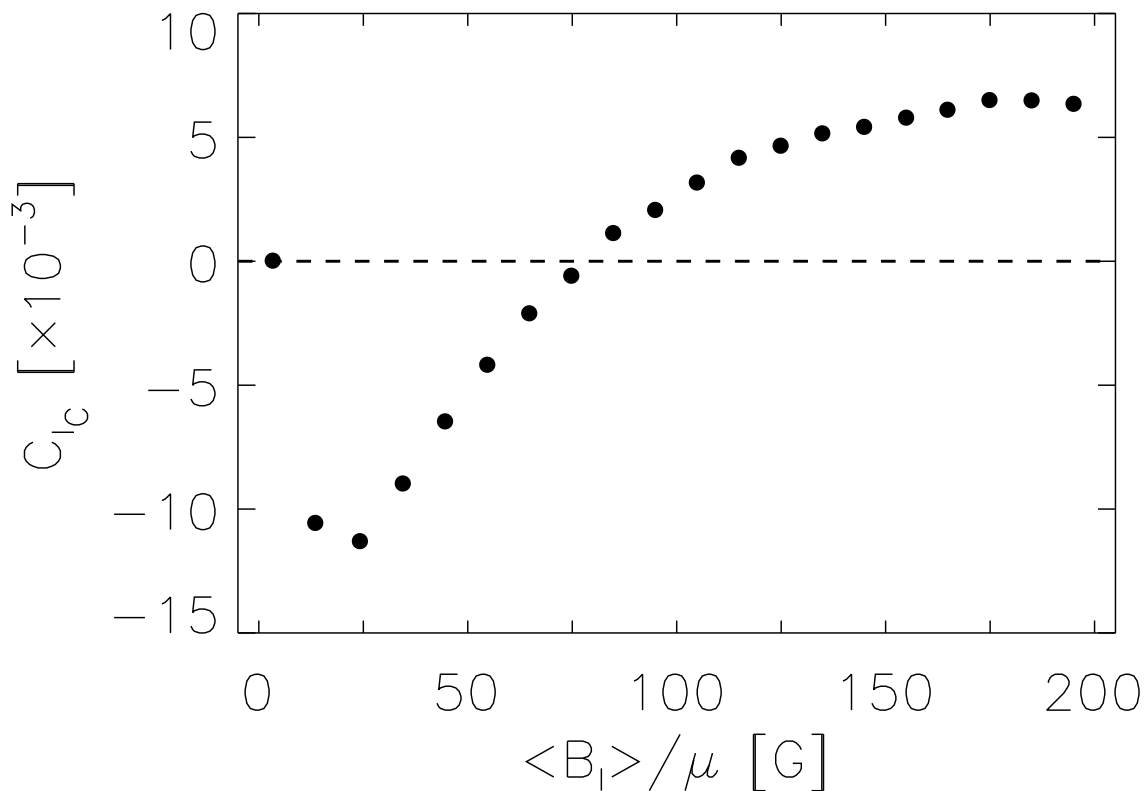


Figure 3.11: Continuum intensity contrast, C_{Ic} of quiet Sun, network and faculae over $0.94 < \mu \leq 1.00$ as a function of $\langle B_l \rangle / \mu$. The filled circles represent the mean of C_{Ic} grouped by $\langle B_l \rangle / \mu$ in bins 10 G wide. The dashed line denotes the mean quiet Sun level.

estimated from the uncertainty in $C_{Ic,max}$ and the standard error of $\langle \langle B_l \rangle / \mu \rangle$ employing standard propagation of errors.

While the position of the continuum intensity contrast CLV maximum varies with $\langle B_l \rangle / \mu$, line core intensity contrast at a given $\langle B_l \rangle / \mu$ is invariably strongest at disc centre (Fig. 3.8) as pointed out in Sect. 3.3.1. Maximum line core intensity contrast (i.e., the value at $\mu = 1$), $C_{Ic,\mu=1}$ and specific contrast, $C_{Ic,\mu=1} / (\langle B_l \rangle / \mu)$ derived similarly as above from the cubic polynomial fit to the contrast CLV profiles are expressed in Fig. 3.15 as a function of $\langle B_l \rangle / \mu$, along with the values obtained from the surface fit (Eq. 3.4). In both instances, there is some disparity between the values obtained from the cubic polynomial fits to the contrast CLV profiles and the surface fit below $\langle B_l \rangle / \mu \sim 100$ G. This is likely due to the truncated coverage of disc positions at low $\langle B_l \rangle / \mu$ discussed in Sect. 3.3.1.

Network and facular features exhibit similar, kilogauss strength magnetic fields (Stenflo 1973, Solanki and Stenflo 1984, Rabin 1992, Rüedi et al. 1992). This means, in general, the intrinsic magnetic field strength of magnetic elements, B does not vary significantly with $\langle B_l \rangle / \mu$ and is also well above the range of $\langle B_l \rangle / \mu$ examined here, thus allowing us to assume that the magnetic filling factor, α never saturates. As mentioned in Sect. 3.2.1, the quantity $\langle B_l \rangle / \mu$ is representative of αB . Taking these into account, within the limits of this study, $\langle B_l \rangle / \mu$ is representative of the magnetic filling factor. Therefore specific contrast, as it is defined and derived here, is a measure of the average intrinsic

3 Intensity contrast of solar network and faculae

(The contents of this chapter are identical to the printed version of Yeo, K. L., Solanki, S. K., Krivova, N. A., 2013, *Intensity contrast of network and faculae*, *Astron. Astrophys.*, 550, A95.)

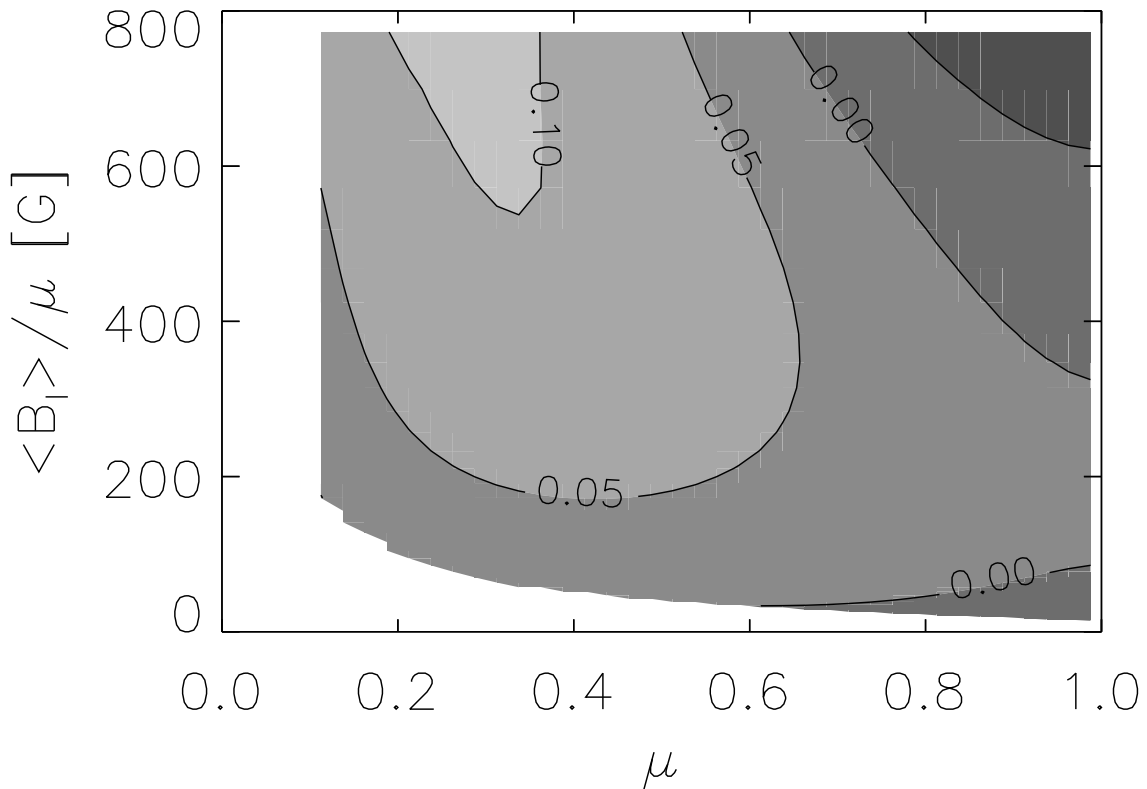


Figure 3.12: Grey scale plot of the polynomial fit to bin-averaged continuum intensity contrast over the region where data exist, sampled at the mid-point of each bin in the 36×41 bins grid employed to compute the averages.

contrast or heating efficiency of magnetic features within a given $\langle B_l \rangle / \mu$ interval. Like the intrinsic field strength, the intrinsic contrast cannot be measured directly because most network and facular features are not resolved at HMI's spatial resolution and due to the effect of scattered light.

Above $\langle B_l \rangle / \mu \sim 100$ G, the heliocentric angle at which continuum intensity contrast reaches its maximum decreases (i.e., the maximum is reached further away from disc centre) with increasing $\langle B_l \rangle / \mu$ (Fig. 3.14). A similar trend was reported by Ortiz et al. (2002) based on MDI continuum observations. Assuming the hot wall model (Spruit 1976) and a simple flux tube geometry, the authors demonstrated this to imply the average size of flux tubes increases with $\langle B_l \rangle / \mu$.

Both continuum and line core intensity specific contrast increases strongly with decreasing $\langle B_l \rangle / \mu$ up to a maximum (at around 200 and 50 G respectively) before gradually declining (Figs. 3.14 and 3.15). The decline at low $\langle B_l \rangle / \mu$ aside, the observed trends suggests that brightness or temperature excess in both the lower and middle photosphere in flux tubes decreases with increasing magnetic filling factor (the continuum and line core formation height of the Fe I 6173 Å line is about 20 and 300 km respectively, Norton et al. 2006). This may partly be due to the increasing average size of flux tubes; larger magnetic elements appear darker as lateral heating is less efficient (Spruit 1976, Spruit and Zwaan 1981, Grossmann-Doerth et al. 1994) and magnetic suppression of surround-

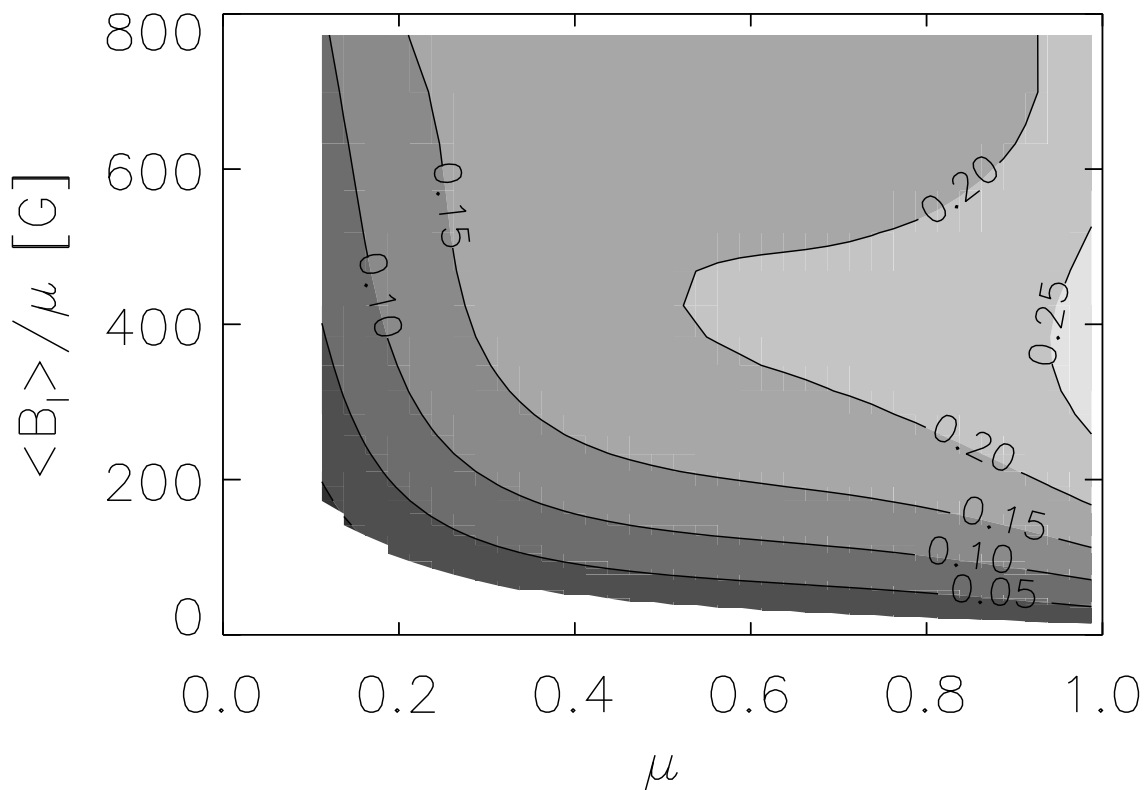


Figure 3.13: Same as Fig. 3.12, but for line core intensity contrast.

ing convective energy transport is more severe (Kobel et al. 2012). The total radiation flux derived from MHD simulations by Vögler (2005) exhibits a similar behaviour. This result also agrees with the observations that network elements appear hotter than facular elements in the lower and middle photosphere (Solanki and Stenflo 1984, Solanki 1986, Keller et al. 1990) and G-band bright points are brighter in the quiet Sun than in active regions (Romano et al. 2012).

The decline in both continuum and line core specific contrast at low $\langle B_l \rangle / \mu$ suggests a diminishing heating efficiency of the smallest magnetic elements but is more likely due to the influence of intergranular lanes on apparent contrast. (As with the low contrast towards $\langle B_l \rangle / \mu = 0$ G in the contrast versus $\langle B_l \rangle / \mu$ profiles discussed in Sect. 3.3.1.) The probable impact of the truncated coverage of disc positions at low $\langle B_l \rangle / \mu$ on the quality of the fits to measured contrast here might have also played a role.

3.4 Discussion

3.4.1 Comparison with Ortiz et al. (2002)

A comparison of the results reported here for continuum intensity with those from the similar study based on full-disc MDI observations by Ortiz et al. (2002) reveal several notable differences.

- The contrast reported here is generally higher, by as much as a factor of about

3 Intensity contrast of solar network and faculae

(The contents of this chapter are identical to the printed version of Yeo, K. L., Solanki, S. K., Krivova, N. A., 2013, *Intensity contrast of network and faculae*, *Astron. Astrophys.*, 550, A95.)

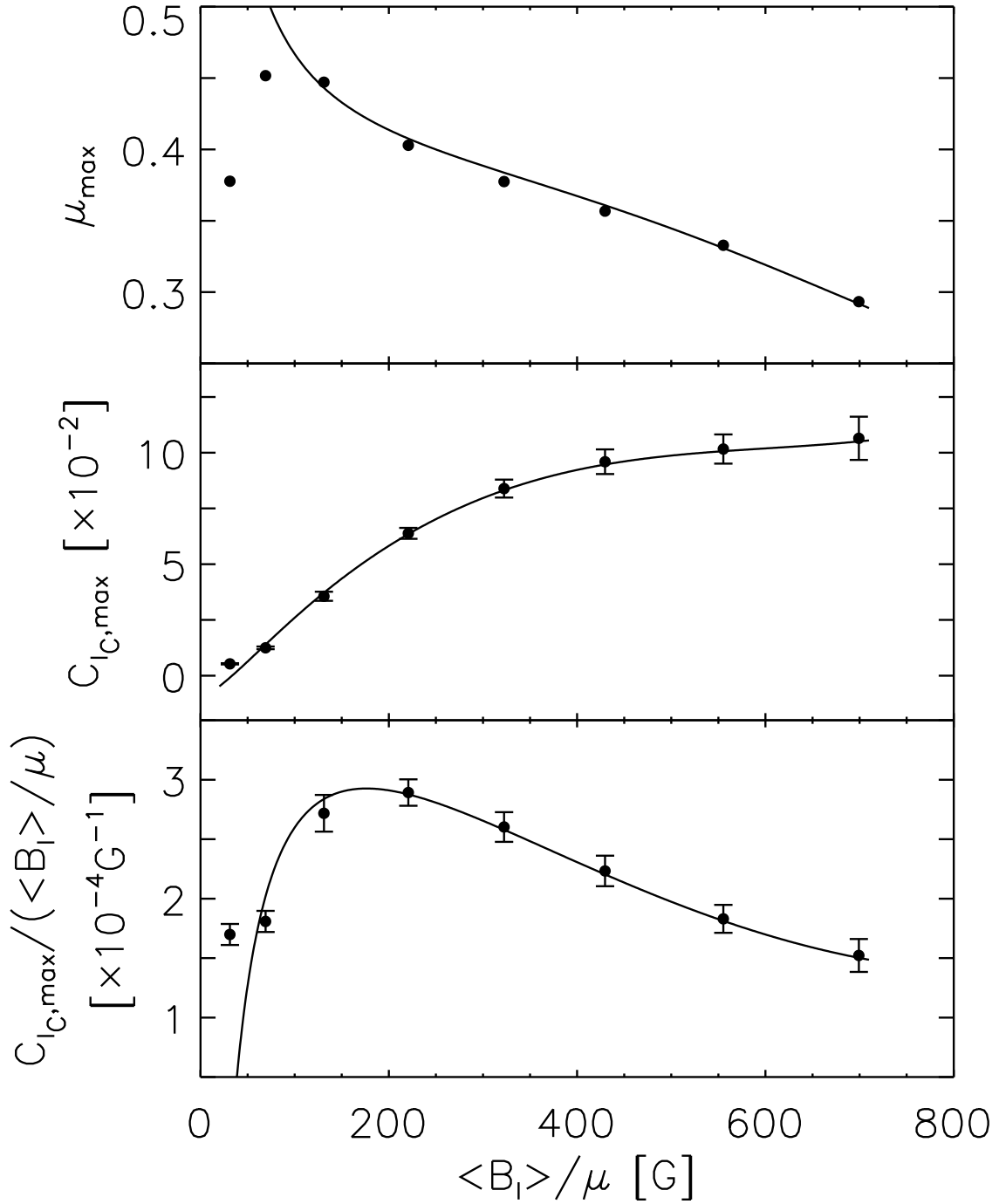


Figure 3.14: Heliocentric angle at which continuum intensity contrast reaches its maximum, μ_{\max} (top), as well as the contrast, $C_{I_C, \max}$ (middle) and specific contrast, $C_{I_C, \max} / (\langle B_l \rangle / \mu)$ (bottom) there, as a function of $\langle B_l \rangle / \mu$. The filled circles represent the values derived from the cubic polynomial fit to the contrast CLV profiles (Fig. 3.7) and the error bars the uncertainty in $C_{I_C, \max}$ and $C_{I_C, \max} / (\langle B_l \rangle / \mu)$. The curves follow the solution from the surface fit to measured continuum intensity contrast (Eq. 3.3).

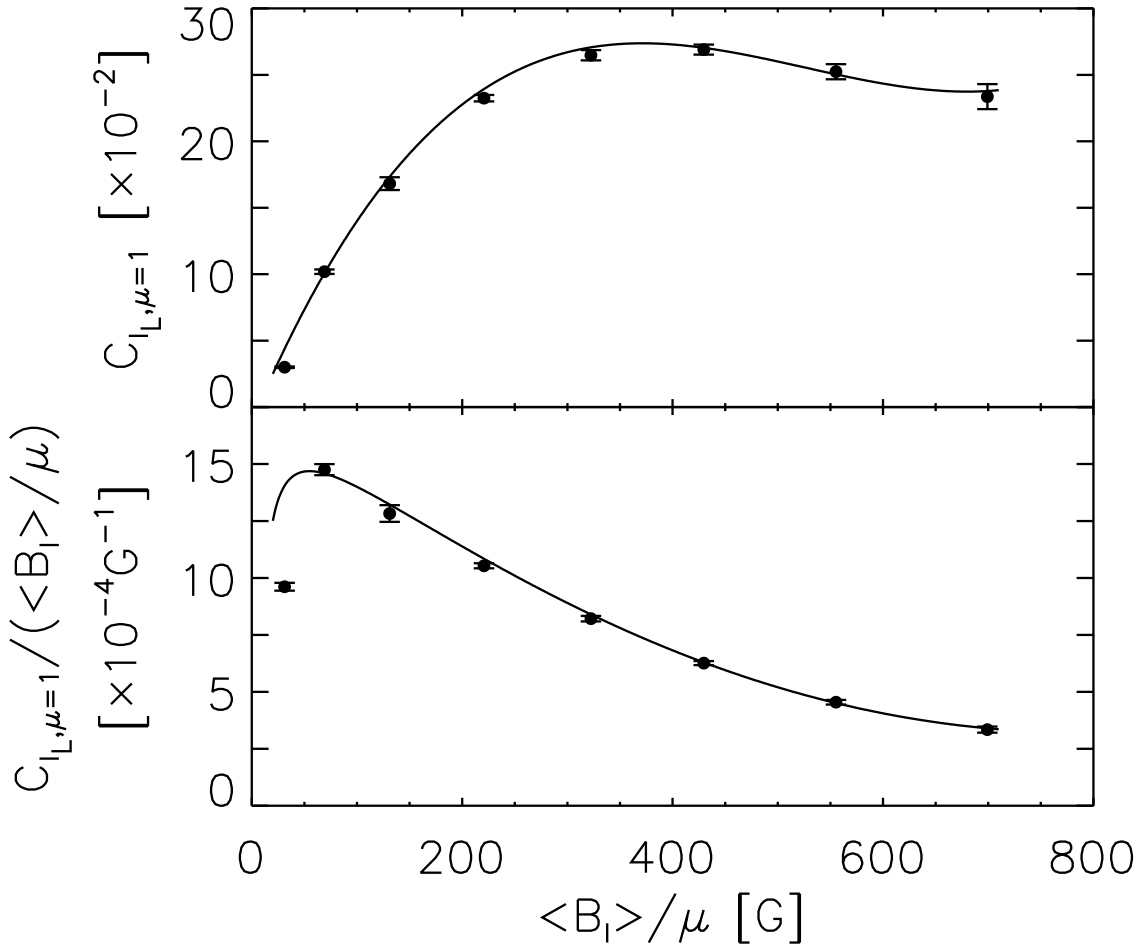


Figure 3.15: Line core intensity contrast, $C_{I_L, \mu=1}$ (top) and specific contrast, $C_{I_L, \mu=1} / (\langle B_l \rangle / \mu)$ (bottom) at disc centre as a function of $\langle B_l \rangle / \mu$. The filled circles represent the values derived from the cubic polynomial fit to the contrast CLV profiles (Fig. 3.8) and the error bars the uncertainty in $C_{I_L, \mu=1}$ and $C_{I_L, \mu=1} / (\langle B_l \rangle / \mu)$. The curves follow the solution from the surface fit to measured line core intensity contrast (Eq. 3.4).

two. The difference between the two studies becomes increasingly pronounced with $\langle B_l \rangle / \mu$ and distance from disc centre.

- Approaching disc centre, contrast appears to level off in our study (Fig. 3.7). In the earlier work, the contrast declines approximately linearly towards $\mu = 1$ and there are also marked fluctuations about $\mu \sim 0.95$ (Fig. 3, Ortiz et al. 2002).
- Near $\langle B_l \rangle / \mu = 0$ G contrast is negative here (Fig. 3.9) but positive in the previous study (Fig. 4, Ortiz et al. 2002).
- The specific contrast (a proxy of intrinsic contrast given by the quotient of contrast at the maximum point on the CLV profile and $\langle B_l \rangle / \mu$) presented here ascends with $\langle B_l \rangle / \mu$ up to $\langle B_l \rangle / \mu \sim 200$ G before descending monotonically thereafter (Fig. 3.14). Ortiz et al. (2002) found specific contrast to decline approximately linearly with $\langle B_l \rangle / \mu$ (Fig. 8 in their paper).

3 Intensity contrast of solar network and faculae

(The contents of this chapter are identical to the printed version of Yeo, K. L., Solanki, S. K., Krivova, N. A., 2013, Intensity contrast of network and faculae, Astron. Astrophys., 550, A95.)

- For $\langle B_l \rangle / \mu \gtrsim 200$ G, the specific contrast reported here is also nearly double that in the earlier work.

The lower contrast and specific contrast (for $\langle B_l \rangle / \mu \gtrsim 200$ G), and difference in CLV towards disc centre reported by Ortiz et al. (2002) is likely, as we will show shortly, to be primarily due to the misidentification of the magnetic signal adjacent to sunspots and pores as network and faculae (discussed in Sect. 3.2.2) by those authors. Care was taken here to minimise such misidentification. The negative contrast towards $\langle B_l \rangle / \mu = 0$ G found here, as argued in Sect. 3.3.1, arises from the resolution of intergranular lanes at HMI's spatial resolution. We demonstrate below that this difference in spatial resolution also contributes to the opposite $\langle B_l \rangle / \mu$ -dependence of specific contrast below $\langle B_l \rangle / \mu \sim 200$ G reported here and by Ortiz et al. (2002).

To recreate the conditions of the study by Ortiz et al. (2002), we recomputed continuum intensity contrast and specific contrast from the HMI data set employed here without applying the magnetic extension removal procedure, binning the data set spatially by 4×4 pixels to be consistent with MDI's spatial resolution and (very approximately) transforming measured contrast to the corresponding value at MDI's operating wavelength, 6768 Å. This last transformation was carried out by describing quiet Sun, network and faculae as black bodies, and taking an effective temperature of 5800 K for the quiet Sun. This allowed us to crudely convert contrast measured at 6173 Å by HMI into the corresponding contrast at 6768 Å. It should be noted that this is a first-order approximation of the wavelength dependence of contrast which ignores the variation of the continuum formation height with wavelength (Solanki and Unruh 1998, Sütterlin et al. 1999, Norton et al. 2006). In Fig. 3.16 we depict the contrast CLV profile of network patterns ($50 \text{ G} < \langle B_l \rangle / \mu \leq 100 \text{ G}$) and active region faculae ($500 \text{ G} < \langle B_l \rangle / \mu \leq 640 \text{ G}$) after the application of the above procedure. Also plotted are the similarly treated contrast versus $\langle B_l \rangle / \mu$ profiles about disc centre ($0.94 < \mu \leq 1.00$) and near limb ($0.36 < \mu \leq 0.50$). The specific contrasts from this process are illustrated in Fig. 3.17.

Excluding the procedure to remove magnetic signal adjoined to sunspots and pores produced the largest effect. It produced an overall drop in contrast (cyan series, Fig. 3.16) and also reproduced the linear CLV near disc centre observed by Ortiz et al. (2002) ($640 \text{ G} < \langle B_l \rangle / \mu \leq 800 \text{ G}$ panel). The effects of the resizing of the data set (blue series) and the projection of measured contrasts to MDI's operating wavelength (green series) are relatively minor. The contrast profiles derived from the application of all three procedures (red series) are, in terms of both form and magnitude, in general agreement with the profiles covering similar disc positions and magnetogram signal levels reported by Ortiz et al. (2002) (Figs. 3 and 4 in their paper).

Similarly for specific contrast, the result of applying all three processes (red series, Fig. 3.17) resembles the measurements presented by Ortiz et al. (2002) (Fig. 8 in their paper) and the greatest effect on magnitude came from the omission of the magnetic extension removal procedure. Binning the data set down to a MDI-like resolution also produced a significant increase in specific contrast at low $\langle B_l \rangle / \mu$. After combining with the other two processes, this rendered specific contrast approximately level below 200 G. The influence of granulation on apparent contrast at HMI's spatial resolution plays a role in the observed decline in specific contrast from $\langle B_l \rangle / \mu \sim 200$ G towards $\langle B_l \rangle / \mu = 0$ G.

The largest effect is produced by the removal of magnetic signal adjoining to sunspots and pores. Hence it is worth considering this process more closely. The procedure by

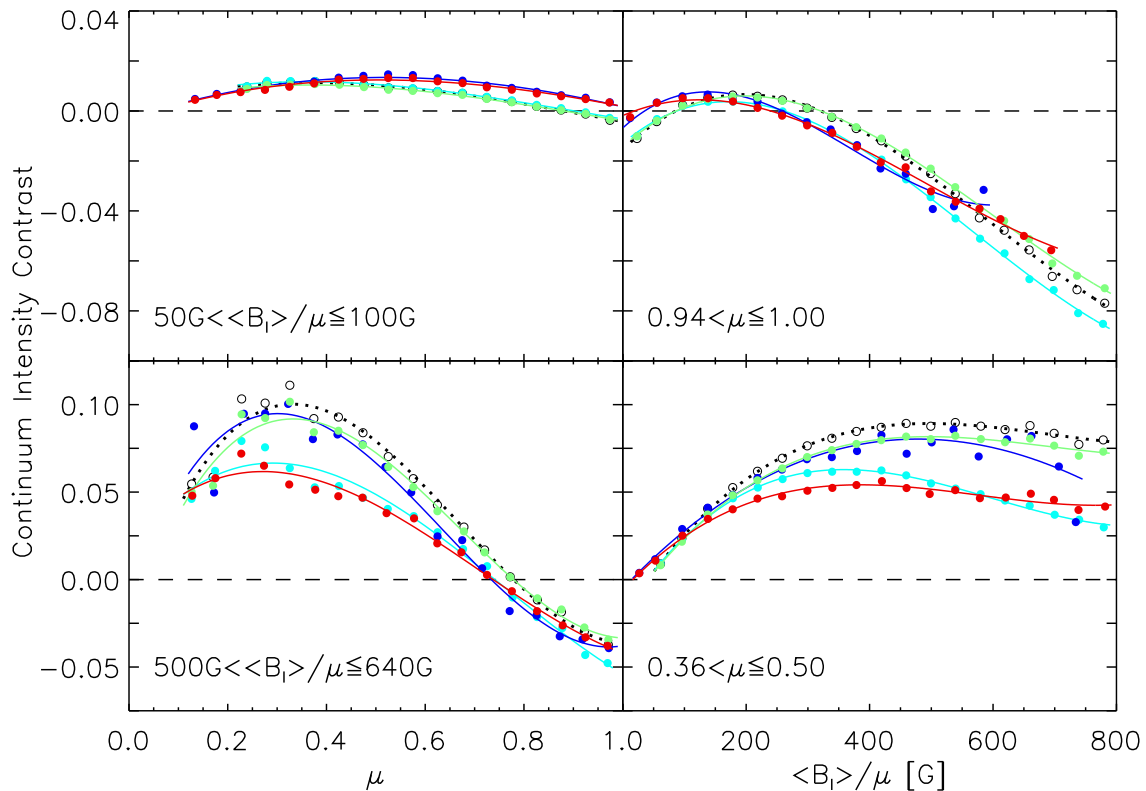


Figure 3.16: Selected continuum intensity contrast CLV (left) and contrast versus $\langle B_l \rangle / \mu$ (right) profiles from Figs. 3.7 and 3.9 (open circles and dotted curves). The selected profiles correspond to quiet Sun network (top left), active region faculae (bottom left), disc centre (top right) and near limb (bottom right). The cyan, blue and green series denote the profiles obtained by omitting the magnetic extension removal procedure, spatially binning the data set by 4×4 pixels and converting measured contrast to 6768 Å respectively. The red series indicates the results of taking into account all these three considerations. The circles represent the mean of measured contrast binned as in the referenced figures and the curves the corresponding third-order polynomial fits. The dashed lines mark the mean quiet Sun level.

which we removed these signals inevitably discriminates against active region faculae, and various authors have noted lower contrast in active region faculae compared to quiet Sun network at similar magnetogram signal levels (Lawrence et al. 1993, Kobel et al. 2011), but we do not reckon this to be the reason for the greater contrast reported here. In spite of the severe steps taken to exclude magnetic signals adjoined to sunspots and pores, there remains a fair representation of active region faculae in the measured contrasts (Fig. 3.5). Also, at HMI's spatial resolution, network patterns are largely confined to the lower half of the $\langle B_l \rangle / \mu$ range considered (Fig. 3.6) while the difference between the contrast reported here and by Ortiz et al. (2002) is more pronounced at higher $\langle B_l \rangle / \mu$.

Following the example of earlier studies (e.g. Chapman 1980), Ortiz et al. (2002) fit quadratic polynomials to continuum intensity contrast CLV profiles derived in their study. Here we fit cubic polynomials instead because of the different CLV near disc centre which

3 Intensity contrast of solar network and faculae

(The contents of this chapter are identical to the printed version of Yeo, K. L., Solanki, S. K., Krivova, N. A., 2013, *Intensity contrast of network and faculae*, *Astron. Astrophys.*, 550, A95.)

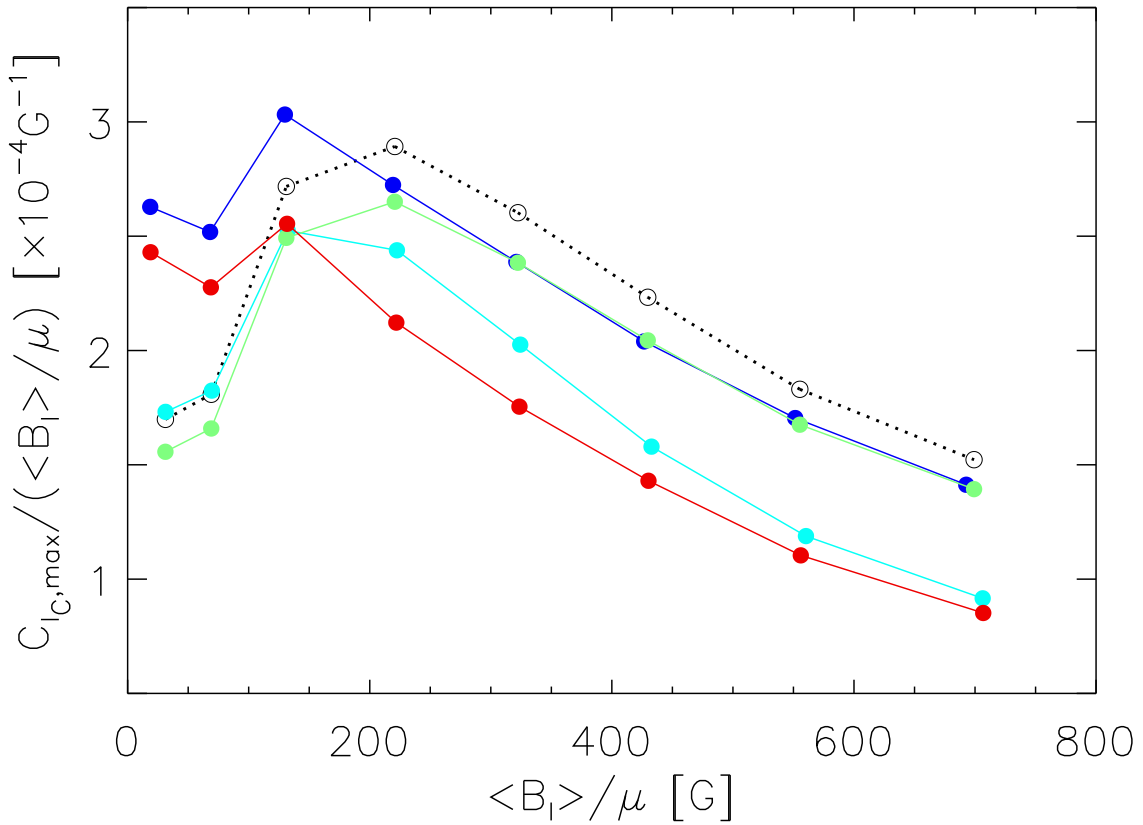


Figure 3.17: Continuum intensity specific contrast as a function of $\langle B_l \rangle / \mu$ from Fig. 3.14 (open circles). The cyan, blue and green filled circles represent the same quantity obtained by omitting the magnetic extension removal procedure, spatially binning the data set by 4×4 pixels and converting measured contrast to 6768 Å respectively. The red filled circles represent the result of taking into account all these three considerations. The points in each series are joined by straight lines to aid the eye.

we just demonstrated to arise from our treatment of magnetic signal adjoined to sunspots and pores.

We surmise that the fluctuations about disc centre in the continuum intensity CLV profiles reported by Ortiz et al. (2002) is due to the non-homogeneous distribution of active regions over the solar disc. Each unit μ represents a greater radial distance towards the disc centre rendering these fluctuations increasingly abrupt. Not accounting for magnetic signal adjoined to sunspots and pores probably accentuated these fluctuations.

3.4.2 Continuum intensity contrast about disc centre

In this section we compare the magnetogram signal dependence of continuum intensity contrast near disc centre reported here with that from other recent studies, summarized in Table 3.2. Apart from the work of Ortiz et al. (2002), the CLV of continuum intensity contrast has been examined in detail previously by Topka et al. (1992, 1997) and Lawrence et al. (1993). While we and Ortiz et al. (2002) employed full-disc observations

made at a single wavelength and spatial resolution, these authors collated telescope scans made at multiple wavelengths and resolutions. The magnetogram signal intervals represented by the contrast CLV profiles presented in these papers also differ considerably from those presented here and by Ortiz et al. (2002). For these reasons it is not straightforward to make any quantitative comparisons with the contrast CLV reported by these studies, therefore the focus on results for near disc centre here.

The negative contrast at low magnetogram signal levels found here and by the majority of the compared works counters expectations from thin flux tube models, which predict intrinsically bright magnetic features in this regime (Knölker et al. 1988). As discussed in Sect. 3.3.1, this is attributed here (and in Title et al. 1992, Topka et al. 1992, Kobel et al. 2011) to the influence of intergranular lanes, an assertion supported by various models (Title and Berger 1996, Schnerr and Spruit 2011). Of the studies compared, only that by Ortiz et al. (2002) noted positive contrasts. Binning the data set here to a MDI-like resolution raised the disc centre end of the contrast CLV profile in the $50 \text{ G} < \langle B_l \rangle / \mu \leq 100 \text{ G}$ interval into positive territory (Fig. 3.16), suggesting that the positive contrasts reported by Ortiz et al. (2002) arose from utilising data at a resolution (the lowest of the studies compared) where granulation is largely unresolved.

From SVST scans of active regions, Title et al. (1992), Topka et al. (1992, 1997) and Lawrence et al. (1993) found contrast to decline monotonically with magnetogram signal. Lawrence et al. (1993) also noted the same with active region data acquired at the San Fernando Observatory (SFO). Kobel et al. (2011) demonstrated the comparatively poorer resolution and straylight from pores to be likely culpable for the monotonic decline observed in the SVST studies. In all the other compared works, contrast exhibits a peak, the position of which varied from $\langle B_l \rangle / \mu \sim 100 \text{ G}$ (Ortiz et al. 2002) to $\langle B_l \rangle \sim 700 \text{ G}$ (Kobel et al. 2011), except for the quiet Sun SST scan examined by Schnerr and Spruit (2011), where contrast saturated at $\langle B_l \rangle \sim 800 \text{ G}$. Generally, the finer the spatial resolution, the higher the position of the peak. Most of these studies were based on observations made at the Fe I 6302 Å line. Even if we discount the studies made at other wavelengths, this broad pattern is still apparent, ruling out differences in wavelength as the major driver. Kobel et al. (2011) reported similar contrast peak positions for quiet Sun and active region scans. Therefore the difference between active region and quiet Sun contrast had likely little role in the spread in reported peak positions amongst the compared works. As shown in the $0.94 < \mu \leq 1.00$ panel of Fig. 3.16, both resizing the HMI data set to a MDI-like spatial resolution and omitting the magnetic extension removal procedure shifted the position of the contrast versus $\langle B_l \rangle / \mu$ profile maximum towards the origin.

The above comparison points to differences in spatial resolution and treatment of magnetic signal near sunspots and pores as the dominant factors behind the spread in reported dependence of contrast on magnetogram signal. Indeed, the recent MHD simulation work of Röhrbein et al. (2011) suggests that the contrast peak at intermediate magnetogram signal levels seen in direct observations, but not observed in MHD simulations, is a product of the limited spatial resolution. The bulk of the studies listed in Table 3.2 were based on higher spatial resolution data than utilised here. For this reason, a more quantitative comparison like we did in Sect. 3.4.1 with the findings of Ortiz et al. (2002) is not workable here.

The recent works of Berger et al. (2007) and Viticchié et al. (2010), examining the contrast of bright points in the G-band, bear tenuous relevance to our study. These studies

3 Intensity contrast of solar network and faculae

(The contents of this chapter are identical to the printed version of Yeo, K. L., Solanki, S. K., Krivova, N. A., 2013, *Intensity contrast of network and faculae*, *Astron. Astrophys.*, 550, A95.)

Table 3.2: Continuum intensity contrast dependence on magnetogram signal near disc centre obtained in the present and from earlier studies.

Reference	Instrument	Target ^b	Resolution [Arcsec]	Wavelength [Å]	Results
Present 1, 2, 3, 4	SDO/HMI	$\mu > 0.94^c$	1	6173	Negative near $\langle B_l \rangle / \mu = 0$ G. Peak at $\langle B_l \rangle / \mu \sim 200$ G.
	SVST	AR	$\gtrsim 0.3$	Various ^d	Negative near $\langle B_l \rangle = 0$ G. Monotonic decline with $\langle B_l \rangle$.
3	SVST	QS	$\gtrsim 0.3$	6302	Negative near $\langle B_l \rangle = 0$ G. Peak at $\langle B_l \rangle \sim 400$ G.
	SFO/SHG ^e	QS	$\gtrsim 1$	6302	Negative near $\langle B_l \rangle = 0$ G. Peak at $100 \text{ G} \lesssim \langle B_l \rangle \lesssim 200$ G.
5	SoHO/MDI	AR	4	6768	Negative near $\langle B_l \rangle = 0$ G. Monotonic decline with $\langle B_l \rangle$.
					Positive near $\langle B_l \rangle / \mu = 0$ G. Peak at $\langle B_l \rangle / \mu \sim 100$ G.
6	SST	AR	0.15	6302	Negative near $\langle B_l \rangle = 0$ G. Peak at $\langle B_l \rangle \sim 650$ G.
7	Hinode/SOT	QS	0.3	6302	Negative near $\langle B_l \rangle = 0$ G. Peak at $\langle B_l \rangle \sim 700$ G.
		AR			Negative near $\langle B_l \rangle = 0$ G. Peak at $\langle B_l \rangle \sim 700$ G.
8	SST	QS	0.15	6302	Negative near $\langle B_l \rangle = 0$ G. Saturate at $\langle B_l \rangle \sim 800$ G.
		Hinode/SOT	QS	0.3	6302

Notes. ^(a) San Fernando Observatory (SFO) 28-cm vacuum telescope and vacuum spectroheliograph (SHG). ^(b) AR and QS denote active region and quiet Sun respectively. ^(c) Segment of full-disc observations considered. ^(d) 5250Å, 5576Å, 6302Å and 6768Å.

References. (1) Title et al. (1992); (2) Topka et al. (1992); (3) Lawrence et al. (1993); (4) Topka et al. (1997); (5) Ortiz et al. (2002); (6) Narayan and Scharmer (2010); (7) Kobel et al. (2011); (8) Schnerr and Spruit (2011).

utilised observations made in a molecular band (i.e., neither continuum nor line core) where the contrast of magnetic features is enhanced (due to CH depletion, Steiner et al. 2001, Schüssler et al. 2003). More importantly, while this study and the works cited in Table 3.2 considered each pixel a separate entity, Berger et al. (2007) and Viticchié et al. (2010) examined the overall contrast of each individual bright structure. As the body of magnetic features isolated by both approaches differ, the results are not directly comparable. Berger et al. (2007) did however also report a pixel-by-pixel consideration of G-band contrast. Scans at four disc positions were surveyed. Barring one that appeared anomalous, the contrast versus magnetogram signal profiles from each scan bear general resemblance to ours in terms of form. Notably, the profile from the disc centre scan, with a spatial resolution of 0.15 arcsec, exhibits a peak at $\langle B_l \rangle \sim 700$ G, consistent with the broad pattern between spatial resolution and peak position described here.

3.4.3 Line core intensity contrast

As pointed out in Sect. 3.3.1, the most notable difference between the continuum and line core intensity contrasts present here is the converse CLV. While continuum intensity contrast is weakest near disc centre and strengthens towards the limb, line core intensity contrast is strongest at disc centre and declines towards the limb. The divergent CLV exhibited by the two sets of measurements stem from their rather different physical sources. Continuum intensity is enhanced largely in the hot walls of magnetic elements, thus the centre-to-limb increase. The line core is formed in the middle photosphere, which is heated either by radiation from deeper layers (Knölker et al. 1991), or by mechanical and Ohmic dissipations (Moll et al. 2012). Also stated in Sect. 3.3.1, line core intensity is modulated by line strength and shape, and continuum intensity. Excluding variation related to continuum excess, line core intensity enhancement arises from the influence of the temperature excess in the middle photosphere and Zeeman splitting on line strength and shape. Given the relatively narrow, vertical geometry of flux tubes, as magnetic elements rotate from disc centre to limb, line-of-sight rays go from being largely confined to single flux tubes to increasingly passing into and out of multiple flux tubes, especially in densely packed facular regions (Bunte et al. 1993). Line core intensity contrast decreases towards the limb as the contribution to the spectral line from magnetic elements diminishes from absorption in the non-magnetic part of the atmosphere transversed by the rays (Solanki et al. 1998). Another probable cause of the centre-to-limb decline is the spatial displacement of the line core with respect to the corresponding continuum towards the limb caused by the difference in formation height and oblique viewing geometry (Stellmacher and Wiehr 1991, 2001). The line core intensity enhancement arising from temperature excess in the middle photosphere and Zeeman splitting discussed here is not to be confused with that from the centre-to-limb broadening of the Fe I 6173 Å line mentioned in Sect. 3.2.2.2, which arises from the viewing geometry independent of magnetic field.

We recomputed line core intensity contrast, this time normalizing the line core intensity images by the corresponding continuum intensity images prior to data reduction. The result, the line core residual intensity contrast, is essentially the component of line core intensity contrast arising from line weakening in magnetic features alone. Line core intensity and residual intensity contrast values can be compared directly. (Line core residual

3 Intensity contrast of solar network and faculae

(The contents of this chapter are identical to the printed version of Yeo, K. L., Solanki, S. K., Krivova, N. A., 2013, *Intensity contrast of network and faculae*, *Astron. Astrophys.*, 550, A95.)

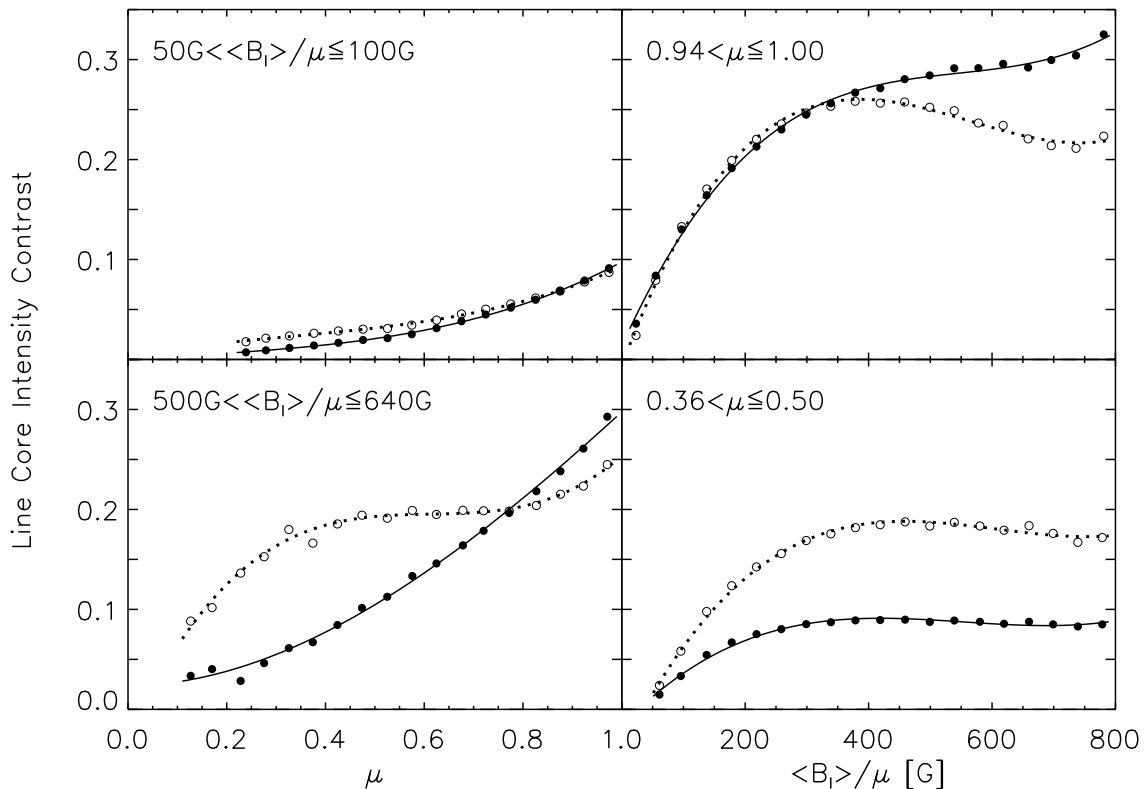


Figure 3.18: Selected line core intensity (open circles and dotted curves) and corresponding residual intensity (filled circles and solid curves) contrast CLV (left) and contrast versus $\langle B_l \rangle / \mu$ (right) profiles. The circles represent the mean of measured contrast binned as in Figs. 3.8 and 3.10 and the curves the corresponding cubic polynomial fits. The selected profiles correspond to quiet Sun network (top left), active region faculae (bottom left), disc centre (top right) and near limb (bottom right).

intensity contrast equates to the line core intensity contrast we would get from scaling the line core intensity of just the network and faculae pixels by $\langle I_{C, QS} \rangle / I_C$.) The line core residual intensity contrast CLV profile of network patterns ($50 \text{ G} < \langle B_l \rangle / \mu \leq 100 \text{ G}$) and active region faculae ($500 \text{ G} < \langle B_l \rangle / \mu \leq 640 \text{ G}$), and contrast versus $\langle B_l \rangle / \mu$ profile about disc centre ($0.94 < \mu \leq 1.00$) and near limb ($0.36 < \mu \leq 0.50$) so derived are plotted along with the corresponding line core intensity contrast profiles from Figs. 3.8 and 3.10 in Fig. 3.18. Line core residual intensity specific contrast is plotted along with the line core intensity specific contrast from Fig. 3.15 in Fig. 3.19.

As expected, excluding the contribution of continuum intensity enhancement to line core intensity contrast results in a more pronounced centre-to-limb decline ($50 \text{ G} < \langle B_l \rangle / \mu \leq 100 \text{ G}$ and $500 \text{ G} < \langle B_l \rangle / \mu \leq 640 \text{ G}$ panels, Fig. 3.18). This decline in the line core residual intensity contrast CLV profiles is also consistent with the spectroscopic observations of Stellmacher and Wiehr (1979) and Hirzberger and Wiehr (2005). Comparing line core intensity and residual intensity contrast (Figs. 3.18 and 3.19), the broad similarity, especially near disc centre, imply that line core intensity contrast is dominated by the contribution from line weakening. Even towards the limb, where magnetic

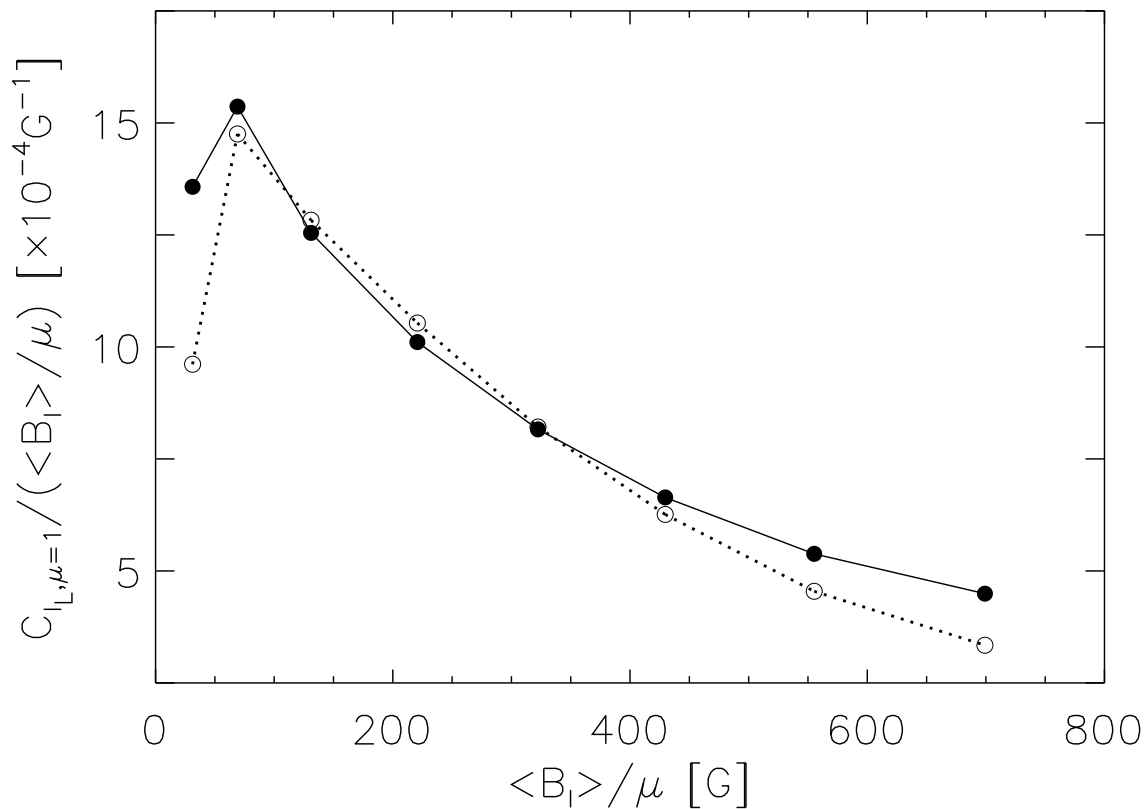


Figure 3.19: Line core intensity (open circles) and corresponding residual intensity (filled circles) specific contrast as a function of $\langle B_l \rangle / \mu$. The circles are joined by straight lines to aid the eye.

line weakening is at its weakest, it still comprises a significant proportion of observed line core intensity contrast. The potential implications of this result and the opposite CLV exhibited by continuum and line core intensity contrast on facular contribution to solar irradiance variations will be discussed in Sect. 3.4.4.

Very few studies examining the disc position and magnetogram signal dependence of line core intensity contrast exist in the literature. Frazier (1971), Lawrence et al. (1991) and Title et al. (1992) measured intensity contrast at disc centre in the core of the Fe I 5250 Å, Fe I 6302 Å and Ni I 6768 Å lines, respectively. Results from different lines are not directly comparable but it is still encouraging to see that in terms of magnitude and general trend with magnetogram signal, the results from these earlier studies express broad agreement with ours. The only notable exception is the steep monotonic decline at $\langle B_l \rangle > 600$ G reported by Title et al. (1992), which largely persisted even after the authors masked out pores. The decline coincides with a similar trend in intensity contrast measured at the nearby continuum, suggesting a greater relative influence of the continuum excess to magnetic line weakening at the Ni I 6768 Å line compared to the Fe I 6173 Å line. Frazier (1971) also made measurements away from disc centre, but due to data scatter the author could do no better than to present a schematic representation of the CLV through visually fitted linear functions. Walton (1987) reported measured line core residual intensities for eight magnetically insensitive lines at various disc positions.

3 Intensity contrast of solar network and faculae

(The contents of this chapter are identical to the printed version of Yeo, K. L., Solanki, S. K., Krivova, N. A., 2013, Intensity contrast of network and faculae, Astron. Astrophys., 550, A95.)

There were however only a small number of scattered measurements for each line, and a relatively narrow range of disc positions ($\mu > 0.6$). To our knowledge, the present study is the first to examine line core intensity contrast employing full-disc observations. Together with the relatively fine resolution and low noise level, this allowed us to describe the magnetogram signal dependence and especially the CLV with greater accuracy and detail than in the previous efforts.

3.4.4 Facular contribution to variation in solar irradiance

Our finding that intensity contrast in the line core is dominated by line weakening rather than continuum intensity enhancement and exhibits the opposite CLV as continuum intensity contrast has potential implications on facular contribution to total solar irradiance variation. Total solar irradiance (TSI) variation is the sum manifest of variation in the continuum and spectral lines. The converse CLV of the continuum and line core intensity contrasts reported here imply a different time variation of the contribution by the continuum and spectral lines to solar irradiance as magnetic features rotate across the solar disc.

In Fig. 3.20a we show the level 2.0 hourly TSI measurements from the DIARAD radiometer (Dewitte et al. 2004a) on the SoHO/VIRGO instrument (Fröhlich et al. 1995) for the 22-day period of August 19 to September 9, 1996 (open circles). Active region NOAA 7986 rotated into view on August 23 and out of view on September 5, and was the only active region on the solar disc for the duration of its passage across the solar disc. The period is otherwise relatively quiet. This data therefore allows us to chart variations in TSI arising mainly from the passage of a single active region across the solar disc. The dip around August 29 corresponds to active region NOAA 7986 crossing disc centre. Even with darkening from sunspots present in the active region, the nadir of the dip is $\sim 0.2 \text{ Wm}^{-2}$ above the level before August 23 and after September 5. This suggests an overall positive contribution to TSI variation by the faculae in NOAA 7986 when it was near disc centre (first pointed out by Fligge et al. 2000).

A schematic representation of facular contribution to variation in TSI during the passage of NOAA 7986 across the solar disc, depicted in Fig. 3.20e, was derived as follows.

- The DIARAD TSI data was interpolated at 0.1 day intervals and the result smoothed (via binomial smoothing, Marchand and Marmet 1983). Sunspot darkening was estimated from the Photometric Sunspot Index (PSI) by Chapman et al. (1994) based on full-disc photometric images acquired with the Cartesian Full Disk Telescope 1 (CFDT1) at SFO. A quadratic polynomial was fitted to the PSI values from the period of interest excluding the points where $\text{PSI} = 0$ (i.e., no sunspots in view). Taking a value of 1365.4 Wm^{-2} for the total irradiance of the quiet Sun, the fit was converted from units of parts per million to Wm^{-2} and subtracted from the DIARAD data. This value for the total irradiance of the quiet Sun is given by the average TSI at the last three solar minima stated in version d41_62_1204 (dated April 2, 2012) of the PMOD TSI composite (Fröhlich 2000). The DIARAD data, after this treatment, represents variation in TSI largely from faculae in NOAA 7986 alone. In Fig. 3.20a we plot the DIARAD data after interpolation and smoothing (red dotted curve), and after removing sunspot darkening (red solid curve) along

the original measurements. In Fig. 3.20b we show the PSI (open circles) and the quadratic polynomial fit to the non-zero segment (curve).

- The trajectory of NOAA 7986 during its passage across the solar disc was estimated from 142 level 1.8 5-minute MDI magnetograms (Scherrer et al. 1995) on which the active region was entirely in view (i.e. not only partially rotated into, or partially rotated off the solar disc). Taking the unsigned magnetogram signal, the magnetograms were binned spatially by 16×16 pixels. For each binned magnetogram, the position of NOAA 7986, in terms of μ , was estimated from the mean position of the five pixels within the active region with the strongest signal. The trajectory of NOAA 7986 is then given by the quadratic polynomial fit to these estimates. In Fig. 3.20c we show the estimated position of NOAA 7986 in the magnetograms (open circles) and the quadratic polynomial fit (curve).
- Facular contribution to variation in TSI was very approximately modelled from the empirical relationships describing contrast as a function of μ and $\langle B_l \rangle / \mu$ derived in this study. Assuming a power law distribution of $\langle B_l \rangle / \mu$ with a scaling exponent of -1.85 (Parnell et al. 2009), we evaluated Eqs. 3.3 and 3.4, scaled by $\left(\frac{\langle B_l \rangle}{\mu} / 15\right)^{-1.85}$ and integrated over $\langle B_l \rangle / \mu = 15$ G to 800 G, at 0.1 day intervals taking μ from the trajectory of NOAA 7986 estimated earlier. The resulting time series were then scaled by μ (to correct for the CLV of projected area on the solar disc) and the limb darkening function from Foukal et al. (2004). Given the approximate manner of this derivation, the results are non-quantitative. However for this analysis it is not the actual values but the temporal trends that is important. Here we had approximated the active region as a point object and so cannot include variation arising from the active region being only partially visible as it rotates into and off the solar disc. This derivation is therefore only valid, and confined to, the period where NOAA 7986 was entirely in view in MDI magnetograms.

The treated DIARAD data, giving TSI variation largely from faculae in NOAA 7986 alone, is plotted in Fig. 3.20d (red curve) along the conjectures based on the observed intensity contrast in the continuum (blue dashed curve) and line core (blue dotted curve). To compare how they varied with time, we subtracted the mean from and normalized each time series by the area bounded by the curve and the zero level. In Fig. 3.20e we show the multiple linear regression fit of the continuum and line core models to the DIARAD series (blue solid curve), which showed a much better agreement to it than either model. Facular contribution to variation in solar irradiance appears to be strongly driven by intensity contrast in both the continuum, and spectral lines, which derives largely from line weakening in magnetic elements. This complies with the observation that solar irradiance variations over the solar cycle seems to be significantly influenced by changes in spectral lines (Mitchell and Livingston 1991, Unruh et al. 1999, Preminger et al. 2002).

Various studies examining the photometric contrast of faculae, as identified in calcium line images, reported positive values near disc centre (Lawrence et al. 1988, Walton et al. 2003, Foukal et al. 2004). The apparent divergence between the findings of these works, and the largely negative contrast near disc centre reported here (Fig. 3.9) and in the similar studies listed in Table 3.2, where network and faculae were characterized by the magnetogram signal, arises from the different selection methods (Ermolli et al. 2007).

3 Intensity contrast of solar network and faculae

(The contents of this chapter are identical to the printed version of Yeo, K. L., Solanki, S. K., Krivova, N. A., 2013, *Intensity contrast of network and faculae*, *Astron. Astrophys.*, 550, A95.)

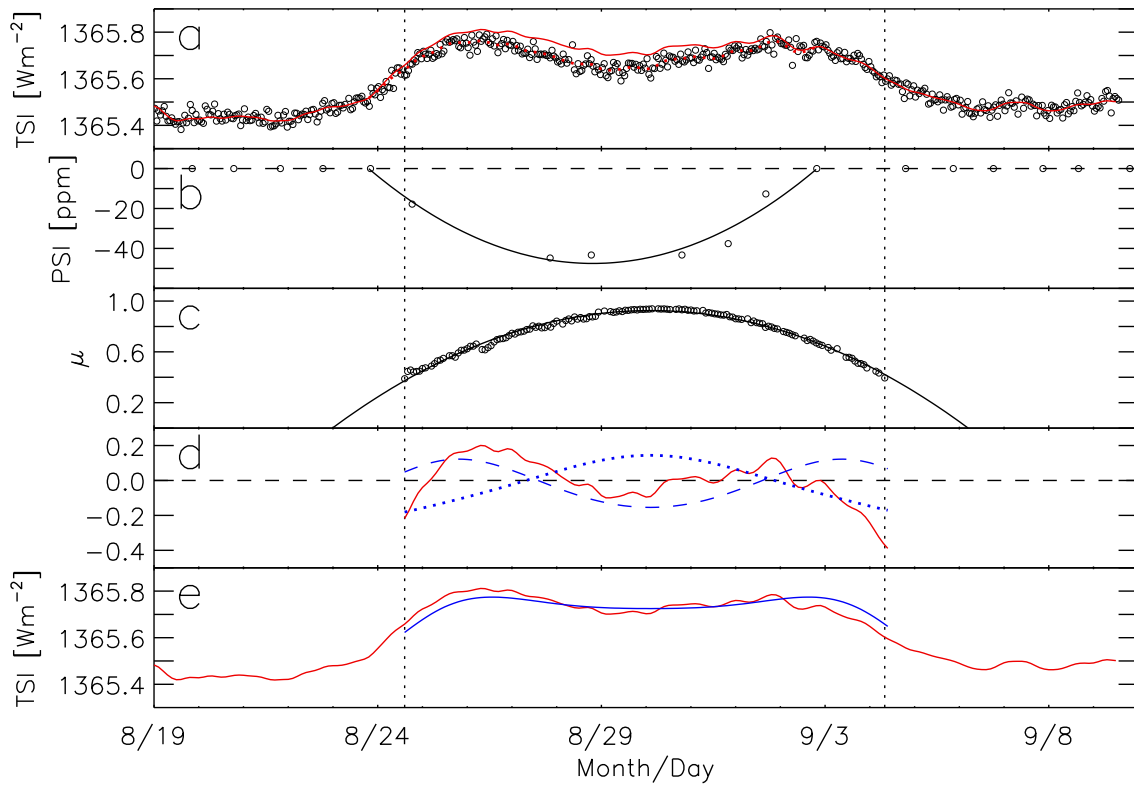


Figure 3.20: a) Total solar irradiance, TSI from DIARAD on SoHO/VIRGO (open circles) for the period of August 19 to September 9, 1996. The dotted and solid red curves represent the interpolated and smoothed version before and after subtracting sunspot darkening. b) Photometric Sunspot Index, PSI (open circles) by Chapman et al. (1994) and the quadratic polynomial fit to the non-zero points (curve). The dashed line marks the zero level. c) Position of NOAA 7986 as estimated from MDI magnetograms (open circles) and the quadratic polynomial fit (curve). d) TSI minus sunspot darkening (red curve) and model of facular contribution to TSI based on observed intensity contrast in the continuum (blue dashed curve) and line core (blue dotted curve), each mean subtracted and normalized by the area bound between the time series and the zero level (black dashed line). e) TSI minus sunspot darkening (red curve) and the multiple linear regression fit of the continuum and line core models (blue solid curve). The dotted lines running down all the panels mark the period where NOAA 7986 was entirely on the solar disc in MDI magnetograms.

Significantly, the results of Foukal et al. (2004) were based on near total light broadband measurements. From the statistical analysis of an extensive catalogue of full-disc photometric observations obtained with the SFO/CFDT1, Walton et al. (2003) found contrast, in a continuum passband (i.e., negligible spectral line contribution) in the visible red, averaged over each facular region (as identified in the Ca II K) to be positive (~ 0.005) near disc centre. The authors took this result to indicate the distribution of flux tube sizes in facular regions is biased to the low end (i.e., more small bright flux tubes than large dark ones), which is reasonable considering the typical distribution of magnetogram sig-

nal (i.e., much more weak signals than strong, Parnell et al. 2009) and the observation that the average flux tube size is greater where magnetogram signal is greater (Ortiz et al. 2002). This suggests the continuum component of facular contribution to TSI variation is on average positive at disc centre in the visible red. From this and the analysis presented above, we conclude that the apparent overall positive contribution to TSI variation by the faculae in NOAA 7986 when it was near disc centre is, at least in part, due to the prevalence of smaller flux tubes and line weakening.

3.5 Conclusion

Here we have presented measured network and facular intensity contrast in the continuum and in the core of the Fe I 6173 Å line from SDO/HMI full-disc observations. We studied the dependence of the contrast on disc position and magnetogram signal, represented by μ and $\langle B_l \rangle / \mu$ respectively. Specifically, we derived empirical relationships describing contrast as a function of μ and $\langle B_l \rangle / \mu$, and specific contrast (contrast per unit $\langle B_l \rangle / \mu$, representative of intrinsic contrast) as a function of $\langle B_l \rangle / \mu$. This study exploits the unprecedented opportunity offered by the SDO mission to examine co-temporal full-disc observations of magnetic field and intensity at a constant intermediate spatial resolution (1 arcsec), relatively low noise, and without atmospheric interference. The quality of the data allowed us to examine intensity contrast for a larger sample at greater accuracy and detail than previous, similar studies, especially in the case of the line core. These results constitute stringent observational constraints on the variation of network and facular intensity with disc position and magnetogram signal in the low and middle photosphere. By constraining atmospheric models of network and faculae, these results should be of utility to solar irradiance reconstructions, especially as HMI data will increasingly be used for this purpose. Given this is the first study of its kind to examine the entire solar disc in both the continuum and line core, it should also be useful to reproduce these results in models of magnetic flux concentrations.

There are significant discrepancies in the continuum intensity contrast reported here and from earlier studies. In this study we had taken steps to account for magnetic signal in the periphery of sunspots and pores, arising from their magnetic canopies and the influence of straylight, which can easily be misidentified as network and faculae. From a comparison with the findings of past efforts, including a recomputation of the results obtained here recreating the conditions of the similar study by Ortiz et al. (2002), we showed differences in resolution, and treatment of magnetic signal adjacent to sunspots and pores to be the likely main factors behind the spread in reported results. The apparent radiant behaviour of network and faculae elements is strongly modulated by spatial resolution (Title and Berger 1996, Röhrbein et al. 2011, Schnerr and Spruit 2011). An understanding of its influence is necessary for the proper interpretation of direct measurements.

In terms of magnitude, trend with magnetogram signal and in particular the CLV, the results obtained here in the continuum and line core differ considerably. While continuum intensity contrast broadly ascends towards the limb, line core intensity contrast is greatest near disc centre and diminishes from disc centre to limb. The divergence between both sets of measurements arises dominantly from spectral line changes due to heating in the middle photosphere and Zeeman splitting in magnetic features, and the different mecha-

3 Intensity contrast of solar network and faculae

(The contents of this chapter are identical to the printed version of Yeo, K. L., Solanki, S. K., Krivova, N. A., 2013, Intensity contrast of network and faculae, Astron. Astrophys., 550, A95.)

nisms by which apparent contrast vary with viewing geometry going from disc centre to limb. From a simple model based on the empirical relationships between contrast, and μ and $\langle B_l \rangle / \mu$ derived here we confirmed that facular contribution to variation in solar irradiance is strongly driven by both continuum excess and spectral line changes.

The specific contrast in both the continuum and line core exhibit a marked decline with increasing magnetogram signal, confirming that network elements are, per unit magnetic flux, hotter and brighter than active region faculae. The different radiant behaviour of network and faculae, not accounted in present models of solar irradiance variations, would be an important factor to consider for more realistic modelling. This observation also implies that secular changes in solar irradiance may be considerably larger than what some models of solar irradiance variations have suggested, given the variation in the number of small-scale magnetic elements on the solar disc is a prime candidate driver of secular changes (Solanki et al. 2002). For example, the model employed by Krivova et al. (2007) to reconstruct variation in TSI from 1700 and by Vieira et al. (2011) for over the Holocene assumed the faculae contrast model by Unruh et al. (1999) for both network and faculae. This renders network and faculae with similar magnetic filling factors equally bright and therefore possibly underestimate the contribution by network to secular variation.

4 Point spread function of SDO/HMI and the effects of stray light correction on the apparent properties of solar surface phenomena

*Yeo, K. L., Feller, A., Solanki, S. K., Couvidat, S., Danilovic, S., Krivova, N. A. Astron. Astrophys., 561, A22 (2014)**

Abstract

Aims. We present a point spread function (PSF) for the Helioseismic and Magnetic Imager (HMI) onboard the Solar Dynamics Observatory (SDO) and discuss the effects of its removal on the apparent properties of solar surface phenomena in HMI data.

Methods. The PSF was retrieved from observations of Venus in transit by matching it to the convolution of a model of the venusian disc and solar background with a guess PSF. We described the PSF as the sum of five Gaussian functions, the amplitudes of which vary sinusoidally with azimuth. This relatively complex functional form was required by the data. Observations recorded near in time to the transit of Venus were corrected for instrumental scattered light by the deconvolution with the PSF. We also examined the variation in the shape of the solar aureole in daily data, as an indication of PSF changes over time.

Results. Granulation contrast in restored HMI data is greatly enhanced relative to the original data and exhibit reasonable agreement with numerical simulations. Image restoration enhanced the apparent intensity and pixel averaged magnetic field strength of photospheric magnetic features significantly. For small-scale magnetic features, restoration enhanced intensity contrast in the continuum and core of the Fe I 6173 Å line by a factor of 1.3, and the magnetogram signal by a factor of 1.7. For sunspots and pores, the enhancement varied strongly within and between features, being more acute for smaller

*The contents of this chapter are identical to the printed version of Yeo, K. L., Feller, A., Solanki, S. K., Couvidat, S., Danilovic, S., Krivova, N. A., 2014, Point spread function of SDO/HMI and the effects of stray light correction on the apparent properties of solar surface phenomena, *Astron. Astrophys.*, 561, A22, reproduced with permission from Astronomy & Astrophysics, © ESO.

features. Magnetic features are also rendered smaller, as signal smeared onto the surrounding quiet Sun is recovered. Image restoration increased the apparent amount of magnetic flux above the noise floor by a factor of about 1.2, most of the gain coming from the quiet Sun. Line-of-sight velocity due to granulation and supergranulation is enhanced by a factor of 1.4 to 2.1, depending on position on the solar disc. The shape of the solar aureole varied, with time and between the two CCDs. There are also indications that the PSF varies across the FOV. However, all these variations were found to be relatively small, such that a single PSF can be applied to HMI data from both CCDs, over the period examined without introducing significant error.

Conclusions. Restoring HMI observations with the PSF presented here returns a reasonable estimate of the stray light-free intensity contrast. Image restoration affects the measured radiant, magnetic and dynamic properties of solar surface phenomena sufficiently to significantly impact interpretation.

4.1 Introduction

Solar telescopes, like any real optical system, diverge from diffraction-limited behaviour due to optical aberrations and, in the case of ground-based instruments, the influence of the Earth's atmosphere. Optical aberrations arise from factors such as design and material constraints, imperfections in the fabrication, presence of impurities, thermal changes and jitter, and are practically unavoidable. Due to aperture diffraction and optical aberrations, radiation entering a given optical system is not entirely confined to the intended area on the focal plane but instead spread out, as described mathematically by the point spread function, PSF. This image blurring or loss of contrast is the so-termed stray light.

The apparent properties of solar phenomena is sensitive to stray light, accounting for its influence on solar imagery is necessary for proper interpretation and comparison with numerical models. This has been demonstrated repeatedly in the literature, for example, in studies looking at the limb darkening function (Pierce and Slaughter 1977, Neckel and Labs 1994), the intensity contrast of granulation (Sánchez Cuberes et al. 2000, Danilovic et al. 2008, Wedemeyer-Böhm and Rouppe van der Voort 2009, Afram et al. 2011), and the brightness of small-scale magnetic concentrations (Title and Berger 1996, Schnerr and Spruit 2011) and sunspots (Albregtsen and Maltby 1981, Mathew et al. 2007).

Sophisticated techniques to correct solar observations for instrumental and atmospheric effects exist, the most common being speckle interferometry (de Boer et al. 1992, von der Lühe 1993) and phase diversity (Gonsalves 1982, Löfdahl and Scharmer 1994) methods. For spaceborne instruments, where variable atmospheric seeing is not a factor, a more conventional approach is often sufficient. Specifically, inferring the PSF from the distribution of intensity about the boundary between the bright and dark parts of partially illuminated scenes (such as, of the solar limb, and of transits of the Moon, Venus or Mercury) and restoring data by the deconvolution with it. Recent examples include the work of Mathew et al. (2007) with observations from SoHO/MDI¹, Wedemeyer-Böhm (2008), Wedemeyer-Böhm and Rouppe van der Voort (2009) and Mathew et al. (2009)

¹The Michelson Doppler Imager onboard the Solar and Heliospheric Observatory (Scherrer et al. 1995).

with Hinode/SOT/BFI², and DeForest et al. (2009) with TRACE³.

In this paper we present an estimate of the PSF of the Helioseismic and Magnetic Imager onboard the Solar Dynamics Observatory, SDO/HMI (Schou et al. 2012b). The PSF was derived from observations of Venus in transit. We also demonstrate the effects of correcting HMI data for stray light with this PSF on the apparent properties of various photospheric phenomena.

This study broadly follows the approach taken with the other spaceborne instruments listed above. It departs from these earlier efforts in that we constrain the PSF not only in the radial dimension but also in the azimuthal direction, recovering the anisotropy. This we will show to be crucial for accurate stray light removal (Sect. 4.2.3).

The relationship between the radiance of magnetic features in the photosphere, and their size and position on the solar disc, is an important consideration in understanding and modelling the variation in solar irradiance (Domingo et al. 2009). HMI returns continuous, seeing-free, full-disc observations of intensity, Doppler shift and magnetic field at a constant, intermediate spatial resolution (~ 1 arcsec) and at relatively low noise. This renders it a suitable tool for constraining the radiant behaviour of photospheric magnetic features (Yeo et al. 2013). It is therefore of interest to enhance the quality of HMI observations by quantifying the stray light performance of the instrument. This would be of utility not only for the accurate examination of the radiant behaviour of magnetic features in HMI data but also any application that can benefit from stray light-free measurements of intensity, line-of-sight velocity and magnetic flux density.

The PSF presented here is, to our knowledge, the first on-orbit measurement of the stray light of HMI reported in the literature (see Wachter et al. 2012, for the pre-launch measurement). This is necessary given that the exact operating conditions of the sensor cannot be exactly simulated on the ground. Also, the stray light of the HMI might have changed from the time of the pre-launch calibration from changes in the condition of the instrument.

The HMI comprises of two identical 4096×4096 pixel CCD cameras, denoted ‘side’ and ‘front’. The PSF was retrieved from images recorded on the side CCD during the transit of Venus on June 5 to 6, 2012. In addition to this transit of Venus, the HMI has also witnessed several partial lunar eclipses (seven, as of the end of 2012). In Sect. 4.2.5 we discuss the reasons for choosing the observations of Venus in transit over data from the partial lunar eclipses or of the solar limb for constraining the PSF, even though Venus has an atmosphere which had to be taken into account in deriving the PSF, introducing additional complexity to the task and uncertainty to the final estimate of the PSF.

In the following section, we detail the data selection (Sect. 4.2.1), the PSF derivation (Sect. 4.2.2) and image restoration method (Sect. 4.2.3), and how we accounted for the influence of Venus’ atmosphere (Sect. 4.2.4). Then, we verify the utility of the PSF presented here for image restoration, comparing the apparent granulation contrast in restored HMI observations and synthetic intensity maps generated from numerical simulation (Sect. 4.3.1). We illustrate the result of image restoration on the intensity, Dopplergram and magnetogram data products of the instrument, looking at its effect on the following.

²The Broadband Filter Imager of the Solar Optical Telescope onboard Hinode (Kosugi et al. 2007).

³The Transition Region And Coronal Explorer (Handy et al. 1998).

4 Point spread function of SDO/HMI and the effects of stray light correction on the apparent properties of solar surface phenomena

(The contents of this chapter are identical to the printed version of Yeo, K. L., Feller, A., Solanki, S. K., Couvidat, S., Danilovic, S., Krivova, N. A., 2014, Point spread function of SDO/HMI and the effects of stray light correction on the apparent properties of solar surface phenomena, Astron. Astrophys., 561, A22.)

- The intensity and magnetic field strength of small-scale magnetic concentrations (Sect. 4.3.2.1).
- The intensity and magnetic field strength of sunspots and pores (Sect. 4.3.2.2).
- The amount of magnetic flux on the solar surface (Sect. 4.3.2.3).
- Line-of-sight velocity (Sect. 4.3.2.4).

The retrieved PSF represents the stray light behaviour of the side CCD at the time of the transit of Venus, at the position in the field-of-view (FOV) occupied by the Venus disc. In Sect. 4.4 we examine the applicability of this PSF to other positions in the FOV, and to observations from the front CCD as well as from other times. Finally, a summary of the study is given in Sect. 4.5.

4.2 PSF derivation

4.2.1 Data selection

The HMI is a full-Stokes capable filtergram instrument. The instrument records full-disc polarimetric filtergrams continuously, at 3.75-s cadence, on the two identical CCDs. The filtergram sequence of the side CCD alternates between six polarizations ($I \pm Q$, $I \pm U$ and $I \pm V$) and six positions across the Fe I 6173 Å line (at ± 34 , ± 103 and ± 172 mÅ from line centre). A set of 36 filtergrams, of each polarization at each line position, is collected every 135-s. The front CCD collects a set of 12 filtergrams, covering the Stokes $I + V$ and $I - V$ polarizations at the same line positions, every 45-s.

Dopplergrams, longitudinal magnetograms and intensity (continuum, and line depth and width) images, collectively termed the line-of-sight data products, are generated from the filtergram sequence of the side CCD at 720-s intervals, and from that of the front CCD at 45-s intervals. Stokes parameters (I, Q, U and V) and the corresponding Milne-Eddington inversion (Borrero et al. 2011) are also produced, at 720-s cadence, from the filtergram sequence of the side CCD.

During the transit of Venus on June 5 to 6, 2012, the side CCD recorded filtergrams in the nearby continuum (-344 mÅ from line centre), instead of the regular filtergram sequence. For the purpose of estimating the PSF of the instrument, we examined the 854×854 pixel crop, centred on the Venus disc, of 249 continuum filtergrams collected between second and third contact (i.e., the period the venusian disc was entirely within the solar disc). Care was taken to avoid filtergrams with pixels with spurious signal levels, a result of cosmic ray hits, on the venusian disc. The pixel scale was 0.504 arcsec/pixel. A summary description of this and the other HMI data employed in this study is given in Table 4.1.

When generating the various data products in the HMI data processing pipeline, filtergrams (from an interval of 1350-s for the 720-s data products and 270-s for the 45-s data products) are corrected for spatial distortion (Wachter et al. 2012), cosmic ray hits, polarization crosstalk (Schou et al. 2012a) and solar rotation, and the filtergrams of similar polarizations averaged. These time-averaged filtergrams are then combined non-linearly

Table 4.1: Summary description of the HMI data employed in this study and the sections in which their analysis is detailed.

Index	Description	UTC time of observation	Section(s)
1	854 × 854 pixel crop, centred on the venusian disc, of 249 continuum (−344 mÅ from line centre) filtergrams recorded on the side CCD during the transit of Venus, between second and third contact.	Between 22:30, June 5 and 04:14, June 6, 2012.	4.2.1
2	The mean of 42 of the 249 images in item 1, between which the spatial distribution of intensity on the venusian disc is relatively similar, termed the mean transit image.	Between 02:04 and 02:46, June 5, 2012.	4.2.1, 4.2.2, 4.2.4
3	One of the 42 images used to produce item 2, referred to as the test transit image.	02:25:37, June 6, 2012.	4.2.3, 4.2.4
4	854 × 854 pixel crop, centred on the venusian disc, of a continuum side CCD filtergram recorded just before second contact, denoted the ingress image.	22:25:33, June 5, 2012.	4.2.4
5	Continuum side CCD filtergram taken right after the venusian disc exited the solar disc completely, termed the test continuum filtergram.	04:35:59, June 6, 2012.	4.3.1, 4.4.1
6	45-s longitudinal magnetogram from the front CCD closest in time (< 1 minute) to item 5.	04:35:22, June 6, 2012.	4.3.1, 4.4.1
7	A set of simultaneous 720-s Dopplergram, longitudinal magnetogram, line depth and continuum intensity images from the side CCD, recorded about an hour after the end of the transit of Venus, when said CCD resumed collection of the regular filtergram sequence.	05:35:32, June 6, 2012.	4.3.2, 4.4.1
8	A pair of filtergrams, one from each CCD, of similar bandpass (−172 mÅ from line centre) and polarization (Stokes $I - V$), taken less than one minute apart of one another.	Around 05:36, June 6, 2012.	4.4.2
9	The continuum filtergram recorded on each CCD whenever the SDO spacecraft passes orbital noon and midnight. A total of 1866 filtergrams from each CCD, from when the HMI commenced regular operation to the time of the study.	Around 06:00 and 18:00 daily, between May 1, 2010 and June 30, 2013.	4.4.2

4 Point spread function of SDO/HMI and the effects of stray light correction on the apparent properties of solar surface phenomena

(The contents of this chapter are identical to the printed version of Yeo, K. L., Feller, A., Solanki, S. K., Couvidat, S., Danilovic, S., Krivova, N. A., 2014, Point spread function of SDO/HMI and the effects of stray light correction on the apparent properties of solar surface phenomena, Astron. Astrophys., 561, A22.)

to form the various data products (Couvidat et al. 2012). For the side CCD, these time-averaged filtergrams are outputted as the 720-s Stokes parameters product.

As a consequence of the correction for spatial distortion, the apparent PSF is different in the unprocessed and time-averaged filtergrams. The non-linearity of the algorithms used to derive the data products means they cannot be corrected for stray light by the deconvolution with the PSF. Instead, their restoration must go via restoring the unprocessed or time-averaged filtergrams.

The 249 continuum filtergrams considered (and all the other filtergram data utilised in the rest of the study) were corrected for spatial distortion. The retrieved PSF therefore represents stray light in undistorted HMI observations. This allows the generation of stray light-free data products through the deconvolution of the PSF from the time-averaged filtergrams. For the line-of-sight data products, this means correcting just the time-averaged Stokes $I + V$ and $I - V$ at each line position, a total of $2 \times 6 = 12$ images in each instance, instead of all the unprocessed filtergrams, which numbers 360 and 72 for the 720-s and 45-s data products respectively.

In this study we assumed Venus to be a perfect sphere (Archinal et al. 2011). Radial distance and azimuth are denoted r and ϕ , respectively. Azimuth is taken anti-clockwise from the CCD column axis such that zero is up.

The spatial distribution of intensity on the venusian disc, predominantly instrumental scattered light (aperture diffraction and stray light), varied significantly over the course of the transit (Fig. 4.1). The figure gives the intensity on the venusian disc in the 249 continuum filtergrams,

- as a function of radial distance from the centre of the venusian disc, averaged over all azimuths and normalized to the level at the point of inflexion (\hat{I}_r , top panel), and
- as a function of azimuth along the edge of the venusian disc as given by the point of inflexion on \hat{I}_r , normalized to the mean level (\hat{I}_ϕ , bottom panel).

Also plotted are the mean \hat{I}_r and \hat{I}_ϕ of all the filtergrams, $\langle \hat{I}_r \rangle$ and $\langle \hat{I}_\phi \rangle$ (red curves). The radius of the venusian disc as given by the point of inflexion on \hat{I}_r is, to 0.1 arcsec, constant at 29.5 arcsec. The fluctuation in the intensity on the venusian disc over the course of the transit arises from changes in the solar background from granulation, p -mode oscillations and limb darkening, as well as the variation of the PSF with position in the FOV.

To quantify the variation in the spatial distribution of intensity on the venusian disc over the course of the transit, and the influence of the changing solar background and the variation of the PSF with position in the FOV, we computed, for each of the 249 continuum filtergrams, the following two quantities.

- The integral under \hat{I}_r from the centre of the venusian disc to the point of inflexion, $\int \hat{I}_r dr$. The broader the PSF at a given position in the FOV, the brighter the venusian disc is relative to the level at its edge, and the greater this integral.
- The root-mean-square or RMS difference between \hat{I}_ϕ and $\langle \hat{I}_\phi \rangle$, $\text{RMS}_{\hat{I}_\phi - \langle \hat{I}_\phi \rangle}$. The closer the agreement in the trend with azimuth between \hat{I}_ϕ and $\langle \hat{I}_\phi \rangle$, the smaller this quantity. $\text{RMS}_{\hat{I}_\phi - \langle \hat{I}_\phi \rangle}$ reflects changes in the isotropy of the PSF (such as, from astigmatism and coma aberrations) and variation in the spatial distribution of intensity of the solar background.

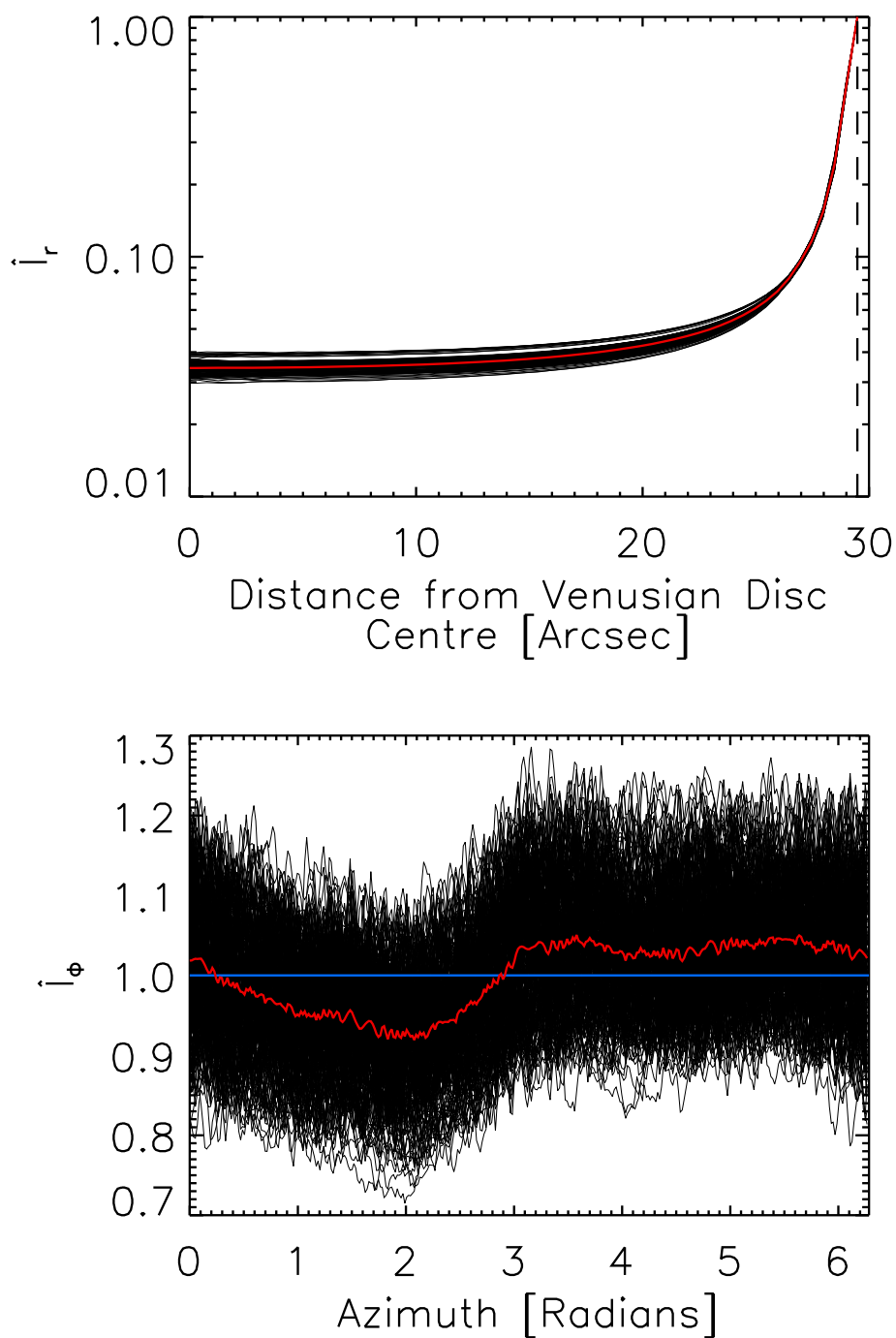


Figure 4.1: Intensity on the venusian disc in the 249 continuum filtergrams from the transit of Venus. Top: Intensity as a function of distance from the centre of the venusian disc, averaged over all azimuths and normalized to the level at the point of inflexion (dashed line), \hat{I}_r . Bottom: Intensity versus azimuth along the edge of the venusian disc as given by the point of inflexion on \hat{I}_r , normalized to the mean level, \hat{I}_ϕ . The red curves follow the mean \hat{I}_r and \hat{I}_ϕ of all the filtergrams, while the blue line represents $\hat{I}_\phi = 1$.

$\int \hat{I}_r dr$ and $\text{RMS}_{\hat{I}_\phi - \langle \hat{I}_\phi \rangle}$ are plotted along the trajectory of the venusian disc, given in terms of the cosine of the heliocentric angle, $\mu = \cos \theta$ of the disc centre, as a function of time in Fig. 4.2.

$\int \hat{I}_r dr$ changed slowly but notably over the course of the transit and the variation appears to be uncorrelated to distance from solar disc centre (and therefore, limb darkening). This suggests that the width of the PSF varies significantly along the path of Venus in the FOV. $\text{RMS}_{\hat{I}_\phi - \langle \hat{I}_\phi \rangle}$ showed a marked point-to-point fluctuation but is otherwise relatively low ($\lesssim 0.1$) and exhibits no obvious trend with time. This indicates that the azimuth dependence of \hat{I}_ϕ and $\langle \hat{I}_\phi \rangle$ is mainly driven by a persistent PSF anisotropy along the path of Venus in the FOV rather than limb darkening (see also Sect. 4.2.2). The marked point-to-point fluctuation is likely from granulation and p -mode oscillations. This is supported by the comparatively smooth time variation of $\int \hat{I}_r dr$, which is less sensitive to these small-scale intensity fluctuations in the solar background due to the averaging over all azimuths.

From the trend of $\int \hat{I}_r dr$ and $\text{RMS}_{\hat{I}_\phi - \langle \hat{I}_\phi \rangle}$ with time, we surmise that the width of the PSF varies significantly along the path of Venus in the FOV and while the anisotropy of the PSF is relatively stable, it is obscured by granulation and p -mode oscillations in individual filtergrams. Based on these considerations, we retained just the 42 filtergrams highlighted in Fig. 4.2 (red circles), taken over a 40-minute period where $\int \hat{I}_r dr$ is relatively stable, for the derivation of the PSF. The selected filtergrams were aligned by the venusian disc and the average, hereafter referred to as the mean transit image, taken. The objective is to derive an image of Venus in transit where the influence of granulation and p -mode oscillations is minimal by averaging filtergrams where the PSF at Venus' position in the FOV is fairly similar.

The 249 continuum filtergrams examined alternated between four polarizations (Stokes $I + Q$, $I - Q$, $I + U$ and $I - U$). We found no systematic differences in the spatial distribution of intensity on the venusian disc between filtergrams of different polarizations and so made no distinction between them here. We repeated the analysis described in this subsection on the filtergrams recorded at the six regular wavelength positions, on the front CCD during the transit of Venus. There are systematic differences (in $\int \hat{I}_r dr$ and $\text{RMS}_{\hat{I}_\phi - \langle \hat{I}_\phi \rangle}$) between different positions, even between positions at similar distance from but opposite sides of the line centre. This suggests spectral line changes from effects unrelated to the stray light behaviour of the instrument may exert an influence on intensity measured on the venusian disc. Specifically, Doppler shifts from the motion of the spacecraft (SDO is in a geosynchronous orbit) and the rotation of the Sun. For this reason we restricted ourselves to the continuum filtergrams from the side CCD.

4.2.2 PSF derivation method

A bivariate polynomial function was fitted to the mean transit image. We excluded the circular area of 50 arcsec radii centred on the venusian disc (about three times the area of the venusian disc) from the regression. The extrapolation of the surface fit over this excluded area represents an estimate of the intensity if Venus had been absent. We filled a circular area in the surface fit, corresponding to the venusian disc, with zeroes. We will refer to the result, essentially a model of the mean transit image in the absence of an atmosphere in Venus, aperture diffraction and stray light, as the artificial image.

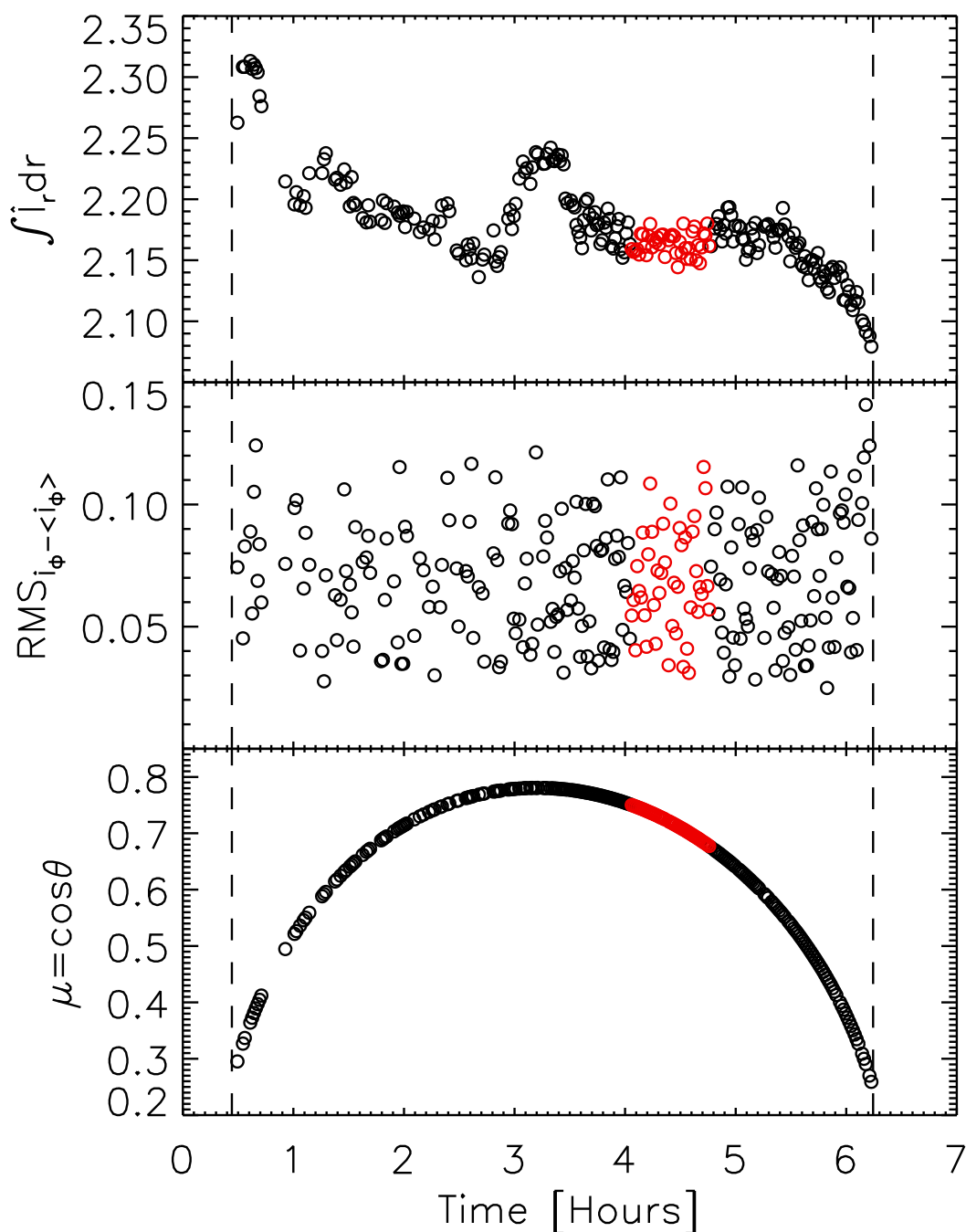


Figure 4.2: The integral under \hat{I}_r , $\int \hat{I}_r dr$ (top), the RMS difference between \hat{I}_ϕ and $\langle \hat{I}_\phi \rangle$, $\text{RMS}_{\hat{I}_\phi - \langle \hat{I}_\phi \rangle}$ (middle) and the position of the centre of the venusian disc in terms of the cosine of the heliocentric angle, $\mu = \cos \theta$ (bottom) as a function of time from 22:00:00 UTC, June 5, 2012. The red circles highlight the values for the filtergrams used to derive the PSF. The dashed lines mark the approximate time of the second and third contacts; the period between which the venusian disc was entirely within the solar disc from SDO's position.

The PSF was determined by minimizing the chi-square between the convolution of the artificial image with a guess PSF and the mean transit image, in the circular area of 50 arcsec radii centred on the venusian disc. For this we employed the implementation of the Levenberg-Marquardt algorithm (LMA) included in the IDL Astronomy User's Library, mpfit2dfun.pro.

Intensity in the circular area was sampled at equal intervals in the radial (0.504 arcsec, the pixel scale) and azimuthal (1/360 radians) dimensions. This is to give intensity measured at each radius from the centre of the venusian disc more equal weight in the LMA optimization. The result is a closer agreement between the convolution of the artificial image with the guess PSF and the mean transit image on convergence than achieved by comparing the circular area in the artificial and mean transit images directly.

We scaled the artificial image by a factor prior to convolution with the guess PSF. We allowed this factor and the radius of the disc of zeroes in the artificial image to be free parameters in the LMA optimization, taking an initial value of unity (i.e., no scaling) and 29.5 arcsec (the position of the point of inflexion on \hat{I}_r). This is to minimize error from any misestimation of the surface fit to the mean transit image and the radius of the venusian disc⁴.

Following the example of previous studies (Martínez Pillet 1992, Mathew et al. 2007, 2009), we attempted to model the guess PSF as the linear sum of various combinations of Gaussian and Lorentzian functions. Except here we allowed the amplitude of each Gaussian and Lorentzian component to vary sinusoidally with azimuth to accommodate PSF anisotropy. We also tried to set the ideal diffraction-limited PSF as one of the components. The guess PSF we found to reproduce the measured intensity in the artificial image best, denoted K , is given by

$$K(r, \phi) = \sum_{i=1}^5 [1 + A_i \cos(u_i \phi + v_i)] w_i \left[\frac{1}{2\pi\sigma_i^2} \exp\left(-\frac{r^2}{2\sigma_i^2}\right) \right]. \quad (4.1)$$

That is, the linear combination of five Gaussian functions, with weight w_i and standard deviation σ_i , the amplitudes of which vary sinusoidally with azimuth, with amplitude A_i , period of $2\pi u_i$ radians (where $u_i \in \mathbb{Z}$) and phase v_i .

Modelling the guess PSF as the linear combination of four Gaussian or three Gaussian and a Lorentzian, as done in the cited works, still reproduces measured intensity in the artificial image reasonably well. The retrieved PSFs are however, negative at parts (i.e., unphysical) from the LMA converging to solutions where $|A_i| > 1$. And introducing additional sinusoidal terms to the azimuth dependence of each Gaussian and Lorentzian function did not alleviate this problem. The linear combination of five Gaussians appeared necessary to reach a physical solution while reproducing the measured intensity in the artificial image in both the radial and azimuthal dimensions.

The guess PSF was applied to the artificial image by evaluating K (Eqn. 4.1) at pixel scale intervals (0.504 arcsec) on a 251×251 grid, the centre element representing the origin ($r = 0$), and taking the convolution of the artificial image with the result. On convergence, the value at each grid element represents the integral of the PSF over the element. The retrieved PSF therefore describes the pixel integrated PSF. This was done,

⁴The point of inflexion on \hat{I}_r is not an accurate indication of the position of the edge of the venusian disc due to the influence of the venusian atmosphere.

instead of filling the grid with the pixel integrated value of K , for a practical reason. When correcting HMI observations for stray light via deconvolution with the PSF, it is the pixel integrated PSF that is required.

Care was taken to repeat the LMA optimization, varying the initial value of the free parameters, to reduce the likelihood that the solution lies in a local chi-square minimum. To accommodate the requirement that $u_i \in \mathbb{Z}$, we executed the LMA optimization with no constraint on the value of u_i , rounded the retrieved u_i to the nearest integer and repeated the process with these parameters fixed.

The PSF derivation method described here implicitly assumes there is no interaction between solar radiation and the venusian atmosphere. We will qualify this statement, and detail the adjustments made to the artificial image and the mean transit image to account for the influence of the venusian atmosphere on the retrieved PSF in Sect. 4.2.4. The method also ignores motion blurring from the lateral movement of the venusian disc relative to the solar disc. The displacement of the venusian disc within the exposure time of the instrument is, on average, about 0.015 pixels and can therefore be neglected without significant loss of accuracy.

In the following, we denote the PSF retrieved as described above, a preliminary estimate of the stray light behaviour of the instrument, by K_1 . The retrieved value of the parameters of K_1 are listed in Table. 4.2. The best fit value of the scale factor applied to the artificial image is 1.0029, and the radius of the disc of zeroes, 29.29 arcsec. Though only a slight departure from the initial values (unity and 29.5 arcsec), this correction to the amplitude of the artificial image and the size of the disc of zeroes effected a marked improvement in the chi-square statistic.

In Fig. 4.3 we plot the intensity along different radii from the centre of the venusian disc; from the mean transit image (black curves) and reproduced in the artificial image by the convolution with K_1 (red curves). Also plotted is the intensity reproduced in the artificial image by fixing the A_i at zero (blue curves). In this instance, the variation with azimuth arises solely from limb darkening, which enters the process through the surface fit to the mean transit image. Evidently, limb darkening alone cannot account for all the observed variation with azimuth, confirming that the PSF of the instrument is significantly anisotropic. By allowing the amplitude of each Gaussian component in the guess PSF to vary sinusoidally with azimuth, we are able to reproduce most of the observed intensity azimuth dependence. The close overall agreement between observed and reproduced intensities in the radial dimension is illustrated in Fig. 4.4.

Here we choose to describe the PSF as the linear combination of five Gaussian functions over more physically realistic models, such as the convolution of the diffraction-limited PSF with a Voigt function (Wedemeyer-Böhm 2008). Apart from yielding a closer agreement between the PSF-blurred artificial image and the mean transit image, this functional form is more amenable to incorporating the complex azimuthal dependence. The retrieved parameter values of K_1 (Table 4.2) and the azimuth dependence of measured intensity on the venusian disc at different radii (Fig. 4.3) suggest that the overall amplitude and phase of the anisotropy of the PSF varies with radial distance.

The linear combination of Gaussian functions is not a physically realistic model of real PSFs for the following reasons:

- It allows solutions with Strehl ratios exceeding unity, which is unphysical.

4 Point spread function of SDO/HMI and the effects of stray light correction on the apparent properties of solar surface phenomena

(The contents of this chapter are identical to the printed version of Yeo, K. L., Feller, A., Solanki, S. K., Couvidat, S., Danilovic, S., Krivova, N. A., 2014, Point spread function of SDO/HMI and the effects of stray light correction on the apparent properties of solar surface phenomena, *Astron. Astrophys.*, 561, A22.)

Table 4.2: Parameter values (and associated formal regression error) of the guess PSF retrieved neglecting (K_1) and accounting for the influence of the venusian atmosphere (K_2).

PSF	Gaussian component	w_i	σ_i [Arcsec]	A_i	u_i	v_i [Radians]
K_1	$i = 1$	0.641 ± 0.002	0.470 ± 0.001	0.131 ± 0.002	1	-1.85 ± 0.02
	$i = 2$	0.211 ± 0.002	1.155 ± 0.008	0.371 ± 0.006	1	2.62 ± 0.01
	$i = 3$	0.066 ± 0.002	2.09 ± 0.02	0.54 ± 0.01	2	-2.34 ± 0.01
	$i = 4$	0.0467 ± 0.0005	4.42 ± 0.02	0.781 ± 0.006	1	1.255 ± 0.004
	$i = 5$	0.035 ± 0.004	25.77 ± 0.04	0.115 ± 0.001	1	2.58 ± 0.01
K_2	$i = 1$	0.747 ± 0.001	0.417	0.164 ± 0.002	1	-2.22 ± 0.01
	$i = 2$	0.126 ± 0.003	1.45 ± 0.01	0.48 ± 0.01	1	2.36 ± 0.01
	$i = 3$	0.049 ± 0.003	2.10 ± 0.02	0.74 ± 0.04	2	-2.36 ± 0.01
	$i = 4$	0.0428 ± 0.0004	4.66 ± 0.02	0.776 ± 0.007	1	1.194 ± 0.006
	$i = 5$	0.035 ± 0.004	26.16 ± 0.05	0.122 ± 0.002	1	2.63 ± 0.01

Notes. The PSFs are given by the linear combination of five Gaussian functions (Eqn. 4.1), denoted by i , with weight w_i and listed in ascending order by the standard deviation, σ_i . The amplitude of each Gaussian component modulates sinusoidally with azimuth, with amplitude A_i , period of $2\pi u_i$ radians (where $u_i \in \mathbb{Z}$) and phase v_i . There are no associated formal regression errors for u_i , and in the case of K_2 , $\sigma_{i=1}$ as the value of these parameters were fixed in the LMA optimization (see text).

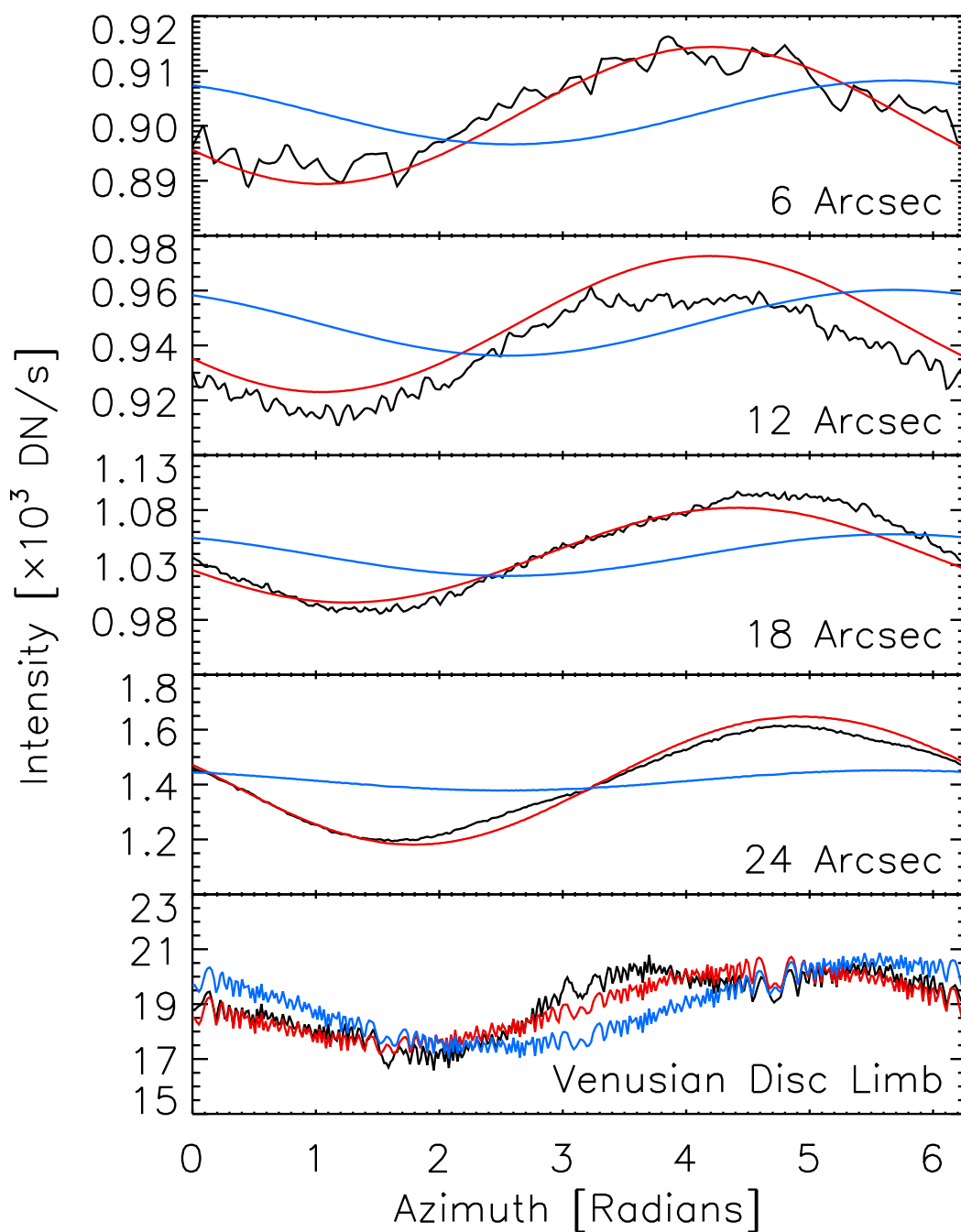


Figure 4.3: Intensity on the venusian disc at distances of 6, 12 18 and 24 arcsec from the centre, and along its limb (taking the radius of the venusian disc retrieved along with K_1 by the LMA optimization, 29.29 arcsec), as a function of azimuth. The black curves follow the values from the mean transit image and the red curves the values reproduced in the artificial image by the convolution with K_1 . The blue curves represent the intensity obtained in the artificial image by fixing A_i at zero. The intensity fluctuations along the venusian limb arises from aliasing artefacts.

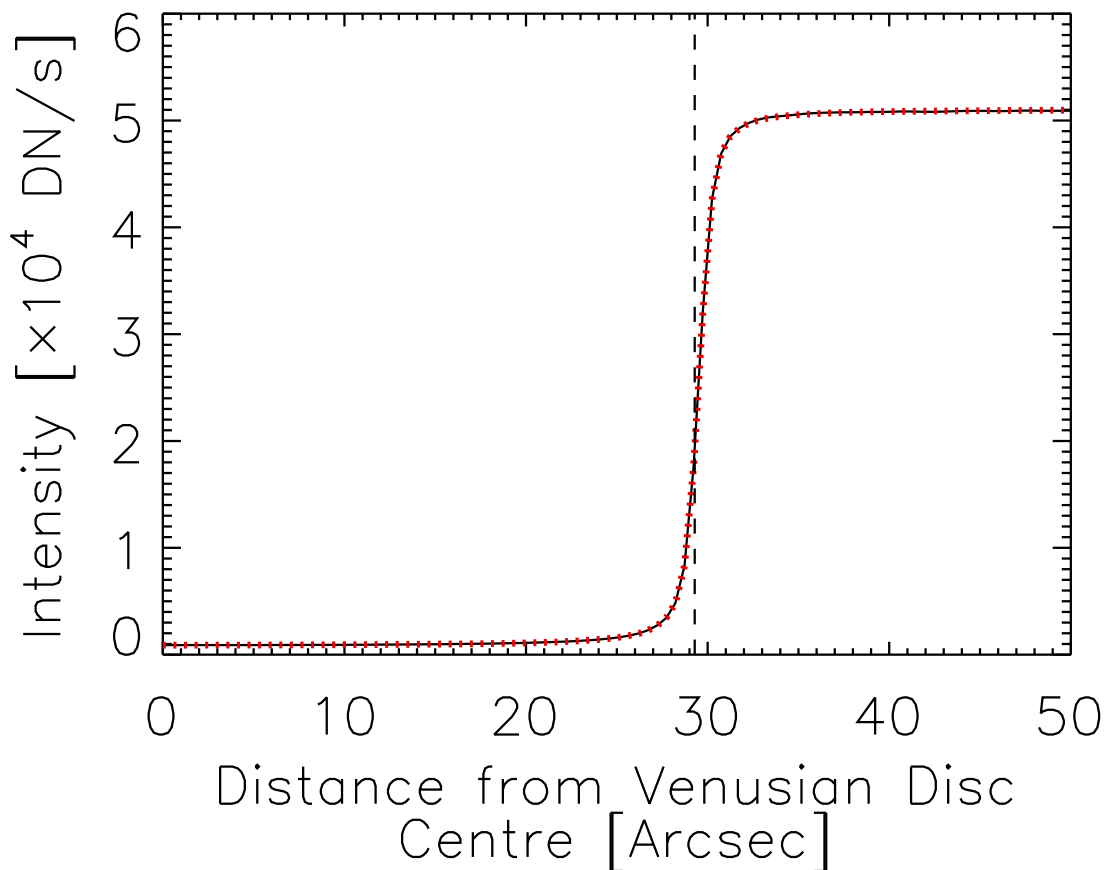


Figure 4.4: Radial intensity as a function of distance from the centre of the venusian disc; from the mean transit image (black solid curve) and the convolution of the artificial image with K_1 (red dotted curve). The dashed line marks the position of the Venus limb as returned along with K_1 by the LMA optimization.

- The Fourier transform of the Gaussian function, and therefore the modulation transfer function (MTF) of such PSF models, is non-zero above the Nyquist limit. Correcting observations for stray light by the deconvolution with such a PSF can introduce aliasing artefacts from the enhancement of spatial frequencies above the Nyquist limit.

We will address these two potential issues in Sects. 4.2.4 and 4.3.1, respectively.

The approach taken here to derive the PSF is broadly similar to that applied to images of Mercury in transit from Hinode/SOT/BFI by Mathew et al. (2009). Specifically, by minimising the difference between observed intensity and that produced in a model of the aperture diffraction and stray light-free image (termed here the artificial image) by the convolution with a guess PSF. There are two significant departures.

Firstly, in this study, the artificial image is given by the surface fit to the mean transit image, with a disc of zeroes representing the venusian disc. In the cited work, the authors filled the mercurian disc in the recorded image with zeroes and took the result as the artificial image. As stated earlier in this subsection, having excluded the venusian disc and surroundings in the regression, the surface fit to the mean transit image is, in this excluded

region, an approximation of the intensity had Venus been absent. For this we consider the approach taken here to yield a more realistic model of the instrumental scattered light-free image.

Secondly, as mentioned in the introduction, while the earlier effort assumed an isotropic form to the PSF, here we allowed the PSF to vary with azimuth. We were motivated by the observation that the stray light behaviour of the instrument is evidently anisotropic (Sect. 4.2.1 and Fig. 4.3).

4.2.3 Image restoration method

To correct HMI observations for aperture diffraction and stray light, we utilised the implementation of the Richardson-Lucy algorithm, RLA (Richardson 1972, Lucy 1974), included in the IDL Astronomy User's Library, `max_likelihood.pro`.

The RLA is an iterative method for restoring an image blurred by a known PSF, in our study, the guess PSF, K . Let f_k denote the estimate of the restored image from the k -th iteration, f_{k+1} is given by

$$f_{k+1} = f_k \circ ((f_k * K) \star K), \quad (4.2)$$

where the \circ , $*$ and \star symbols represent the pixel-by-pixel product, convolution and correlation, respectively. The method has been shown, empirically, for data obeying Poisson statistics, to converge towards the maximum likelihood solution (Shepp and Vardi 1982). Following Mathew et al. (2009), we employed a threshold for the chi-square between the original image and $f_k * K$ as the stopping rule. Here we set the threshold at 99.99% confidence level.

In Figs. 4.5 and 4.6a we show the result of restoring one of the 42 continuum filtergrams averaged to yield the mean transit image (recorded at 02:25:37 UTC, June 6, 2012), hereafter referred to as the test transit image, with K_1 . The image restoration sharpened the test transit image considerably and removed most of the signal on the venusian disc. The restoration however, also left a ringing artefact around the venusian disc; manifest as the bright halo in the grey scale plot (middle panel, Fig. 4.5) and the peak in the radial intensity profile (black solid curve, Fig. 4.6a). Restoring other observations taken nearby in time (within a few hours of the test transit image), we found similar artefacts in the boundary of active region faculae, and sunspot penumbra and umbra.

Mathew et al. (2009) in the similar study with images of Mercury in transit from Hinode/SOT/BFI noted similar ringing artefacts around the mercurian disc upon image restoration with the RLA. The authors attributed it to Gibb's phenomenon, ringing artefacts in the Fourier series representation of discontinuous signals. In the PSF derivation and image restoration process described here, discrete Fourier transforms, DFTs were executed in convolution and correlation computations. We found that repeating the derivation of K_1 and the restoration of the test transit image without performing any DFTs in the convolution and correlation computations had negligible effect on the ringing artefact, ruling out Gibb's phenomenon as the main cause in this instance. In the following subsection we will demonstrate the ringing artefact found here to arise from us not taking the interaction between solar radiation and the venusian atmosphere into account in deriving K_1 .

Figure 4.7 is a colour scale plot of the venusian disc in the restored test transit image (left panel). The plot is saturated at about 2% of the mean photospheric level to reveal

4 Point spread function of SDO/HMI and the effects of stray light correction on the apparent properties of solar surface phenomena

(The contents of this chapter are identical to the printed version of Yeo, K. L., Feller, A., Solanki, S. K., Couvidat, S., Danilovic, S., Krivova, N. A., 2014, Point spread function of SDO/HMI and the effects of stray light correction on the apparent properties of solar surface phenomena, Astron. Astrophys., 561, A22.)

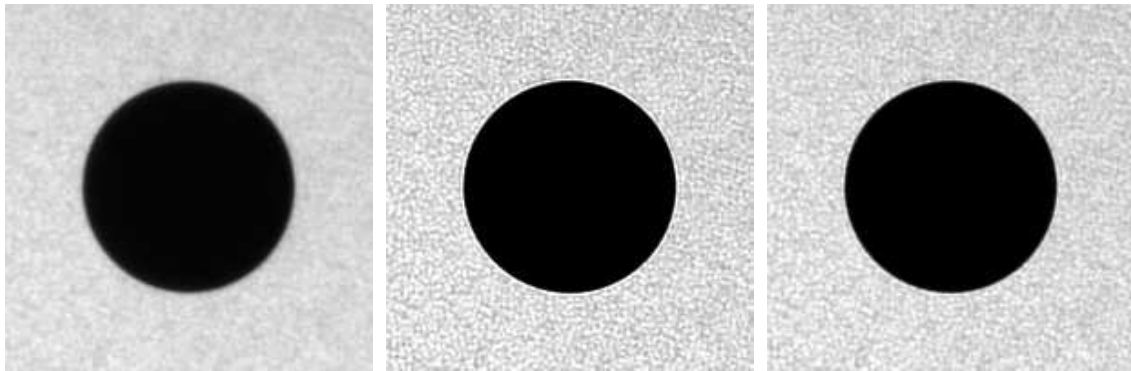


Figure 4.5: 201×201 pixel inset, centred on Venus, of the test transit image; before (left) and after image restoration with K_1 (middle), and with K_2 (right). The three grey scale plots are saturated at 6×10^4 DN/s, about 120% of the mean photospheric level.

the spatial distribution of residual intensity (instrumental scattered light not removed by the image restoration) on the venusian disc. Also shown is the result of restoring the test transit image with K_1 excluding the anisotropy of the PSF by setting A_i at zero (right panel). There is a gross, broadly east-west graduation of the residual intensity in the latter, not apparent in the former, where the residual intensity level is significantly more uniform across the venusian disc. This demonstrates the necessity to constrain the anisotropy of the PSF to properly correct HMI observations for instrumental scattered light.

4.2.4 Interaction between solar radiation and the venusian atmosphere

As stated in Sect. 4.2.2, the PSF derivation method described so far builds on the assumption that there is no interaction between solar radiation and the venusian atmosphere.

In representing the venusian disc as a disc of zeroes in the artificial image, we have presumed that the body would, in the absence of aperture diffraction and stray light, be completely dark and exhibit a discrete edge. Diffusion and scattering of solar radiation in the venusian atmosphere can, however, render the edge of the venusian disc diffused.

The PSF is retrieved from matching the mean transit image to the convolution of the artificial image and the guess PSF. This is valid if all measured intensity came directly from the Sun. This is, however, not the case; there is a bright halo around the venusian disc when it is in transit (termed the aureole) from the refraction of solar radiation by the upper layers of the atmosphere towards the observer.

4.2.4.1 Diffusion and scattering of solar radiation in the venusian atmosphere

To elucidate the influence of diffusion and scattering of solar radiation in the venusian atmosphere on the retrieved PSF we repeated the derivation, approximating the action of diffusion and scattering by blurring the edge of the disc of zeroes in the artificial image prior to the convolution with the guess PSF. We generated a copy of the artificial image that is unity everywhere outside the venusian disc and zero inside, convolved it with a Gaussian kernel, and scaled the original artificial image by the result. This procedure

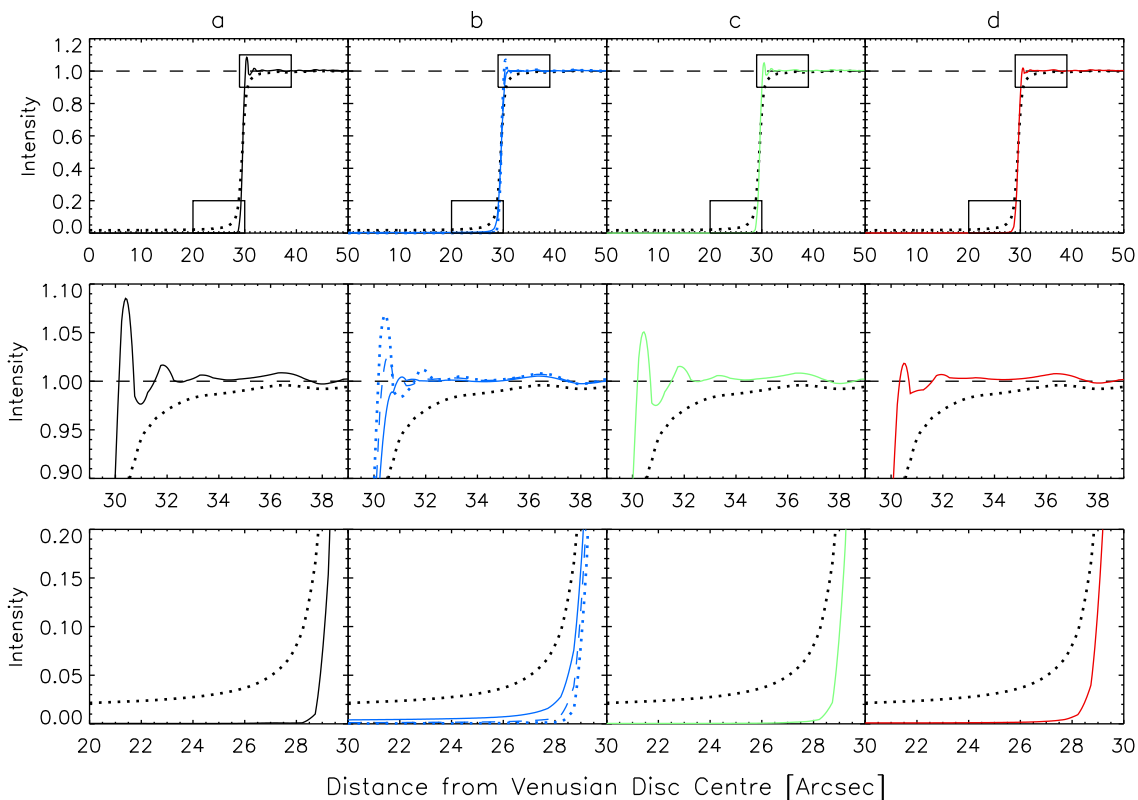


Figure 4.6: Top: Radial intensity in the test transit image, corrected for limb darkening, as a function of distance from the centre of the venusian disc before (black dotted curves) and after image restoration with the various PSF estimates. a) With K_1 (black solid curve). b) With the PSFs obtained by blurring the edge of the disc of zeroes in the artificial image with kernels representing Gaussian functions with standard deviations of 0.2, 0.3 and 0.4 arcsec (blue dotted, dashed and solid curves). c) With the PSF retrieved by subtracting the estimated aureole intensity from the mean transit image (green solid curve). d) With K_2 (red solid curve). Middle and bottom: Blow-up insets of the boxed areas. The radius of the venusian disc, a free parameter in the LMA optimization, is in all instances about 29.3 arcsec and not marked to avoid cluttering. The horizontal dashed lines follow unit intensity. The test transit image was corrected for limb darkening by normalizing it by the surface fit, computed as done for the mean transit image in Sect. 4.2.2.

introduces Gaussian blur that is confined to near the edge of the disc of zeroes. We repeated the derivation of the PSF with different degrees of Gaussian blurring.

In Fig. 4.8 (top panel) we display the PSFs retrieved after blurring the edge of the disc of zeroes with kernels representing Gaussian functions with standard deviations of 0.2, 0.3 and 0.4 arcsec (blue dotted, dashed and solid curves) along K_1 (black dashed curve). In Fig. 4.6b we have the radial intensity profile of the test transit image before and after image restoration with these PSFs. The stronger the blurring, the narrower the core of the PSF and the weaker the ringing artefact. The narrowest Gaussian kernel (0.2 arcsec) returned a PSF that is still very similar to K_1 while the broadest (0.4 arcsec) yielded a PSF that is unphysical, significantly narrower at the core than the ideal diffraction-limited PSF.

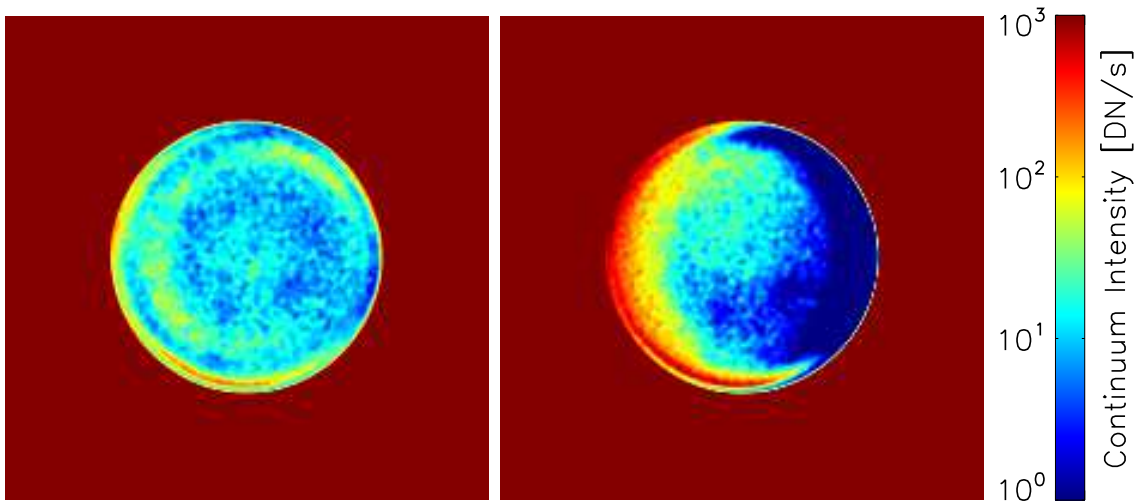


Figure 4.7: 201×201 pixel inset, centred on Venus, of the test transit image after image restoration with K_1 (left) and the same, except with A_i set to zero (right).

As the Gaussian blurring is confined to near the edge of the disc of zeroes, the retrieved PSFs do not differ significantly from K_1 beyond a few arcseconds from the centre of the PSF.

4.2.4.2 Refraction of solar radiation in the venusian atmosphere

We estimated the contribution by the aureole to apparent intensity in the mean transit image. For this purpose we examined the 854×854 pixel crop, centred on the venusian disc, of a continuum filtergram taken shortly (~ 10 seconds) before the venusian disc moved completely into the solar disc (recorded at 22:25:33 UTC, June 5, 2012), hereafter referred to as the ingress image. The ingress image is expressed as a grey scale plot in Fig. 4.9.

The aureole is only directly observable at ingress and egress (i.e., when the venusian disc is only partially within the solar disc), in the part of the venusian disc outside the solar disc. This is because the aureole is much dimmer than the photosphere and therefore difficult to distinguish from direct solar radiation. Generally, the intensity of the aureole increases with the proportion of the venusian disc sitting inside the solar disc (Tanga et al. 2012). Therefore, observations taken right before second contact (such as the ingress image) or right after third contact give the closest direct indication of the intensity of the aureole when the venusian disc is entirely within the solar disc. The intensity of the aureole also varies with azimuth. This is, at least in part, because it is modulated by the spatial distribution of photospheric intensity (Tanga et al. 2012) and variation in the physical structure of the venusian atmosphere with latitude (Pasachoff et al. 2011).

Here we looked at the intensity of the aureole in the ingress image over the minor sector marked in Fig. 4.9 (blue lines), where it is relatively stable with azimuth.

The radial intensity profile over the minor sector marked in Fig. 4.9 is plotted in Fig. 4.10 (circles, top panel). The peak near the edge of the venusian disc (dashed line) corresponds to the aureole while the slowly varying background is largely instrumental

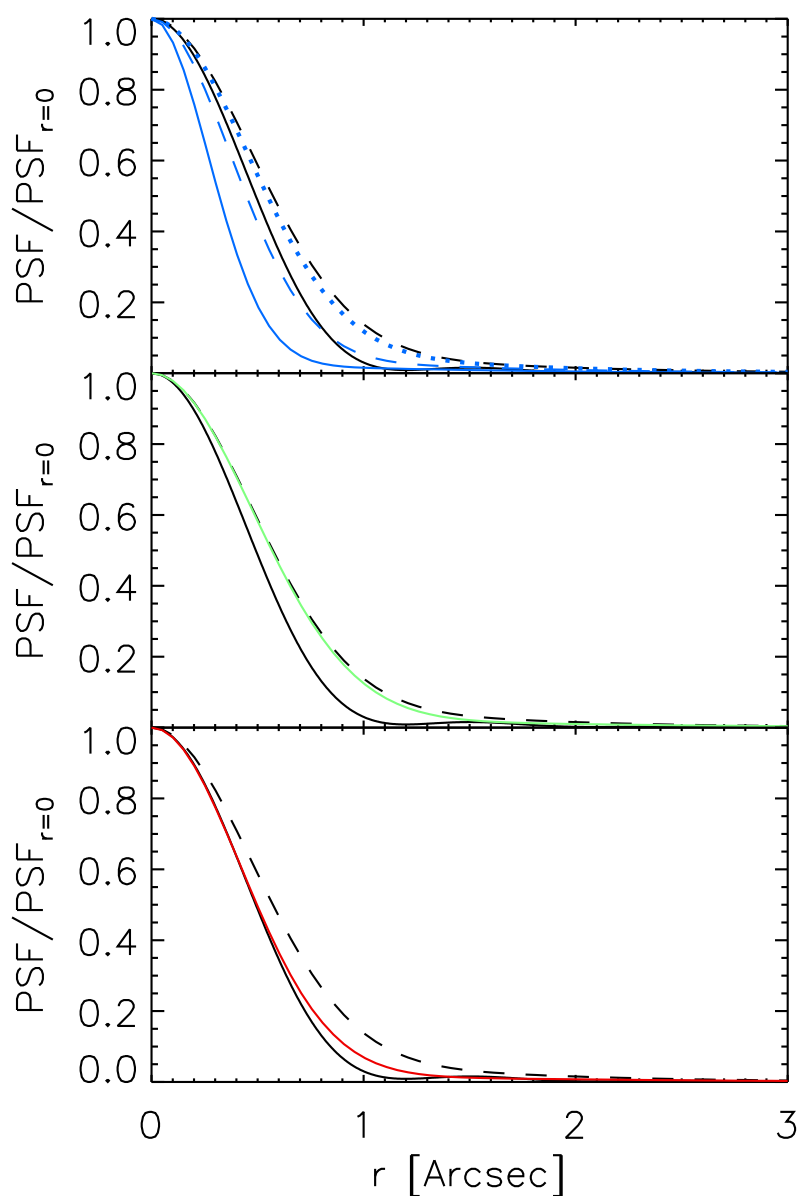


Figure 4.8: Comparison between K_1 (black dashed curves), the ideal diffraction-limited PSF (black solid curves) and the other retrieved PSFs. The blue curves (top) represent the PSFs retrieved after blurring the edge of the disc of zeroes in the artificial image by kernels representing Gaussian functions with standard deviations of 0.2 (dotted), 0.3 (dashed) and 0.4 arcsec (solid). The green curve (middle) corresponds to the PSF found by subtracting the estimated aureole intensity from the mean transit image. The red curve (bottom) corresponds to K_2 . For illustration purposes, we set the value of A_i at zero (i.e., ignoring the azimuthal dependence) and normalized each PSF to the level at $r = 0$. As the retrieved PSFs represent estimates of the pixel integrated true PSF, the ideal diffraction-limited PSF was smoothed with a box function of pixel scale width to allow a direct comparison.

4 Point spread function of SDO/HMI and the effects of stray light correction on the apparent properties of solar surface phenomena

(The contents of this chapter are identical to the printed version of Yeo, K. L., Feller, A., Solanki, S. K., Couvidat, S., Danilovic, S., Krivova, N. A., 2014, *Point spread function of SDO/HMI and the effects of stray light correction on the apparent properties of solar surface phenomena*, *Astron. Astrophys.*, 561, A22.)

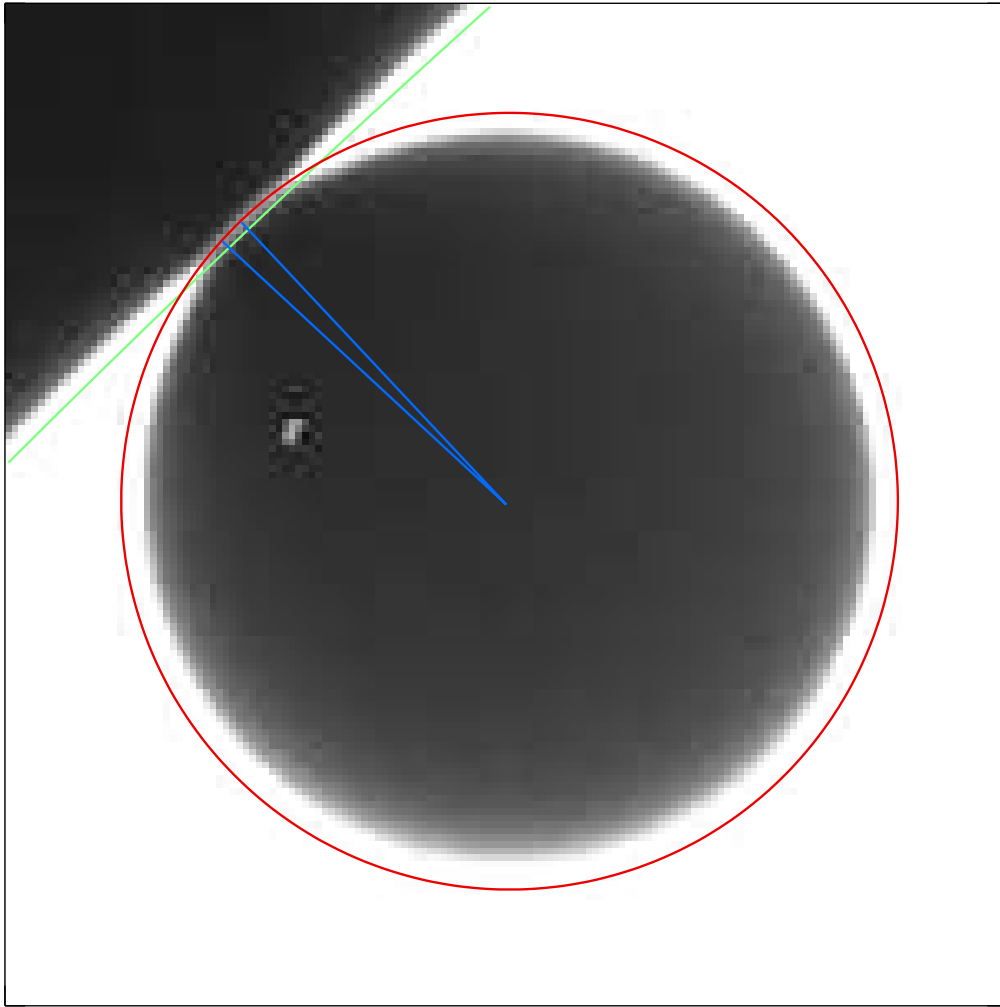


Figure 4.9: 151×151 pixel inset, centred on Venus, of the ingress image. The edge of the venusian disc (as given by the point of inflexion on \hat{I}_r) and of the solar disc are indicated by the red and green contours respectively. They do not coincide with the apparent boundaries due to the low grey scale saturation level. The grey scale is saturated at 3000 DN/s ($\sim 5\%$ of the mean photospheric level at disc centre) to allow the aureole, the bright arc on the part of the venusian disc outside the solar disc, which is much dimmer than the solar disc, to be visible. The blue lines mark the minor sector within which the intensity of the aureole is relatively stable with azimuth. The bright feature on the northwest quadrant of the venusian disc is an artefact of cosmic ray hits on the CCD.

scattered light from the solar disc. We subtracted the polynomial fit to the background (red curve) from the radial intensity profile. To the background-subtracted radial intensity profile (circles, bottom panel) we fit the linear combination of two Gaussian functions (blue curve). We then scaled this fit by the quotient of the integrated photospheric intensity behind the venusian disc in the mean transit image and in the ingress image⁵. The result

⁵The intensity of the photosphere behind the venusian disc in the mean transit image is given by the surface fit described in Sect. 4.2.2. For the ingress image, we binned the image pixels on the solar disc by

(green curve) represents an estimate of the radial intensity profile of the aureole in the mean transit image.

In Fig. 4.8 (middle panel) we compare the PSF retrieved after first subtracting the estimated radial intensity profile of the aureole from the mean transit image (green curve) with K_1 (black dashed curve). In Fig. 4.6c we have the radial intensity profile in the test transit image, before and after image restoration with this PSF. The effect of removing the contribution by the aureole to observed intensity on the retrieved PSF and the ringing artefact in the restored test transit image is similar as that from introducing Gaussian blur to the edge of the disc of zeroes in the artificial image. The retrieved PSF is slightly narrower than K_1 at the core. The ringing artefact in the restored test transit image is slightly weaker. As the aureole is concentrated near the edge of the venusian disc, removing it from the mean transit image made little difference to the retrieved PSF beyond a few arcseconds from the core.

In removing the contribution of the aureole from the mean transit image as described above, we have made two simplifying assumptions:

- One, that the intensity of the aureole is directly proportional to the integrated photospheric intensity behind the venusian disc.
- Two, that the intensity of the aureole does not change with azimuth.

Tanga et al. (2012) recently published a model of aureole intensity, relating it to the spatial distribution of photospheric intensity and physical structure of the venusian atmosphere. This is, to our knowledge, the only model of its kind reported in the literature. Given the fact that the aureole is blurred by instrumental scattered light, the uncertainties over the structure of the venusian atmosphere, and in the interest of simplicity, we favoured the rather approximate approach taken here over a more rigorous computation based on the model of Tanga et al. (2012). The estimated peak intensity of the aureole in the mean transit image is about 1500 DN/s (blue curve, Fig. 4.10), much smaller than the photospheric level ($\sim 5 \times 10^4$ DN/s, Fig. 4.4). Taking into account this as well as the relatively minor effect of subtracting the radial intensity profile of the aureole from the mean transit image on the retrieved PSF, we surmise that the uncertainty introduced by the two assumptions listed is likely minimal.

By repeating the derivation of the PSF and restoration of the test transit image, first blurring the edge of the disc of zeroes in the artificial image or subtracting the estimated contribution by the aureole to the mean transit image, we have demonstrated that the interaction between solar radiation and the venusian atmosphere has a palpable impact on the width of the core of the retrieved PSF. Both adjustments yielded PSFs that were narrower at the core compared to K_1 (Fig. 4.8). And the narrower the core of the PSF, the weaker the ringing artefact in the restored test transit image (Fig. 4.6). The width of the core of K_1 , derived with no consideration of the venusian atmosphere, is over-estimated and the over-sharpening this produces when used to restore HMI data shows up as ringing artefacts near where the signal is changing rapidly.

μ , excluding the venusian disc and surroundings, and took the bin-averaged intensity. The intensity behind the venusian disc was then estimated from the polynomial fit to these bin-averaged intensities given the μ of each image pixel within the venusian disc.

4 Point spread function of SDO/HMI and the effects of stray light correction on the apparent properties of solar surface phenomena

(The contents of this chapter are identical to the printed version of Yeo, K. L., Feller, A., Solanki, S. K., Couvidat, S., Danilovic, S., Krivova, N. A., 2014, Point spread function of SDO/HMI and the effects of stray light correction on the apparent properties of solar surface phenomena, *Astron. Astrophys.*, 561, A22.)

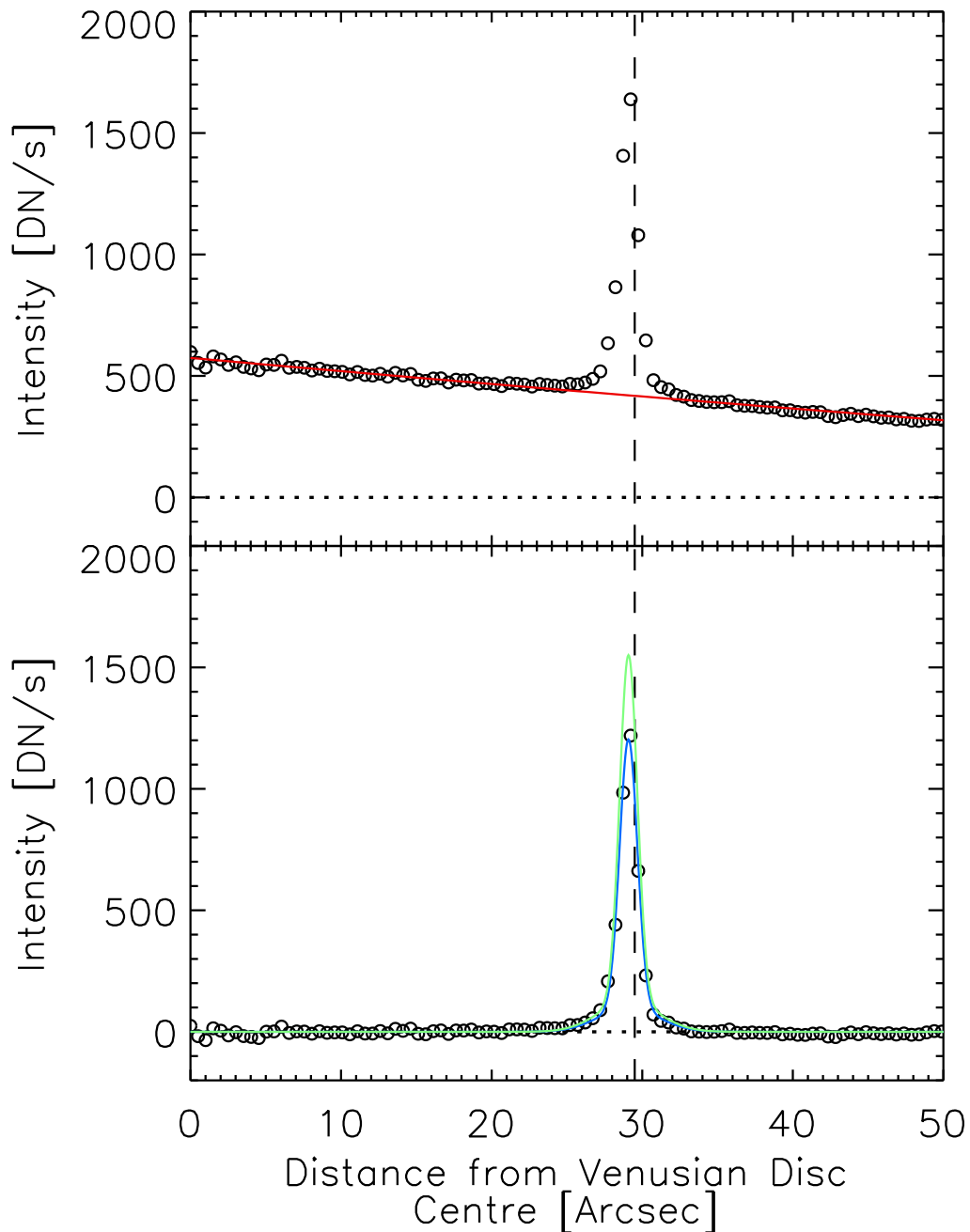


Figure 4.10: Intensity in the ingress image, averaged over the minor sector marked in Fig. 4.9, as a function of distance from the centre of the venusian disc (circles); before (top panel) and after (bottom panel) subtracting the polynomial fit to the slowly varying background (red curve). The blue curve corresponds to the sum-of-two-Gaussians fit to the background-subtracted series, while the green curve is the same after scaling by the quotient of the total photospheric intensity behind the venusian disc in the mean transit image and in the ingress image. The black dashed and dotted lines denote the position of the Venus limb (as given by the point of inflexion on \hat{I}_r) and the zero intensity level, respectively.

4.2.4.3 Final estimate of the PSF

We arrived at our final estimate of the PSF by making the following changes to the derivation procedure described in Sect. 4.2.2.

- Firstly, we subtracted the estimate of the radial intensity profile of the aureole from the mean transit image.
- Secondly, we blurred the edge of the disc of zeroes in the artificial image with a Gaussian kernel, the width of which we allowed to be a free parameter in the LMA optimization.
- Lastly, we fixed the width of the narrowest Gaussian component in the guess PSF such that the full width at half maximum, FWHM of the component is similar to that of the pixel-integrated ideal diffraction-limited PSF. The pixel integration was achieved by smoothing the ideal diffraction-limited PSF with a box filter of HMI pixel scale width.

The parameters of the PSF so derived, hereafter referred to as K_2 , are summarized in Table 4.2. The adjustments to the PSF derivation procedure yielded a PSF that is significantly narrower at the core compared to K_1 , though not more than the ideal diffraction-limited PSF (bottom panel, Fig. 4.8). The agreement between the aureole-subtracted mean transit image, and the convolution of the Gaussian-blurred artificial image with K_2 is similar as in the K_1 instance, illustrated in Figs. 4.3 and 4.4, and therefore not plotted here.

The best fit value of the scale factor applied to the artificial image is 1.0028 and the radius of the disc of zeroes 29.33 arcsec. The retrieved standard deviation of the Gaussian kernel is 0.26 arcsec. The scale height of the venusian atmosphere, at 15.9 km or approximately 0.08 arcsec, is of similar order. The degree of Gaussian blurring introduced is, as far as one can infer from such a comparison, physically plausible.

The intention here is to recover a conservative estimate of the PSF, making use of the fact that the PSF of the instrument cannot be narrower at the core than the ideal diffraction-limited PSF. Also, it was necessary to fix the width of the narrowest Gaussian component as allowing both this and the standard deviation of the Gaussian kernel to be free parameters leads to a degeneracy of the LMA optimization⁶. Though a conservative estimate, restoring the test transit image with K_2 still removed most of the intensity on the venusian disc while largely suppressing the ringing artefacts (Figs. 4.5 and 4.6d).

As stated in Sect. 4.2.2, a potential hazard of modelling the PSF as the linear combination of Gaussian functions is that it allows solutions with Strehl ratios greater than unity. This functional form is only appropriate when the weight and width of the broader Gaussian components, representing the non-ideal contribution to the PSF (instrumental effects other than aperture diffraction) are sufficiently high to avoid this (Wedemeyer-Böhm 2008). As evident in Fig. 4.11, this is indeed the case here for both K_1 (dashed curve) and K_2 (red curve). The greater integral under both PSFs compared to the pixel-integrated ideal diffraction-limited PSF, all normalized to the level at $r = 0$, indicates Strehl ratios of less than unity. (We cannot compute the Strehl ratio of K_1 and K_2 directly as they describe the pixel-integrated PSF.)

⁶Specifically, the LMA converged to different solutions for the PSF, some of which are narrower at the core than the ideal diffraction-limited PSF, depending on the initial value of the free parameters.

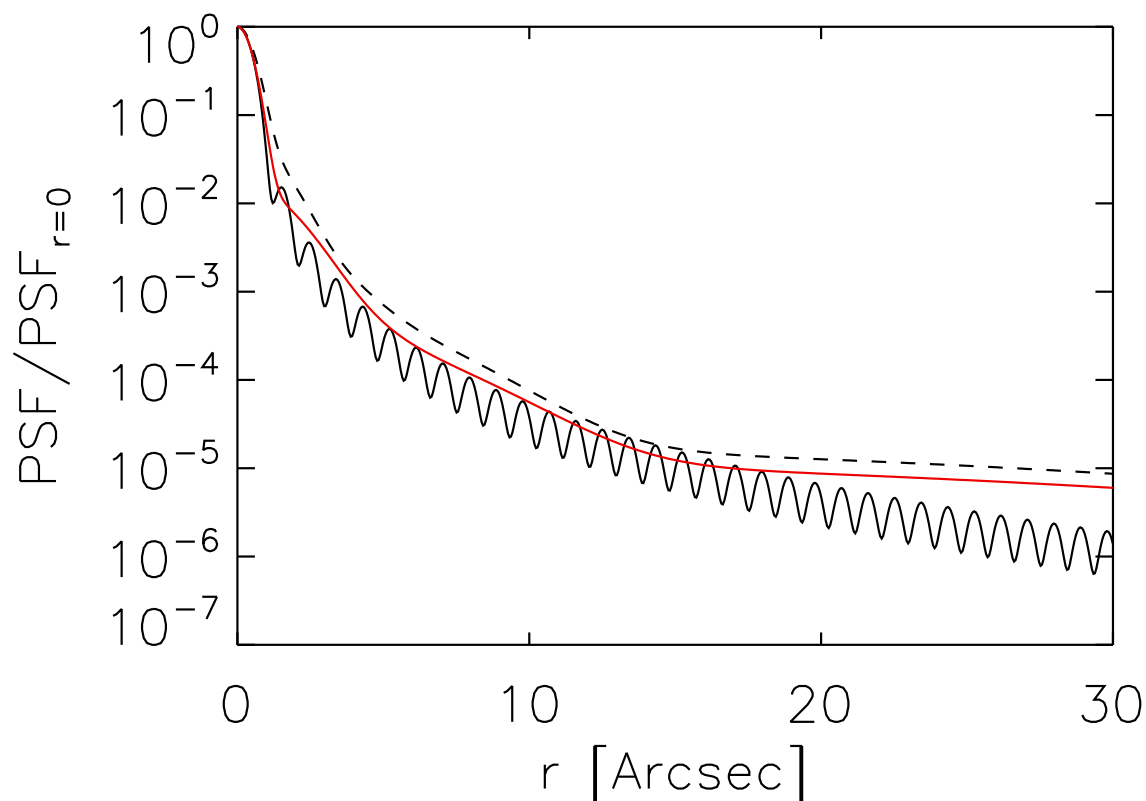


Figure 4.11: As in Fig. 4.8 (bottom panel), but with the PSF on a logarithmic scale and over an extended radial range.

4.2.5 Partial lunar eclipse and solar limb observations

As stated in the introduction, we consider the observations of Venus in transit the most appropriate available for recovering the PSF of the HMI, preferring them over data from partial lunar eclipses and of the solar limb.

It is challenging to constrain the PSF in both the radial and azimuthal dimensions with data from partial lunar eclipses due to the combination of the geometry, as well as jitter and defocus issues brought on by the lunar occultation itself.

- The radius of curvature of the terminator, the edge of the lunar disc, is much greater than the width of the PSF. So at any given point along the terminator, the spatial distribution of signal smeared onto the lunar disc largely reflects the PSF in the direction of the centre of curvature. Therefore, a given partial lunar eclipse image only contains information about the PSF within a limited range of azimuths. Circumventing this limitation by looking at multiple images with the terminator at different orientations is not straightforward due to the variation of the PSF with position in the FOV.
- The terminator is uneven from lunar terrain. This makes it complicated to model the aperture diffraction and stray light-free image as we did here for the mean transit image with the artificial image (Sect. 4.2.2). A possible solution is to reduce the

problem from 2D to 1D by looking at the radial intensity profile over segments of the terminator relatively free of lunar terrain features. This is, however, only appropriate when the terminator is near solar disc centre, where we can take the solar background to be uniform.

- The image stabilization system, ISS of the instrument was not always functional during the partial lunar eclipses due to the lunar disc blocking the diodes necessary for its operation, increasing the jitter.
- Having the lunar disc occult a significant proportion of the solar disc, and therefore greatly reducing the amount of impinging radiation, causes the front window of the instrument to cool, resulting in defocus (Schou et al. 2012b).
- There are observations made when the lunar disc was just starting to cover the solar disc and not blocking the ISS diodes. These data do not suffer jitter and defocus problems, but we cannot resolve the lunar terrain issue by reducing the problem from 2D to 1D as described above, as the variation in the solar background from limb darkening is significant here.

Our approach in this study is to constraint the PSF by the spatial distribution of intensity about a closed bright and dark boundary as this allows us to recover the full azimuthal dependence (i.e., all directions). For this we can either employ observations of Venus in transit or of the solar limb. The PSF of HMI likely varies with position in the FOV, as shown for the part of the FOV transversed by Venus in Sect. 4.2.1. The longer the boundary used to constrain the PSF, the greater the contribution by the variation of the PSF with position in the FOV to observed intensity fluctuation along and near the boundary, which introduces bias to the retrieved PSF. The venusian disc occupies only about 0.06% of the FOV by area, and the solar disc, over 60%. The variation of the PSF over the part of the FOV occupied by the venusian disc is likely minimal, making these observations more suited for the purpose.

In view of the issues associated with deducing the PSF from partial lunar eclipse and solar limb data, we utilised the observations of Venus in transit though the interaction between solar radiation and the venusian atmosphere is challenging to account for, leaving us with only a conservative estimate of the PSF (Sect. 4.2.4).

4.3 Application of the derived PSF to HMI observations

4.3.1 Granulation contrast

Restoring HMI data with K_2 is not exact. This is due to the approximate account of the influence of the venusian atmosphere in the derivation of K_2 (Sect. 4.2.4) and from applying a single PSF to the entire FOV (so ignoring the variation of the PSF with position in the FOV, discussed in detail in Sect. 4.4.1). In this subsection we examine the effect of image restoration with K_2 on apparent granulation contrast, represented by the RMS intensity contrast of the quiet Sun⁷. We compare the values deduced from HMI continuum

⁷Intensity variation in the quiet Sun arises mainly from granulation.

4 Point spread function of SDO/HMI and the effects of stray light correction on the apparent properties of solar surface phenomena

(The contents of this chapter are identical to the printed version of Yeo, K. L., Feller, A., Solanki, S. K., Couvidat, S., Danilovic, S., Krivova, N. A., 2014, Point spread function of SDO/HMI and the effects of stray light correction on the apparent properties of solar surface phenomena, Astron. Astrophys., 561, A22.)

observations and from synthetic intensity maps generated from a 3D MHD simulation. The purpose is to demonstrate that image restoration with K_2 , with all its limitations, still yields reasonable estimates of the aperture diffraction and stray light-free intensity contrast.

The side CCD continued to observe in the continuum for about an hour after the end of the transit of Venus. For this analysis we employed a continuum filtergram from this period (recorded at 04:35:59 UTC, June 6, 2012), hereafter referred to as the test continuum filtergram. Of the various types of data available from HMI, the continuum filtergram represents the closest to a near instantaneous continuum capture (exposure time of ~ 0.135 seconds). This implies minimal loss of apparent contrast from averaging in time. It is worth noting however, that the continuum bandpass (-344 m\AA from line centre), whilst close to the clean continuum, may be slightly affected by the far wing of the Fe I 6173 \AA line.

The intensity contrast of pixels corresponding to quiet Sun in the test continuum filtergram was computed largely following the method of Yeo et al. (2013), who examined the intensity contrast of small-scale magnetic concentrations utilizing the 45-s continuum intensity and line depth data products from the front CCD. As in the cited work, the intensity contrast at a given image pixel is defined here as the normalized difference to the mean quiet-Sun intensity.

First, we identified magnetic activity present using the 45-s longitudinal magnetogram from the front CCD closest in time (< 1 minute) to the test continuum filtergram⁸. Let $\langle B_l \rangle / \mu$ denote the magnetogram signal, the mean line-of-sight magnetic flux density within a given image pixel, corrected (to first order) for foreshortening by the quotient with μ . The magnetogram was resampled to register with the test continuum filtergram. Image pixels in the test continuum filtergram corresponding to points where $\langle B_l \rangle / \mu > 10 \text{ G}$ in the resampled magnetogram were taken to contain significant magnetic activity and masked, leaving quiet Sun.

The test continuum filtergram was corrected for limb darkening by normalizing it by a fifth order polynomial in μ fit to the quiet Sun pixels (following Neckel and Labs 1994). Let I/I_0 denote the limb darkening corrected intensity. Next, we derived the mean I/I_0 of the quiet Sun, $\langle I/I_0 \rangle_{\text{QS}}$ as a function of position on the solar disc. As similarly noted for the 45-s continuum and line depth data products by Yeo et al. (2013), there are distortions in HMI filtergrams such that $\langle I/I_0 \rangle_{\text{QS}}$ is not at unity but varying with position on the solar disc. (This is not to be confused with the spatial distortion present in HMI data discussed in Sect. 4.2.1.)

We sampled the solar disc at 16-pixel intervals in both the vertical and horizontal directions. At each sampled point, we retrieved the median intensity of all the quiet Sun pixels inside a 401×401 pixel window centred on the point. We then fit a bivariate polynomial surface to the values so obtained from the entire disc. This surface describes $\langle I/I_0 \rangle_{\text{QS}}$ as a function of position on the solar disc. The intensity contrast at a given image pixel is then given by the value of $\frac{I/I_0}{\langle I/I_0 \rangle_{\text{QS}}} - 1$ there.

Finally, we derived the RMS intensity contrast of the quiet Sun as a function of μ . To this end we grouped the quiet Sun pixels by μ in bins with a width of 0.01 and took

⁸The 720-s longitudinal magnetogram data product from the side CCD, generated from the regular filtergram sequence, is evidently not available when this CCD is observing in the continuum.

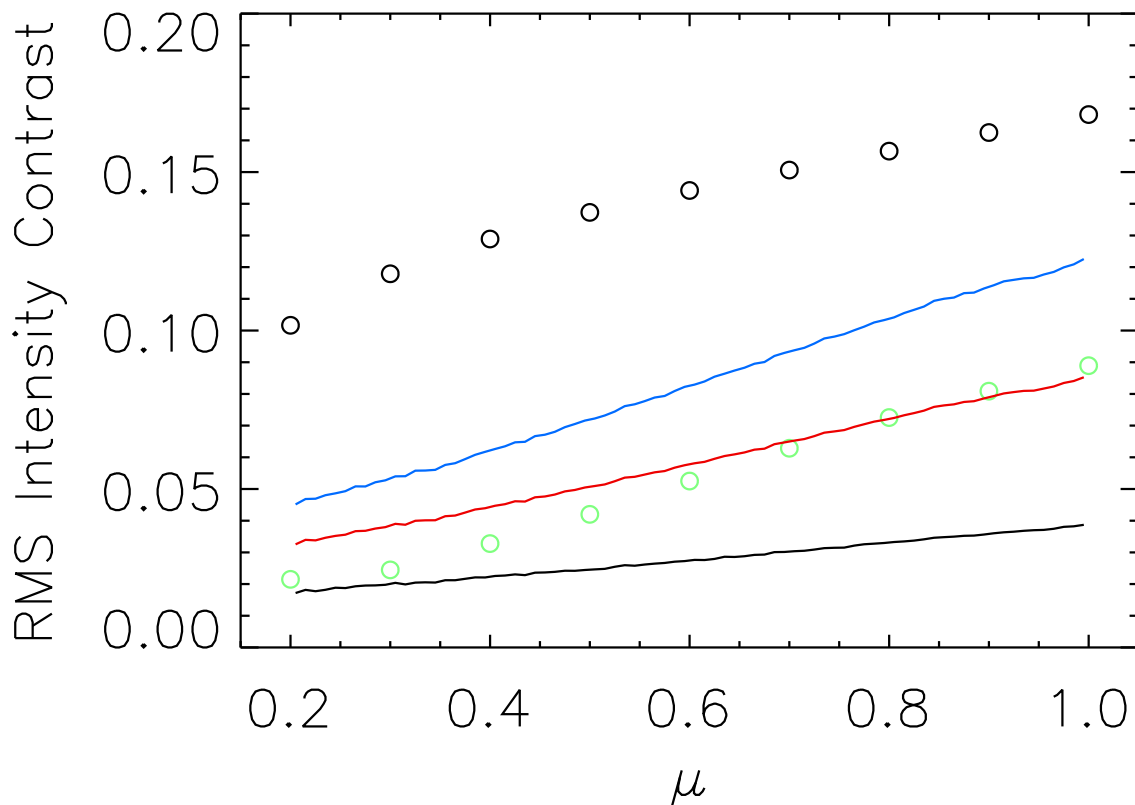


Figure 4.12: RMS intensity contrast of the quiet Sun in the test continuum filtergram as a function of μ , before (black curve), and after image restoration with K_1 (blue curve) and with K_2 (red curve). The black circles represent the values from the synthetic intensity maps and the green circles the same, rescaled to reflect the proportion arising from spatial frequencies up to the cutoff spatial frequency of the restored (with K_2) test continuum filtergram (see text).

the RMS intensity contrast within each bin. The results are expressed in Fig. 4.12 (black curve). Also plotted are the values from first restoring the test continuum filtergram with K_1 (blue curve), and with K_2 (red curve). Quiet Sun pixels near the limb ($\mu < 0.2$) were excluded. Towards the limb, the spread in measured intensity contrast in HMI data is dominated by scatter from the combination of the diminishing signal-to-noise ratio and the limb darkening correction (Yeo et al. 2013).

The decline in granulation contrast with distance from disc centre, seen here for the test continuum filtergram, is a known, well reported phenomenon (see Sánchez Cuberes et al. 2000, 2003, and references therein). Also within expectation, image restoration resulted in greater RMS contrasts, by a factor of about 2.6 near limb in the K_1 instance, going up to 3.2 at disc centre, and going from 1.9 to 2.2 for K_2 .

The apparent granulation contrast is not only significantly enhanced by image restoration but also rather sensitive to differences between K_1 and K_2 . This makes the RMS intensity contrast of the quiet Sun a suitable check of the goodness of K_2 for the restoration of HMI data. We compared the values obtained here with values from synthetic intensity maps, artificial images of the quiet Sun produced from a numerical simulation.

4 Point spread function of SDO/HMI and the effects of stray light correction on the apparent properties of solar surface phenomena

(The contents of this chapter are identical to the printed version of Yeo, K. L., Feller, A., Solanki, S. K., Couvidat, S., Danilovic, S., Krivova, N. A., 2014, Point spread function of SDO/HMI and the effects of stray light correction on the apparent properties of solar surface phenomena, Astron. Astrophys., 561, A22.)

To this end, synthetic Stokes spectra were generated by applying the LTE radiative transfer package SPINOR/STOPRO (Solanki 1987, Frutiger et al. 2000), to snapshots of a 3D MHD simulation performed with the MURaM code (Vögler 2003, Vögler et al. 2005), as done in, for example, Danilovic et al. (2010, 2013).

The simulation, set up as in Danilovic et al. (2013), represents a layer encompassing the solar surface in the quiet Sun. The mean vertical magnetic flux density is 50 G. The simulation ran over about 23 minutes solar time after reaching a statistically steady state. Synthetic Stokes profiles were computed for ten snapshots of the simulation output, recorded at intervals of approximately two minutes solar time. From each snapshot we produced nine synthetic intensity maps corresponding to μ of 0.2, 0.3, 0.4 and so on, up to 1.0, rotating the snapshot along one dimension. The computational domain of the simulation spans 6×6 Mm in the horizontal, 1.4 Mm in depth, the top of the box lying about 0.5 Mm above the mean optical depth unity level, in a $288 \times 288 \times 100$ grid. This translates into a pixel scale of (0.0287μ) arcsec and 0.0287 arcsec, in the rotated and static direction, in the synthetic intensity maps.

The Stokes I and Q components of the synthetic spectra were convolved with a Gaussian function with a FWHM of 75 mÅ and sampled at -327 mÅ from the centre of the Fe I 6173 Å line in order to yield synthetic intensity maps mimicking the polarization (Stokes $I + Q$) and bandpass of the test continuum filtergram. The FWHM and central wavelength of the continuum bandpass were estimated from the main lobe of the CCD centre filter transmission profile⁹.

The synthetic intensity maps were resampled in the foreshortened direction such that the pixel scale is similar along both dimensions. The RMS contrast of a given intensity map is given by the RMS value of $\frac{I}{\langle I \rangle} - 1$ over all points, $\langle I \rangle$ denoting the mean intensity of the map. The mean RMS contrasts from the synthetic intensity maps at each μ level for which we simulated data are plotted along the measured values from the test continuum filtergram in Fig. 4.12 (black circles).

The RMS intensity contrast of the quiet Sun in the test continuum filtergram and the synthetic intensity maps cannot be compared directly due to the gross difference in the pixel scale (0.504 versus 0.0287 arcsec). Resampling the synthetic intensity maps to HMI's pixel scale is not feasible as the resampled synthetic intensity maps will extend only 16×16 pixels in the $\mu = 1.0$ case, going down to 3×16 pixels for $\mu = 0.2$. Simulations with considerably larger computational domains are necessary to yield synthetic intensity maps from which we can compute the RMS contrast at HMI's pixel scale with statistical confidence. What we did instead was to estimate, by comparing the power spectra of the synthetic intensity maps and the test continuum filtergram, the contribution to intensity variations in the synthetic intensity maps by spatial frequencies up to the resolution limit of the test continuum filtergram.

In Fig. 4.13 we plot the encircled energy of the power spectrum of the 361×361 pixel crop, centred on solar disc centre, of the test continuum filtergram. There are no sunspots present in this crop. We define the cutoff spatial frequency as the spatial frequency at which the encircled energy of the power spectrum reaches 0.99, taken here as an indication

⁹The filter transmission profiles of the HMI varies slightly with position in the CCD. The central wavelength of the main lobe, at -327 Å from line centre, differs from the bandpass position of -344 Å stated earlier. Quoted bandpass positions for HMI are theoretical figures derived assuming the filter transmission profiles are delta functions.

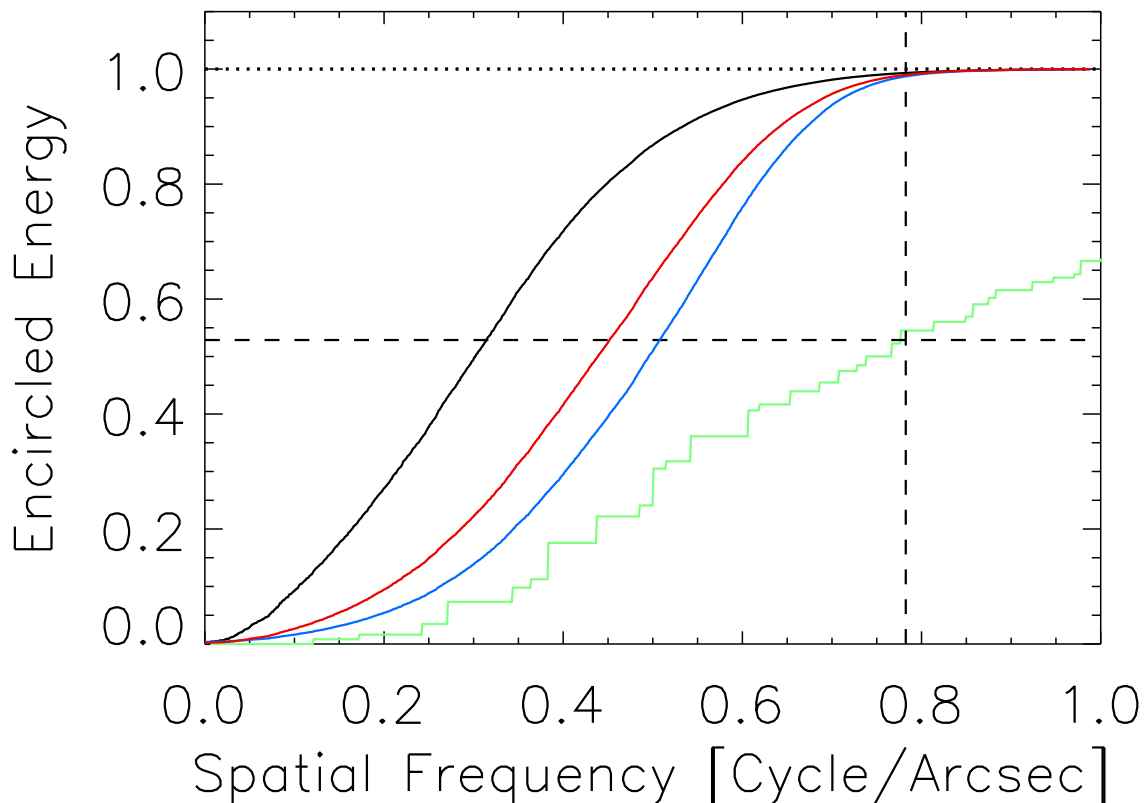


Figure 4.13: The encircled energy of the power spectrum of the 361×361 pixel inset, centred on the centre of the solar disc, of the test continuum filtergram, before (black), and after image restoration with K_1 (blue) and with K_2 (red). The green series gives the encircled energy of the mean power spectrum of the synthetic intensity maps corresponding to $\mu = 1.0$. The vertical dashed line marks the cutoff spatial frequency (see text) of the restored (with K_2) test continuum filtergram and the horizontal dashed line the encircled energy of the mean power spectrum of the $\mu = 1.0$ synthetic intensity maps at this spatial frequency. The dotted line denotes encircled energy of unity.

of the resolution limit. The cutoff spatial frequency is 0.75 cycle/arcsec for the original test continuum filtergram (black curve), and 0.79 cycle/arcsec and 0.78 cycle/arcsec for the iterations restored with K_1 (blue curve) and with K_2 (red curve).

As mentioned in Sect. 4.2.2, image restoration with a PSF that is the linear combination of Gaussian functions can potentially introduce aliasing artefacts from the enhancement of spatial frequencies above the Nyquist limit (0.99 cycle/arcsec for HMI). While image restoration with K_1 and K_2 enhanced image contrast, indicated here by the rightward displacement of the encircled energy profile for the restored iterations of the test continuum filtergram, it made little difference to the resolution limit which is also significantly lower than the Nyquist limit. Even after image restoration, almost all energy is confined to spatial frequencies well below the Nyquist limit. Aliasing artefacts from the restoration, if present, are likely negligible.

At each μ level for which we generated synthetic intensity maps, we computed the power spectrum of each intensity map and then the encircled energy of the mean power

4 Point spread function of SDO/HMI and the effects of stray light correction on the apparent properties of solar surface phenomena

(The contents of this chapter are identical to the printed version of Yeo, K. L., Feller, A., Solanki, S. K., Couvidat, S., Danilovic, S., Krivova, N. A., 2014, Point spread function of SDO/HMI and the effects of stray light correction on the apparent properties of solar surface phenomena, Astron. Astrophys., 561, A22.)

spectrum. Following that we estimated the encircled energy at the spatial cutoff frequency of the restored (with K_2) test continuum filtergram, illustrated in Fig. 4.13 for $\mu = 1.0$. The encircled energy here gives the proportion of observed intensity variation in the synthetic intensity maps arising from spatial frequencies up to the spatial cutoff frequency of the test continuum filtergram. The product of this quantity with the RMS intensity contrast of the quiet Sun from the synthetic intensity maps (green circles, Fig. 4.12) then represents an approximation of the RMS contrast if the spatial resolution of the synthetic intensity maps were similar to that of the test continuum filtergram. This treatment is very approximate, ignoring the fact that the spatial frequency response of the test continuum filtergram and synthetic intensity maps, up to the cutoff, are in all likelihood not similar.

In this analysis we had,

- defined the cutoff spatial frequency as the level where the encircled energy of the power spectrum reaches 0.99, and
- used the cutoff spatial frequency of the copy of the test continuum filtergram restored with K_2 to find the factors by which to rescale the RMS intensity contrast of the synthetic intensity maps (as the comparison between this restored version of the test continuum filtergram and the synthetic intensity maps is of greatest interest).

As stated above, the restoration of the test continuum filtergram made little difference to the cutoff spatial frequency. Also, the encircled energy of the power spectrum of the synthetic intensity maps does not vary strongly with spatial frequency in the regime of the cutoff spatial frequency of the test continuum filtergram, as visibly evident for the $\mu = 1.0$ example in Fig. 4.13. Hence, tests showed that the level of the rescaled RMS contrast is not sensitive to small variations in the threshold encircled energy level chosen in the definition of the cutoff spatial frequency. The result is also not changed significantly if we employ the cutoff spatial frequency of the unrestored and restored with K_1 versions of the test continuum filtergram to derive the rescaling factors instead.

The RMS intensity contrast of the quiet Sun in the restored (with K_2) test continuum filtergram (red curve, Fig. 4.12) and in the synthetic intensity maps, rescaled as described above (green circles), are of gratifyingly similar magnitude, less than or close to 0.01 apart at most μ , especially near disc centre. They do, however, differ in that the latter exhibits a steeper decline with distance from disc centre. The diverging trend with decreasing μ is likely, at least in part, from

- the approximate way of accounting for the influence of the venusian atmosphere in the derivation of K_2 (Sect. 4.2.4),
- applying a single PSF to the entire FOV, so ignoring the variation of the PSF with position in the FOV (discussed in detail in Sect. 4.4.1),
- the difference in the spatial frequency response of the test continuum filtergram and the synthetic intensity maps,
- sensor noise and its centre-to-limb variation (CLV), and
- Doppler shift of the spectral line from the motion of SDO and the rotation of the Sun, which may produce small, μ -dependent effects on apparent intensity in the continuum bandpass through the line wing.

The observation that these two series are close, even with these factors present, confers confidence that image restoration with K_2 , though not exact, returns a reasonable approximation of the true aperture diffraction and stray light-free intensity contrast.

A quantitative comparison of the RMS intensity contrast of the quiet Sun presented here for HMI and other measurements reported in the literature would require taking into account instrumental differences such as the spatial resolution and bandpass, which is beyond the scope of this study. Due to HMI's limited spatial resolution, the RMS contrast, even after image restoration with K_2 , remains below the values returned from spaceborne and balloon-borne (i.e., similarly seeing-free) observatories at finer spatial resolutions, namely Hinode (Danilovic et al. 2008, Mathew et al. 2009, Wedemeyer-Böhm and Rouppe van der Voort 2009) and SUNRISE (Hirzberger et al. 2010). (Note though, that the divergence is also due in part to the different bandpass of the various instruments.)

4.3.2 Effect of image restoration on the Dopplergram, longitudinal magnetogram, continuum intensity and line depth data products

In this subsection we discuss the effect of image restoration with K_2 on the Dopplergram, longitudinal magnetogram, continuum intensity and line depth data products. We examine the influence on the apparent continuum and line-core intensity, and magnetic field strength of small-scale magnetic concentrations, as well as sunspots and pores. We will also describe the result of image restoration on the apparent amount of magnetic flux on the solar surface and the line-of-sight velocity.

For this purpose we utilised a set of simultaneous (generated from the same sequence of filtergrams) 720-s Dopplergram, longitudinal magnetogram, continuum intensity and line depth images from the side CCD, taken shortly after this CCD resumed collection of the regular filtergram sequence, about an hour after Venus left the solar disc (at 05:35:32 UTC, June 6, 2012). Here we will refer to the result of subtracting the line depth image from the continuum intensity image, giving the intensity in the Fe I 6173 Å line, as the line-core intensity image.

As mentioned in Sect. 4.2.1, HMI data products cannot be corrected for stray light by the deconvolution with the PSF but instead we must correct either the Stokes parameters or the filtergrams used to compute the data products. The data set was restored for stray light by applying image restoration with K_2 to the corresponding 720-s Stokes parameters, and returning the result to the HMI data processing pipeline. A 200×200 pixel inset of the original and restored version of the data set, near disc centre ($\mu > 0.93$), featuring active region NOAA 11494, is shown in Fig. 4.14. The enhanced image contrast and visibility of small-scale structures is clearly evident.

The 720-s Milne-Eddington inversion data product includes the vector magnetogram. Since the inversion procedure employed to obtain this data product assumes a magnetic filling factor of unity everywhere, the process treats noise in the Stokes Q , U and V parameters as signal, creating pixel-averaged horizontal magnetic field strengths of ~ 100 G in the vector magnetogram even in the very quiet Sun. For ease of interpretation we confined ourselves to the longitudinal magnetogram data product here.

4 Point spread function of SDO/HMI and the effects of stray light correction on the apparent properties of solar surface phenomena

(The contents of this chapter are identical to the printed version of Yeo, K. L., Feller, A., Solanki, S. K., Couvidat, S., Danilovic, S., Krivova, N. A., 2014, *Point spread function of SDO/HMI and the effects of stray light correction on the apparent properties of solar surface phenomena*, *Astron. Astrophys.*, 561, A22.)

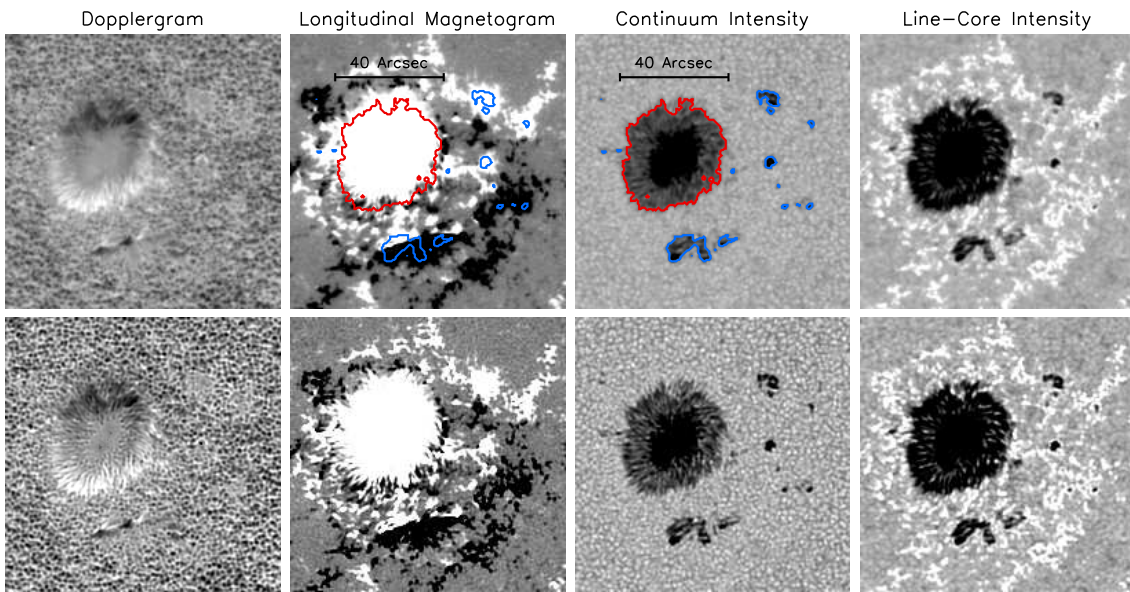


Figure 4.14: 200×200 pixel (101×101 arcsec) inset, near disc centre ($\mu > 0.93$), encompassing active region NOAA 11494, of the simultaneously recorded 720-s data products examined, before (top) and after (bottom) image restoration with K_2 . The grey scale is saturated at -1200 and 1200 ms^{-1} for the Dopplergrams, at -100 and 100 G for the longitudinal magnetograms, and at 0.6 and 1.2 for the continuum and line-core intensity images. The Dopplergram was corrected for the velocity of SDO relative to the Sun and for differential rotation (Sect. 4.3.2.4). Both the continuum and line-core intensity images were normalized to the mean quiet-Sun level (Sect. 4.3.2.1). The red and blue contours in the grey scale plot of the uncorrected longitudinal magnetogram and continuum intensity image follow $I/I_0 = (I/I_0)_{\text{QS,P}}$, the quiet Sun to penumbra boundary. The colour coding is to distinguish the big sunspot feature (red) from the smaller sunspots and pores (blue), treated separately in Fig. 4.17.

4.3.2.1 Intensity contrast and magnetogram signal of small-scale magnetic concentrations

Both the original and restored continuum and line-core intensity images were normalized by the fifth order polynomial in μ fit to the quiet Sun pixels. Then the intensity contrast at each image pixel was computed following the procedure applied to the test continuum filtergram in Sect. 4.3.1. For the line-core intensity image, the normalization not only corrects for limb darkening, but also the centre-to-limb weakening of the Fe I 6173 \AA line (Norton et al. 2006, Yeo et al. 2013).

Sunspots were identified by applying a continuum intensity threshold representing the quiet Sun-to-penumbra boundary, denoted $(I/I_0)_{\text{QS,P}}$. We took the threshold value for MDI continuum intensity images, taken at 6768 \AA , from Ball et al. (2012), 0.89 , and estimated the equivalent level at HMI's wavelength, 6173 \AA . Assuming sunspots to be perfect blackbodies and an effective temperature of 5800 K for the quiet Sun, the result is a threshold value of 0.88 . This is a crude approximation, ignoring the difference in spatial resolution and variation in the continuum formation height with wavelength (Solanki and

Unruh 1998, Sütterlin et al. 1999, Norton et al. 2006). Pores were also isolated by the application of this threshold. In the following we count these features to the sunspots and do not mention them separately.

We selected the image pixels where $\mu > 0.94$ (i.e., near disc centre), excluding sunspots (i.e., all points with $I/I_0 < (I/I_0)_{\text{QS,P}}$) and all points within three pixels of a sunspot. The selected points were binned by $\langle B_l \rangle / \mu$ such that we end up with 800 bins of equal population. We then took the mean $\langle B_l \rangle / \mu$, as well as the median continuum and line-core intensity contrast within each bin. The values for the uncorrected and restored copy of the data set are represented by the black and red curves respectively in Fig. 4.15. These profiles depict the intensity contrast of small-scale magnetic concentrations as a function of $\langle B_l \rangle / \mu$, which serves as an approximate proxy of the magnetic filling factor (Ortiz et al. 2002, Yeo et al. 2013), in the continuum and core of the Fe I 6173 Å line. This is effectively a repeat of part of the analysis of Yeo et al. (2013), except now on HMI observations corrected for aperture diffraction and stray light.

Comparing the magnetogram with the continuum intensity image, we found the magnetogram signal associated with sunspots to extend beyond the continuum intensity boundary, given by the $I/I_0 = (I/I_0)_{\text{QS,P}}$ locus (for example, in Fig. 4.14). This was similarly noted by Yeo et al. (2013), who attributed it to the encroachment of the magnetic canopy of sunspots, and the smearing of polarized signal originating from sunspots onto its surrounds by instrumental scattered light. Hence, close to sunspots, the magnetogram signal is not entirely from local, non-sunspot magnetic features alone and would introduce a bias into the intensity contrast versus $\langle B_l \rangle / \mu$ profiles (Fig. 4.15) if left unaccounted for. In the cited work pixels contiguous to sunspots and with $\langle B_l \rangle / \mu$ above a certain threshold level were masked. Here, we excluded only all points within three pixels of each sunspot, observing that excluding pixels further than this distance made no appreciable difference to the resulting intensity contrast versus $\langle B_l \rangle / \mu$ profiles. This measure is sufficient here as, unlike in the earlier study which examined almost all disc positions ($\mu > 0.1$), we are only looking at image pixels near disc centre ($\mu > 0.94$). Near disc centre, the influence of magnetic canopies, which are largely horizontal, on the longitudinal magnetogram signal near sunspots is not as significant or extensive as at disc positions closer to the limb.

The continuum and line-core intensity contrast versus $\langle B_l \rangle / \mu$ profile of small-scale magnetic concentrations near disc centre presented here for the uncorrected data set (black curves, Fig. 4.15) is nearly identical to that by Yeo et al. (2013) (Figs. 9 and 10 in their paper), who employed similar data and method of derivation. The profiles from the restored data set (red curves) span a wider range, by a factor of about 1.3 in the continuum and line-core intensity contrast, and 1.7 in $\langle B_l \rangle / \mu$, but are qualitatively similar in form.

Image restoration produced an absolute increase in the continuum and line-core intensity contrast everywhere except around the peak of the continuum contrast versus $\langle B_l \rangle / \mu$ profile. The lower maximum in the profile from the restored data set, compared to the profile from the uncorrected data set (2.6×10^{-3} versus 5.7×10^{-3}), is likely from the enhanced contrast of dark intergranular lanes.

In Fig. 4.16 we show the uncorrected and restored continuum intensity and $\langle B_l \rangle / \mu$ along a 21-pixel cut across example magnetic features near disc centre ($\mu = 0.97$). The troughs and peaks in the intensity curve (top panel) correspond to intergranular lanes and granules respectively. The magnetic features, the peaks in the $\langle B_l \rangle / \mu$ curve (bottom panel), sit inside the intergranular lanes. The $\langle B_l \rangle / \mu$ level at the core of these magnetic

4 Point spread function of SDO/HMI and the effects of stray light correction on the apparent properties of solar surface phenomena

(The contents of this chapter are identical to the printed version of Yeo, K. L., Feller, A., Solanki, S. K., Couvidat, S., Danilovic, S., Krivova, N. A., 2014, *Point spread function of SDO/HMI and the effects of stray light correction on the apparent properties of solar surface phenomena*, *Astron. Astrophys.*, 561, A22.)

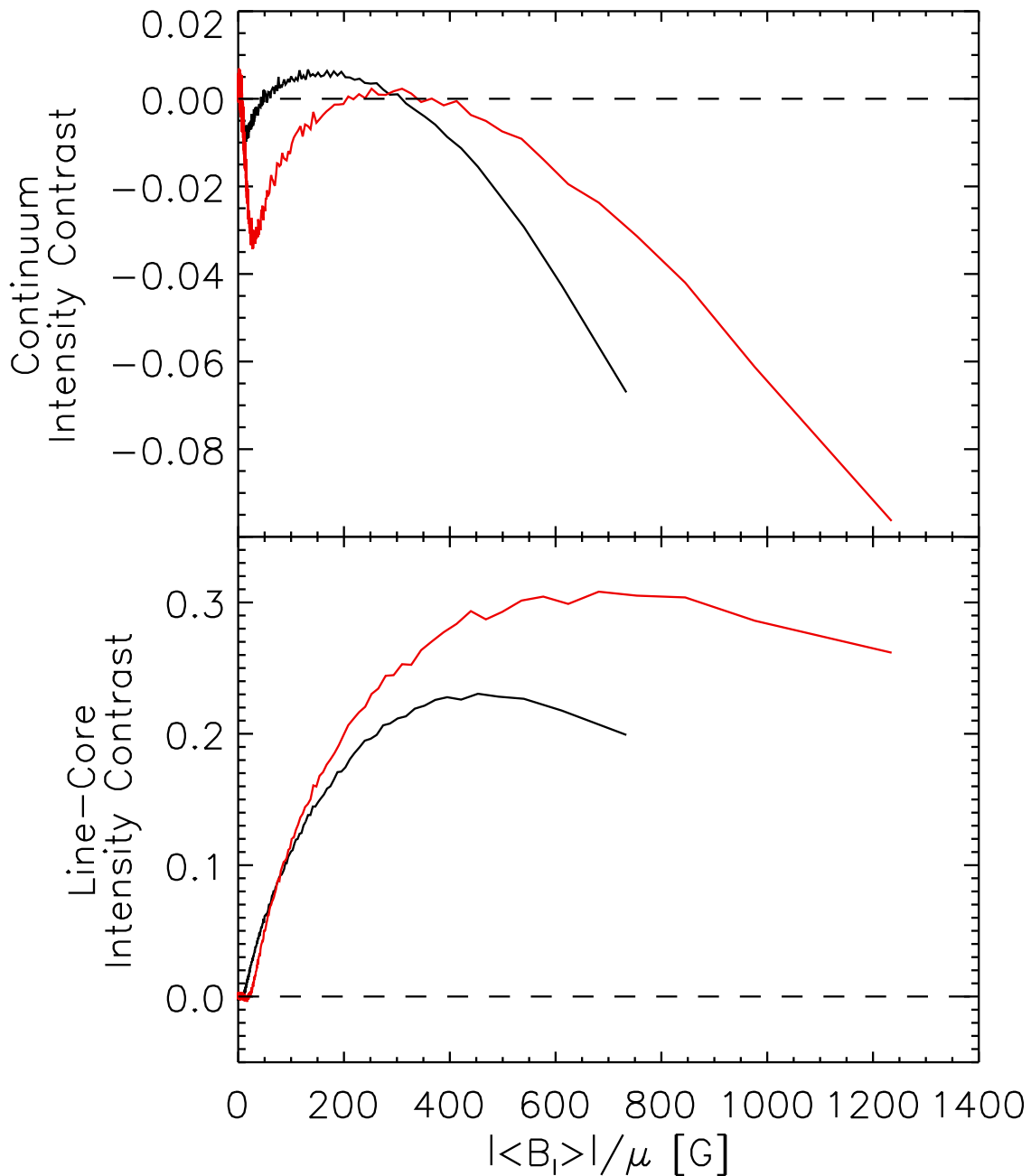


Figure 4.15: The continuum (top) and line core (bottom) intensity contrast of small-scale magnetic concentrations, near disc centre ($\mu > 0.94$), as a function of $\langle B_l \rangle / \mu$. The black and red curves correspond to the values from the original and restored (with K_2) data sets, respectively.

features lie in the regime of the peak of the continuum contrast versus $\langle B_l \rangle / \mu$ profile. The stray light correction boosted the magnetogram signal at the core of these magnetic features but also rendered them darker here, even from positive contrast to negative, as radiation originating from nearby granulation is removed from the intergranular lanes. The spatial resolution of HMI is insufficient to resolve many of the magnetic elements.

Consequently, measured intensities contain contributions not only from magnetic features but also from the intergranular lanes that host them.

The intensity contrast of small-scale magnetic concentrations in both the continuum and spectral lines component of the solar spectrum, in particular the variation with position on the solar disc and magnetic field strength, is an important consideration in understanding the contribution by these features to variation in solar irradiance (Yeo et al. 2013). To the extent tested, image restoration with K_2 enhanced measured intensity contrast and $\langle B_l \rangle / \mu$ significantly but made little qualitative difference to the dependence of apparent contrast on $\langle B_l \rangle / \mu$. The analysis here was restricted to image pixels near disc centre ($\mu > 0.94$). To extend the analysis to other disc positions, we would need to examine multiple full-disc images from different times featuring active regions at various disc positions as done by Ortiz et al. (2002) and Yeo et al. (2013), beyond the scope of this paper.

4.3.2.2 Intensity and magnetogram signal of sunspots and pores

In Fig. 4.17 we illustrate the change introduced by image restoration with K_2 on $\langle B_l \rangle$, as well as the continuum and line-core intensity of the sunspots and pores defined by the $I/I_0 = (I/I_0)_{\text{QS,P}}$ contours in Fig. 4.14. Signal enhancement is expressed as a function of the original level, separately for the big sunspot bounded by the red contours, and the smaller sunspots and pores bounded by the blue contours. We binned the image pixels by the uncorrected $\langle B_l \rangle$ in intervals of 100 G and plotted the bin-averaged change in $\langle B_l \rangle$ against the bin-averaged original $\langle B_l \rangle$ (Fig. 4.17a). This was repeated for the continuum and line-core intensity (Figs. 4.17b and 4.17c), taking a bin size of 0.05 in both instances.

Within expectation, the influence of image restoration on $\langle B_l \rangle$ and intensity is highly correlated to the original values of these quantities. This comes largely from the fact that the darker regions, where $\langle B_l \rangle$ is also typically higher, are more affected by stray light as scattered radiation forms a greater proportion of measured intensity, and therefore respond more strongly to image restoration. Also within expectation, the effect of restoration is more pronounced (greater absolute change) for smaller features, which are more susceptible to instrumental scattered light. An exception is the peak in the line-core intensity profile for the big sunspot feature (red curve, Fig. 4.17c), which arose from the enhanced brightness of the bright filaments in the penumbra from the restoration, visible in Fig. 4.14.

Given the variation in the response of sunspots to image restoration, it could have a profound effect on the apparent radiant and magnetic properties of these features. A full account of the effect of image restoration on sunspots, including the variation with size and disc position, would require examining a much larger sample of sunspots from multiple images taken at different times, which is outside the scope of this work (see Mathew et al. (2007) for such a study, based on MDI data).

4.3.2.3 Amount of magnetic flux on the solar surface

We segmented the solar disc in the 720-s longitudinal magnetogram by μ (excluding points where $\mu < 0.1$, $\sim 1\%$ of the solar disc by area) into 50 annuli of equal area. Within each annulus, we computed the quantities listed below, plotted in Fig. 4.18. For

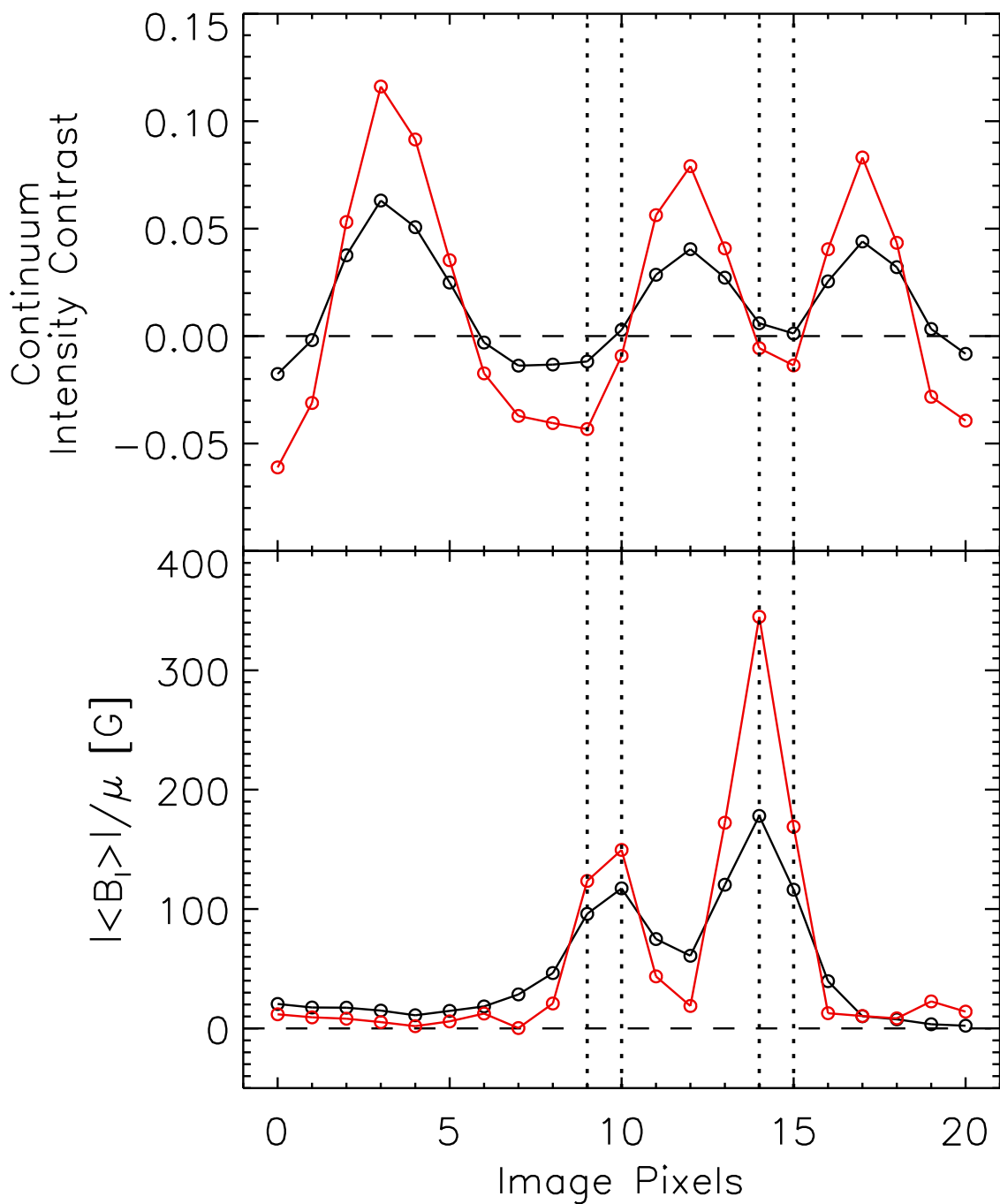


Figure 4.16: The uncorrected (black circles) and restored (with K_2 , red circles) continuum intensity contrast (top) and $\langle B_l \rangle / \mu$ (bottom) along a 21-pixel section across magnetic features near disc centre ($\mu = 0.97$). The plotted points represent image pixel values and are connected by straight lines to aid the eye. The dotted lines highlight the image pixels inside the magnetic features where the stray light correction effected a decrease in continuum intensity contrast accompanied by an increase in $\langle B_l \rangle / \mu$. The dashed lines follow the zero level.

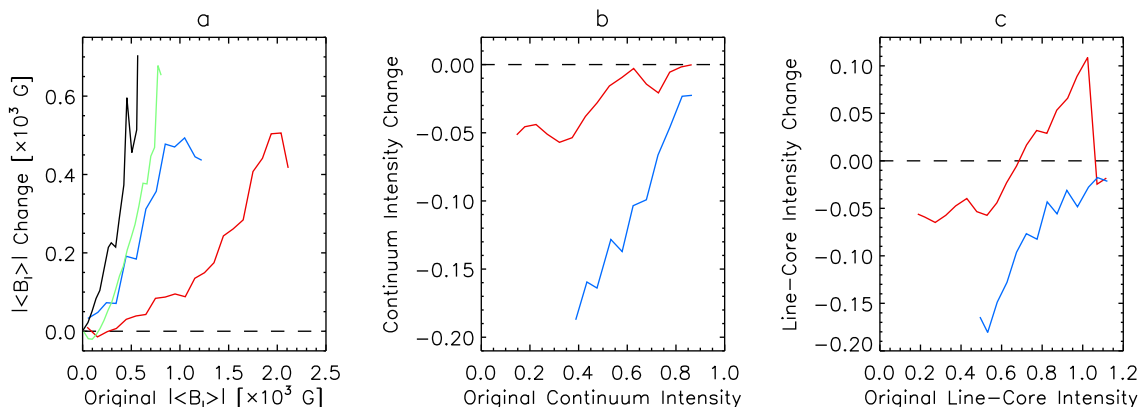


Figure 4.17: The change in $\langle B_l \rangle$ (left), as well as in the continuum (middle) and line-core intensity (right) introduced by image restoration with K_2 , as a function of the original value. Both the continuum and line core intensities are normalized to the quiet-Sun level. The red and blue series follow the values derived from the sunspot and pore features encircled by the similarly colour-coded contours in Fig. 4.14. The black and green curves (left) correspond to the change in $\langle B_l \rangle$ in the quiet Sun field depicted in Fig. 4.19, and in a 201×201 pixel active region field near disc centre ($\mu > 0.92$), respectively. The dashed lines mark the zero level.

each quantity, we derived the level in the uncorrected and restored magnetogram (black and red series, left axes), and the ratio of the restored and the uncorrected values (blue series, right axes), denoted by the Δ prefix.

- The noise level, $\sigma_{\langle B_l \rangle}$ (Fig. 4.18a), given by the standard deviation of $\langle B_l \rangle$. The standard deviation was computed iteratively, points more than three standard deviations from the mean were excluded from succeeding iterations till convergence, to exclude magnetic activity. The variation of the noise level of HMI longitudinal magnetograms with position on the solar disc is dominated by a centre-to-limb increase (Liu et al. 2012, Yeo et al. 2013). It is therefore reasonable to represent the noise level within a given annulus by a single value of $\sigma_{\langle B_l \rangle}$. Image restoration increased the noise level, on average, by a factor of 1.6.
- The proportion of image pixels counted as containing significant magnetic activity, n_{mag} (Fig. 4.18b), taken here as the points where $\langle B_l \rangle > 3\sigma_{\langle B_l \rangle}$.
- The mean $\langle B_l \rangle$ of the image pixels counted as magnetic, $\epsilon_{\langle B_l \rangle, \text{mag}}$ (Fig. 4.18c).
- The product of n_{mag} and $\epsilon_{\langle B_l \rangle, \text{mag}}$ (Fig. 4.18d). The quantity $\Delta(n_{\text{mag}}\epsilon_{\langle B_l \rangle, \text{mag}})$ represents the factor by which the apparent amount of line-of-sight magnetic flux changed from stray light removal.

Image restoration resulted in less image pixels being counted as magnetic (around -10% to -25% , Fig. 4.18b), though the enhancement to the magnetogram signal (30% to 60% , Fig. 4.18c) meant that there is an overall increase in the apparent amount of line-of-sight magnetic flux (10% to 40% , Fig. 4.18d). Computing $\Delta(n_{\text{mag}}\epsilon_{\langle B_l \rangle, \text{mag}})$ taking all the

4 Point spread function of SDO/HMI and the effects of stray light correction on the apparent properties of solar surface phenomena

(The contents of this chapter are identical to the printed version of Yeo, K. L., Feller, A., Solanki, S. K., Couvidat, S., Danilovic, S., Krivova, N. A., 2014, Point spread function of SDO/HMI and the effects of stray light correction on the apparent properties of solar surface phenomena, *Astron. Astrophys.*, 561, A22.)

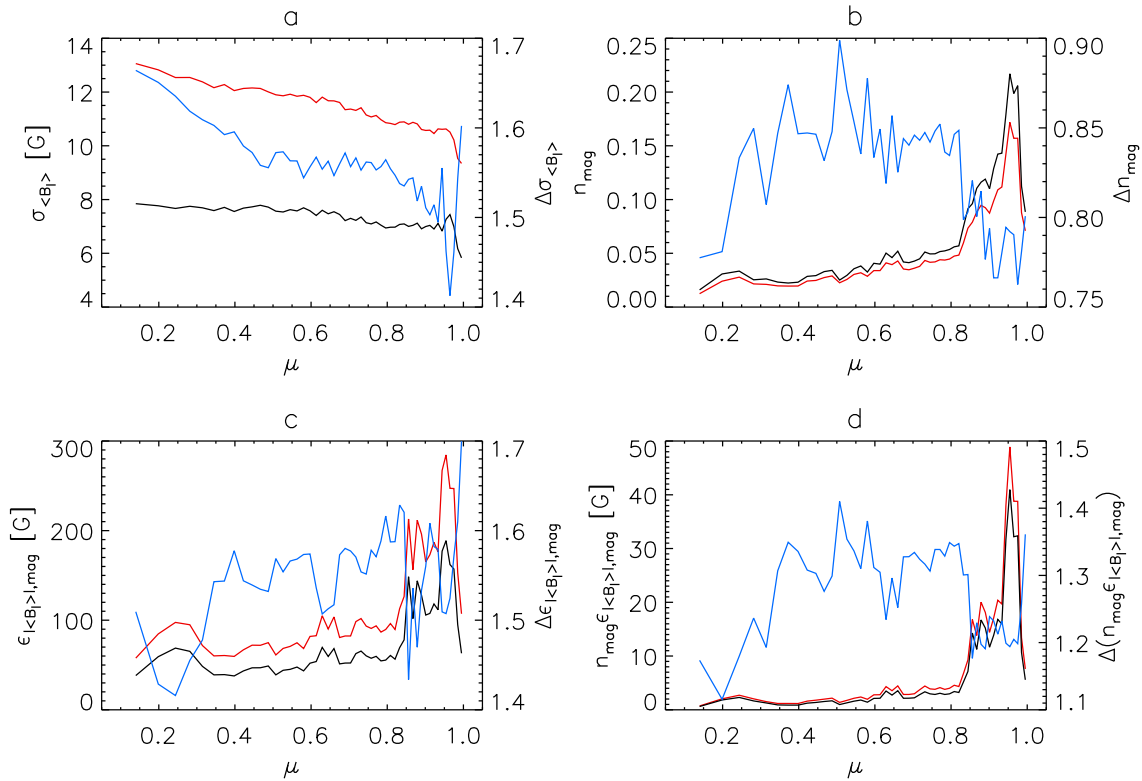


Figure 4.18: Plotted as a function of μ , a) the noise level of the 720-s longitudinal magnetogram, $\sigma_{\langle B_l \rangle}$, b) the proportion of image pixels counted as containing significant magnetic activity, n_{mag} , c) the mean $\langle B_l \rangle$ of these points, $\epsilon_{\langle B_l \rangle, \text{mag}}$, d) and the product of n_{mag} and $\epsilon_{\langle B_l \rangle, \text{mag}}$. Left axes: the uncorrected (black series) and restored with K_2 levels (red series). Right axes: the quotient of the restored and uncorrected values (blue series).

annulus as a whole, the total amount of line-of-sight magnetic flux over the solar disc increased by a factor of 1.2.

In Fig. 4.19, we mark the location of image pixels counted as magnetic in the original and restored data, in a 201×201 pixel inset centred on the disc centre. Image restoration renders magnetic features spatially smaller as polarized radiation originating from these features, lost to the surrounding quiet Sun by aperture diffraction and stray light, is recovered (illustrated by the blue and red clusters). This change in the size of magnetic features likely depends on factors such as the surface area, and circumference to surface area ratio. The enhanced noise level also contributes to the smaller count in the restored data. Image restoration does recover some magnetic features smeared below the magnetogram signal threshold ($\langle B_l \rangle = 3\sigma_{\langle B_l \rangle}$) in the original data by instrumental scattered light (green clusters). Overall, less image pixels are counted as magnetic.

The overall increase in $\sigma_{\langle B_l \rangle}$ towards the limb is partly related to the increase in low-level magnetogram signal fluctuations from the ubiquitous weak horizontal magnetic fields in the quiet Sun internetwork (Lites et al. 1996, 2008, Beck and Rezaei 2009), which obtain a line-of-sight component near the limb, and magnetic features foreshortening towards the background noise regime when approaching the limb. A probable cause

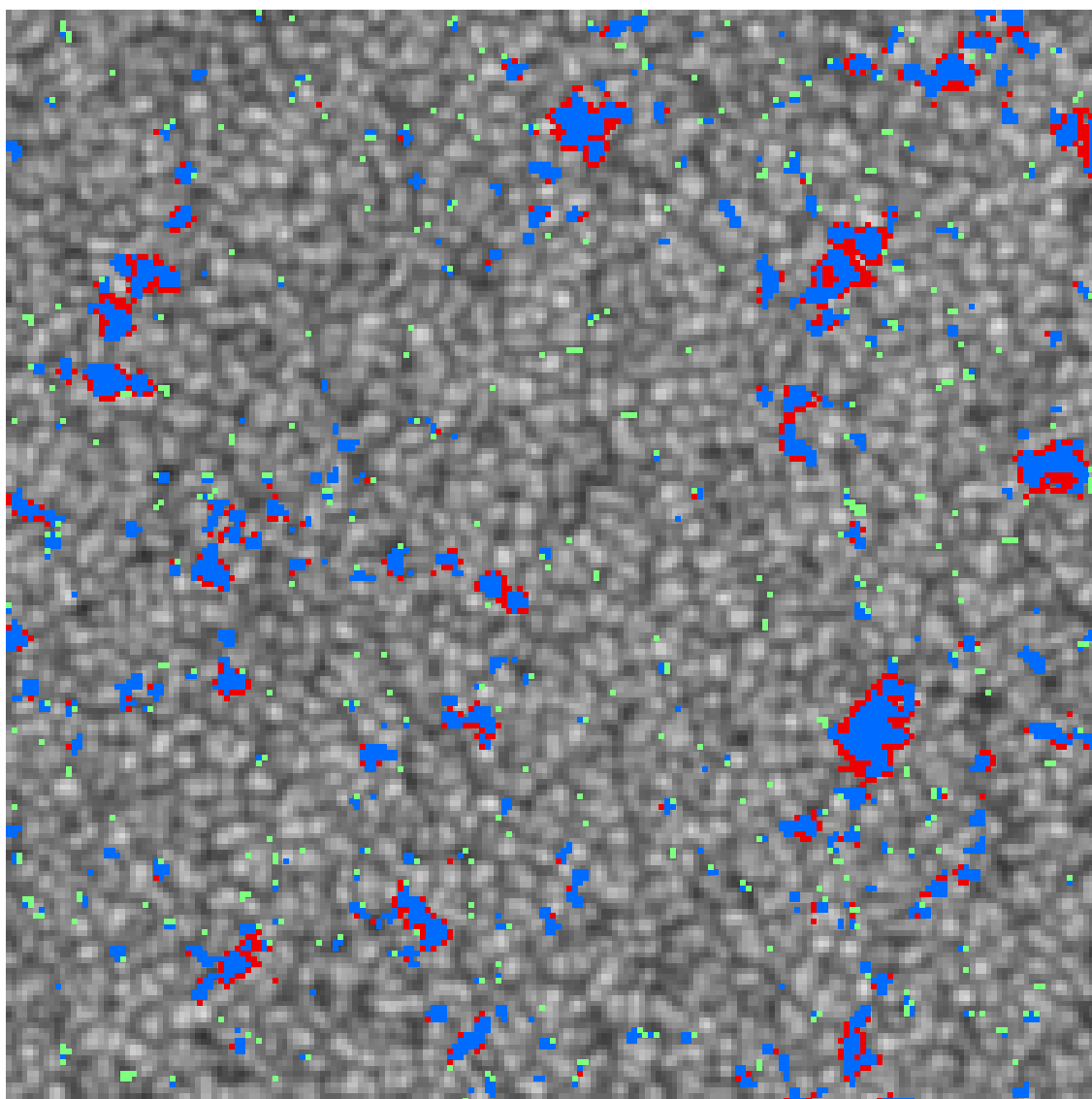


Figure 4.19: 201×201 pixel inset, centred on disc centre, of the 720-s continuum intensity image, with the points displaying $\langle B_l \rangle > 3\sigma_{\langle B_l \rangle}$ in the 720-s longitudinal magnetogram highlighted. Blue corresponds to the points realizing this condition in both the uncorrected and restored magnetogram, red the points fulfilling it only in the uncorrected data and green the points satisfying it only in the restored data. The grey scale is saturated at 0.8 and 1.2 times the mean quiet-Sun level.

of the overall centre-to-limb increase in $\Delta\sigma_{\langle B_l \rangle}$ is the enhancement of these true signal contributions to apparent noise.

In Fig. 4.17a we display the change in magnetogram signal as a function of the original signal, in the quiet Sun field illustrated in Fig. 4.19 and in a 201×201 pixel crop of an active region near the disc centre ($\mu > 0.92$), represented by the green and black curves, respectively. This was computed as done in Sect. 4.3.2.3 for the sunspots and pores in Fig. 4.14, the results of which are also plotted for comparison (blue and red curves). The only

4 Point spread function of SDO/HMI and the effects of stray light correction on the apparent properties of solar surface phenomena

(The contents of this chapter are identical to the printed version of Yeo, K. L., Feller, A., Solanki, S. K., Couvidat, S., Danilovic, S., Krivova, N. A., 2014, Point spread function of SDO/HMI and the effects of stray light correction on the apparent properties of solar surface phenomena, Astron. Astrophys., 561, A22.)

difference is here we binned the image pixels by the uncorrected $\langle B_I \rangle$ in intervals of 40 G instead of 100 G. As done in Sect. 4.3.2.1, we minimised the influence of pores present in the active region field by excluding the image pixels where $I/I_0 < (I/I_0)_{\text{QS,P}}$ and points up to three pixels away from them. (There are no image pixels where $I/I_0 < (I/I_0)_{\text{QS,P}}$ in the quiet Sun field.) The result from the quiet Sun and active region fields represent the effect of image restoration on the magnetogram signal of quiet Sun network, and active region faculae, respectively.

As noted for sunspots and pores (Sect. 4.3.2.2), the enhancement of the magnetogram signal of network and faculae from image restoration is highly correlated to the original level. This is possibly from the restoration enhancing the signal in the core of magnetic features, where it is also typically stronger, while depressing the signal in the fringes, from the recovery of polarized radiation scattered from the core to the fringes and surrounding quiet Sun, as discussed above and visible for the magnetic features depicted in Fig. 4.16.

The effect of image restoration on network and faculae is also more pronounced than in sunspots and pores, in particular for network. This is likely related to the smaller spatial scale of these features, which makes them more susceptible to stray light, and consequently they respond more acutely to restoration, than sunspots and pores. The stronger response of network compared to faculae is probably due to the fact that they appear in smaller clusters and the restoration of small-scale mixed polarities in the quiet Sun smeared out by instrumental scattered light.

As image restoration affects different magnetic features differently, the overall effect on the apparent amount of magnetic flux fluctuates with prevailing magnetic activity. This is the likely reason neither Δn_{mag} , $\Delta \epsilon_{\langle B_I \rangle, \text{mag}}$ nor $\Delta (n_{\text{mag}} \epsilon_{\langle B_I \rangle, \text{mag}})$ exhibit any obvious trend with μ , modulated by the magnetic features present within each annulus. Importantly, the relatively acute effect of image restoration on network, and the fact that the solar disc is, by area, predominantly quiet Sun means most of the increase in the measured amount of magnetic flux comes from the enhancement of these features. This is consistent with the findings of Krivova and Solanki (2004).

4.3.2.4 Line-of-sight velocity

Here we are interested in the part of measured line-of-sight velocities in HMI Dopplergrams arising from convective motions on the solar surface. To this end, we corrected the 720-s Dopplergram for the contribution by the rotation of the Sun and the relative velocity of SDO to the Sun¹⁰, \vec{v}_{SDO} , following the procedure of Welsch et al. (2013). Oscillatory motions associated with p -modes are largely undetectable in the 720-s Dopplergram data product as it is a weighted combination of filtergram observations from a 1350-s period, much longer than the period of these oscillations (~ 5 minutes).

The rotation rate of the Sun varies with heliographic latitude, Φ . Let \vec{v}_{rot} denote the velocity of the surface of the Sun from its rotation. We first determined the Stonyhurst latitude and longitude at each image pixel within the solar disc. Then, we derived the \vec{v}_{rot} at each latitude from the differential rotation profile by Snodgrass (1983),

$$w(\Phi) = 2.902 - 0.464 \sin^2 \Phi - 0.328 \sin^4 \Phi, \quad (4.3)$$

¹⁰Given by the radial, heliographic west and north velocity of the spacecraft relative to the Sun listed in the data header.

which relates angular velocity, $w = \frac{|\vec{v}_{\text{rot}}|}{R_{\text{S}} \cos \Phi}$ (R_{S} being the radius of the Sun in metres) to Φ . The contribution by \vec{v}_{rot} and \vec{v}_{SDO} to measured velocity at a given image pixel is then given by the projection of \vec{v}_{rot} and \vec{v}_{SDO} onto the line-of-sight to the point, taking the small-angle approximation. The projection of \vec{v}_{SDO} , in this instance, varied between 500 and 800 ms^{-1} with position on the solar disc. The significant magnitude and variation of this with disc position arises from SDO's geosynchronous orbit about Earth and Earth's orbit about the Sun.

Let $\langle \vec{v}_1 \rangle$ represent the signed Dopplergram signal, the mean line-of-sight component of the vector velocity over a given image pixel.

As done in Sect. 4.3.2.3, we segmented the solar disc by μ , into 50 equal annuli, excluding points where $\mu < 0.1$. The image pixels where $\langle B_l \rangle / \mu > 10\text{G}$ in the 720-s longitudinal magnetogram were masked, leaving quiet Sun. Within each annulus, we binned the unmasked points by the uncorrected $\langle \vec{v}_1 \rangle$ in intervals of 20 ms^{-1} , and retrieved the median original and restored $\langle \vec{v}_1 \rangle$ within each bin, ignoring bins with less than 100 points. The factor enhancement of $\langle \vec{v}_1 \rangle$ from image restoration, $\Delta \langle \vec{v}_1 \rangle_{\text{QS}}$ is then given by the slope of the linear regression fit to the restored bin-median $\langle \vec{v}_1 \rangle$ against the original, illustrated for the disc centremost interval of μ ($\mu > 0.99$) in Fig. 4.20a. By performing this computation over small intervals of μ , we avoid introducing scatter or bias in $\Delta \langle \vec{v}_1 \rangle_{\text{QS}}$ from the μ dependence of the convective blueshift of the spectral line.

The enhancement of the Dopplergram signal in the quiet Sun from image restoration with K_2 is significant and exhibits an acute CLV; $\Delta \langle \vec{v}_1 \rangle_{\text{QS}}$ increases monotonically with μ , from about 1.4 near the limb to 2.1 at disc centre (Fig. 4.20b).

In looking only at the quiet Sun, we excluded phenomena localised in active regions (for example, Evershed flow in sunspots), leaving signal largely from granulation and supergranulation. Supergranulation flows are largely horizontal. The line-of-sight velocities of supergranulation flows are thus greatest near the limb and diminishes towards disc centre from foreshortening. In contrast, the apparent line-of-sight velocities of granulation flows diminish towards the limb. Approaching the limb, granulation is more and more difficult to resolve from foreshortening and the line-of-sight increasingly crossing into multiple granulation cells. The typical diameter of granulation and supergranulation cells is about 1 Mm and 30 Mm, respectively. Granulation is therefore more affected by stray light and experiences greater signal enhancement from image restoration than supergranulation. The observed CLV of $\Delta \langle \vec{v}_1 \rangle_{\text{QS}}$ is consistent with the converse CLV of the line-of-sight velocities of granulation and supergranulation flows, and the stronger effect of image restoration on granulation compared to supergranulation.

By correcting both the original and restored Dopplergram for differential rotation with Eqn. 4.3, we had implicitly assumed that this component of measured line-of-sight velocity is not significantly changed by stray light or its removal. Given the line-of-sight component of \vec{v}_{rot} varies gradually across the solar disc, this is true except very close to the limb. Therefore, the effect on this analysis is likely minute and confined to the annuli closest to the limb.

The pronounced Dopplergram signal enhancement effected by image restoration with K_2 could have an impact on the characterization of plasma flows in the solar surface with HMI data. In this study we will not attempt to examine the effects of image restoration on apparent Doppler shifts in active regions, p -mode oscillations (detectable in the 45-s Dopplergram data product of the front CCD) or the individual physical processes driving

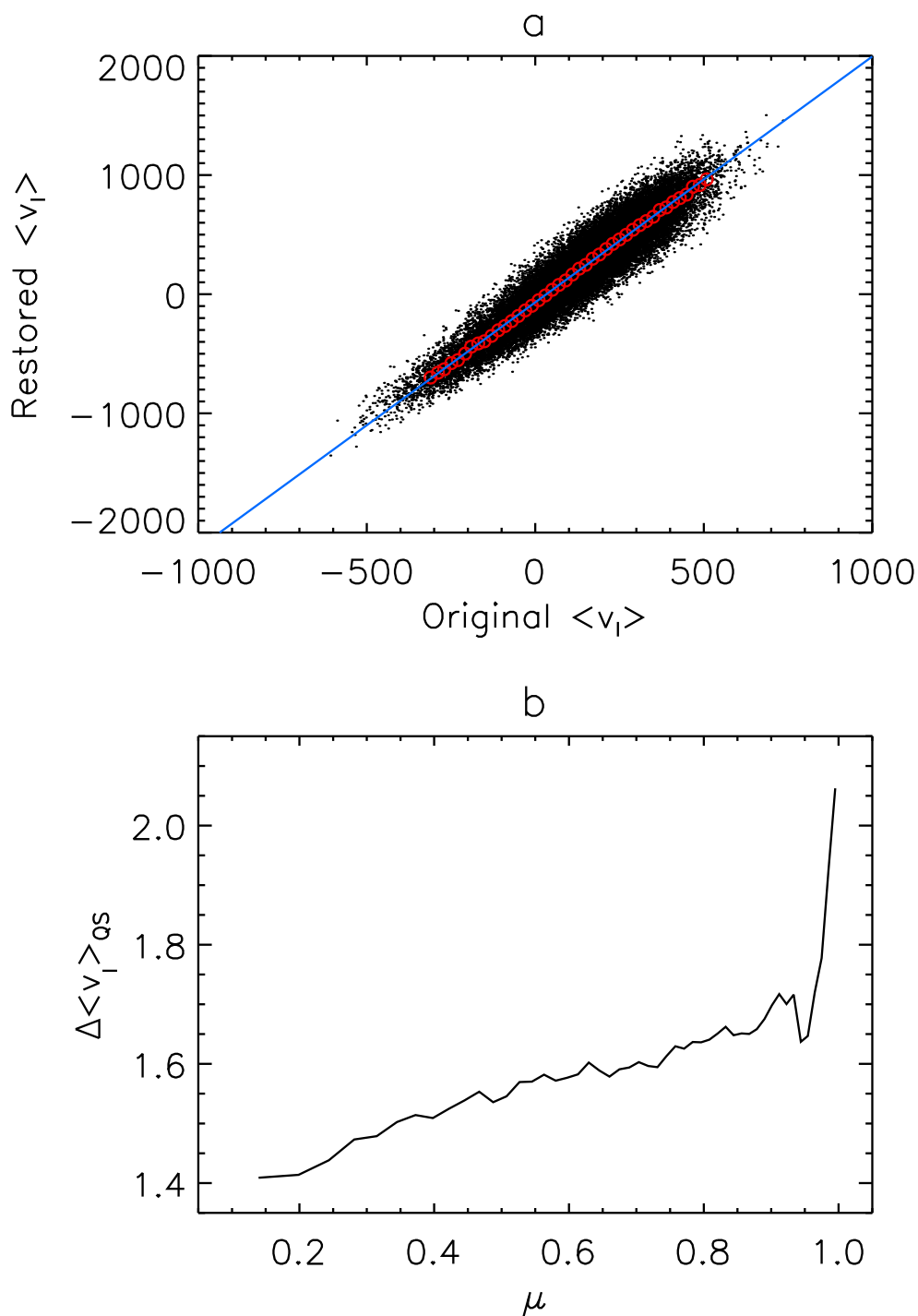


Figure 4.20: a) Scatter plot of the Dopplergram signal, $\langle \vec{v}_1 \rangle$ in the quiet Sun, near disc centre ($\mu > 0.99$), in the restored (with K_2) and uncorrected versions of the 720-s Dopplergram. The red circles denote the bin-median (from binning the points by the uncorrected $\langle \vec{v}_1 \rangle$ in intervals of 20 ms^{-1}) and the blue line the corresponding linear regression fit. b) The factor enhancement of $\langle \vec{v}_1 \rangle$ in the quiet Sun from image restoration, $\Delta \langle \vec{v}_1 \rangle_{\text{QS}}$ as a function of μ .

plasma motion on the solar surface.

4.4 Variation of the PSF within the FOV, between the HMI CCDs and with time

Derived from observations of Venus in transit recorded on the side CCD, K_2 characterizes the stray light in the employed data, at the position in the FOV occupied by the venusian disc. Here we discuss the applicability of K_2 to the entire FOV, to data from the front CCD and, importantly, from other times.

4.4.1 Variation of the PSF with FOV position

Taking the test continuum filtergram (from Sect. 4.3.1), we segmented the solar disc into eight equal sectors and computed the RMS intensity contrast of the quiet Sun within each sector. The level before and after image restoration with K_2 are illustrated in Fig. 4.21a. There is scatter in the RMS contrast between the sectors which is more pronounced in the restored data. This enhanced divergence is, at least in part, caused by the fact that we restored the entire solar disc with a single PSF when the true PSF varies from sector to sector.

The scatter in RMS contrast is, however, at least to the extent tested, relatively small in comparison to the absolute level. More importantly, the divergence between the sectors in the restored data (red curves) is small compared to the difference between the restored and the original data (black curves). This implies that the inhomogeneity introduced by applying a single PSF to the entire FOV is small in comparison to the contrast enhancement. Nonetheless, for sensitive measurements, care should be taken, where possible, to average measurements from different positions in the FOV after deconvolution with the PSF deduced here.

Next, we looked at the variation, over the solar disc, of the effect of image restoration with K_2 on the 720-s longitudinal magnetogram from Sect. 4.3.2. Sampling the solar disc at 16-pixel intervals in both the north-south and east-west directions, we centred a 401×401 pixel window over each sampled point and took the mean $\langle B_l \rangle$ of all the solar disc pixels within the window, denoted $\epsilon_{\langle B_l \rangle}$. Let $\Delta\epsilon_{\langle B_l \rangle}$ represent the ratio of $\epsilon_{\langle B_l \rangle}$ in the restored and uncorrected data, representing the factor enhancement to $\epsilon_{\langle B_l \rangle}$ from the restoration.

Expectedly, $\Delta\epsilon_{\langle B_l \rangle}$ varied with position on the solar disc (Fig. 4.22b). This variation is driven by:

- differences in the magnetic activity present in the sampling window (image restoration affects different magnetic features differently, Sect. 4.3.2.3) and
- fluctuations in the effect of image restoration from the variation of the stray light behaviour of the instrument across the FOV.

The scatter plot of $\Delta\epsilon_{\langle B_l \rangle}$ versus the original $\epsilon_{\langle B_l \rangle}$ reveals an inverse relationship between the two quantities (Fig. 4.22c). The cause of this correlation is that the restoration enhances the magnetogram signal in the quiet Sun more strongly than in active regions (Fig.

4 Point spread function of SDO/HMI and the effects of stray light correction on the apparent properties of solar surface phenomena

(The contents of this chapter are identical to the printed version of Yeo, K. L., Feller, A., Solanki, S. K., Couvidat, S., Danilovic, S., Krivova, N. A., 2014, Point spread function of SDO/HMI and the effects of stray light correction on the apparent properties of solar surface phenomena, *Astron. Astrophys.*, 561, A22.)

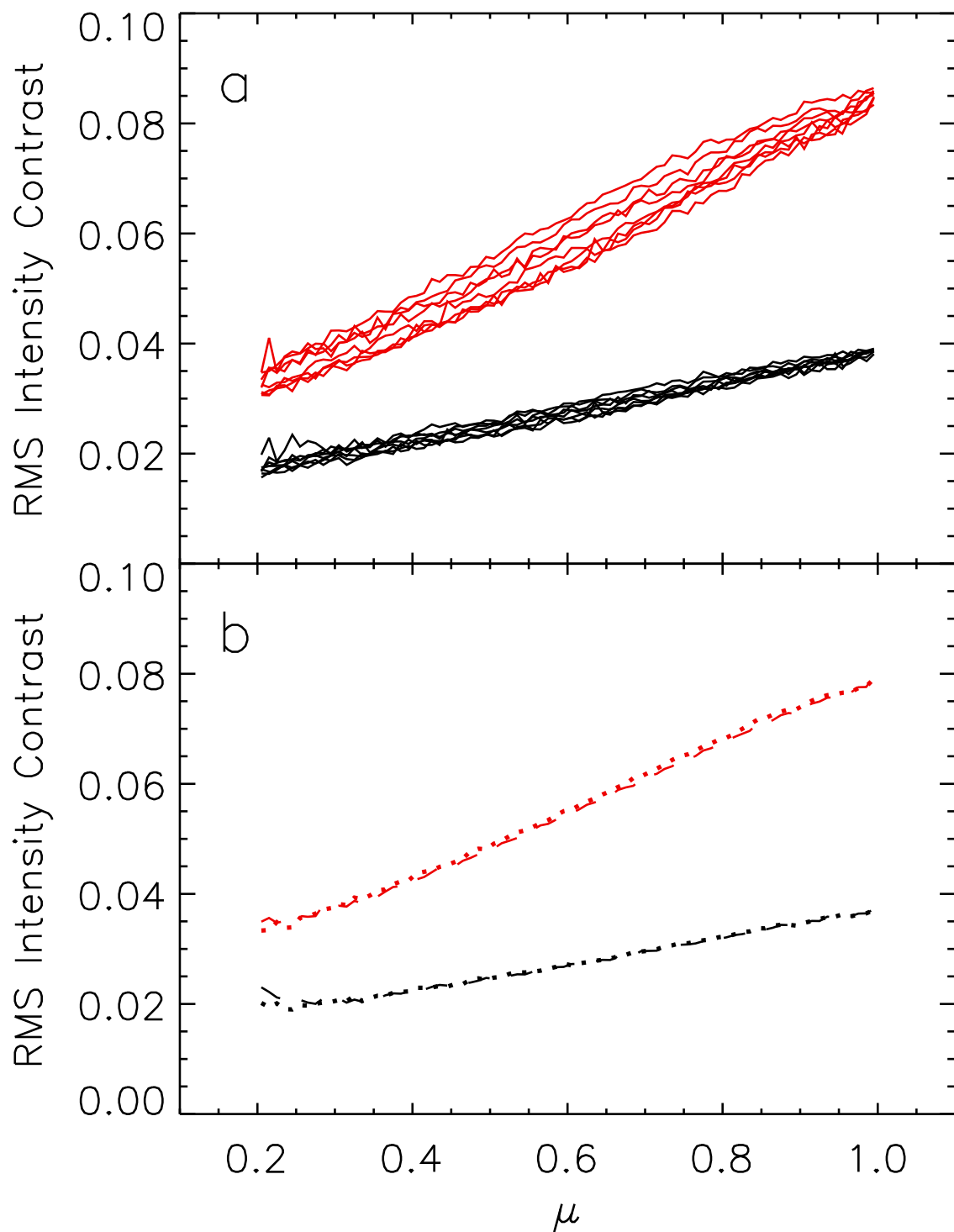


Figure 4.21: RMS intensity contrast of the quiet Sun as a function of μ , before (black lines) and after (red) image restoration with K_2 . a) In the test continuum filtergram, the solar disc segmented into eight equal sectors. b) In the near-simultaneous filtergrams of similar bandpass and polarization from the side (dotted lines) and front (dashed) CCD.

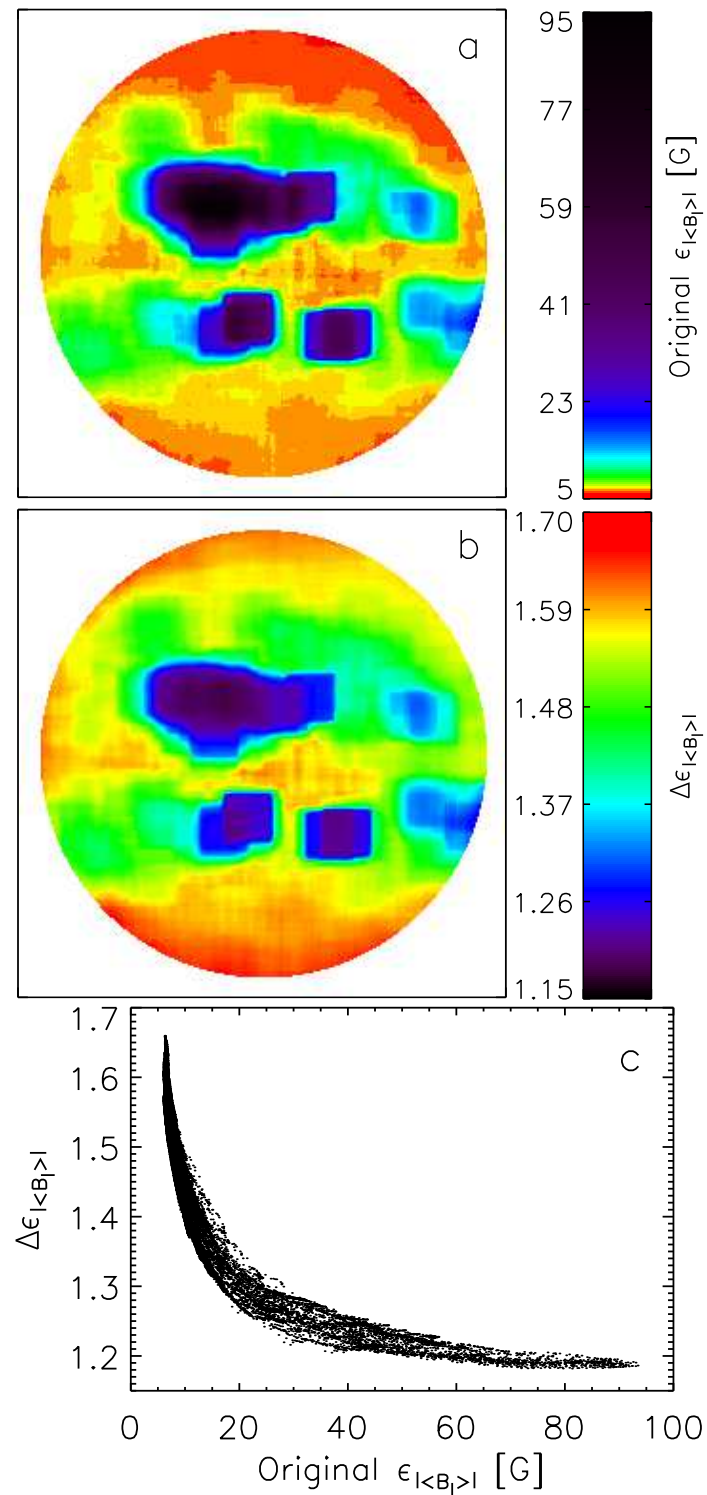


Figure 4.22: a) Mean unsigned magnetogram signal, $\epsilon_{\langle B_l \rangle}$ of the original (not corrected for stray light) 720-s longitudinal magnetogram. b) Factor enhancement of $\epsilon_{\langle B_l \rangle}$ from image restoration with K_2 , $\Delta\epsilon_{\langle B_l \rangle}$. c) Scatter plot of $\Delta\epsilon_{\langle B_l \rangle}$ against the original $\epsilon_{\langle B_l \rangle}$.

4.17a). The relatively weak spread of the scatter plot suggests the variation in $\Delta\epsilon_{(B_1)}$ with disc position is dominantly due to the inhomogeneous distribution of magnetic activity (Fig. 4.22a) and the diverging effects of restoration on different magnetic features. This is further evidence that it is a reasonable approximation to restore the entire FOV of HMI for instrumental scattered light with a single PSF.

4.4.2 Variation of the PSF between the HMI CCDs and with time

In Fig. 4.21b we show the RMS intensity contrast of the quiet Sun in two near-simultaneous filtergrams, one from each CCD, taken less than one minute apart. The two filtergrams were recorded about an hour after Venus left the solar disc (at around 05:36 UTC, June 6, 2012), shortly after the side CCD resumed collection of the regular filtergram sequence.

The two near-simultaneous filtergrams were taken in the same bandpass (-172 m\AA from line centre) and polarization (Stokes $I - V$). Any disparity in the RMS contrast between the two would arise mainly from differences in the performance of the two CCDs, including the stray light behaviour. The RMS contrast in the two filtergrams is very similar, even after image restoration with K_2 (red curves). Since we expect any disparity due to differences in the stray light behaviour of the two CCDs to be amplified by the application of the side CCD PSF to a front CCD filtergram, this agreement is encouraging.

Comparing the close similarity in the RMS intensity contrast of the quiet Sun in the two near-simultaneous filtergrams to the scatter between different FOV positions in the test continuum filtergram (top panel), it appears that the difference in the stray light behaviour of the two CCDs is much smaller than the variation with position in the FOV of the side CCD. The side and front CCDs are identical and share a common optical path (Schou et al. 2012b), it is therefore within reason that the stray light behaviour, even the variation of the PSF with position in the FOV, is broadly similar.

The SDO satellite is in a geosynchronous orbit. Since the HMI commenced regular operation (May 1, 2010), the side and front CCDs recorded a continuum filtergram each during the daily pass through orbital noon and midnight. For the purpose of investigating the stability of the stray light behaviour of the instrument over time, we examined the solar aureole, the intensity observed outside the solar disc arising from instrumental scattered light, in these daily data¹¹. We examined 2307 orbital noon and midnight continuum filtergrams from each CCD, spanning the 1157-day period of May 1, 2010 to June 30, 2013.

For each continuum filtergram, we averaged the solar aureole over all azimuths. From the resulting radial intensity profile, we determined the intensity of the solar aureole at distances of 1 and 10 arcsec from the edge of the solar disc. The derived intensities, normalized to the limb level, are expressed in Figs. 4.23a and 4.23b, respectively.

We excluded the points that are spurious or from continuum filtergrams with missing pixel values, leaving 2248 and 2288 points from the side and front CCDs respectively. To show up the broad trend with time we interpolated each time series at one day intervals and smoothed the result by means of binomial smoothing (Marchand and Marmet 1983). The time variation in the relative (to the limb level) intensity of the solar aureole at 1 and

¹¹The solar aureole is not to be confused with the aureole about the venusian disc when it is in transit, discussed in Sect. 4.2.4.

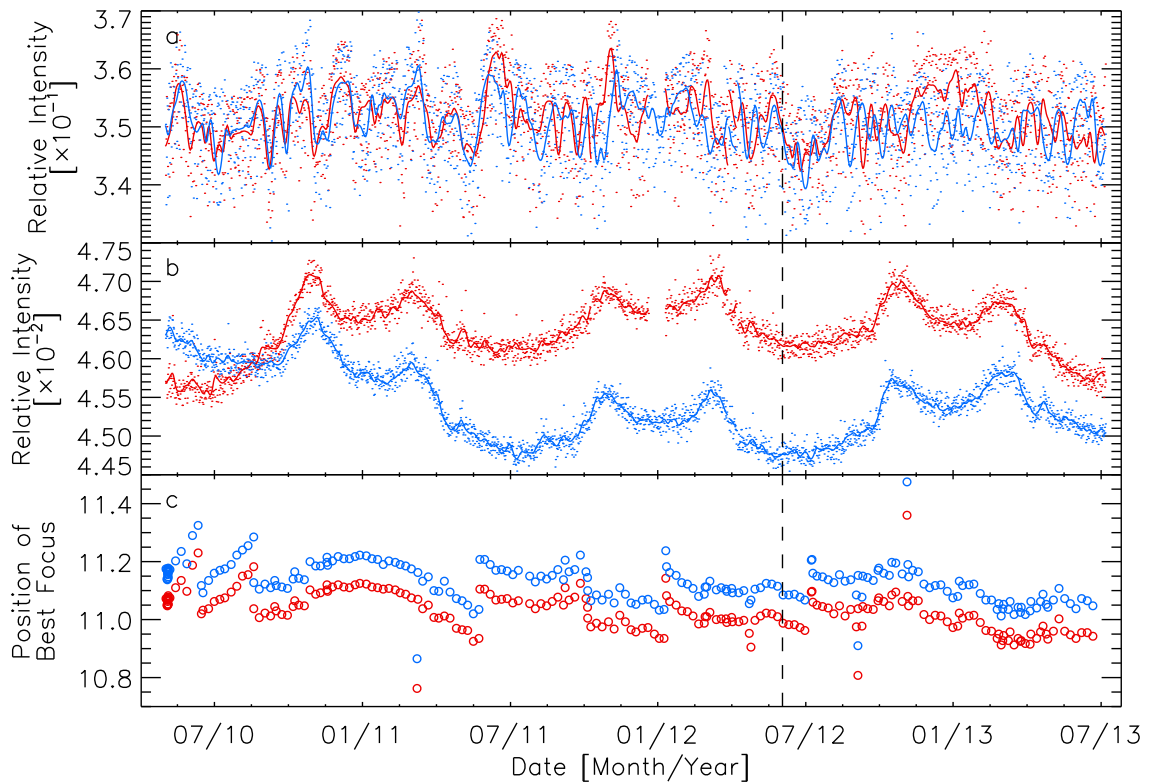


Figure 4.23: Radial intensity of the solar aureole, at distances of a) 1 and b) 10 arcsec from the edge of the solar disc, in the orbital noon and midnight continuum filtergrams from the side (red) and front (blue) CCDs. The value from each filtergram is normalized to the level at the edge of the solar disc. The dots represent the measured values and the curves the smoothed time series. Segments of measured values spaced more than one day apart were treated as separate time series, giving the gaps in the curves. c) The position of best focus, in units of focus steps (see text), from the (approximately) weekly focus calibration of the side (red circles) and front CCDs (blue circles). The dashed line marks the time of the transit of Venus.

10 arcsec from the limb reflects changes to the shape of the PSF near the core and in the wings respectively.

There is clear point-to-point fluctuation in the relative intensity of the solar aureole at 1 arcsec from the limb. This is due to the fact that near the limb, the intensity of the solar aureole decays rapidly with radial distance such that small variations in the width of the core of the PSF show up as large swings in the relative intensity at a fixed distance from and near the limb. Overall, the magnitude of the scatter, given by the standard deviation, is below 2% of the mean level. Also, the side and front CCD series are relatively stable and similar, with no overt long term trends or divergence from one another. This suggests that the width of the core of the PSFs of the two CCDs are, to the extent tested, broadly similar and constant over the period examined.

For the relative intensity of the solar aureole at 10 arcsec from the limb, there is an approximately synchronous periodic variation between the two CCDs. There is also a gradual overall drift between May 2010 and July 2011, and between August 2012 and

June 2013. The fluctuation of the two time series and the divergence between them is minute, less than 5% of the overall level. The time variation of, and difference between the wings of the PSFs of the two CCDs, implied by these fluctuations, has likely little effect on image contrast. Even with the $\sim 3\%$ offset between the front and side CCD time series around the time of the Venus transit, the RMS intensity contrast of the quiet Sun in the near-simultaneous filtergrams from the two CCDs (taken about an hour after the end of the transit) is practically identical (Fig. 4.21b).

Going from 1 to 10 arcsec from the limb, the time dependence of the relative intensity of the solar aureole changes gradually from the trend seen at 1 arcsec to that seen at 10 arcsec. Beyond 10 arcsec the variation with time does not change significantly. The relative intensity of the solar aureole at 1 and 10 arcsec from the limb therefore constitute a reasonable representation of variation in the shape of the PSFs of the two CCDs with time.

From the near identity of the RMS intensity contrast of the quiet Sun in the near-simultaneous filtergrams from the two CCDs (Fig. 4.21b) and the minute time variation of the PSFs of the two CCDs implied by the relative stability of the shape of the solar aureole in daily data (Figs. 4.23a and 4.23b), we assert that K_2 can be applied to observations from both CCDs for the period examined (May 1, 2010 to June 30, 2013) without introducing significant error.

This assertion is consistent with the state of the focus of the instrument over the period examined. The PSF of HMI, like any optical system, is strongly modulated by the focus. The instrument is maintained in focus by varying the heating of the front window and the position of two five-element optical wheels (Schou et al. 2012b). By varying the elements of the two optical wheels placed in the optical path, they allow the focus to be adjusted in 16 uniform, discrete steps, each corresponding to about two-thirds of a depth of focus. In Fig. 4.23c we plot the position of best focus, in units of the focus steps, from the regular (roughly weekly) focus calibration of the sensor, over the same period as the daily data. The focus of the two CCDs are remarkably similar and stable, differing from one another and varying over the period of interest by much less than a depth of focus. The contribution by focus to the variation of the PSF between the two CCDs and with time is most probably minute.

4.5 Summary

In this paper we present an estimate of the PSF of the SDO/HMI instrument. The PSF was derived from observations of Venus in transit. We convolved a simple model of the venusian disc and solar background with a guess PSF iteratively, optimizing the agreement between the result of the convolution and observation. We modelled the PSF as the linear sum of five Gaussian functions, the amplitude of which we allowed to vary sinusoidally with azimuth. This azimuthal variation was necessary to reproduce the observations accurately. Recovering the anisotropy of the PSF was also shown to be important for the proper removal of stray light from HMI data by the deconvolution with the PSF. The interaction between solar radiation and the venusian atmosphere is complex and not straightforward to account for. The result is a conservative estimate of the PSF, similar in width to the ideal diffraction-limited PSF in the core but with more extended wings.

The PSF was derived with data from one of the two identical CCDs in the sensor. It therefore represents the stray light behaviour of that particular CCD, at the time of the transit of Venus, at the position in the FOV occupied by the venusian disc in the employed observations.

Comparing the apparent granulation contrast in different parts of a single image, we showed that although the variation in the stray light behaviour of the instrument with position in the FOV introduces uncertainty to measured contrast, amplified by restoring observations with a single PSF, the scatter is relatively minute and will likely have little quantitative influence if care is taken to average measurements from multiple FOV positions. This was confirmed by an examination of the uniformity, over the FOV, of the effect of image restoration on the 720-s longitudinal magnetogram data product.

The time variation of the shape of the solar aureole in daily data was taken as an indication of PSF changes over the period examined (May 1, 2010 to June 30, 2013). Based on the relatively weak time variation of the aureole, and the similarity of the aureole and granulation contrast in data from the two CCDs, we assert that the PSF derived here can be applied to observations from both CCDs over the period examined without introducing significant error.

Apparent granulation contrast, given here by the RMS intensity contrast of the quiet Sun, in HMI continuum observations restored by the deconvolution with the PSF, exhibit reasonable agreement with that in artificial images generated from a 3D MHD simulation at equal spatial sampling. This demonstrates that the PSF, though an approximation, returns a competent estimate of the aperture diffraction and stray light-free contrast. The restoration enhanced the RMS intensity contrast of the quiet Sun by a factor of about 1.9 near the limb ($\mu = 0.2$), rising up to 2.2 at disc centre.

We also illustrated the effect of image restoration with the PSF on the 720-s Dopplergram and longitudinal magnetogram data products, and the apparent intensity of magnetic features.

- For small-scale magnetic concentrations, image restoration enhanced the intensity contrast in the continuum and core of the Fe I 6173 Å line by a factor of about 1.3, and the magnetogram signal by a factor of about 1.7.
- Magnetic features in the longitudinal magnetogram are rendered smaller, as polarized radiation smeared onto surrounding quiet Sun by instrumental scattered light is recovered.
- Image restoration increased the apparent amount of magnetic flux above the noise floor by a factor of about 1.2, mainly in the quiet Sun. This may be, in part, from the recovery of magnetic flux in opposite magnetic polarities lying close to one another partially cancelled out by stray light.
- The influence of image restoration on sunspots and pores varied strongly, as expected, within a given feature and between features of different sizes.
- Line-of-sight velocity due to plasma motions on the solar atmosphere increases by a factor of about 1.4 to 2.1. The variation comes from the restoration enhancing granulation flows more strongly than larger scale supergranulation flows. Given the

4 Point spread function of SDO/HMI and the effects of stray light correction on the apparent properties of solar surface phenomena

(The contents of this chapter are identical to the printed version of Yeo, K. L., Feller, A., Solanki, S. K., Couvidat, S., Danilovic, S., Krivova, N. A., 2014, Point spread function of SDO/HMI and the effects of stray light correction on the apparent properties of solar surface phenomena, Astron. Astrophys., 561, A22.)

spatial scale dependence, the effect on Doppler shifts from large scale motions such as the meridional flow and differential rotation is probably minute.

The pronounced effect of image restoration on the apparent radiant, magnetic and motional properties of solar surface phenomena could have a significant impact on the interpretation of HMI observations. For instance, the observation that restoring HMI longitudinal magnetograms renders magnetic features smaller while boosting the magnetogram signal, and the increase in the amount of magnetic flux is dominantly in the quiet Sun, can influence models of variation in solar irradiance based on HMI data. Specifically, with models that relate the contribution by small-scale magnetic concentrations to solar irradiance variations to the number density and magnetogram signal (for example, Wenzler et al. 2006, Foukal et al. 2011, Ball et al. 2012).

5 Reconstruction of total and spectral solar irradiance from 1974 to 2013 based on KPVT, SoHO/MDI and SDO/HMI observations

Yeo, K. L., Krivova, N. A., Solanki, S. K., Glassmeier, K. H.
Astron. Astrophys., **570**, A85 (2014)*

Abstract

Context. Total and spectral solar irradiance are key parameters in the assessment of solar influence on changes in the Earth's climate.

Aims. We present a SATIRE-S reconstruction of daily solar irradiance spanning 1974 to 2013, based on full-disc observations from the KPVT, SoHO/MDI and SDO/HMI.

Methods. SATIRE-S ascribes variation in solar irradiance, on timescales greater than a day, to photospheric magnetism. The solar spectrum is reconstructed from the apparent surface coverage of bright magnetic features and sunspots in the daily data using the modelled intensity spectra of these magnetic structures. We cross-calibrated the various data sets, harmonizing the model input so to yield a single consistent time series as the output.

Results. The model replicates 92% ($R = 0.957$) of the variability, and the secular decline between the 1996 and 2008 solar cycle minima in the PMOD TSI composite. The model also reproduced most of the variability in solar Lyman- α irradiance and the Mg II index. The ultraviolet solar irradiance measurements from the UARS and SORCE missions exhibit discrepant solar cycle variation, especially above 240 nm. As a result, the model while able to replicate the rotational variability in these records, aligned with certain observations better than others in terms of the long-term trends. The solar cycle variation in the ultraviolet in the reconstruction is confirmed by the close match to that in a SUSIM-based empirical model from a previous study. As with earlier similar investigations, the reconstruction cannot reproduce the long-term trends in SORCE/SIM spectrometry. We argue, from the apparent lack of solar cycle modulation in SIM SSI and the dissimilarity

*The contents of this chapter are identical to the submitted version of Yeo, K. L., Krivova, N. A., Solanki, S. K., Glassmeier, K. H., 2014, Reconstruction of total and spectral solar irradiance from 1974 to 2013 based on KPVT, SoHO/MDI and SDO/HMI observations, *Astron. Astrophys.*, 570, A85, reproduced with permission from Astronomy & Astrophysics, © ESO.

between the total flux recorded by the instrument and TSI, that unaccounted instrumental trends are present.

Conclusions. The daily solar irradiance time series is consistent with observations from multiple sources, demonstrating its validity and utility for climate models. It also provides further evidence that photospheric magnetism is the prime driver of variation in solar irradiance on timescales greater than a day.

5.1 Introduction

Solar radiation is the principle source of energy entering the Earth system. As such, the variation in the Sun's radiative output, solar irradiance, is a prime candidate driver of externally driven changes to the Earth's climate. A significant body of publications citing correlations between solar variability and climate parameters exist in the literature, and numerous mechanisms have been mooted to explain these observations (see e.g., Gray et al. 2010, for a review). The Earth's climate is believed to be modulated by variations in solar irradiance through effects related to its absorption at the Earth's surface, and in the atmosphere. An established mechanism is the interaction between ultraviolet irradiance and stratospheric ozone (e.g., Haigh 1994, Solanki et al. 2013). These mechanisms are wavelength dependent, from the wavelength dependence of the variation in solar irradiance and its absorption in the Earth's surface and atmosphere (Haigh 2007). Consequently, both total and spectral solar irradiance, TSI and SSI, are of interest in assessing the impact of variation in solar irradiance on the Earth's climate.

TSI has been monitored since 1978 through a succession of spaceborne radiometers. The measurements from individual radiometers diverge, mainly in terms of the absolute level and long-term trends, due to instrument-related factors such as the radiometric calibration, degradation with time and design. Accounting for these influences to combine the various data sets into a single time series is non-trivial and still a topic of debate (e.g., Scafetta and Willson 2009, Krivova et al. 2009a, Fröhlich 2012). There are, at present, three published composites. Namely, the ACRIM (Willson and Mordvinov 2003), IRMB (Dewitte et al. 2004b, Mekaoui and Dewitte 2008) and PMOD (Fröhlich 2000) composites. The long-term trends in these competing series do not agree. Notably, the successive solar minima in 1986, 1996 and 2008 exhibit conflicting levels and cycle-to-cycle variation in the three composites, encapsulating the difficulty in observing secular changes in TSI unambiguously.

As in the case of TSI, ultraviolet spectral irradiance (120 to 400 nm) has been measured from space on a regular basis since 1978. Again, the combination of the measurements from the succession of instruments into a single time series is an ongoing challenge (DeLand and Cebula 2008, 2012). The difficulty in producing a composite record is, in this instance, compounded by the wavelength dependence of instrumental influences.

The series of GOME instruments (the first of which was launched in 1996 onboard ERS-2, Weber et al. 1998, Munro et al. 2006) and ENVISAT/SCIAMACHY (launched in 2002, Skupin et al. 2005a) made regular measurements of the solar spectrum in the 240 to 790 nm and 240 to 2380 nm range, respectively. However, these instruments are designed for atmospheric sounding measurements which do not require absolute radiometry rather than the monitoring of solar irradiance. As they lack the capability to track instrument

degradation in-flight, long-term trends in solar irradiance cannot be recovered from the spectral observations. The spectral measurements from the Sun PhotoMeter, SPM on the SoHO/VIRGO experiment (Fröhlich et al. 1995, 1997), spanning 1996 to the present, cover just three narrow (FWHM of 5 nm) bandpass, at 402, 500 and 862 nm. In the visible and infrared, continuous observation of spectral irradiance only started, in effect, with SORCE/SIM (Harder et al. 2005a,b), which has been surveying the wavelength range of 200 to 2416 nm since 2003. SIM provides what is, at present, the only extended, radiometrically calibrated, record of SSI covering the ultraviolet to the infrared available.

The available body of solar irradiance observations is invaluable. However, given the limited period in time covered and uncertainties in the long-term variation, there is a need to augment observations with models relating solar variability to irradiance. Such models have been reported for almost as long as irradiance measurements were made from space (e.g., Willson et al. 1981b, Oster et al. 1982). The models that ascribe fluctuations in solar irradiance to the time evolution of magnetic concentrations in the photosphere (from its influence on the temperature structure of the solar surface and atmosphere, Spruit and Roberts 1983) have been particularly successful (Domingo et al. 2009). This is especially true of TSI. The recent TSI reconstructions by Ball et al. (2012) and Chapman et al. (2013), based on such models, replicated 96% and 95% of the observed variation in SORCE/TIM radiometry (Kopp and Lawrence 2005, Kopp et al. 2005a,b), respectively. The model by Ball et al. (2012) also reproduced 92% of the variation in the PMOD TSI composite.

In the case of SSI, gaping disagreements between models and observations persist, exemplified in the current debate on the long-term trends in the SORCE/SIM record (Harder et al. 2009, Lean and DeLand 2012, Unruh et al. 2012, Wehrli et al. 2013, Ermolli et al. 2013). The ultraviolet irradiance (200 to 400 nm) measured by SIM declined from 2004 to 2008 by a factor of two to six more than in other measurements and models (sans Fontenla et al. 2011, discussed below). The range of two to six reflects the spread between these other measurements and models. The pronounced drop in the ultraviolet, almost twice the decrease in TSI level over the same period, is accompanied and so compensated by an increase in visible irradiance (400 to 700 nm). Coming at a time where solar activity is declining, this elevation in the visible runs counter to models of solar irradiance, which point to visible solar irradiance varying in phase with the solar cycle instead.

The reconstruction of TSI and SSI by Fontenla et al. (2011), based on PSPT observations (Coulter and Kuhn 1994, Ermolli et al. 1998) and the model atmospheres of Fontenla et al. (2009) with certain adjustments, is the only model so far to reproduce the long-term trends in SIM SSI, albeit qualitatively. However, the reconstruction failed to reproduce the solar cycle variation in TSI, which other models have generally been able to with reasonable success. Employing similar PSPT images and the model atmospheres of Fontenla et al. (2009) without modification, the analogous computation by Ermolli et al. (2013), as with preceding models, reproduced observed rotational and cyclic variation in TSI but not the long-term behaviour of SIM SSI.

Apart from the models based on the regression of indices of solar activity to measured solar irradiance, commonly referred to as proxy models (e.g., Lean et al. 1997, Lean 2000, Pagaran et al. 2009, Chapman et al. 2013), present day models of spectral solar irradiance have a similar architecture to one another (reviewed in Ermolli et al. 2013). The proportion of the solar disc covered by magnetic features (such as faculae and sunspots) is

deduced from full-disc observations. This information is converted to solar irradiance by means of the calculated intensity spectra of said features (derived by applying radiative transfer codes to semi-empirical model atmospheres). The Spectral And Total Irradiance REconstruction for the Satellite era, SATIRE-S (Fligge et al. 2000, Krivova et al. 2003, 2011b) is an established model of this type.

The SATIRE-S model has been applied to full-disc observations of intensity and magnetic flux from the Kitt Peak Vacuum Telescope (KPVT, Livingston et al. 1976, Jones et al. 1992) and the Michelson Doppler Imager onboard the Solar and Heliospheric Observatory (SoHO/MDI, Scherrer et al. 1995). The solar irradiance reconstructions by Krivova et al. (2003, 2006, 2009b, 2011a), Wenzler et al. (2005, 2006, 2009), Unruh et al. (2008) and Ball et al. (2011, 2012, 2014), spanning various periods between 1974 to 2009, achieved considerable success in replicating observed fluctuations in TSI, SSI measurements from the missions preceding SORCE and, at rotational timescales, SORCE SSI.

The reconstruction of solar irradiance with SATIRE-S has been curtailed by the deactivation of MDI in 2011. (The KPVT had ceased operation earlier in 2003.) In this study, we present a SATIRE-S reconstruction of total and spectral solar irradiance from 1974 to 2013. This work sought to update the preceding efforts based on KPVT and MDI data with similar observations from the Helioseismic and Magnetic Imager onboard the Solar Dynamics Observatory (SDO/HMI, Schou et al. 2012b).

The apparent surface coverage of the solar disc by magnetic features, the main input to the model, is instrument dependent. Concurrent observations from different instruments can diverge significantly from differences in spatial resolution, bandpass, calibration, stray light, noise and the like. The combination of the model output based on data from multiple instruments into a single time series constitutes one of the main challenges to such a study. Apart from the extension to the present time with HMI data, this study departs from the earlier efforts with the SATIRE-S model in how this combination is done. This improvement in the methodology is one of the main advances of this paper.

In the following, we briefly describe the SATIRE-S model (Sect. 5.2) and the data used in the reconstruction (Sect. 5.3). Thereafter, we detail the reconstruction process (Sect. 5.4), before a discussion of the result (Sect. 5.5) and summary statements (Sect. 5.6).

5.2 The SATIRE-S model

SATIRE-S is currently the most precise version of the SATIRE model. The main assumption of the SATIRE model is that variations in solar irradiance, on timescales of days and longer, arise from solar surface magnetism alone. The different versions of the model differ by the data used to deduce the surface coverage of magnetic features (see Krivova et al. 2007, 2011b, Vieira et al. 2011). The SATIRE-S utilises continuum intensity images and longitudinal magnetograms. In the present iteration, the solar surface is modelled as being composed of quiet Sun, faculae, and sunspot umbrae and penumbrae.

Image pixels with continuum intensity below threshold levels representing the umbral (umbra to penumbra), and the penumbral (penumbra to granulation) boundary are classified as umbra and penumbra, respectively. Points with magnetogram signals exceeding a certain threshold and not already classed as umbra or penumbra (i.e., bright magnetic

features), are denoted as faculae. (While bright magnetic features include both network and faculae, in this study we refer to them collectively as faculae for the sake of brevity.) The remaining image pixels are then taken to correspond to quiet Sun. Standalone facular pixels (i.e., not contiguous with any other) are reassigned as quiet Sun to minimize the misidentification of magnetogram noise fluctuations as bright magnetic features.

Let $\langle B_l \rangle$ denote the longitudinal magnetogram signal (the pixel-averaged line-of-sight magnetic flux density) and μ the cosine of the heliocentric angle. At the spatial resolution of available full-disc magnetograms, the small-scale magnetic concentrations associated with bright magnetic features remain largely unresolved. This is approximately accounted for by scaling the filling factor of facular pixels (defined here as the effective proportion of the resolution element occupied) linearly with $\langle B_l \rangle / \mu$, from zero at 0 G, to unity at what is denoted $(\langle B_l \rangle / \mu)_{\text{sat}}$, where after it saturates (see Fligge et al. 2000, for details). The quantity $(\langle B_l \rangle / \mu)_{\text{sat}}$ is the sole free parameter in the model.

As small-scale magnetic concentrations are generally orientated roughly normally to the solar surface (due to magnetic buoyancy), the quantity $\langle B_l \rangle / \mu$ represents a first-order approximation of the pixel-averaged magnetic flux density. This approximation breaks down very close to the limb from the combined action of foreshortening and magnetogram noise. For this reason, image pixels near the limb ($\mu < 0.1$, about 1% of the solar disc by area) are ignored. Following Ball et al. (2011, 2012), we counted facular pixels with $\langle B_l \rangle / \mu$ above an arbitrary but conservative cutoff value, denoted $(\langle B_l \rangle / \mu)_{\text{cut}}$, as quiet Sun instead. These points correspond, especially towards the limb, mainly to the magnetic canopy of sunspots, rather than legitimate faculae (Yeo et al. 2013).

In this study, we used the same set of calculated intensity spectra, of umbra, penumbra, faculae and quiet Sun (at various values of μ) as Wenzler et al. (2006), Ball et al. (2012) to convert the surface coverage of magnetic features to solar irradiance (the derivation of these spectra is detailed in Unruh et al. 1999). The model output is the summation, over all the image pixels within the solar disc, of the intensity spectrum corresponding to each point as defined by the above analysis. The resulting spectrum, spanning the wavelength range of 115 to 160000 nm, and the integral represent the prevailing SSI and TSI at the sampled point in time.

The appropriate value of the free parameter, $(\langle B_l \rangle / \mu)_{\text{sat}}$ is recovered by comparing the reconstruction to measured TSI (see Sect. 5.4.2).

5.3 Data selection and preparation

5.3.1 Daily full-disc continuum intensity images and longitudinal magnetograms

In this study, we employed full-disc longitudinal magnetograms and continuum intensity images collected at the KPVT, and from the first-ever spaceborne magnetograph, SoHO/MDI (Scherrer et al. 1995) and its successor instrument, SDO/HMI (Schou et al. 2012b). The NASA/NSO 512-channel diode array magnetograph (Livingston et al. 1976), installed at the KPVT, started operation in 1974. In 1992, it was replaced with the NASA/NSO spectromagnetograph (Jones et al. 1992), itself retired in 2003. Here, we will refer to the two configurations of the KPVT, effectively two unique instruments for

the purpose of this study, as KP_{512} and KP_{SPM} , respectively.

To the extent permitted by available data (see Sects. 5.3.1.1 to 5.3.1.3), we selected, for each instrument, a continuum intensity image and a longitudinal magnetogram, recorded simultaneously or close in time, from each observation day. The number of selected daily continuum intensity images and longitudinal magnetograms from each instrument, and the period covered are summarized in Table 5.1. Also listed is the image size, pixel scale and spectral line surveyed.

5.3.1.1 HMI

The HMI is a full-Stokes capable filtergram instrument. The instrument captures full-disc filtergrams continuously at 1.875s cadence, alternating between two CCDs, six positions across the Fe I 6173 Å line and six polarizations. The filtergram data is combined to form continuum intensity images and longitudinal magnetograms at 45-s cadence. Generated from similar filtergram data, the two data products are exactly co-temporal.

For each day since the instrument commenced regular operation in April 30, 2010, up to 31 May, 2013, we took the average of seven consecutive 45-s continuum intensity images, resampled in space and time to co-register, and likewise the average of the corresponding 45-s longitudinal magnetograms. We will refer to the result as the 315-s continuum intensity image and longitudinal magnetogram. The averaging is to facilitate the segmentation of the solar disc by suppressing intensity and magnetogram signal fluctuations from noise and p -mode oscillations.

We took the first 315-s continuum intensity image and longitudinal magnetogram from each day, except for the period where we also have selected MDI observations (April 30 to December 24, 2010, see Sect. 5.3.1.2). On these days we took the HMI data taken closest in time to the MDI longitudinal magnetogram.

Aided by the absence of atmospheric seeing, granulation and sunspot structures are starting to be resolved at HMI's spatial resolution (~ 1 arcsec). To minimize the misclassification of darker non-sunspot and brighter sunspot features, the 315-s continuum intensity images were (after the correction for limb darkening, see Sect. 5.4.1.1) convolved with a 7×7 pixel (3.5×3.5 arcsec) Gaussian kernel.

5.3.1.2 MDI

The MDI returned observations from March 19, 1996 to April 11, 2011. The instrument recorded full-disc filtergrams at five positions, one near and four within the Ni I 6768 Å line. A number of continuum intensity images and longitudinal magnetograms are produced each observation day. Unlike HMI, the two data products are generated from separate filtergrams and are therefore not co-temporal.

The SoHO spacecraft suffered two extended outages between June 1998 and February 1999 (usually referred to as the SoHO vacation). Ball et al. (2012) presented evidence that the response of MDI to magnetic flux might have changed over this period. Following the cited work, we excluded MDI data from before February 1999.

The flat field of MDI continuum intensity images is severe enough to impede the reliable identification of sunspots by the method employed in SATIRE-S (see Sect. 5.4.1.1), and varied over the lifetime of the instrument (Krivova et al. 2011a). As in this earlier

Table 5.1: Summary description of the daily full-disc continuum intensity images and longitudinal magnetograms selected for this study.

Instrument	No. of data days	Period [year.month.day]	Proportion of			Image size [pixel]	Pixel scale [arcsec]	Spectral line
			period covered	period covered	period covered			
KP ₅₁₂	1371	1974.08.23 to 1993.04.04	0.20	0.20	2048 × 2048	1	Fe I 8688 Å	
KP _{SPM}	2055	1992.11.21 to 2003.09.21	0.52	0.52	1788 × 1788	1.14	Fe I 8688 Å	
MDI	3941	1999.02.02 to 2010.12.24	0.91	0.91	1024 × 1024	1.98	Ni I 6768 Å	
HMI	1128	2010.04.30 to 2013.05.31	1.00	1.00	4096 × 4096	0.504	Fe I 6173 Å	

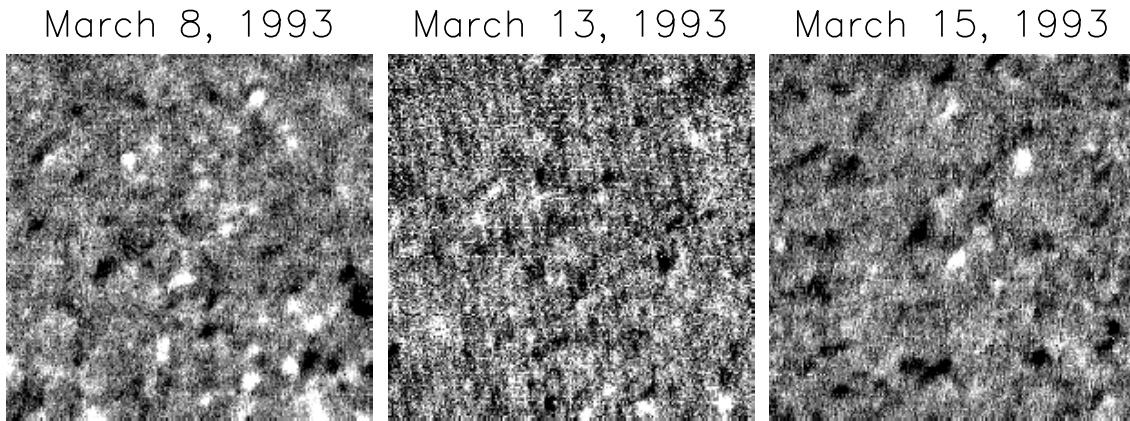


Figure 5.1: 200×200 arcsec crop of one of the KP_{512} magnetogram excluded from the analysis because of grid-like noise artefacts, described in the text (middle), contrasted against the similar inset of two magnetograms from nearby days that are markedly less affected by these instrumental artefacts (left and right). The grey scale is saturated at ± 20 G.

study, we corrected the intensity images for flat field by the division with the appropriate median filter, kindly provided by the MDI team. At least one median filter is produced per Carrington rotation period, but only up to Carrington period 2104 (November 26 to December 24, 2010). For this reason we did not consider data from after this Carrington period.

For each observation day between February 02, 1999 and December 24, 2010, we selected the level 1.5 continuum intensity image and level 1.8.2 5-min longitudinal magnetogram (Liu et al. 2012) recorded closest in time and no more than 12 hours apart of one another. The continuum intensity images were rotated to the observation time of the corresponding longitudinal magnetogram and spatially resampled to co-register with the latter. We discarded the daily data from 18 days that were beset with gross instrumental artefacts, such as unusually strong noise fluctuations and smearing.

5.3.1.3 KPVT

Co-temporal full-disc continuum intensity images and longitudinal magnetograms, from spectropolarimetry of the Fe I 8688 Å line, were collected at the KPVT on a daily basis with the KP_{512} between February 1, 1974 and April 10, 1993, and with the KP_{SPM} between November 19, 1992 and September 21, 2003.

Some of these data carry artefacts from atmospheric seeing and instrumental effects, described in Wenzler et al. (2004, 2006). In this study we consider just the 1757 KP_{512} and 2055 KP_{SPM} daily continuum intensity image and longitudinal magnetogram identified by Wenzler et al. 2006 (out of the 4665 and 2894 available) to be sufficiently free of these artefacts for the magnetic features of interest to be identified with confidence.

On visual examination, we still found instrumental artefacts in some of the KP_{512} magnetograms similar to what is depicted in Fig. 5.1 (middle panel). The magnetogram signal is spurious along rows and columns of image pixels, producing the line and cross

features in the grey scale plot. In 386 of the 1757 KP₅₁₂ magnetograms, large parts of the solar disc is pervaded with this grid-like noise pattern (concentrated between 1989 and 1992, where 268 of the 321 magnetograms are so affected). We excluded the data from these 386 days from the succeeding analysis.

Arge et al. (2002) compared the Carrington rotation synoptic charts of full-disc magnetograms from KPVT, Mount Wilson Observatory (MWO) and Wilcox Solar Observatory (WSO). The data sets spanned the period of 1974 to 2002. The authors noted that the total amount of unsigned magnetic flux in the KPVT charts, up to around 1990, appear slightly lower than the level in the MWO and WSO charts (Fig. 1 in their paper). This was attributed to the bias in the zero level of KP₅₁₂ magnetograms, which was stated to vary with time and with position in the solar disc (from centre to limb, and from east to west). The authors brought the magnetic flux levels in a subset of the KPVT synoptic charts from before 1990 to closer agreement with the MWO and WSO data by modifying the procedure by which KP₅₁₂ magnetograms are combined to form the synoptic charts. Wenzler et al. (2006) and Ball et al. (2012) attempted, by various approximations, to replicate the effect of this correction in KP₅₁₂ magnetograms from before 1990. Wenzler et al. (2006) multiplied the magnetogram signal by a factor of 1.242 while Ball et al. (2012) added 5.9 G to the absolute value.

Here, instead of trying to reproduce the effect of the procedure of Arge et al. (2002), we examined the zero level bias of KP₅₁₂ magnetogram. In this study, we introduce the trimmed mean and trimmed standard deviation. These are the mean and standard deviation of a sample, computed iteratively, with data points more than three standard deviations from the mean omitted from succeeding iterations till no more points are removed.

We divided the solar disc along the central meridian and the $\mu = 0.72$ locus, yielding four segments approximately equal in area. We computed, for each magnetogram, the trimmed mean of the signed magnetogram signal within each segment. The 361-day moving average of the time series of the trimmed mean within each segment (Fig. 5.2) was taken as the zero level bias. The purpose of taking the moving average was to minimise error from the influence of magnetic activity on the trimmed mean in individual magnetograms. Consistent with the claims of Arge et al. (2002), the zero level bias is non-zero, and it varied with time and between the four segments.

However, we found that subtracting the zero level bias from the magnetogram signal made negligible difference to the rest of the analysis, having on the whole, no appreciable effect on the apparent surface coverage and magnetic field strength of bright magnetic features. This is likely due to the fact that the zero level bias, though non-zero, is much weaker than noise fluctuations in the magnetogram signal (the noise level of KP₅₁₂ magnetograms is around 8 G, Wenzler et al. 2006). In SATIRE-S, image pixels with magnetogram signals below the magnetogram signal threshold, which is based on the noise level, are counted as quiet Sun.

Arge et al. (2002) interpreted the observation that the magnetic flux level in the KPVT synoptic charts is slightly lower than in the MWO and WSO charts up to around 1990 (and broadly similar after) to indicate a problem with pre-1990 KP₅₁₂ data. As reported earlier in this section, most of the KP₅₁₂ magnetograms from between 1989 to 1992 are affected by the grid-like noise pattern depicted in Fig. 5.1 (middle panel). The influence by these instrumental artefacts on the magnetogram signal might have contributed to the fact that the flux level in the KPVT charts from this period are no longer lower than in

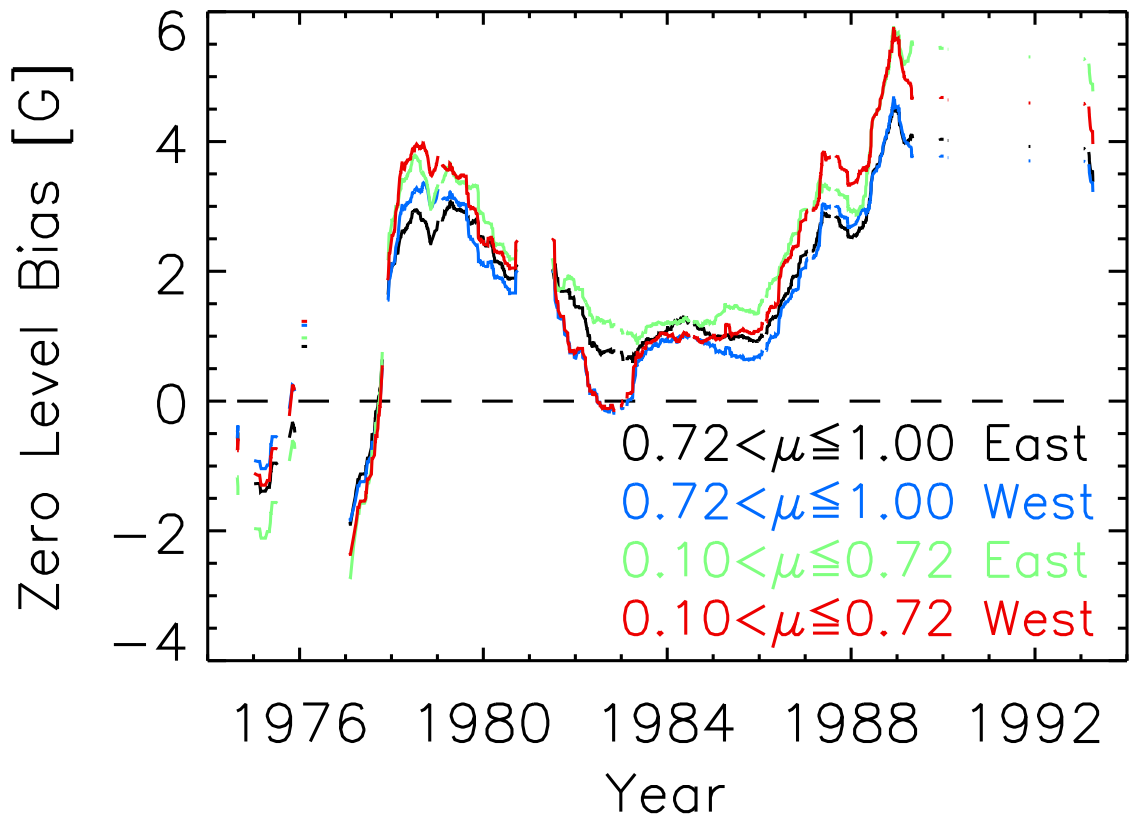


Figure 5.2: Zero level bias of KP_{512} magnetograms, around disc centre ($0.72 < \mu \leq 1.00$) and limb ($0.1 < \mu \leq 0.72$), and east and west of the central meridian. Here (and in all the subsequent time series plots in this paper), segments spaced more than 27 days apart are drawn separately, giving the gaps in the plots. The dashed line follows the null level.

the MWO and WSO charts. (After this period, the KPVT charts are based on KP_{SPM} magnetograms.) We surmise that the disparity between the pre-1990 KPVT charts, and the MWO and WSO charts might be from systematic effects not accounted for in the analysis of Arge et al. (2002) and does not constitute any conclusive indication that a correction of pre-1990 KP_{512} magnetograms is necessary.

We did not introduce the corrections to KP_{512} magnetograms from before 1990 proposed by Wenzler et al. (2006) and Ball et al. (2012), or subtract the zero level bias, determined here, from the magnetogram signal, leaving the KP_{512} magnetograms as they are for the succeeding analysis.

5.3.2 TSI measurements

As stated in Sect. 5.2, the appropriate value of the free parameter, $(\langle B_l \rangle / \mu)_{\text{sat}}$ was recovered by comparing the reconstruction to TSI measurements (to be detailed in Sect. 5.4.2). For this purpose, we took the daily TSI measurements from four radiometers in current operation. They are, namely, ACRIMSAT/ACRIM3 (version 11/13, Willson and Mordvinov 2003), the DIARAD (Crommelynck and Domingo 1984, Dewitte et al. 2004a) and PMO6V (Brusa and Fröhlich 1986) radiometers on SoHO/VIRGO (level 2, version

6_002_1302, Fröhlich et al. 1995, 1997), and SORCE/TIM (level 3, version 14, Kopp and Lawrence 2005, Kopp et al. 2005a,b).

There are two calibrations of the TSI measurements from DIARAD, one by IRMB and the other by PMOD/WRC. Hereafter, we will denote the two calibrations of the DIARAD record, both considered in the analysis, as $\text{DIARAD}_{\text{IRMB}}$ and $\text{DIARAD}_{\text{PMOD}}$, respectively.

The final reconstruction was also evaluated against the three published TSI composites (Sect. 5.5.1.1); ACRIM (version 11/13), IRMB (dated December 19, 2013, kindly provided by Steven Dewitte) and PMOD (version d41_62_1302).

The absolute radiometric calibration of the various radiometers differ, in particular, TIM measurements are about 5 Wm^{-2} lower than that from preceding instruments. Tests conducted at the TSI radiometer facility, TRF with ground copies of ACRIM3, TIM and VIRGO revealed stray light effects in the ACRIM3 and VIRGO instruments (Kopp and Lean 2011). Stray light correction introduced to the ACRIM3 record based on these tests brought it down to within 0.5 Wm^{-2} of TIM TSI (Kopp et al. 2012). The TSI measurements from Picard/PREMOS (Schmutz et al. 2009, Fehlmann et al. 2012), launched in 2011, the only TSI radiometer calibrated in vacuum at full TSI power levels before launch (also at the TRF), agree with TIM to within a similar margin. The results of these efforts have established the lower TSI level first registered by TIM as likely the more accurate.

Taking the 2008 solar minimum as the reference, we normalized all the TSI measurements and composites listed in this section, and the SATIRE-S reconstruction to the mean level in the TIM record over the period of November 2008 to January 2009¹.

5.4 Solar irradiance reconstruction

5.4.1 Harmonizing the model input from multiple instruments

The apparent surface coverage of magnetic features, the key input to the model, is modulated by the properties of the observing instrument. The influence of instrumental differences, left unaccounted for, can introduce inconsistencies between segments of the reconstruction based on data from different instruments. This is avoided here by treating the KP_{512} , KP_{SPM} , MDI and HMI data sets in such a manner (described below in Sects. 5.4.1.1 and 5.4.1.2), that we bring the apparent surface coverage of magnetic features in the various data sets, in the periods of overlap between instruments, to agreement.

5.4.1.1 Umbra and penumbra

First, KP_{SPM} , MDI and HMI continuum intensity images were corrected for limb darkening by the normalization to the fifth order polynomial in μ fit (following Neckel and Labs 1994).

In this study, we adopt the umbra and penumbra continuum intensity threshold for KP_{SPM} determined by Wenzler et al. (2006), and for MDI by Ball et al. (2012). Wenzler et al. (2006) set the KP_{SPM} penumbra threshold at 0.92, where the resulting sunspot area agrees with the sunspot area record by Balmaceda et al. (2009). Assuming this value for

¹In this study, we took the position of solar cycle minima and maxima from the table published by NOAA at www.ngdc.noaa.gov/stp/space-weather/solar-data/solar-indices/sunspot-numbers/cycle-data/.

KP_{SPM} . Ball et al. (2012) found the penumbra threshold for MDI that brought the sunspot area in KP_{SPM} and MDI data into agreement over the period of overlap between the two to be 0.89. In both instances, the umbra threshold (0.70 for KP_{SPM} and 0.64 for MDI) was such that the umbra to sunspot area ratio is 0.2, a figure consistent with observations (Solanki 2003, Wenzler 2005).

We set the umbra and penumbra threshold for HMI as done for MDI by Ball et al. (2012). Comparing MDI and HMI continuum intensity images from the period of overlap, we fixed the HMI penumbra threshold at 0.87, the level that equalized the sunspot area in the two data sets. An umbra to sunspot area ratio of 0.2 was achieved with an umbra threshold of 0.59.

The difference in the umbra and penumbra threshold for the three data sets is primarily due to the fact that sunspot contrast is wavelength dependent.

Due to the 4-bit digitization, KP_{512} continuum intensity images cannot be treated in a similar manner. For this data set, we employed the sunspot masks (indicating the image pixels occupied by sunspots) determined by Wenzler et al. (2006). The sunspot masks were generated by binning the solar disc by μ and estimating from the intensity distribution within each bin the penumbra threshold for the bins closer to disc centre. This procedure overlooks pore-like structures that lack an umbral core. Following the cited work, we derived the umbra and penumbra area from the sunspot masks by

- giving the image pixels marked as sunspots in the masks, umbra and penumbra filling factors of 0.2 and 0.8, respectively, and
- reclassifying the faculae pixels with the highest $\langle B_l \rangle / \mu$, up to 0.127 of the sunspot area, as penumbra.

The latter measure approximately recovers the pore-like structures omitted by the sunspot identification process, bringing the sunspot area in KP_{512} into agreement with the sunspot area record by Balmaceda et al. (2009).

5.4.1.2 Faculae

While it is relatively straightforward to account for the effect of instrumental differences on apparent sunspot area, doing the same for faculae is considerably more subtle. The small-scale magnetic concentrations associated with bright magnetic features are largely unresolved even at HMI's spatial resolution (~ 1 arcsec), leaving us to infer their presence and filling factor from the magnetogram signal. The magnetogram properties of the instruments considered in this study diverge significantly (Jones and Ceja 2001, Wenzler et al. 2004, 2006, Ball et al. 2012, Liu et al. 2012). Applying the same magnetogram signal threshold, $(\langle B_l \rangle / \mu)_{\text{cut}}$ and $(\langle B_l \rangle / \mu)_{\text{sat}}$ to all the data sets with no regards for these differences would create significant discrepancies between the segments of the reconstruction based on data from the different instruments.

The SATIRE-S reconstruction by Ball et al. (2012, 2014) combined the model output from KP_{512} , KP_{SPM} and MDI data into a single TSI/SSI time series. The authors accounted for instrumental differences by adjusting the parameters of the model to each data set (in a manner that does not introduce additional free parameters). This brought the model output from the various data sets into broad agreement. The small residual disagreement

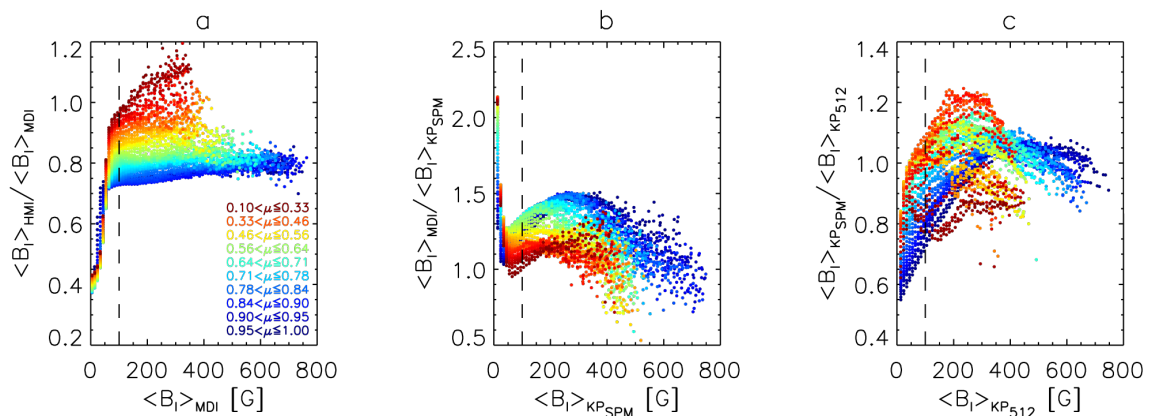


Figure 5.3: a) Ratio of the HMI and MDI magnetogram signal, $\langle B_l \rangle_{\text{HMI}} / \langle B_l \rangle_{\text{MDI}}$ as a function of $\langle B_l \rangle_{\text{MDI}}$, within 68 partially overlapping intervals of μ (the boundary of ten of which are annotated). The dashed line, at $\langle B_l \rangle_{\text{MDI}} = 100$ G, marks the threshold below which the points are excluded from the derivation of the MDI magnetogram signal conversion function due to the increasing influence of magnetogram noise (see text). Also illustrated is the same from the comparison between b) KP_{SPM} and rescaled MDI magnetograms, and c) KP_{512} and rescaled KP_{SPM} magnetograms.

between the KP_{512} , KP_{SPM} and MDI segments of the reconstruction, caused by differences in the magnetogram response of the various instruments, was empirically corrected for by regression.

In this study, we took an alternative approach. We cross-calibrated the magnetograms and the faculae filling factor from the various data sets such that we can apply the same magnetogram signal threshold, $(\langle B_l \rangle / \mu)_{\text{cut}}$ and $(\langle B_l \rangle / \mu)_{\text{sat}}$ to all the data sets. Together with the harmonized umbra and penumbra areas (Sect. 5.4.1.1), this yielded a consistent TSI/SSI time series without the need for any additional correction of the reconstructed spectra.

For these modifications, we relied on the data from the various instruments taken close in time to one another. There are 11 days, between Jan 22 and April 4, 1993, with daily data from both KP_{512} and KP_{SPM} , recorded within about three hours of one another. We will term these observations the KP_{512} - KP_{SPM} co-temporal data. For the period of overlap between KP_{SPM} and MDI, and MDI and HMI, there are considerably more days with daily data from both instruments. For KP_{SPM} and MDI, 910 days between February 2, 1999 and September 21, 2003, and for MDI and HMI, 196 days between April 30 and December 24, 2010. This afforded us the option to restrict ourselves to just the observations taken closest in time to one another. We will denote the KP_{SPM} and MDI observations from 67 days, taken within one hour of one another, and MDI and HMI observations from 187 days, taken within five minutes of one another, as the KP_{SPM} -MDI and MDI-HMI co-temporal data, respectively. It was in the interest of cross-calibrating the data sets as accurately as possible that we balanced examining just the daily data taken closest in time to one another and considering as many as possible, to the extent permitted by available data.

Taking the MDI-HMI co-temporal data, we derived the ratio of the magnetogram

(The contents of this chapter are identical to the submitted version of Yeo, K. L., Krivova, N. A., Solanki, S. K., Glassmeier, K. H., 2014, Reconstruction of total and spectral solar irradiance from 1974 to 2013 based on KPVT, SoHO/MDI and SDO/HMI observations, *Astron. Astrophys.*, 570, A85.)

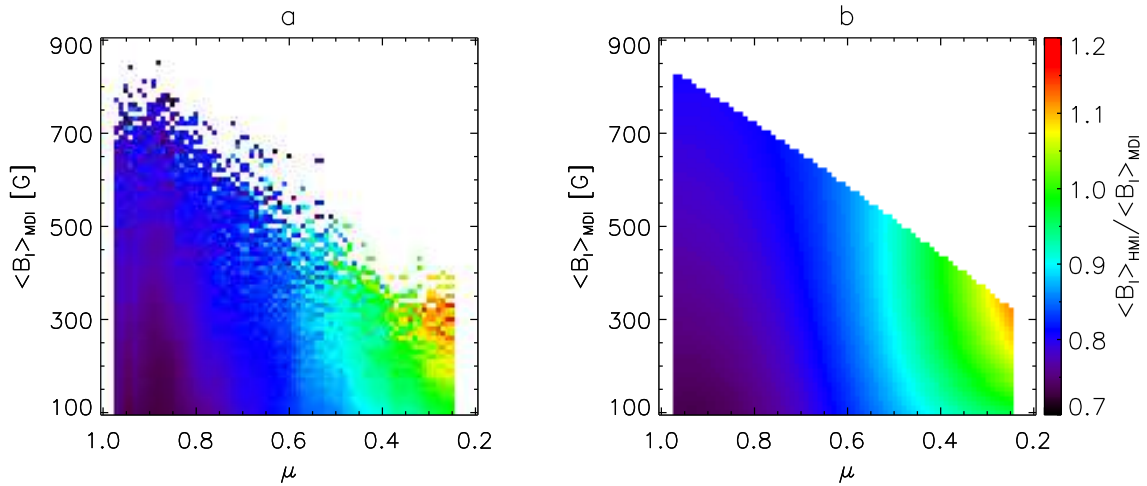


Figure 5.4: a) The same as Fig. 5.3a, except as a colour scale plot and excluding the points where $\langle B_l \rangle_{\text{MDI}} < 100$ G. b) The corresponding bivariate polynomial fit, the MDI magnetogram signal conversion function, over a similar range of μ and $\langle B_l \rangle_{\text{MDI}}$.

signal in HMI and MDI magnetograms, $\langle B_l \rangle_{\text{HMI}} / \langle B_l \rangle_{\text{MDI}}$ as a function of the MDI magnetogram signal and μ .

- First, we resampled the HMI observations in space and time, to co-register with the corresponding MDI data.
- Following that, we masked the image pixels counted as umbra or penumbra. Our interest here is the magnetogram signal of bright magnetic features. The influence of instrument-related factors on the magnetogram signal of these features, and of sunspots and pores differ (e.g., Yeo et al. 2014a), therefore the need to exclude the latter. Another consideration is the saturation of MDI and HMI magnetograms in sunspot umbrae. For MDI, this is due to limitations in the onboard algorithm used to generate the magnetograms (Liu et al. 2007, 2012), and for HMI, the Fe I 6173 Å line shifting out of the spectral sampling range of the instrument (Sebastien Couvidat, personal communication).
- We divided the solar disc by μ into 68 partially overlapping intervals, each representing $\sim 10\%$ of the solar disc by area. Within each μ interval, we compared the magnetogram signal in the MDI and HMI data by the following, based broadly on the histogram equalization method of Jones and Ceja (2001).
- Taking each magnetogram, we ranked the unmasked image pixels by the signed magnetogram signal and took the mean of each successive ten points. We then matched the ranked and averaged MDI magnetogram signal to the corresponding values from the HMI magnetogram from the same day. Collating the MDI and HMI magnetogram signal pairs so derived from all the data days, we binned them by the MDI magnetogram signal in bins of 10 G width. Finally, we took the median MDI and HMI magnetogram signal within each bin, and the quotient of the two, $\langle B_l \rangle_{\text{HMI}} / \langle B_l \rangle_{\text{MDI}}$, expressed in Figs. 5.3a and 5.4a.

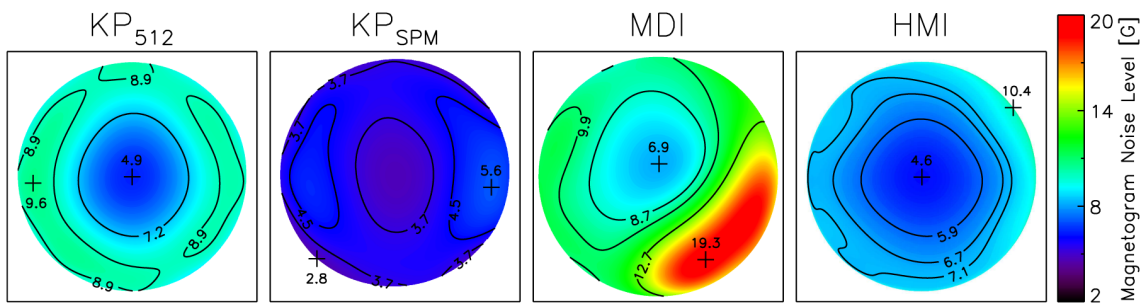


Figure 5.5: Noise level of rescaled KP_{512} , KP_{SPM} and MDI magnetograms, and of HMI magnetograms, as a function of position in the field-of-view. The contours correspond to the first, second and third quartiles, and the crosses to the minimum and maximum points. The contour and point labels are in units of Gauss. We omit the second quartile in the KP_{512} and KP_{SPM} plots to avoid cluttering. The KP_{512} , KP_{SPM} and HMI noise surfaces were resampled to MDI image size to allow a direct comparison.

As evident in Figs. 5.3a and 5.4a, the relationship between the HMI and MDI magnetogram signal, represented by $\langle B_l \rangle_{\text{HMI}} / \langle B_l \rangle_{\text{MDI}}$, varies significantly with magnetogram signal and μ . The marked decline in $\langle B_l \rangle_{\text{HMI}} / \langle B_l \rangle_{\text{MDI}}$ towards $\langle B_l \rangle_{\text{MDI}} = 0$ G comes from the fact that MDI 5-min longitudinal magnetograms are significantly noisier than HMI 315-s longitudinal magnetograms (see the noise level estimates by Ball et al. 2012, Liu et al. 2012, Yeo et al. 2013), and so does not reflect the true relationship between HMI and MDI magnetogram signal in this regime. Excluding the points where $\langle B_l \rangle_{\text{MDI}} < 100$ G (a conservative threshold), we fit a bivariate polynomial (second order in $\langle B_l \rangle_{\text{MDI}}$ and third order in μ) to $\langle B_l \rangle_{\text{HMI}} / \langle B_l \rangle_{\text{MDI}}$, illustrated in Fig. 5.4b. This surface fit, hereafter referred to as the MDI magnetogram signal conversion function, gives the multiplicative factor for a given μ and $\langle B_l \rangle_{\text{MDI}}$ that would convert the magnetogram signal in MDI magnetograms to the HMI equivalent.

We rescaled the magnetogram signal in the entire MDI data set to the HMI equivalent by applying the MDI magnetogram signal conversion function.

We repeated the entire process described above for the other data sets. That is, using the KP_{SPM} -MDI co-temporal data to bring the magnetogram signal in the SPM data set to the rescaled MDI equivalent, and then the KP_{512} - KP_{SPM} co-temporal data to bring the magnetogram signal in the KP_{512} data set to the rescaled KP_{SPM} equivalent. As between MDI and HMI, the relationship between KP_{SPM} and rescaled MDI, and KP_{512} and rescaled KP_{SPM} magnetogram signal fluctuates with magnetogram signal and μ (Figs. 5.3b and 5.3c). Though there are only observations from 11 days in the KP_{512} - KP_{SPM} co-temporal data set, each magnetogram presents the order of 10^6 point measurements of magnetic flux, providing sufficient statistics for the analysis.

The noise level of rescaled MDI magnetograms was estimated following the analysis of Yeo et al. (2013) with HMI 315-s longitudinal magnetograms. We selected the magnetogram from ten sunspot-free, low-activity days near the 2008 solar cycle minimum. For each magnetogram, we centred a 101×101 pixel window on each point on the solar disc and computed the trimmed standard deviation (defined in Sect. 5.3.1.3). Then, we took the median of the trimmed standard deviation from the ten magnetograms at each point

5 Reconstruction of total and spectral solar irradiance from 1974 to 2013 based on KPVT, SoHO/MDI and SDO/HMI observations

(The contents of this chapter are identical to the submitted version of Yeo, K. L., Krivova, N. A., Solanki, S. K., Glassmeier, K. H., 2014, *Reconstruction of total and spectral solar irradiance from 1974 to 2013 based on KPVT, SoHO/MDI and SDO/HMI observations*, *Astron. Astrophys.*, 570, A85.)

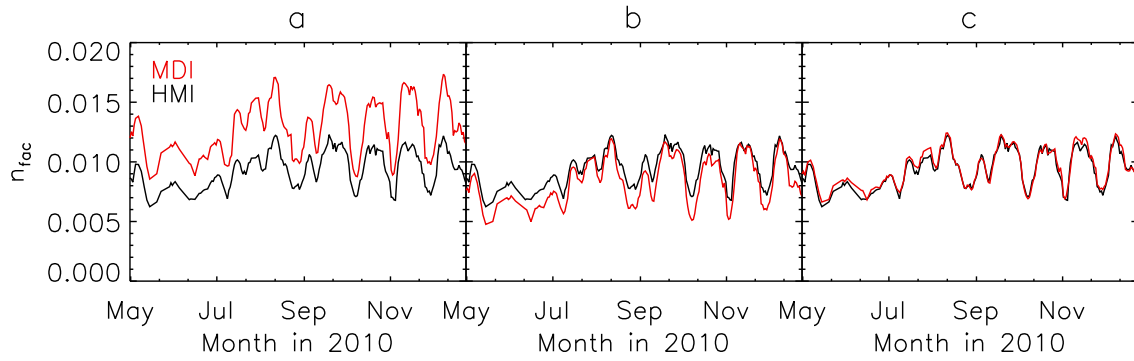


Figure 5.6: a) Proportion of the solar disc covered by faculae, n_{fac} in the MDI (red) and HMI (black) data sets over the period of overlap if we do not rescale the MDI magnetogram signal and faculae filling factor. b) The same, after rescaling the MDI magnetogram signal. c) The final result, incorporating the rescaled MDI magnetogram signal and faculae filling factor.

on the solar disc. To these values we fit a polynomial surface, which represents the noise level of rescaled MDI magnetograms, plotted in Fig. 5.5. Also illustrated are the noise surfaces of rescaled KP_{512} and KP_{SPM} magnetograms, derived in a similar manner, and the noise surface of HMI magnetograms (determined by Yeo et al. 2013). The noise level of rescaled MDI magnetograms is, at every (relative) position in the field-of-view, higher than the noise level of the other data sets.

The area covered by faculae was derived taking into account the fact that the MDI data set has (after the rescaling of the magnetogram signal) the highest magnetogram noise level (Fig. 5.5) and the coarsest pixel scale of the data sets considered in this study (Table 5.1). To this end, we took the following measures.

- We applied the same magnetogram signal threshold, given by three times the noise surface of rescaled MDI magnetograms, to all the data sets.
- In SATIRE-S, standalone facular pixels are reclassified as quiet Sun to minimise the inclusion of magnetogram noise fluctuations. This is at the expense of legitimate bright magnetic features occupying just a single image pixel. To ensure that we are discriminating against similar sized features in all the data sets, we excluded the bright magnetic features in the KP_{512} , KP_{SPM} and HMI data sets that would appear standalone if we resample the magnetograms to MDI pixel scale.
- Taking an arbitrary but conservative value of 600 G for $(\langle B_l \rangle / \mu)_{\text{cut}}$, facular pixels with magnetogram signals above this level were also reclassified as quiet Sun (following Ball et al. 2011, 2012). As stated in Sect. 5.2, this is to minimise the misclassification of the magnetic canopy of sunspots as faculae.
- The filling factor of each facular pixel was then determined by the linear relationship described in Sect. 5.2. We obtained a value of 230 G for $(\langle B_l \rangle / \mu)_{\text{sat}}$ (see Sect. 5.4.2).

Let n_{fac} represent the proportion of the solar disc covered by faculae, given by the sum over all facular pixels of the filling factor, normalised by the number of solar disc pixels. The n_{fac} in the MDI and HMI data sets over the period of overlap is shown in Fig. 5.6. In Fig. 5.6a, we compare the n_{fac} if we do not rescale the magnetogram signal in the MDI data set. As stated at the beginning of this section, applying the same model parameters to the MDI and HMI data sets without any consideration of the different magnetogram properties results in a gross divergence in the apparent faculae area. Rescaling the magnetogram signal of the MDI data set to the HMI equivalent removed most of this disparity (Fig. 5.6b). The residual difference, though small, is not negligible. The apparent facular area in the overlap between the KP₅₁₂, KP_{SPM} and MDI data sets exhibit a similar response to the analysis, not shown here to avoid repetition.

The magnetogram signal conversion functions are determined from the fit to observed magnetogram signal ratios (Fig. 5.4), excluding the data below 100 G, where the apparent ratio is increasingly biased by magnetogram noise (Fig. 5.3). The factors used to rescale the magnetogram signal below 100 G are given by the extrapolation of the fit to this regime. As a test, we repeated the analysis described in this section, fixing the $\langle B_l \rangle < 100$ G segment of the conversion functions at the value at $\langle B_l \rangle = 100$ G instead. This adjustment to the conversion function made no appreciable difference to n_{fac} , excluding the uncertainty in the conversion functions below 100 G as the main cause of the residual disparity in n_{fac} between the various data sets.

The residual disparity in n_{fac} is probably due to differences in spatial resolution. Specifically, in the point spread function and how it is sampled by the detector array. The effect of spatial resolution on apparent area is especially relevant to bright magnetic features, as they remain largely unresolved even at HMI's resolving power they are particularly susceptible to effects such as stray light and undersampling. (As an example, the pronounced effect of stray light on the apparent surface area of bright magnetic features in HMI magnetograms was recently demonstrated by Yeo et al. 2014a). To correct for this directly, we would have to convolve the various data sets by suitable filters and resample the KP₅₁₂, KP_{SPM} and HMI data to MDI image size. These filters, different for each instrument, are not straightforward to determine (see the discussions in Wedemeyer-Böhm 2008, Yeo et al. 2014a). Here, we account for the residual effect of instrumental differences on n_{fac} by the following steps instead.

- Taking each magnetogram in the MDI-HMI co-temporal data, we divided the solar disc by μ in intervals of 0.01, and calculated the n_{fac} within each segment.
- Interval by interval, we fit a second order polynomial to the scatter plot of the n_{fac} from the MDI magnetograms versus the n_{fac} from the corresponding HMI magnetograms. To improve the statistics, we included the values from adjacent μ intervals. The result is a series of functions that relate the apparent faculae area in MDI and HMI magnetograms at different distances from disc centre.
- With these functions, we rescaled the faculae filling factor of the entire MDI data set to the HMI equivalent.
- This adjustment was then propagated to the KP_{SPM} and KP₅₁₂ data sets. We rescaled the faculae filling factor of the KP_{SPM} data set repeating the above analysis on the

Table 5.2: To the nearest Gauss, the value of $(\langle B_l \rangle / \mu)_{\text{sat}}$ that optimises the agreement between reconstructed and measured TSI. Also tabulated is the correlation (R and R^2) and RMS difference (k) between each TSI record and the corresponding candidate reconstruction.

TSI record	$(\langle B_l \rangle / \mu)_{\text{sat}}$ [G]	R	R^2	k [Wm^{-2}]
ACRIM3	204	0.963	0.928	0.155
DIARAD _{IRMB}	255	0.962	0.925	0.141
DIARAD _{PMOD}	230	0.969	0.940	0.131
PMO6V	230	0.979	0.959	0.107
TIM	220	0.960	0.921	0.108

KP_{SPM}-MDI co-temporal data, and finally of the KP₅₁₂ data set using the KP₅₁₂-KP_{SPM} co-temporal data.

This procedure brought the apparent faculae area in the KP₅₁₂, KP_{SPM}, MDI and HMI data sets, in the periods of overlap, to agreement, illustrated for the overlap between MDI and HMI in Fig. 5.6c.

5.4.2 The free parameter

In the SATIRE-S model, the faculae filling factor of bright magnetic features is deduced from the magnetogram signal. It is given by the quotient of $\langle B_l \rangle / \mu$ and $(\langle B_l \rangle / \mu)_{\text{sat}}$, up to $\langle B_l \rangle / \mu = (\langle B_l \rangle / \mu)_{\text{sat}}$, beyond which it is fixed at unity (Fligge et al. 2000). The higher the value of $(\langle B_l \rangle / \mu)_{\text{sat}}$, the sole free parameter in the model, the lower the apparent facular area, and vice versa. This is accentuated by the fact that the distribution of magnetogram signals is skewed towards lower magnetogram signal levels (Parnell et al. 2009). As a result, facular contribution to variation in reconstructed solar irradiance scales nearly inversely with $(\langle B_l \rangle / \mu)_{\text{sat}}$. The appropriate value of $(\langle B_l \rangle / \mu)_{\text{sat}}$ is obtained by optimizing the agreement between reconstructed and measured TSI. As mentioned in Sect. 5.3.2, we considered the observations from ACRIM3, DIARAD, PMO6V and TIM for this purpose.

There are discrepancies in the long-term trends in the TSI time series produced by ACRIM3, DIARAD, PMO6V and TIM (Fig. 5.7). The most notable is the conflicting secular variation between the 1996 and 2008 solar minima, between the DIARAD_{IRMB}, and the DIARAD_{PMOD} and PMO6V records. This disparity is one of the reasons we considered multiple TSI records, all of which extend for at least about a decade for this part of the analysis. The motivation is to avoid introducing bias in $(\langle B_l \rangle / \mu)_{\text{sat}}$ from relying on just a single or shorter TSI records (such as, from Picard/PREMOS, launched only in 2011, Schmutz et al. 2009).

Let TSI_{obs} and TSI_{mod} denote observed and reconstructed TSI. In the earlier implementations of SATIRE-S by Ball et al. (2011, 2012), $(\langle B_l \rangle / \mu)_{\text{sat}}$ was fixed at the value that brought the slope of the linear fit to the scatter plot of TSI_{obs} and TSI_{mod} to unity, taken as an indication of a close match in the overall trend. While a regression coefficient of unity would be a property of two TSI series that are similar, it is not by itself sufficient to indicate similarity or a linear relationship between the two. The divergence of the slope from unity is suitable as a measure of similarity only in the case where a linear relation between the two series in question can be assumed. Additionally, differences

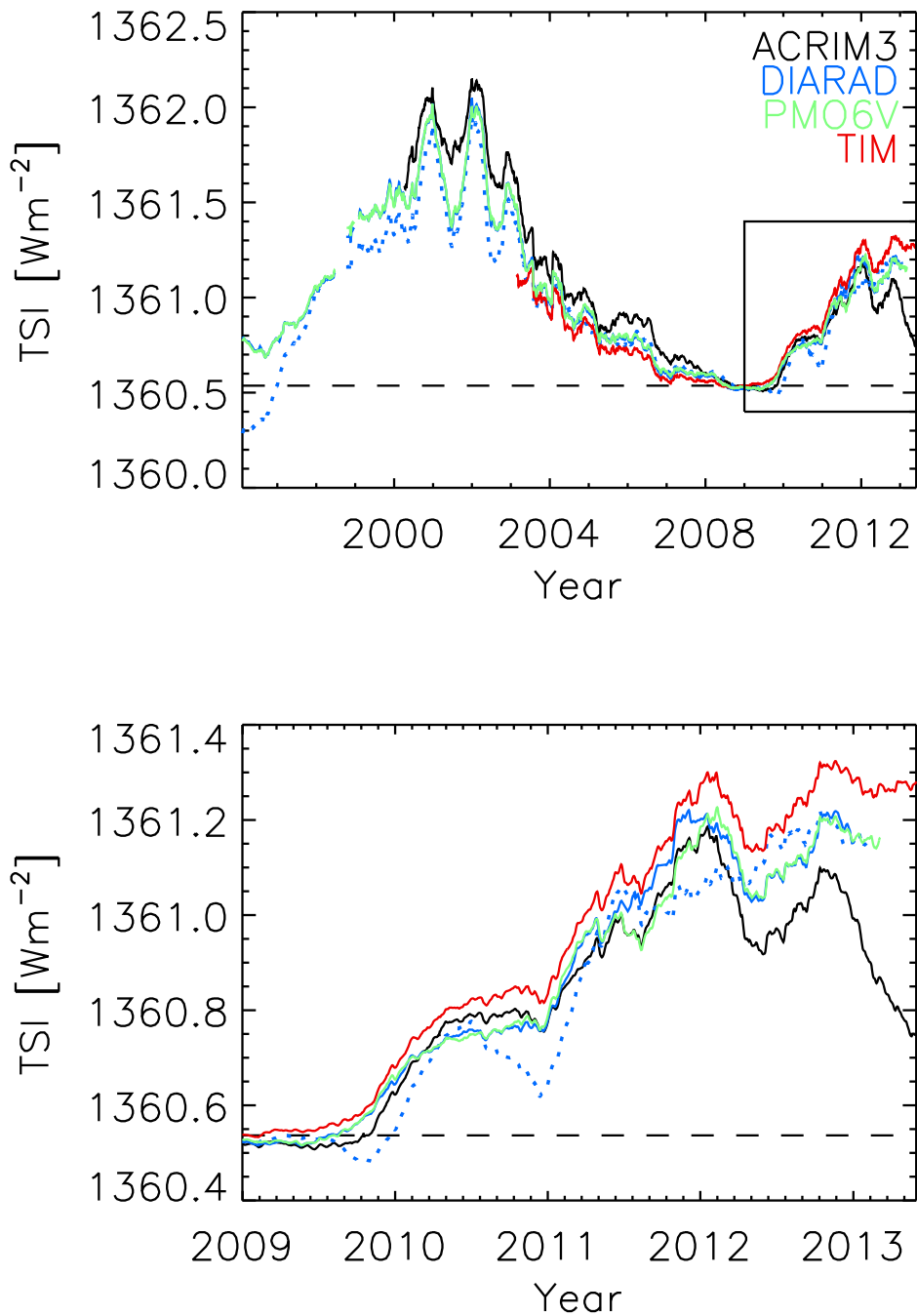


Figure 5.7: 181-day moving average of the daily TSI measurements from the ACRIM3 (black), DIARAD (blue), PMO6V (green) and TIM (red) radiometers. The dotted and solid blue curves correspond to $\text{DIARAD}_{\text{IRMB}}$ and $\text{DIARAD}_{\text{PMOD}}$, the calibration of the DIARAD record by IRMB and by PMOD/WRC. The $\text{DIARAD}_{\text{PMOD}}$ series is almost completely hidden by the PMO6V series due to the close similarity. The dashed lines follow the mean TIM TSI level over the period of November 2008 to January 2009. The lower plot is a blow up of the boxed inset in the upper plot.

in the long-term trend between TSI_{obs} and TSI_{mod} can possibly shift the slope towards, rather than away from unity. Here, we set $(\langle B_l \rangle / \mu)_{\text{sat}}$ at the value that minimizes the root mean square, RMS difference between TSI_{obs} and TSI_{mod} , denoted k , instead. It can be shown that the RMS difference between TSI_{obs} and TSI_{mod} is, apart from a factor, equivalent to the RMS of the normal distance of the scatter plot of TSI_{obs} and TSI_{mod} to the $\text{TSI}_{\text{obs}} = \text{TSI}_{\text{mod}}$ line. Quantifying the scatter about $\text{TSI}_{\text{obs}} = \text{TSI}_{\text{mod}}$, this quantity measures the similarity between the two series independent of the underlying relationship.

We generated five candidate reconstructions by taking each of the five TSI records considered as the reference for recovering $(\langle B_l \rangle / \mu)_{\text{sat}}$. The retrieved value of $(\langle B_l \rangle / \mu)_{\text{sat}}$ in each case, determined to the nearest Gauss, is summarized in Table 5.2. Recall, that facular contribution to variation in reconstructed solar irradiance scales nearly inversely with $(\langle B_l \rangle / \mu)_{\text{sat}}$. The spread in the recovered value of $(\langle B_l \rangle / \mu)_{\text{sat}}$ reflects the differences in the cyclical variation in the five TSI records (Fig. 5.7). The retrieved values of $(\langle B_l \rangle / \mu)_{\text{sat}}$ in the DIARAD_{PMOD} and PMO6V cases (and therefore the corresponding candidate reconstructions) are exactly identical due to the close similarity in the long-term trend in these TSI records.

In Fig. 5.8, we plot the TSI from the candidate reconstructions, along the respective reference TSI record (top row), and the difference between the two (centre row). To elucidate the long-term fluctuations, we smoothed each time series with a 181-day boxcar filter.

- ACRIM3 (Fig. 5.8a): The reconstruction is broadly lower than the TSI record, by $\lesssim 0.1 \text{ Wm}^{-2}$, up to 2007, after which it starts to drift (almost monotonically) higher, by $\sim 0.25 \text{ Wm}^{-2}$ between 2007 and 2012, and by the same margin in 2013 alone.
- DIARAD_{IRMB} (Fig. 5.8b): The reconstruction and the TSI record differ, for much of the period of comparison, by more than $\sim 0.1 \text{ Wm}^{-2}$. Notably, the level at the solar cycle minimum in 1996 is higher in the reconstruction by a gross margin of $\sim 0.4 \text{ Wm}^{-2}$.
- DIARAD_{PMOD} (Fig. 5.8c) and PMO6V (Fig. 5.8d): In both cases, modelled and measured TSI agree, to within $\sim 0.05 \text{ Wm}^{-2}$, over nearly the entire period of comparison.
- TIM (Fig. 5.8e): There is a continuous drift, of $\sim 0.25 \text{ Wm}^{-2}$ between 2003 and 2013, between model and measurement.

We derived the coefficient of determination, R^2 between reconstructed and observed TSI within a 361-day window centred on each data day (bottom row, Fig. 5.8), representing the short-term agreement. The agreement between modelled and measured TSI is relatively close, with R^2 generally above 0.8, except around solar cycle minima, where it dips as variation in solar irradiance diminishes and noise starts to play a role. In the ACRIM3 and DIARAD_{PMOD} cases, there are also other periods where the agreement deteriorated markedly. The closest short-term agreement is seen with the TIM data set.

In terms of the overall agreement, given by the correlation and the RMS difference, k over the entire period of comparison, the closest alignment was found between the PMO6V record and the corresponding candidate reconstruction (Table 5.2).

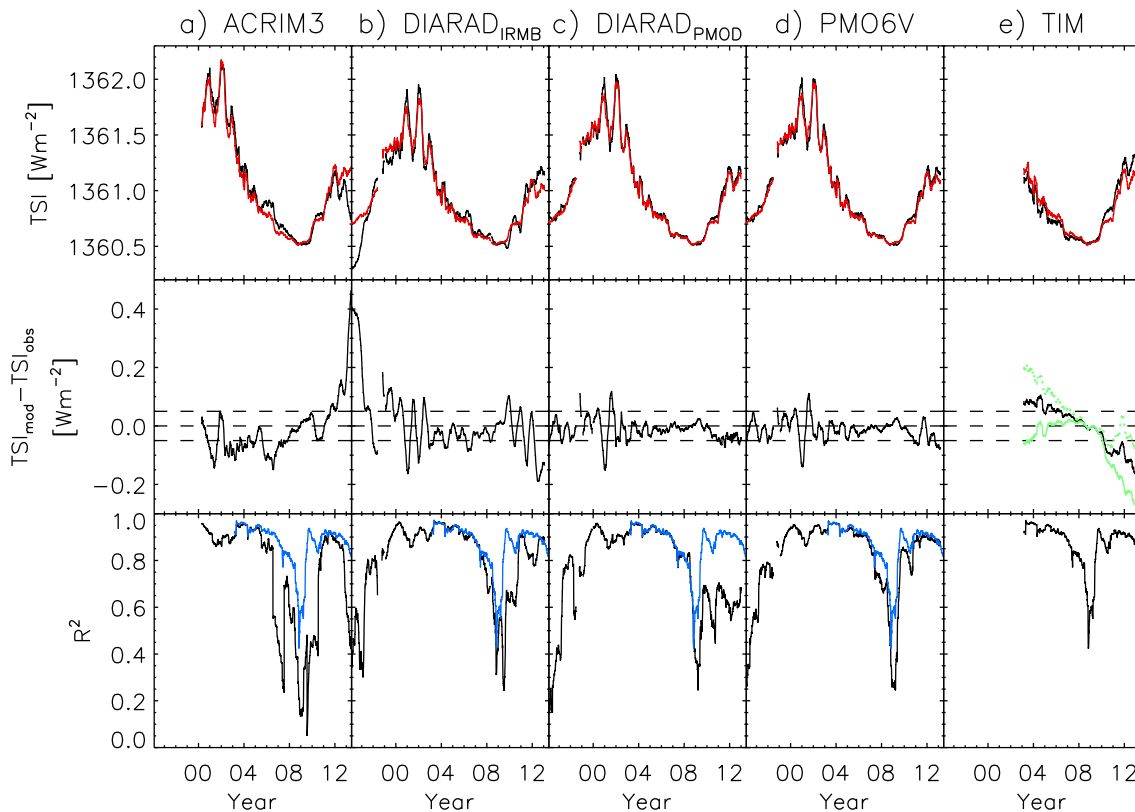


Figure 5.8: Top: 181-day moving average of the five TSI records examined (black) and the TSI reconstructed by taking them as the reference for recovering $(\langle B_l \rangle / \mu)_{\text{sat}}$ (red). Middle: The difference between the two, $\text{TSI}_{\text{mod}} - \text{TSI}_{\text{obs}}$. The solid and dotted green curves in the TIM panel depict the same from taking just TIM measurements from before, and from after October 1, 2009 as the reference. The dashed lines mark the zero level and $\text{TSI}_{\text{mod}} - \text{TSI}_{\text{obs}} = \pm 0.05 \text{ Wm}^{-2}$. Bottom: The R^2 between measured and modelled TSI within a 361-day window centred on each data day. The TIM series is plotted over the other series in blue for comparison.

Only with the PMO6V record did reconstructed TSI exhibit consistent close agreement at both rotational and cyclical timescales (Fig. 5.8). For this reason, we retained the candidate reconstruction, derived taking the PMO6V record as the reference for recovering $(\langle B_l \rangle / \mu)_{\text{sat}}$, for the succeeding analysis.

This is a departure from the preceding SATIRE-S reconstruction by Ball et al. (2012). The authors determined $(\langle B_l \rangle / \mu)_{\text{sat}}$ comparing the model output to TIM TSI over the period of 2003 to 2009. Their reconstruction exhibited close long-term agreement with the TIM record, while we noted an almost continuous drift between the TIM record and the corresponding candidate reconstruction (Fig. 5.8e). This disparity stems largely from the difference in the period of comparison (discussed below), although the fact that we had derived facular area by a significantly different analysis (Sect. 5.4.1.2) may have contributed to a minor extent.

Here, the period of comparison extends to 2013. Taking, as in the earlier study, just TIM data up to October 31, 2009 (termed, for this discussion, the cutoff date) as the

reference, we retrieved a higher value of 261 G for $\langle B_I \rangle / \mu_{\text{sat}}$. This brought the pre-cutoff segment of the reconstruction down closer to the TIM record but at the same time amplified the post-cutoff divergence (green solid curve, Fig. 5.8e). Likewise, using only TIM measurements from after the cutoff date as the reference returned a lower $\langle B_I \rangle / \mu_{\text{sat}}$ of 185 G, which raised the post-cutoff segment closer to TIM levels but also widened the pre-cutoff disparity (green dotted curve). As the solar cycle amplitude of modelled TSI is modulated by $\langle B_I \rangle / \mu_{\text{sat}}$ and the cutoff date is incidentally near the 2008 solar cycle minimum, the slow, near-monotonic drift between the reconstruction and the TIM record found here is largely undetectable looking at data from before, or from after the cutoff date alone. No significance should be attached to this value of the cutoff date. Repeating this analysis, setting the cutoff date at earlier and later times around the 2008 minimum, we found similar trends in the recovered value of $\langle B_I \rangle / \mu_{\text{sat}}$, and the pre-cutoff and post-cutoff segments of the reconstruction.

This observation, that disparity between model and measurement can possibly be hidden if we recover $\langle B_I \rangle / \mu_{\text{sat}}$ comparing them over a span of time that sits largely within the ascending or descending phase of a solar cycle, is another reason for considering multiple, extended (> 10 years) TSI records for this part of the analysis.

5.4.3 Ultraviolet solar irradiance

As detailed in Unruh et al. (1999), the intensity spectra of umbra, penumbra, faculae and quiet Sun utilised in the reconstruction were synthesized with the ATLAS9 radiative transfer code (which assumes local thermodynamic equilibrium, LTE, Kurucz 1993) representing spectral lines by opacity distribution functions, ODFs. Consequently, below ~ 300 nm, modelled solar irradiance starts to diverge from observation and progressively so with decreasing wavelength (as previously noted by Krivova et al. 2006, Unruh et al. 2008, and illustrated in Fig. 5.9). The effects of the LTE and ODF simplifications emerge in the ultraviolet from the breakdown of the LTE approximation in the upper layers of the solar atmosphere, and estimating line blanketing using ODFs.

The limitations of the SATIRE-S model in the ultraviolet imposed by the LTE and ODF simplifications were previously accounted for as follows. Krivova et al. (2006) reported a close agreement between their SATIRE-S reconstruction of ultraviolet solar irradiance and the measurements from UARS/SUSIM (Brueckner et al. 1993, Floyd et al. 2003) in the wavelength range of 220 to 240 nm (termed the reference interval). Taking the SUSIM record, the authors found, by regression, the relationship between each wavelength channel and the integrated flux in the reference interval. Solar irradiance over the wavelength range of 115 to 270 nm was then regenerated applying these relationships to the reconstruction of the integrated flux in the reference interval.

In this study, we accounted for the LTE and ODF simplifications by a modified analysis.

- 180 to 300 nm: We offset this segment of the reconstruction (wavelength element by wavelength element) to the Whole Heliospheric Interval (WHI) reference solar spectra (version 2, Woods et al. 2009). This somewhat less obtrusive approach was prompted by our observations that in this spectral range the model reproduces variations in SSI observations well (see Sect. 5.5.1.3), though less so the absolute

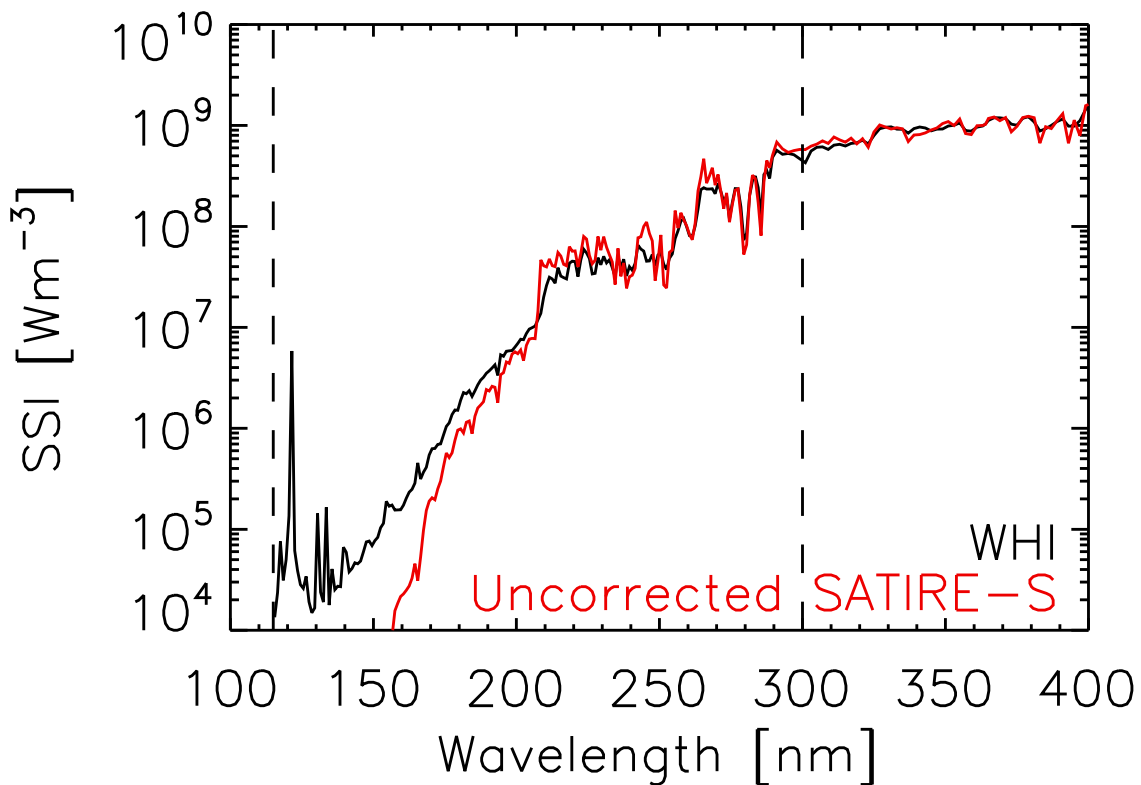


Figure 5.9: The WHI reference solar spectrum for the period of April 10 to April 16, 2008, and the mean SATIRE-S spectrum over the same period prior to the correction of the 115 to 300 nm segment (see text), bounded by the dashed lines. The WHI reference solar spectrum is binned to the wavelength scale of the reconstruction.

level. The intention here is to bring the absolute level of the reconstruction in this spectral range to a more realistic level, while retaining the variation returned by the model. We are prohibited from extending this approximation below 180 nm due to the gross disparity in the absolute level between modelled and measured solar irradiance there (Fig. 5.9).

- 115 to 180 nm: We regenerated this segment of the reconstruction by an analysis similar to that previously employed by Krivova et al. (2006), described above. Except here we based the correction on the observations from the FUV (115 to 180 nm) instrument on *SORCE/SOLSTICE* (level 3, version 12, McClintock et al. 2005, Snow et al. 2005a) instead. This is in the interest of consistency with the correction introduced in the 180 to 300 nm segment; the wavelength range of 115 to 310 nm in the WHI reference solar spectra is provided by *SOLSTICE* spectrometry.

The WHI reference solar spectra represent the mean SSI over three periods within Carrington rotation 2068 (March 25 to March 29, March 30 to April 4, and April 10 to April 16, 2008). First, we binned the higher spectral resolution reference spectra to the wavelength scale of the reconstruction (given basically by the *ATLAS9* code). Next, we took the difference between the reference spectra and the average reconstructed spectra

(The contents of this chapter are identical to the submitted version of Yeo, K. L., Krivova, N. A., Solanki, S. K., Glassmeier, K. H., 2014, Reconstruction of total and spectral solar irradiance from 1974 to 2013 based on KPVT, SoHO/MDI and SDO/HMI observations, *Astron. Astrophys.*, 570, A85.)

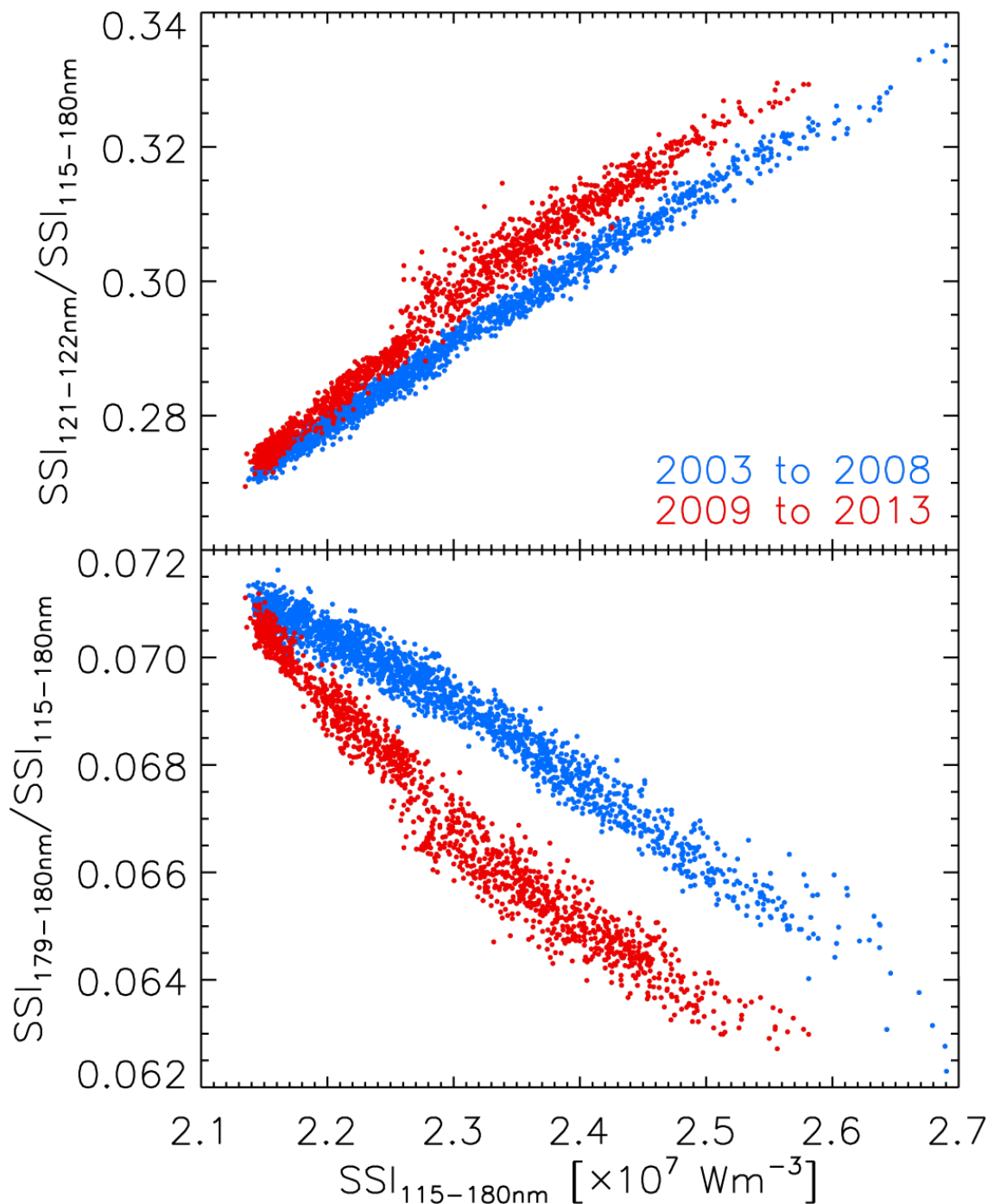


Figure 5.10: Scatter plot of the ratio of SOLSTICE FUV SSI to the total flux registered by the instrument against the total flux, in the 121 to 122 nm (top), and 179 to 180 nm wavelength channels (bottom). The points from up to December 31, 2008 are drawn in blue, and from January 1, 2009 on in red.

over the same periods. Finally, we took the mean of the three difference spectra and offset the 180 to 300 nm segment of the SSI reconstruction by the result.

The SOLSTICE FUV data set spans May 14, 2003 to July 15, 2013. We found a

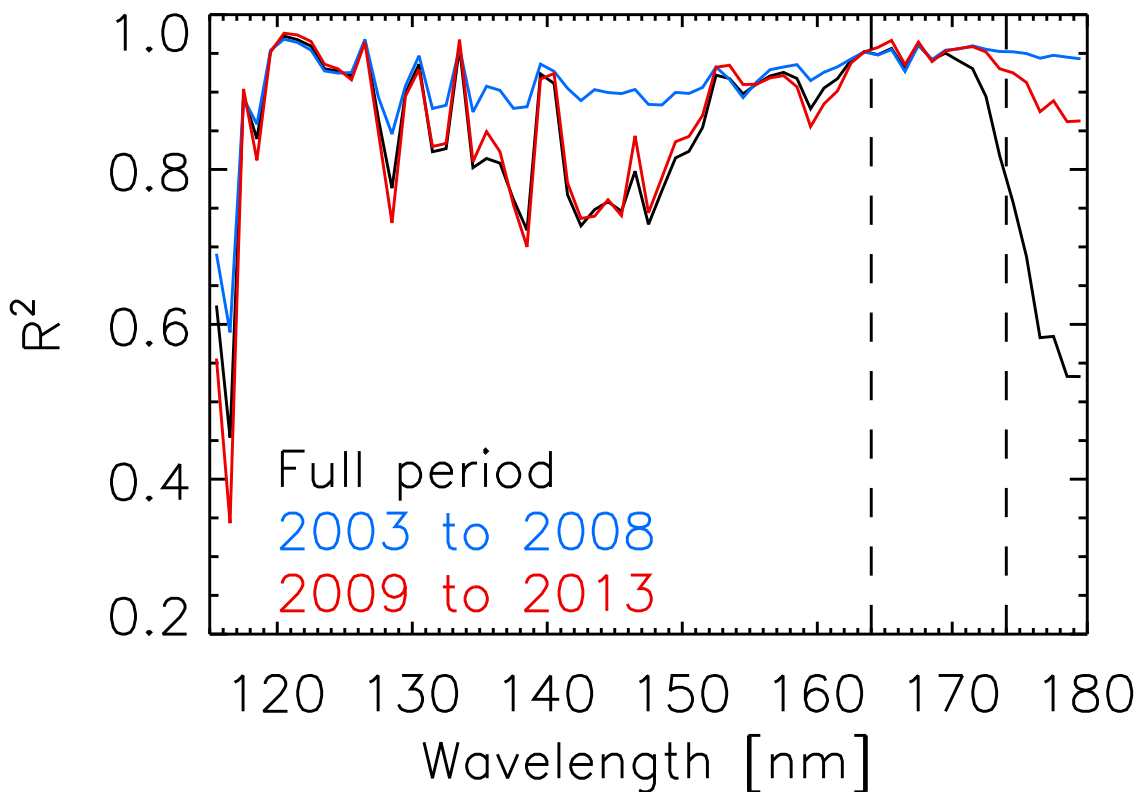


Figure 5.11: The R^2 between the reconstruction (prior to the correction of the 115 to 300 nm segment) and SOLSTICE FUV, as a function of wavelength. The black curve represents the values obtained when considering the entire period of overlap between the two series, the blue and red curves data from before 2009 and from 2009 onwards alone. The dashed lines mark the reference interval, 164 to 174 nm (see text).

distinct disparity between the measurements from before 2009, and from 2009 onwards. This can be seen from the scatter plot of the ratio of measured flux in a given wavelength channel to the total flux registered by the instrument versus the total flux (two examples of which are illustrated in Fig. 5.10). The two intervals of time, differently coloured, visibly do not overlap. This behaviour is seen for most of the wavelength channels and suggests that around the turn of 2008 to 2009, there was a shift in how the shape of SOLSTICE FUV spectra scaled with total flux. We will not speculate here if this shift is solar or instrumental in origin.

We also compared the reconstruction with the SOLSTICE FUV record, deriving the R^2 between the two as a function of wavelength. (The wavelength scale of the reconstruction and the SOLSTICE FUV record is similar, allowing us to make a channel-to-channel comparison.) Looking at data from before 2009 alone, measurement and model are highly correlated everywhere above ~ 120 nm (blue curve, Fig. 5.11). Once we include data from 2009 onwards or examine them alone (black and red curves, respectively), the correlation at most wavelengths deteriorate significantly. Given the apparent shift in the property of SOLSTICE FUV observations around the turn of 2008 to 2009 (Fig. Fig. 5.10), and the excellent consistency between measurement and model before this shift, we confined

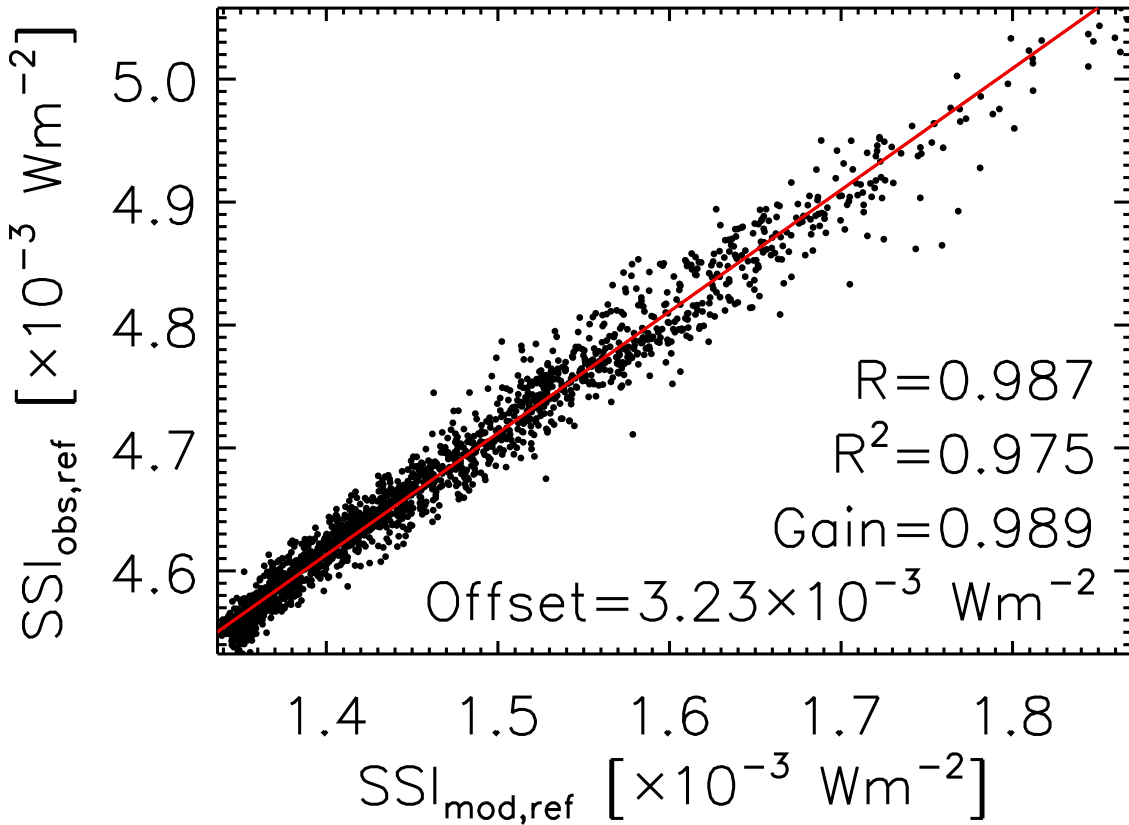


Figure 5.12: Scatter plot of the integrated flux over the reference interval (164 to 174 nm) in the SOLSTICE FUV record, $SSI_{\text{obs,ref}}$ and in the reconstruction, $SSI_{\text{mod,ref}}$ (prior to the correction of the 115 to 300 nm segment). The red line is the straight line fit to the scatter plot. The R and R^2 between the two series, and the gain and offset of the fit are indicated.

ourselves to the SOLSTICE FUV observations from up to December 31, 2008 for the following.

We took the 10 nm interval, 164 to 174 nm, as the reference interval. Let $SSI_{\text{obs,ref}}$ and $SSI_{\text{mod,ref}}$ denote the observed and reconstructed integrated flux in the reference interval. The linear regression of $SSI_{\text{obs,ref}}$ to $SSI_{\text{mod,ref}}$ is plotted along with the scatter plot of the two in Fig. 5.12. The overall levels of $SSI_{\text{obs,ref}}$ and $SSI_{\text{mod,ref}}$ differ by a factor of about three. The variation with time however, is remarkably similar, as indicated by the proximity of the correlation coefficient, R (0.987) and the gain of the fit (0.989) to unity. A regression slope that is close to unity, as discussed in Sect. 5.4.2, is inadequate by itself as a metric of similarity. However, together with a high R , it denotes that the two series are not only correlated, but the scale of the variation is closely similar. To a good approximation, $SSI_{\text{obs,ref}}$ and $SSI_{\text{mod,ref}}$ differ only by an offset of $3.23 \times 10^{-3} \text{ Wm}^{-2}$, the vertical intercept of the straight line fit.

Following, we fit a second order polynomial in $SSI_{\text{obs,ref}}$ to the scatter plot of the measured solar irradiance in each SOLSTICE FUV channel versus $SSI_{\text{obs,ref}}$. Finally, we applied the relationships defined by these fits to $SSI_{\text{mod,ref}} + 3.23 \times 10^{-3} \text{ Wm}^{-2}$ from the entire reconstruction to regenerate the 115 to 180 nm segment.

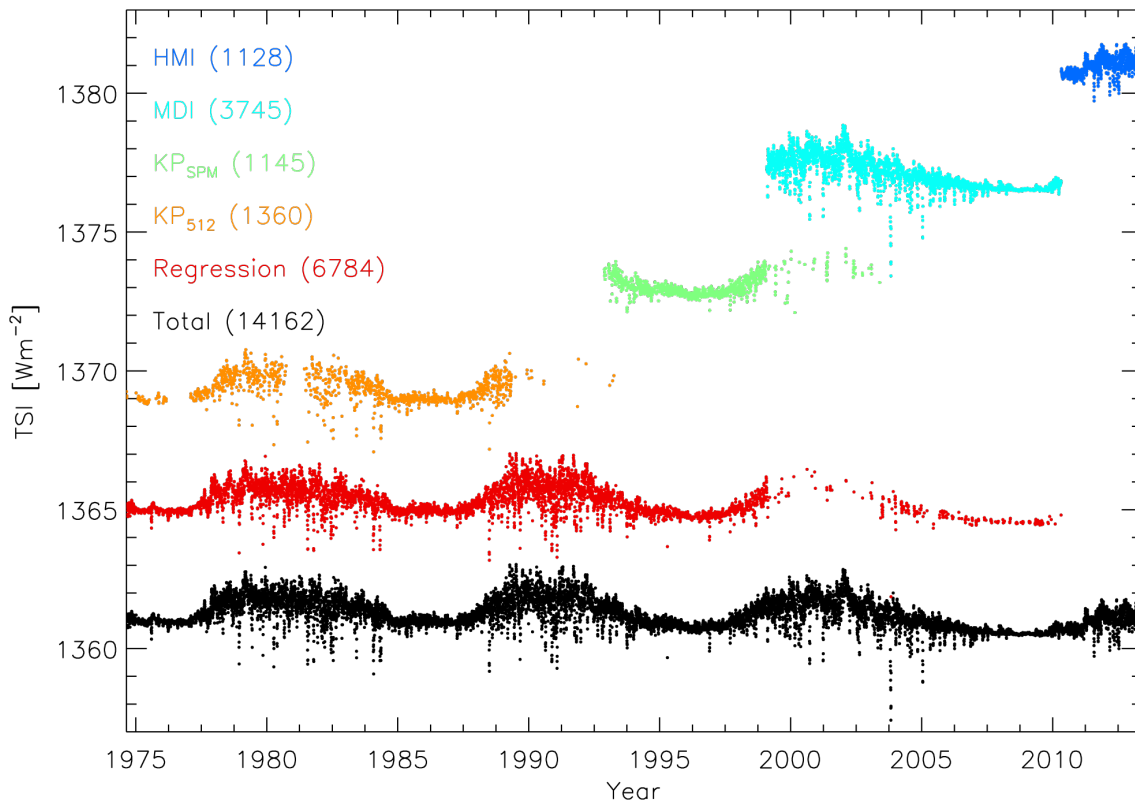


Figure 5.13: Reconstructed daily total solar irradiance (black). The other series indicate the contribution to this time series by the SATIRE-S reconstruction based on the various data sets, and the regression series (see text), progressively offset to aid visibility. The values in parentheses indicate the number of daily values.

It must be emphasized that we are only introducing, into the reconstruction, an offset to the absolute level in the reference interval and the wavelength channel to reference interval relationships in SOLSTICE FUV data. The variation of the regenerated SSI with time is defined by the original reconstruction through $SSI_{\text{obs,ref}}$, not by the SOLSTICE FUV record. By using the WHI reference solar spectra to correct the absolute level between 180 to 300nm, we are able to confine this regeneration to within 115 and 180 nm, a narrower wavelength range than in the analysis of Krivova et al. 2006 (115 to 270 nm).

5.4.4 Data gaps

Reconstructed solar irradiance from the KP_{512} , KP_{SPM} , MDI and HMI data sets were collated into a single time series taking, on the days where the model output from more than one data set is available, the value from the succeeding instrument. That is, taking the model output from KP_{SPM} during the days with both KP_{512} and KP_{SPM} data, from MDI where KP_{SPM} and MDI overlap, and from HMI where MDI and HMI overlap.

The reconstruction extends over the period of August 23, 1974 to May 31, 2013. Restricted by the availability of suitable magnetograms (Sect. 5.3.1), it covers just 7378 of the 14162 days within this period (Fig. 5.13). The daily data cover, on average, just

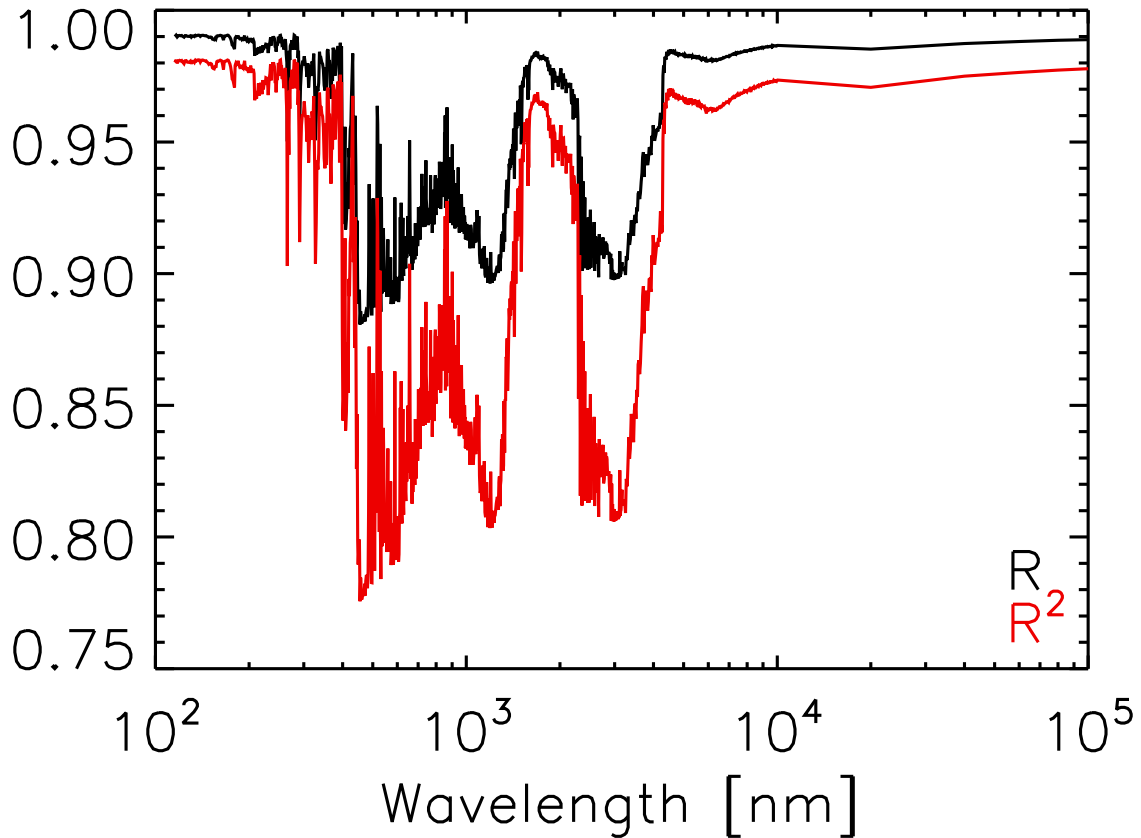


Figure 5.14: The R (black) and R^2 (red) between the SATIRE-S reconstruction and the regression series, as a function of wavelength.

one of every five days in the KP_{512} data set, one of every two for the KP_{SPM} data set and nine of every ten for the MDI data set (Table 5.1). The HMI data set is the only one that has no gaps. To yield an uninterrupted time series, we regressed indices of solar activity to the reconstruction, and used the relationships derived to estimate the solar spectra in the gaps from index data (loosely following the method set out in Ball et al. 2014).

We employed the following solar activity index records; the Ottawa and Penticton adjusted 10.7 cm radio flux, F10.7 (Tapping 1987, 2013), the LASP Lyman- α composite (Woods et al. 2000), the IUP Mg II index composite (version 4, Viereck and Puga 1999, Skupin et al. 2005b,c) and the projected sunspot area composite by Balmaceda et al. 2009 (version 0613). Apart from the Mg II index composite by IUP, there is a competing composite by LASP (Viereck et al. 2004, Snow et al. 2005b). We selected the IUP record as the result of the regression agreed better with the SATIRE-S reconstruction.

For each wavelength element, we performed the (multiple) linear regression of each index, and each combination of two indices to the reconstruction. The indices-to-irradiance relationships so derived were then ranked by the correlation between the result of the regression and the reconstruction. The irradiance over the period of the reconstruction was estimated by applying, for each day, the highest ranked relationship for which the required index data is available. For this discussion, we will term this the regression series.

Next, we offset each entry in the regression series by the average difference between

the reconstruction and the regression series over the nearest 100 days where the reconstruction is available. This is to factor out any discrepancy in the long-term trend between the reconstruction and the regression series by adopting the long-term trend of the reconstruction in the regression series. The correlation between the SATIRE-S reconstruction and the regression series as a function of wavelength is depicted in Fig. 5.14. Comparing the TSI from the two series, the R (R^2) is 0.940 (0.883). Not unexpectedly, the regression series cannot reproduce all the variability in the SATIRE-S reconstruction. The agreement is, however, relatively good, sufficient for the intended purpose of the regression series. Finally, the gaps in the reconstruction were filled with values from the regression series.

It is worth noting that the indices-to-irradiance relationships were derived by regressing index records to the reconstruction, not to observations as in proxy models (e.g., Lean et al. 1997, Lean 2000, Pagaran et al. 2009, Chapman et al. 2013). We are filling the gaps in the reconstruction by the regression of index data to the reconstruction, not a second independent model of solar irradiance.

5.4.5 Error analysis

The reconstruction process is complex and involved multiple data sets. A rigorous determination of the uncertainty is far from straightforward, compounded by the following extenuating factors.

- We did not examine the KP_{512} , KP_{SPM} , MDI and HMI data sets for possible variation with time from changes in instrumental properties. This and uncertainty in the apparent surface coverage of magnetic features cannot be ascertained unambiguously from the data sets themselves.
- Magnetogram noise and finite resolution hinder us from identifying and including bright magnetic features that are weak and/or small (Krivova and Solanki 2004), and bright kilogauss magnetic concentrations have been observed even in the quiet Sun internetwork (Riethmüller et al. 2013). The amount of unresolved magnetic flux and its variation with time is not known and cannot be determined directly from the magnetogram data.
- The radiant behaviour of small-scale magnetic concentrations is not sufficiently understood to model its complexities fully. The LTE and ODF simplifications aside (Sect. 5.4.3), the faculae intensity spectra utilised in the SATIRE-S reconstruction are based on a 1-D model atmosphere and applied to all bright magnetic features. This ignores 3-D effects on the apparent intensity contrast of small-scale magnetic concentrations (Solanki et al. 1998, Holzreuter and Solanki 2013). This also overlooks the fact that their intensity contrast scales with magnetogram signal differently in the continuum and in spectral lines (Yeo et al. 2013), and quiet Sun network is, on a per unit magnetogram signal basis, brighter than active region faculae (Ortiz et al. 2002, Foukal et al. 2011, Kobel et al. 2011). It is our intention to refine this part of the model in the future, considering 3-D MHD simulations (which are reaching the maturity required for quantitative comparison with observations, Afram et al. 2011) and high spatial resolution observations from missions such as SUNRISE (Solanki et al. 2010, Barthol et al. 2011).

While a comprehensive error analysis is clearly onerous, a reasonable estimate of the reconstruction uncertainty can be obtained considering the uncertainty introduced by the steps taken to harmonize the model input from the various data sets (Sect. 5.4.1), and in the free parameter, $(\langle B_l \rangle / \mu)_{\text{sat}}$. This is similar to the approach taken by Ball et al. (2012, 2014). The apparent uncertainty from these processes is influenced by, and would therefore largely encompass the error from other sources such as the indeterminate factors discussed above. We performed the following, for each wavelength element in the reconstruction and the TSI time series.

The uncertainty arising from the cross-calibration of the KP_{512} , KP_{SPM} , MDI and HMI data sets is given by the RMS difference between the reconstruction based on the various data sets over the periods where they overlap. For the days with no SATIRE-S reconstruction, plugged with the regression series (Sect. 5.4.4), we adopted the RMS difference between the SATIRE-S reconstruction and the regression series as the uncertainty.

As stated in Sect. 5.4.2, the amplitude of faculae contribution to variation in reconstructed solar irradiance scales nearly inversely with $(\langle B_l \rangle / \mu)_{\text{sat}}$. The TSI records considered as the reference with which to recover $(\langle B_l \rangle / \mu)_{\text{sat}}$ exhibit differences in terms of the amplitude of solar cycle variation (Fig. 5.7). Due to these discrepancies, we arrived at estimates of $(\langle B_l \rangle / \mu)_{\text{sat}}$ ranging from 204 to 255 G (Table 5.2). Eventually, we adopted 230 G, the value recovered with the PMO6V record as the reference (on account of the consistency between the resulting reconstruction and the record). We assume an uncertainty of ± 30 G for $(\langle B_l \rangle / \mu)_{\text{sat}}$.

The upper (lower) bound of the uncertainty range of the reconstruction is then given by the reconstruction generated with $(\langle B_l \rangle / \mu)_{\text{sat}}$ set at 200 G (260 G), plus (minus) the cross-calibration error.

5.5 Discussion

5.5.1 Comparison with observations

In this section, we evaluate the reconstruction against

- the ACRIM, IRMB and PMOD composite records of TSI (Sect. 5.5.1.1),
- the LASP Lyman- α composite, the Mg II index composites by IUP and by LASP (Sect. 5.5.1.2), and
- SSI observations from the UARS and SORCE missions (Sects. 5.5.1.3 and 5.5.1.4).

5.5.1.1 TSI composites

While broadly consistent with one another, the ACRIM, IRMB and PMOD composites do exhibit divergent decadal trends (Fig. 5.15). This is readily apparent in the conflicting cycle-to-cycle variation of the solar cycle minimum level (both in strength and direction, Table 5.3), the focal point of the ensuing debate (Scafetta and Willson 2009, Krivova et al. 2009a, Fröhlich 2012).

Preceding efforts with the SATIRE-S model, based on KPVT and/or MDI data, have found the greatest success in replicating the variability of the PMOD composite (Wenzler

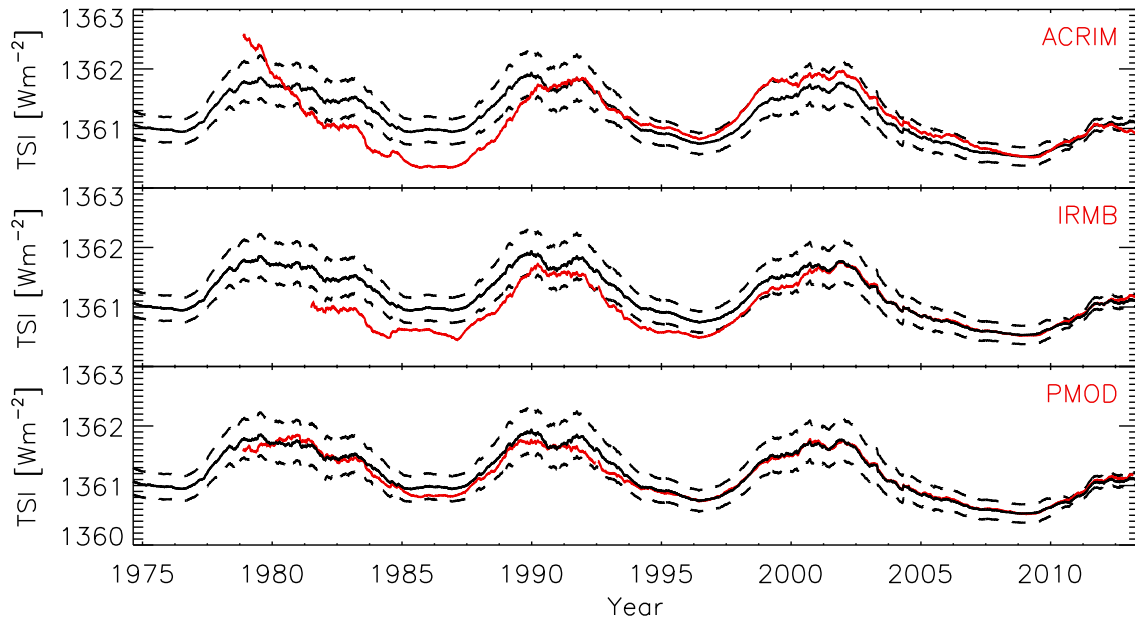


Figure 5.15: 361-day moving average of the TSI reconstruction (black), and the ACRIM, IRMB and PMOD composites (red). The dashed lines denote the uncertainty range of the reconstruction.

Table 5.3: The difference between the TSI level at the solar cycle minima of 1976, 1986 and 1996, and the level at the 2008 minimum. We considered the mean level over the 3-month period centred on each minima.

Series	1976 [Wm^{-2}]	1986 [Wm^{-2}]	1996 [Wm^{-2}]
ACRIM		-0.205	0.341
IRMB		-0.084	-0.048
PMOD		0.273	0.188
SATIRE-S	0.423	0.399	0.236

et al. 2009, Krivova et al. 2011a, Ball et al. 2012). Here, having updated the reconstruction method and extended the model to the present with HMI data, a re-evaluation is necessary.

More than with the ACRIM or IRMB composites, the reconstruction replicated the variability of the PMOD composite (Table 5.4). The reconstruction and the PMOD composite are not only highly correlated to one another ($R = 0.957$ and $R^2 = 0.916$) but as

Table 5.4: The R , R^2 and k (RMS difference) between the reconstruction, and the ACRIM, IRMB and PMOD composites. Here and in the rest of the paper, these quantities are calculated excluding the part of the reconstruction provided by the regression series.

Series	R	R^2	k [Wm^{-2}]
ACRIM	0.864	0.747	0.301
IRMB	0.897	0.805	0.251
PMOD	0.957	0.916	0.149

(The contents of this chapter are identical to the submitted version of Yeo, K. L., Krivova, N. A., Solanki, S. K., Glassmeier, K. H., 2014, Reconstruction of total and spectral solar irradiance from 1974 to 2013 based on KPVT, SoHO/MDI and SDO/HMI observations, *Astron. Astrophys.*, 570, A85.)

Table 5.5: The same as Table 5.4, except between the reconstruction and the TSI measurements from ACRIM3, TIM and VIRGO. (This is not to be confused with Table 5.2, where we compared the same TSI records with the corresponding candidate reconstruction, see Sect. 5.4.2.)

Series	R	R^2	k [Wm^{-2}]
ACRIM3	0.965	0.931	0.175
DIARAD _{IRMB}	0.958	0.917	0.159
DIARAD _{PMOD}	0.969	0.940	0.131
PMO6V	0.979	0.959	0.107
TIM	0.961	0.924	0.109

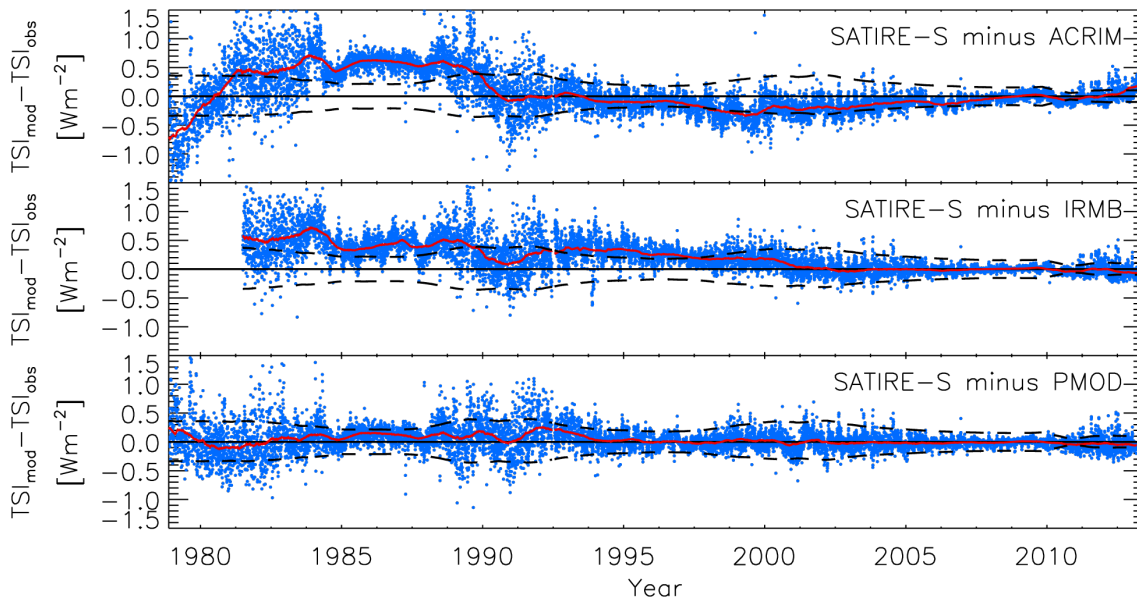


Figure 5.16: The difference between the TSI reconstruction, and the ACRIM, IRMB and PMOD composites (blue dots), and the corresponding 361-day moving average (red curves). The dashed and solid black lines represent the reconstruction uncertainty and the zero level, respectively.

indicated by the weak RMS difference ($k = 0.149 \text{ Wm}^{-2}$) the absolute variation is similar.

In Table 5.5, we also listed the correlation and RMS difference between the reconstruction and the TSI measurements from ACRIM3, TIM and VIRGO. Obviously, the closest alignment was found with the PMO6V record ($R = 0.979$, $R^2 = 0.959$ and $k = 0.107 \text{ Wm}^{-2}$). This excellent agreement is all the more significant considering the fact that the PMO6V record, which extends 1996 to the present, encompasses an entire solar cycle minimum to minimum.

In terms of the long-term trends, it is evident that the reconstruction is most consistent with the PMOD composite (Figs. 5.15 and 5.16). The cyclic variation of the PMOD composite is replicated to well within the uncertainty limits of the reconstruction (bottom panel, Fig. 5.15), including the secular decline between the solar cycle minima of 1986, 1996 and 2008 (Table 5.3).

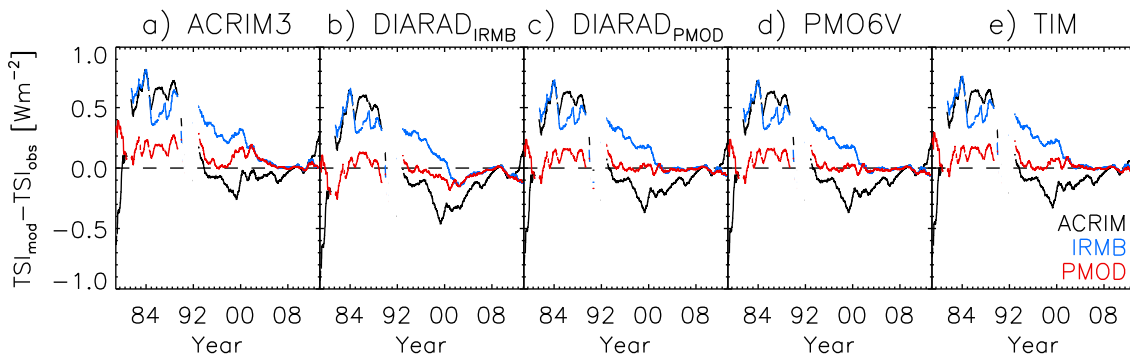


Figure 5.17: 361-day moving average of the difference between the five candidate TSI reconstructions described in Sect. 5.4.2 (denoted by the TSI record referenced to determine $\langle\langle B_l \rangle\rangle / \mu_{\text{sat}}$), and the ACRIM (black), IRMB (blue) and PMOD composites (red). The dashed line represents the zero level.

The fact that we had relied on the PMO6V record to fix the free parameter, $\langle\langle B_l \rangle\rangle / \mu_{\text{sat}}$ is not the reason the reconstruction is more aligned towards the PMOD composite (which uses the PMOD/WRC calibration of VIRGO radiometry in solar cycles 23 and 24) than the ACRIM and IRMB composites. In Fig. 5.17 we express the smoothed difference between the five candidate reconstructions examined in Sect. 5.4.2 and the three composites. There is no qualitative difference in how the candidate reconstructions compare with the three composites. For solar cycles 23 and 24, the ACRIM composite is based on the ACRIM2 and ACRIM3 records. For the IRMB composite, measurements from ACRIM2, ERBS, TIM and VIRGO (IRMB calibration). Using the ACRIM3 record as the reference to determine $\langle\langle B_l \rangle\rangle / \mu_{\text{sat}}$ does not swing the comparison towards the ACRIM composite (Fig. 5.17a). Neither does employing the DIARAD_{IRMB} and TIM records particularly favour the IRMB composite (Figs. 5.17b and 5.17e), nor the DIARAD_{PMOD} and PMO6V records the PMOD composite (Figs. 5.17c and 5.17d).

We noted earlier (in Sect. 5.4.2) that the candidate reconstructions generated taking the ACRIM3, DIARAD_{IRMB} and TIM records as the reference to recover $\langle\langle B_l \rangle\rangle / \mu_{\text{sat}}$ differ significantly from the respective reference in terms of the long-term variations (Fig. 5.8). $\langle\langle B_l \rangle\rangle / \mu_{\text{sat}}$ modulates the solar cycle amplitude of the reconstruction through its effect on apparent facular area. In using a given TSI record to determine $\langle\langle B_l \rangle\rangle / \mu_{\text{sat}}$, we are not adopting its long-term trend but rather just taking it as a reference to scale the overall amplitude of the reconstruction. The long-term trend, including the secular decline between the solar cycle minima of 1986, 1996 and 2008 in the reconstruction is inherent to it and not an outcome of using the PMO6V record to fix $\langle\langle B_l \rangle\rangle / \mu_{\text{sat}}$.

The observation here that we are able to replicate the secular change between the 1996 and 2008 solar cycle minima in the PMOD composite (i.e., PMOD/WRC calibration of VIRGO radiometry) using a model based on photospheric magnetism alone runs contrary to the claims of Fröhlich (2009, 2012, 2013). The author noted that proxy models using chromospheric indices such as the Mg II index to represent bright magnetic features cannot fully replicate this secular decline and attributed the difference to a possible cooling/dimming of the photosphere. Foukal et al. (2011) proposed that the differing decadal trends exhibited by TSI and chromospheric indices might be due to the non-linear re-

lationship between the two (Solanki and Krivova 2004). Another probable contributing factor is the long-term uncertainty in index data. We provide evidence for these in Sect. 5.5.1.2.

The long-term trend in the PMOD composite is well reproduced almost everywhere. A notable exception is the offset between the reconstruction and the PMOD composite between 1984 and 1994; the reconstruction is broadly higher by 0.1 to 0.3 Wm^{-2} (Fig. 5.16). Consequently, the reconstruction registers a stronger secular decline between the 1986 and 1996 solar cycle minima than the PMOD composite (Table 5.3). To put this apparent disparity in context though, it is minute compared to the spread between the three composites, between the reconstruction and the other two composites, and between recent measurements of TSI (Fig. 5.7).

The offset between the reconstruction and the PMOD composite between 1984 and 1994 is unlikely to be related to the cross-calibration of the KP_{512} and KP_{SPM} data sets (Sect. 5.4.1). Going back in time, the reconstruction and the PMOD composite started to differ in 1994, while the period of overlap between KP_{512} and KP_{SPM} data sets is November 1992 to April 1993. Also, any drift between model and measurement from how we combined the model output based on the KP_{512} data set to the rest of the reconstruction would most likely amplify going back in time. The apparent discrepancy could possibly be from unaccounted instrumental variation in the KP_{512} and KP_{SPM} data sets, or in the PMOD composite, especially as the period of 1984 to 1994 encompasses the ACRIM gap (Scafetta and Willson 2009, Krivova et al. 2009a).

5.5.1.2 Solar Lyman- α irradiance and Mg II index composites

Next, we compare the reconstruction with the LASP Lyman- α composite, and the competing Mg II index composites by IUP and by LASP (introduced in Sect. 5.4.4).

In the wavelength range of 115 to 290 nm, the wavelength sampling of the reconstruction is 1 nm. We took the reconstructed solar irradiance in the 121 to 122 nm wavelength element, $\text{SSI}_{\text{mod},121-122\text{nm}}$, as the solar Lyman- α irradiance. The ‘Mg II index’ of the reconstruction is given by

$$\frac{2 \times \text{SSI}_{\text{mod},279-281\text{nm}}}{\text{SSI}_{\text{mod},276-277\text{nm}} + \text{SSI}_{\text{mod},283-284\text{nm}}}, \quad (5.1)$$

crudely following the definition by Heath and Schlesinger (1986). The Lyman- α and Mg II index series so taken from the reconstruction are obviously not exactly equivalent to that from measurement, which are computed from the examination of higher spectral resolution line profiles. However, as we are only interested in comparing the relative variation, these approximations are still appropriate. The correlation between measurement and model is excellent. The reconstruction reproduced over 94% of the variability in the LASP Lyman- α composite ($R = 0.970$ and $R^2 = 0.942$), and over 96% for the IUP Mg II index composite ($R = 0.981$ and $R^2 = 0.963$). The agreement with the LASP Mg II index composite is poorer by a significant margin, but still very good ($R = 0.948$ and $R^2 = 0.899$).

A direct quantitative comparison is not feasible given the approximate manner by which we estimated the solar Lyman- α irradiance and Mg II index from the reconstruction. Also, the absolute level of the LASP Mg II index composite is nearly twice that of

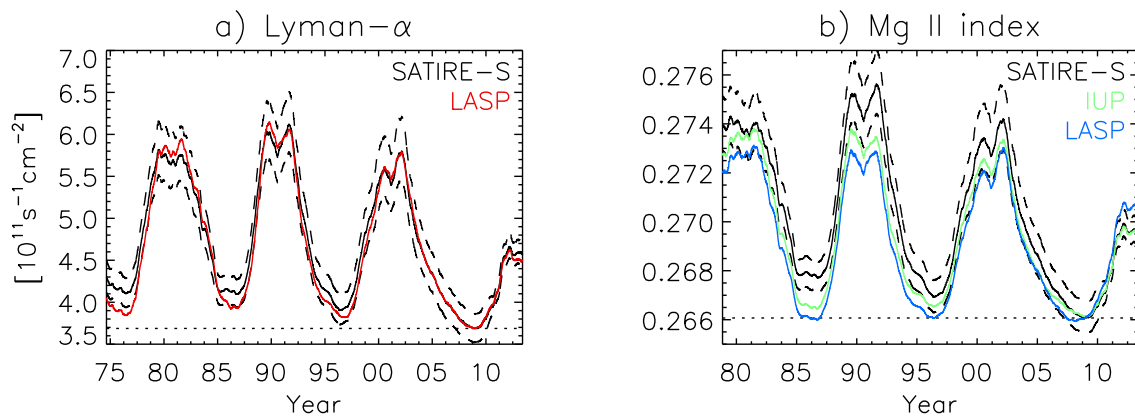


Figure 5.18: 361-day moving average of the a) solar Lyman- α irradiance and the b) Mg II index. The various time series were matched, in terms of the rotational variability and the level at the 2008 solar cycle minimum (dotted lines), to the time series generated from the SATIRE-S reconstruction to allow a direct comparison of the long-term trends (see text). The dashed lines indicate the lower and upper uncertainty of the SATIRE-S Lyman- α and Mg II index series.

the IUP composite². To compare the long-term trends, we did the following. Take the Lyman- α instance, we regressed the LASP Lyman- α composite, detrended by subtracting the 361-moving average, to the similarly detrended reconstruction series. We rescaled the original LASP Lyman- α composite by the regression coefficient, in so doing matching the rotational variability to that of the reconstruction series. Finally, we offset the LASP Lyman- α composite to the reconstruction series at the 2008 solar cycle minimum. The IUP and LASP Mg II index composites were similarly rescaled and offset to the Mg II index generated from the reconstruction.

The long-term trend in the LASP Lyman- α composite is reproduced in the reconstruction series to, at most places, well within the limits of uncertainty (Fig. 5.18a). A notable exception is the noticeably higher levels in the reconstruction series at the solar cycle minima of 1976, 1986 and 1996. Even with this discrepancy, the secular trend in the solar cycle minima level in the LASP Lyman- α composite is largely replicated in the reconstruction. The lower solar cycle minima levels in the LASP Lyman- α composite compared to reconstructed solar irradiance at 121 to 122 nm is likely from the non-linear relationship between the two.

In the case of the Mg II index, the two composites and the Mg II index based on the reconstruction exhibit differences in the long-term trend greater than can be accounted within the reconstruction uncertainty (Fig. 5.18b). The IUP composite does, however, register a similar, albeit weaker, secular decline between the 1996 and 2008 solar cycle minima as in the reconstruction series. The Mg II index, the line core-to-wing ratio of the Mg II h and k doublet at 280 nm, is relatively robust to instrument degradation as

²The Mg II index produced from measurements from different spectrometers differ in absolute terms since the wavelength sampling is usually not identical. There is therefore a degree of arbitrariness in how the Mg II index records generated from the various instruments are rescaled when combining them together to form the composite time series.

that largely cancels out in the division. The discrepancy between the two composites, of similar order as the difference to the reconstruction series, highlight the uncertainty still present (likely from the variation in instrument degradation with wavelength within the line profile).

The non-linear relationship between chromospheric indices and solar irradiance, and the long-term uncertainty in index data has a significant impact on how the decadal trends in chromospheric indices and the reconstruction compare to one another (Fig. 5.18). As noted in Sect. 5.5.1.1, these are the probable reasons why proxy models employing chromospheric indices to represent faculae brightening cannot replicate the secular decline in VIRGO TSI radiometry.

5.5.1.3 UARS and SORCE ultraviolet solar irradiance

Compared to TSI, greater uncertainty persists over the measurement and modelling of ultraviolet solar irradiance. Measurements and models are broadly consistent at rotational timescales but diverge significantly in terms of the absolute level and long-term trends (DeLand and Cebula 2008, 2012, Lean and DeLand 2012, Unruh et al. 2012, Ermolli et al. 2013, Solanki et al. 2013). This is due in part to the challenge in making reliable measurements (complicated by the wavelength dependence of instrumental influences), and the varying approaches taken by models of solar irradiance to account for non-LTE effects on reconstructed spectra (see Fontenla et al. 1999, Krivova et al. 2006, Shapiro et al. 2010, and Sect. 5.4.3).

In this section, we compare the reconstruction with the daily ultraviolet spectral measurements from the SOLSTICE (as archived on lasp.colorado.edu/lisird/, covering 119 to 420 nm, Rottman et al. 2001) and SUSIM (version 22, 115 to 410 nm, Brueckner et al. 1993, Floyd et al. 2003) experiments onboard the UARS mission, and SOLSTICE (level 3, version 12, 114 to 310 nm, McClintock et al. 2005, Snow et al. 2005a) and SIM (level 3, version 19, 240 to 2416 nm, Harder et al. 2005a,b) onboard SORCE. The UARS/SOLSTICE, SUSIM and SIM data sets contain glitches which manifest themselves as null or spurious measurements. We omitted the daily spectra with null measurements but otherwise employed these records as they are.

For this discussion, we examine the integrated flux between 120 and 180 nm, 180 and 240 nm, and 240 and 300 nm. We excluded UARS/SOLSTICE and SUSIM observations from the comparison of 240 to 300 nm flux; approaching 300 nm, solar cycle variation is increasingly obscured by long-term stability issues (DeLand et al. 2004). The integrated flux time series from the UARS and SORCE data sets were offset to the reconstruction at the 1996 and 2008 solar cycle minima, respectively. Given the spread in observed solar cycle variation, it is within expectation that in terms of the overall agreement (given by the correlation and RMS difference, Table 5.6) and long-term variation (Fig. 5.19), the reconstruction is aligned towards certain records more than others.

- 120 to 180 nm (top panel, Fig. 5.19): The overall agreement between the reconstruction, and the measurements from SUSIM and the two SOLSTICE experiments is excellent ($R > 0.97$, $R^2 > 0.94$ and $k < 3 \times 10^{-3} \text{ Wm}^{-2}$). The long-term variation in the three records is replicated to largely within the uncertainty of the reconstruction.

Table 5.6: The correlation (R and R^2) and RMS difference (k and k_{rot} , for the complete and detrended series, respectively) between the reconstruction and ultraviolet solar irradiance observations from the UARS and SORCE missions, over the indicated spectral intervals.

Spectral interval	Series	R	R^2	k [Wm^{-2}]	k_{rot} [Wm^{-2}]
120 to 180 nm	UARS/SOLSTICE	0.979	0.959	3.85×10^{-4}	3.10×10^{-4}
	UARS/SUSIM	0.971	0.943	4.41×10^{-4}	3.86×10^{-4}
	SORCE/SOLSTICE	0.979	0.959	3.04×10^{-3}	1.98×10^{-4}
180 to 240 nm	UARS/SOLSTICE	0.521	0.271	2.51×10^{-2}	1.83×10^{-2}
	UARS/SUSIM	0.943	0.890	6.97×10^{-3}	3.99×10^{-3}
	SORCE/SOLSTICE	0.789	0.623	3.91×10^{-2}	2.83×10^{-3}
	Morrill et al. (2011)	0.976	0.952	5.48×10^{-3}	3.40×10^{-3}
240 to 300 nm	SORCE/SOLSTICE	0.432	0.187	0.102	2.05×10^{-2}
	SORCE/SIM	0.818	0.670	0.140	1.02×10^{-2}
	Morrill et al. (2011)	0.964	0.929	2.41×10^{-2}	1.07×10^{-2}

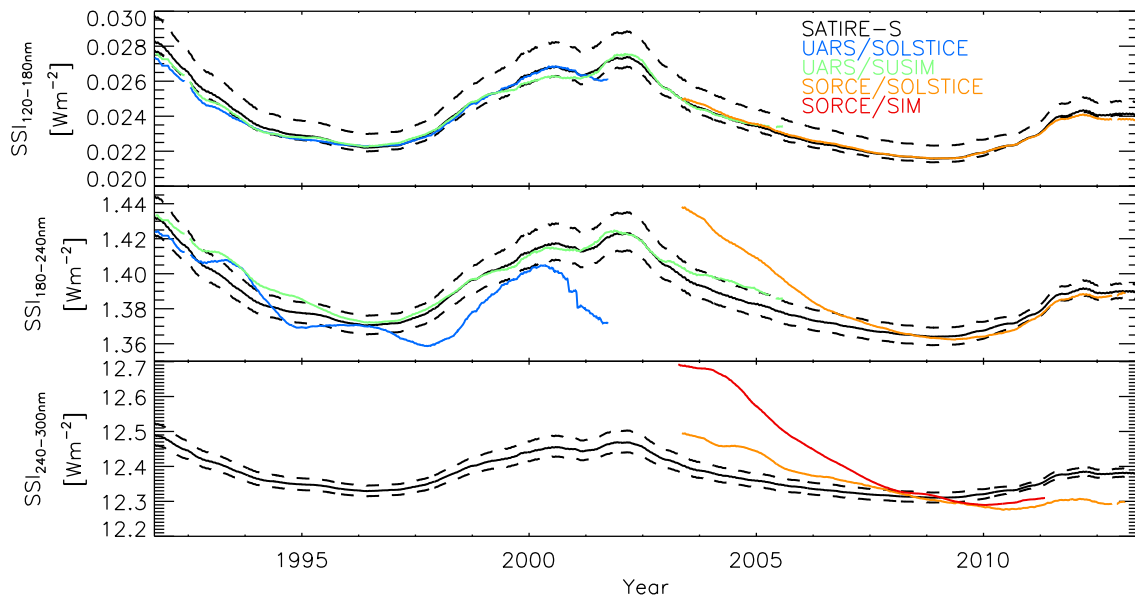


Figure 5.19: 361-day moving average of the integrated flux between 120 to 180 nm (top), 180 to 240 nm (middle) and 240 to 300 nm (bottom), in the reconstruction and the spectral measurements from the UARS and SORCE missions. The UARS and SORCE time series are offset to the level of the reconstruction at the 1996 and 2008 solar cycle minima, respectively. The dashed lines mark the uncertainty range of the reconstruction.

- 180 to 240 nm (middle panel, Fig. 5.19): The reconstruction is a close match to the SUSIM record ($R = 0.943$, $R^2 = 0.890$ and $k = 6.97 \times 10^{-3} \text{ Wm}^{-2}$) but much less so with the observations from the two SOLSTICE experiments. There is a periodic modulation in the UARS/SOLSTICE record that is not present in the reconstruction or any of the other records. The SORCE/SOLSTICE record declined, between 2003 and 2008, by about twice as much as the reconstruction over the same period, but exhibited a similar overall trend after.

5 Reconstruction of total and spectral solar irradiance from 1974 to 2013 based on KPVT, SoHO/MDI and SDO/HMI observations

(The contents of this chapter are identical to the submitted version of Yeo, K. L., Krivova, N. A., Solanki, S. K., Glassmeier, K. H., 2014, Reconstruction of total and spectral solar irradiance from 1974 to 2013 based on KPVT, SoHO/MDI and SDO/HMI observations, *Astron. Astrophys.*, 570, A85.)

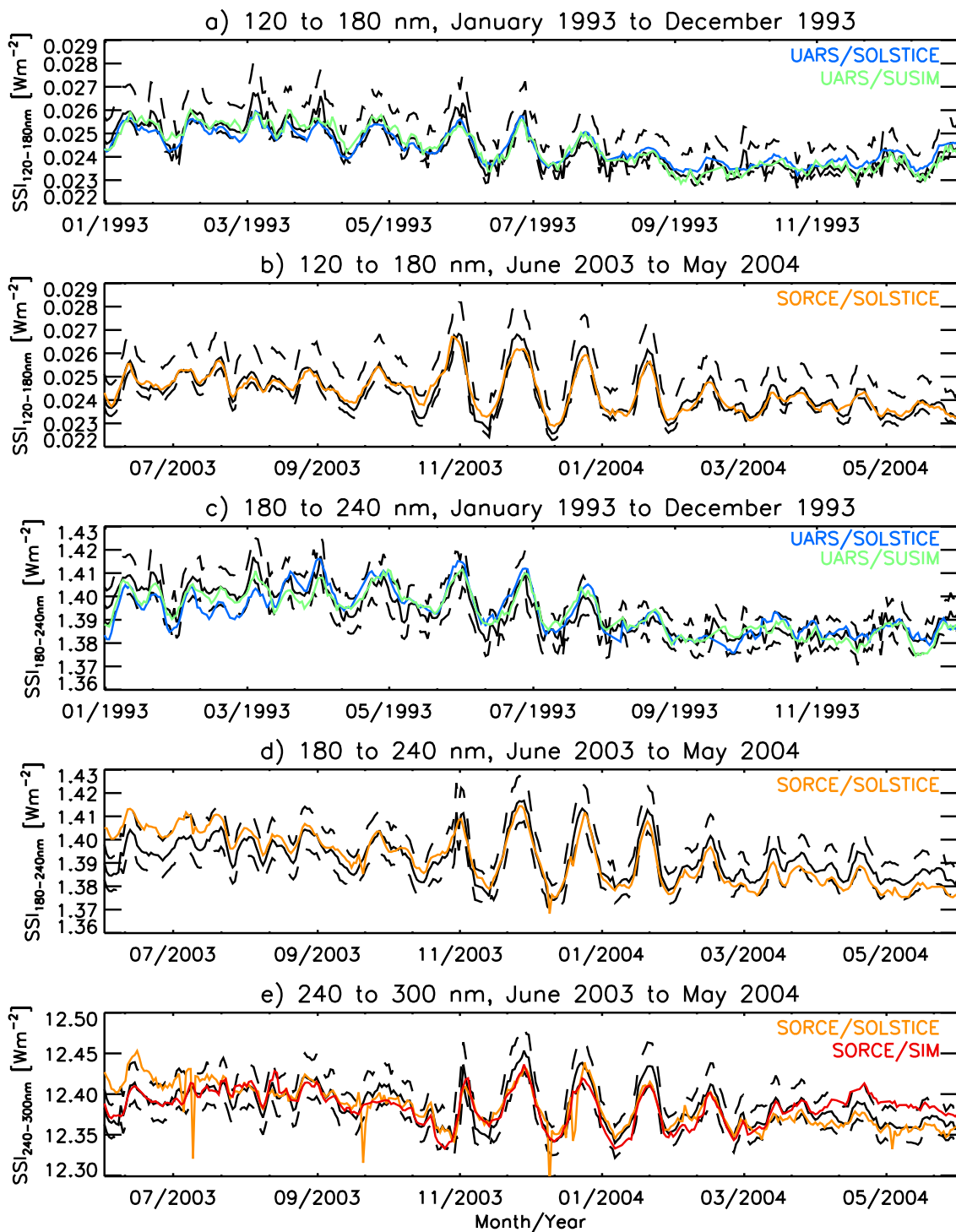


Figure 5.20: Integrated flux between 120 to 180 nm, 180 to 240 nm and 240 to 300 nm, in the reconstruction (black curves) and in the spectral measurements from the UARS and SORCE missions, over the annotated periods. The UARS and SORCE time series are offset to the level of the reconstruction. The dashed lines represent the reconstruction uncertainty.

- 240 to 300 nm (bottom panel, Fig. 5.19): The overall agreement between the reconstruction and the two SORCE records is poor, primarily from the gross divergence in the solar cycle variation. Between 2003 and 2008, the overall level in the SORCE/SOLSTICE and SIM records decreased by a factor of about two and four, respectively, more than in the reconstruction over the same period. Both records continued to decline after the solar cycle minimum of 2008, thus going from varying in phase to being in anti-phase with the solar cycle. This behaviour is not replicated in the reconstruction.

To compare the rotational variability, we detrended both measurement and model by the 361-day moving average. The corresponding RMS difference, denoted k_{rot} , is listed in Table 5.6. The rotational variability of all the records examined is, at most places, reproduced to within the reconstruction uncertainty (Fig. 5.20), encapsulated in the weak k_{rot} values. This suggests that the discrepancy between the reconstruction and certain measurements, detailed above, is likely a result of residual instrumental influences in said observations.

Ultraviolet solar irradiance below 242 nm, and between 242 and 310 nm is responsible for the production and destruction of ozone in the stratosphere, respectively. While the long-term variability of ultraviolet solar irradiance below 240 nm is relatively well constrained, above 240 nm the amplitude of solar cycle variation in measurements and models differ from one another by up to a factor of six (see Ermolli et al. 2013, Table 5.6 and Fig. 5.19). Due to this spread, their application to climate models has led to qualitatively different results for the variation in mesospheric ozone (Haigh et al. 2010, Merkel et al. 2011, Ball et al. 2014).

As previously noted for SATIRE-S by Krivova et al. (2006), Ermolli et al. (2013), Ball et al. (2014), between 240 and 400 nm, the amplitude of solar cycle variation in the SATIRE-S reconstruction is around twice that in the NRLSSI model (Lean et al. 1997, Lean 2000), illustrated in Fig. 5.21, and multiple times weaker than indicated by SIM SSI (Fig. 6.5, discussed in the following section).

We contrasted the SATIRE-S reconstruction against the empirical model of ultraviolet solar irradiance by Morrill et al. 2011 (courtesy of Jeff Morrill). This model, covering 150 to 400 nm, is based on the regression of the Mg II index to SUSIM SSI. It therefore represents an approximation of SUSIM-like SSI with the long-term degradation corrected to that of the Mg II index. The Morrill et al. (2011) reconstruction, covering 1978 to 2013, is a close match to the SATIRE-S reconstruction (Table 5.6 and Fig. 5.22). The differences in the level at solar cycle minima reflect the similar divergence between the IUP Mg II index composite and the Mg II index taken from the SATIRE-S reconstruction, discussed in Sect. 5.5.1.2. Even with this discrepancy in the decadal trend, the amplitude of solar cycle variation is similar (Fig. 5.21).

Between 120 and 400 nm, NRLSSI solar irradiance is given by the regression of the Mg II index to the rotational variability of the UARS/SOLSTICE record. The observation here that the solar cycle variation in the SATIRE-S reconstruction and the SUSIM-based model of Morrill et al. (2011) is similar lends credence to the variability reproduced in both models. It also supports the suggestion, stated in Ermolli et al. (2013), that solar cycle variability in the ultraviolet in the NRLSSI might be underestimated from extending the result of the regression to rotational variability to longer timescales.

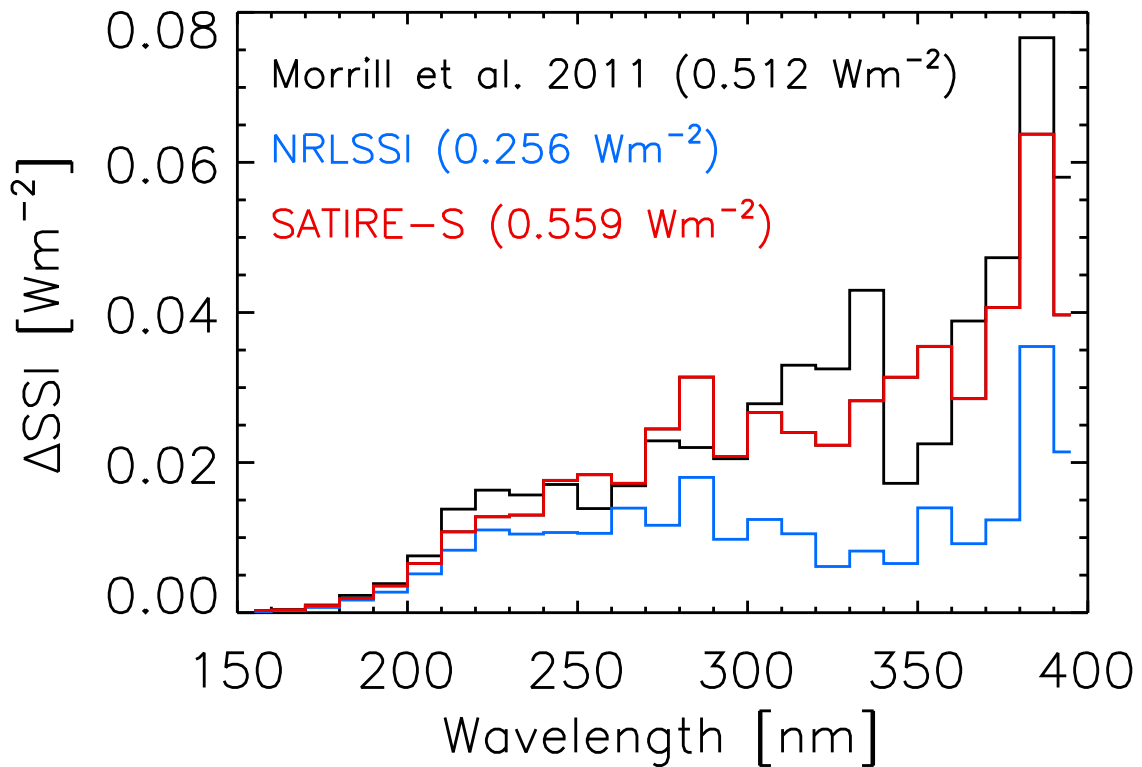


Figure 5.21: The change in SSI, between the solar cycle maximum of 2000 and the minimum of 2008, in the Morrill et al. 2011 (black), NRLSSI (blue) and SATIRE-S (red) models, as a function of wavelength. We considered the mean spectra over the 3-month period centred on the stated activity maximum/minimum, binned by wavelength in intervals of 10 nm. The integral between 240 and 400 nm is given in parentheses.

5.5.1.4 SORCE/SIM SSI

The recent release of SORCE/SIM SSI (level 3, version 19, dated November 19, 2013) spans the wavelength range of 240 to 2416 nm. As stated in the introduction, this is, at present, the only extended and continuous (in time) radiometrically calibrated SSI record covering the ultraviolet to infrared available. For this discussion, we examine the integrated flux in the reconstruction and the SIM data set over the ultraviolet (240 to 400 nm), visible (400 to 700 nm), near-infrared (700 to 1000 nm) and shortwave-infrared (1000 to 2416 nm).

In terms of the overall level, the reconstruction is, up to the near-infrared, varying broadly in phase with TSI (Fig. 5.23). In the shortwave-infrared, the radiation deficit due to sunspots become dominant due to the low (negative at parts) facular intensity contrast here (as noted earlier for SATIRE-S by Unruh et al. 2008, Krivova et al. 2011a, Ball et al. 2011).

Also depicted in Fig. 5.23 is the ratio of the variation (with respect to the level at the 2008 solar cycle minimum) within each spectral interval and in TSI, $\Delta\text{SSI}/\Delta\text{TSI}$. The value of $\Delta\text{SSI}/\Delta\text{TSI}$ around solar cycle maxima gives the relative contribution by the spectral interval to solar cycle variation in TSI (approximately, ultraviolet: 55%, visible:

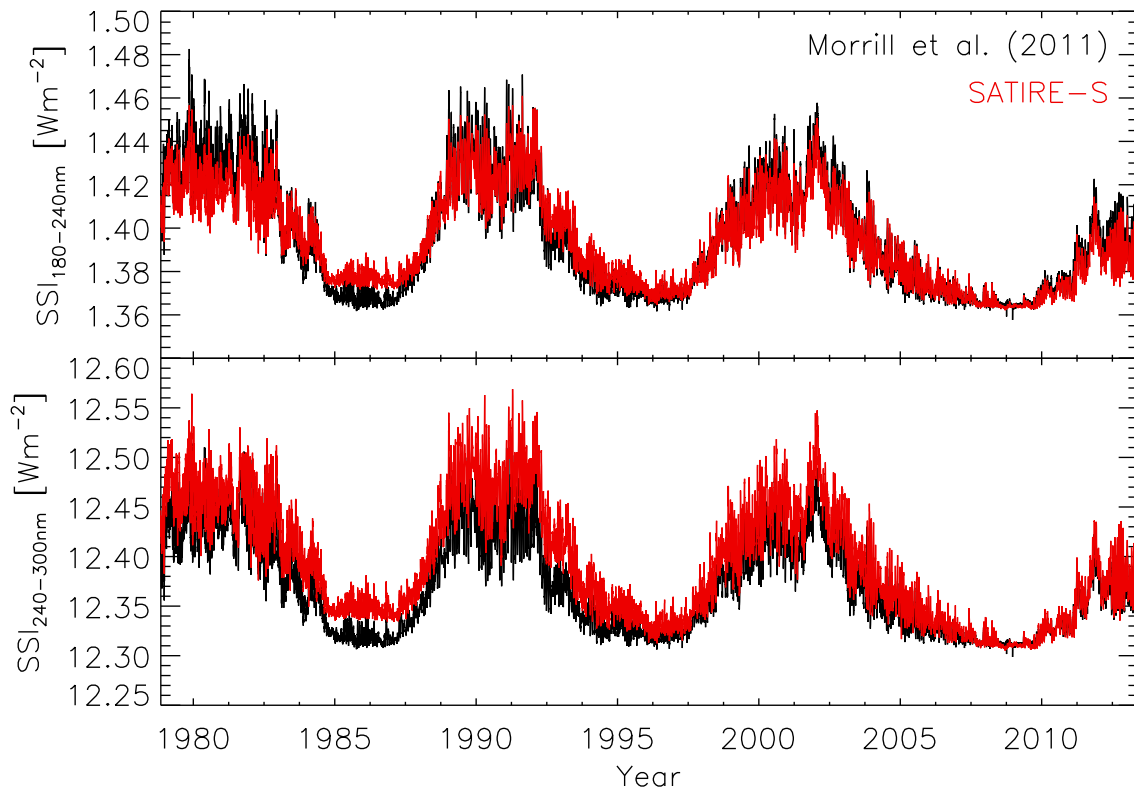


Figure 5.22: Integrated flux between 180 and 240 nm (top), and 240 and 300 nm (bottom), in the Morrill et al. 2011 (black) and the SATIRE-S reconstructions (red).

30%, near-infrared: 16% and shortwave-infrared: -5%). $\Delta\text{SSI}/\Delta\text{TSI}$ at solar cycle minima represents the same for the secular variation in the TSI level at solar cycle minima (ultraviolet: 40%, visible: 35%, near-infrared: 17% and shortwave-infrared: 5%). The variation in $\Delta\text{SSI}/\Delta\text{TSI}$ between solar cycle maxima and minima, including the change of sign in the shortwave-infrared, arises mainly from the fact that sunspots and pores are largely absent around activity minima (see Sect. 5.5.2).

The SIM record indicates a steady decline in ultraviolet and near-infrared flux since 2004 (Fig. 5.24a and 5.24c). Counter to expectation (that solar irradiance display solar cycle variation), there was no reversal in the overall trend after the 2008 solar cycle minimum. Between 2003 and 2006, SIM recorded a pronounced, almost monotonic increase in visible and shortwave-infrared flux (Fig. 5.24b and 5.24d), during a period solar activity is diminishing. Thereafter, the variation is much weaker and largely in phase with the solar cycle, declining till 2008 before ascending again. There is no obvious indication of any consistent trend (neither in phase nor in anti-phase) between the integrated flux within each spectral interval and the solar cycle.

The apparent non-correlation between the SIM record and the solar cycle is in conflict with what we found in the reconstruction (Fig. 5.23). It also does not corroborate with most other observations of ultraviolet solar irradiance (Fig. 5.19) and VIRGO SPM photometry (Wehrli et al. 2013), which demonstrate clear solar cycle variation. The SATIRE-S model describes the effect of photospheric magnetism on the solar spectrum. As the

5 Reconstruction of total and spectral solar irradiance from 1974 to 2013 based on KPVT, SoHO/MDI and SDO/HMI observations

(The contents of this chapter are identical to the submitted version of Yeo, K. L., Krivova, N. A., Solanki, S. K., Glassmeier, K. H., 2014, *Reconstruction of total and spectral solar irradiance from 1974 to 2013 based on KPVT, SoHO/MDI and SDO/HMI observations*, *Astron. Astrophys.*, 570, A85.)

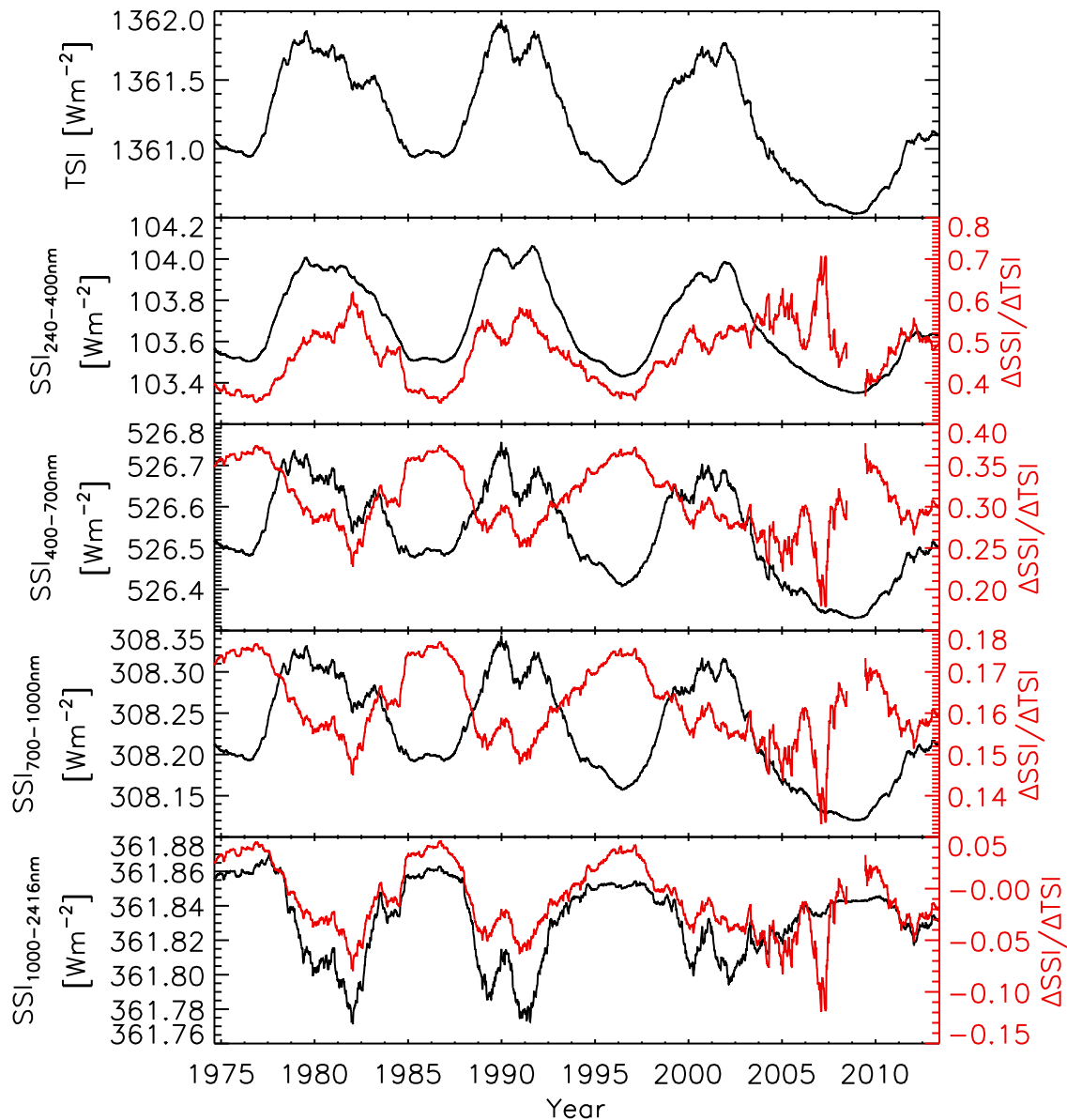


Figure 5.23: Left: 361-day moving average of the TSI reconstruction and the integrated flux over the annotated spectral intervals in the SSI reconstruction (black). Right: Ratio of the variation (with respect to the 2008 solar cycle minimum) in SSI and in TSI, $\Delta\text{SSI}/\Delta\text{TSI}$, as given by the smoothed TSI and SSI time series, drawn in red. As $\Delta\text{SSI}/\Delta\text{TSI}$ is sensitive to noise where ΔTSI is weak, the values from near the 2008 minimum are ignored, therefore the gap in the plots there.

amount of resolved magnetic flux and sunspots exhibit solar cycle variation, obviously so does reconstructed solar irradiance. The amplitude of the overall trend in the SIM record is also grossly stronger than what is reproduced in the reconstruction (Fig. 5.24). Expectedly, the overall agreement between the reconstruction and SIM SSI, as given by the correlation and the RMS difference, is very poor (Table 5.7).

In Fig. 5.25, we compare the total flux recorded by SIM (red), the integrated flux in

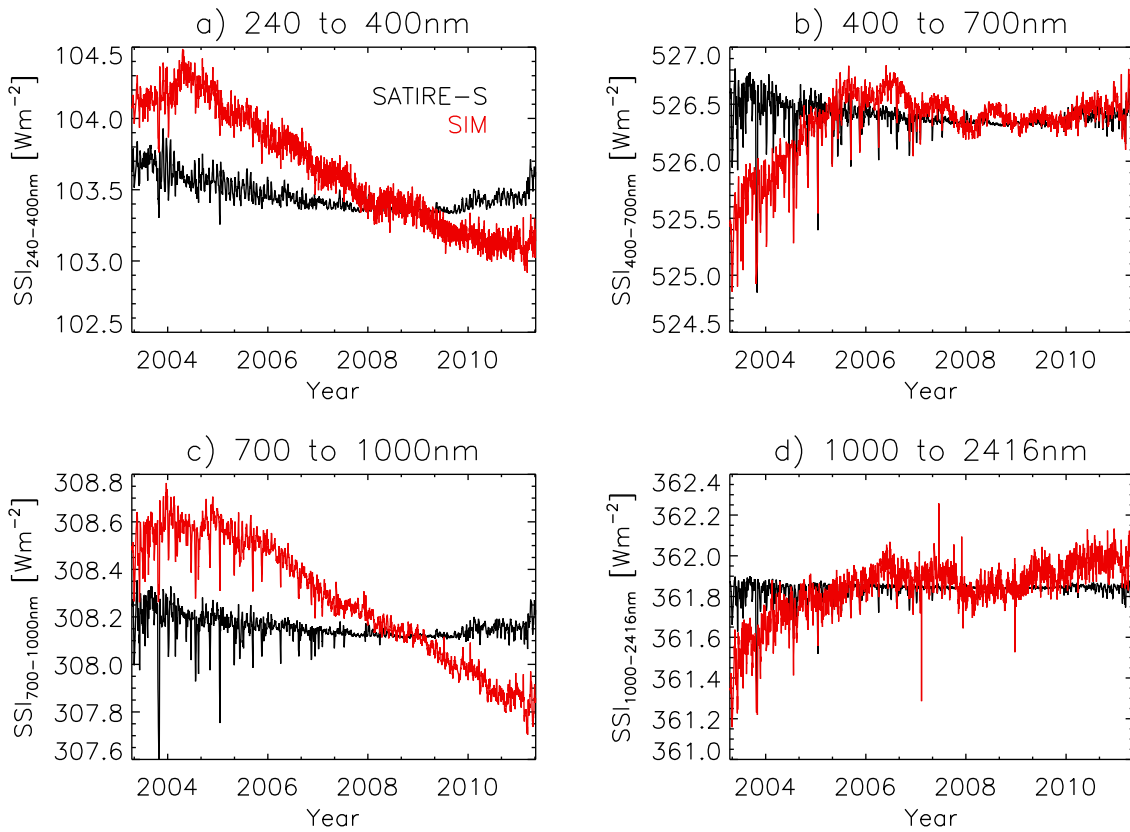


Figure 5.24: Integrated flux over the annotated spectral intervals in the reconstruction (black) and in SIM SSI (red). The SIM time series are offset to the level of the reconstruction at the 2008 solar cycle minimum.

Table 5.7: The correlation (R and R^2) and scatter (k and k_{rot}) between the integrated flux over the indicated spectral intervals in the SIM record and in the SSI reconstruction.

Spectral interval	R	R^2	k [Wm^{-2}]	k_{rot} [Wm^{-2}]
240 to 400 nm	0.675	0.456	0.367	6.61×10^{-2}
400 to 700 nm	0.088	0.008	0.312	8.35×10^{-2}
700 to 1000 nm	0.380	0.145	0.258	3.39×10^{-2}
1000 to 2416 nm	0.427	0.182	0.124	5.47×10^{-2}
240 to 2416 nm	0.411	0.169	0.583	0.179

the reconstruction over the same wavelength range (black) and PMO6V TSI (blue). With the bulk of the energy in solar radiation confined within the spectral range surveyed by SIM ($> 97\%$), the integrated flux over this spectral range should at least resemble TSI (as similarly argued by Lean and DeLand 2012). The total flux registered by SIM, as with the integrated flux over each of the spectral intervals examined earlier (Fig. 5.24), exhibits no clear consistent relation to TSI or the solar cycle. For the reconstruction, the integrated flux over the spectral range of SIM reproduces at least 88% ($R > 0.94$ and $R^2 > 0.88$) of the variability in ACRIM3, TIM and VIRGO TSI radiometry, and effectively all of the variability in the TSI from the reconstruction (Table 5.8). The total flux registered

(The contents of this chapter are identical to the submitted version of Yeo, K. L., Krivova, N. A., Solanki, S. K., Glassmeier, K. H., 2014, Reconstruction of total and spectral solar irradiance from 1974 to 2013 based on KPVT, SoHO/MDI and SDO/HMI observations, *Astron. Astrophys.*, 570, A85.)

Table 5.8: The correlation (R and R^2) between the total flux registered by SIM and the integrated flux in the SSI reconstruction over a similar wavelength range (i.e., 240 to 2416 nm), and the five TSI records discussed in Sect. 5.4.2 and the TSI reconstruction. We only considered the data from the days where the reconstruction, SIM SSI and all the TSI records are available.

SSI Series	TSI Series	R	R^2
SIM SSI _{240–2416nm}	ACRIM3	0.481	0.232
	DIARAD _{IRMB}	0.474	0.225
	DIARAD _{PMOD}	0.418	0.175
	PMO6V	0.428	0.183
	TIM	0.328	0.108
	SATIRE-S TSI	0.412	0.170
SATIRE-S SSI _{240–2416nm}	ACRIM3	0.940	0.883
	DIARAD _{IRMB}	0.963	0.927
	DIARAD _{PMOD}	0.965	0.931
	PMO6V	0.971	0.942
	TIM	0.966	0.933
	SATIRE-S TSI	0.999	0.999

by SIM reproduces, in the best case, about 23% of the variability in the ACRIM3 record ($R = 0.481$ and $R^2 = 0.232$).

As with the ultraviolet solar irradiance records discussed in Sect. 5.5.1.3, the reconstruction replicates the rotational variability in SIM SSI, largely to within uncertainty, in all the spectral intervals examined except the shortwave-infrared (the k_{rot} between measurement and model is tabulated in Table 5.7). That said, even with the more pronounced scatter, there is still a broad agreement between model and measurement in terms of the rotational variation in the shortwave-infrared (top row, Fig. 5.26).

During periods of significant sunspot activity, the dip corresponding to the passage of sunspots across the solar disc is in some instances significantly deeper in the reconstruction than in SIM SSI, an example of which is illustrated in Fig. 5.26 (bottom row). If we examine the integrated flux in the reconstruction over the spectral range of SIM, the dip is much closer to that registered in concurrent TSI measurements. It is unlikely that the discrepancy between the total flux recorded by SIM and TSI measurements at these times can be accounted for by sunspot contrast below 240 nm and above 2416 nm. The weaker dips registered by SIM as compared to the reconstruction during periods of heightened sunspot activity is likely instrumental in origin.

Earlier in this section, we noted that there is no obvious solar cycle modulation in the SIM record (Fig. 5.24), and the total flux recorded by the instrument fails to reproduce much of the observed variability in TSI (Fig. 5.25 and Table 5.8). In comparison, the reconstruction exhibits clear solar cycle variation (Fig. 5.23) and the integrated flux over the spectral range of SIM replicates most of the variability in ACRIM3, TIM and VIRGO TSI radiometry. These observations, together with the broad consistency between the reconstruction and the SIM record at rotational timescales implies that the overall discord between measurement and model (Fig. 5.24 and Table 5.7) is probably the result of residual instrumental trends in the SIM data set.

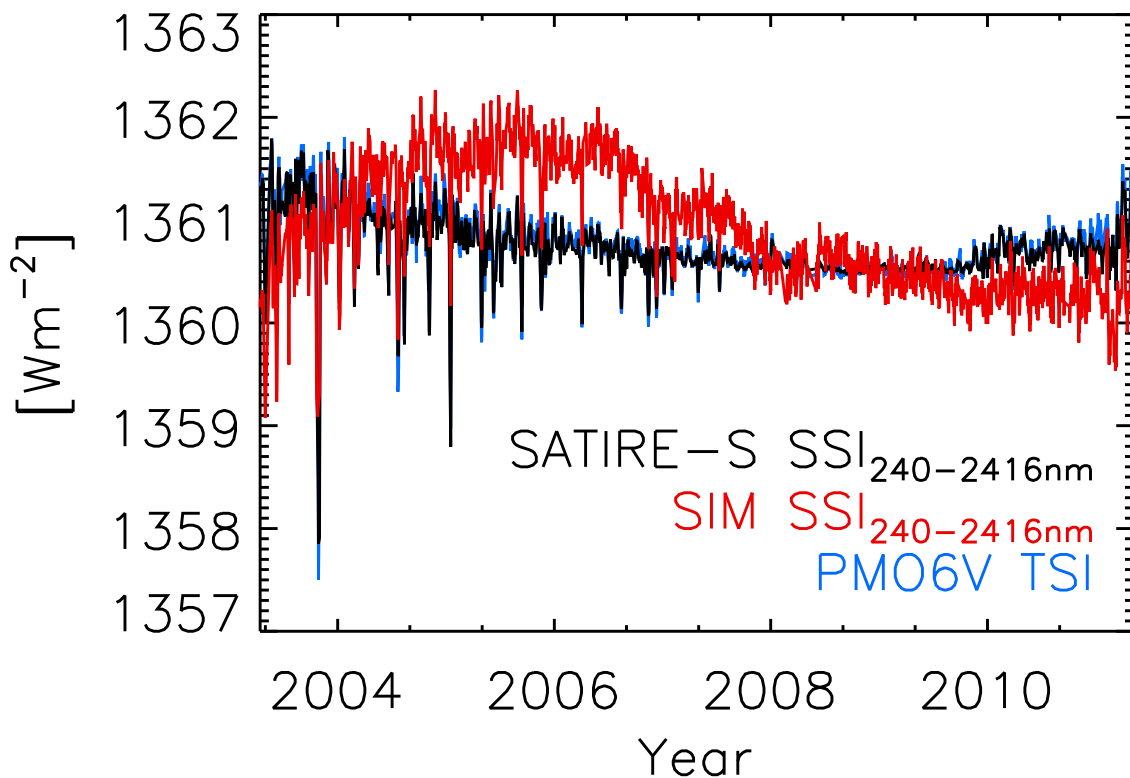


Figure 5.25: The total flux recorded by SIM (red), the integrated flux in the reconstruction over a similar wavelength range (black) and PMO6V TSI (blue). The SIM and SATIRE-S time series were offset to the PMO6V series at the 2008 solar cycle minimum. The PMO6V series is largely hidden by the SATIRE-S series due to the close similarity.

5.5.2 Facular and sunspot contribution to variation in TSI

From the intermediate products of the SATIRE-S reconstruction process, it is straightforward to compute the (magnetically) quiet solar spectrum (reconstructed solar spectrum assuming a solar disc that is entirely quiet Sun) and the variation in solar irradiance with respect to this base level from faculae, and from sunspots. Of course, this analysis excludes the part of the reconstruction provided by the regression series (Sect. 5.4.4).

The variation in TSI from faculae (denoted $\Delta\text{TSI}_{\text{fac}}$), and from sunspots ($\Delta\text{TSI}_{\text{spt}}$), with respect to the calculated quiet Sun level, 1360.122 Wm^{-2} (the integral under the quiet solar spectrum) is illustrated in Fig. 5.27. Between the solar cycle minima of 1986, 1996 and 2008, $\Delta\text{TSI}_{\text{fac}}$ (red) diminished, minimum-to-minimum, by over 0.2 Wm^{-2} , while $\Delta\text{TSI}_{\text{spt}}$ (blue) declined, in absolute terms, by around 0.02 Wm^{-2} . (We do not have any figures for the 1976 minimum as this period in the reconstruction is mainly covered by the regression series.) The secular variation of the solar cycle minima level in the TSI reconstruction (Table 5.3) is dominantly from the variation in the intensity excess from faculae.

We histogrammed $\Delta\text{TSI}_{\text{fac}}$ and $\Delta\text{TSI}_{\text{spt}}$ from each data day by sine latitude (bin width of 0.01) and concatenated the monthly average histogram from the entire reconstruction, expressed in Fig. 5.28. This is an update and extension of the similar figure by Wenzler

5 Reconstruction of total and spectral solar irradiance from 1974 to 2013 based on KPVT, SoHO/MDI and SDO/HMI observations

(The contents of this chapter are identical to the submitted version of Yeo, K. L., Krivova, N. A., Solanki, S. K., Glassmeier, K. H., 2014, Reconstruction of total and spectral solar irradiance from 1974 to 2013 based on KPVT, SoHO/MDI and SDO/HMI observations, *Astron. Astrophys.*, 570, A85.)

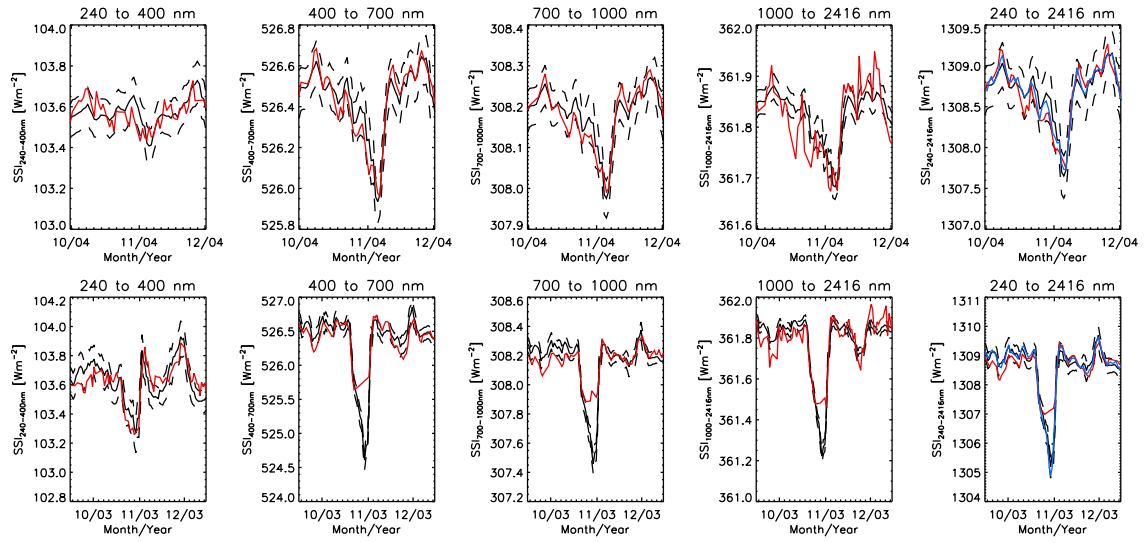


Figure 5.26: The integrated flux over the annotated spectral intervals, in the reconstruction (black) and in the SIM record (red), between October 1 and November 30, 2004 (top), and September 15 and December 15, 2003 (bottom). The maximum sunspot number over the depicted periods is 99 (October 24, 2004) and 167 (October 29, 2003), respectively. PMO6V TSI is plotted along the integrated flux over 240 to 2416 nm (blue). The SIM and PMO6V time series are offset to the level of the reconstruction. The dashed lines denote the uncertainty range of the reconstruction.

2005, generated with the SATIRE-S model using similar KP_{512} and KP_{SPM} data.

Obviously, since ΔTSI_{fac} traces bright magnetic features (concentrated in active regions) and ΔTSI_{spt} , sunspots and pores, the figure demonstrates Spörer's law, bearing resemblance to butterfly diagrams of sunspot area/position and magnetic flux (e.g., Figs. 4 and 14 in Hathaway 2010). A similar diagram to the ΔTSI_{spt} butterfly diagram (Fig. 5.28b), based on the photometric sunspot index, was recently presented by Fröhlich 2013 (Fig. 5 in their paper). The vertical stripes in the ΔTSI_{fac} butterfly diagram (Fig. 5.28a) correspond to an annual modulation associated with Earth's inclined orbit about the Sun. The northern and southern hemispheres of the Sun, and therefore the photospheric magnetism present in each, come alternately into greater view.

We took the average of the daily ΔTSI_{fac} histograms over the three-month period centred on each of the last three solar cycle minima. Then, we summed the values from the southern and northern hemispheres, giving the mean intensity excess from faculae around each minimum as a function of distance from the equator (top panel, Fig. 5.29).

Looking at the mean ΔTSI_{fac} histogram from the 1986 minimum (black series), there are three broad peaks. The maximum near the equator is from active regions associated with the preceding cycle, and that at middle latitude active regions associated with the succeeding cycle. The elevation towards high latitude corresponds to magnetic flux transported polewards over the previous cycle by meridional circulation. (What these peaks represent is visibly apparent in the ΔTSI_{fac} butterfly diagram, Fig. 5.28a.) Comparing the mean ΔTSI_{fac} histogram from the three solar cycle minima, the secular trend in total ΔTSI_{fac} (the main component of the corresponding secular variation in reconstructed TSI)

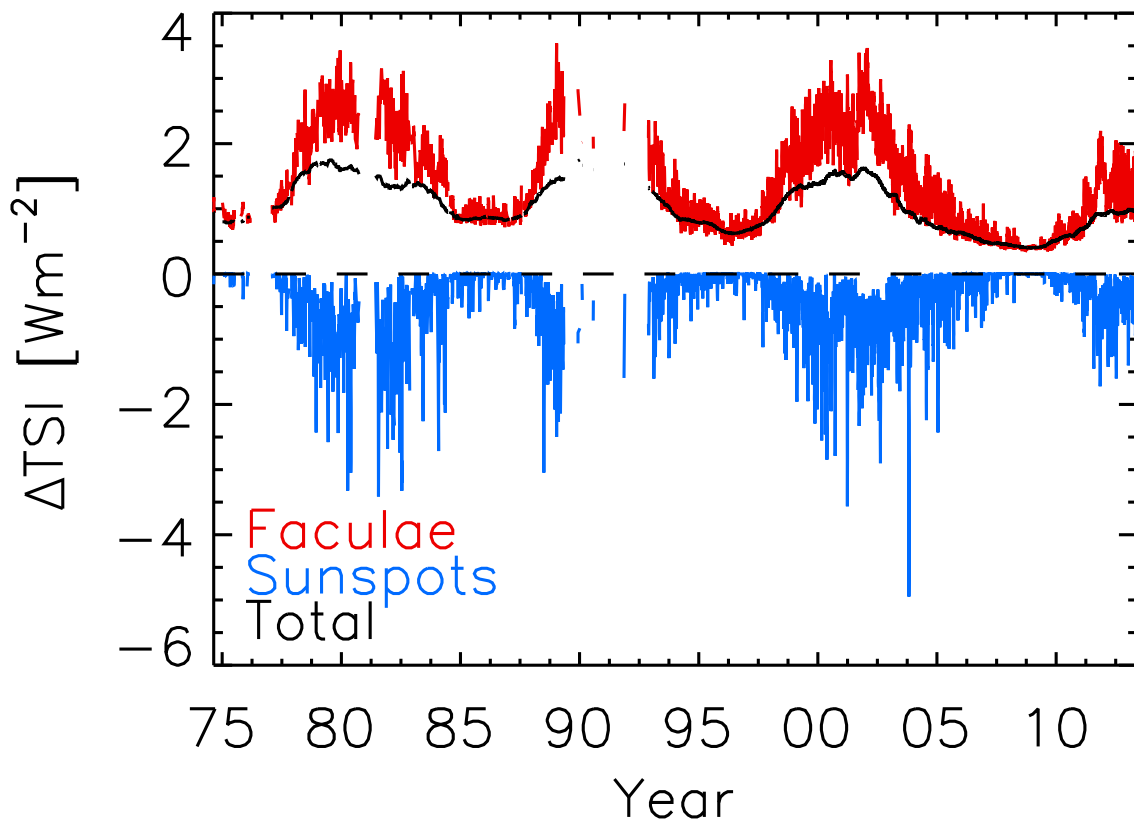


Figure 5.27: TSI excess from faculae (red), and deficit from sunspots (blue), with respect to the calculated quiet Sun level (1360.122 Wm^{-2} , denoted by the dashed line) in the reconstruction. The sum, giving the net variation in TSI, is drawn in black, smoothed by means of a 361-day boxcar filter so as not to obscure the other series.

is influenced by the prevailing magnetic activity in the three latitude regions.

We repeated this analysis with the $\Delta\text{TSI}_{\text{spt}}$ histograms (bottom panel, Fig. 5.29). The dips in the mean $\Delta\text{TSI}_{\text{spt}}$ histograms are located at similar latitudes as the low and middle latitude peaks in the the mean $\Delta\text{TSI}_{\text{fac}}$ histograms, associated with the same active regions. They are much weaker in terms of the magnitude and minimum-to-minimum variation, showing, as in Fig. 5.27, that the secular trend of the solar cycle minima level in the TSI reconstruction is primarily faculae-driven.

5.6 Summary

In this paper, we present a SATIRE-S model reconstruction of daily total and spectral solar irradiance. The reconstruction, spanning the period of 1974 to 2013, is based on full-disc observations of continuum intensity and line-of-sight magnetic field from the KPVT, SoHO/MDI and SDO/HMI. Gaps in the time series, from the limited availability of suitable magnetogram data, were plugged by the regression of indices of solar activity to the reconstruction.

This work extends the preceding reconstruction based on similar observations from the

5 Reconstruction of total and spectral solar irradiance from 1974 to 2013 based on KPVT, SoHO/MDI and SDO/HMI observations

(The contents of this chapter are identical to the submitted version of Yeo, K. L., Krivova, N. A., Solanki, S. K., Glassmeier, K. H., 2014, *Reconstruction of total and spectral solar irradiance from 1974 to 2013 based on KPVT, SoHO/MDI and SDO/HMI observations*, *Astron. Astrophys.*, 570, A85.)

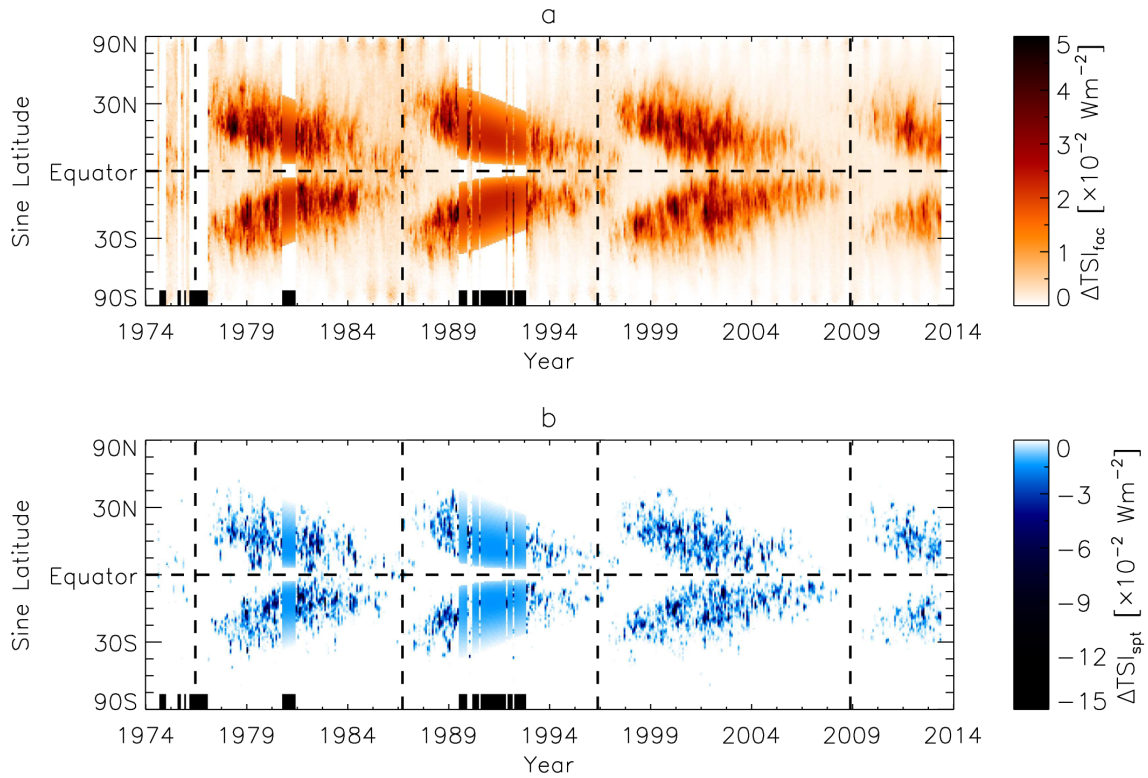


Figure 5.28: Variation in reconstructed TSI with respect to the calculated quiet Sun level due to a) faculae ($\Delta\text{TSI}_{\text{fac}}$) and b) sunspots ($\Delta\text{TSI}_{\text{spt}}$), as a function of time and latitude (the monthly average in sine latitude intervals of 0.01). The black bars along the horizontal axes mark the months with no values from the lack of suitable magnetogram data. The gaps around the maxima of solar cycles 21 and 22 are filled by the interpolation. The vertical dashed lines denote solar cycle minima and the horizontal dashed lines the equator.

KPVT and MDI by Ball et al. (2012, 2014), which covered the period of 1974 to 2009. Apart from the extension to the present time with HMI data, we updated the reconstruction method.

The most significant change to the reconstruction method is the procedure by which the model input from the various data sets were combined such that they yield a consistent time series as the model output. The approach taken in previous studies tailored the parameters of the model to each data set (in such a manner that it does not introduce additional free parameters) and any residual discrepancy between the reconstructed spectra generated from the various data sets were accounted for by regression.

In this study, we compared the magnetogram signal and the computed faculae filling factor in the various data sets and brought them into agreement in the periods of overlap between them by regression. This allowed us to apply the same model parameters (apart from the umbra and penumbra intensity thresholds, which are wavelength dependent) to all the data sets. The updated procedure yielded a consistent TSI/SSI time series without the need for any additional correction of the reconstructed spectra.

The model has a single free parameter which modulates the contribution by bright

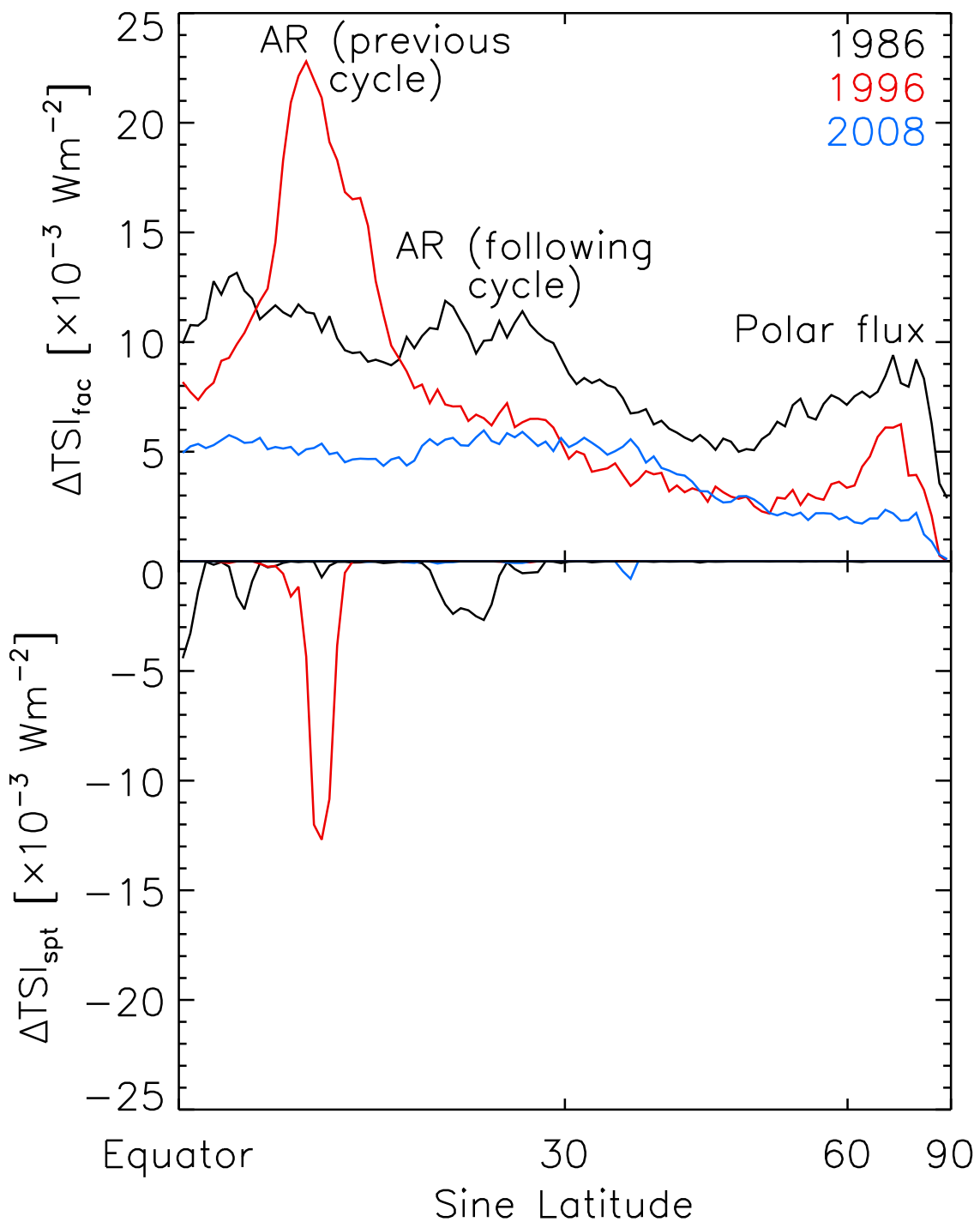


Figure 5.29: Top: Mean variation in reconstructed TSI, with respect to the calculated quiet Sun level, from faculae ($\Delta\text{TSI}_{\text{fac}}$, top) and from sunspots ($\Delta\text{TSI}_{\text{spt}}$, bottom) around the solar cycle minima in 1986 (black), 1996 (red) and 2008 (blue), as a function of distance from the equator in sine latitude. AR is short for active regions.

magnetic features to variability in reconstructed solar irradiance. This free parameter is recovered by the comparison with TSI measurements. We considered the observations

from four TSI radiometers in current operation, ACRIM3, DIARAD (both the IRMB and PMOD/WRC calibrations of the instrument output) and PMO6V on VIRGO, and TIM. Each of these TSI record resulted in a somewhat different value for the free parameter (and hence reconstructed solar irradiance time series). Based on the particularly close consistency between the PMO6V record and the TSI reconstruction generated using it as the reference to retrieve the free parameter, we adopted this candidate reconstruction for further study.

The agreement between the reconstruction and the PMO6V record, which extends 1996 to 2013, is excellent. The correlation coefficient, R is 0.979 ($R^2 = 0.959$), implying that over solar cycles 23 and 24, at least 96% of TSI variability is due to the time evolution of solar surface magnetism. The reconstruction also reproduces the secular decline between the 1996 and 2008 solar cycle minima in the PMO6V record. This counters the suggestion by Fröhlich (2009) that a dimming of the solar photosphere, rather than photospheric magnetism, might be responsible for the observed secular decline.

We also evaluated the reconstruction against the ACRIM, IRMB and PMOD composite records of TSI, the LASP Lyman- α composite, the Mg II index composites by IUP and by LASP, and SSI measurements from the UARS and SORCE missions.

As with previous efforts with SATIRE-S, we found the closest match with the PMOD composite ($R = 0.957$ and $R^2 = 0.916$ over the span of the series, 1978 to 2013). The long-term trend in the PMOD composite is well reproduced in the reconstruction almost everywhere except between 1984 and 1994, where the reconstruction is broadly higher by 0.1 to 0.3 Wm^{-2} . This discrepancy is, however, minute compared to the spread between TSI composites, or between the TSI radiometers in current operation. We attribute this apparent disparity to possible unresolved instrumental trends in the KPVT data set or in the PMOD composite, especially as the period in question encompasses the ACRIM gap.

The solar Lyman- α irradiance and Mg II index taken from the reconstruction exhibit excellent correlation with the LASP Lyman- α composite ($R = 0.970$ and $R^2 = 0.942$) and the IUP Mg II index composite ($R = 0.981$ and $R^2 = 0.963$), respectively. The secular trend in the solar cycle minima level in the LASP Lyman- α composite is also, to largely within uncertainty, reproduced. There are weak but palpable discrepancies, in terms of the amplitude of solar cycle variation, between the IUP and LASP Mg II index composites, and the reconstruction series. The implied long-term uncertainty of the two Mg II index composites could have contributed to the observation that proxy models of solar irradiance based on the Mg II index cannot replicate the secular decline between the 1996 and 2008 solar cycle minima in VIRGO TSI radiometry.

We contrasted the reconstruction against the ultraviolet (120 to 300 nm) solar irradiance measurements from the SOLSTICE and SUSIM experiments onboard UARS, and SOLSTICE and SIM onboard SORCE. As observations of ultraviolet solar irradiance exhibit divergent long-term trends, especially above 240 nm, the agreement between measurement and model varied. The reconstruction reproduces at least 89% of the variability between 120 and 240 nm in SUSIM SSI ($R > 0.94$ and $R^2 > 0.89$), and 95% for 120 to 180 nm observations from the two SOLSTICE instruments ($R > 0.97$ and $R^2 > 0.95$). It was less successful with measurements above 180 nm from the two SOLSTICE experiments and SIM SSI. At rotational timescales however, the reconstruction exhibits reasonable agreement with all the records examined, implying that the disparity between the model and some of these measurements at longer timescales arises from unresolved instrumental

trends in the latter. The validity of the reconstruction in the ultraviolet is further supported by the excellent alignment with the SUSIM-based proxy model of ultraviolet solar irradiance by Morrill et al. 2011 ($R > 0.96$ and $R^2 > 0.92$). Importantly, the solar cycle variation between 240 and 400 nm in the SATIRE-S and the Morrill et al. (2011) reconstructions is similar (this spectral interval is crucial for climate models but the long-term trend is very poorly constrained by measurements and preceding models).

As stated in the introduction, SIM is the first and, at present, only instrument purpose-built to return radiometrically calibrated spectral measurements spanning the ultraviolet to the infrared at a regular basis. Also stated, the record indicates long-term trends that are difficult to reconcile with other observations and models of solar irradiance. The reconstruction reproduces the rotational variability in the SIM record but as with previous similar studies, failed to reproduce the long-term trends. We argue, from the lack of constancy in how SIM SSI relate to the solar cycle, and the disparity between the total flux recorded by the instrument and TSI (the wavelength range surveyed by SIM accounts for over 97% of the energy in solar radiation), that unaccounted instrumental trends are present in the data set. In contrast, the reconstruction exhibits clear solar cycle variation at all wavelengths and the integrated flux over the wavelength range of SIM replicates at least 88% of the variability in ACRIM3, TIM and VIRGO TSI radiometry ($R > 0.94$ and $R^2 > 0.88$). The present quandary between SIM observations, and other measurements and models of solar irradiance emphasizes the need for continual monitoring of the solar spectrum over a wide spectral range.

The SATIRE-S model describes the variation in the solar spectrum from bright magnetic features (classed as ‘faculae’), and sunspots and pores (classed as ‘sunspots’). We examined the intensity excess from faculae, and the intensity deficit from sunspots, at the solar cycle minimum of 1986, 1996 and 2008 (there was insufficient data around the 1976 minima) as a function of latitude. This allowed us to visualize the contribution by low and middle latitude magnetic activity (mostly from active regions), and polar magnetic flux to the observed secular variation.

The results of this work significantly strengthen support for the hypothesis that variation in solar irradiance on timescales greater than a day is driven by photospheric magnetic activity (Foukal and Lean 1986, Fligge et al. 2000, Solanki et al. 2002, Preminger et al. 2002, Krivova et al. 2003). The reconstruction is consistent with observations from multiple sources, confirming its reliability and utility for climate modelling. The SATIRE-S daily total and spectral solar irradiance time series is available for download at www.mps.mpg.de/projects/sun-climate/data.html.

6 Solar cycle variation in solar irradiance

Yeo, K. L., Krivova, N. A., Solanki, S. K.
Space Sci. Rev., online (2014)*

Abstract

The correlation between solar irradiance and the 11-year solar activity cycle is evident in the body of measurements made from space, which extend over the past four decades. Models relating variation in solar irradiance to photospheric magnetism have made significant progress in explaining most of the apparent trends in these observations. There are however, persistent discrepancies between different measurements and models, in terms of the absolute radiometry, secular variation and the spectral dependence of the solar cycle variability. We present an overview of solar irradiance measurements and models, and discuss the key challenges in reconciling the divergence between the two.

6.1 Introduction

The 11-year solar activity cycle, the observational manifest of the solar dynamo, is apparent in indices of solar surface magnetism such as the sunspot area and number, 10.7 cm radio flux, and in the topic of this paper, solar irradiance. The observational and modelling aspects of the solar cycle are reviewed in Hathaway (2010) and Charbonneau (2010), respectively. Solar irradiance is described in terms of what is referred to as the total and spectral solar irradiance, TSI and SSI. They are defined, respectively, as the aggregate and spectrally resolved solar radiative flux (i.e., power per unit area, and power per unit area and wavelength) above the Earth's atmosphere, normalized to one AU from the Sun. Factoring out the Earth's atmosphere and the variation in the Earth-Sun distance, TSI and SSI characterize the radiant behaviour of the Earth-facing hemisphere of the Sun.

Although the variation of the radiative output of the Sun with solar activity has long been suspected (Abbot et al. 1923, Smith and Gottlieb 1975, Eddy 1976), it was not observed directly till satellite measurements, free from the effects of atmospheric seeing, became available. TSI and SSI (at least in the ultraviolet) have been monitored regularly

*The contents of this chapter are identical to the submitted version of Yeo, K. L., Krivova, N. A., Solanki, S. K., 2014, Solar cycle variation in solar irradiance, Space Sci. Rev., online, reproduced with permission from Space Science Reviews, © Springer Science+Business Media.

from space through a succession of satellite missions, starting with Nimbus-7 in 1978 (Hickey et al. 1980, Willson and Hudson 1988, Fröhlich 2006, DeLand and Cebula 2008, Kopp et al. 2012). A correlation between variations in TSI and the passage of active regions across the solar disc was soon apparent (Willson et al. 1981a, Hudson et al. 1982, Oster et al. 1982, Foukal and Lean 1986), leading to the development of models relating the variation in solar irradiance to the occurrence of bright and dark magnetic structures on the solar surface. While not the only mechanism mooted, models that ascribe variation in solar irradiance at timescales greater than a day to solar surface magnetism have been particularly successful in reproducing observations (Domingo et al. 2009). At timescales shorter than a day, excluded from the discussion here, intensity fluctuations from acoustic oscillations, convection and flares begin to dominate (Hudson 1988, Woods et al. 2006, Seleznyov et al. 2011).

The measurement and modeling of the variation in solar irradiance over solar cycle timescales, a minute proportion of the overall level (about 0.1% in the case of TSI), is a considerable achievement. Though significant progress has been made over the past four decades, considerable discrepancies remain between different measurements and models, chiefly in terms of the absolute radiometry, secular variation and the spectral dependence of the cyclic variability (see the recent reviews by Ermolli et al. 2013, Solanki et al. 2013). In the following, we present a brief overview of the current state of solar irradiance observations (Sect. 6.2) and models (Sect. 6.3). We then discuss the key issues in reconciling measurements and models (Sect. 6.4), before giving a summary (Sect. 6.5).

6.2 Measurements

6.2.1 Total solar irradiance, TSI

The measurements from the succession of TSI radiometers sent into space since 1978, collectively representing a nearly uninterrupted record, exhibit clear solar cycle modulation. This is illustrated in Fig. 6.1 by the comparison with the monthly sunspot number. All these instruments are based on active cavity electrical substitution radiometry (Butler et al. 2008, Frohlich 2010). Succinctly, TSI is measured by allowing solar radiation into a heated absorptive cavity intermittently and adjusting the heating power as necessary to maintain thermal equilibrium. While these observations are sufficiently accurate to trace solar cycle variability (only about 0.1% of the overall level), the measurements from the various instruments are offset from one another by a greater margin, reflecting the uncertainty in the absolute radiometry.

With the early instruments, specifically, Nimbus-7/ERB (Hickey et al. 1980, Hoyt et al. 1992), SMM/ACRIM1 (Willson 1979) and ERBS/ERBE¹ (Lee et al. 1987), the spread in absolute radiometry arose mainly from the uncertainty in the aperture area. As the determination of the aperture area improved, so the absolute radiometry from the succeeding missions converged. That is, up till the Total Irradiance Monitor, TIM (Kopp and Lawrence 2005, Kopp et al. 2005a,b) onboard the SOLar Radiation and Climate Experi-

¹Nimbus-7/ERB denotes the Earth Radiation Budget instrument onboard Nimbus-7, SMM/ACRIM1 the Active Cavity Radiometer Irradiance Monitor onboard the Solar Maximum Mission, and ERBS/ERBE the Earth Radiation Budget Experiment onboard the similarly named satellite.

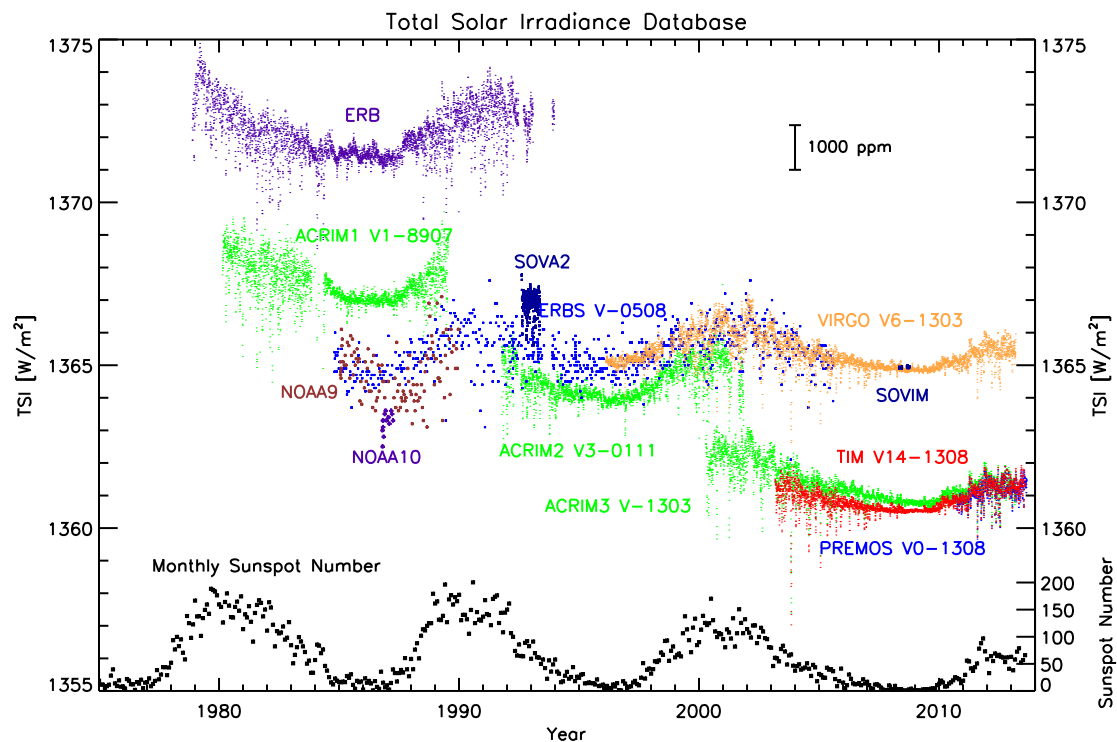


Figure 6.1: The measurements from the succession of TSI radiometers sent into orbit since 1978 (colour coded) and the monthly mean of the sunspot number (lower right axis, black). Each TSI record is annotated by the name of the instrument name, and where applicable, the version number, and/or the year and month of the version. Courtesy of G. Kopp (<http://spot.colorado.edu/kopp/TSI/>).

ment, *SORCE* (launched in 2003, Rottman 2005).

The measurements from *TIM* were about 5 Wm^{-2} lower than the concurrent observations from *ACRIMSAT/ACRIM3* (Willson and Mordvinov 2003) and *SoHO/VIRGO*² (Fröhlich et al. 1995, 1997). Tests conducted at the TSI Radiometer Facility, TRF (Kopp et al. 2007) with ground copies of *ACRIM3*, *TIM* and *VIRGO* revealed unaccounted stray light effects in *ACRIM3* and *VIRGO* (Kopp and Lean 2011, Kopp et al. 2012, Fehlmann et al. 2012). Correction for scattered light subsequently introduced to the *ACRIM3* record based on these tests brought the absolute radiometry down to significantly closer agreement with *TIM* (within 0.5 Wm^{-2}). The similar proximity between the measurements from the *PREcision MONitor Sensor*, *PREMOS* onboard *Picard* (launched in 2010, Schmutz et al. 2009, Fehlmann et al. 2012) with *TIM* radiometry provided further evidence that the lower absolute level first registered by *TIM* is likely the more reliable. (*PREMOS* is the first TSI radiometer to be calibrated in vacuum at full solar power levels prior to flight, also at the TRF.)

Due to the limited lifetime of TSI radiometers, there is no single mission that covered

²*ACRIMSAT/ACRIM3* refers to the ACRIM radiometer onboard the ACRIM SATellite, and *SoHO/VIRGO* the Variability of IRradiance and Gravity Oscillations experiment onboard the Solar and Heliospheric Observatory.

6 Solar cycle variation in solar irradiance

(The contents of this chapter are identical to the submitted version of Yeo, K. L., Krivova, N. A., Solanki, S. K., 2014, *Solar cycle variation in solar irradiance*, *Space Sci. Rev.*, online.)

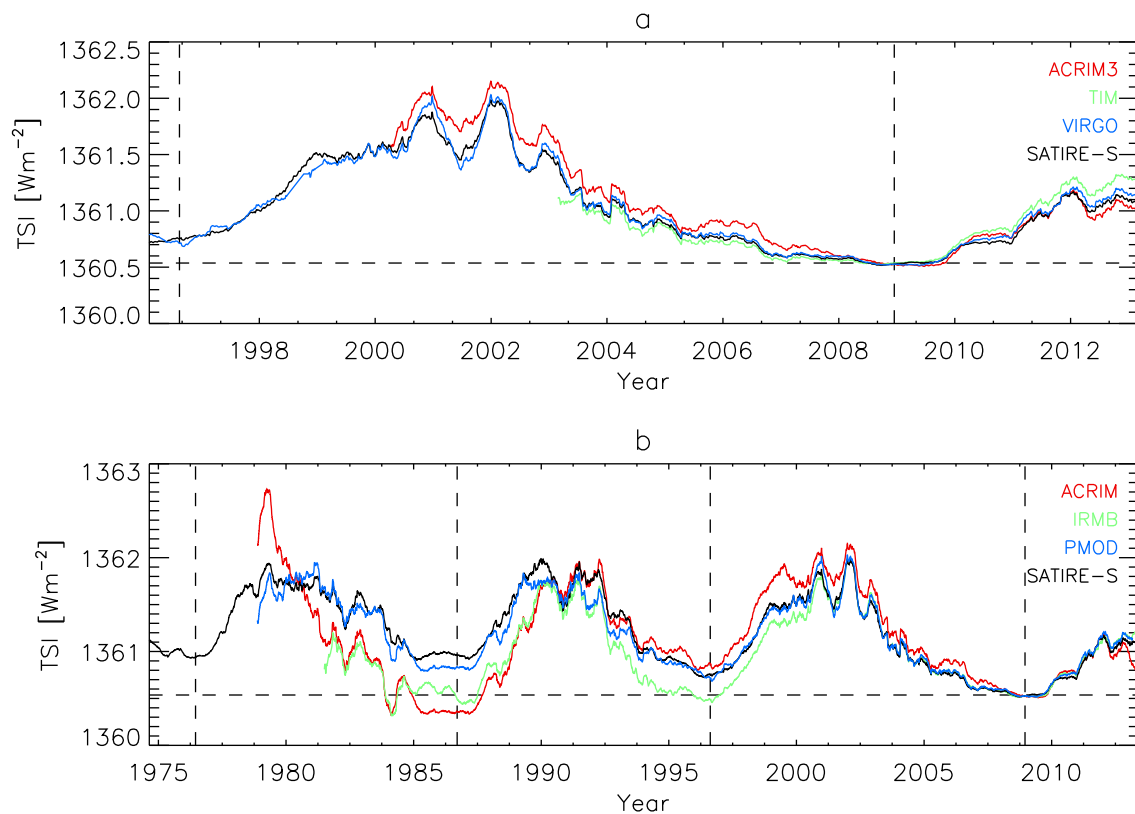


Figure 6.2: a) TSI measurements from ACRIMSAT/ACRIM3 (version 11/13), *SORCE/TIM* (level 3, version 14) and *SoHO/VIRGO* (level 2, version 6_002_1302). b) The ACRIM (version 11/13), IRMB (version dated December 19, 2013, provided by S. Dewitte) and PMOD (version d41_62_1302) composite records of TSI. Also plotted is the SATIRE-S reconstruction of TSI. The vertical dashed lines mark the position of solar cycle minima. All the time series were normalized to TIM at the 2008 solar cycle minimum (horizontal dashed line) and smoothed with a 181-day boxcar filter.

the entire period of observation, and apart from *VIRGO* (1996 to present), there is no other record that extends more than a complete solar cycle minimum-to-minimum. The composition of the observations from the various missions into a single time series, obviously essential, is non-trivial due to ageing/exposure degradation, calibration uncertainty and other instrumental issues. The ACRIM, *PREMOS*, *TIM* and *VIRGO* instruments are designed with redundant cavities to allow in-flight degradation tracking. Even with this capability and the best efforts of the respective instrument teams, significant uncertainty persists over the long-term stability (conservatively, 0.2Wm^{-2} or 20 ppm per year, Solanki et al. 2013), reflected in the discrepant amplitude of solar cycle variation in the ACRIM3, *TIM* and *VIRGO* records (Fig. 6.2a). Accounting for changes in instrument sensitivity, which are often particularly severe during early operation and can see discrete shifts (such as that suffered by *ERB* and *VIRGO*), has proven to be particularly precarious (Hoyt et al. 1992, Lee et al. 1995, Dewitte et al. 2004a, Fröhlich 2006). It is worth mentioning here that the observations from the various radiometers do largely agree at solar rotational timescales (roughly one month), where apparent variability is much less affected by the

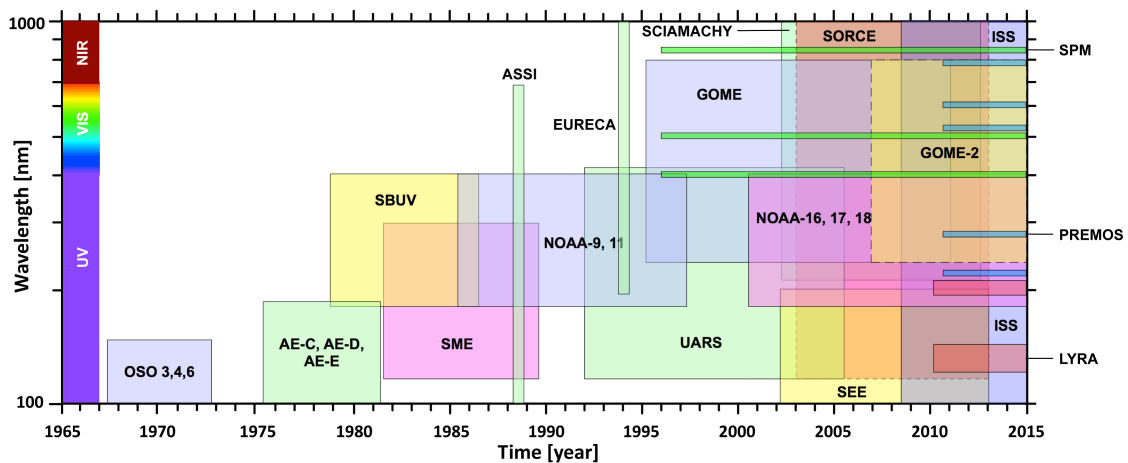


Figure 6.3: Timeline and spectral range of the space missions making observations of the solar spectrum (above 100 nm). Taken from Ermolli et al. (2013).

instrumental influences discussed above.

There are, at present, three composite records of TSI, published by the ACRIM science team (Willson and Mordvinov 2003), IRMB (Dewitte et al. 2004b, Mekaoui and Dewitte 2008) and PMOD/WRC³ (Fröhlich 2000, 2006). These competing time series, while broadly similar, do differ in terms of the amplitude of solar cycle variation (discussed in detail by Fröhlich 2006, 2012), most readily apparent in the conflicting secular trend of the solar cycle minima level (Fig. 6.2b). The TSI reconstructions presented by Wenzler et al. (2009), Ball et al. (2012), Yeo et al. (2014b), based on the SATIRE-S model (Fligge et al. 2000, Krivova et al. 2003, 2011b), have found the greatest success in replicating the solar cycle variation in the PMOD composite (see Sect. 6.3.3.1 for more details).

6.2.2 Spectral solar irradiance, SSI

The solar spectrum has been probed through a miscellany of spaceborne instruments over the past five decades (Fig. 6.3), differing in the regularity of measurements and the spectral range surveyed. As with TSI, ultraviolet solar irradiance (120 to 400 nm) has been monitored, almost without interruption, from space since 1978.

The key features of the body of ultraviolet solar irradiance measurements is similar to that of TSI, discussed in Sect. 6.2.1. The observations from the various spectrometers display similar rotational variability but diverge in terms of the absolute radiometry and the amplitude of solar cycle variation, especially at wavelengths above 240 nm (see DeLand and Cebula 2012, Unruh et al. 2012, Ermolli et al. 2013, Yeo et al. 2014b, and Fig. 6.4). In particular, the measurements from the SIM (Harder et al. 2005b,a) and SOLSTICE (McClintock et al. 2005, Snow et al. 2005a) experiments onboard SORCE exhibit much stronger solar cycle variation than registered by the SOLSTICE (Rottman et al. 2001) and SUSIM (Brueckner et al. 1993, Floyd et al. 2003) instruments onboard

³IRMB is short for L'Institut Royal Météorologique de Belgique, and PMOD/WRC Physikalisch-Meteorologisches Observatorium Davos/World Radiation Center. The composite by IRMB is also variously referred to as the RMIB or SARR composite.

6 Solar cycle variation in solar irradiance

(The contents of this chapter are identical to the submitted version of Yeo, K. L., Krivova, N. A., Solanki, S. K., 2014, *Solar cycle variation in solar irradiance*, *Space Sci. Rev.*, online.)

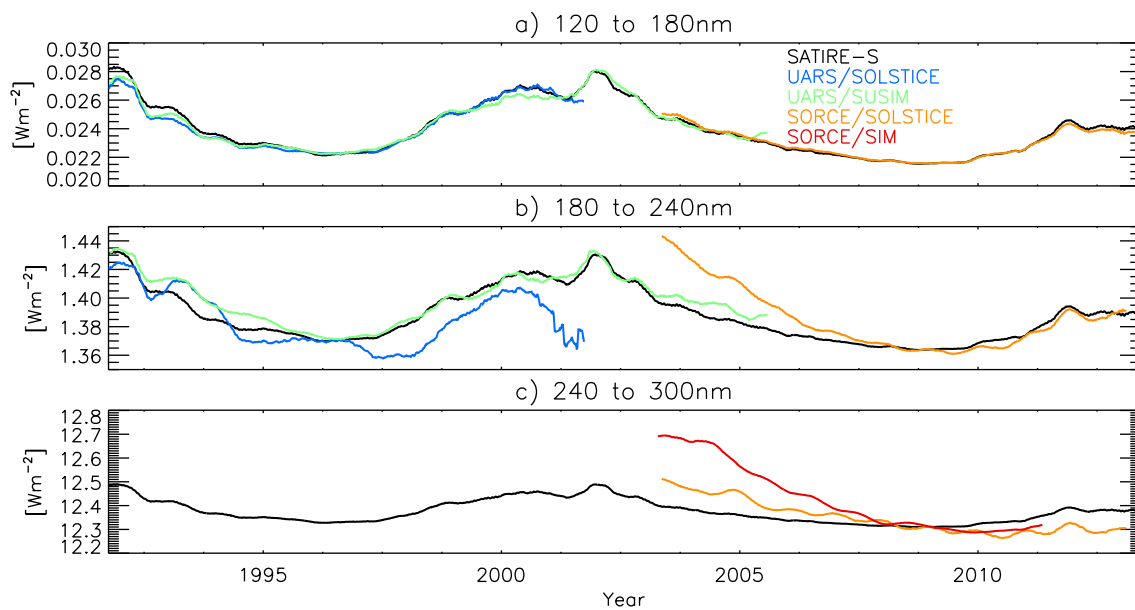


Figure 6.4: Integrated solar irradiance between a) 120 and 180 nm, b) 180 and 240 nm (centre), and c) 240 and 300 nm (bottom), in the SATIRE-S reconstruction of SSI (black). Also drawn are the measurements from the UARS and SORCE missions, offset to SATIRE-S at the 1996 and 2008 solar cycle minima, respectively. All the time series were smoothed by taking the 181-day moving average. Adapted from Yeo et al. (2014b).

the predecessor mission, UARS⁴ (by a factor of three to ten, depending on wavelength, see Fig. 7 in DeLand and Cebula 2012). This disparity, while broadly within the uncertainty in the long-term stability of said instruments, is much greater than encountered between pre-SORCE instruments (DeLand and Cebula 2012, Ermolli et al. 2013). The uncertainty in the long-term stability of ultraviolet solar irradiance observations, on the order of 0.1 to 1% per year (varying with wavelength and between instruments, Snow et al. 2005a, Merkel et al. 2011, DeLand and Cebula 2012), is of similar magnitude as the variation over the solar cycle. It is also grossly greater than the uncertainty afflicting TSI measurements. Again, due to the limited lifetime of spaceborne instrumentation, there is no record that extends beyond a complete solar cycle minimum-to-minimum, with the exception of the observations from NOAA-9 SBUV/2⁵ (DeLand and Cebula 1998).

The solar cycle modulation in, and disparity between the pre-SORCE measurements is illustrated in the time series plot by DeLand and Cebula 2008 (Fig. 2 in their paper), which is qualitatively analogous to Fig. 6.1. The authors presented the first published effort to compose the ultraviolet solar irradiance observations from these instruments into a single time series. The result, spanning the period of 1978 to 2005, still contains overt instrumental trends for which the appropriate correction is not known. The challenge in

⁴SIM denotes the Spectral Irradiance Monitor, SOLSTICE the SOLar STellar Irradiance Comparison Experiment, SUSIM the Solar Ultraviolet Spectral Irradiance Monitor and UARS the Upper Atmosphere Research Satellite.

⁵The second generation Solar Backscatter UltraViolet spectrometer onboard the ninth National Oceanic and Atmospheric Administration satellite.

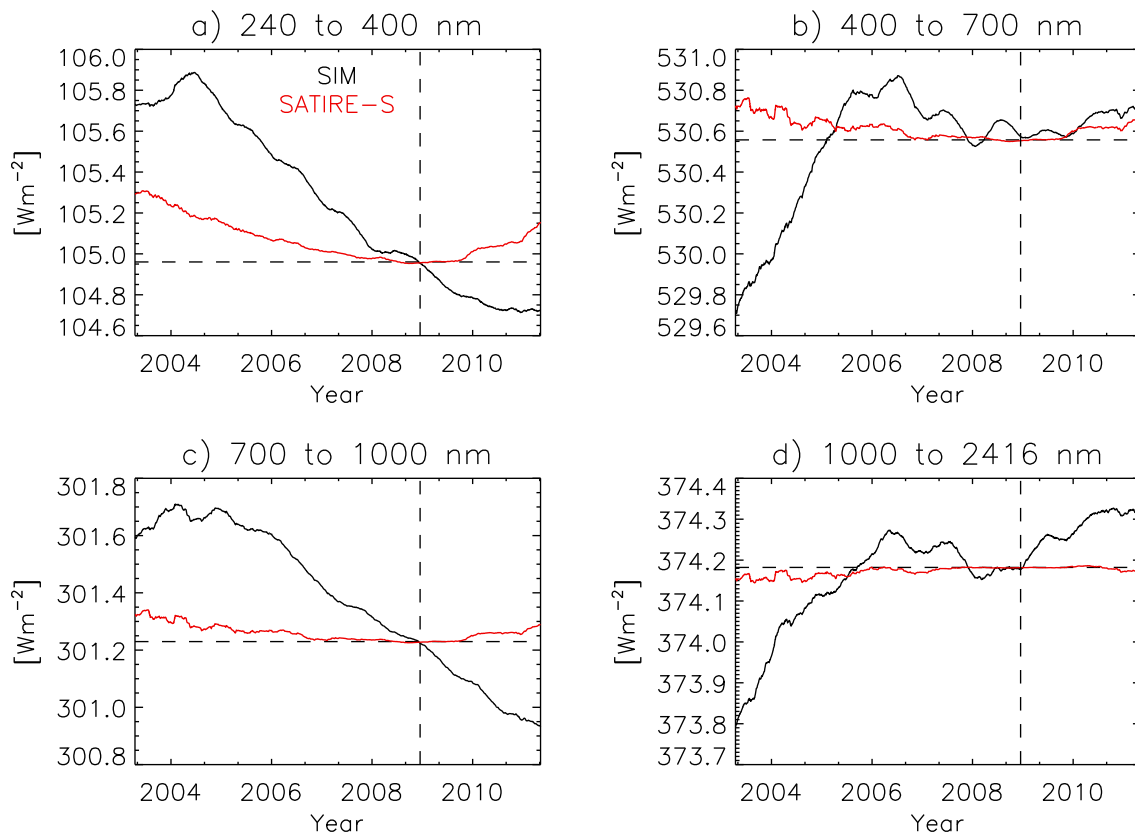


Figure 6.5: 181-day moving average of the integrated solar irradiance over the spectral intervals specified above each panel, in the SORCE/SIM record (red) and the SATIRE-S reconstruction (black). The SATIRE-S time series were offset to the corresponding SIM time series at the 2008 solar cycle minimum, the position and level at which is indicated by the dashed lines. Adapted from Yeo et al. (2014b).

the account of instrumental influences is substantially greater than with TSI, exacerbated by the wavelength dependence of instrumental effects, and differences in the design, operation and calibration.

The series of GOME instruments (the first of which was onboard ERS-2, launched in 1996, Weber et al. 1998, Munro et al. 2006) and ENVISAT/SCIAMACHY⁶ (launched in 2002, Skupin et al. 2005a) made regular measurements of the solar spectrum in the 240 to 790 nm and 240 to 2380 nm wavelength range, respectively. However, these instruments, purpose built for atmospheric sounding rather than solar irradiance monitoring, lack the capability for in-flight degradation tracking. This renders the observations unsuitable for tracing the solar cycle variation of the solar spectrum. The long-term stability of the narrowband (FWHM of 5 nm) photometry at 402, 500 and 862 nm from the Sun PhotoMeter, SPM on the SoHO/VIRGO experiment (Fröhlich et al. 1995, 1997) is similarly problematic (though considerable progress has been made, see Wehrli et al. 2013).

⁶GOME is short for Global Ozone Monitoring Experiment. ERS-2 refers to the second European Remote Sensing satellite, and ENVISAT/SCIAMACHY the SCanning Imaging Absorption spectroMeter for Atmospheric CHartography onboard the ENVironmental SATellite.

6 Solar cycle variation in solar irradiance

(The contents of this chapter are identical to the submitted version of Yeo, K. L., Krivova, N. A., Solanki, S. K., 2014, *Solar cycle variation in solar irradiance*, *Space Sci. Rev.*, online.)

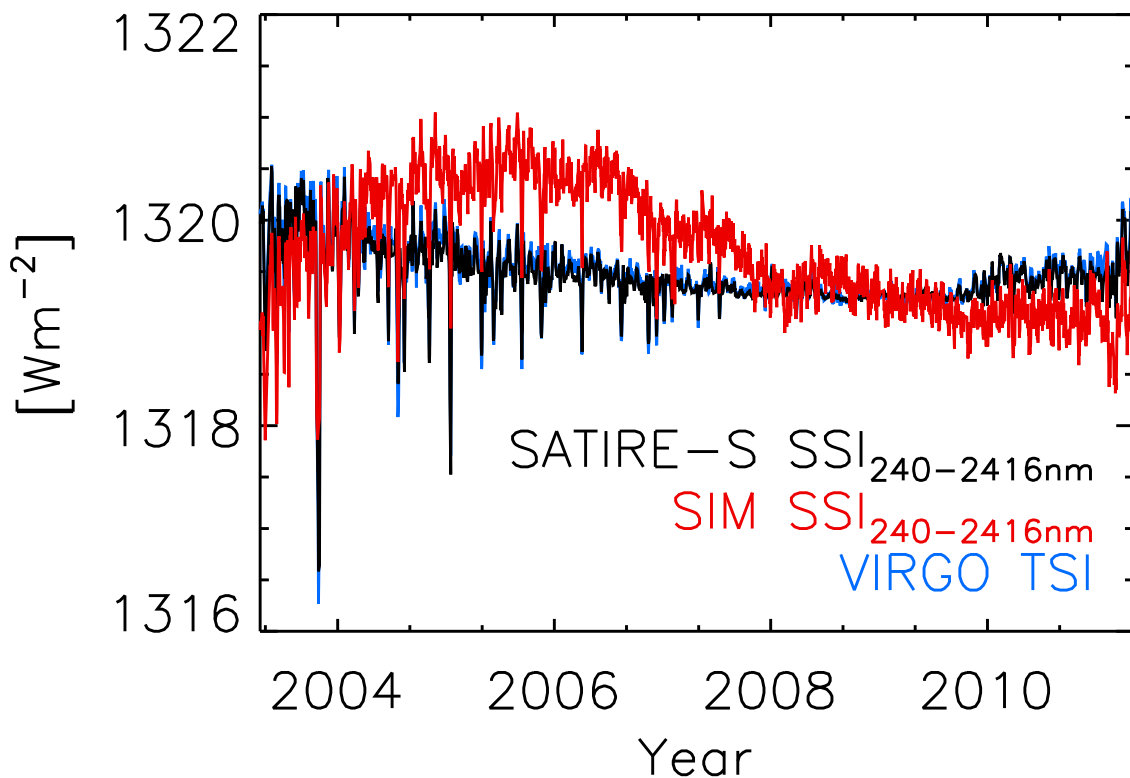


Figure 6.6: Total flux registered by SIM (red). Also drawn is the integrated flux in the SATIRE-S reconstruction over a similar wavelength range (black) and VIRGO TSI (blue), both offset to match the level of the SIM time series at the 2008 solar cycle minimum. The VIRGO time series is largely hidden by the SATIRE-S time series due to the close similarity. Adapted from Yeo et al. (2014b).

Regular monitoring of the solar spectrum beyond the ultraviolet only started, in effect, with SIM. This instrument provides the only radiometrically calibrated, continuous/extended (in time) record of the solar spectrum spanning the ultraviolet to infrared (the latest release, version 19, dated November 19, 2013, covers 240 to 2416 nm) presently available, illustrated in Figs. 6.5 and 6.6.

Between 2004 and 2008 (which is within the declining phase of solar cycle 23), SIM registered a decline in ultraviolet flux (integrated solar irradiance between 240 and 400 nm, Fig. 6.5a) that is, in absolute terms, almost double the drop in TSI over the same period (Fig. 6.7). Up to 2006, this pronounced downward trend was accompanied by a comparable increase in the visible (400 to 700 nm, Fig. 6.5b), in apparent anti-phase with the solar cycle. The decline in the ultraviolet is multiple times greater than projections from other measurements (i.e., pre-SORCE ultraviolet solar irradiance) and models of solar irradiance, summarized in Fig. 6.7 (Harder et al. 2009, Ball et al. 2011, DeLand and Cebula 2012, Lean and DeLand 2012, Unruh et al. 2012, Ermolli et al. 2013, Yeo et al. 2014b). (We exclude, for now, the solar irradiance reconstruction presented by Fontenla et al. 2011, where steps were taken to bring the model into qualitative agreement with SIM SSI, to be discussed in Sect. 6.3.3.2.) The increase in the visible prior to 2006 is in conflict with VIRGO SPM photometry (see next paragraph) and present-day models, all

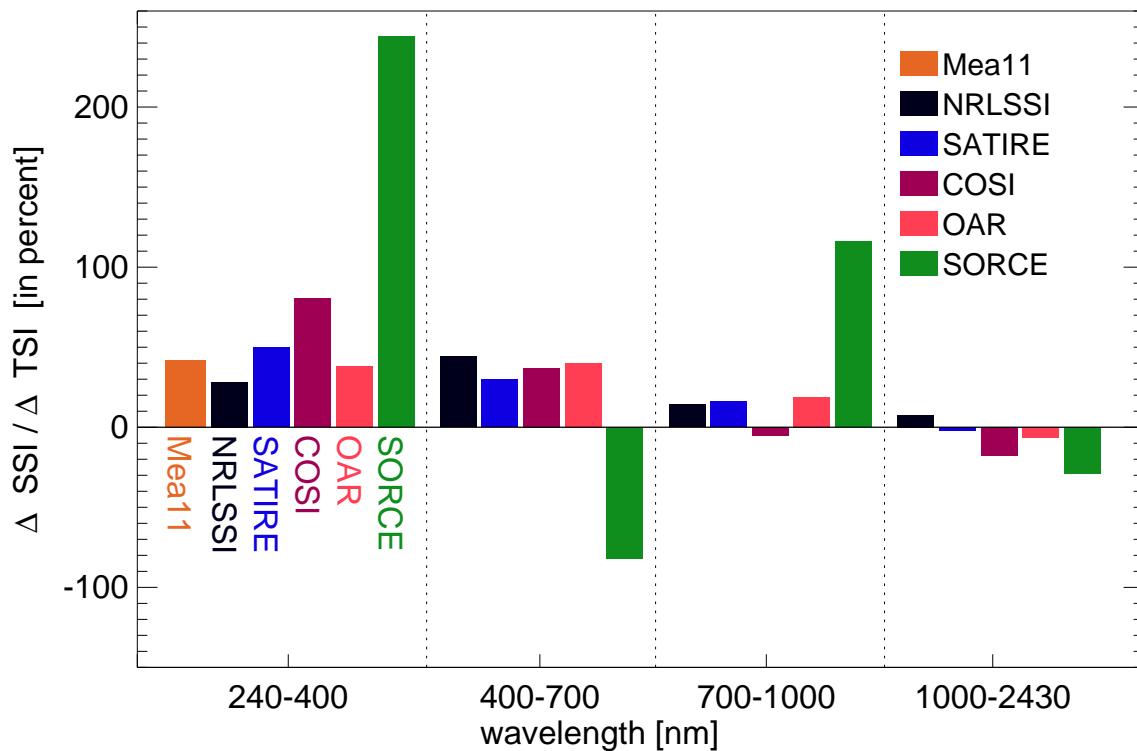


Figure 6.7: Ratio of the integrated variation in the same spectral intervals examined in Fig. 6.5, Δ SSI and the corresponding variation in TSI, Δ TSI between solar cycle maximum and minimum (2002 and 2008) in the models discussed in Sect. 6.3.3. For the model by Morrill et al. (2011), denoted Mea11, we took Δ TSI from the SATIRE-S model. Also depicted is the same for SORCE measurements between 2004 and 2008, with Δ SSI and Δ TSI from the SIM and TIM records, respectively. Adapted from Ermolli et al. (2013).

of which see visible solar irradiance varying in phase with the solar cycle. The variation in the infrared (700 to 2416 nm, Figs. 6.5c and 6.5d) over this period is also significantly stronger than in model reconstructions. The investigations of Ball et al. (2011), DeLand and Cebula (2012), Lean and DeLand (2012), Unruh et al. (2012), Yeo et al. (2014b) did, however, note similar rotational variability in SIM SSI and in these other measurements and models.

Looking at the entire SIM record (the current version extends from 2003 to 2011), there is no constancy in how the overall trend in SIM SSI (at a given wavelength) relate to the solar cycle, neither in phase nor in anti-phase (Fig. 6.5). Apart from the solar cycle modulation evident in pre-SORCE ultraviolet solar irradiance measurements, this also runs counter to the positive correlation between SPM visible (500 nm) photometry and TSI over the similar period of 2002 to 2012 reported by Wehrli et al. (2013). There being no other extended record of SSI covering a similar spectral range, we cannot rule out completely that segments of the solar spectrum may vary in a non-cyclic manner as apparent in SIM SSI but it is almost irrefutable that the integral of the solar spectrum over all wavelengths, TSI, does exhibit variation that is clearly in phase with the solar cycle. The spectral range surveyed by SIM accounts for more than 97% of the power

in solar radiation; the total flux recorded by SIM should closely replicate the variability in TSI, but that is evidently not the case (Fig. 6.6). In contrast, the reconstruction of the integrated solar irradiance over the spectral range of SIM from SSI models replicates most of the variability in measured TSI (see Ball et al. 2011, Lean and DeLand 2012, Yeo et al. 2014b, and Fig. 6.6).

The discrepancies between SIM SSI, and other measurements and models, discussed above, were taken in various studies to indicate that there are unaccounted instrumental effects in the SIM record (Ball et al. 2011, DeLand and Cebula 2012, Lean and DeLand 2012, Unruh et al. 2012, Yeo et al. 2014b). This is favoured over alternative interpretations such as the apparent trends between 2004 and 2008 implying a change in the physics of the Sun during this period compared to earlier times, or that there are gaping insufficiencies in our understanding/modeling of the physical processes driving variations in solar irradiance. As we will argue in Sect. 6.3.1, the decline in visible flux between 2003 and 2006 (Fig. 6.5a) is not consistent with our current understanding of solar surface magnetism and its effect on solar irradiance.

Evidently, considerable uncertainty afflicts the direct observation of the variation in SSI over solar cycle timescales. The situation is set to improve, with the continuing efforts to calibrate SCIAMACHY and SORCE spectrometry, and spectral measurements expected from ISS/SOLSPEC (intermittent in time but radiometrically calibrated, Thuillier et al. 2009) and the upcoming JPSS⁷ mission (set to be launched in 2016), which will carry an improved version of the SIM instrument (Richard et al. 2011). For more extensive reviews of the measurement of solar irradiance, we refer the reader to DeLand and Cebula (2008, 2012), Domingo et al. (2009), Kopp et al. (2012), Fröhlich (2012), Ermolli et al. (2013), Solanki et al. (2013).

6.3 Models

The collection of satellite measurements of solar irradiance, while evidently core to our understanding of the solar cycle variation in the radiative output of the Sun, cover a limited period in time and suffer significant uncertainty. Models of solar irradiance serve both to complement these observations and to advance our understanding of the physical processes driving the apparent variability.

6.3.1 Solar surface magnetism

A feature of the 11-year solar activity cycle is the cyclical emergence and evolution of kilogauss strength magnetic concentrations in the photosphere (Solanki and Schmidt 1993), the main properties of which can be explained by describing them as magnetic flux tubes (see Fig. 6.8 and Spruit 1976, Spruit and Roberts 1983, Solanki 1993). They range in physical extent, from on the order of 10^1 to 10^5 km in cross section. The lower end corresponds to the small-scale magnetic elements which make up active region faculae, quiet Sun network and internetwork (Lagg et al. 2010, Riethmüller et al. 2013), and the upper end, sunspots and pores.

⁷ISS/SOLSPEC denotes the SOLar SPECTrum experiment onboard the International Space Station, and JPSS the Joint Polar Satellite System.

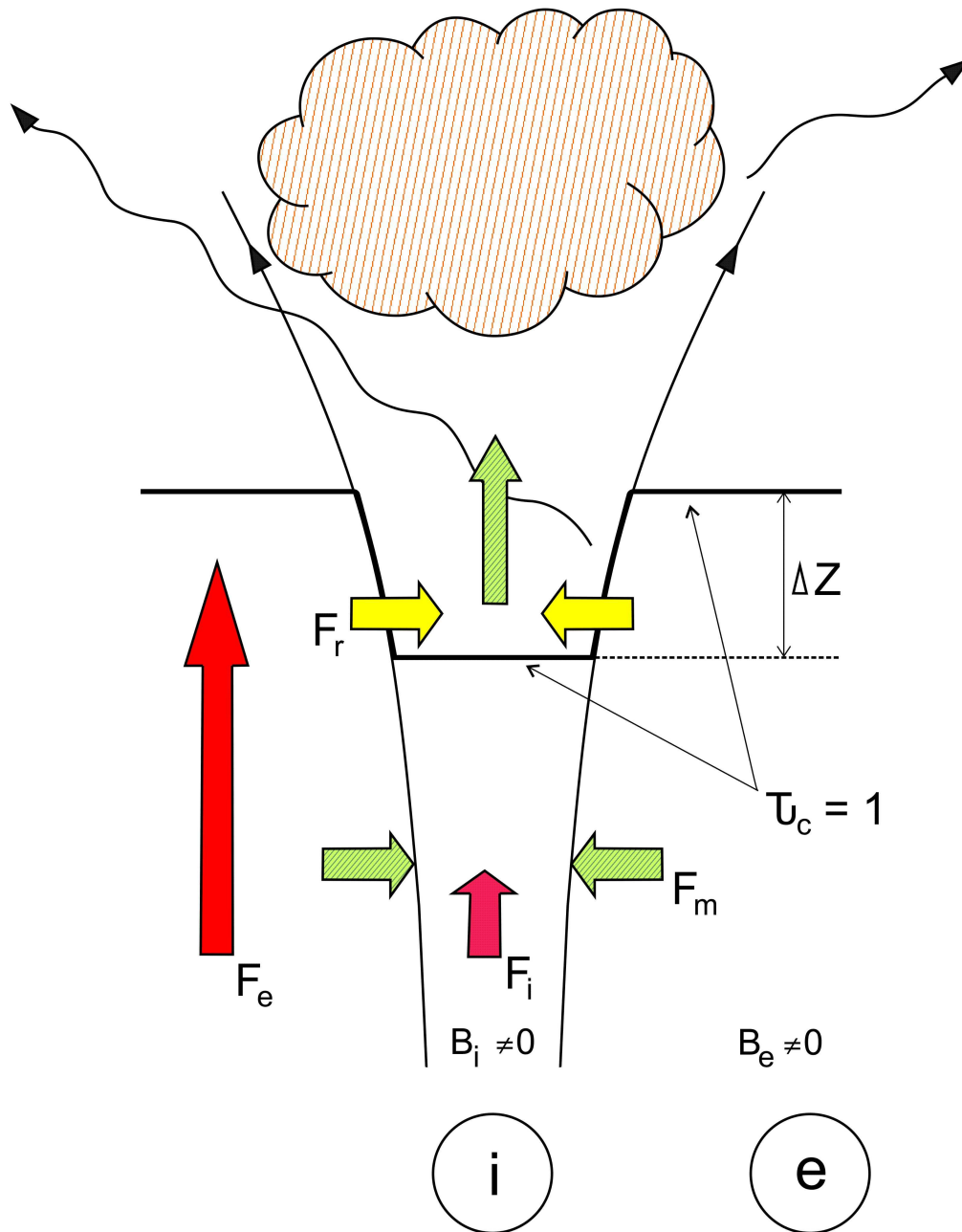


Figure 6.8: Schematic of a thin magnetic flux tube. The thickened line follow the optical depth unity ($\tau_c = 1$) surface, depressed by ΔZ within the flux tube. The red arrows represent convective and radiative energy transport in the interior and exterior of the flux tube (denoted by the i and e subscripts, respectively). The yellow arrows correspond to radiative heating through the side walls of the depression, and the gree arrows mechanical energy transfers. The cloud symbolizes the heated chromospheric layers of the magnetic structure. Reproduced from Solanki et al. (2013), which followed Zwaan (1978).

6 Solar cycle variation in solar irradiance

(The contents of this chapter are identical to the submitted version of Yeo, K. L., Krivova, N. A., Solanki, S. K., 2014, Solar cycle variation in solar irradiance, Space Sci. Rev., online.)

a) HMI Longitudinal Magnetogram b) HMI Continuum Intensity (617.3nm) c) AIA Continuum Intensity (170nm)

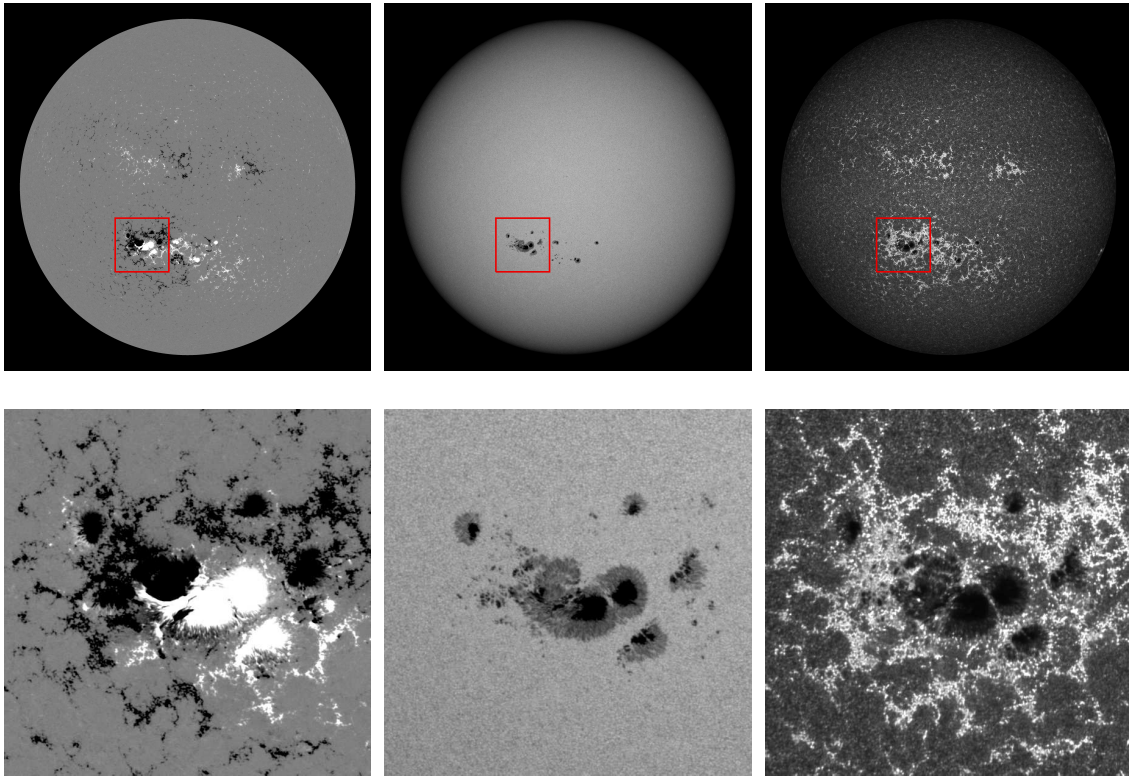


Figure 6.9: Top: Concurrent observations, from July 11, 2012, of the a) line-of-sight magnetic field, and the continuum intensity at b) 617.3 nm and c) 170 nm from the Helioseismic and Magnetic Imager, HMI (Schou et al. 2012b) and the Atmospheric Imaging Assembly, AIA (Lemen et al. 2012) onboard the Solar Dynamics Observatory. Bottom: Blow up of the boxed region, featuring active region NOAA 11520. The grey scale is saturated at ± 30 G, and at about 60% and 120%, and 20% and 300% of the mean quiet Sun level at disc centre, respectively.

Solar irradiance is modulated by photospheric magnetic activity from its effect on the thermal/radiant property of the solar surface and atmosphere. The influence of magnetic concentrations on the local temperature structure of the solar surface and atmosphere varies strongly with the size of the magnetic feature, as described below.

As a consequence of pressure balance, the interior of magnetic concentrations is evacuated. The lower density creates a depression in the optical depth unity surface and magnetic buoyancy (the result of which is flux tubes are largely vertical). The intensity contrast in the continuum is influenced by the competing effects of magnetic suppression of convection and radiative heating from surrounding granulation through the side walls of the depression. Sunspots and pores are dark from the magnetic suppression of convection within these features (see the reviews by Solanki 2003, Rempel and Schlichenmaier 2011, and Fig. 6.9). For small-scale magnetic concentrations, this is overcome by the lateral heating, rendering them bright (Spruit 1976, Spruit and Zwaan 1981, Grossmann-Doerth

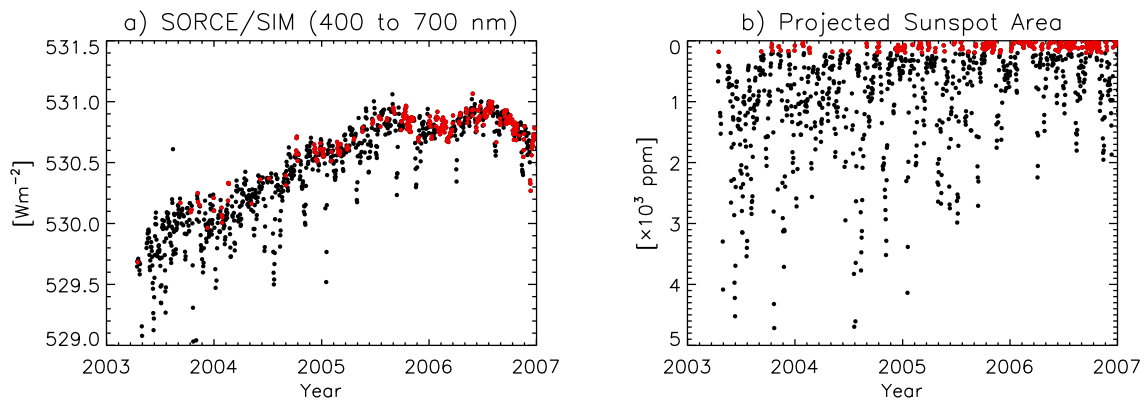


Figure 6.10: a) Integrated solar irradiance in the visible in SORCE/SIM spectroscopy, and b) the concurrent projected sunspot area (from the composite record by Balmaceda et al. 2009, version 0613). Points corresponding to days where the projected sunspot area is less than 200 ppm are highlighted in red. The vertical axis of the projected sunspot area plot is inverted to aid interpretation.

et al. 1994), especially away from the disc centre as the side walls come into greater view (Spruit 1976, Keller et al. 2004, Carlsson et al. 2004, Steiner 2005). Heated by mechanical and resistive dissipations (Musielak and Ulmschneider 2003, Moll et al. 2012), and radiation from deeper layers (Knölker et al. 1991), the temperature gradient within small-scale magnetic elements is steeper, so enhancing their intensity within spectral lines and in the ultraviolet, formed at greater heights than the visible continuum (see Frazier 1971, Mitchell and Livingston 1991, Morrill et al. 2001, Ermolli et al. 2007, Yeo et al. 2013, Riethmüller et al. 2010, and Fig. 6.9c).

Models describing the variation in solar irradiance, at timescales greater than a day, by the intensity deficit and excess facilitated by photospheric magnetism have achieved substantial success in reproducing measured solar irradiance (see Domingo et al. 2009, and Sects. 6.3.2 and 6.3.3). While other plausible mechanisms have been proposed (Wolff and Hickey 1987, Kuhn et al. 1988, Cossette et al. 2013), related to physical processes in the solar interior, direct evidence is not straightforward to obtain and consequently still largely lacking.

The increase in visible solar irradiance registered by SIM between 2003 and 2006 (Fig. 6.5b, discussed in Sect. 6.2.2) came at a time solar activity is declining. For the solar cycle variation in photospheric magnetism to be compatible with this trend in visible solar irradiance, small-scale magnetic concentrations would have to be dark in the visible. The intensity deficit from sunspots and pores, while declining over this period, is not driving the upward trend in SIM visible solar irradiance. This is demonstrated in Fig. 6.10 by the variation of SIM visible flux over the days with minimal sunspot activity.

Indeed, studies examining the intensity contrast of small-scale magnetic concentrations in the visible continuum as a function of magnetogram signal have noted negative contrasts near disc centre at both low and high magnetogram signal levels (summarized in Table 2 of Yeo et al. 2013). However, the results of recent investigations suggest that these apparent negative contrasts are related to the fact that small-scale magnetic ele-

ments congregate mainly within dark intergranular lanes (Schnerr and Spruit 2011, Kobel et al. 2011), and observational effects related to the limited spatial resolution and telescope diffraction (Röhrbein et al. 2011), than any indication that small-scale magnetic concentrations are, near disc centre, dark in the visible continuum. Taken together with the intensity enhancement towards the limb and within spectral lines (Topka et al. 1997, Ortiz et al. 2002, Yeo et al. 2013), it is highly unlikely that small-scale magnetic concentrations (at least overall) might be dark in the visible. The upward trend in early SIM visible solar irradiance is not consistent with our current understanding of solar surface magnetism and its effect on solar irradiance.

6.3.2 Model architectures

There are two broad categories of solar irradiance models, commonly referred to as proxy and semi-empirical models, distinguished by the modelling approach.

As stated in the introduction, the measurement of solar irradiance from space quickly revealed an apparent correlation between TSI and the passage of active regions across the solar disc. This was followed by the development of proxy models, aimed at reconstructing solar irradiance by the multivariate regression of indices of solar activity to measured solar irradiance. The index data serve as proxies of the effects of bright and dark magnetic structures on the radiative output of the Sun.

Sunspot darkening is usually represented by sunspot area or the PSI (photometric sunspot index, Hudson et al. 1982, Fröhlich et al. 1994), and facular brightening by chromospheric indices such as the Ca II K (Keil et al. 1998), Mg II (Heath and Schlesinger 1986) or F10.7 (10.7 cm radio flux, Tapping 1987) indices. (In this context the term sunspots includes pores, and faculae, quiet Sun network.) The Ca II K and Mg II indices are given by the ratio of the disc-integrated flux in the line core (of the Ca II K line, and the Mg II h and k doublet, respectively) to that at nearby reference wavelengths. The line core to ‘continuum’ ratio is preferred over absolute flux as it is more robust to instrument degradation.

The TSI reconstructions by the group at the San Fernando Observatory, SFO (Chapman et al. 1996, 2012, 2013, Preminger et al. 2002) employ sunspot and faculae indices derived from full-disc photometric images obtained at the observatory. These models proved to be particularly successful among proxy models. By employing full-disc imagery instead of Sun-as-a-star measures such as the indices listed above, they include the centre-to-limb variation of sunspot and faculae contrast, albeit only at the photometric bandpass. The latest iteration, based on visible red and Ca II K observations, reproduced most of the variation in TIM radiometry ($R^2 = 0.95$, Chapman et al. 2013).

Since the proxy model approach relies on the availability of reliable solar irradiance measurements, it is not straightforward to reconstruct SSI by this method due to the long-term stability issues in available measurements and the relative paucity of observations outside the ultraviolet (Sect. 6.2). Making use of the fact that the effects of instrument degradation on apparent variability is relatively benign at shorter timescales, long-term stability issues are sometimes circumvented by fitting index data to measured rotational variability (either by detrending the data or confining the regression to rotational periods, Lean et al. 1997, Pagaran et al. 2009, Thuillier et al. 2012) and then assuming the indices-to-irradiance relationships so derived to all timescales. As we will discuss in Sect.

6.4.1, the assumption that the underlying relationship between indices of solar activity and solar irradiance is similar at all timescales is not likely valid.

The next level of sophistication in the modelling of solar irradiance is realized by semi-empirical models. In these models, the solar disc is segmented by surface feature type, termed ‘components’. The filling factor (proportion of the solar disc or a given area covered) and time evolution of each component is deduced from indices of solar activity or suitable full-disc observations. This information is converted to solar irradiance employing the intensity spectra of the various components, calculated using spectral synthesis codes with semi-empirical model atmospheres of said feature types (Fontenla et al. 1999, 2009, Unruh et al. 1999, Shapiro et al. 2010). The reconstruction of the solar spectrum is given by the filling factor weighted-sum of the component intensity spectra. The semi-empirical model atmospheres describe the temperature and density stratification of the solar atmosphere within each component, constrained and validated by observations (therefore the term ‘semi-empirical’).

The semi-empirical approach has the advantage that it yields SSI independent of the availability of reliable measurements. Additionally, for the models that rely on full-disc imagery for the filling factor of the solar surface components (i.e., the exact disc position of magnetic features is known), the centre-to-limb variation of the radiant behaviour of each component can be taken into account by generating and applying the corresponding intensity spectrum at varying heliocentric angles.

At present, there are five models reported in the literature capable of returning the full solar spectrum, reviewed in Ermolli et al. (2013). They are,

- NRLSSI (Naval Research Laboratory Solar Spectral Irradiance, Lean et al. 1997, Lean 2000),
- SATIRE-S (Spectral And Total Irradiance REconstruction for the Satellite era, Unruh et al. 1999, Fligge et al. 2000, Krivova et al. 2003, 2006, 2011b, Yeo et al. 2014b),
- SRPM (Solar Radiation Physical modelling, Fontenla et al. 1999, 2004, 2006, 2009, 2011),
- OAR (Observatorio Astronomico di Roma, Penza et al. 2003, Ermolli et al. 2011, 2013) and
- COSI (COde for Solar Irradiance, Haberreiter et al. 2008, Shapiro et al. 2010, 2011, 2013).

Apart from the NRLSSI, these models adopt the semi-empirical approach. In the following, we discuss the recent results obtained with the SATIRE-S model by Yeo et al. 2014b (Sect. 6.3.3.1) before giving an overview of the other models listed (Sect. 6.3.3.2). For a broader review of models of solar irradiance, we refer the reader to Domingo et al. (2009), Ermolli et al. (2013), Solanki et al. (2013).

6.3.3 SSI models capable of returning the full solar spectrum

6.3.3.1 SATIRE-S

The SATIRE-S model (Fligge et al. 2000, Krivova et al. 2003, 2011b) relies on full-disc observations of magnetic field and intensity to segment the solar disc into quiet Sun, faculae, sunspot umbra and sunspot penumbra. It has been applied to longitudinal magnetograms and continuum intensity images collected at the KPVT (in operation from 1974 to 2003, Livingston et al. 1976, Jones et al. 1992), as well as from SoHO/MDI (1996 to 2011, Scherrer et al. 1995) and SDO/HMI⁸ (2010 to the present, Schou et al. 2012b) to reconstruct total and spectral solar irradiance over various periods between 1974 and 2013 (Krivova et al. 2003, Wenzler et al. 2006, Ball et al. 2012, 2014, Yeo et al. 2014b). In the latest iteration (Yeo et al. 2014b), KPVT, MDI and HMI magnetograms were cross-calibrated in such a way that the model input from all the data sets combine to yield a single consistent TSI/SSI time series spanning the entire period of 1974 to 2013 as the output. Apart from the NRLSSI, which extends back to 1950, this is the only other daily reconstruction of the full solar spectrum (from present-day models) to cover multiple solar cycles.

At present, the model employs the intensity spectra of quiet Sun, faculae, umbra and penumbra from Unruh et al. (1999), generated with the ATLAS9 spectral synthesis code (Kurucz 1993). As ATLAS9 assumes local thermodynamic equilibrium (LTE), it fails in the ultraviolet or below approximately 300 nm. (Solar ultraviolet radiation is formed in the upper photosphere and lower chromosphere, where the plasma is increasingly collisionless.) This is accounted for by offsetting/rescaling the 115 to 300 nm segment of the reconstructed spectra to the Whole Heliospheric Interval (WHI) reference solar spectra by Woods et al. (2009) and SORCE/SOLSTICE spectrometry (detailed in Yeo et al. 2014b). SATIRE-S is the only semi-empirical model to include non-LTE effects through such an approach. The SRPM, OAR and COSI models make use of various non-LTE spectral synthesis codes, which differ from one another in the method non-LTE effects are approximated (see Fontenla et al. 1999, Uitenbroek 2002, Shapiro et al. 2010).

Recall, due to uncertainties in the amplitude of solar cycle variation, the three published TSI composites exhibit conflicting decadal trends (Sect. 6.2.1). The TSI from the reconstruction is a significantly closer match to the PMOD composite than to the ACRIM and IRMB time series, replicating most of the variability ($R^2 = 0.92$), including the solar cycle variation (Fig. 6.2b). Reconstructed TSI also exhibits excellent agreement with the measurements from individual instruments such as ACRIM3, TIM and VIRGO. In particular, the record produced by the PMO6V⁹ radiometer on VIRGO ($R^2 = 0.96$). The secular decline between the 1996 and 2008 solar cycle minima in VIRGO radiometry is reproduced to within 0.05 Wm^{-2} (Fig. 6.2a). This agreement between SATIRE-S TSI and VIRGO radiometry, which extends all of solar cycle 23 and on to the present, is signif-

⁸In full, the Kitt Peak Vacuum Telescope (KPVT), the Michelson Doppler Imager onboard the Solar and Heliospheric Observatory (SoHO/MDI), and the Helioseismic and Magnetic Imager onboard the Solar Dynamics Observatory (SDO/HMI).

⁹VIRGO TSI is actually given by the combination of the measurements from two onboard radiometers, DIARAD and PMO6V. The solar cycle variation in the DIARAD and PMO6V records is nearly identical but they do differ at rotational timescales resulting in very different results for the correlation on comparison with other measurements or models.

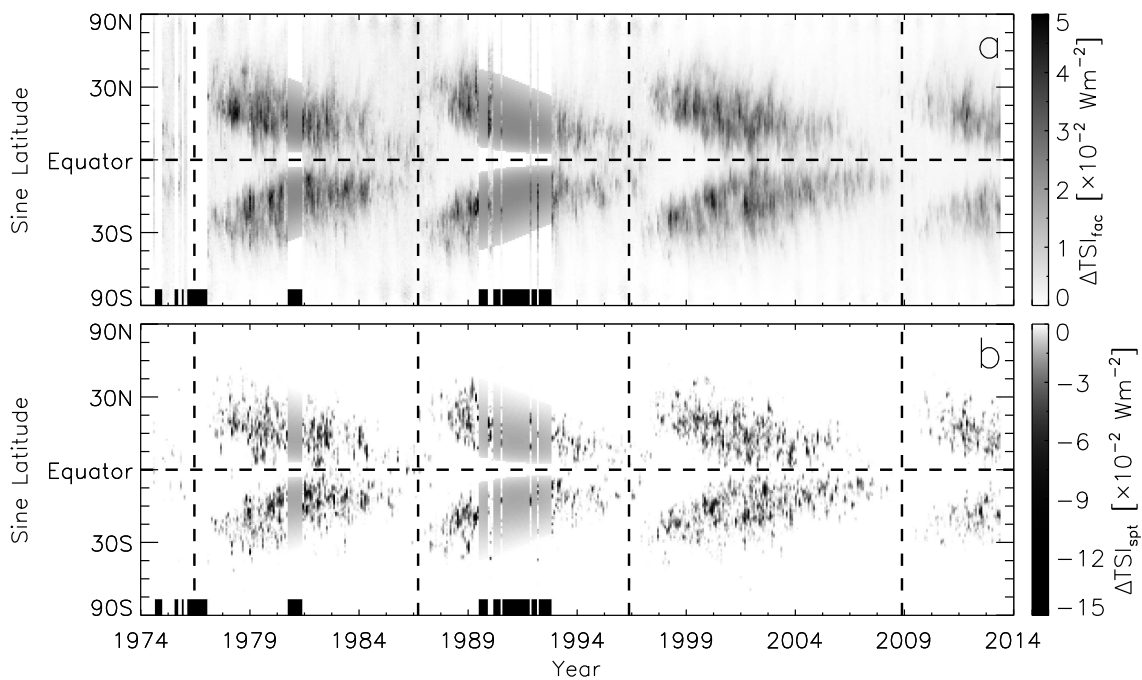


Figure 6.11: Variation in TSI from a) faculae brightening, $\Delta\text{TSI}_{\text{fac}}$ and b) sunspot darkening, $\Delta\text{TSI}_{\text{spt}}$ in the SATIRE-S model, as a function of time and latitude (the monthly average in sine latitude intervals of 0.01). The black bars along the horizontal axes mark the months with no values from the lack of suitable magnetogram data. The gaps around the maxima of solar cycles 21 and 22 are filled by the interpolation. The horizontal and vertical dashed lines denote the equator and position of solar cycle minima, respectively. Adapted from Yeo et al. (2014b).

icant. It implies that at least 96% of the variability in solar irradiance, over this period, including the secular variation between the 1996 and 2008 solar cycle minima can be explained by solar surface magnetism alone.

The bolometric facular brightening and sunspot darkening, $\Delta\text{TSI}_{\text{fac}}$ and $\Delta\text{TSI}_{\text{spt}}$ (with respect to the TSI level of the magnetically quiet Sun, which emerges in the computation), binned and averaged by month and sine latitude, is expressed in Fig. 6.11. Since solar surface magnetism is concentrated in active regions, it follows then that the latitudinal distribution of the associated intensity excess/deficit demonstrate Spörer’s law, resembling butterfly diagrams of sunspot area/position and magnetic flux (for example, Figs. 4 and 14 in Hathaway 2010). A diagram similar to Fig. 6.11b, based on the PSI, was recently presented by Fröhlich (2013).

Since sunspots are largely absent around solar cycle minima, the minimum-to-minimum variation in SATIRE-S TSI is dominantly from the change in facular brightening. In Fig. 6.12, we illustrate the latitudinal distribution of faculae brightening at the last three solar cycle minima, obtained from the butterfly diagram (Fig. 6.11a). Around the 1986 solar cycle minimum, facular brightening is elevated close to the equator, around mid-latitudes, and towards high latitudes (red curve). The broad peak near the equator and at mid-latitudes correspond to active regions associated with the preceding cycle and the

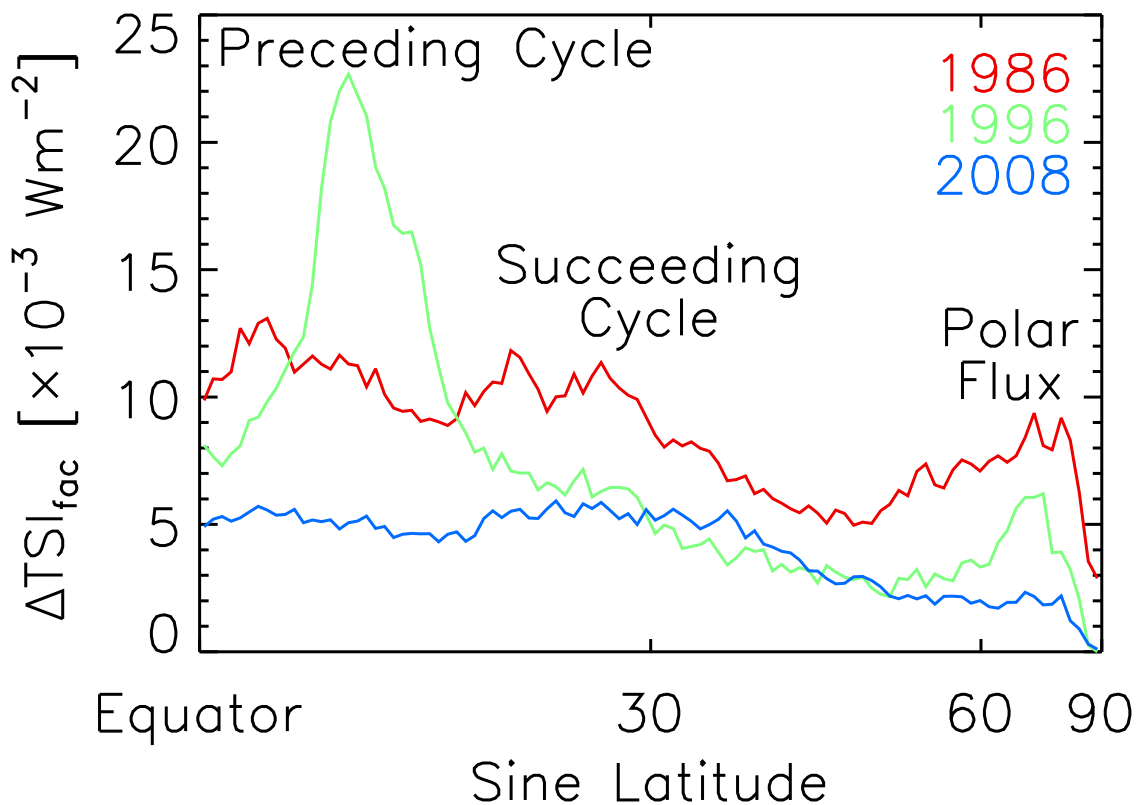


Figure 6.12: Latitudinal distribution of facular brightening ($\Delta\text{TSI}_{\text{fac}}$) in SATIRE-S at the 1986, 1996 and 2008 solar cycle minima, taken from Fig. 6.11a. Facular brightening is influenced by active regions in the low and mid-latitudes (associated with the preceding and succeeding solar cycles, respectively), and polar flux at high latitudes. Adapted from Yeo et al. (2014b).

succeeding cycle, respectively. The increase towards high latitudes relate to magnetic elements transported polewards by meridional circulation over the course of the previous cycle (i.e., polar flux). Comparing the latitudinal distribution at the three solar cycle minima depicted, the minimum-to-minimum trend in faculae brightening (and therefore TSI) is modulated by the prevailing magnetic activity in the three latitude regions. The low flat profile of the blue curve, which corresponds to the 2008 solar cycle minimum, reflects the near-complete absence of any form of activity during this period, which contributed significantly to the secular decline between the 1996 and 2008 solar cycle minima.

As discussed in Sect. 6.2.2, ultraviolet solar irradiance (120 to 400 nm) measurements exhibit similar rotational variability but diverge in terms of the amplitude of solar cycle variation, especially above 240 nm, and between *SORCE* and pre-*SORCE* missions. Consequently, while the SATIRE-S reconstruction reproduces the rotational variability in ultraviolet solar irradiance observations from the *UARS* and *SORCE* missions, in terms of the variation over the solar cycle, it replicates certain records better than others (Fig. 6.4). It reproduced the solar cycle variation in *SUSIM* spectrometry between 115 and 240 nm, and in *UARS/SOLSTICE* and *SORCE/SOLSTICE* measurements between 115 and 180 nm. The reconstruction is also a very close match to the empirical model by Morrill

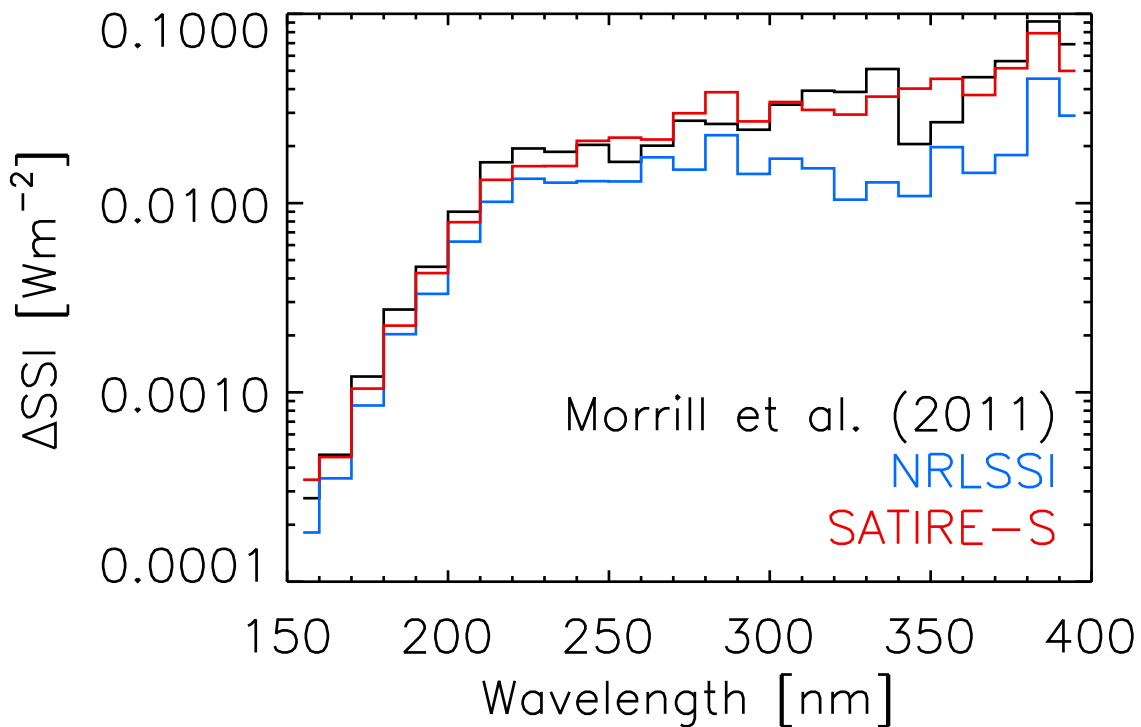


Figure 6.13: The change in solar irradiance (ΔSSI), integrated over 10 nm intervals, between 2000 and 2008 (solar cycle maximum and minimum), in the Morrill et al. (2011), NRLSSI and SATIRE-S models. Adapted from Yeo et al. (2014b).

et al. (2011). (This model, based on matching the Mg II index to SUSIM SSI, represents an estimation of SUSIM-like spectrometry over the wavelength range of 150 to 400 nm.) Notably, the amplitude of solar cycle variation is similar, even above 240 nm (Figs. 6.7 and 6.13). The reconstruction also replicated the rotational variability in SIM SSI over the entire wavelength range of the record (240 to 2416 nm) but not the overall trend (Fig. 6.5). It is worth noting here that there is no model reported thus far that is able to replicate the solar cycle variation in SIM SSI and TSI simultaneously.

The Lyman- α irradiance of the reconstruction reproduces most of the variability ($R^2 = 0.94$), including the solar cycle trend (Fig. 6.14a), in the LASP Lyman- α composite (Woods et al. 2000). The Mg II index taken from the reconstruction is also highly correlated to the competing Mg II index composites by LASP (Viereck et al. 2004, Snow et al. 2005b), and by IUP (Viereck and Puga 1999, Skupin et al. 2005c,b), in particular the latter ($R^2 = 0.96$). It was, however, less successful in replicating the decadal trend (Fig. 6.14b). That said, it did reproduce, to within model uncertainty, the secular decline between the 1996 and 2008 solar cycle minima in the IUP Mg II index composite.

6.3.3.2 Other present-day models

The present-day models capable of returning the full solar spectrum, with the exception of the SRPM, are broadly consistent with one another. There are some differences, most notably in terms of the spectral dependence of the cyclic variability (Fig. 6.7). In this

6 Solar cycle variation in solar irradiance

(The contents of this chapter are identical to the submitted version of Yeo, K. L., Krivova, N. A., Solanki, S. K., 2014, *Solar cycle variation in solar irradiance*, *Space Sci. Rev.*, online.)

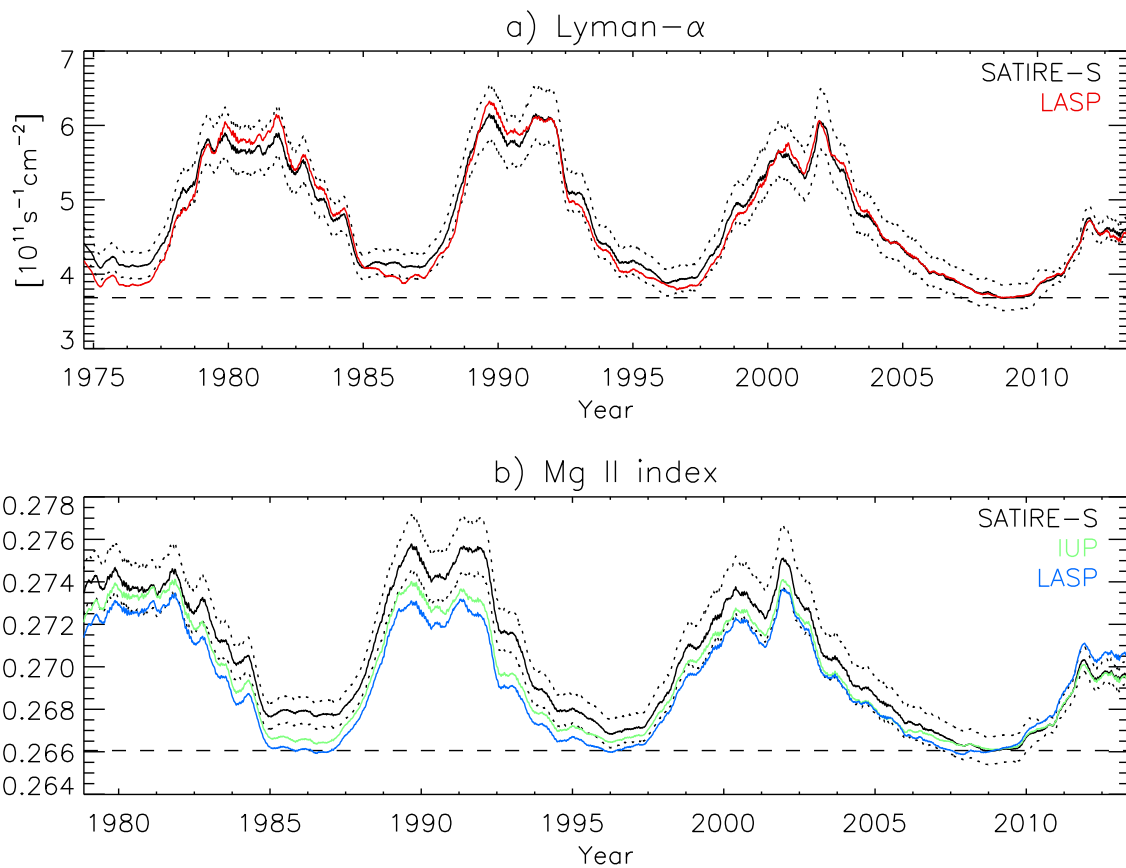


Figure 6.14: a) The Lyman- α irradiance and b) Mg II index based on the SATIRE-S reconstruction of SSI (black solid lines). The reconstruction uncertainty is denoted by the dotted lines. Also illustrated, the LASP Lyman- α composite (red), and the IUP (green) and LASP (blue) Mg II index composites, regressed to the rotational variability and offset to the 2008 solar cycle minimum level (dashed lines) in the respective SATIRE-S time series. All the time series were smoothed with a 181-day boxcar filter. Adapted from Yeo et al. (2014b).

section, we will give a brief description of the NRLSSI, SRPM, OAR and COSI models, and highlight the key discrepancies between these models and SATIRE-S.

The NRLSSI (Lean et al. 1997, Lean 2000) describes the effect of sunspot darkening and faculae brightening on a model spectrum of the quiet Sun. The time evolution of sunspot darkening is given by the PSI calculated from sunspot area records, and facular brightening by the Ca II K, Mg II and F10.7 indices. In the ultraviolet (120 to 400 nm), the variation in solar irradiance is inferred from the multivariate regression of the index data to the rotational variability in UARS/SOLSTICE SSI (by first detrending both index and solar irradiance data). Above 400 nm, it is given by the sunspot and faculae contrast (as a function of wavelength) model from Solanki and Unruh (1998), modulated in time by the index data.

The models discussed here, apart from the SRPM, all see reconstructed SSI varying in phase with the solar cycle in the ultraviolet and visible (Fig. 6.7). In the infrared,

facular contrast is weak (and depending on the model, negative at certain wavelengths), allowing sunspot darkening to dominate, such that the overall level at activity maximum can be lower than at minimum (illustrated for SATIRE-S in Fig. 6.5d). Depending on the computed sunspot/faculae contrast adopted by the various models, they differ in the wavelength range and strength of this effect (see Fig. 7 in Ermolli et al. 2013). This effect is relatively weak in the NRLSSI such that the integrated flux over the shortwave-infrared (1000 to 2416 nm) still varies in phase with the solar cycle, contrary to the other models (Fig. 6.7). The variation over the solar cycle between 240 and 400 nm is also weaker, almost half of that in SATIRE-S, attributed to confining the regression to rotational variability (Ermolli et al. 2013). The consistency between SATIRE-S and the SUSIM-based model of Morrill et al. (2011) gives further support to the amplitude of solar cycle variation in the ultraviolet exhibited by these two models (Fig. 6.13). While SATIRE-S replicates the secular decline between the 1996 and 2008 solar cycle minima in VIRGO TSI radiometry (Fig. 6.2a), the NRLSSI does not as this minimum-to-minimum variation is absent in the Mg II index composite employed (the one released by LASP, Fig. 6.14b).

The SRPM denotes the set of data and tools for semi-empirical modeling of solar irradiance, including a non-LTE spectral synthesis code, developed by Fontenla et al. (1999, 2004, 2006, 2009, 2011). Currently, the package features semi-empirical model atmospheres for nine solar surface components, namely, quiet Sun internetwork, quiet Sun network lane, enhanced network, plage, bright plage, sunspot umbra and sunspot penumbra (presented in Fontenla et al. 2009), and dark quiet Sun internetwork and hot facula (introduced in Fontenla et al. 2011, but not incorporated into the solar irradiance reconstruction reported by the authors). Earlier SRPM reconstructions (or indeed, all other models) cannot replicate the strong decline in the ultraviolet or the accompanying increase in the visible, in apparent anti-phase with the solar cycle, registered by SIM between 2004 and 2008 (Sect. 6.2.2). Fontenla et al. (2011) took this to indicate that the temperature gradient inside small-scale magnetic concentrations might be steeper than previous estimations and proceeded to adjust the temperature stratification of the model atmospheres introduced in Fontenla et al. 2009 (see Fig. 1 in Fontenla et al. 2011). The solar irradiance reconstruction presented, extending 2000 to 2009, is based on these modified model atmospheres and filling factors for the various components derived from full-disc images (in the visible red and Ca II K) acquired with the Precision Solar Photometric Telescope, PSPT at OAR (Coulter and Kuhn 1994, Ermolli et al. 1998).

The modifications to the Fontenla et al. (2009) model atmospheres did result in reconstructed visible solar irradiance varying in anti-phase with the solar cycle. However, the solar cycle variation in the ultraviolet is still weaker than what was registered by SORCE/SOLSTICE. The model thus failed to reproduce the solar cycle variation in measured TSI, which all the other present-day models are able to do with reasonable success. All these shortcomings were taken by the authors to imply that the number of solar surface components is insufficient.

The full-disc images recorded with the PSPT at OAR were also employed in the series of proxy and semi-empirical reconstructions of solar irradiance reported by the OAR team (Penza et al. 2003, Domingo et al. 2009, Ermolli et al. 2011). Work on a new semi-empirical model is in progress (Ermolli et al. 2013). This latest effort considers the seven solar surface components defined in Fontenla et al. (2009). The filling factors were obtained from PSPT observations spanning the period of 1997 to 2012 following Ermolli

et al. (2010). The intensity spectra corresponding to each component were calculated with the Fontenla et al. (2009) model atmospheres (without the more recent modifications introduced by Fontenla et al. 2011) using the non-LTE spectral synthesis code RH¹⁰ (Uitenbroek 2002). The computation is therefore, apart from employing the Fontenla et al. (2009) model atmospheres as is, broadly analogous to the SRPM reconstruction presented by Fontenla et al. 2011.

In the ultraviolet and visible, the OAR reconstruction is consistent with NRLSSI, SATIRE-S and COSI, exhibiting a similar disparity with SIM SSI (Fig. 6.7). Also in line with these other models, the reconstruction replicates most of the variability in TSI observations (specifically, TIM radiometry and the PMOD composite). In apparent contradiction to the conclusion of Fontenla et al. (2011), the agreement with measured TSI suggests that the seven solar surface components described in Fontenla et al. (2009) are sufficient for the semi-empirical modeling of (at least) TSI. This also supports the conclusions of Ball et al. (2011), DeLand and Cebula (2012), Lean and DeLand (2012), Unruh et al. (2012), Yeo et al. (2014b), that the discrepancy between SIM SSI and models arise from unaccounted instrumental effects in SIM observations, than any indication that a significant rethink in how solar irradiance is modelled in current models is necessary (discussed in Sect. 6.2.2).

The non-LTE spectral synthesis code COSI (Haberreiter et al. 2008, Shapiro et al. 2010) has been utilised to generate intensity spectra of solar surface components for semi-empirical modeling of solar irradiance (Haberreiter et al. 2005). The current implementation utilizes intensity spectra generated with the model atmospheres by Fontenla et al. (1999). These were applied to sunspot number, ¹⁰Be and neutron monitor data to reconstruct solar irradiance back to the Maunder minimum period and over the Holocene (at 1-year and 22-year cadence, respectively, Shapiro et al. 2011), and to SRPM PSPT-based filling factors covering a two week period in 2010 (Shapiro et al. 2013).

Contrary to the NRLSSI, SATIRE-S and OAR models, the Shapiro et al. (2011) reconstruction varied in anti-phase with the solar cycle in the near-infrared (700 to 1000 nm, Fig. 6.7), accompanied and compensated by an enhanced variability in the ultraviolet. This is attributed to the use of a single model atmosphere for sunspots, and for plage (so not distinguishing between sunspot umbra and penumbra, and plage and bright plage, Ermolli et al. 2013). In response, Shapiro et al. (2013) reduced sunspot and plage contrast in such a manner that brought the reconstruction presented into alignment with SORCE/SOLSTICE measurements in the Herzberg continuum (190 to 222 nm). A more comprehensive approach is in development.

6.4 Reconciling measurements and models

6.4.1 Proxy models

Solar irradiance observations, in particular SSI, suffer non-trivial uncertainty in the long-term stability (Sect. 6.2). As mentioned in Sect. 6.3.2, in the regression of indices of solar activity to observations, certain proxy models confine the fitting to rotational variability

¹⁰Based on the work of, and abbreviated after Rybicki and Hummer (1991, 1992).

to circumvent bias from instrumental trends, implicitly assuming that the relationship between the two is similar at all timescales.

Rotational variability in solar surface magnetism is dominated by active regions, and at longer timescales, by the magnetic flux distributed in the quiet Sun. The response of chromospheric indices to magnetic flux in active regions and quiet Sun is, evidently, not the same (Tapping 1987, Solanki and Krivova 2004, Ermolli et al. 2010, Foukal et al. 2011). The weak solar cycle variation in the ultraviolet in the NRLSSI highlights the limitation of applying the relationship between chromospheric indices and solar irradiance at rotational timescales to longer timescales.

The NRLSSI also does not replicate the secular decline between the 1996 and 2008 solar cycle minima in VIRGO TSI radiometry as it is absent in the LASP Mg II index composite. Fröhlich (2009, 2012, 2013) attributed the discrepant decadal trend in the LASP Mg II index composite and VIRGO TSI to a possible cooling/dimming of the photosphere between the two solar cycle minima. This disparity is more likely related to the non-linear relationship between chromospheric indices and solar irradiance, discussed in the previous paragraph (Foukal et al. 2011), and the uncertainty in the long-term stability of Mg II index data. While the LASP Mg II index composite is effectively level between the 1996 and 2008 solar cycle minima, the competing composite by IUP does exhibit a secular decline (Fig. 6.14b). This minimum-to-minimum drop in the IUP composite is replicated in the Mg II index produced from the SATIRE-S reconstruction, the TSI from which reproduces the secular decline in VIRGO TSI (Sect. 6.3.3.1). The discrepancy between the IUP and LASP composites demonstrates the sensitivity of the apparent decadal trend, even in a quantity as robust to instrumental effects as the Mg II index, to the long-term stability.

The rigorous reconstruction of solar irradiance through proxy models would require a greater understanding of the relationship between indices of solar activity and solar irradiance, and of the long-term stability in index data (still largely unknown).

6.4.2 Semi-empirical models

Present-day semi-empirical models (reviewed in Sect. 6.3.3) all employ one-dimensional or plane-parallel model atmospheres. Various studies have pointed out that the intensity spectra synthesized from one-dimensional representations of the spatially inhomogeneous solar atmosphere do not necessarily reflect the true average property (Uitenbroek and Criscuoli 2011, Holzreuter and Solanki 2013).

The intensity contrast of network and facular magnetic features varies with distance from disc centre and magnetic field strength. In SATIRE-S, the magnetic field strength dependence is included by scaling the faculae filling factor of non-sunspot image pixels above the magnetogram noise floor by the magnetogram signal (up to a saturation level, the free parameter in the model, Fligge et al. 2000). For the SRPM, OAR and COSI models, which employ full-disc Ca II K images as a proxy of magnetic field strength, after identifying sunspots, the rest of the solar disc is segmented into multiple components. These measures are not only empirical but also do not account (at least not fully) for the observation that the continuum and line core intensity contrast of small-scale magnetic concentrations scale differently with magnetogram signal (Yeo et al. 2013). As set out by Unruh et al. (2009), three-dimensional model atmospheres would allow the possibility to

relate the appropriate calculated intensity spectra to the magnetogram signal or Ca II K intensity directly.

At present, the centre-to-limb variation of the intensity of solar surface components is accounted in semi-empirical models by generating the intensity spectra at varying limb angles (by rotating the respective model atmospheres). In the continuum, the intensity contrast of small-scale magnetic elements increases with distance from disc centre before declining again close to the limb. The converse is observed within spectral lines, the difference coming primarily from the differing interaction between the line-of-sight and magnetic flux tubes at the continuum and spectral lines formation heights (Yeo et al. 2013). In employing one-dimensional model atmospheres, we do not capture these effects.

Three-dimensional model atmospheres based on observations (Socas-Navarro 2011) and magnetohydrodynamics (MHD) simulations (Vögler 2005), while growing in sophistication and realism, cannot as yet reproduce observations at all heights (Afram et al. 2011). A limiting factor is our understanding of the effects of spatial resolution (that is, the point spread function and how it is sampled by the imaging array) on observations (Danilovic et al. 2008, 2013, Röhrbein et al. 2011). This is especially severe for the small-scale magnetic elements which make up network and faculae, largely unresolved in current observations. The increasing availability of atmospheric seeing free observations from space and balloon-borne missions, in particular high spatial resolution imagery such as those from SUNRISE (Solanki et al. 2010, Barthol et al. 2011), will provide stringent constraints on model atmospheres. Space and balloon-borne telescopes have the advantage that the point spread function can be well constrained (Mathew et al. 2007, 2009, Wedemeyer-Böhm 2008, Yeo et al. 2014a), rendering them particularly useful for this purpose.

Another source of uncertainty is the treatment of non-LTE effects, which are highly complex and not fully understood. As a matter of necessity, the SATIRE-S, SRPM, OAR and COSI models take varying approximations to include non-LTE effects. While inexact, the one-dimensional model atmospheres and non-LTE approximations employed in present-day semi-empirical models are a practical necessity. As these simplifications are tested against and so constrained by observations, the output from current models are still reasonably realistic, demonstrated by the broad consistency between reconstructed solar irradiance and measurements (Sect. 6.3.3).

6.5 Summary

The TSI observations from the succession of radiometers sent into space since 1978 readily reveal solar cycle modulation. The records from the various instruments however, differ in terms of the absolute level and the apparent amplitude of solar cycle variation, chiefly from the difficulty in accounting for instrument degradation. With the collaborative efforts of various teams, the absolute radiometry of present-day instruments is converging. The uncertainty in the long-term stability is evident in the conflicting decadal trends exhibited by the three published TSI composites.

Like TSI, ultraviolet (120 to 400 nm) solar irradiance has been monitored from space, almost without interruption, since 1978. Spectrometry is obviously a more complicated

measurement, the uncertainty in the absolute radiometry and the amplitude of solar cycle variation is more severe than with TSI. Compounded by the wavelength dependence of instrumental influences, this translates into uncertainty in the spectral dependence of the cyclical variability. The problem is particularly acute above 240 nm, and between measurements from the *SORCE* satellite and preceding missions.

The SIM instrument onboard *SORCE* provides what is still the only extended (2003 to 2011) and radiometrically calibrated record of SSI spanning the ultraviolet to the infrared (240 to 2416 nm) available. The measurements from the first few years of operation (2003 to 2008) saw ultraviolet solar irradiance declining almost twice as rapidly as TSI, and visible solar irradiance ascending, in apparent anti-phase with the solar cycle. These trends conflict with the projections from other measurements and models (except for Fontenla et al. 2011). Looking at the full period, the overall trend shows no obvious solar cycle modulation. The total flux recorded by the instrument, which surveys a wavelength range responsible for more than 97% of the power in solar radiative flux, also fails to replicate the solar cycle variation evident in TSI.

Satellite monitoring of solar irradiance has been accompanied by the development of models aimed at recreating the observed variability. Solar irradiance is modulated by photospheric magnetism from its effect on the thermal structure and consequently the radiant behavior of the solar surface and atmosphere. Models of solar irradiance based on the assumption that variations at timescales greater than a day are driven by solar surface magnetism have achieved considerable success in replicating observations.

There are two broad categories of solar irradiance models, termed proxy and semi-empirical. Proxy models are based on the regression of indices of solar activity to solar irradiance observations. Semi-empirical models employ the intensity spectra of various types of solar surface features (calculated with spectral synthesis codes from semi-empirical model atmospheres) to reconstruct the solar spectrum from the apparent surface coverage of these feature types (derived from index data or full-disc observations).

We discussed the present-day models capable of returning the full solar spectrum; NRLSSI, SATIRE-S, SRPM, OAR and COSI. Apart from the NRLSSI, these models adopt the semi-empirical approach.

In the regression of index data to solar irradiance observations, certain proxy models including the NRLSSI (in the ultraviolet) restrict the fitting to the rotational variability to factor out any bias from the uncertainty in the long-term stability of the solar irradiance measurements employed. In doing so, these models implicitly assume that the relationship between chromospheric indices (utilized in these models as a proxy of faculae brightening) and solar irradiance at rotational timescales is applicable to longer timescales. Likely a consequence of the fact that the relationship between chromospheric indices and solar irradiance is really non-linear, the amplitude of solar cycle variation in the ultraviolet in the NRLSSI is weaker than in other present-day models.

Another limitation of the proxy approach is the fact that the reconstructed solar irradiance adopts the variability of the index records used in the reconstruction, along with the associated uncertainty. The uncertainty in the long-term stability of Mg II index data was argued to be the probable reason why the NRLSSI does not replicate the secular decline between the 1996 and 2008 solar cycle minima in *VIRGO* TSI radiometry.

The SRPM reconstruction of solar irradiance presented by Fontenla et al. (2011) is the only where visible flux varied in anti-phase with the solar cycle, in qualitative agreement

6 Solar cycle variation in solar irradiance

(The contents of this chapter are identical to the submitted version of Yeo, K. L., Krivova, N. A., Solanki, S. K., 2014, Solar cycle variation in solar irradiance, Space Sci. Rev., online.)

with early SIM observations. This was achieved with modifications to the temperature stratification in the Fontenla et al. (2009) model atmospheres. However, the TSI from the reconstruction failed to replicate the solar cycle variation in measured TSI. The other models reviewed see visible solar irradiance varying in-phase with the solar cycle and reproduced TSI variability, including the solar cycle modulation, with reasonable success. Significantly, the OAR computation is, apart from the use of the Fontenla et al. (2009) model atmospheres without any modifications, largely analogous to the Fontenla et al. (2011) study in terms of the approach.

Considering the role of photospheric magnetism in driving variations in solar irradiance, the increase in the visible registered by SIM during its early operation, coming at a time where solar activity is declining, requires that small-scale magnetic concentrations be darker than the quiet Sun in this spectral region. However, our current understanding of the radiant properties of these solar surface features point to the converse.

Apart from the NRLSSI, the semi-empirical model SATIRE-S, recently updated by Yeo et al. (2014b), gives the only other daily reconstruction of the full solar spectrum from present-day models to cover multiple solar cycles (1974 to 2013). Of the three competing and conflicting TSI composites, the model found the greatest success in replicating the solar cycle variation in the PMOD composite. The TSI reconstruction is also a good match to present-day measurements, reproducing about 95% of the variability in the PMO6V record and the secular decline between the 1996 and 2008 solar cycle minima in VIRGO radiometry. The SSI reconstruction reproduced the rotational variability in UARS and SORCE spectrometry, and the cyclical variability in certain records below 240 nm. Above 240 nm, as the amplitude of solar cycle variation is poorly constrained in current measurements, SATIRE-S, as with all other models, cannot exactly replicate SORCE solar cycle variation. The amplitude of solar cycle variation between 240 and 400 nm in the reconstruction is however, matches closely to the empirical model of Morrill et al. (2011), which represents an approximation of SUSIM-like SSI with the long-term stability corrected to that of the Mg II index. The model also replicates the solar cycle variation in the LASP Lyman- α composite, and the secular decline between the 1996 and 2008 solar cycle minima in the IUP Mg II index composite.

The intensity spectra of solar surface features employed in present-day semi-empirical models are derived from one-dimensional model atmospheres, which do not capture all the complexities of the radiant behaviour of the solar surface and atmosphere. Three-dimensional model atmospheres, though increasingly realistic, still cannot reproduce observations at all heights. Their development is impeded by the limited availability of high spatial resolution observations, and the challenge in understanding instrumental influences on apparent radiance. Current semi-empirical models also include non-LTE effects by various approximations. Constrained by observations, the intensity spectra of solar surface features generated from one-dimensional model atmospheres and present non-LTE schemes, while not exact, are sufficiently reliable for the intended purpose. This is demonstrated by the broad consistency between the various semi-empirical models, and their success in replicating measurements.

The direct observation of solar irradiance is a challenging endeavour. While the body of spaceborne measurements is still afflicted by uncertainties in the absolute radiometry, secular variation and spectral dependence of the cyclical variability, one cannot discount the considerable progress made over the past four decades with the collective effort of the

community. Models of solar irradiance based on solar surface magnetism have proved to be an able complement, augmenting our understanding of the observations and the physical processes underlying solar cycle variation in solar irradiance. While open questions remain, continual observational and modeling efforts will undoubtedly see the emergence of a more cohesive picture of solar cycle variation in solar irradiance.

7 Summary and outlook

This thesis is the compilation of four publications (each forming a chapter), detailing investigations into the nature of variations in solar irradiance over the 11-year activity cycle of the Sun. They are summarized below in the order presented in the thesis.

Chapter 3: Yeo, K. L., Solanki, S. K., Krivova, N. A., 2013, Intensity contrast of network and faculae, *Astron. Astrophys.*, 550, A95

In this work, we examined the relationship between the intensity contrast of network and faculae, in the continuum and core of the Fe I 6173 Å line in full-disc SDO/HMI observations, with disc position and magnetogram signal. Never before has any other solar telescope been able to return simultaneous, atmospheric seeing free, full-disc measurements of intensity and magnetic flux density at similar spatial resolutions or noise level (Chap. 1.2). So, while similar studies have been reported in the literature, the image quality of HMI data gave us the chance to look at the disc position and magnetogram signal dependence of the intensity contrast of network and faculae at unprecedented accuracy and detail, particularly in the line core (which was, up to this study, largely unstudied).

The results from this study and preceding investigations into the continuum intensity contrast of network and faculae exhibit significant discrepancies. In the case of the analogous study by Ortiz et al. (2002) with SoHO/MDI (the predecessor instrument to the HMI) data, this is due to the fact that we had taken care to exclude image pixels around sunspots and pores, where the apparent magnetogram signal is affected by stray light from and the magnetic canopy of these features, from consideration. Comparing the results obtained around disc centre from the various studies, we argued that the spread in apparent magnetogram signal dependence is largely due to differences in spatial resolution.

Not surprisingly, the radiant behaviour of network and faculae in the continuum and in the line core, formed at different heights, is very different. The most notable divergence is the converse centre-to-limb variation. While the intensity contrast in the continuum increases away from disc centre before decreasing again near the limb, in the line core, the intensity contrast is strongest at disc centre and declines monotonically towards the limb. This is due to the steeper temperature gradient and Zeeman splitting within magnetic concentrations, and the different mechanisms by which apparent contrast is modulated by viewing geometry at the continuum and spectral line formation heights.

Earlier works had shown, but only indirectly, that variation in solar irradiance is the sum manifestation of changes in the continuum and within spectral lines. From the data set, we derived empirical relationships relating the intensity contrast in the continuum and line core to the heliocentric angle and magnetogram signal. Using a simple model based

on these relationships, we demonstrated that the variation in total solar irradiance during a three-week period in 1996, where only a single active region is visible on the solar disc, can only be explained if we consider facular contrast in both the continuum and the line core.

The study also provided further evidence that magnetic elements in quiet Sun network have a higher heating efficiency than the facular counterpart, as implied by the higher intensity contrast per unit magnetogram signal there.

Since looking at the variation in intensity contrast with magnetic field strength obviously requires co-temporal and co-spatial measurements of intensity and magnetic field, studies have largely relied on such observations from magnetographs and so mostly confined to the visible part of the spectrum. (With few exceptions, magnetographs are designed to observe the photosphere and therefore operate in the visible.) The intensity contrast of network and faculae (and therefore their contribution to variation in solar irradiance) is highest in the ultraviolet from how the Planck function responds to temperature. Yet, the relationship between the intensity contrast in the ultraviolet with magnetic field strength is not nearly as well studied as in the visible (Berger et al. 2007, Viticchié et al. 2010).

In order to plug this gap in our knowledge, it will be of interest to extend this study, examining

- HMI magnetograms together with the concurrent full-disc ultraviolet filtergrams from AIA (Atmospheric Imaging Assembly, also onboard SDO, Lemen et al. 2012), and the
- co-temporal magnetic field and ultraviolet intensity observations from the IMAx magnetograph (Imaging Magnetograph eXperiment, Martínez Pillet et al. 2011) and the SuFI filtergram instrument (SUNRISE Filter Imager, Gandorfer et al. 2011) onboard the SUNRISE balloon-borne observatory.

The AIA surveys three narrow passbands between 304 and 1700 Å, and SuFI, five between 2140 and 3968 Å, formed at different heights in the solar atmosphere between the photosphere and the transition region¹. The observations from SUNRISE are not only free from atmospheric seeing but are also at the highest spatial resolutions achieved to date. They reveal the fine structure of the small-scale magnetic concentrations that make up network and faculae, largely unresolved in preceding observations, at an unsurpassed level of detail (Lagg et al. 2010, Riethmüller et al. 2013). The spatial resolution of AIA is also the highest of full-disc solar telescopes operating in a similar wavelength range. The co-temporal magnetic field and ultraviolet intensity measurements from SDO and from SUNRISE are well-suited for the intended purpose, covering a wide range of heights in the solar atmosphere at unprecedented spatial resolutions and atmospheric seeing free quality.

The complex radiant behaviour of network and faculae uncovered in this study is not completely represented in present-day semi-empirical models of solar irradiance, primarily due to the use of one-dimensional model atmospheres. Three-dimensional model atmospheres have not reached the maturity required for use in such models. As discussed

¹The AIA has a total of nine passbands, the other six, located between 94 and 335 Å, are formed in the corona.

in Chap. 6.4.2, while they are increasingly realistic, current three-dimensional model atmospheres cannot replicate observations at all heights. This renders the extension of this study to AIA and SUNRISE data all the more pertinent. The results of this investigation form a stringent constraint on three-dimensional model atmospheres at the HMI wavelength, 6173 Å. Such an endeavour will however, also require an understanding of the effects of stray light on the apparent intensity contrast in HMI observations, investigated in the following publication.

Chapter 4: Yeo, K. L., Feller, A., Solanki, S. K., Couvidat, S., Danilovic, S., Krivova, N. A., 2014, Point spread function of SDO/HMI and the effects of stray light correction on the apparent properties of solar surface phenomena, *Astron. Astrophys.*, 561, A22

Here, we reported an estimate of the PSF of the HMI instrument and examined the effects of restoring HMI data for the influence of straylight by the deconvolution of this PSF. We modelled the PSF as a bivariate function of radial distance and azimuth, recovering the anisotropy of the underlying stray light behaviour. This is a departure from preceding efforts with other spaceborne solar telescopes, which had for simplicity assumed isotropy (i.e., modelling the PSF as a function of radial distance alone). The anisotropic PSF was demonstrated to perform better than an isotropic solution for stray light removal. It was also verified by comparing the image contrast in restored HMI data and in artificial solar images generated from a MHD simulation.

Restoring HMI observations for stray light with the retrieved PSF had a pronounced effect on the apparent intensity, magnetic field strength and line-of-sight velocity. Of particular relevance to solar irradiance studies is the effect on small-scale magnetic concentrations.

Image restoration decreased the surface area and increased the magnetic field strength of network and faculae. It also recovered otherwise undetectable magnetic features smeared below the noise floor by stray light. Overall, the apparent amount of magnetic flux, at least in the HMI data examined, increased by about 20%, most of it arising in the quiet Sun. The greater influence on quiet Sun network simply reflects the fact that the magnetic features there, generally smaller than those in active region faculae, are more affected by stray light. The observation that network elements have a higher heating efficiency than faculae and are also more obscured by stray light is not accounted in present-day models of solar irradiance that rely on full-disc imagery. The contribution by the network to variation in solar irradiance might therefore be underestimated in these models.

The PSF was recovered from observations of Venus in transit from one of the two CCDs in the instrument. It therefore represents the stray light property of this particular CCD at the time of the transit and the position of Venus in the field of view. Another important result of this study is the demonstration that the PSF reported can be applied to the entire field of view, to HMI data from either CCD and from the beginning of regular operation to the time of the study (April 2010 to June 2013) without introducing significant error. In other words, the stray light property of the instrument is sufficiently uniform across the field of view, similar between the two CCDs, and stable in time for this to be the case. Current models of solar irradiance assume that the intrinsic intensity contrast of photospheric magnetic features is invariable over time. Studies investigating

if sunspot contrast varies over the solar cycle have returned conflicting results (see for example, Mathew et al. 2007, Rezaei et al. 2012, Norton et al. 2013, de Toma et al. 2013). The possible time variation of network and faculae contrast is much less studied (Walton et al. 2003, Ortiz et al. 2006, Ermolli et al. 2007). An obstacle had been the lack of stable, extended time series of observations. The finding here that HMI data are, in terms of stray light, relatively stable over the period examined (which encompassed much of the ascending phase of solar cycle 24) demonstrates its suitability for such investigations.

HMI data products (described in Chap. 1.2) are archived and distributed through several repositories such as JSOC and GDC-SDO². We plan to incorporate straylight correction by the deconvolution with the PSF reported here into the HMI data processing pipeline, with the aim to make a straylight-corrected version of the extended, near continuous time series of observations from the instrument available to the scientific community through one or more of these repositories. This will be of utility not only to investigations into the possible time variation of the intrinsic intensity contrast of solar surface features and semi-empirical models of solar irradiance such as the SATIRE-S, but any study that would benefit from accurate full-disc measurements of magnetic flux density, Doppler shift and intensity.

As stated in Chap. 1.4, an overall objective with the two studies discussed so far is to derive the information necessary to make quantitative comparisons of the radiant properties of small-scale magnetic concentrations in HMI data, and in artificial solar observations (of intensity and magnetic field³) synthesized from three-dimensional model atmospheres based on MURaM MHD simulations (Chap. 2.3.4). By blurring such artificial observations with the PSF of HMI, we can compare the relationship between intensity contrast, and disc position and magnetogram signal in the result with that in HMI data (obtained in the first study) directly.

Chapter 5: Yeo, K. L., Krivova, N. A., Solanki, S. K., Glassmeier, K. H., 2014, Reconstruction of total and spectral solar irradiance from 1974 to 2013 based on KPVT, SoHO/MDI and SDO/HMI observations, *Astron. Astrophys.*, **570, A85**

We presented a daily reconstruction of total and spectral solar irradiance, extending from 1974 to 2013, based on the SATIRE-S model.

SATIRE-S had previously been applied to full-disc continuum intensity images and longitudinal magnetograms from the KPVT and SoHO/MDI to reconstruct TSI and SSI between 1974 and 2009. The parameters of the model were adjusted to the data from the two spectromagnetographs operated at the KPVT, and from MDI to combine the model output from the various data sets into a single TSI/SSI time series. This, however, still left some discrepancy in reconstructed spectra based on data from different instruments, which had to be accounted for empirically by regression. The decommissioning of MDI in 2011 also curtailed the possibility of extending these modelling efforts to the present and beyond.

²In full, the Joint Science Operations Center (<http://jsoc.stanford.edu/>) and the German Data Center for SDO (<http://www2.mps.mpg.de/projects/seismo/GDC-SDO/>).

³By generating artificial intensity images at the various HMI bandpass and polarizations (as described in Chap. 4.3.1), and combining them together as done for HMI filtergrams to yield artificial HMI-like magnetograms.

In this study, we made significant improvements to the reconstruction method and extended the model to the present with similar observations from HMI. Of the improvements made, the most important is the more sophisticated cross-calibration of the model input from the various instruments. The magnetogram signal and faculae filling factor in the various data sets were brought into agreement in the periods of overlap between the different instruments (by taking into account non-linearities and variations between solar disc centre and limb) such that they yielded a consistent TSI/SSI time series as the output without the need for any additional adjustment of the reconstructed spectra.

The TSI from the reconstruction exhibited excellent agreement with the observations from the instruments in current operation, in particular, from the PMO6V radiometer on the SoHO/VIRGO experiment (which covers the period from 1996 to the present). The reconstruction reproduced most of the variability ($R^2 = 0.96$) including the secular decline between the 1996 and 2008 solar cycle minima. This result indicates that at least 96% of the variability in solar irradiance over this period, including the secular variation, can be accounted for by photospheric magnetism alone. The reported alignment is all the more significant considering the fact that VIRGO is, of the TSI monitors sent into orbit since 1978, the only to return measurements covering an entire solar cycle minimum-to-minimum; extending all of solar cycle 23 and beyond to the current maximum.

Examining the latitudinal distribution of faculae brightening and sunspot darkening in the model at the last three solar cycle minima (1986, 1996 and 2008), we were able to illustrate, for the first time, the contribution by prevailing magnetism in the low and middle latitudes from active regions, and polar flux at high latitudes, to the minimum-to-minimum trend in TSI. The reconstruction also reproduced the solar cycle variation in the PMOD TSI composite (between 1978 and 2013) and the LASP Lyman- α composite (between 1974 and 2013), confirming the long-term stability of the reconstruction.

Like TSI, ultraviolet solar irradiance has been measured from space regularly since 1978. The measurements from the succession of missions, while broadly consistent at rotational timescales, exhibit discrepant solar cycle variation, especially above 240 nm. The reconstruction replicates the rotational variability in the ultraviolet solar irradiance measurements from the UARS and SORCE missions rather well but had mixed results in terms of the amplitude of solar cycle variation (which is to be expected given the gross scatter in observations). The amplitude of solar cycle variation in the reconstruction is, however, a very close match to that in the Morrill et al. (2011) model, even above 240 nm. This purely data-based model, extending 150 to 400 nm, is an estimation of SUSIM-equivalent SSI, with the long-term stability corrected with the Mg II index as reference. The agreement renders support to the cyclic variability in the SATIRE-S reconstruction.

The observations from SORCE/SIM represent the only extended (2003 to 2011) and continuous, radiometrically calibrated record of SSI covering the ultraviolet to the infrared (240 to 2416 nm) available. As with all other present-day models, the SATIRE-S reconstruction failed to replicate the overall trend in SIM SSI. The spectral range surveyed by SIM is accountable for more than 97% of the power in solar radiation. Therefore, the integrated solar irradiance over this range should reproduce most of the variability in TSI. The total flux recorded by the instrument exhibits little resemblance to concurrent TSI measurements while the integrated solar irradiance over the spectral range of the instrument in the reconstruction replicated most of the variability in ACRIM3, VIRGO and TIM TSI radiometry ($R^2 > 0.88$). This suggests that the discrepancy in the overall trend

between the reconstruction and SIM SSI is likely due to unresolved instrumental effects in the latter, an assertion strengthened in the review discussed next.

The reconstruction is, within uncertainty, an excellent match to observations, providing further evidence that variations in solar irradiance at timescales greater than a day is, if not solely at least predominantly driven by photospheric magnetism. The incorporation of the results from the study on the intensity contrast of network and faculae, and on the PSF of HMI, discussed earlier, into future efforts with SATIRE-S will certainly lead to even more sophisticated, reliable reconstructions of solar irradiance. (For example, the finding that network magnetic features are hotter/brighter than facular magnetic features, and the observations on the influence of sunspots/pores on the apparent magnetogram signal near these features and the effects of stray light on the manifest surface area and magnetic field strength of bright magnetic features.)

Currently, the variation in the intensity of bright magnetic features with magnetic field strength is included in SATIRE-S by the empirical relationship between the faculae filling factor and magnetogram signal described in Chap. 1.3, which introduced the sole free parameter in the model, $\langle\langle B_I \rangle\rangle / \mu_{\text{sat}}$. This is another motivation for the studies detailed in Chaps. 3 and 4, and our aim to reconcile the intensity contrast of small-scale magnetic concentrations and its magnetogram signal dependence in HMI data and in artificial observations synthesized from three-dimensional model atmospheres, discussed earlier in this chapter. As suggested by Unruh et al. (2009), this would allow us to relate the intensity spectra synthesized from said three-dimensional model atmospheres to the magnetogram signal in HMI observations directly, obviating the empirical filling factor model and the associated free parameter.

Apart from the use of plane-parallel model atmospheres, another significant source of uncertainty in SATIRE-S is the assumption of local thermodynamic equilibrium, LTE (see Chap. 2.3.2) and the use of opacity distribution functions, ODFs (Chap. 2.3.3) to represent spectral lines in the ATLAS9 spectral synthesis code. The detrimental effects of these simplifications are largely confined to wavelengths below 300 nm. Incidentally, this is where the variation in solar irradiance with solar activity is strongest (Fig. 6.7) and it is also a critical spectral region for climate models. So, while the empirical correction introduced in this study produced satisfactory results, going forward it is needful to tackle the LTE and ODF simplifications directly.

The approach taken to generate the intensity spectra of solar surface components in SATIRE-S has not been updated since the work of Unruh et al. (1999). Since then, the application of various non-LTE spectral synthesis codes to semi-empirical modelling of solar irradiance has been demonstrated by several groups, reviewed in Chap. 6. These and other similar codes published in the literature differ by the approximations taken to include non-LTE effects and line opacity. A favoured alternative to the use of ODFs is the opacity sampling (OS) approach (described in Chap. 2.3.3), which allows a more accurate account of line opacity, at the expense of computing time. It is our intention to examine the non-LTE and OS schemes reported in the literature, with the eventual aim to employ them in the generation of intensity spectra of solar surface components for solar irradiance modelling.

In order to reconstruct solar irradiance over as long a period as possible, we employed full-disc observations from multiple instruments. Of the instruments considered, MDI has the coarsest spatial resolution and also the highest magnetogram noise level. To compose

the model output based on data from the various instruments into a single, consistent time series, we had to disregard bright magnetic features in the KPVT and HMI data sets that are small and/or weak (in terms of the magnetogram signal) such that they would be undetectable at MDI's spatial resolution and magnetogram noise. Compared to other full-disc spectromagnetographs, the unsurpassed image quality of HMI observations allows prevailing photospheric magnetism to be resolved and quantified as accurately as currently achievable. On top of the proposed enhancements to the SATIRE-S model discussed, a reconstruction based on HMI data alone (optimized to the limits of the HMI instrument rather than that of MDI), though limited in timespan, will be informative of the limit to which variations in solar irradiance can be explained by photospheric magnetism.

Chapter 6: Yeo, K. L., Krivova, N. A., Solanki, S. K., 2014, Solar cycle variation in solar irradiance, *Space Sci. Rev.*, online

In this paper, we reviewed the current state of the measurement and modelling of solar irradiance, and the key challenges in refining present-day models.

While tremendous progress have been made over the past four decades since satellite measurements were first available, the direct observation of solar irradiance is still plagued by considerable uncertainty. Specifically, in terms of the absolute radiometry, the secular variation and the spectral dependence of the variation over the solar cycle. This is due mainly due to the immense challenge in accounting for aging and exposure degradation. For this reason, models of solar irradiance have emerged to become an important complement to measurements, augmenting our understanding not just of the apparent variability but the underlying physical processes.

We reviewed the present-day models that are able to recreate the full solar spectrum, placing the SATIRE-S reconstruction discussed above in the context of contemporary models (namely NRLSSI, SRPM, OAR and COSI).

There are two main approaches to the modelling of solar irradiance, termed proxy and semi-empirical. The models discussed, apart from NRLSSI, take the semi-empirical approach. The SATIRE-S, NRLSSI, OAR and COSI models are broadly consistent with one another, though not without disagreement. Specifically, the NRLSSI and COSI models exhibit discrepant solar cycle variation at certain spectral ranges. We showed that in the case of NRLSSI, these differences are due to shortcomings in the proxy approach, and for COSI certain limitations in the current implementation of the model.

Present-day models, with the exception of SRPM, are successful in reproducing TSI variability but not the overall trend in SIM SSI, in particular, the anti-phase (with the solar cycle) variation in the visible registered by the instrument between 2003 and 2006. The SRPM is the only model where visible solar irradiance varies in anti-phase with the solar cycle. However, the adjustments made to the model to achieve this result almost completely suppressed the solar cycle modulation in the TSI from the reconstruction. From a review of the literature and an examination of the SIM record, we summarized the evidence that the overall trend in SIM SSI is likely dominated by instrumental effects. We also argued that an inverse variation with the solar cycle in the visible is not consistent with our current knowledge of the intensity contrast of network and faculae. All these serve to refute claims that the failure of present-day models, including SATIRE-S, to replicate SIM SSI might be due to a change in the physics of the Sun or gross insufficien-

cies in current models of solar irradiance.

The daily reconstruction of TSI and SSI detailed in this thesis, based on the semi-empirical SATIRE-S model, was shown to be more reliable than the proxy reconstruction provided by the NRLSSI and highly consistent with measurements from multiple instruments. It also extends multiple decades, much longer than the daily reconstructions from contemporary semi-empirical models. This reconstruction is of utility not only to solar irradiance studies but also to climate models (which require solar irradiance inputs). The application of the SATIRE-S reconstruction to climate models, and a comparison of the results with that obtained with other solar irradiance models and measurements, is planned.

A Appendix

A.1 **Yeo, K. L., Solanki, S. K., Krivova, N. A., 2013, Intensity contrast of network and faculae, *Astron. Astrophys.*, 550, A95**

The contents of Chapter 3 are identical to the printed version of Yeo, K. L., Solanki, S. K., Krivova, N. A., 2013, Intensity contrast of network and faculae, *Astron. Astrophys.*, 550, A95. The printed version is reproduced here with permission from Astronomy & Astrophysics, © ESO.

Intensity contrast of solar network and faculae

K. L. Yeo^{1,2}, S. K. Solanki^{1,3}, and N. A. Krivova¹

¹ Max-Planck Institut für Sonnensystemforschung, Max-Planck-Straße 2, 37191 Katlenburg-Lindau, Germany
e-mail: yeo@mps.mpg.de

² Technische Universität Braunschweig, Institut für Geophysik und Extraterrestrische Physik, Mendelssohnstraße 3,
38106 Braunschweig, Germany

³ School of Space Research, Kyung Hee University, Yongin, 446-701 Gyeonggi, Korea

Received 1 November 2012 / Accepted 20 December 2012

ABSTRACT

Aims. This study aims at setting observational constraints on the continuum and line core intensity contrast of network and faculae, specifically, their relationship with magnetic field and disc position.

Methods. Full-disc magnetograms and intensity images by the Helioseismic and Magnetic Imager (HMI) onboard the Solar Dynamics Observatory (SDO) were employed. Bright magnetic features, representing network and faculae, were identified and the relationship between their intensity contrast at continuum and line core with magnetogram signal and heliocentric angle examined. Care was taken to minimize the inclusion of the magnetic canopy and straylight from sunspots and pores as network and faculae.

Results. In line with earlier studies, network features, on a per unit magnetic flux basis, appeared brighter than facular features. Intensity contrasts in the continuum and line core differ considerably, most notably, they exhibit opposite centre-to-limb variations. We found this difference in behaviour to likely be due to the different mechanisms of the formation of the two spectral components. From a simple model based on bivariate polynomial fits to the measured contrasts we confirmed spectral line changes to be a significant driver of facular contribution to variation in solar irradiance. The discrepancy between the continuum contrast reported here and in the literature was shown to arise mainly from differences in spatial resolution and treatment of magnetic signals adjacent to sunspots and pores.

Conclusions. HMI is a source of accurate contrasts and low-noise magnetograms covering the full solar disc. For irradiance studies it is important to consider not just the contribution from the continuum but also from the spectral lines. In order not to underestimate long-term variations in solar irradiance, irradiance models should take the greater contrast per unit magnetic flux associated with magnetic features with low magnetic flux into account.

Key words. Sun: activity – Sun: faculae, plages – Sun: photosphere – Sun: surface magnetism

1. Introduction

Photospheric magnetic activity is the dominant driver of variation in solar irradiance on rotational and cyclical timescales (Domingo et al. 2009). Magnetic flux in the photosphere is partly confined to discrete concentrations of kilogauss strengths, generally described in terms of flux tubes (Stenflo 1973; Spruit & Roberts 1983). The brightness excess, or contrast relative to the Quiet Sun, of flux tubes is strongly modulated by their size and position on the solar disc (see Solanki 1993, for a review). Within these magnetic concentrations, pressure balance dictates an evacuation of the interior and consequent depression of the optical depth unity surface (Spruit 1976). The horizontal extent influences the effect of radiative heating from the surroundings through the side walls on the temperature structure and contrast (Spruit & Zwaan 1981; Grossmann-Doerth et al. 1994). The position on the solar disc changes the viewing geometry, and therefore the degree to which the hot walls are visible and the apparent contrast (Steiner 2005). Models describing the counteracting effects on solar irradiance of dark sunspots, and bright network and faculae, characterizing the latter by the magnetic filling factor (related to number density) and position have been successful in reproducing more than 90% of observed variation over multiple solar cycles (Wenzler et al. 2006; Ball et al. 2012). Other factors, such as inclination, internal dynamics, phase of evolution and surrounding convective motions affect the brightness excess

of a given flux tube, but become less important when considering the overall behaviour of an ensemble as is the case with such models (Fligge et al. 2000). The same is assumed of flux tube size, which enters these models only very indirectly, though it is known to have a significant effect on contrast.

Evidently, the robust reconstruction of solar irradiance variation from models based on photospheric magnetic activity is contingent, amongst other factors, on a firm understanding of the radiant behaviour of magnetic elements, in particular the variation with size and position on the solar disc. While the radiant behaviour of sunspots is relatively well known (Chapman et al. 1994; Mathew et al. 2007) and sufficiently described by current models (Maltby et al. 1986; Collados et al. 1994; Unruh et al. 1999), the converse is true of network and faculae, and constitutes one of the main uncertainties in current solar irradiance reconstructions. This is primarily due to the difficulty in observing such small-scale features, the detailed structure of which are only starting to be resolved (Lites et al. 2004; Lagg et al. 2010) with instruments such as the Swedish 1-m Solar Telescope (SST, Scharmer et al. 2003) and the Imaging Magnetograph eXperiment (IMaX, Martínez Pillet et al. 2011) onboard SUNRISE (Solanki et al. 2010; Barthol et al. 2011). As such, the relationship between radiance and size cannot, as yet, be studied directly. It is however appropriate and more straightforward to consider instead the relationship between apparent intensity contrast and magnetogram signal. Apart from small-scale magnetic

fields observed in the quiet Sun internetwork (Khomenko et al. 2003; Lites et al. 2008; Beck & Rezaei 2009), magnetic concentrations carrying more than a minimum amount of flux exhibit similar field strengths regardless of size (Solanki & Schmidt 1993; Solanki et al. 1999). Flux tubes also tend towards vertical orientation due to magnetic buoyancy. As flux tubes exhibit a narrow range of magnetic field strengths and are largely vertical, on average the magnetogram signal at a given image pixel approximately scales with the proportion of the resolution element occupied by magnetic fields. Also, although the relationship between magnetogram signal and distribution of flux tube sizes is degenerate (a given magnetogram signal can, for example, correspond to either a single flux tube or a concentration of numerous smaller ones), flux tube size appears, on average, to be greater where the magnetogram signal is greater (Ortiz et al. 2002).

Relatively few studies examining network and faculae contrast variation with magnetogram signal and position on the solar disc have been reported in the literature. The majority of studies from the past two decades employed high-resolution (<0.5 arcsec) scans made with ground-based telescopes. For example, the efforts of Topka et al. (1992, 1997) and Lawrence et al. (1993) with the Swedish Vacuum Solar Telescope (SVST) and of Berger et al. (2007) with the SST. These studies suffer from variable seeing effects introduced by the Earth's atmosphere and poor representation of disc positions, a limitation imposed by the relatively narrow fields-of-view (FOVs). Ortiz et al. (2002) and Kobel et al. (2011) repeated the work of Topka et al. (1992, 1997) and Lawrence et al. (1993) utilising observations from spaceborne instruments, and in so doing avoided seeing effects. Ortiz et al. (2002) employed full-disc continuum intensity images and longitudinal magnetograms from the Michelson Doppler Imager (MDI) onboard the Solar and Heliospheric Observatory (SoHO). While full-disc MDI observations presented a more complete coverage of disc positions, allowing the authors to derive an empirical relationship relating contrast to heliocentric angle and magnetogram signal, the spatial resolution is significantly poorer than in the SVST studies (4 arcsec versus ≥ 0.3 arcsec). Kobel et al. (2011) examined the relationship between contrast and magnetogram signal near disc centre using spectropolarimetric scans from the Solar Optical Telescope (SOT) onboard Hinode (Kosugi et al. 2007). In this instance, the spatial resolution (0.3 arcsec) is comparable.

In this paper we discuss continuum and line core intensity contrast of network and facular elements from full-disc observations by the Helioseismic and Magnetic Imager (HMI) onboard the Solar Dynamics Observatory (SDO) spacecraft (Schou et al. 2012), and their relationship with heliocentric angle and magnetogram signal. The aim here is to derive stringent observational constraints on the relationship between intensity contrast, and position on the solar disc and magnetic field. This will be of utility to solar irradiance reconstructions, especially as HMI data will increasingly be used for this purpose.

This study partly echoes the similar studies discussed above, in particular that by Ortiz et al. (2002) utilising MDI observations. It presents a significant extension of the effort by Ortiz et al. (2002) in that we examined the entire solar disc not just in the continuum but also in the core of the HMI spectral line (Fe I 6173 Å). This is of particular relevance to solar irradiance variation given the observation that spectral line changes appear to have a significant influence on such variations (Mitchell & Livingston 1991; Unruh et al. 1999; Preminger et al. 2002). Both here and in the study by Ortiz et al. (2002), network and facular elements were distinguished from quiet Sun by the magnetogram

signal, and sunspots and pores by the continuum intensity. HMI magnetograms are significantly less noisy than MDI magnetograms, allowing us to achieve a similar magnetogram signal threshold while averaging over a much shorter period (315 s versus 20 min). Network and facular features evolve at granular timescales (~ 10 min, Berger & Title 1996; Wiegmann et al. 2012). It is pertinent to keep the averaging period below this in order to avoid smearing and loss of signal. HMI also has a finer spatial resolution (1 arcsec compared to 4 arcsec), allowing weaker unresolved features to be detected at the same noise level than with MDI. The finer resolution however, also renders intensity fluctuations from small-scale phenomena such as granulation and filamentation more severe, which complicates the clear segmentation of sunspots and pores.

In Sect. 2.1 we briefly present the HMI instrument, the observables considered and the data set. The data reduction process by which we identified and derived the intensity contrast of network and facular features is detailed in Sect. 2.2. Following that we describe the results of our analysis of these measured contrasts (Sect. 3). In Sect. 4 we discuss our findings in the context of earlier studies and of their relevance to facular contribution to solar irradiance variation, before presenting our conclusions in Sect. 5.

2. Method

2.1. SDO/HMI data

SDO/HMI (Schou et al. 2012) is designed for the continuous, full-disc observation of velocity, magnetic field and intensity on the solar surface. The instrument comprises two 4096×4096 pixel CCD cameras observing the Sun at a spatial resolution of 1 arcsec (corresponding to two pixels). By means of a tunable Lyot filter and two tunable Michelson interferometers, the instrument records 3.75-s cadence filtergrams at various polarizations and wavelengths across the Fe I absorption line at 6173 Å. 45-s cadence Dopplergrams, longitudinal magnetograms and intensity (continuum, line depth and width) images are generated from the filtergram sequence. For this work we considered the longitudinal magnetic field, continuum intensity and line depth observables. HMI is full-Stokes capable, however, at time of study, only 720-s cadence Stokes IQUV parameters and Milne-Eddington inversions were available. As argued in Sect. 1, for this study it is important to keep the integration period of measurements below ~ 10 min. We opted to utilise the 45-s longitudinal magnetograms also to keep in line with earlier studies, which examined intensity contrast variation with line-of-sight magnetic field (e.g. Topka et al. 1992, 1997; Lawrence et al. 1993; Ortiz et al. 2002; Kobel et al. 2011). More details on the instrument can be found in Schou et al. (2012).

The data set comprises simultaneous longitudinal magnetograms, continuum intensity and line depth images from 15 high activity days in the period May 2010 to July 2011. From each day, for each observable we took the average of the seven 45-s cadence images from a 315-s period, each rotated to the observation time of the middle image to co-register. Aside from signal-to-noise considerations, this averaging is to suppress variance from p-mode oscillations. The dates and times of the employed observations are listed in Table 1.

Longitudinal magnetograms describe the line-of-sight component of the average magnetic flux density over each resolution element. To first order, for a given flux tube of intrinsic magnetic field strength B , the unsigned longitudinal magnetogram signal, $\langle B_l \rangle$, is $\alpha B |\cos \gamma|$, scaled by α , the magnetic filling factor and γ ,

Table 1. Observation date and time of the data set.

Date (year.month.date)	Time (hour.minute.second)
2010.05.04	00:03:00
2010.06.11	00:00:00
2010.07.24	00:05:15
2010.08.11	00:00:00
2010.09.02	00:00:00
2010.10.25	00:00:00
2010.11.13	00:00:00
2010.12.04	00:00:00
2011.01.01	00:00:00
2011.02.14	00:00:00
2011.03.08	00:00:00
2011.04.15	00:00:00
2011.05.30	00:00:00
2011.06.02	00:00:00
2011.07.18	00:12:00

Notes. The time listed is the nominal time, in International Atomic Time (TAI), of the middle cadence in the sequence of seven considered from each day.

the inclination of the magnetic field from the line-of-sight. As mentioned in the introduction (Sect. 1), flux tubes tend towards vertical orientation. In this study we examined the overall properties of an ensemble of magnetic elements. Under this condition it is reasonable to assume that on average $\gamma \approx \theta$, the heliocentric angle, allowing us to employ the magnetogram signal as a proxy for αB via the quantity $\langle B_l \rangle / \mu$, where $\mu = \cos \theta$. This quantity also represents a first-order approximation of the unsigned average magnetic flux density over each resolution element. At time of writing, HMI Dopplergrams and longitudinal magnetograms were generated from just the first Fourier component of the filtergram sequence resulting in a $\sqrt{2}$ factor increase in photon noise from the optimal level (Couvidat 2011; Couvidat et al. 2012).

Each line depth image was subtracted from the corresponding continuum intensity image to yield the line core intensity image. Hereafter we will denote the continuum and line core intensity I_C and I_L respectively. At time of writing, HMI data products are generated from the filtergram sequence assuming a Gaussian form to the Fe I 6173 Å line and delta filter transmission profiles. The effect of these approximations on Doppler velocity and longitudinal magnetic field measurements are accounted for, but not completely for the intensity observables (Couvidat 2011; Couvidat et al. 2012). The impact on this study is assumed minimal as we are only interested in contrast relative to the local mean quiet Sun level.

2.2. Data reduction

2.2.1. Magnetogram noise level

The noise level of 315-s HMI magnetograms as a function of position on the solar disc was determined. For this purpose we used 10 spot-free 315-s magnetograms recorded over a seven month period in 2010. First, we estimated the centre-to-limb variation (CLV) of the noise level. The pixels within each magnetogram were ordered by distance from the disc centre and sampled in successive blocks of 5000 pixels. The blocks represent concentric rings (near the limb, arcs, as the circumference of the solar disc is greater than 5000 pixels) of pixels of similar distance from the disc centre. Within each block we computed the average distance from the disc centre and the standard deviation

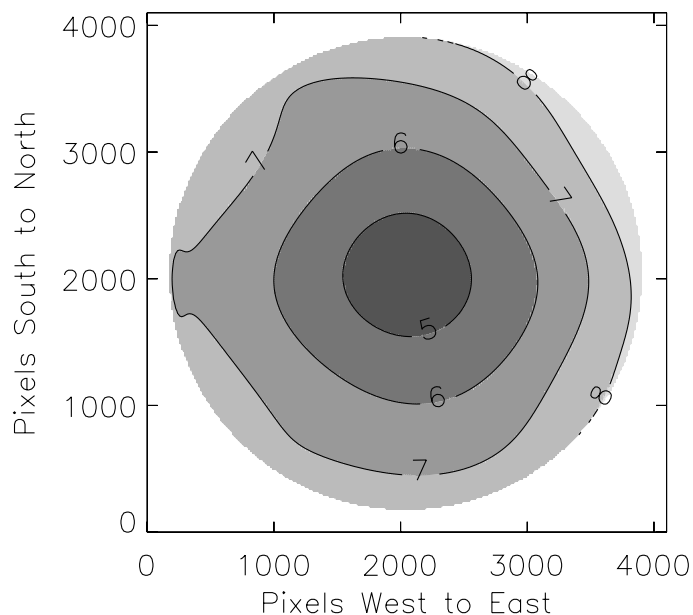


Fig. 1. Magnetogram noise level in units of Gauss, as a function of disc position, sampled at 16-pixel intervals in either direction on the CCD.

of the magnetogram signal (iteratively, with points outside three standard deviations from the mean excluded from the succeeding iteration till convergence). A fifth-order polynomial in μ was fitted to the noise CLV; the mean of the standard deviation versus distance profiles so derived from the magnetograms. The magnetograms were then normalized by the noise CLV fit. At each disc position, the standard deviation over a 401×401 pixel window centred on the pixel of interest was computed (iteratively as above) for each normalized magnetogram and the median taken (following Ortiz et al. 2002). (Near the limb, the standard deviation was computed from just the image pixels that lie within the solar disc.) A sixth-order polynomial was fitted to the resultant surface (termed here the noise residue). This fit represents the noise level after the removal of the CLV as a function of position on the solar disc. The noise level, $\sigma_{\langle B_l \rangle}$, shown in Fig. 1, is then the product of the noise CLV fit and the noise residue fit. The noise level is lowest near disc centre and increases radially up to the limb (mean of 4.9 G for $\mu > 0.95$ and 8.6 G for $\mu < 0.05$). The root-mean-square (RMS) difference between the noise level and the noise CLV fit is 0.4 G. The correlation with distance from disc centre and relatively small deviation from circular symmetry suggests photon noise is the dominant component. The noise level of 45-s magnetograms, derived by a like analysis, has a similar, albeit accentuated form. The ratio between the noise level, averaged over the solar disc, of 45-s and 315-s magnetograms is 2.7 (approximately $\sqrt{7}$). The noise level of 45-s magnetograms determined by Liu et al. (2012), via a vastly different method, also exhibits a similar CLV.

2.2.2. Quiet Sun intensity

For this part of the data reduction process, where we examined how quiet Sun intensity and the noise level of the intensity images vary with position on the solar disc, we counted all pixels with $\langle B_l \rangle / \mu \leq 10$ G as corresponding to quiet Sun (QS).

The continuum and line core intensity images were normalized by the fifth-order polynomial in μ fit to the quiet Sun pixels to correct for limb-darkening (following Neckel & Labs 1994). In the case of the line core intensity images, this was also to

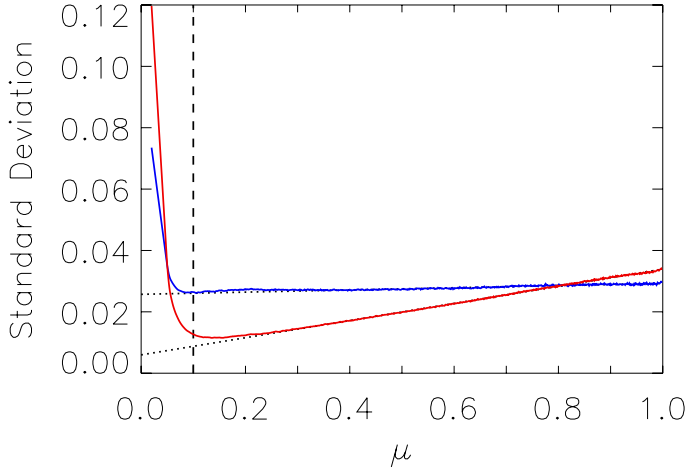


Fig. 2. Standard deviation of quiet Sun ($\langle B_1 \rangle / \mu \leq 10$ G) intensity at continuum, $\sigma_{I_{C, QS}}$ (red) and line core, $\sigma_{I_{L, QS}}$ (blue) as a function of μ . The dotted lines represent the linear fit to $\sigma_{I_{C, QS}}$ and $\sigma_{I_{L, QS}}$ over the range $0.3 \leq \mu \leq 1.0$ (largely hidden due to the close agreement), extrapolated to $\mu = 0$. The dashed line denotes the threshold ($\mu = 0.1$) below which pixels were excluded from the rest of the study in view of the scatter in measured intensity.

correct for the centre-to-limb broadening of the Fe I 6173 Å line (Norton et al. 2006). There are distortions in the intensity images such that after this normalization, the mean quiet Sun intensity is not constant at unity but varying with position on the solar disc. The mean quiet Sun intensity at the continuum and line core as a function of position on the solar disc, denoted $\langle I_{C, QS} \rangle$ and $\langle I_{L, QS} \rangle$ respectively, were determined for each of the selected days. A 401×401 pixel window was centred on each disc position and the mean continuum and line core intensity of all quiet Sun pixels inside the window computed. For each day represented in the data set, $\langle I_{C, QS} \rangle$ and $\langle I_{L, QS} \rangle$ were given by the fifth-order polynomial fits to the mean quiet Sun continuum and line core intensity surfaces so derived from the images from the day. This analysis had to be repeated for each selected day as we found the spatial distribution of $\langle I_{C, QS} \rangle$ and $\langle I_{L, QS} \rangle$ to vary significantly over the period of observation. The RMS value of $\langle I_{C, QS} \rangle - 1$ and $\langle I_{L, QS} \rangle - 1$, the scale of the image distortions, is on average 0.004 and 0.01 respectively.

The CLV of the standard deviation of quiet Sun intensity at continuum, $\sigma_{I_{C, QS}}$ and line core, $\sigma_{I_{L, QS}}$ were determined, from $I_C / \langle I_{C, QS} \rangle$ and $I_L / \langle I_{L, QS} \rangle$, by an analysis similar to the procedure used to derive the magnetogram noise CLV. In Fig. 2, we express $\sigma_{I_{C, QS}}$ and $\sigma_{I_{L, QS}}$, which carry information on the noise level of the intensity images and granulation contrast, as a function of μ . Going from disc centre, $\sigma_{I_{C, QS}}$ decreases gradually down to $\mu \sim 0.15$ before increasing rapidly towards the limb. The monotonic decline from disc centre to $\mu \sim 0.15$ resembles a similar trend in the CLV of granulation contrast reported by various authors (Sánchez Cuberes et al. 2000, 2003, and references therein). $\sigma_{I_{L, QS}}$ exhibits a similar, though less accentuated, trend. For both $\sigma_{I_{C, QS}}$ and $\sigma_{I_{L, QS}}$, the μ -dependence from disc centre to $\mu \sim 0.3$ is approximately linear, as highlighted by the linear fits (dotted lines). The elevation near limb is a direct consequence of limb-darkening; the diminishing signal-to-noise ratio translates into an escalating noise level in the normalized intensity. Given the gross scatter towards the limb, we excluded pixels outside $\mu = 0.1$, representing about 1% of the solar disc by area, from further consideration.

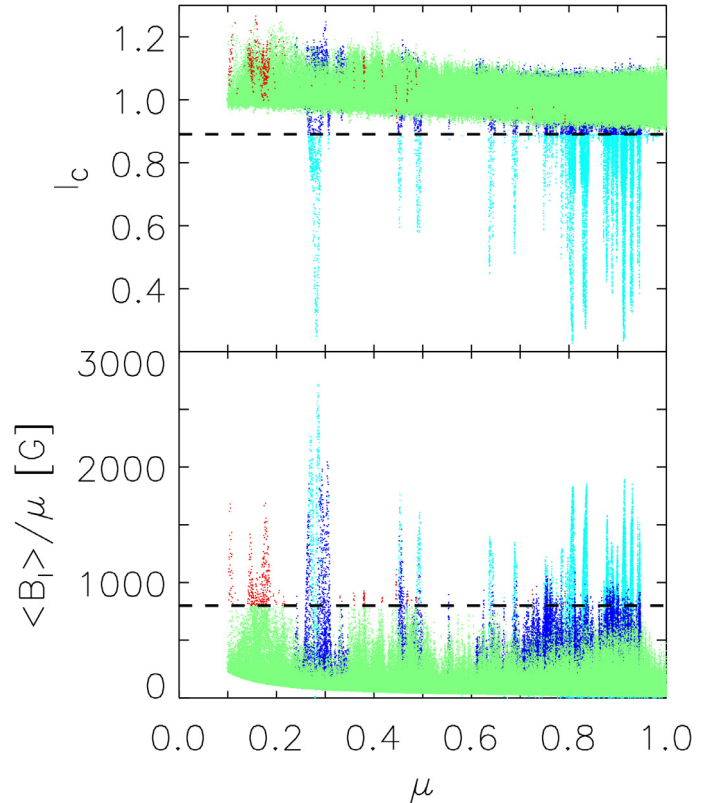


Fig. 3. Continuum intensity, I_C versus μ (top) and $\langle B_1 \rangle / \mu$ versus μ (bottom) scatter plots of pixels counted as network and faculae (green) from June 2, 2011. The pixels counted as sunspots and pores by the continuum intensity threshold and the magnetic extension removal procedure (see text) are represented by the cyan and blue dots respectively. The red dots represent network and faculae pixels that lie above the cutoff $\langle B_1 \rangle / \mu$ level. The dashed lines denote the continuum intensity threshold (top) and the cutoff $\langle B_1 \rangle / \mu$ level (bottom).

2.2.3. Identification of network and faculae

Network and facular features, the subject of this work, were identified by first distinguishing them from quiet Sun by the magnetogram signal and from sunspots and pores by the continuum intensity. Pixels with $\langle B_1 \rangle / \mu > 3\sigma_{\langle B_1 \rangle} / \mu$ (~ 14 G near disc centre, where $\sigma_{\langle B_1 \rangle}$ is lowest) were considered to harbour substantive magnetic fields. Isolated pixels above this threshold were assumed false positives and excluded. Hereafter we will denote $3\sigma_{\langle B_1 \rangle} / \mu$ as $(\langle B_1 \rangle / \mu)_{TH}$. Pixels with $I_C < 0.89$ were counted as sunspots and pores. This value of the threshold is given by the mean of the minimum value of $\langle I_{C, QS} \rangle - 3\sigma_{I_{C, QS}}$ from each selected day. It was so defined to distinguish sunspots and pores with minimal wrongful inclusion of intergranular lanes and magnetic features darker than the quiet Sun in the continuum. The continuum intensity versus μ scatter plot of network and facular pixels for one of the selected days (June 2, 2011) is shown in Fig. 3 (top panel). The pixels identified as network and faculae lie clearly above the continuum intensity threshold.

In HMI magnetograms, magnetic signals produced by sunspots and pores extend beyond their boundary (in our analysis, the $I_C = 0.89$ locus). This is illustrated for a sunspot near disc centre and another that is close to the limb on one of the selected days (July 18, 2011) in Fig. 4. The $I_C = 0.89$ locus is plotted over the continuum intensity image and magnetogram of both sunspots (red contours) to highlight the extension of the magnetogram signal. This arises predominantly from the

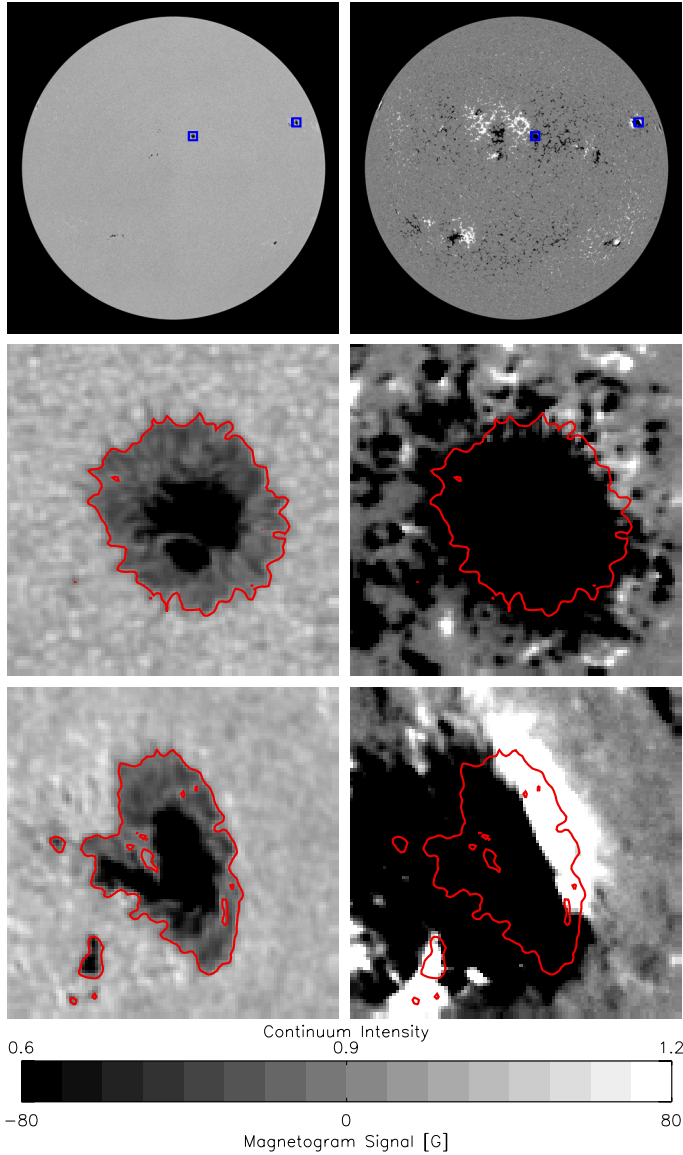


Fig. 4. Continuum intensity image (*top left*) and magnetogram (*top right*) from July 18, 2011 and the corresponding 50×50 arcsec insets of the boxed sunspot features near disc centre (*middle panels*) and limb (*bottom panels*). The red contours represent the continuum intensity sunspot boundary (the $I_C = 0.89$ locus). The magnetograms have been saturated at ± 80 G to highlight the extension of the magnetic signal from these sunspots beyond the intensity boundary (see grey scale below the figure).

lateral expansion of their magnetic field with height (i.e., magnetic canopy) and partly also from the effect of straylight from sunspots and pores on nearby pixels. Towards the limb, these magnetic features become more extensive and bipolar due to the acute orientation of the largely horizontal magnetic canopy with the line-of-sight (Giovanelli 1980), as illustrated by the near limb example (bottom panels). Figure 4 also highlights the presence of bright sunspot structures (such as bright penumbral filaments) that lie above the continuum intensity threshold. All of these could easily be misidentified as network and faculae by the simple application of the magnetogram signal and continuum intensity thresholds described earlier.

To account for the effects of straylight around sunspots and pores, magnetic canopies and bright sunspot structures, we expanded sunspots and pores to include adjoining magnetic signal.

Pixels adjacent to sunspots and pores that lie above $(\langle B_1 \rangle / \mu)_{TH}$ are reassigned to these features. This was iterated till no more pixels could be added. Here we will refer to this process as magnetic extension removal. Simply adding only adjoining pixels within a threshold distance from sunspots and pores instead is not useful as the physical extent of magnetic canopies exhibits a broad dynamic range, dependent on the position and physical properties of the associated feature. Kobel et al. (2011), in a similar study with Hinode/SOT scans, expanded pores to include adjoining pixels above a threshold magnetogram signal level of 200 G to account for their influence on surrounding pixels from telescope diffraction. While this technique appears to work for Hinode/SOT scans, here we observed that adding only adjoining pixels above a threshold magnetogram signal level results in the appearance of a knee in contrast versus $\langle B_1 \rangle / \mu$ plots at this threshold level regardless of the value chosen. For these reasons we expanded sunspots and pores to include all adjoining magnetic signal, though this conservative approach inevitably assigns too many pixels, including legitimate faculae, to sunspots and pores.

All pixels identified as magnetic, and not as sunspots and pores or their extensions, were taken to correspond to network and faculae. Figure 3 shows the continuum intensity versus μ (top panel) and $\langle B_1 \rangle / \mu$ versus μ (bottom panel) scatter plots of pixels identified as network and faculae (green), and counted as sunspots and pores by the magnetic extension removal procedure (blue) from June 2, 2011. The pixels captured by the magnetic extension removal procedure are not well distinguished from network and faculae by the continuum intensity; largely hidden by network and faculae in the continuum intensity versus μ scatter plot. It is clear from the $\langle B_1 \rangle / \mu$ versus μ scatter plots however that the two classes are significantly different magnetic populations. As noted earlier, this procedure is likely too severe and results in the exclusion of some true faculae. However, for the purpose of this study it is not necessary to identify all faculae present and far more important to avoid false positives.

Finally, network and facular pixels with $\langle B_1 \rangle / \mu$ above a conservative cutoff level of 800 G were excluded from the subsequent analysis (following Ball et al. 2011, 2012). They are mostly bright features concentrated near the limb (as illustrated for June 2, 2011 by the red dots in Fig. 3) associated with sunspots and pores. (The relatively high $\langle B_1 \rangle / \mu$ values likely reflect nearly horizontal fields, for which $|\cos \gamma| \gg \mu$ towards the limb.) This is to account for non-facular magnetic signals that might have been missed by the continuum intensity threshold and the magnetic extension removal procedure.

The classification image, indicating the positions of the pixels classed as sunspot and pores, and network and faculae for another of the selected days (May 30, 2011) is shown in Fig. 5. In spite of the severe measures taken to minimise the influence of sunspots and pores, a fair fraction of active region faculae remains. In total, 7.6×10^6 pixels were identified as corresponding to network and facular features from the data set (i.e. 4.5% of all solar disc pixels in the 15 continuum intensity image and magnetogram pairs examined).

2.2.4. Definition of intensity contrast

The average continuum and line core intensity contrast over a given resolution element, C_{I_C} and C_{I_L} were defined as:

$$C_{I_C}(x, y) = \frac{I_C(x, y) - \langle I_{C, QS} \rangle(x, y)}{\langle I_{C, QS} \rangle(x, y)} \quad (1)$$

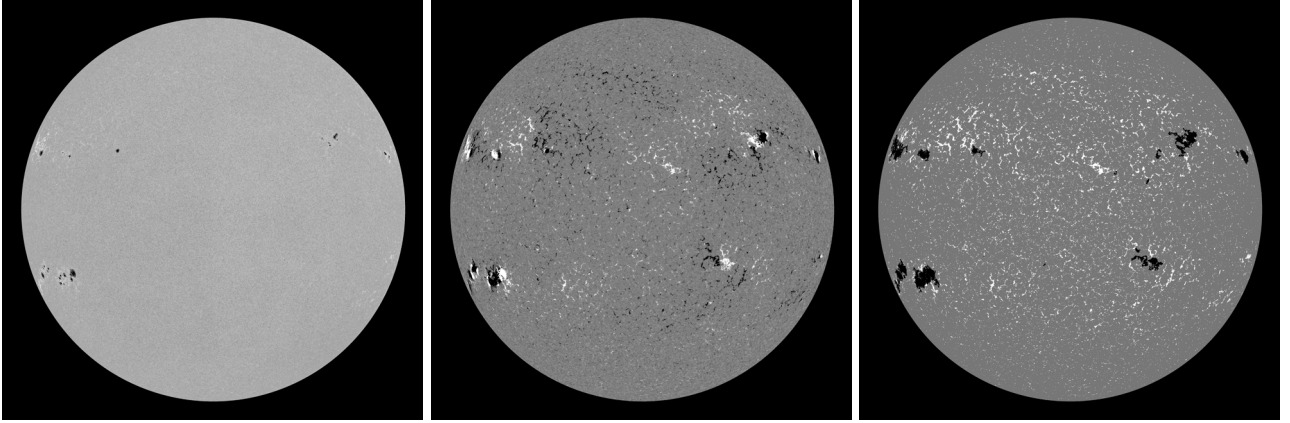


Fig. 5. HMI continuum intensity image (*left*), magnetogram (*middle*) and classification image (*right*) from May 30, 2011. The classification image indicates the positions of the pixels classed as network and faculae (white), and sunspots and pores (black). The latter includes magnetic signal adjoined to sunspots and pores, counted to them to avoid counting their magnetic canopy, possible bright structures within penumbrae and straylight as network and faculae erroneously. The continuum intensity image and magnetogram are scaled between 0.6 and 1.2, and -80 G and 80 G respectively as in Fig. 4.

and

$$C_{I_L}(x, y) = \frac{I_L(x, y) - \langle I_{L, QS} \rangle(x, y)}{\langle I_{L, QS} \rangle(x, y)} \quad (2)$$

respectively, where (x, y) denote position on the CCD array. These two quantities, computed for each of the pixels identified as corresponding to network and facular features, represent the normalized difference between the continuum and line core intensities at a given pixel and the local mean quiet Sun levels as given by the mean quiet Sun continuum and line core intensity surfaces, $\langle I_{C, QS} \rangle$ and $\langle I_{L, QS} \rangle$, defined earlier in Sect. 2.2.2.

In summary, here we extracted an ensemble of 7.6×10^6 continuum and line core intensity contrast measurements corresponding to network and facular features covering as wide a range of heliocentric angles ($0.1 \leq \mu \leq 1.0$) and magnetogram signal ($(\langle B_1 \rangle / \mu)_{TH} < \langle B_1 \rangle / \mu \leq 800$ G) as reasonably possible from the data set for the succeeding analysis.

3. Results

3.1. Variation with position and magnetogram signal

The positions of pixels identified as network and faculae, classified by $\langle B_1 \rangle / \mu$, in a quiet region and an active region on one of the selected days (April 15, 2011) is shown in Fig. 6. As expected, at HMI's spatial resolution, magnetic signals with higher $\langle B_1 \rangle / \mu$ are largely concentrated in active regions. Though magnetic signals with lower $\langle B_1 \rangle / \mu$ are present in both quiet Sun and active regions, the fact that the solar disc is predominantly quiet Sun means these signals correspond largely to quiet Sun network and internetwork.

To elucidate the CLV of intensity contrast, we grouped the measured contrasts into eight intervals of $\langle B_1 \rangle / \mu$ spanning the range $(\langle B_1 \rangle / \mu)_{TH} < \langle B_1 \rangle / \mu \leq 800$ G and within each interval into μ bins 0.05 wide. As the distribution of magnetogram signal is skewed towards the lower bound (Wenzler et al. 2004; Parnell et al. 2009), the $\langle B_1 \rangle / \mu$ intervals were defined such that the widths slide from about 36 G ($(\langle B_1 \rangle / \mu)_{TH} < \langle B_1 \rangle / \mu \leq 50$ G) to 160 G (640 G $< \langle B_1 \rangle / \mu \leq 800$ G) to ensure reasonable statistics in every interval. In grouping the measured contrasts into these broad $\langle B_1 \rangle / \mu$ intervals we are effectively grouping the network and facular features by αB (Sect. 2.1), neglecting differences in quiet Sun network and active region faculae contrast

(Lawrence et al. 1993; Kobel et al. 2011). This is reasonable since the lower intervals are mainly populated by quiet Sun network and the higher intervals by active region faculae. The bin-averaged continuum and line core intensity contrast as a function of μ and the cubic polynomial fit for each of the $\langle B_1 \rangle / \mu$ intervals are expressed in Figs. 7 and 8 respectively. For brevity we will refer to these bin-averaged contrasts as the contrast CLV profiles.

The truncated μ coverage in the lower $\langle B_1 \rangle / \mu$ intervals is due to foreshortening. As flux tubes are mainly vertical, going from disc centre to the limb the corresponding longitudinal magnetogram signal diminishes, eventually dropping below the threshold level which itself rises towards the limb (Fig. 1). The fluctuations near the limb, more pronounced in the higher $\langle B_1 \rangle / \mu$ intervals, is due to the inhomogeneous distribution of active regions on the solar disc, where stronger magnetic signals are concentrated on the selected days. Diminishing statistics also play a role; there are comparatively fewer pixels in the higher $\langle B_1 \rangle / \mu$ intervals.

To investigate the $\langle B_1 \rangle / \mu$ -dependence of intensity contrast, the measured contrasts were grouped into eight μ intervals spanning the range $0.1 \leq \mu \leq 1.0$ and within each interval into $\langle B_1 \rangle / \mu$ bins 40 G wide. The μ intervals were defined such that they represent an approximately equal proportion of the solar disc by area. The bin-averaged continuum and line core intensity contrasts as a function of $\langle B_1 \rangle / \mu$ and the cubic polynomial fit for each of the μ intervals are shown in Figs. 9 and 10 respectively. For brevity we will refer to these bin-averaged contrasts as the contrast versus $\langle B_1 \rangle / \mu$ profiles. These profiles represent the variation of continuum and line core intensity contrast ranging from internetwork and weak network to active region faculae at different distances from disc centre.

The cubic polynomial fit to each contrast versus $\langle B_1 \rangle / \mu$ profile included the zeroth-degree term. This produced better fits to data at low $\langle B_1 \rangle / \mu$ than constraining the fits to pass through the origin by excluding it. Approaching $\langle B_1 \rangle / \mu = 0$ G, the contrast versus $\langle B_1 \rangle / \mu$ profiles decline to weak, broadly negative levels. Although the cubic polynomial fits express good agreement with measurements, they are too simple to accommodate this decline well without including the unphysical zeroth-degree term. For similar considerations we included the zeroth-degree term in the cubic polynomial fits to the contrast CLV profiles, so rendering them non-zero at $\mu = 0$. These apparent offsets in the contrast

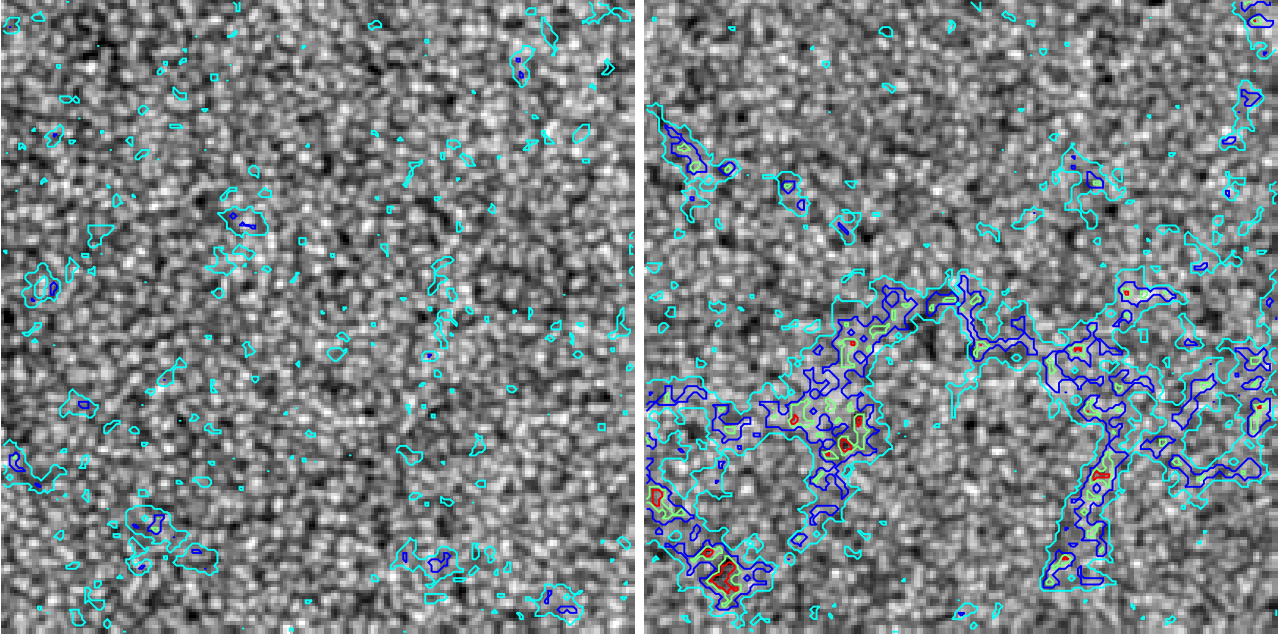


Fig. 6. 100×100 arcsec insets of a quiet region near disc centre ($\mu > 0.99$, *left*) and active region NOAA 11187 ($0.82 < \mu < 0.91$, *right*) of the continuum intensity image from April 15, 2011. The cyan contours indicate the boundary of network and faculae. The blue, green and red contours correspond to $\langle B_1 \rangle / \mu = 100$ G, 280 G and 500 G, respectively.

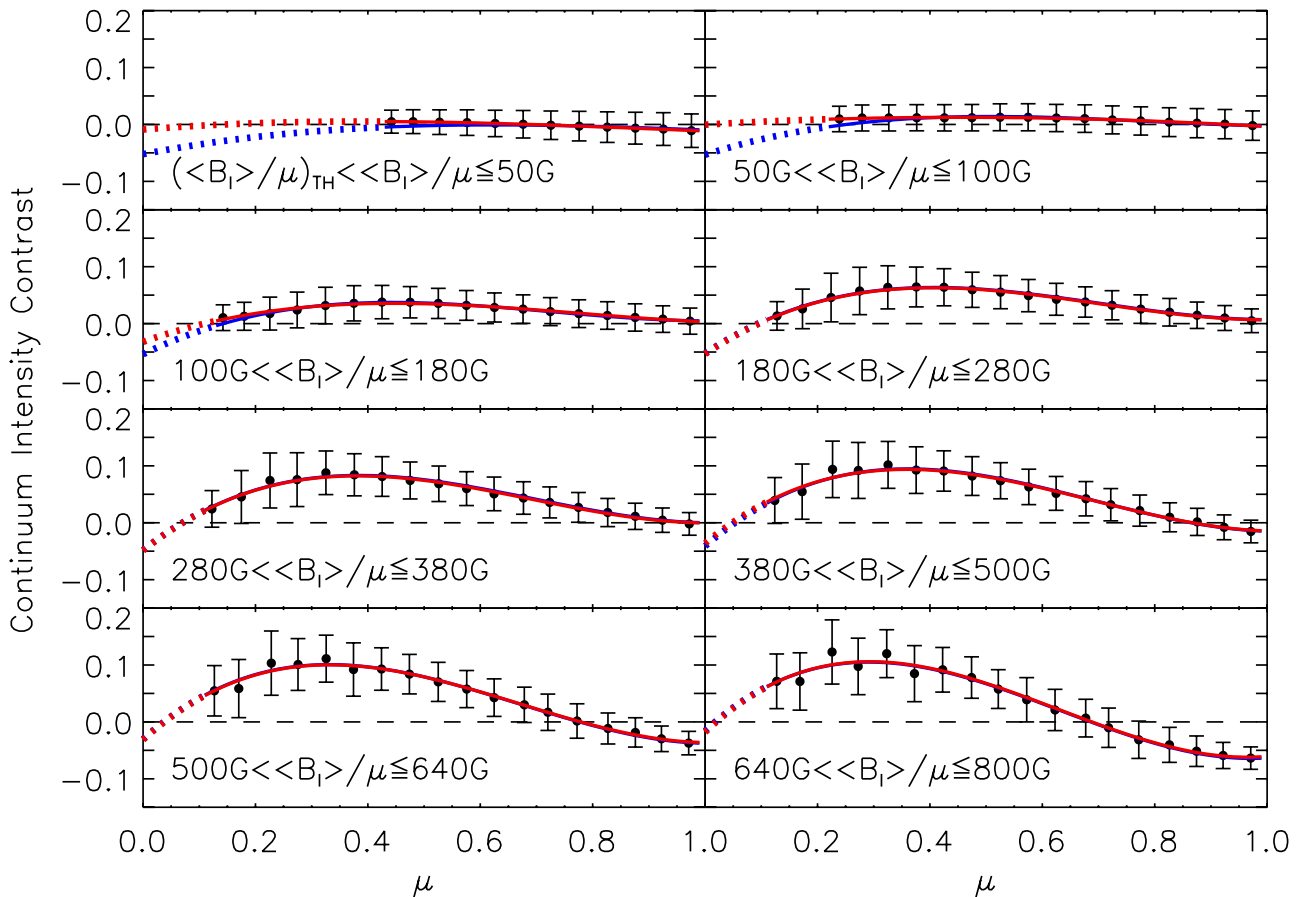


Fig. 7. CLV of continuum intensity contrast, C_{I_C} over eight $\langle B_1 \rangle / \mu$ intervals. The filled circles and error bars represent the mean and standard deviation of C_{I_C} grouped by μ in bins 0.05 wide. The red curves are third-order polynomial fits to the filled circles and the blue curves are the cross-sections of the surface fit to C_{I_C} at the mean $\langle B_1 \rangle / \mu$ within each interval (largely hidden due to the close agreement), extrapolated to $\mu = 0$ (dotted segments). The horizontal dashed lines denote the mean quiet Sun level.

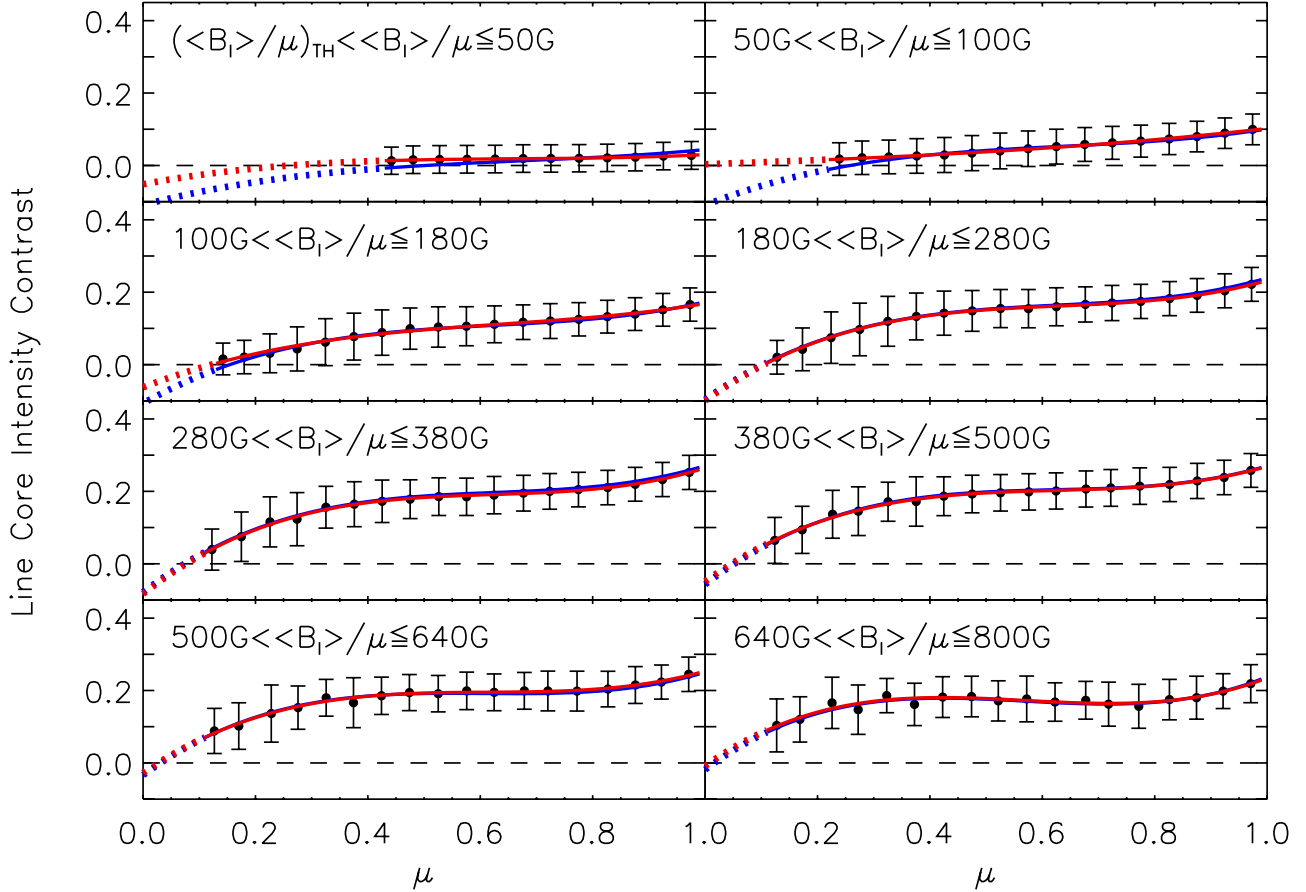


Fig. 8. Similar to Fig. 7, but for line core intensity contrast.

CLV and contrast versus $\langle B_1 \rangle / \mu$ profiles probably reflects the fact that magnetic elements are generally located in dark intergranular lanes.

In Fig. 11 we show a recomputation of the continuum intensity contrast versus $\langle B_1 \rangle / \mu$ profile over $0.94 < \mu \leq 1.00$ from Fig. 9 where we included pixels below the magnetogram signal threshold and not identified as sunspots and pores (i.e., quiet Sun), and grouped the measurements by $\langle B_1 \rangle / \mu$ in bins 10 G (instead of 40 G) wide. Approaching $\langle B_1 \rangle / \mu = 0$ G, contrast declines gradually to below the reference level before turning back up sharply towards the origin. Similar trends were reported by Narayan & Scharmer (2010), Kobel et al. (2011) and Schnerr & Spruit (2011), who termed it the fishhook feature, based on SST and Hinode/SOT disc centre scans. Schnerr & Spruit (2011) demonstrated the resolution of granules and dark intergranular lanes, where magnetic flux concentrates, at the relatively fine spatial resolution of both instruments (0.15 and 0.3 arcsec respectively) to be the cause of the fishhook feature at low magnetogram signal levels. Though HMI has a coarser resolution (1 arcsec) than either Hinode/SOT or SST, the fishhook feature near $\langle B_1 \rangle / \mu = 0$ G in Fig. 11 indicates granulation is still sufficiently resolved to have a measurable impact on apparent contrast.

Comparing the measured intensity contrast at continuum and line core derived here, the most distinct difference is the opposite CLV. Confining this discussion to broad trends in the measurements, continuum intensity contrast is weakest near disc centre and increases up to a maximum before declining quite significantly towards the limb (Fig. 7). Conversely, line core intensity contrast is strongest near disc centre and declines monotonically

from disc centre to limb (Fig. 8). Line core intensity is modulated by line strength and shape, and continuum intensity. The centre-to-limb decline exhibited by the measured line core intensity contrast arises from variation in line strength and shape (if this were absent the continuum and line core intensity contrast would vary proportionally) and would be even more acute than reflected in the CLV profiles if not partially offset by the accompanying increase in continuum intensity. This will be demonstrated, along with a closer discussion of the diverging trends exhibited by both sets of measurements in Sect. 4.3.

3.2. Surface fits

The cubic polynomial fit to the contrast CLV and contrast versus $\langle B_1 \rangle / \mu$ profiles reproduced the observations well (Figs. 7 to 10). Given this, we fit the entire set of measured network and faculae continuum and line core intensity contrast as functions of μ and $\langle B_1 \rangle / \mu$ (following Ortiz et al. 2002). The measured contrasts were grouped by μ and the natural logarithm of $\langle B_1 \rangle / \mu$ into a grid of 36×41 bins. The grid spans $0.1 \leq \mu \leq 1.0$ and $2.6 \leq \ln(\langle B_1 \rangle / \mu) \leq 6.7$ or about 14 G to 810 G. Each bin represents an interval of 0.025 in μ and 0.1 in $\ln(\langle B_1 \rangle / \mu)$. The logarithmic binning in $\langle B_1 \rangle / \mu$ is to compensate for the bottom-heavy distribution of magnetogram signal, to ensure the distribution of points is not too concentrated in the lower magnetogram signal bins. At each grid element we considered the mean μ , $\langle B_1 \rangle / \mu$, continuum and line core intensity contrast of the points within the bin. In accord with the cubic polynomial fits to the individual contrast CLV and contrast versus $\langle B_1 \rangle / \mu$ profiles, bivariate polynomials cubic in μ and $\langle B_1 \rangle / \mu$ were fitted

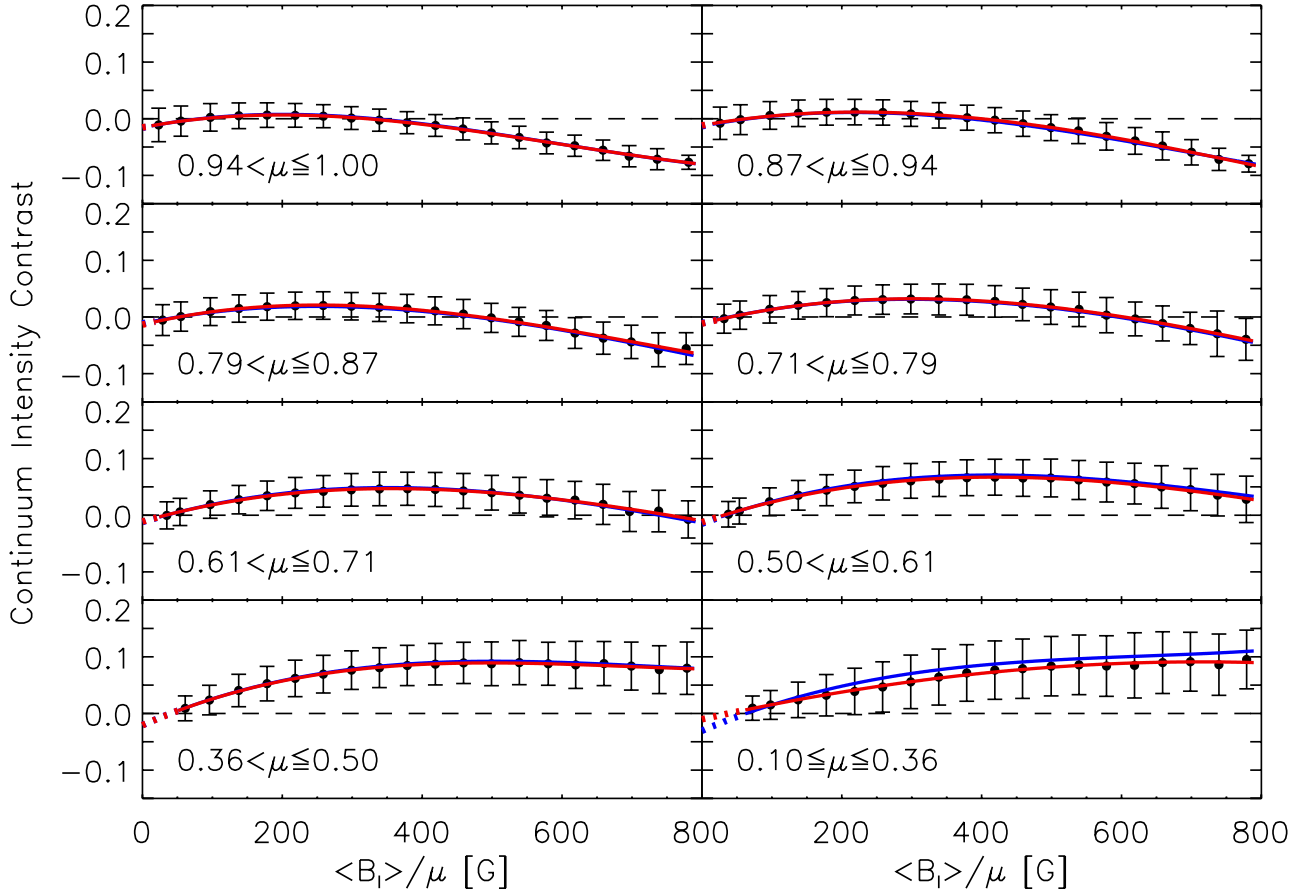


Fig. 9. Continuum intensity contrast, C_{Ic} as a function of $\langle B_1 \rangle / \mu$ over eight μ intervals. The filled circles and error bars represent the mean and standard deviation of C_{Ic} grouped by $\langle B_1 \rangle / \mu$ in 40 G bins. The red and blue curves and the horizontal dashed lines have the same meanings as in Fig. 7.

to the bin-averaged continuum and line core intensity contrast. The zeroth μ and $\langle B_1 \rangle / \mu$ orders were included based on similar considerations as with the polynomial fits to the contrast CLV and contrast versus $\langle B_1 \rangle / \mu$ profiles. In linear algebra notation, the surface fit to the bin-averaged continuum and line core intensity contrast are:

$$C_{Ic} \left(\mu, \frac{\langle B_1 \rangle}{\mu} \right) = \begin{bmatrix} 10^{-2} \left(\frac{\langle B_1 \rangle}{\mu} \right)^0 \\ 10^{-3} \left(\frac{\langle B_1 \rangle}{\mu} \right)^1 \\ 10^{-6} \left(\frac{\langle B_1 \rangle}{\mu} \right)^2 \\ 10^{-9} \left(\frac{\langle B_1 \rangle}{\mu} \right)^3 \end{bmatrix}^T \begin{bmatrix} -5.11 & 7.74 & 0.34 & -4.72 \\ -0.04 & 3.84 & -7.42 & 3.90 \\ 0.19 & -6.27 & 12.03 & -6.78 \\ -0.08 & 3.58 & -8.04 & 5.04 \end{bmatrix} \begin{bmatrix} \mu^0 \\ \mu^1 \\ \mu^2 \\ \mu^3 \end{bmatrix} \quad (3)$$

and

$$C_{I_l} \left(\mu, \frac{\langle B_1 \rangle}{\mu} \right) = \begin{bmatrix} 10^{-1} \left(\frac{\langle B_1 \rangle}{\mu} \right)^0 \\ 10^{-3} \left(\frac{\langle B_1 \rangle}{\mu} \right)^1 \\ 10^{-5} \left(\frac{\langle B_1 \rangle}{\mu} \right)^2 \\ 10^{-8} \left(\frac{\langle B_1 \rangle}{\mu} \right)^3 \end{bmatrix}^T \begin{bmatrix} -1.08 & 2.09 & -1.78 & 0.66 \\ -0.08 & 6.84 & -11.22 & 6.34 \\ 0.07 & -1.50 & 2.52 & -1.48 \\ -0.06 & 1.03 & -1.90 & 1.18 \end{bmatrix} \begin{bmatrix} \mu^0 \\ \mu^1 \\ \mu^2 \\ \mu^3 \end{bmatrix} \quad (4)$$

respectively. Since contrast is wavelength dependent and bright magnetic features are largely unresolved at HMI's spatial

resolution, these relationships are valid only at the instrument's operating wavelength (6173 Å) and spatial resolution (1 arcsec).

The surface fits are illustrated as surface and grey scale plots in Figs. 12 and 13. Cross-sections to the surface fits are plotted in Figs. 7 to 10 (blue curves) along the contrast CLV and contrast versus $\langle B_1 \rangle / \mu$ profiles, and the corresponding cubic polynomial fits (red curves). The surface fits are in excellent agreement with the cubic polynomial fits almost everywhere. The agreement is so close that the surface fit cross-sections are completely hidden by the cubic polynomial fits in most places. The advantage with these surface fits is that they allow us to describe how the measured contrasts vary with μ and $\langle B_1 \rangle / \mu$ almost equally well and with far fewer free parameters than by the cubic polynomial fit to each individual contrast CLV and contrast versus $\langle B_1 \rangle / \mu$ profile (32 versus 128 free parameters; 4 from each of 32 profiles).

3.3. Intrinsic contrast

At each $\langle B_1 \rangle / \mu$ interval, we estimated the maximum continuum intensity contrast, $C_{Ic,max}$ and the heliocentric angle at which it is reached, μ_{max} from the cubic polynomial fit to the contrast CLV profile (Fig. 7). Following Ortiz et al. (2002) we term $C_{Ic,max} / \langle \langle B_1 \rangle / \mu \rangle$ the specific contrast; estimated here from the quotient of $C_{Ic,max}$ and $\langle \langle B_1 \rangle / \mu \rangle$, the mean $\langle B_1 \rangle / \mu$ of all the points within a given $\langle B_1 \rangle / \mu$ interval. The values of μ_{max} , $C_{Ic,max}$ and $C_{Ic,max} / \langle \langle B_1 \rangle / \mu \rangle$ are shown in Fig. 14 as a function of $\langle B_1 \rangle / \mu$ where the abscissa is given by $\langle \langle B_1 \rangle / \mu \rangle$. Also plotted are the values obtained from the surface fit (Eq. (3)). The

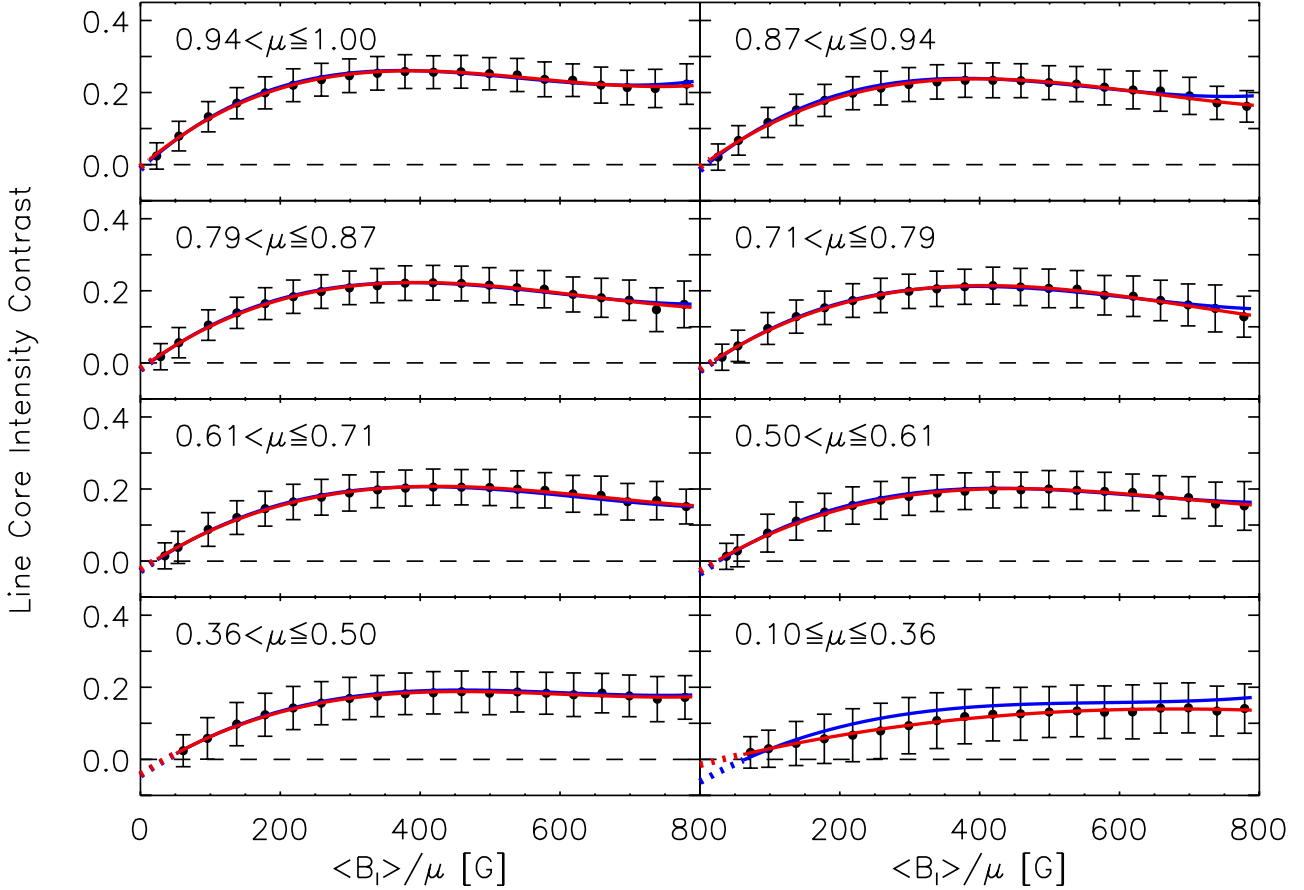


Fig. 10. Similar to Fig. 9, but for line core intensity contrast.

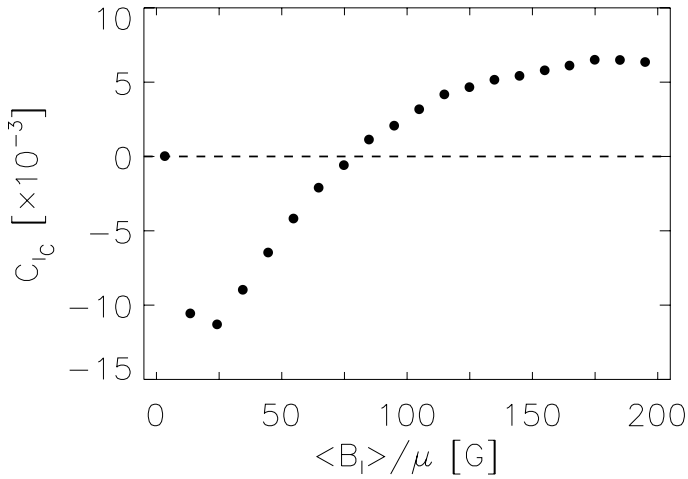


Fig. 11. Continuum intensity contrast, C_{lc} of quiet Sun, network and faculae over $0.94 < \mu \le 1.00$ as a function of $\langle B_1 \rangle / \mu$. The filled circles represent the mean of C_{lc} grouped by $\langle B_1 \rangle / \mu$ in bins 10 G wide. The dashed line denotes the mean quiet Sun level.

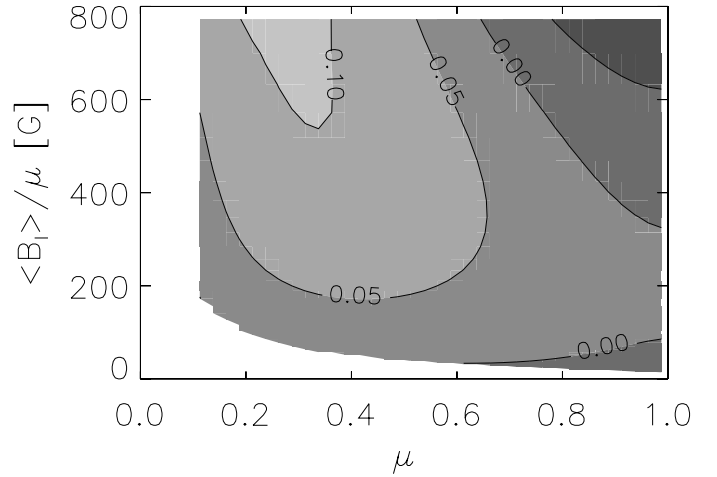


Fig. 12. Grey scale plot of the polynomial fit to bin-averaged continuum intensity contrast over the region where data exist, sampled at the mid-point of each bin in the 36×41 bins grid employed to compute the averages.

uncertainty in $C_{lc,max}$ is given by the RMS difference between the contrast CLV profiles and their cubic polynomial fits. The uncertainty in $C_{lc,max} / (\langle B_1 \rangle / \mu)$ was estimated from the uncertainty in $C_{lc,max}$ and the standard error of $\langle \langle B_1 \rangle / \mu \rangle$ employing standard propagation of errors.

While the position of the continuum intensity contrast CLV maximum varies with $\langle B_1 \rangle / \mu$, line core intensity contrast at a given $\langle B_1 \rangle / \mu$ is invariably strongest at disc centre (Fig. 8)

as pointed out in Sect. 3.1. Maximum line core intensity contrast (i.e., the value at $\mu = 1$), $C_{lc,\mu=1}$ and specific contrast, $C_{lc,\mu=1} / (\langle B_1 \rangle / \mu)$ derived similarly as above from the cubic polynomial fit to the contrast CLV profiles are expressed in Fig. 15 as a function of $\langle B_1 \rangle / \mu$, along with the values obtained from the surface fit (Eq. (4)). In both instances, there is some disparity between the values obtained from the cubic polynomial fits to the contrast CLV profiles and the surface fit below $\langle B_1 \rangle / \mu \sim 100$ G.

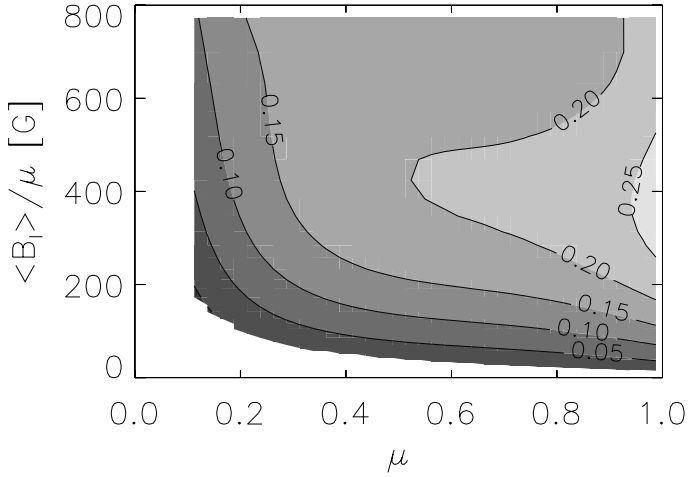


Fig. 13. Same as Fig. 12, but for line core intensity contrast.

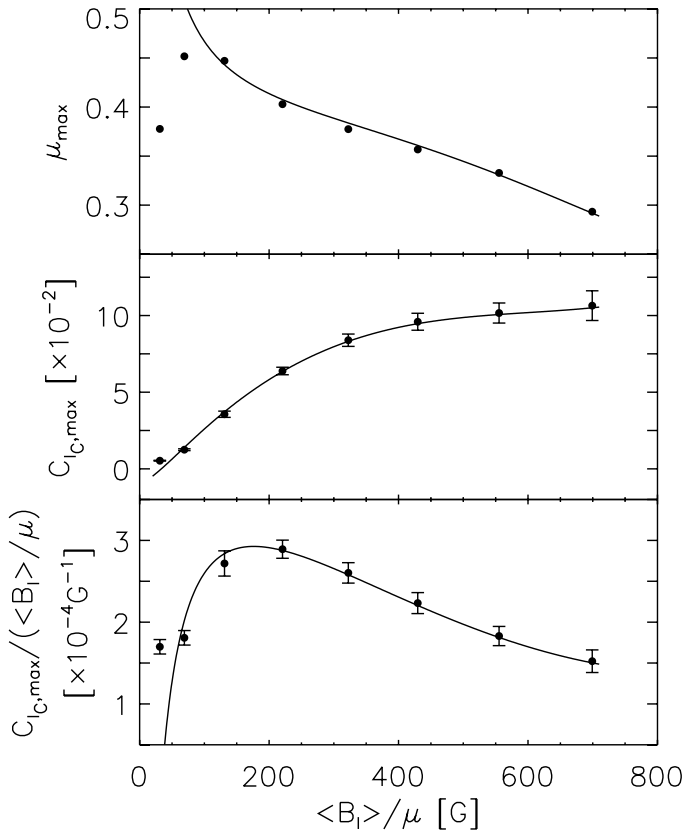


Fig. 14. Heliocentric angle at which continuum intensity contrast reaches its maximum, μ_{\max} (top), as well as the contrast, $C_{I_C, \max}$ (middle) and specific contrast, $C_{I_C, \max} / (\langle B_l \rangle / \mu)$ (bottom) there, as a function of $\langle B_l \rangle / \mu$. The filled circles represent the values derived from the cubic polynomial fit to the contrast CLV profiles (Fig. 7) and the error bars the uncertainty in $C_{I_C, \max}$ and $C_{I_C, \max} / (\langle B_l \rangle / \mu)$. The curves follow the solution from the surface fit to measured continuum intensity contrast (Eq. (3)).

This is likely due to the truncated coverage of disc positions at low $\langle B_l \rangle / \mu$ discussed in Sect. 3.1.

Network and facular features exhibit similar, kilogauss strength magnetic fields (Stenflo 1973; Solanki & Stenflo 1984; Rabin 1992; Rüedi et al. 1992). This means, in general, the intrinsic magnetic field strength of magnetic elements, B does not vary significantly with $\langle B_l \rangle / \mu$ and is also well above the

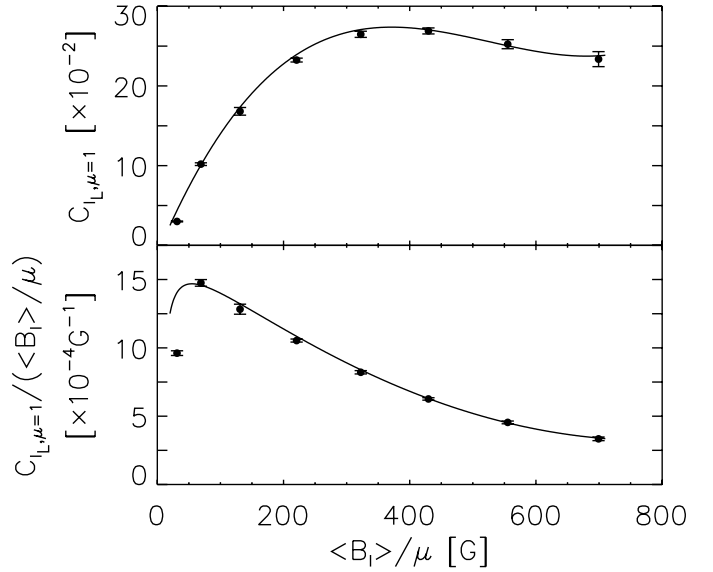


Fig. 15. Line core intensity contrast, $C_{I_L, \mu=1}$ (top) and specific contrast, $C_{I_L, \mu=1} / (\langle B_l \rangle / \mu)$ (bottom) at disc centre as a function of $\langle B_l \rangle / \mu$. The filled circles represent the values derived from the cubic polynomial fit to the contrast CLV profiles (Fig. 8) and the error bars the uncertainty in $C_{I_L, \mu=1}$ and $C_{I_L, \mu=1} / (\langle B_l \rangle / \mu)$. The curves follow the solution from the surface fit to measured line core intensity contrast (Eq. (4)).

range of $\langle B_l \rangle / \mu$ examined here, thus allowing us to assume that the magnetic filling factor, α never saturates. As mentioned in Sect. 2.1, the quantity $\langle B_l \rangle / \mu$ is representative of αB . Taking these into account, within the limits of this study, $\langle B_l \rangle / \mu$ is representative of the magnetic filling factor. Therefore specific contrast, as it is defined and derived here, is a measure of the average intrinsic contrast or heating efficiency of magnetic features within a given $\langle B_l \rangle / \mu$ interval. Like the intrinsic field strength, the intrinsic contrast cannot be measured directly because most network and facular features are not resolved at HMI's spatial resolution and due to the effect of scattered light.

Above $\langle B_l \rangle / \mu \sim 100$ G, the heliocentric angle at which continuum intensity contrast reaches its maximum decreases (i.e., the maximum is reached further away from disc centre) with increasing $\langle B_l \rangle / \mu$ (Fig. 14). A similar trend was reported by Ortiz et al. (2002) based on MDI continuum observations. Assuming the hot wall model (Spruit 1976) and a simple flux tube geometry, the authors demonstrated this to imply the average size of flux tubes increases with $\langle B_l \rangle / \mu$.

Both continuum and line core intensity specific contrast increases strongly with decreasing $\langle B_l \rangle / \mu$ up to a maximum (at around 200 and 50 G respectively) before gradually declining (Figs. 14 and 15). The decline at low $\langle B_l \rangle / \mu$ aside, the observed trends suggests that brightness or temperature excess in both the lower and middle photosphere in flux tubes decreases with increasing magnetic filling factor (the continuum and line core formation height of the Fe I 6173 Å line is about 20 and 300 km respectively, Norton et al. 2006). This may partly be due to the increasing average size of flux tubes; larger magnetic elements appear darker as lateral heating is less efficient (Spruit 1976; Spruit & Zwaan 1981; Grossmann-Doerth et al. 1994) and magnetic suppression of surrounding convective energy transport is more severe (Kobel et al. 2012). The total radiation flux derived from MHD simulations by Vögler (2005) exhibits a similar behaviour. This result also agrees with the observations that network elements appear hotter than facular elements in the lower

and middle photosphere (Solanki & Stenflo 1984; Solanki 1986; Keller et al. 1990) and G-band bright points are brighter in the quiet Sun than in active regions (Romano et al. 2012).

The decline in both continuum and line core specific contrast at low $\langle B_1 \rangle / \mu$ suggests a diminishing heating efficiency of the smallest magnetic elements but is more likely due to the influence of intergranular lanes on apparent contrast. (As with the low contrast towards $\langle B_1 \rangle / \mu = 0$ G in the contrast versus $\langle B_1 \rangle / \mu$ profiles discussed in Sect. 3.1.) The probable impact of the truncated coverage of disc positions at low $\langle B_1 \rangle / \mu$ on the quality of the fits to measured contrast here might have also played a role.

4. Discussion

4.1. Comparison with Ortiz et al. (2002)

A comparison of the results reported here for continuum intensity with those from the similar study based on full-disc MDI observations by Ortiz et al. (2002) reveal several notable differences.

- The contrast reported here is generally higher, by as much as a factor of about two. The difference between the two studies becomes increasingly pronounced with $\langle B_1 \rangle / \mu$ and distance from disc centre.
- Approaching disc centre, contrast appears to level off in our study (Fig. 7). In the earlier work, the contrast declines approximately linearly towards $\mu = 1$ and there are also marked fluctuations about $\mu \sim 0.95$ (Fig. 3, Ortiz et al. 2002).
- Near $\langle B_1 \rangle / \mu = 0$ G contrast is negative here (Fig. 9) but positive in the previous study (Fig. 4, Ortiz et al. 2002).
- The specific contrast (a proxy of intrinsic contrast given by the quotient of contrast at the maximum point on the CLV profile and $\langle B_1 \rangle / \mu$) presented here ascends with $\langle B_1 \rangle / \mu$ up to $\langle B_1 \rangle / \mu \sim 200$ G before descending monotonically thereafter (Fig. 14). Ortiz et al. (2002) found specific contrast to decline approximately linearly with $\langle B_1 \rangle / \mu$ (Fig. 8 in their paper).
- For $\langle B_1 \rangle / \mu \gtrsim 200$ G, the specific contrast reported here is also nearly double that in the earlier work.

The lower contrast and specific contrast (for $\langle B_1 \rangle / \mu \gtrsim 200$ G), and difference in CLV towards disc centre reported by Ortiz et al. (2002) is likely, as we will show shortly, to be primarily due to the misidentification of the magnetic signal adjacent to sunspots and pores as network and faculae (discussed in Sect. 2.2) by those authors. Care was taken here to minimise such misidentification. The negative contrast towards $\langle B_1 \rangle / \mu = 0$ G found here, as argued in Sect. 3.1, arises from the resolution of intergranular lanes at HMI's spatial resolution. We demonstrate below that this difference in spatial resolution also contributes to the opposite $\langle B_1 \rangle / \mu$ -dependence of specific contrast below $\langle B_1 \rangle / \mu \sim 200$ G reported here and by Ortiz et al. (2002).

To recreate the conditions of the study by Ortiz et al. (2002), we recomputed continuum intensity contrast and specific contrast from the HMI data set employed here without applying the magnetic extension removal procedure, binning the data set spatially by 4×4 pixels to be consistent with MDI's spatial resolution and (very approximately) transforming measured contrast to the corresponding value at MDI's operating wavelength, 6768 Å. This last transformation was carried out by describing quiet Sun, network and faculae as black bodies, and taking an effective temperature of 5800 K for the quiet Sun. This allowed us to crudely convert contrast measured at 6173 Å by HMI into the corresponding contrast at 6768 Å. It should be noted that this

is a first-order approximation of the wavelength dependence of contrast which ignores the variation of the continuum formation height with wavelength (Solanki & Unruh 1998; Sütterlin et al. 1999; Norton et al. 2006). In Fig. 16 we depict the contrast CLV profile of network patterns ($50 \text{ G} < \langle B_1 \rangle / \mu \leq 100 \text{ G}$) and active region faculae ($500 \text{ G} < \langle B_1 \rangle / \mu \leq 640 \text{ G}$) after the application of the above procedure. Also plotted are the similarly treated contrast versus $\langle B_1 \rangle / \mu$ profiles about disc centre ($0.94 < \mu \leq 1.00$) and near limb ($0.36 < \mu \leq 0.50$). The specific contrasts from this process are illustrated in Fig. 17.

Excluding the procedure to remove magnetic signal adjoined to sunspots and pores produced the largest effect. It produced an overall drop in contrast (cyan series, Fig. 16) and also reproduced the linear CLV near disc centre observed by Ortiz et al. (2002) ($640 \text{ G} < \langle B_1 \rangle / \mu \leq 800 \text{ G}$ panel). The effects of the resizing of the data set (blue series) and the projection of measured contrasts to MDI's operating wavelength (green series) are relatively minor. The contrast profiles derived from the application of all three procedures (red series) are, in terms of both form and magnitude, in general agreement with the profiles covering similar disc positions and magnetogram signal levels reported by Ortiz et al. (2002) (Figs. 3 and 4 in their paper).

Similarly for specific contrast, the result of applying all three processes (red series, Fig. 17) resembles the measurements presented by Ortiz et al. (2002) (Fig. 8 in their paper) and the greatest effect on magnitude came from the omission of the magnetic extension removal procedure. Binning the data set down to a MDI-like resolution also produced a significant increase in specific contrast at low $\langle B_1 \rangle / \mu$. After combining with the other two processes, this rendered specific contrast approximately level below 200 G. The influence of granulation on apparent contrast at HMI's spatial resolution plays a role in the observed decline in specific contrast from $\langle B_1 \rangle / \mu \sim 200$ G towards $\langle B_1 \rangle / \mu = 0$ G.

The largest effect is produced by the removal of magnetic signal adjoining to sunspots and pores. Hence it is worth considering this process more closely. The procedure by which we removed these signals inevitably discriminates against active region faculae, and various authors have noted lower contrast in active region faculae compared to quiet Sun network at similar magnetogram signal levels (Lawrence et al. 1993; Kobel et al. 2011), but we do not reckon this to be the reason for the greater contrast reported here. In spite of the severe steps taken to exclude magnetic signals adjoining to sunspots and pores, there remains a fair representation of active region faculae in the measured contrasts (Fig. 5). Also, at HMI's spatial resolution, network patterns are largely confined to the lower half of the $\langle B_1 \rangle / \mu$ range considered (Fig. 6) while the difference between the contrast reported here and by Ortiz et al. (2002) is more pronounced at higher $\langle B_1 \rangle / \mu$.

Following the example of earlier studies (e.g. Chapman 1980), Ortiz et al. (2002) fit quadratic polynomials to continuum intensity contrast CLV profiles derived in their study. Here we fit cubic polynomials instead because of the different CLV near disc centre which we just demonstrated to arise from our treatment of magnetic signal adjoining to sunspots and pores.

We surmise that the fluctuations about disc centre in the continuum intensity CLV profiles reported by Ortiz et al. (2002) is due to the non-homogeneous distribution of active regions over the solar disc. Each unit μ represents a greater radial distance towards the disc centre rendering these fluctuations increasingly abrupt. Not accounting for magnetic signal adjoining to sunspots and pores probably accentuated these fluctuations.

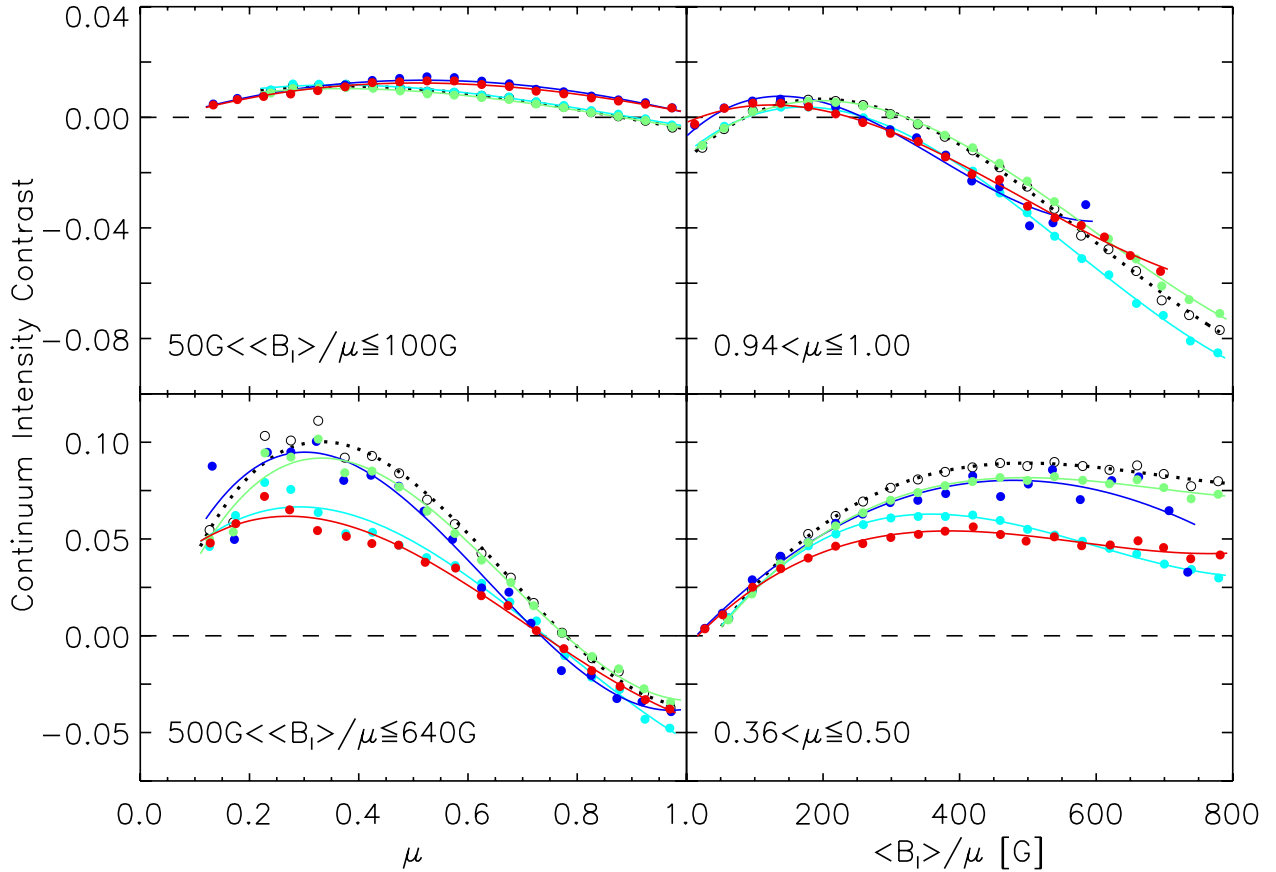


Fig. 16. Selected continuum intensity contrast CLV (*left*) and contrast versus $\langle B_1 \rangle / \mu$ (*right*) profiles from Figs. 7 and 9 (open circles and dotted curves). The selected profiles correspond to quiet Sun network (*top left*), active region faculae (*bottom left*), disc centre (*top right*) and near limb (*bottom right*). The cyan, blue and green series denote the profiles obtained by omitting the magnetic extension removal procedure, spatially binning the data set by 4×4 pixels and converting measured contrast to 6768 \AA respectively. The red series indicates the results of taking into account all these three considerations. The circles represent the mean of measured contrast binned as in the referenced figures and the curves the corresponding third-order polynomial fits. The dashed lines mark the mean quiet Sun level.

4.2. Continuum intensity contrast about disc centre

In this section we compare the magnetogram signal dependence of continuum intensity contrast near disc centre reported here with that from other recent studies, summarized in Table 2. Apart from the work of Ortiz et al. (2002), the CLV of continuum intensity contrast has been examined in detail previously by Topka et al. (1992, 1997) and Lawrence et al. (1993). While we and Ortiz et al. (2002) employed full-disc observations made at a single wavelength and spatial resolution, these authors collated telescope scans made at multiple wavelengths and resolutions. The magnetogram signal intervals represented by the contrast CLV profiles presented in these papers also differ considerably from those presented here and by Ortiz et al. (2002). For these reasons it is not straightforward to make any quantitative comparisons with the contrast CLV reported by these studies, therefore the focus on results for near disc centre here.

The negative contrast at low magnetogram signal levels found here and by the majority of the compared works counters expectations from thin flux tube models, which predict intrinsically bright magnetic features in this regime (Knölker et al. 1988). As discussed in Sect. 3.1, this is attributed here (and in Title et al. 1992; Topka et al. 1992; Kobel et al. 2011) to the influence of intergranular lanes, an assertion supported by various models (Title & Berger 1996; Schnerr & Spruit 2011). Of the studies compared, only that by Ortiz et al. (2002) noted positive contrasts. Binning the data set here to a MDI-like

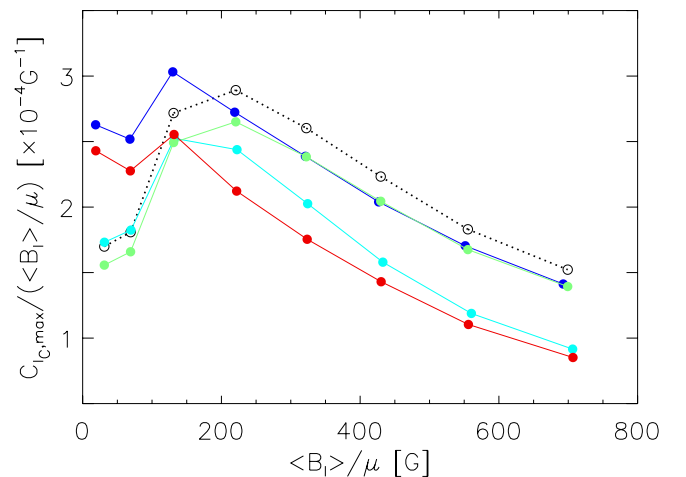


Fig. 17. Continuum intensity specific contrast as a function of $\langle B_1 \rangle / \mu$ from Fig. 14 (open circles). The cyan, blue and green filled circles represent the same quantity obtained by omitting the magnetic extension removal procedure, spatially binning the data set by 4×4 pixels and converting measured contrast to 6768 \AA respectively. The red filled circles represent the result of taking into account all these three considerations. The points in each series are joined by straight lines to aid the eye.

resolution raised the disc centre end of the contrast CLV profile in the $50 \text{ G} < \langle B_1 \rangle / \mu \leq 100 \text{ G}$ interval into positive

Table 2. Continuum intensity contrast dependence on magnetogram signal near disc centre obtained in the present and from earlier studies.

Reference	Instrument	Target ^b	Resolution [Arcsec]	Wavelength [Å]	Results
Present	SDO/HMI	$\mu > 0.94^c$	1	6173	Negative near $\langle B_1 \rangle / \mu = 0$ G. Peak at $\langle B_1 \rangle / \mu \sim 200$ G.
1, 2, 3, 4	SVST	AR	≥ 0.3	Various ^d	Negative near $\langle B_1 \rangle = 0$ G. Monotonic decline with $\langle B_1 \rangle$.
3	SVST	QS	≥ 0.3	6302	Negative near $\langle B_1 \rangle = 0$ G. Peak at $\langle B_1 \rangle \sim 400$ G.
	SFO/SHG ^a	QS	≥ 1	6302	Negative near $\langle B_1 \rangle = 0$ G. Peak at $100 \text{ G} \lesssim \langle B_1 \rangle \lesssim 200 \text{ G}$.
		AR			Negative near $\langle B_1 \rangle = 0$ G. Monotonic decline with $\langle B_1 \rangle$.
5	SoHO/MDI	$\mu > 0.92^c$	4	6768	Positive near $\langle B_1 \rangle / \mu = 0$ G. Peak at $\langle B_1 \rangle / \mu \sim 100$ G.
6	SST	AR	0.15	6302	Negative near $\langle B_1 \rangle = 0$ G. Peak at $\langle B_1 \rangle \sim 650$ G.
7	Hinode/SOT	QS	0.3	6302	Negative near $\langle B_1 \rangle = 0$ G. Peak at $\langle B_1 \rangle \sim 700$ G.
		AR			Negative near $\langle B_1 \rangle = 0$ G. Peak at $\langle B_1 \rangle \sim 700$ G.
8	SST	QS	0.15	6302	Negative near $\langle B_1 \rangle = 0$ G. Saturate at $\langle B_1 \rangle \sim 800$ G.
	Hinode/SOT	QS	0.3	6302	Negative near $\langle B_1 \rangle = 0$ G. Peak at $\langle B_1 \rangle \sim 500$ G.

Notes. ^(a) San Fernando Observatory (SFO) 28-cm vacuum telescope and vacuum spectroheliograph (SHG). ^(b) AR and QS denote active region and quiet Sun respectively. ^(c) Segment of full-disc observations considered. ^(d) 5250 Å, 5576 Å, 6302 Å and 6768 Å.

References. (1) Title et al. (1992); (2) Topka et al. (1992); (3) Lawrence et al. (1993); (4) Topka et al. (1997); (5) Ortiz et al. (2002); (6) Narayan & Schärmer (2010); (7) Kobel et al. (2011); (8) Schnerr & Spruit (2011).

territory (Fig. 16), suggesting that the positive contrasts reported by Ortiz et al. (2002) arose from utilising data at a resolution (the lowest of the studies compared) where granulation is largely unresolved.

From SVST scans of active regions, Title et al. (1992), Topka et al. (1992, 1997) and Lawrence et al. (1993) found contrast to decline monotonically with magnetogram signal. Lawrence et al. (1993) also noted the same with active region data acquired at the San Fernando Observatory (SFO). Kobel et al. (2011) demonstrated the comparatively poorer resolution and straylight from pores to be likely culpable for the monotonic decline observed in the SVST studies. In all the other compared works, contrast exhibits a peak, the position of which varied from $\langle B_1 \rangle / \mu \sim 100$ G (Ortiz et al. 2002) to $\langle B_1 \rangle \sim 700$ G (Kobel et al. 2011), except for the quiet Sun SST scan examined by Schnerr & Spruit (2011), where contrast saturated at $\langle B_1 \rangle \sim 800$ G. Generally, the finer the spatial resolution, the higher the position of the peak. Most of these studies were based on observations made at the Fe I 6302 Å line. Even if we discount the studies made at other wavelengths, this broad pattern is still apparent, ruling out differences in wavelength as the major driver. Kobel et al. (2011) reported similar contrast peak positions for quiet Sun and active region scans. Therefore the difference between active region and quiet Sun contrast had likely little role in the spread in reported peak positions amongst the compared works. As shown in the $0.94 < \mu \leq 1.00$ panel of Fig. 16, both resizing the HMI data set to a MDI-like spatial resolution and omitting the magnetic extension removal procedure shifted the position of the contrast versus $\langle B_1 \rangle / \mu$ profile maximum towards the origin.

The above comparison points to differences in spatial resolution and treatment of magnetic signal near sunspots and pores as the dominant factors behind the spread in reported dependence of contrast on magnetogram signal. Indeed, the recent MHD simulation work of Röhrbein et al. (2011) suggests that the contrast peak at intermediate magnetogram signal levels seen in direct observations, but not observed in MHD simulations, is a product of the limited spatial resolution. The bulk of the studies listed in Table 2 were based on higher spatial resolution data than utilised here. For this reason, a more quantitative comparison like we did in Sect. 4.1 with the findings of Ortiz et al. (2002) is not workable here.

The recent works of Berger et al. (2007) and Viticchié et al. (2010), examining the contrast of bright points in the G-band,

bear tenuous relevance to our study. These studies utilised observations made in a molecular band (i.e., neither continuum nor line core) where the contrast of magnetic features is enhanced (due to CH depletion, Steiner et al. 2001; Schüssler et al. 2003). More importantly, while this study and the works cited in Table 2 considered each pixel a separate entity, Berger et al. (2007) and Viticchié et al. (2010) examined the overall contrast of each individual bright structure. As the body of magnetic features isolated by both approaches differ, the results are not directly comparable. Berger et al. (2007) did however also report a pixel-by-pixel consideration of G-band contrast. Scans at four disc positions were surveyed. Barring one that appeared anomalous, the contrast versus magnetogram signal profiles from each scan bear general resemblance to ours in terms of form. Notably, the profile from the disc centre scan, with a spatial resolution of 0.15 arcsec, exhibits a peak at $\langle B_1 \rangle \sim 700$ G, consistent with the broad pattern between spatial resolution and peak position described here.

4.3. Line core intensity contrast

As pointed out in Sect. 3.1, the most notable difference between the continuum and line core intensity contrasts present here is the converse CLV. While continuum intensity contrast is weakest near disc centre and strengthens towards the limb, line core intensity contrast is strongest at disc centre and declines towards the limb. The divergent CLV exhibited by the two sets of measurements stem from their rather different physical sources. Continuum intensity is enhanced largely in the hot walls of magnetic elements, thus the centre-to-limb increase. The line core is formed in the middle photosphere, which is heated either by radiation from deeper layers (Knölker et al. 1991), or by mechanical and Ohmic dissipations (Moll et al. 2012). Also stated in Sect. 3.1, line core intensity is modulated by line strength and shape, and continuum intensity. Excluding variation related to continuum excess, line core intensity enhancement arises from the influence of the temperature excess in the middle photosphere and Zeeman splitting on line strength and shape. Given the relatively narrow, vertical geometry of flux tubes, as magnetic elements rotate from disc centre to limb, line-of-sight rays go from being largely confined to single flux tubes to increasingly passing into and out of multiple flux tubes, especially in densely packed facular regions (Büntje et al. 1993). Line core intensity contrast decreases towards the limb as the contribution

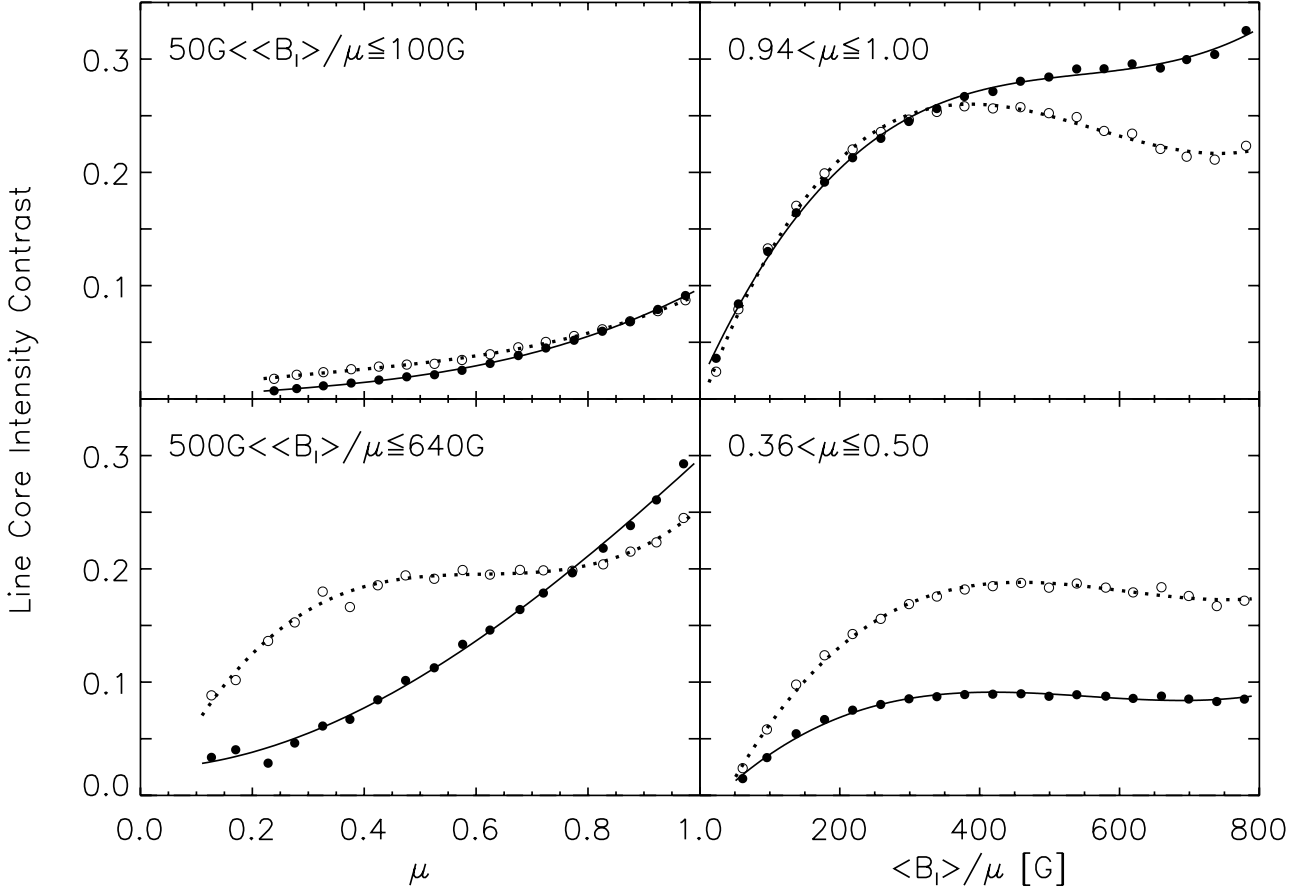


Fig. 18. Selected line core intensity (open circles and dotted curves) and corresponding residual intensity (filled circles and solid curves) contrast CLV (*left*) and contrast versus $\langle B_1 \rangle / \mu$ (*right*) profiles. The circles represent the mean of measured contrast binned as in Figs. 8 and 10 and the curves the corresponding cubic polynomial fits. The selected profiles correspond to quiet Sun network (*top left*), active region faculae (*bottom left*), disc centre (*top right*) and near limb (*bottom right*).

to the spectral line from magnetic elements diminishes from absorption in the non-magnetic part of the atmosphere transversed by the rays (Solanki et al. 1998). Another probable cause of the centre-to-limb decline is the spatial displacement of the line core with respect to the corresponding continuum towards the limb caused by the difference in formation height and oblique viewing geometry (Stelmacher & Wiehr 1991, 2001). The line core intensity enhancement arising from temperature excess in the middle photosphere and Zeeman splitting discussed here is not to be confused with that from the centre-to-limb broadening of the Fe I 6173 Å line mentioned in Sect. 2.2.2, which arises from the viewing geometry independent of magnetic field.

We recomputed line core intensity contrast, this time normalizing the line core intensity images by the corresponding continuum intensity images prior to data reduction. The result, the line core residual intensity contrast, is essentially the component of line core intensity contrast arising from line weakening in magnetic features alone. Line core intensity and residual intensity contrast values can be compared directly. (Line core residual intensity contrast equates to the line core intensity contrast we would get from scaling the line core intensity of just the network and faculae pixels by $\langle I_{C,QS} \rangle / I_C$.) The line core residual intensity contrast CLV profile of network patterns ($50 \text{ G} < \langle B_1 \rangle / \mu \leq 100 \text{ G}$) and active region faculae ($500 \text{ G} < \langle B_1 \rangle / \mu \leq 640 \text{ G}$), and contrast versus $\langle B_1 \rangle / \mu$ profile about disc centre ($0.94 < \mu \leq 1.00$) and near limb ($0.36 < \mu \leq 0.50$) so derived are plotted along with the corresponding line core intensity contrast profiles from Figs. 8 and 10 in Fig. 18. Line core

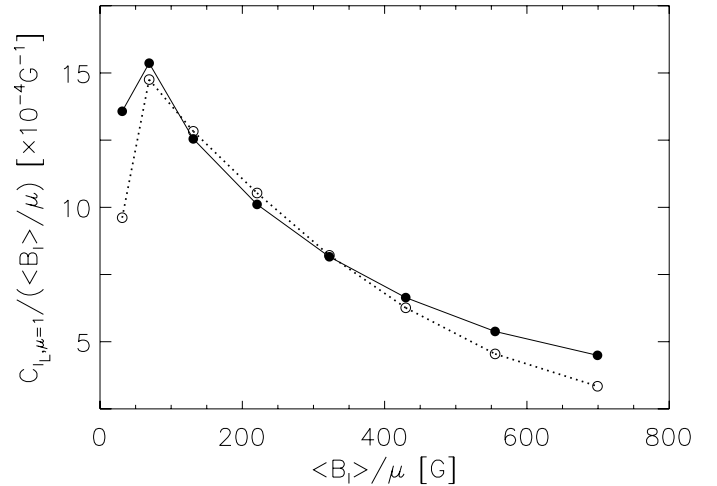


Fig. 19. Line core intensity (open circles) and corresponding residual intensity (filled circles) specific contrast as a function of $\langle B_1 \rangle / \mu$. The circles are joined by straight lines to aid the eye.

residual intensity specific contrast is plotted along with the line core intensity specific contrast from Fig. 15 in Fig. 19.

As expected, excluding the contribution of continuum intensity enhancement to line core intensity contrast results in a more pronounced centre-to-limb decline ($50 \text{ G} < \langle B_1 \rangle / \mu \leq 100 \text{ G}$ and $500 \text{ G} < \langle B_1 \rangle / \mu \leq 640 \text{ G}$ panels, Fig. 18). This decline

in the line core residual intensity contrast CLV profiles is also consistent with the spectroscopic observations of [Stellmacher & Wiehr \(1979\)](#) and [Hirzberger & Wiehr \(2005\)](#). Comparing line core intensity and residual intensity contrast (Figs. 18 and 19), the broad similarity, especially near disc centre, imply that line core intensity contrast is dominated by the contribution from line weakening. Even towards the limb, where magnetic line weakening is at its weakest, it still comprises a significant proportion of observed line core intensity contrast. The potential implications of this result and the opposite CLV exhibited by continuum and line core intensity contrast on facular contribution to solar irradiance variations will be discussed in Sect. 4.4.

Very few studies examining the disc position and magnetogram signal dependence of line core intensity contrast exist in the literature. [Frazier \(1971\)](#), [Lawrence et al. \(1991\)](#) and [Title et al. \(1992\)](#) measured intensity contrast at disc centre in the core of the Fe I 5250 Å, Fe I 6302 Å and Ni I 6768 Å lines, respectively. Results from different lines are not directly comparable but it is still encouraging to see that in terms of magnitude and general trend with magnetogram signal, the results from these earlier studies express broad agreement with ours. The only notable exception is the steep monotonic decline at $\langle B_1 \rangle > 600$ G reported by [Title et al. \(1992\)](#), which largely persisted even after the authors masked out pores. The decline coincides with a similar trend in intensity contrast measured at the nearby continuum, suggesting a greater relative influence of the continuum excess to magnetic line weakening at the Ni I 6768 Å line compared to the Fe I 6173 Å line. [Frazier \(1971\)](#) also made measurements away from disc centre, but due to data scatter the author could do no better than to present a schematic representation of the CLV through visually fitted linear functions. [Walton \(1987\)](#) reported measured line core residual intensities for eight magnetically insensitive lines at various disc positions. There were however only a small number of scattered measurements for each line, and a relatively narrow range of disc positions ($\mu > 0.6$). To our knowledge, the present study is the first to examine line core intensity contrast employing full-disc observations. Together with the relatively fine resolution and low noise level, this allowed us to describe the magnetogram signal dependence and especially the CLV with greater accuracy and detail than in the previous efforts.

4.4. Facular contribution to variation in solar irradiance

Our finding that intensity contrast in the line core is dominated by line weakening rather than continuum intensity enhancement and exhibits the opposite CLV as continuum intensity contrast has potential implications on facular contribution to total solar irradiance variation. Total solar irradiance (TSI) variation is the sum manifest of variation in the continuum and spectral lines. The converse CLV of the continuum and line core intensity contrasts reported here imply a different time variation of the contribution by the continuum and spectral lines to solar irradiance as magnetic features rotate across the solar disc.

In Fig. 20a we show the level 2.0 hourly TSI measurements from the DIARAD radiometer ([Dewitte et al. 2004](#)) on the SoHO/VIRGO instrument ([Fröhlich et al. 1995](#)) for the 22-day period of August 19 to September 9, 1996 (open circles). Active region NOAA 7986 rotated into view on August 23 and out of view on September 5, and was the only active region on the solar disc for the duration of its passage across the solar disc. The period is otherwise relatively quiet. This data therefore allows us to chart variations in TSI arising mainly from the passage

of a single active region across the solar disc. The dip around August 29 corresponds to active region NOAA 7986 crossing disc centre. Even with darkening from sunspots present in the active region, the nadir of the dip is ~ 0.2 Wm⁻² above the level before August 23 and after September 5. This suggests an overall positive contribution to TSI variation by the faculae in NOAA 7986 when it was near disc centre (first pointed out by [Fligge et al. 2000](#)).

A schematic representation of facular contribution to variation in TSI during the passage of NOAA 7986 across the solar disc, depicted in Fig. 20e, was derived as follows.

- The DIARAD TSI data was interpolated at 0.1 day intervals and the result smoothed (via binomial smoothing, [Marchand & Marmet 1983](#)). Sunspot darkening was estimated from the Photometric Sunspot Index (PSI) by [Chapman et al. \(1994\)](#) based on full-disc photometric images acquired with the Cartesian Full Disk Telescope 1 (CFDT1) at SFO. A quadratic polynomial was fitted to the PSI values from the period of interest excluding the points where PSI = 0 (i.e., no sunspots in view). Taking a value of 1365.4 Wm⁻² for the total irradiance of the quiet Sun, the fit was converted from units of parts per million to Wm⁻² and subtracted from the DIARAD data. This value for the total irradiance of the quiet Sun is given by the average TSI at the last three solar minima stated in version d41_62_1204 (dated April 2, 2012) of the PMOD TSI composite ([Fröhlich 2000](#)). The DIARAD data, after this treatment, represents variation in TSI largely from faculae in NOAA 7986 alone. In Fig. 20a we plot the DIARAD data after interpolation and smoothing (red dotted curve), and after removing sunspot darkening (red solid curve) along the original measurements. In Fig. 20b we show the PSI (open circles) and the quadratic polynomial fit to the non-zero segment (curve).
- The trajectory of NOAA 7986 during its passage across the solar disc was estimated from 142 level 1.8 5-min MDI magnetograms ([Scherrer et al. 1995](#)) on which the active region was entirely in view (i.e. not only partially rotated into, or partially rotated off the solar disc). Taking the unsigned magnetogram signal, the magnetograms were binned spatially by 16×16 pixels. For each binned magnetogram, the position of NOAA 7986, in terms of μ , was estimated from the mean position of the five pixels within the active region with the strongest signal. The trajectory of NOAA 7986 is then given by the quadratic polynomial fit to these estimates. In Fig. 20c we show the estimated position of NOAA 7986 in the magnetograms (open circles) and the quadratic polynomial fit (curve).
- Facular contribution to variation in TSI was very approximately modelled from the empirical relationships describing contrast as a function of μ and $\langle B_1 \rangle / \mu$ derived in this study. Assuming a power law distribution of $\langle B_1 \rangle / \mu$ with a scaling exponent of -1.85 ([Parnell et al. 2009](#)), we evaluated Eqs. (3) and (4), scaled by $\left(\frac{\langle B_1 \rangle}{\mu} / 15\right)^{-1.85}$ and integrated over $\langle B_1 \rangle / \mu = 15$ G to 800 G, at 0.1 day intervals taking μ from the trajectory of NOAA 7986 estimated earlier. The resulting time series were then scaled by μ (to correct for the CLV of projected area on the solar disc) and the limb darkening function from [Foukal et al. \(2004\)](#). Given the approximate manner of this derivation, the results are non-quantitative. However for this analysis it is not the actual values but the temporal trends that is important. Here we had approximated the active region as a point object and so cannot include variation arising from the active region being only partially

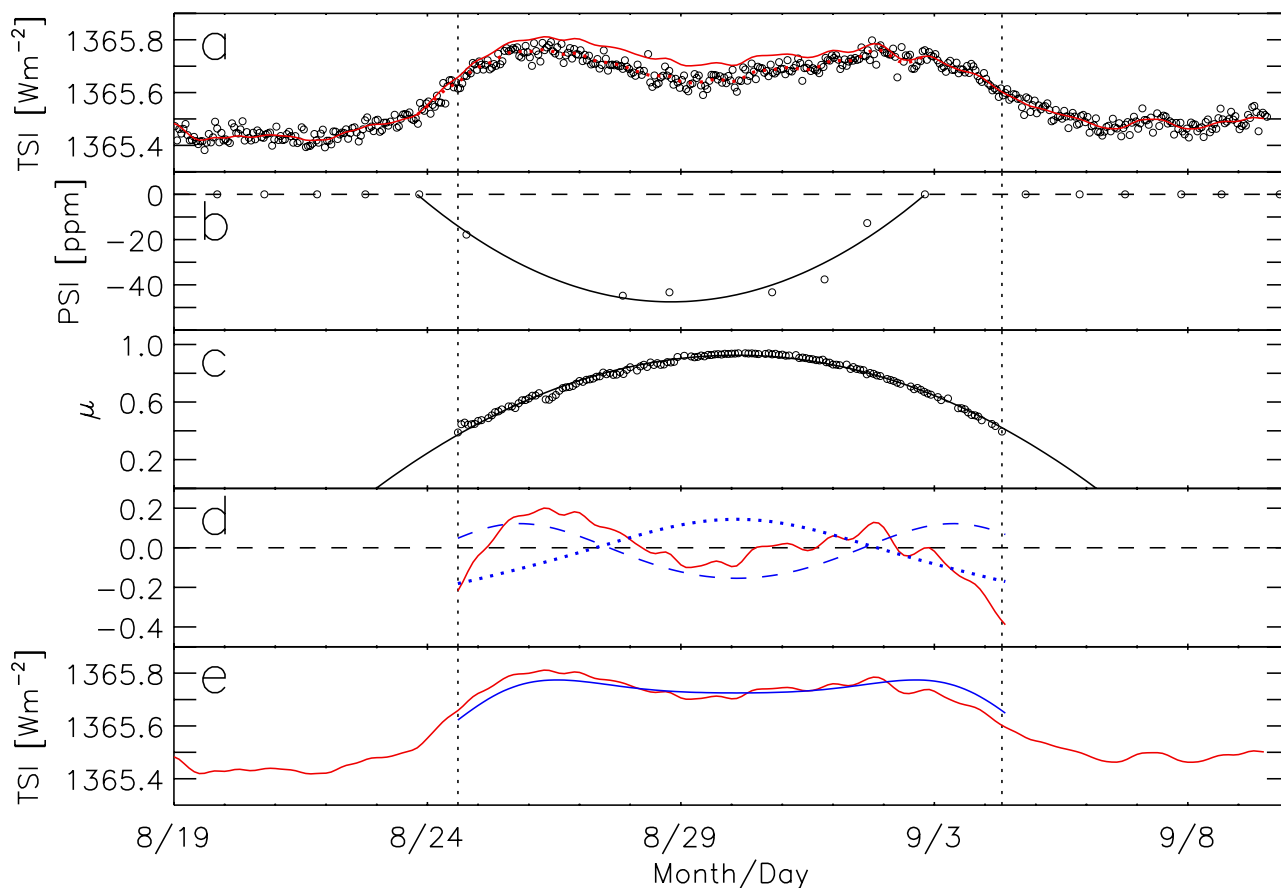


Fig. 20. **a)** Total solar irradiance, TSI from DIARAD on SoHO/VIRGO (open circles) for the period of August 19 to September 9, 1996. The dotted and solid red curves represent the interpolated and smoothed version before and after subtracting sunspot darkening. **b)** Photometric Sunspot Index, PSI (open circles) by Chapman et al. (1994) and the quadratic polynomial fit to the non-zero points (curve). The dashed line marks the zero level. **c)** Position of NOAA 7986 as estimated from MDI magnetograms (open circles) and the quadratic polynomial fit (curve). **d)** TSI minus sunspot darkening (red curve) and model of facular contribution to TSI based on observed intensity contrast in the continuum (blue dashed curve) and line core (blue dotted curve), each mean subtracted and normalized by the area bound between the time series and the zero level (black dashed line). **e)** TSI minus sunspot darkening (red curve) and the multiple linear regression fit of the continuum and line core models (blue solid curve). The dotted lines running down all the panels mark the period where NOAA 7986 was entirely on the solar disc in MDI magnetograms.

visible as it rotates into and off the solar disc. This derivation is therefore only valid, and confined to, the period where NOAA 7986 was entirely in view in MDI magnetograms.

The treated DIARAD data, giving TSI variation largely from faculae in NOAA 7986 alone, is plotted in Fig. 20d (red curve) along the conjectures based on the observed intensity contrast in the continuum (blue dashed curve) and line core (blue dotted curve). To compare how they varied with time, we subtracted the mean from and normalized each time series by the area bounded by the curve and the zero level. In Fig. 20e we show the multiple linear regression fit of the continuum and line core models to the DIARAD series (blue solid curve), which showed a much better agreement to it than either model. Facular contribution to variation in solar irradiance appears to be strongly driven by intensity contrast in both the continuum, and spectral lines, which derives largely from line weakening in magnetic elements. This complies with the observation that solar irradiance variations over the solar cycle seems to be significantly influenced by changes in spectral lines (Mitchell & Livingston 1991; Unruh et al. 1999; Preminger et al. 2002).

Various studies examining the photometric contrast of faculae, as identified in calcium line images, reported positive values near disc centre (Lawrence et al. 1988; Walton et al. 2003; Foukal et al. 2004). The apparent divergence between the

findings of these works, and the largely negative contrast near disc centre reported here (Fig. 9) and in the similar studies listed in Table 2, where network and faculae were characterized by the magnetogram signal, arises from the different selection methods (Ermolli et al. 2007). Significantly, the results of Foukal et al. (2004) were based on near total light broadband measurements. From the statistical analysis of an extensive catalogue of full-disc photometric observations obtained with the SFO/CFDT1, Walton et al. (2003) found contrast, in a continuum passband (i.e., negligible spectral line contribution) in the visible red, averaged over each facular region (as identified in the Ca II K) to be positive (~ 0.005) near disc centre. The authors took this result to indicate the distribution of flux tube sizes in facular regions is biased to the low end (i.e., more small bright flux tubes than large dark ones), which is reasonable considering the typical distribution of magnetogram signal (i.e., much more weak signals than strong, Parnell et al. 2009) and the observation that the average flux tube size is greater where magnetogram signal is greater (Ortiz et al. 2002). This suggests the continuum component of facular contribution to TSI variation is on average positive at disc centre in the visible red. From this and the analysis presented above, we conclude that the apparent overall positive contribution to TSI variation by the faculae in NOAA 7986 when it was near disc centre is, at least in part, due to the prevalence of smaller flux tubes and line weakening.

5. Conclusion

Here we have presented measured network and facular intensity contrast in the continuum and in the core of the Fe I 6173 Å line from SDO/HMI full-disc observations. We studied the dependence of the contrast on disc position and magnetogram signal, represented by μ and $\langle B_1 \rangle / \mu$ respectively. Specifically, we derived empirical relationships describing contrast as a function of μ and $\langle B_1 \rangle / \mu$, and specific contrast (contrast per unit $\langle B_1 \rangle / \mu$, representative of intrinsic contrast) as a function of $\langle B_1 \rangle / \mu$. This study exploits the unprecedented opportunity offered by the SDO mission to examine co-temporal full-disc observations of magnetic field and intensity at a constant intermediate spatial resolution (1 arcsec), relatively low noise, and without atmospheric interference. The quality of the data allowed us to examine intensity contrast for a larger sample at greater accuracy and detail than previous, similar studies, especially in the case of the line core. These results constitute stringent observational constraints on the variation of network and facular intensity with disc position and magnetogram signal in the low and middle photosphere. By constraining atmospheric models of network and faculae, these results should be of utility to solar irradiance reconstructions, especially as HMI data will increasingly be used for this purpose. Given this is the first study of its kind to examine the entire solar disc in both the continuum and line core, it should also be useful to reproduce these results in models of magnetic flux concentrations.

There are significant discrepancies in the continuum intensity contrast reported here and from earlier studies. In this study we had taken steps to account for magnetic signal in the periphery of sunspots and pores, arising from their magnetic canopies and the influence of straylight, which can easily be misidentified as network and faculae. From a comparison with the findings of past efforts, including a recomputation of the results obtained here recreating the conditions of the similar study by Ortiz et al. (2002), we showed differences in resolution, and treatment of magnetic signal adjacent to sunspots and pores to be the likely main factors behind the spread in reported results. The apparent radiant behaviour of network and faculae elements is strongly modulated by spatial resolution (Title & Berger 1996; Röhrbein et al. 2011; Schnerr & Spruit 2011). An understanding of its influence is necessary for the proper interpretation of direct measurements.

In terms of magnitude, trend with magnetogram signal and in particular the CLV, the results obtained here in the continuum and line core differ considerably. While continuum intensity contrast broadly ascends towards the limb, line core intensity contrast is greatest near disc centre and diminishes from disc centre to limb. The divergence between both sets of measurements arises dominantly from spectral line changes due to heating in the middle photosphere and Zeeman splitting in magnetic features, and the different mechanisms by which apparent contrast vary with viewing geometry going from disc centre to limb. From a simple model based on the empirical relationships between contrast, and μ and $\langle B_1 \rangle / \mu$ derived here we confirmed that facular contribution to variation in solar irradiance is strongly driven by both continuum excess and spectral line changes.

The specific contrast in both the continuum and line core exhibit a marked decline with increasing magnetogram signal, confirming that network elements are, per unit magnetic flux, hotter and brighter than active region faculae. The different radiant behaviour of network and faculae, not accounted in present models of solar irradiance variations, would be an important factor to consider for more realistic modelling. This observation also

implies that secular changes in solar irradiance may be considerably larger than what some models of solar irradiance variations have suggested, given the variation in the number of small-scale magnetic elements on the solar disc is a prime candidate driver of secular changes (Solanki et al. 2002). For example, the model employed by Krivova et al. (2007) to reconstruct variation in TSI from 1700 and by Vieira et al. (2011) for over the Holocene assumed the faculae contrast model by Unruh et al. (1999) for both network and faculae. This renders network and faculae with similar magnetic filling factors equally bright and therefore possibly underestimate the contribution by network to secular variation.

Acknowledgements. K.L.Y. acknowledges postgraduate fellowship of the International Max Planck Research School on Physical Processes in the Solar System and Beyond. The authors would like to express their gratitude to the SDO/HMI team for providing the data and members of the German Data Center for SDO (GDC-SDO) team, in particular R. Burston, for assistance rendered over the course of this work. This work has been partly supported by WCU grant No. R31-10016 funded by the Korean Ministry of Education, Science and Technology.

References

- Ball, W. T., Unruh, Y. C., Krivova, N. A., Solanki, S., & Harder, J. W. 2011, *A&A*, 530, A71
- Ball, W. T., Unruh, Y. C., Krivova, N. A., et al. 2012, *A&A*, 541, A27
- Barthol, P., Gandorfer, A., Solanki, S. K., et al. 2011, *Sol. Phys.*, 268, 1
- Beck, C., & Rezaei, R. 2009, *A&A*, 502, 969
- Berger, T. E., & Title, A. M. 1996, *ApJ*, 463, 365
- Berger, T. E., Rouppe van der Voort, L., & Löfdahl, M. 2007, *ApJ*, 661, 1272
- Bünte, M., Solanki, S. K., & Steiner, O. 1993, *A&A*, 268, 736
- Chapman, G. A. 1980, *ApJ*, 242, L45
- Chapman, G. A., Cookson, A. M., & Dobias, J. J. 1994, *ApJ*, 432, 403
- Collados, M., Martínez Pillet, V., Ruiz Cobo, B., del Toro Iniesta, J. C., & Vázquez, M. 1994, *A&A*, 291, 622
- Couvidat, S. 2011, Calculation of Observables from HMI Data, <http://hmi.stanford.edu/doc/HMI-S031.pdf>, July 15, 2011 revision
- Couvidat, S., Rajaguru, S. P., Wachter, R., et al. 2012, *Sol. Phys.*, 278, 217
- Dewitte, S., Crommelynck, D., & Joukoff, A. 2004, *J. Geophys. Res.*, 109, 2102
- Domingo, V., Ermolli, I., Fox, P., et al. 2009, *Space Sci. Rev.*, 145, 337
- Ermolli, I., Criscuolo, S., Centrone, M., Giorgi, F., & Penza, V. 2007, *A&A*, 465, 305
- Fligge, M., Solanki, S. K., & Unruh, Y. C. 2000, *A&A*, 353, 380
- Foukal, P., Bernasconi, P., Eaton, H., & Rust, D. 2004, *ApJ*, 611, L57
- Frazier, E. N. 1971, *Sol. Phys.*, 21, 42
- Fröhlich, C. 2000, *Space Sci. Rev.*, 94, 15
- Fröhlich, C., Romero, J., Roth, H., et al. 1995, *Sol. Phys.*, 162, 101
- Giovanelli, R. G. 1980, *Sol. Phys.*, 68, 49
- Grossmann-Doerth, U., Knölker, M., Schüssler, M., & Solanki, S. K. 1994, *A&A*, 285, 648
- Hirzberger, J., & Wiehr, E. 2005, *A&A*, 438, 1059
- Keller, C. U., Steiner, O., Stenflo, J. O., & Solanki, S. K. 1990, *A&A*, 233, 583
- Khomenko, E. V., Collados, M., Solanki, S. K., Lagg, A., & Trujillo Bueno, J. 2003, *A&A*, 408, 1115
- Knölker, M., Schüssler, M., & Weisshaar, E. 1988, *A&A*, 194, 257
- Knölker, M., Grossmann-Doerth, U., Schüssler, M., & Weisshaar, E. 1991, *Adv. Space Res.*, 11, 285
- Kobel, P., Solanki, S. K., & Borrero, J. M. 2011, *A&A*, 531, A112
- Kobel, P., Solanki, S. K., & Borrero, J. M. 2012, *A&A*, 542, A96
- Kosugi, T., Matsuzaki, K., Sakao, T., et al. 2007, *Sol. Phys.*, 243, 3
- Krivova, N. A., Balmaceda, L., & Solanki, S. K. 2007, *A&A*, 467, 335
- Lagg, A., Solanki, S. K., Riethmüller, T. L., et al. 2010, *ApJ*, 723, L164
- Lawrence, J. K., Chapman, G. A., & Herzog, A. D. 1988, *ApJ*, 324, 1184
- Lawrence, J. K., Chapman, G. A., & Walton, S. R. 1991, *ApJ*, 375, 771
- Lawrence, J. K., Topka, K. P., & Jones, H. P. 1993, *J. Geophys. Res.*, 98, 18911
- Lites, B. W., Scharmer, G. B., Berger, T. E., & Title, A. M. 2004, *Sol. Phys.*, 221, 65
- Lites, B. W., Kubo, M., Socas-Navarro, H., et al. 2008, *ApJ*, 672, 1237
- Liu, Y., Hoeksema, J. T., Scherrer, P. H., et al. 2012, *Sol. Phys.*, 279, 295
- Malthby, P., Avrett, E. H., Carlsson, M., et al. 1986, *ApJ*, 306, 284
- Marchand, P., & Marmet, L. 1983, *Rev. Sci. Instrum.*, 54, 1034
- Martínez Pillet, V., Del Toro Iniesta, J. C., Álvarez-Herrero, A., et al. 2011, *Sol. Phys.*, 268, 57
- Mathew, S. K., Martínez Pillet, V., Solanki, S. K., & Krivova, N. A. 2007, *A&A*, 465, 291

- Mitchell, Jr., W. E., & Livingston, W. C. 1991, *ApJ*, 372, 336
- Moll, R., Cameron, R. H., & Schüssler, M. 2012, *A&A*, 541, A68
- Narayan, G., & Scharmer, G. B. 2010, *A&A*, 524, A3
- Neckel, H., & Labs, D. 1994, *Sol. Phys.*, 153, 91
- Norton, A. A., Graham, J. P., Ulrich, R. K., et al. 2006, *Sol. Phys.*, 239, 69
- Ortiz, A., Solanki, S. K., Domingo, V., Fligge, M., & Sanahuja, B. 2002, *A&A*, 388, 1036
- Parnell, C. E., DeForest, C. E., Hagenaar, H. J., et al. 2009, *ApJ*, 698, 75
- Preminger, D. G., Walton, S. R., & Chapman, G. A. 2002, *J. Geophys. Res.*, 107, 1354
- Rabin, D. 1992, *ApJ*, 391, 832
- Röhrbein, D., Cameron, R., & Schüssler, M. 2011, *A&A*, 532, A140
- Romano, P., Berrilli, F., Criscuoli, S., et al. 2012, *Sol. Phys.*, 280, 407
- Rüedi, I., Solanki, S. K., Livingston, W., & Stenflo, J. O. 1992, *A&A*, 263, 323
- Sánchez Cuberes, M., Bonet, J. A., Vázquez, M., & Wittmann, A. D. 2000, *ApJ*, 538, 940
- Sánchez Cuberes, M., Vázquez, M., Bonet, J. A., & Sobotka, M. 2003, *A&A*, 397, 1075
- Scharmer, G. B., Bjelksjo, K., Korhonen, T. K., Lindberg, B., & Petterson, B. 2003, in *SPIE Conf. Ser.* 4853, eds. S. L. Keil, & S. V. Avakyan, 341
- Scherrer, P. H., Bogart, R. S., Bush, R. I., et al. 1995, *Sol. Phys.*, 162, 129
- Schnerr, R. S., & Spruit, H. C. 2011, *A&A*, 532, A136
- Schou, J., Scherrer, P. H., Bush, R. I., et al. 2012, *Sol. Phys.*, 275, 229
- Schüssler, M., Shelyag, S., Berdyugina, S., Vögler, A., & Solanki, S. K. 2003, *ApJ*, 597, L173
- Solanki, S. K. 1986, *A&A*, 168, 311
- Solanki, S. K. 1993, *Space Sci. Rev.*, 63, 1
- Solanki, S. K., & Schmidt, H. U. 1993, *A&A*, 267, 287
- Solanki, S. K., & Stenflo, J. O. 1984, *A&A*, 140, 185
- Solanki, S. K., & Unruh, Y. C. 1998, *A&A*, 329, 747
- Solanki, S. K., Steiner, O., Bünte, M., Murphy, G., & Ploner, S. R. O. 1998, *A&A*, 333, 721
- Solanki, S. K., Finsterle, W., Rüedi, I., & Livingston, W. 1999, *A&A*, 347, L27
- Solanki, S. K., Schüssler, M., & Fligge, M. 2002, *A&A*, 383, 706
- Solanki, S. K., Barthol, P., Danilovic, S., et al. 2010, *ApJ*, 723, L127
- Spruit, H. C. 1976, *Sol. Phys.*, 50, 269
- Spruit, H. C., & Roberts, B. 1983, *Nature*, 304, 401
- Spruit, H. C., & Zwaan, C. 1981, *Sol. Phys.*, 70, 207
- Steiner, O. 2005, *A&A*, 430, 691
- Steiner, O., Hauschildt, P. H., & Bruls, J. 2001, *A&A*, 372, L13
- Stellmacher, G., & Wiehr, E. 1979, *A&A*, 75, 263
- Stellmacher, G., & Wiehr, E. 1991, *A&A*, 248, 227
- Stellmacher, G., & Wiehr, E. 2001, *Sol. Phys.*, 202, 259
- Stenflo, J. O. 1973, *Sol. Phys.*, 32, 41
- Sütterlin, P., Wiehr, E., & Stellmacher, G. 1999, *Sol. Phys.*, 189, 57
- Title, A. M., & Berger, T. E. 1996, *ApJ*, 463, 797
- Title, A. M., Topka, K. P., Tarbell, T. D., et al. 1992, *ApJ*, 393, 782
- Topka, K. P., Tarbell, T. D., & Title, A. M. 1992, *ApJ*, 396, 351
- Topka, K. P., Tarbell, T. D., & Title, A. M. 1997, *ApJ*, 484, 479
- Unruh, Y. C., Solanki, S. K., & Fligge, M. 1999, *A&A*, 345, 635
- Vieira, L. E. A., Solanki, S. K., Krivova, N. A., & Usoskin, I. 2011, *A&A*, 531, A6
- Viticchié, B., Del Moro, D., Criscuoli, S., & Berrilli, F. 2010, *ApJ*, 723, 787
- Vögler, A. 2005, *Mem. Sos. Astron. It.*, 76, 842
- Walton, S. R. 1987, *ApJ*, 312, 909
- Walton, S. R., Preminger, D. G., & Chapman, G. A. 2003, *Sol. Phys.*, 213, 301
- Wenzler, T., Solanki, S. K., Krivova, N. A., & Fluri, D. M. 2004, *A&A*, 427, 1031
- Wenzler, T., Solanki, S. K., Krivova, N. A., & Fröhlich, C. 2006, *A&A*, 460, 583
- Wiegmann, T., Solanki, S. K., Borrero, J. M., et al. 2012, *Sol. Phys.*, submitted

A.2 Yeo, K. L., Feller, A., Solanki, S. K., Couvidat, S., Danilovic, S., Krivova, N. A., 2014, Point spread function of SDO/HMI and the effects of stray light correction on the apparent properties of solar surface phenomena, *Astron. Astrophys.*, 561, A22

A.2 Yeo, K. L., Feller, A., Solanki, S. K., Couvidat, S., Danilovic, S., Krivova, N. A., 2014, Point spread function of SDO/HMI and the effects of stray light correction on the apparent properties of solar surface phenomena, *Astron. Astrophys.*, 561, A22

The contents of Chapter 4 are identical to the printed version of Yeo, K. L., Feller, A., Solanki, S. K., Couvidat, S., Danilovic, S., Krivova, N. A., 2014, Point spread function of SDO/HMI and the effects of stray light correction on the apparent properties of solar surface phenomena, *Astron. Astrophys.*, 561, A22. The printed version is reproduced here with permission from Astronomy & Astrophysics, © ESO.

Point spread function of SDO/HMI and the effects of stray light correction on the apparent properties of solar surface phenomena

K. L. Yeo^{1,2}, A. Feller¹, S. K. Solanki^{1,3}, S. Couvidat⁴, S. Danilovic¹, and N. A. Krivova¹

¹ Max-Planck-Institut für Sonnensystemforschung, Max-Planck-Straße 2, 37191 Katlenburg-Lindau, Germany
e-mail: yeo@mps.mpg.de

² Technische Universität Braunschweig, Institut für Geophysik und Extraterrestrische Physik, Mendelssohnstraße 3, 38106 Braunschweig, Germany

³ School of Space Research, Kyung Hee University, Yongin, 446-701 Gyeonggi, Korea

⁴ W.W. Hansen Experimental Physics Laboratory, Stanford University, Stanford, CA 94305-4085, USA

Received 19 August 2013 / Accepted 15 October 2013

ABSTRACT

Aims. We present a point spread function (PSF) for the Helioseismic and Magnetic Imager (HMI) onboard the Solar Dynamics Observatory (SDO) and discuss the effects of its removal on the apparent properties of solar surface phenomena in HMI data.

Methods. The PSF was retrieved from observations of Venus in transit by matching it to the convolution of a model of the Venusian disc and solar background with a guess PSF. We described the PSF as the sum of five Gaussian functions, the amplitudes of which vary sinusoidally with azimuth. This relatively complex functional form was required by the data. Observations recorded near in time to the transit of Venus were corrected for instrumental scattered light by the deconvolution with the PSF. We also examined the variation in the shape of the solar aureole in daily data, as an indication of PSF changes over time.

Results. Granulation contrast in restored HMI data is greatly enhanced relative to the original data and exhibit reasonable agreement with numerical simulations. Image restoration enhanced the apparent intensity and pixel averaged magnetic field strength of photospheric magnetic features significantly. For small-scale magnetic features, restoration enhanced intensity contrast in the continuum and core of the Fe I 6173 Å line by a factor of 1.3, and the magnetogram signal by a factor of 1.7. For sunspots and pores, the enhancement varied strongly within and between features, being more acute for smaller features. Magnetic features are also rendered smaller, as signal smeared onto the surrounding quiet Sun is recovered. Image restoration increased the apparent amount of magnetic flux above the noise floor by a factor of about 1.2, most of the gain coming from the quiet Sun. Line-of-sight velocity due to granulation and supergranulation is enhanced by a factor of 1.4 to 2.1, depending on position on the solar disc. The shape of the solar aureole varied, with time and between the two CCDs. There are also indications that the PSF varies across the FOV. However, all these variations were found to be relatively small, such that a single PSF can be applied to HMI data from both CCDs, over the period examined without introducing significant error.

Conclusions. Restoring HMI observations with the PSF presented here returns a reasonable estimate of the stray light-free intensity contrast. Image restoration affects the measured radiant, magnetic and dynamic properties of solar surface phenomena sufficiently to significantly impact interpretation.

Key words. instrumentation: miscellaneous – space vehicles: instruments – Sun: faculae, plages – Sun: granulation – Sun: photosphere – sunspots

1. Introduction

Solar telescopes, like any real optical system, diverge from diffraction-limited behaviour due to optical aberrations and, in the case of ground-based instruments, the influence of the Earth's atmosphere. Optical aberrations arise from factors such as design and material constraints, imperfections in the fabrication, presence of impurities, thermal changes and jitter, and are practically unavoidable. Due to aperture diffraction and optical aberrations, radiation entering a given optical system is not entirely confined to the intended area on the focal plane but instead spread out, as described mathematically by the point spread function (PSF). This image blurring or loss of contrast is the so-termed stray light.

The apparent properties of solar phenomena is sensitive to stray light, accounting for its influence on solar imagery is necessary for proper interpretation and comparison with numerical

models. This has been demonstrated repeatedly in the literature, for example, in studies looking at the limb darkening function (Pierce & Slaughter 1977; Neckel & Labs 1994), the intensity contrast of granulation (Sánchez Cuberes et al. 2000; Danilovic et al. 2008; Wedemeyer-Böhm & Rouppe van der Voort 2009; Afram et al. 2011), and the brightness of small-scale magnetic concentrations (Title & Berger 1996; Schnerr & Spruit 2011) and sunspots (Albregtsen & Maltby 1981; Mathew et al. 2007).

Sophisticated techniques to correct solar observations for instrumental and atmospheric effects exist, the most common being speckle interferometry (de Boer et al. 1992; von der Lühse 1993) and phase diversity (Gonsalves 1982; Löfdahl & Scharmer 1994) methods. For spaceborne instruments, where variable atmospheric seeing is not a factor, a more conventional approach is often sufficient. Specifically, inferring the PSF from the distribution of intensity about the boundary between the bright and dark parts of partially illuminated scenes (such as, of the

solar limb, and of transits of the Moon, Venus or Mercury) and restoring data by the deconvolution with it. Recent examples include the work of Mathew et al. (2007) with observations from SoHO/MDI¹, Wedemeyer-Böhm (2008), Wedemeyer-Böhm & Ruppe van der Voort (2009) and Mathew et al. (2009) with Hinode/SOT/BFI², and DeForest et al. (2009) with TRACE³.

In this paper we present an estimate of the PSF of the Helioseismic and Magnetic Imager onboard the Solar Dynamics Observatory, SDO/HMI (Schou et al. 2012b). The PSF was derived from observations of Venus in transit. We also demonstrate the effects of correcting HMI data for stray light with this PSF on the apparent properties of various photospheric phenomena.

This study broadly follows the approach taken with the other spaceborne instruments listed above. It departs from these earlier efforts in that we constrain the PSF not only in the radial dimension but also in the azimuthal direction, recovering the anisotropy. This we will show to be crucial for accurate stray light removal (Sect. 2.3).

The relationship between the radiance of magnetic features in the photosphere, and their size and position on the solar disc, is an important consideration in understanding and modelling the variation in solar irradiance (Domingo et al. 2009). HMI returns continuous, seeing-free, full-disc observations of intensity, Doppler shift and magnetic field at a constant, intermediate spatial resolution (~ 1 arcsec) and at relatively low noise. This renders it a suitable tool for constraining the radiant behaviour of photospheric magnetic features (Yeo et al. 2013). It is therefore of interest to enhance the quality of HMI observations by quantifying the stray light performance of the instrument. This would be of utility not only for the accurate examination of the radiant behaviour of magnetic features in HMI data but also any application that can benefit from stray light-free measurements of intensity, line-of-sight velocity and magnetic flux density.

The PSF presented here is, to our knowledge, the first on-orbit measurement of the stray light of HMI reported in the literature (see Wachter et al. 2012, for the pre-launch measurement). This is necessary given that the exact operating conditions of the sensor cannot be exactly simulated on the ground. Also, the stray light of the HMI might have changed from the time of the pre-launch calibration from changes in the condition of the instrument.

The HMI comprises of two identical 4096×4096 pixel CCD cameras, denoted “side” and “front”. The PSF was retrieved from images recorded on the side CCD during the transit of Venus on June 5 to 6, 2012. In addition to this transit of Venus, the HMI has also witnessed several partial lunar eclipses (seven, as of the end of 2012). In Sect. 2.5 we discuss the reasons for choosing the observations of Venus in transit over data from the partial lunar eclipses or of the solar limb for constraining the PSF, even though Venus has an atmosphere which had to be taken into account in deriving the PSF, introducing additional complexity to the task and uncertainty to the final estimate of the PSF.

In the following section, we detail the data selection (Sect. 2.1), the PSF derivation (Sect. 2.2) and image restoration method (Sect. 2.3), and how we accounted for the influence of Venus’ atmosphere (Sect. 2.4). Then, we verify the utility of the PSF presented here for image restoration, comparing

the apparent granulation contrast in restored HMI observations and synthetic intensity maps generated from numerical simulation (Sect. 3.1). We illustrate the result of image restoration on the intensity, Dopplergram and magnetogram data products of the instrument, looking at its effect on the following.

- The intensity and magnetic field strength of small-scale magnetic concentrations (Sect. 3.2.1).
- The intensity and magnetic field strength of sunspots and pores (Sect. 3.2.2).
- The amount of magnetic flux on the solar surface (Sect. 3.2.3).
- Line-of-sight velocity (Sect. 3.2.4).

The retrieved PSF represents the stray light behaviour of the side CCD at the time of the transit of Venus, at the position in the field-of-view (FOV) occupied by the Venus disc. In Sect. 4 we examine the applicability of this PSF to other positions in the FOV, and to observations from the front CCD as well as from other times. Finally, a summary of the study is given in Sect. 5.

2. PSF derivation

2.1. Data selection

The HMI is a full-Stokes capable filtergram instrument. The instrument records full-disc polarimetric filtergrams continuously, at 3.75 s cadence, on the two identical CCDs. The filtergram sequence of the side CCD alternates between six polarizations ($I \pm Q$, $I \pm U$ and $I \pm V$) and six positions across the Fe I 6173 Å line (at ± 34 , ± 103 and ± 172 mÅ from line centre). A set of 36 filtergrams, of each polarization at each line position, is collected every 135 s. The front CCD collects a set of 12 filtergrams, covering the Stokes $I + V$ and $I - V$ polarizations at the same line positions, every 45 s.

Dopplergrams, longitudinal magnetograms and intensity (continuum, and line depth and width) images, collectively termed the line-of-sight data products, are generated from the filtergram sequence of the side CCD at 720 s intervals, and from that of the front CCD at 45 s intervals. Stokes parameters (I , Q , U and V) and the corresponding Milne-Eddington inversion (Borrero et al. 2011) are also produced, at 720 s cadence, from the filtergram sequence of the side CCD.

During the transit of Venus on June 5 to 6, 2012, the side CCD recorded filtergrams in the nearby continuum (-344 mÅ from line centre), instead of the regular filtergram sequence. For the purpose of estimating the PSF of the instrument, we examined the 854×854 pixel crop, centred on the Venus disc, of 249 continuum filtergrams collected between second and third contact (i.e., the period the Venusian disc was entirely within the solar disc). Care was taken to avoid filtergrams with pixels with spurious signal levels, a result of cosmic ray hits, on the Venusian disc. The pixel scale was 0.504 arcsec/pixel. A summary description of this and the other HMI data employed in this study is given in Table 1.

When generating the various data products in the HMI data processing pipeline, filtergrams (from an interval of 1350 s for the 720 s data products and 270 s for the 45 s data products) are corrected for spatial distortion (Wachter et al. 2012), cosmic ray hits, polarization crosstalk (Schou et al. 2012a) and solar rotation, and the filtergrams of similar polarizations averaged. These time-averaged filtergrams are then combined non-linearly to form the various data products (Couvidat et al. 2012). For the side CCD, these time-averaged filtergrams are outputted as the 720 s Stokes parameters product.

¹ The Michelson Doppler Imager onboard the Solar and Heliospheric Observatory (Scherrer et al. 1995).

² The Broadband Filter Imager of the Solar Optical Telescope onboard Hinode (Kosugi et al. 2007).

³ The Transition Region And Coronal Explorer (Handy et al. 1998).

Table 1. Summary description of the HMI data employed in this study and the sections in which their analysis is detailed.

Index	Description	UTC time of observation	Denotation	Section(s)
1	854 × 854 pixel crop, centred on the Venusian disc, of 249 continuum (−344 mÅ from line centre) filtergrams recorded on the side CCD during the transit of Venus, between second and third contact.	Between 22:30, June 5 and 04:14, June 6, 2012.		2.1
2	The mean of 42 of the 249 images in item 1, between which the spatial distribution of intensity on the Venusian disc is relatively similar.	Between 02:04 and 02:46, June 5, 2012.	Mean transit image	2.1, 2.2, 2.4
3	One of the 42 images used to produce item 2.	02:25:37, June 6, 2012.	Test transit image	2.3, 2.4
4	854 × 854 pixel crop, centred on the Venusian disc, of a continuum side CCD filtergram recorded just before second contact.	22:25:33, June 5, 2012.	Ingress image	2.4
5	Continuum side CCD filtergram taken right after the Venusian disc exited the solar disc completely.	04:35:59, June 6, 2012.	Test continuum filtergram	3.1, 4.1
6	45 s longitudinal magnetogram from the front CCD closest in time (<1 min) to item 5.	04:35:22, June 6, 2012.		3.1, 4.1
7	A set of simultaneous 720 s Dopplergram, longitudinal magnetogram, line depth and continuum intensity images from the side CCD, recorded about an hour after the end of the transit of Venus, when said CCD resumed collection of the regular filtergram sequence.	05:35:32, June 6, 2012.		3.2, 4.1
8	A pair of filtergrams, one from each CCD, of similar band-pass (−172 mÅ from line centre) and polarization (Stokes $I - V$), taken less than one minute apart of one another.	Around 05:36, June 6, 2012.		4.2
9	The continuum filtergram recorded on each CCD whenever the SDO spacecraft passes orbital noon and midnight. A total of 1866 filtergrams from each CCD, from when the HMI commenced regular operation to the time of the study.	Around 06:00 and 18:00 daily, between May 1, 2010 and June 30, 2013.		4.2

As a consequence of the correction for spatial distortion, the apparent PSF is different in the unprocessed and time-averaged filtergrams. The non-linearity of the algorithms used to derive the data products means they cannot be corrected for stray light by the deconvolution with the PSF. Instead, their restoration must go via restoring the unprocessed or time-averaged filtergrams.

The 249 continuum filtergrams considered (and all the other filtergram data utilised in the rest of the study) were corrected for spatial distortion. The retrieved PSF therefore represents stray light in undistorted HMI observations. This allows the generation of stray light-free data products through the deconvolution of the PSF from the time-averaged filtergrams. For the line-of-sight data products, this means correcting just the time-averaged Stokes $I + V$ and $I - V$ at each line position, a total of $2 \times 6 = 12$ images in each instance, instead of all the unprocessed filtergrams, which numbers 360 and 72 for the 720 s and 45 s data products respectively.

In this study we assumed Venus to be a perfect sphere (Archinal et al. 2011). Radial distance and azimuth are denoted r and ϕ , respectively. Azimuth is taken anti-clockwise from the CCD column axis such that zero is up.

The spatial distribution of intensity on the Venusian disc, predominantly instrumental scattered light (aperture diffraction and stray light), varied significantly over the course of the transit (Fig. 1). The figure gives the intensity on the Venusian disc in the 249 continuum filtergrams,

- as a function of radial distance from the centre of the Venusian disc, averaged over all azimuths and normalized to the level at the point of inflexion (\hat{I}_r , top panel), and

- as a function of azimuth along the edge of the Venusian disc as given by the point of inflexion on \hat{I}_r , normalized to the mean level (\hat{I}_ϕ , bottom panel).

Also plotted are the mean \hat{I}_r and \hat{I}_ϕ of all the filtergrams, $\langle \hat{I}_r \rangle$ and $\langle \hat{I}_\phi \rangle$ (red curves). The radius of the Venusian disc as given by the point of inflexion on \hat{I}_r is, to 0.1 arcsec, constant at 29.5 arcsec. The fluctuation in the intensity on the Venusian disc over the course of the transit arises from changes in the solar background from granulation, p -mode oscillations and limb darkening, as well as the variation of the PSF with position in the FOV.

To quantify the variation in the spatial distribution of intensity on the Venusian disc over the course of the transit, and the influence of the changing solar background and the variation of the PSF with position in the FOV, we computed, for each of the 249 continuum filtergrams, the following two quantities.

- The integral under \hat{I}_r from the centre of the Venusian disc to the point of inflexion, $\int \hat{I}_r dr$. The broader the PSF at a given position in the FOV, the brighter the Venusian disc is relative to the level at its edge, and the greater this integral.
- The root-mean-square or rms difference between \hat{I}_ϕ and $\langle \hat{I}_\phi \rangle$, $\text{rms}_{\hat{I}_\phi - \langle \hat{I}_\phi \rangle}$. The closer the agreement in the trend with azimuth between \hat{I}_ϕ and $\langle \hat{I}_\phi \rangle$, the smaller this quantity. $\text{rms}_{\hat{I}_\phi - \langle \hat{I}_\phi \rangle}$ reflects changes in the isotropy of the PSF (such as, from astigmatism and coma aberrations) and variation in the spatial distribution of intensity of the solar background.

$\int \hat{I}_r dr$ and $\text{rms}_{\hat{I}_\phi - \langle \hat{I}_\phi \rangle}$ are plotted along the trajectory of the Venusian disc, given in terms of the cosine of the heliocentric angle, $\mu = \cos \theta$ of the disc centre, as a function of time in Fig. 2.

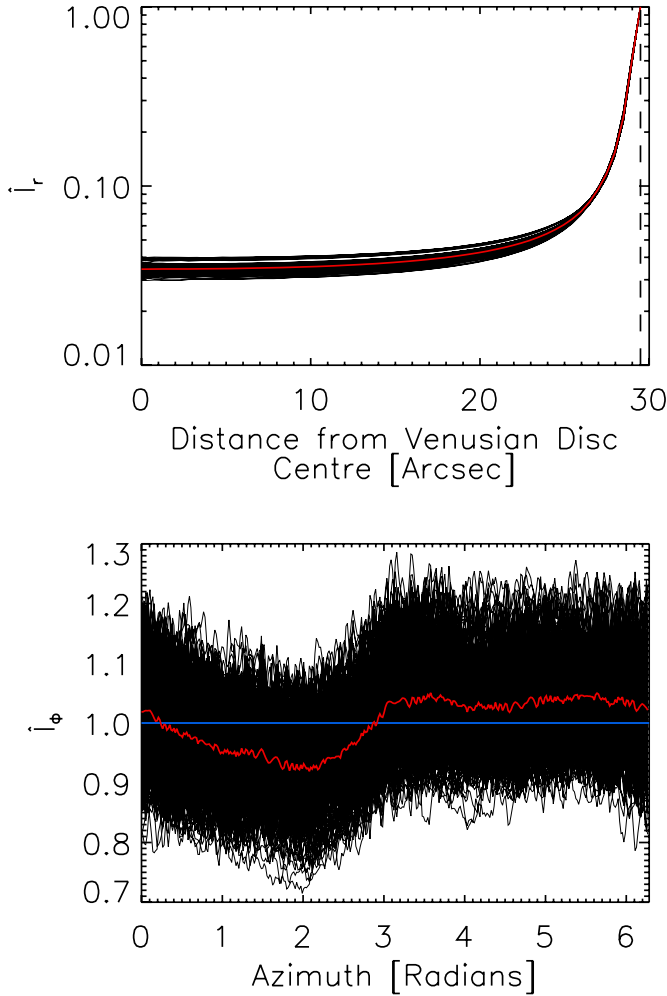


Fig. 1. Intensity on the Venusian disc in the 249 continuum filtergrams from the transit of Venus. *Top*: intensity as a function of distance from the centre of the Venusian disc, averaged over all azimuths and normalized to the level at the point of inflexion (dashed line), \hat{I}_r . *Bottom*: intensity versus azimuth along the edge of the Venusian disc as given by the point of inflexion on \hat{I}_r , normalized to the mean level, \hat{I}_ϕ . The red curves follow the mean \hat{I}_r and \hat{I}_ϕ of all the filtergrams, while the blue line represents $\hat{I}_\phi = 1$.

$\int \hat{I}_r dr$ changed slowly but notably over the course of the transit and the variation appears to be uncorrelated to distance from solar disc centre (and therefore, limb darkening). This suggests that the width of the PSF varies significantly along the path of Venus in the FOV. $\text{rms}_{\hat{I}_\phi - \langle \hat{I}_\phi \rangle}$ showed a marked point-to-point fluctuation but is otherwise relatively low (≤ 0.1) and exhibits no obvious trend with time. This indicates that the azimuth dependence of \hat{I}_ϕ and $\langle \hat{I}_\phi \rangle$ is mainly driven by a persistent PSF anisotropy along the path of Venus in the FOV rather than limb darkening (see also Sect. 2.2). The marked point-to-point fluctuation is likely from granulation and p -mode oscillations. This is supported by the comparatively smooth time variation of $\int \hat{I}_r dr$, which is less sensitive to these small-scale intensity fluctuations in the solar background due to the averaging over all azimuths.

From the trend of $\int \hat{I}_r dr$ and $\text{rms}_{\hat{I}_\phi - \langle \hat{I}_\phi \rangle}$ with time, we surmise that the width of the PSF varies significantly along the path of Venus in the FOV and while the anisotropy of the PSF is relatively stable, it is obscured by granulation and p -mode oscillations in individual filtergrams. Based on these considerations, we

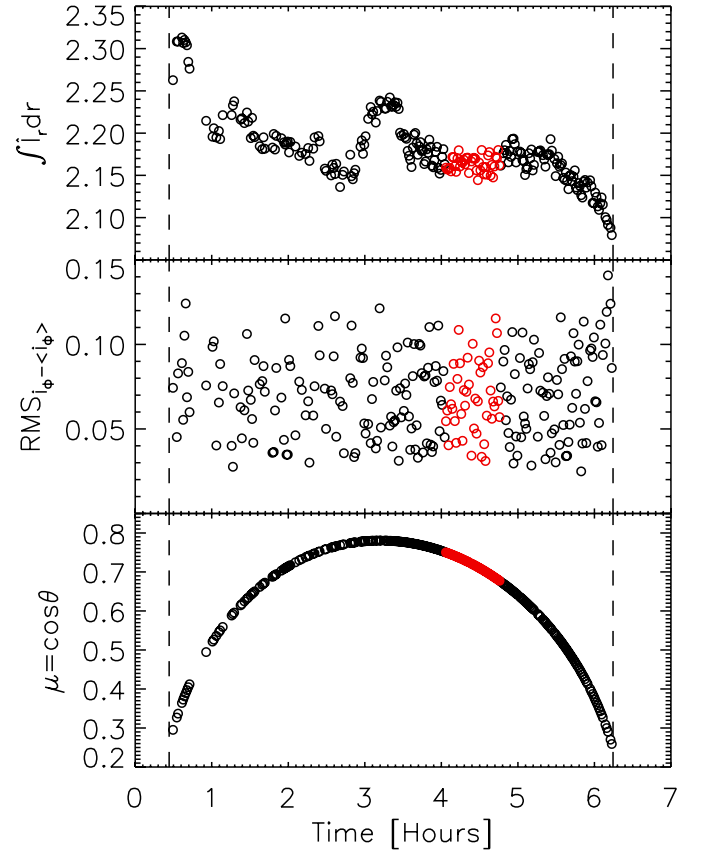


Fig. 2. Integral under \hat{I}_r , $\int \hat{I}_r dr$ (*top*), rms difference between \hat{I}_ϕ and $\langle \hat{I}_\phi \rangle$, $\text{rms}_{\hat{I}_\phi - \langle \hat{I}_\phi \rangle}$ (*middle*), and position of the centre of the Venusian disc in terms of the cosine of the heliocentric angle, $\mu = \cos \theta$ (*bottom*) as a function of time from 22:00:00 UTC, June 5, 2012. The red circles highlight the values for the filtergrams used to derive the PSF. The dashed lines mark the approximate time of the second and third contacts; the period between which the Venusian disc was entirely within the solar disc from SDO's position.

retained just the 42 filtergrams highlighted in Fig. 2 (red circles), taken over a 40 min period where $\int \hat{I}_r dr$ is relatively stable, for the derivation of the PSF. The selected filtergrams were aligned by the Venusian disc and the average, hereafter referred to as the mean transit image, taken. The objective is to derive an image of Venus in transit where the influence of granulation and p -mode oscillations is minimal by averaging filtergrams where the PSF at Venus' position in the FOV is fairly similar.

The 249 continuum filtergrams examined alternated between four polarizations (Stokes $I + Q$, $I - Q$, $I + U$ and $I - U$). We found no systematic differences in the spatial distribution of intensity on the Venusian disc between filtergrams of different polarizations and so made no distinction between them here. We repeated the analysis described in this subsection on the filtergrams recorded at the six regular wavelength positions, on the front CCD during the transit of Venus. There are systematic differences (in $\int \hat{I}_r dr$ and $\text{rms}_{\hat{I}_\phi - \langle \hat{I}_\phi \rangle}$) between different positions, even between positions at similar distance from but opposite sides of the line centre. This suggests spectral line changes from effects unrelated to the stray light behaviour of the instrument may exert an influence on intensity measured on the Venusian disc. Specifically, Doppler shifts from the motion of the spacecraft (SDO is in a geosynchronous orbit) and the rotation of the

Sun. For this reason we restricted ourselves to the continuum filtergrams from the side CCD.

2.2. PSF derivation method

A bivariate polynomial function was fitted to the mean transit image. We excluded the circular area of 50 arcsec radii centred on the Venusian disc (about three times the area of the Venusian disc) from the regression. The extrapolation of the surface fit over this excluded area represents an estimate of the intensity if Venus had been absent. We filled a circular area in the surface fit, corresponding to the Venusian disc, with zeroes. We will refer to the result, essentially a model of the mean transit image in the absence of an atmosphere in Venus, aperture diffraction and stray light, as the artificial image.

The PSF was determined by minimizing the chi-square between the convolution of the artificial image with a guess PSF and the mean transit image, in the circular area of 50 arcsec radii centred on the Venusian disc. For this we employed the implementation of the Levenberg-Marquardt algorithm (LMA) included in the IDL Astronomy User's Library, `mpfit2dfun.pro`.

Intensity in the circular area was sampled at equal intervals in the radial (0.504 arcsec, the pixel scale) and azimuthal (1/360 radians) dimensions. This is to give intensity measured at each radius from the centre of the Venusian disc more equal weight in the LMA optimization. The result is a closer agreement between the convolution of the artificial image with the guess PSF and the mean transit image on convergence than achieved by comparing the circular area in the artificial and mean transit images directly.

We scaled the artificial image by a factor prior to convolution with the guess PSF. We allowed this factor and the radius of the disc of zeroes in the artificial image to be free parameters in the LMA optimization, taking an initial value of unity (i.e., no scaling) and 29.5 arcsec (the position of the point of inflexion on \hat{I}_r). This is to minimize error from any misestimation of the surface fit to the mean transit image and the radius of the Venusian disc⁴.

Following the example of previous studies (Martínez Pillet 1992; Mathew et al. 2007, 2009), we attempted to model the guess PSF as the linear sum of various combinations of Gaussian and Lorentzian functions. Except here we allowed the amplitude of each Gaussian and Lorentzian component to vary sinusoidally with azimuth to accommodate PSF anisotropy. We also tried to set the ideal diffraction-limited PSF as one of the components. The guess PSF we found to reproduce the measured intensity in the artificial image best, denoted K , is given by

$$K(r, \phi) = \sum_{i=1}^5 [1 + A_i \cos(u_i \phi + v_i)] w_i \left[\frac{1}{2\pi\sigma_i^2} \exp\left(-\frac{r^2}{2\sigma_i^2}\right) \right]. \quad (1)$$

That is, the linear combination of five Gaussian functions, with weight w_i and standard deviation σ_i , the amplitudes of which vary sinusoidally with azimuth, with amplitude A_i , period of $2\pi u_i$ radians (where $u_i \in \mathbb{Z}$) and phase v_i .

Modelling the guess PSF as the linear combination of four Gaussian or three Gaussian and a Lorentzian, as done in the cited works, still reproduces measured intensity in the artificial image reasonably well. The retrieved PSFs are however, negative at parts (i.e., unphysical) from the LMA converging to solutions where $|A_i| > 1$. And introducing additional sinusoidal terms to

the azimuth dependence of each Gaussian and Lorentzian function did not alleviate this problem. The linear combination of five Gaussians appeared necessary to reach a physical solution while reproducing the measured intensity in the artificial image in both the radial and azimuthal dimensions.

The guess PSF was applied to the artificial image by evaluating K (Eq. (1)) at pixel scale intervals (0.504 arcsec) on a 251×251 grid, the centre element representing the origin ($r = 0$), and taking the convolution of the artificial image with the result. On convergence, the value at each grid element represents the integral of the PSF over the element. The retrieved PSF therefore describes the pixel integrated PSF. This was done, instead of filling the grid with the pixel integrated value of K , for a practical reason. When correcting HMI observations for stray light via deconvolution with the PSF, it is the pixel integrated PSF that is required.

Care was taken to repeat the LMA optimization, varying the initial value of the free parameters, to reduce the likelihood that the solution lies in a local chi-square minimum. To accommodate the requirement that $u_i \in \mathbb{Z}$, we executed the LMA optimization with no constraint on the value of u_i , rounded the retrieved u_i to the nearest integer and repeated the process with these parameters fixed.

The PSF derivation method described here implicitly assumes there is no interaction between solar radiation and the Venusian atmosphere. We will qualify this statement, and detail the adjustments made to the artificial image and the mean transit image to account for the influence of the Venusian atmosphere on the retrieved PSF in Sect. 2.4. The method also ignores motion blurring from the lateral movement of the Venusian disc relative to the solar disc. The displacement of the Venusian disc within the exposure time of the instrument is, on average, about 0.015 pixels and can therefore be neglected without significant loss of accuracy.

In the following, we denote the PSF retrieved as described above, a preliminary estimate of the stray light behaviour of the instrument, by K_1 . The retrieved value of the parameters of K_1 are listed in Table 2. The best fit value of the scale factor applied to the artificial image is 1.0029, and the radius of the disc of zeroes, 29.29 arcsec. Though only a slight departure from the initial values (unity and 29.5 arcsec), this correction to the amplitude of the artificial image and the size of the disc of zeroes effected a marked improvement in the chi-square statistic.

In Fig. 3 we plot the intensity along different radii from the centre of the Venusian disc; from the mean transit image (black curves) and reproduced in the artificial image by the convolution with K_1 (red curves). Also plotted is the intensity reproduced in the artificial image by fixing the A_i at zero (blue curves). In this instance, the variation with azimuth arises solely from limb darkening, which enters the process through the surface fit to the mean transit image. Evidently, limb darkening alone cannot account for all the observed variation with azimuth, confirming that the PSF of the instrument is significantly anisotropic. By allowing the amplitude of each Gaussian component in the guess PSF to vary sinusoidally with azimuth, we are able to reproduce most of the observed intensity azimuth dependence. The close overall agreement between observed and reproduced intensities in the radial dimension is illustrated in Fig. 4.

Here we choose to describe the PSF as the linear combination of five Gaussian functions over more physically realistic models, such as the convolution of the diffraction-limited PSF with a Voigt function (Wedemeyer-Böhm 2008). Apart from yielding a closer agreement between the PSF-blurred artificial image and the mean transit image, this functional form is more

⁴ The point of inflexion on \hat{I}_r is not an accurate indication of the position of the edge of the Venusian disc due to the influence of the Venusian atmosphere.

Table 2. Parameter values (and associated formal regression error) of the guess PSF retrieved neglecting (K_1) and accounting for the influence of the Venusian atmosphere (K_2).

PSF	Gaussian component	w_i	σ_i [Arcsec]	A_i	u_i	v_i [Radians]
K_1	$i = 1$	0.641 ± 0.002	0.470 ± 0.001	0.131 ± 0.002	1	-1.85 ± 0.02
	$i = 2$	0.211 ± 0.002	1.155 ± 0.008	0.371 ± 0.006	1	2.62 ± 0.01
	$i = 3$	0.066 ± 0.002	2.09 ± 0.02	0.54 ± 0.01	2	-2.34 ± 0.01
	$i = 4$	0.0467 ± 0.0005	4.42 ± 0.02	0.781 ± 0.006	1	1.255 ± 0.004
	$i = 5$	0.035 ± 0.004	25.77 ± 0.04	0.115 ± 0.001	1	2.58 ± 0.01
K_2	$i = 1$	0.747 ± 0.001	0.417	0.164 ± 0.002	1	-2.22 ± 0.01
	$i = 2$	0.126 ± 0.003	1.45 ± 0.01	0.48 ± 0.01	1	2.36 ± 0.01
	$i = 3$	0.049 ± 0.003	2.10 ± 0.02	0.74 ± 0.04	2	-2.36 ± 0.01
	$i = 4$	0.0428 ± 0.0004	4.66 ± 0.02	0.776 ± 0.007	1	1.194 ± 0.006
	$i = 5$	0.035 ± 0.004	26.16 ± 0.05	0.122 ± 0.002	1	2.63 ± 0.01

Notes. The PSFs are given by the linear combination of five Gaussian functions (Eq. (1)), denoted by i , with weight w_i and listed in ascending order by the standard deviation, σ_i . The amplitude of each Gaussian component modulates sinusoidally with azimuth, with amplitude A_i , period of $2\pi u_i$ radians (where $u_i \in \mathbb{Z}$) and phase v_i . There are no associated formal regression errors for u_i , and in the case of K_2 , $\sigma_{i=1}$ as the value of these parameters were fixed in the LMA optimization (see text).

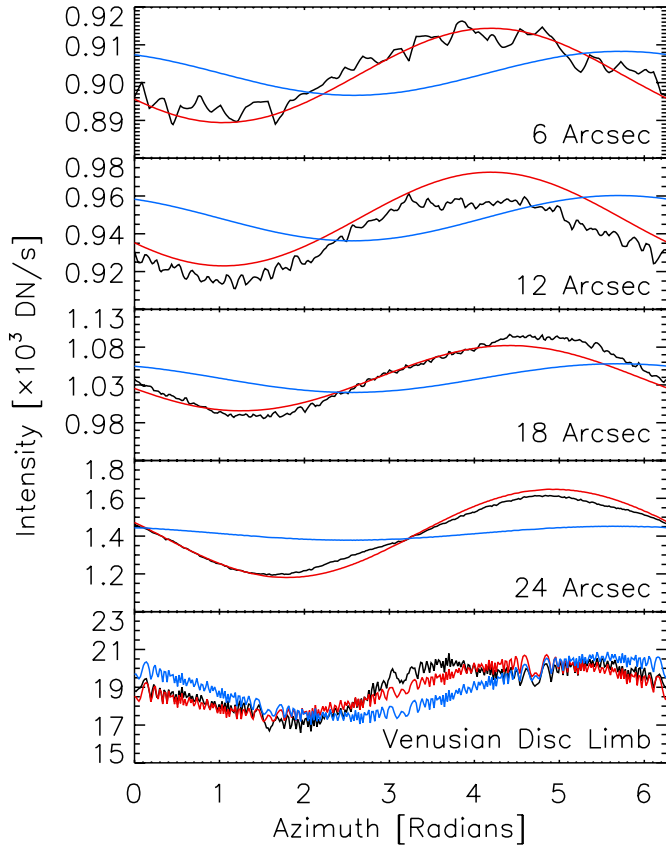


Fig. 3. Intensity on the Venusian disc at distances of 6, 12, 18, and 24 arcsec from the centre, and along its limb (taking the radius of the Venusian disc retrieved along with K_1 by the LMA optimization, 29.29 arcsec), as a function of azimuth. The black curves follow the values from the mean transit image and the red curves the values reproduced in the artificial image by the convolution with K_1 . The blue curves represent the intensity obtained in the artificial image by fixing A_i at zero. The intensity fluctuations along the Venusian limb arises from aliasing artefacts.

amenable to incorporating the complex azimuthal dependence. The retrieved parameter values of K_1 (Table 2) and the azimuth dependence of measured intensity on the Venusian disc at different radii (Fig. 3) suggest that the overall amplitude and phase of the anisotropy of the PSF varies with radial distance.

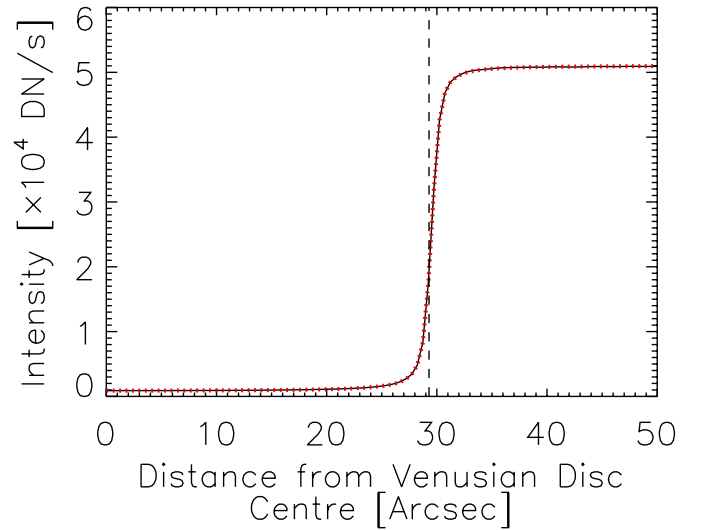


Fig. 4. Radial intensity as a function of distance from the centre of the Venusian disc; from the mean transit image (black solid curve) and the convolution of the artificial image with K_1 (red dotted curve). The dashed line marks the position of the Venus limb as returned along with K_1 by the LMA optimization.

The linear combination of Gaussian functions is not a physically realistic model of real PSFs for the following reasons:

- It allows solutions with Strehl ratios exceeding unity, which is unphysical.
- The Fourier transform of the Gaussian function, and therefore the modulation transfer function (MTF) of such PSF models, is non-zero above the Nyquist limit. Correcting observations for stray light by the deconvolution with such a PSF can introduce aliasing artefacts from the enhancement of spatial frequencies above the Nyquist limit.

We will address these two potential issues in Sects. 2.4 and 3.1, respectively.

The approach taken here to derive the PSF is broadly similar to that applied to images of Mercury in transit from Hinode/SOT/BFI by Mathew et al. (2009). Specifically, by minimising the difference between observed intensity and that produced in a model of the aperture diffraction and stray light-free

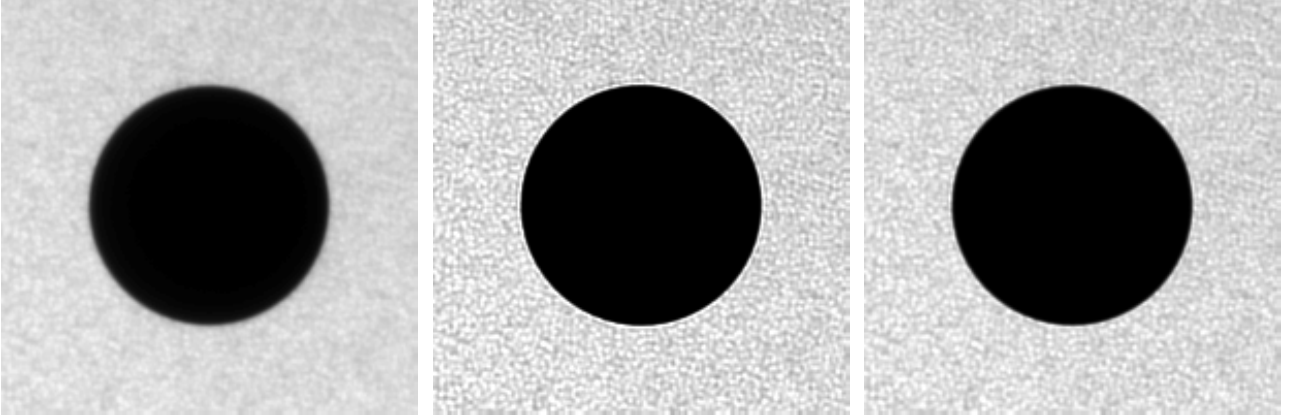


Fig. 5. 201×201 pixel inset, centred on Venus, of the test transit image; before (*left*) and after image restoration with K_1 (*middle*), and with K_2 (*right*). The three grey scale plots are saturated at 6×10^4 DN/s, about 120% of the mean photospheric level.

image (termed here the artificial image) by the convolution with a guess PSF. There are two significant departures.

Firstly, in this study, the artificial image is given by the surface fit to the mean transit image, with a disc of zeroes representing the Venusian disc. In the cited work, the authors filled the mercurian disc in the recorded image with zeroes and took the result as the artificial image. As stated earlier in this subsection, having excluded the Venusian disc and surroundings in the regression, the surface fit to the mean transit image is, in this excluded region, an approximation of the intensity had Venus been absent. For this we consider the approach taken here to yield a more realistic model of the instrumental scattered light-free image.

Secondly, as mentioned in the introduction, while the earlier effort assumed an isotropic form to the PSF, here we allowed the PSF to vary with azimuth. We were motivated by the observation that the stray light behaviour of the instrument is evidently anisotropic (Sect. 2.1 and Fig. 3).

2.3. Image restoration method

To correct HMI observations for aperture diffraction and stray light, we utilised the implementation of the Richardson-Lucy algorithm, RLA (Richardson 1972; Lucy 1974), included in the IDL Astronomy User's Library, `max_likelihood.pro`.

The RLA is an iterative method for restoring an image blurred by a known PSF, in our study, the guess PSF, K . Let f_k denote the estimate of the restored image from the k -th iteration, f_{k+1} is given by

$$f_{k+1} = f_k \circ ((f_k * K) \star K), \quad (2)$$

where the \circ , $*$ and \star symbols represent the pixel-by-pixel product, convolution and correlation, respectively. The method has been shown, empirically, for data obeying Poisson statistics, to converge towards the maximum likelihood solution (Shepp & Vardi 1982). Following Mathew et al. (2009), we employed a threshold for the chi-square between the original image and $f_k * K$ as the stopping rule. Here we set the threshold at 99.99% confidence level.

In Figs. 5 and 6a we show the result of restoring one of the 42 continuum filtergrams averaged to yield the mean transit image (recorded at 02:25:37 UTC, June 6, 2012), hereafter referred to as the test transit image, with K_1 . The image restoration sharpened the test transit image considerably and removed most of the signal on the Venusian disc. The restoration however, also left a

ringing artefact around the Venusian disc; manifest as the bright halo in the grey scale plot (middle panel, Fig. 5) and the peak in the radial intensity profile (black solid curve, Fig. 6a). Restoring other observations taken nearby in time (within a few hours of the test transit image), we found similar artefacts in the boundary of active region faculae, and sunspot penumbra and umbra.

Mathew et al. (2009) in the similar study with images of Mercury in transit from Hinode/SOT/BFI noted similar ringing artefacts around the mercurian disc upon image restoration with the RLA. The authors attributed it to Gibb's phenomenon, ringing artefacts in the Fourier series representation of discontinuous signals. In the PSF derivation and image restoration process described here, discrete Fourier transforms, DFTs were executed in convolution and correlation computations. We found that repeating the derivation of K_1 and the restoration of the test transit image without performing any DFTs in the convolution and correlation computations had negligible effect on the ringing artefact, ruling out Gibb's phenomenon as the main cause in this instance. In the following subsection we will demonstrate the ringing artefact found here to arise from us not taking the interaction between solar radiation and the Venusian atmosphere into account in deriving K_1 .

Figure 7 is a colour scale plot of the Venusian disc in the restored test transit image (left panel). The plot is saturated at about 2% of the mean photospheric level to reveal the spatial distribution of residual intensity (instrumental scattered light not removed by the image restoration) on the Venusian disc. Also shown is the result of restoring the test transit image with K_1 excluding the anisotropy of the PSF by setting A_i at zero (right panel). There is a gross, broadly east-west graduation of the residual intensity in the latter, not apparent in the former, where the residual intensity level is significantly more uniform across the Venusian disc. This demonstrates the necessity to constrain the anisotropy of the PSF to properly correct HMI observations for instrumental scattered light.

2.4. Interaction between solar radiation and the Venusian atmosphere

As stated in Sect. 2.2, the PSF derivation method described so far builds on the assumption that there is no interaction between solar radiation and the Venusian atmosphere.

In representing the Venusian disc as a disc of zeroes in the artificial image, we have presumed that the body would, in the absence of aperture diffraction and stray light, be completely dark

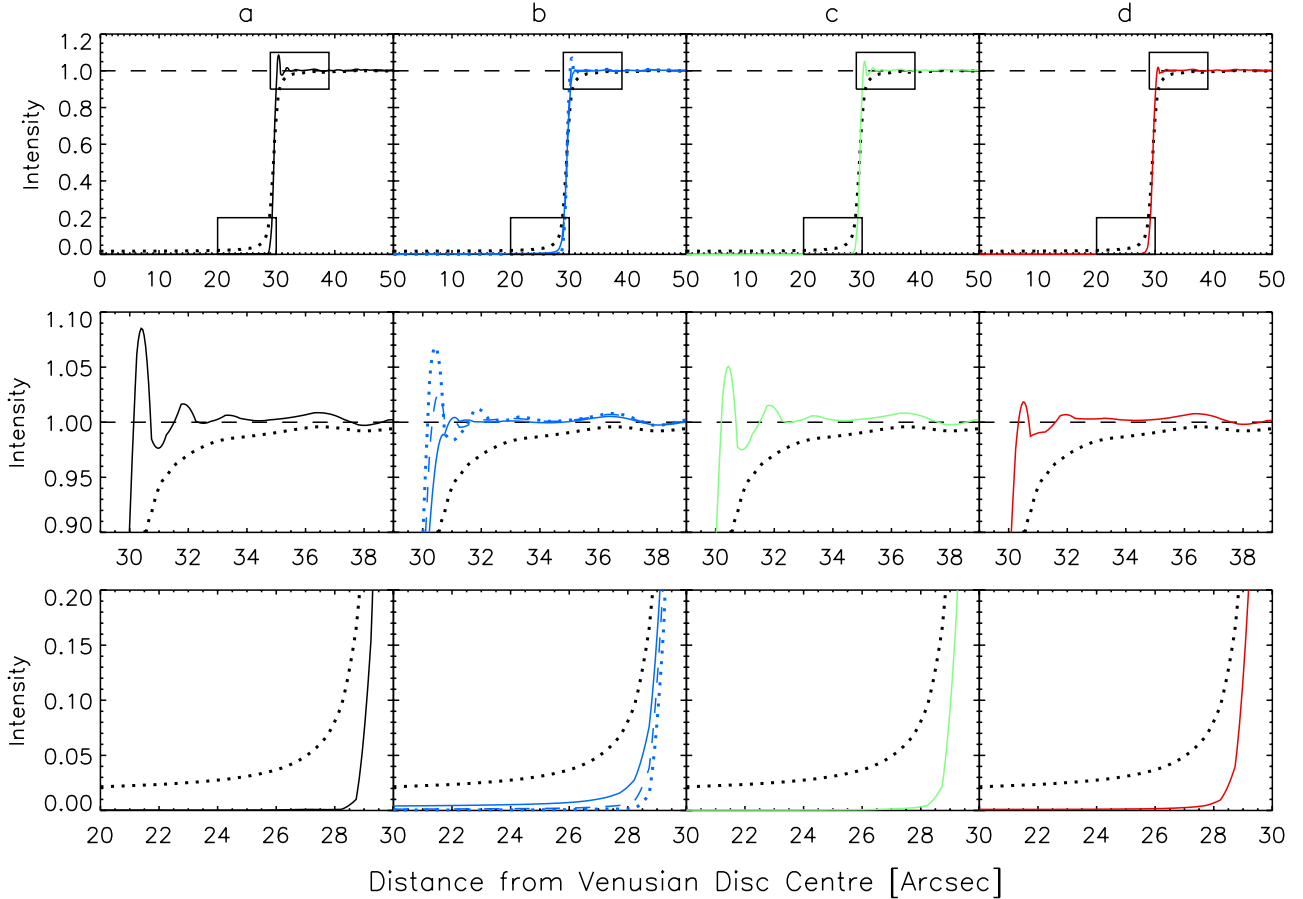


Fig. 6. *Top:* radial intensity in the test transit image, corrected for limb darkening, as a function of distance from the centre of the Venusian disc before (black dotted curves) and after image restoration with the various PSF estimates. **a)** With K_1 (black solid curve). **b)** With the PSFs obtained by blurring the edge of the disc of zeroes in the artificial image with kernels representing Gaussian functions with standard deviations of 0.2, 0.3 and 0.4 arcsec (blue dotted, dashed and solid curves). **c)** With the PSF retrieved by subtracting the estimated aureole intensity from the mean transit image (green solid curve). **d)** With K_2 (red solid curve). *Middle and bottom:* blow-up insets of the boxed areas. The radius of the Venusian disc, a free parameter in the LMA optimization, is in all instances about 29.3 arcsec and not marked to avoid cluttering. The horizontal dashed lines follow unit intensity. The test transit image was corrected for limb darkening by normalizing it by the surface fit, computed as done for the mean transit image in Sect. 2.2.

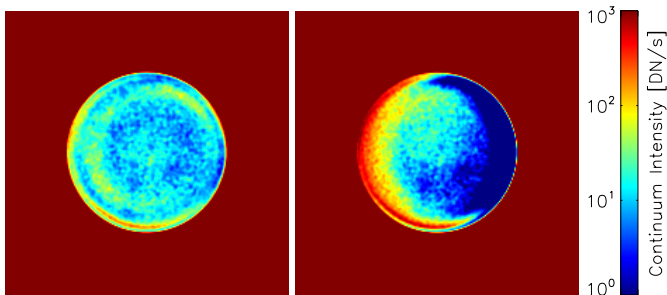


Fig. 7. 201×201 pixel inset, centred on Venus, of the test transit image after image restoration with K_1 (left) and the same, except with A_i set to zero (right).

and exhibit a discrete edge. Diffusion and scattering of solar radiation in the Venusian atmosphere can, however, render the edge of the Venusian disc diffused.

The PSF is retrieved from matching the mean transit image to the convolution of the artificial image and the guess PSF. This is valid if all measured intensity came directly from the Sun. This is, however, not the case; there is a bright halo around the Venusian disc when it is in transit (termed the aureole) from

the refraction of solar radiation by the upper layers of the atmosphere towards the observer.

2.4.1. Diffusion and scattering of solar radiation in the Venusian atmosphere

To elucidate the influence of diffusion and scattering of solar radiation in the Venusian atmosphere on the retrieved PSF we repeated the derivation, approximating the action of diffusion and scattering by blurring the edge of the disc of zeroes in the artificial image prior to the convolution with the guess PSF. We generated a copy of the artificial image that is unity everywhere outside the Venusian disc and zero inside, convolved it with a Gaussian kernel, and scaled the original artificial image by the result. This procedure introduces Gaussian blur that is confined to near the edge of the disc of zeroes. We repeated the derivation of the PSF with different degrees of Gaussian blurring.

In Fig. 8 (top panel) we display the PSFs retrieved after blurring the edge of the disc of zeroes with kernels representing Gaussian functions with standard deviations of 0.2, 0.3 and 0.4 arcsec (blue dotted, dashed and solid curves) along K_1 (black dashed curve). In Fig. 6b we have the radial intensity profile of the test transit image before and after image restoration with

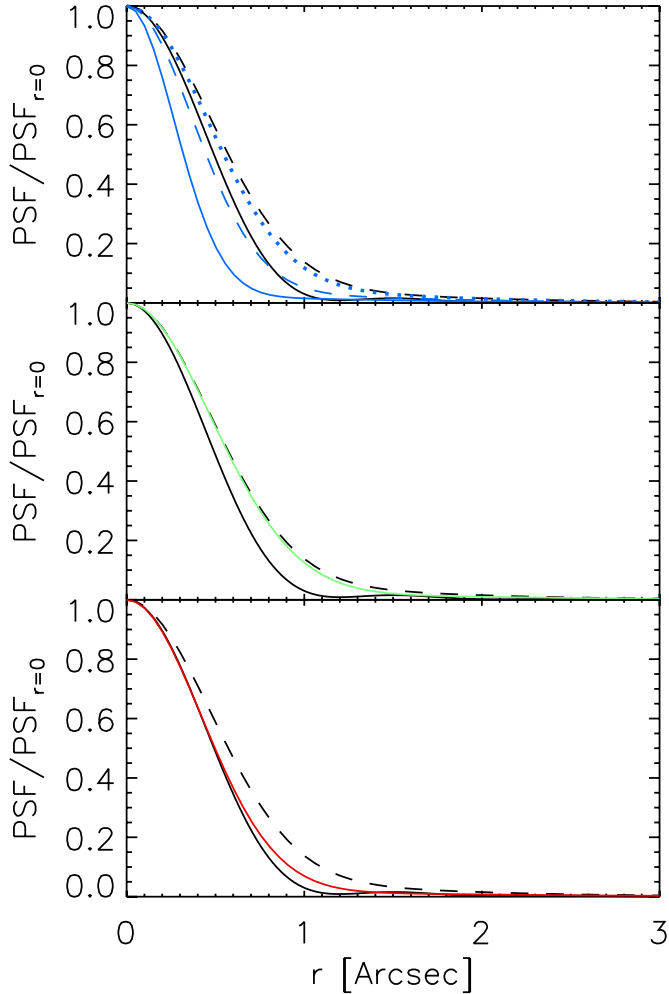


Fig. 8. Comparison between K_1 (black dashed curves), the ideal diffraction-limited PSF (black solid curves) and the other retrieved PSFs. The blue curves (*top*) represent the PSFs retrieved after blurring the edge of the disc of zeroes in the artificial image by kernels representing Gaussian functions with standard deviations of 0.2 (dotted), 0.3 (dashed) and 0.4 arcsec (solid). The green curve (*middle*) corresponds to the PSF found by subtracting the estimated aureole intensity from the mean transit image. The red curve (*bottom*) corresponds to K_2 . For illustration purposes, we set the value of A_i at zero (i.e., ignoring the azimuthal dependence) and normalized each PSF to the level at $r = 0$. As the retrieved PSFs represent estimates of the pixel integrated true PSF, the ideal diffraction-limited PSF was smoothed with a box function of pixel scale width to allow a direct comparison.

these PSFs. The stronger the blurring, the narrower the core of the PSF and the weaker the ringing artefact. The narrowest Gaussian kernel (0.2 arcsec) returned a PSF that is still very similar to K_1 while the broadest (0.4 arcsec) yielded a PSF that is unphysical, significantly narrower at the core than the ideal diffraction-limited PSF. As the Gaussian blurring is confined to near the edge of the disc of zeroes, the retrieved PSFs do not differ significantly from K_1 beyond a few arcseconds from the centre of the PSF.

2.4.2. Refraction of solar radiation in the Venusian atmosphere

We estimated the contribution by the aureole to apparent intensity in the mean transit image. For this purpose we examined the

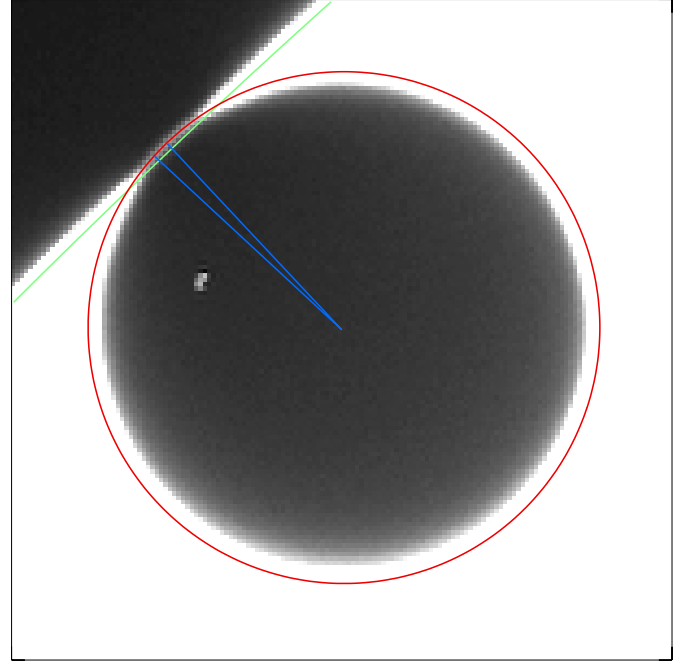


Fig. 9. 151×151 pixel inset, centred on Venus, of the ingress image. The edge of the Venusian disc (as given by the point of inflexion on \hat{I}_r) and of the solar disc are indicated by the red and green contours respectively. They do not coincide with the apparent boundaries due to the low grey scale saturation level. The grey scale is saturated at 3000 DN/s ($\sim 5\%$ of the mean photospheric level at disc centre) to allow the aureole, the bright arc on the part of the Venusian disc outside the solar disc, which is much dimmer than the solar disc, to be visible. The blue lines mark the minor sector within which the intensity of the aureole is relatively stable with azimuth. The bright feature on the northwest quadrant of the Venusian disc is an artefact of cosmic ray hits on the CCD.

854×854 pixel crop, centred on the Venusian disc, of a continuum filtergram taken shortly (~ 10 s) before the Venusian disc moved completely into the solar disc (recorded at 22:25:33 UTC, June 5, 2012), hereafter referred to as the ingress image. The ingress image is expressed as a grey scale plot in Fig. 9.

The aureole is only directly observable at ingress and egress (i.e., when the Venusian disc is only partially within the solar disc), in the part of the Venusian disc outside the solar disc. This is because the aureole is much dimmer than the photosphere and therefore difficult to distinguish from direct solar radiation. Generally, the intensity of the aureole increases with the proportion of the Venusian disc sitting inside the solar disc (Tanga et al. 2012). Therefore, observations taken right before second contact (such as the ingress image) or right after third contact give the closest direct indication of the intensity of the aureole when the Venusian disc is entirely within the solar disc. The intensity of the aureole also varies with azimuth. This is, at least in part, because it is modulated by the spatial distribution of photospheric intensity (Tanga et al. 2012) and variation in the physical structure of the Venusian atmosphere with latitude (Pasachoff et al. 2011).

Here we looked at the intensity of the aureole in the ingress image over the minor sector marked in Fig. 9 (blue lines), where it is relatively stable with azimuth.

The radial intensity profile over the minor sector marked in Fig. 9 is plotted in Fig. 10 (circles, top panel). The peak near the edge of the Venusian disc (dashed line) corresponds to the aureole while the slowly varying background is largely instrumental scattered light from the solar disc. We subtracted the polynomial

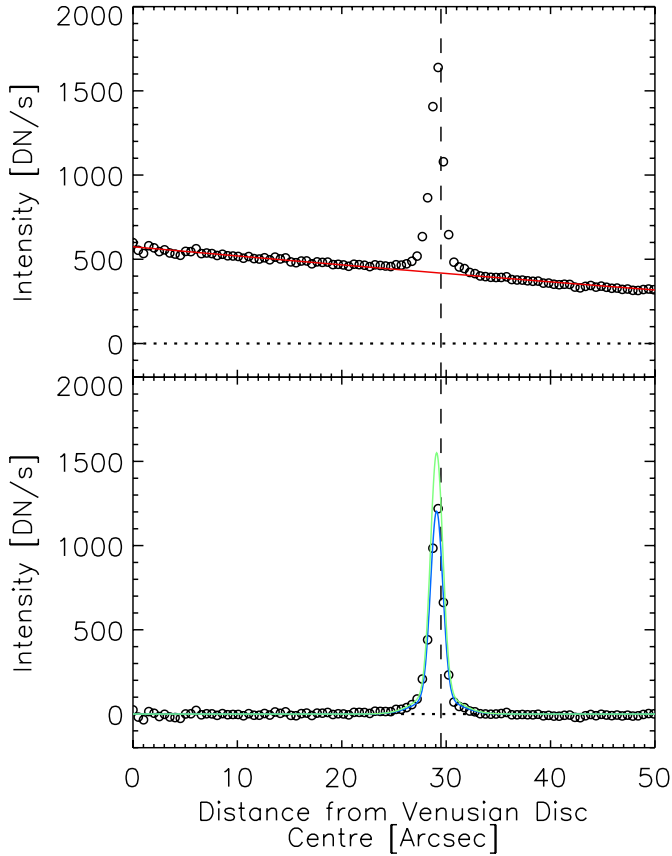


Fig. 10. Intensity in the ingress image, averaged over the minor sector marked in Fig. 9, as a function of distance from the centre of the Venusian disc (circles); before (*top panel*) and after (*bottom panel*) subtracting the polynomial fit to the slowly varying background (red curve). The blue curve corresponds to the sum-of-two-Gaussians fit to the background-subtracted series, while the green curve is the same after scaling by the quotient of the total photospheric intensity behind the Venusian disc in the mean transit image and in the ingress image. The black dashed and dotted lines denote the position of the Venus limb (as given by the point of inflexion on \hat{I}_r) and the zero intensity level, respectively.

fit to the background (red curve) from the radial intensity profile. To the background-subtracted radial intensity profile (circles, bottom panel) we fit the linear combination of two Gaussian functions (blue curve). We then scaled this fit by the quotient of the integrated photospheric intensity behind the Venusian disc in the mean transit image and in the ingress image⁵. The result (green curve) represents an estimate of the radial intensity profile of the aureole in the mean transit image.

In Fig. 8 (middle panel) we compare the PSF retrieved after first subtracting the estimated radial intensity profile of the aureole from the mean transit image (green curve) with K_1 (black dashed curve). In Fig. 6c we have the radial intensity profile in the test transit image, before and after image restoration with this PSF. The effect of removing the contribution by the aureole to observed intensity on the retrieved PSF and the ringing

artefact in the restored test transit image is similar as that from introducing Gaussian blur to the edge of the disc of zeroes in the artificial image. The retrieved PSF is slightly narrower than K_1 at the core. The ringing artefact in the restored test transit image is slightly weaker. As the aureole is concentrated near the edge of the Venusian disc, removing it from the mean transit image made little difference to the retrieved PSF beyond a few arcseconds from the core.

In removing the contribution of the aureole from the mean transit image as described above, we have made two simplifying assumptions:

- One, that the intensity of the aureole is directly proportional to the integrated photospheric intensity behind the Venusian disc.
- Two, that the intensity of the aureole does not change with azimuth.

Tanga et al. (2012) recently published a model of aureole intensity, relating it to the spatial distribution of photospheric intensity and physical structure of the Venusian atmosphere. This is, to our knowledge, the only model of its kind reported in the literature. Given the fact that the aureole is blurred by instrumental scattered light, the uncertainties over the structure of the Venusian atmosphere, and in the interest of simplicity, we favoured the rather approximate approach taken here over a more rigorous computation based on the model of Tanga et al. (2012). The estimated peak intensity of the aureole in the mean transit image is about 1500 DN/s (blue curve, Fig. 10), much smaller than the photospheric level ($\sim 5 \times 10^4$ DN/s, Fig. 4). Taking into account this as well as the relatively minor effect of subtracting the radial intensity profile of the aureole from the mean transit image on the retrieved PSF, we surmise that the uncertainty introduced by the two assumptions listed is likely minimal.

By repeating the derivation of the PSF and restoration of the test transit image, first blurring the edge of the disc of zeroes in the artificial image or subtracting the estimated contribution by the aureole to the mean transit image, we have demonstrated that the interaction between solar radiation and the Venusian atmosphere has a palpable impact on the width of the core of the retrieved PSF. Both adjustments yielded PSFs that were narrower at the core compared to K_1 (Fig. 8). And the narrower the core of the PSF, the weaker the ringing artefact in the restored test transit image (Fig. 6). The width of the core of K_1 , derived with no consideration of the Venusian atmosphere, is over-estimated and the over-sharpening this produces when used to restore HMI data shows up as ringing artefacts near where the signal is changing rapidly.

2.4.3. Final estimate of the PSF

We arrived at our final estimate of the PSF by making the following changes to the derivation procedure described in Sect. 2.2.

- Firstly, we subtracted the estimate of the radial intensity profile of the aureole from the mean transit image.
- Secondly, we blurred the edge of the disc of zeroes in the artificial image with a Gaussian kernel, the width of which we allowed to be a free parameter in the LMA optimization.
- Lastly, we fixed the width of the narrowest Gaussian component in the guess PSF such that the full width at half maximum, FWHM of the component is similar to that of the pixel-integrated ideal diffraction-limited PSF. The pixel integration was achieved by smoothing the ideal diffraction-limited PSF with a box filter of HMI pixel scale width.

⁵ The intensity of the photosphere behind the Venusian disc in the mean transit image is given by the surface fit described in Sect. 2.2. For the ingress image, we binned the image pixels on the solar disc by μ , excluding the Venusian disc and surroundings, and took the bin-averaged intensity. The intensity behind the Venusian disc was then estimated from the polynomial fit to these bin-averaged intensities given the μ of each image pixel within the Venusian disc.

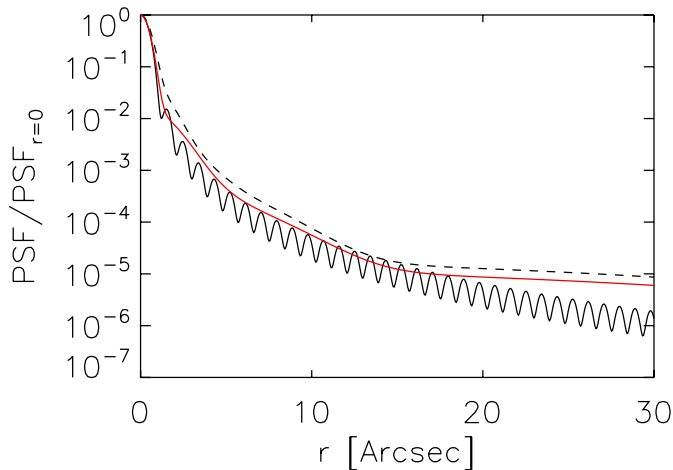


Fig. 11. As in Fig. 8 (bottom panel), but with the PSF on a logarithmic scale and over an extended radial range.

The parameters of the PSF so derived, hereafter referred to as K_2 , are summarized in Table 2. The adjustments to the PSF derivation procedure yielded a PSF that is significantly narrower at the core compared to K_1 , though not more than the ideal diffraction-limited PSF (bottom panel, Fig. 8). The agreement between the aureole-subtracted mean transit image, and the convolution of the Gaussian-blurred artificial image with K_2 is similar as in the K_1 instance, illustrated in Figs. 3 and 4, and therefore not plotted here.

The best fit value of the scale factor applied to the artificial image is 1.0028 and the radius of the disc of zeroes 29.33 arcsec. The retrieved standard deviation of the Gaussian kernel is 0.26 arcsec. The scale height of the Venusian atmosphere, at 15.9 km or approximately 0.08 arcsec, is of similar order. The degree of Gaussian blurring introduced is, as far as one can infer from such a comparison, physically plausible.

The intention here is to recover a conservative estimate of the PSF, making use of the fact that the PSF of the instrument cannot be narrower at the core than the ideal diffraction-limited PSF. Also, it was necessary to fix the width of the narrowest Gaussian component as allowing both this and the standard deviation of the Gaussian kernel to be free parameters leads to a degeneracy of the LMA optimization⁶. Though a conservative estimate, restoring the test transit image with K_2 still removed most of the intensity on the Venusian disc while largely suppressing the ringing artefacts (Figs. 5 and 6d).

As stated in Sect. 2.2, a potential hazard of modelling the PSF as the linear combination of Gaussian functions is that it allows solutions with Strehl ratios greater than unity. This functional form is only appropriate when the weight and width of the broader Gaussian components, representing the non-ideal contribution to the PSF (instrumental effects other than aperture diffraction) are sufficiently high to avoid this (Wedemeyer-Böhm 2008). As evident in Fig. 11, this is indeed the case here for both K_1 (dashed curve) and K_2 (red curve). The greater integral under both PSFs compared to the pixel-integrated ideal diffraction-limited PSF, all normalized to the level at $r = 0$, indicates Strehl ratios of less than unity. (We cannot compute the Strehl ratio of K_1 and K_2 directly as they describe the pixel-integrated PSF.)

⁶ Specifically, the LMA converged to different solutions for the PSF, some of which are narrower at the core than the ideal diffraction-limited PSF, depending on the initial value of the free parameters.

2.5. Partial lunar eclipse and solar limb observations

As stated in the introduction, we consider the observations of Venus in transit the most appropriate available for recovering the PSF of the HMI, preferring them over data from partial lunar eclipses and of the solar limb.

It is challenging to constrain the PSF in both the radial and azimuthal dimensions with data from partial lunar eclipses due to the combination of the geometry, as well as jitter and defocus issues brought on by the lunar occultation itself.

- The radius of curvature of the terminator, the edge of the lunar disc, is much greater than the width of the PSF. So at any given point along the terminator, the spatial distribution of signal smeared onto the lunar disc largely reflects the PSF in the direction of the centre of curvature. Therefore, a given partial lunar eclipse image only contains information about the PSF within a limited range of azimuths. Circumventing this limitation by looking at multiple images with the terminator at different orientations is not straightforward due to the variation of the PSF with position in the FOV.
- The terminator is uneven from lunar terrain. This makes it complicated to model the aperture diffraction and stray light-free image as we did here for the mean transit image with the artificial image (Sect. 2.2). A possible solution is to reduce the problem from 2D to 1D by looking at the radial intensity profile over segments of the terminator relatively free of lunar terrain features. This is, however, only appropriate when the terminator is near solar disc centre, where we can take the solar background to be uniform.
- The image stabilization system, ISS of the instrument was not always functional during the partial lunar eclipses due to the lunar disc blocking the diodes necessary for its operation, increasing the jitter.
- Having the lunar disc occult a significant proportion of the solar disc, and therefore greatly reducing the amount of impinging radiation, causes the front window of the instrument to cool, resulting in defocus (Schou et al. 2012b).
- There are observations made when the lunar disc was just starting to cover the solar disc and not blocking the ISS diodes. These data do not suffer jitter and defocus problems, but we cannot resolve the lunar terrain issue by reducing the problem from 2D to 1D as described above, as the variation in the solar background from limb darkening is significant here.

Our approach in this study is to constraint the PSF by the spatial distribution of intensity about a closed bright and dark boundary as this allows us to recover the full azimuthal dependence (i.e., all directions). For this we can either employ observations of Venus in transit or of the solar limb. The PSF of HMI likely varies with position in the FOV, as shown for the part of the FOV transversed by Venus in Sect. 2.1. The longer the boundary used to constrain the PSF, the greater the contribution by the variation of the PSF with position in the FOV to observed intensity fluctuation along and near the boundary, which introduces bias to the retrieved PSF. The Venusian disc occupies only about 0.06% of the FOV by area, and the solar disc, over 60%. The variation of the PSF over the part of the FOV occupied by the Venusian disc is likely minimal, making these observations more suited for the purpose.

In view of the issues associated with deducing the PSF from partial lunar eclipse and solar limb data, we utilised the observations of Venus in transit though the interaction between solar radiation and the Venusian atmosphere is challenging to account

for, leaving us with only a conservative estimate of the PSF (Sect. 2.4).

3. Application of the derived PSF to HMI observations

3.1. Granulation contrast

Restoring HMI data with K_2 is not exact. This is due to the approximate account of the influence of the Venusian atmosphere in the derivation of K_2 (Sect. 2.4) and from applying a single PSF to the entire FOV (so ignoring the variation of the PSF with position in the FOV, discussed in detail in Sect. 4.1). In this subsection we examine the effect of image restoration with K_2 on apparent granulation contrast, represented by the rms intensity contrast of the quiet Sun⁷. We compare the values deduced from HMI continuum observations and from synthetic intensity maps generated from a 3D MHD simulation. The purpose is to demonstrate that image restoration with K_2 , with all its limitations, still yields reasonable estimates of the aperture diffraction and stray light-free intensity contrast.

The side CCD continued to observe in the continuum for about an hour after the end of the transit of Venus. For this analysis we employed a continuum filtergram from this period (recorded at 04:35:59 UTC, June 6, 2012), hereafter referred to as the test continuum filtergram. Of the various types of data available from HMI, the continuum filtergram represents the closest to a near instantaneous continuum capture (exposure time of ~ 0.135 s). This implies minimal loss of apparent contrast from averaging in time. It is worth noting however, that the continuum bandpass (-344 mÅ from line centre), whilst close to the clean continuum, may be slightly affected by the far wing of the Fe I 6173 Å line.

The intensity contrast of pixels corresponding to quiet Sun in the test continuum filtergram was computed largely following the method of Yeo et al. (2013), who examined the intensity contrast of small-scale magnetic concentrations utilizing the 45 s continuum intensity and line depth data products from the front CCD. As in the cited work, the intensity contrast at a given image pixel is defined here as the normalized difference to the mean quiet-Sun intensity.

First, we identified magnetic activity present using the 45 s longitudinal magnetogram from the front CCD closest in time (< 1 min) to the test continuum filtergram⁸. Let $\langle B_1 \rangle / \mu$ denote the magnetogram signal, the mean line-of-sight magnetic flux density within a given image pixel, corrected (to first order) for foreshortening by the quotient with μ . The magnetogram was resampled to register with the test continuum filtergram. Image pixels in the test continuum filtergram corresponding to points where $|\langle B_1 \rangle| / \mu > 10$ G in the resampled magnetogram were taken to contain significant magnetic activity and masked, leaving quiet Sun.

The test continuum filtergram was corrected for limb darkening by normalizing it by a fifth order polynomial in μ fit to the quiet Sun pixels (following Neckel & Labs 1994). Let I/I_0 denote the limb darkening corrected intensity. Next, we derived the mean I/I_0 of the quiet Sun, $\langle I/I_0 \rangle_{\text{QS}}$ as a function of position on the solar disc. As similarly noted for the 45 s continuum and line depth data products by Yeo et al. (2013), there are distortions

⁷ Intensity variation in the quiet Sun arises mainly from granulation.

⁸ The 720 s longitudinal magnetogram data product from the side CCD, generated from the regular filtergram sequence, is evidently not available when this CCD is observing in the continuum.

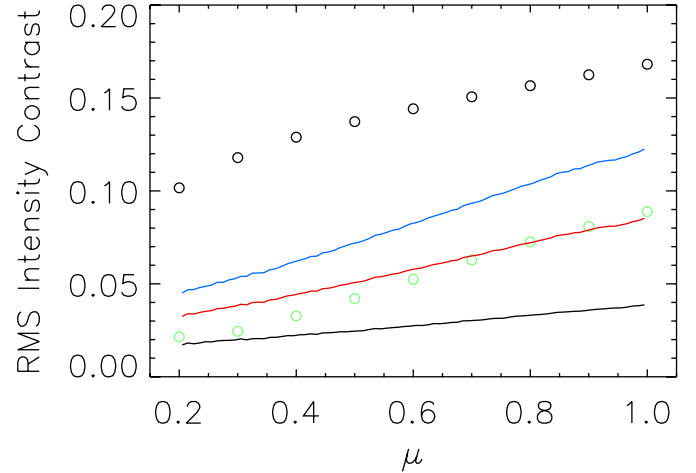


Fig. 12. RMS intensity contrast of the quiet Sun in the test continuum filtergram as a function of μ , before (black curve), and after image restoration with K_1 (blue curve) and with K_2 (red curve). The black circles represent the values from the synthetic intensity maps and the green circles the same, rescaled to reflect the proportion arising from spatial frequencies up to the cutoff spatial frequency of the restored (with K_2) test continuum filtergram (see text).

in HMI filtergrams such that $\langle I/I_0 \rangle_{\text{QS}}$ is not at unity but varying with position on the solar disc. (This is not to be confused with the spatial distortion present in HMI data discussed in Sect. 2.1.)

We sampled the solar disc at 16pixel intervals in both the vertical and horizontal directions. At each sampled point, we retrieved the median intensity of all the quiet Sun pixels inside a 401×401 pixel window centred on the point. We then fit a bivariate polynomial surface to the values so obtained from the entire disc. This surface describes $\langle I/I_0 \rangle_{\text{QS}}$ as a function of position on the solar disc. The intensity contrast at a given image pixel is then given by the value of $\frac{I/I_0}{\langle I/I_0 \rangle_{\text{QS}}} - 1$ there.

Finally, we derived the rms intensity contrast of the quiet Sun as a function of μ . To this end we grouped the quiet Sun pixels by μ in bins with a width of 0.01 and took the rms intensity contrast within each bin. The results are expressed in Fig. 12 (black curve). Also plotted are the values from first restoring the test continuum filtergram with K_1 (blue curve), and with K_2 (red curve). Quiet Sun pixels near the limb ($\mu < 0.2$) were excluded. Towards the limb, the spread in measured intensity contrast in HMI data is dominated by scatter from the combination of the diminishing signal-to-noise ratio and the limb darkening correction (Yeo et al. 2013).

The decline in granulation contrast with distance from disc centre, seen here for the test continuum filtergram, is a known, well reported phenomenon (see Sánchez Cuberes et al. 2000, 2003, and references therein). Also within expectation, image restoration resulted in greater rms contrasts, by a factor of about 2.6 near limb in the K_1 instance, going up to 3.2 at disc centre, and going from 1.9 to 2.2 for K_2 .

The apparent granulation contrast is not only significantly enhanced by image restoration but also rather sensitive to differences between K_1 and K_2 . This makes the rms intensity contrast of the quiet Sun a suitable check of the goodness of K_2 for the restoration of HMI data. We compared the values obtained here with values from synthetic intensity maps, artificial images of the quiet Sun produced from a numerical simulation. To this end, synthetic Stokes spectra were generated by applying the LTE radiative transfer package SPINOR/STOPRO (Solanki 1987; Frutiger et al. 2000), to snapshots of a 3D MHD

simulation performed with the MURaM code (Vögler 2003; Vögler et al. 2005), as done in, for example, Danilovic et al. (2010, 2013).

The simulation, set up as in Danilovic et al. (2013), represents a layer encompassing the solar surface in the quiet Sun. The mean vertical magnetic flux density is 50 G. The simulation ran over about 23 min solar time after reaching a statistically steady state. Synthetic Stokes profiles were computed for ten snapshots of the simulation output, recorded at intervals of approximately two minutes solar time. From each snapshot we produced nine synthetic intensity maps corresponding to μ of 0.2, 0.3, 0.4 and so on, up to 1.0, rotating the snapshot along one dimension. The computational domain of the simulation spans 6×6 Mm in the horizontal, 1.4 Mm in depth, the top of the box lying about 0.5 Mm above the mean optical depth unity level, in a $288 \times 288 \times 100$ grid. This translates into a pixel scale of (0.0287μ) arcsec and 0.0287 arcsec, in the rotated and static direction, in the synthetic intensity maps.

The Stokes I and Q components of the synthetic spectra were convolved with a Gaussian function with a FWHM of 75 mÅ and sampled at -327 mÅ from the centre of the Fe I 6173 Å line in order to yield synthetic intensity maps mimicking the polarization (Stokes $I + Q$) and bandpass of the test continuum filtergram. The FWHM and central wavelength of the continuum bandpass were estimated from the main lobe of the CCD centre filter transmission profile⁹.

The synthetic intensity maps were resampled in the foreshortened direction such that the pixel scale is similar along both dimensions. The rms contrast of a given intensity map is given by the rms value of $\frac{I}{\langle I \rangle} - 1$ over all points, $\langle I \rangle$ denoting the mean intensity of the map. The mean rms contrasts from the synthetic intensity maps at each μ level for which we simulated data are plotted along the measured values from the test continuum filtergram in Fig. 12 (black circles).

The rms intensity contrast of the quiet Sun in the test continuum filtergram and the synthetic intensity maps cannot be compared directly due to the gross difference in the pixel scale (0.504 versus 0.0287 arcsec). Resampling the synthetic intensity maps to HMI's pixel scale is not feasible as the resampled synthetic intensity maps will extend only 16×16 pixels in the $\mu = 1.0$ case, going down to 3×16 pixels for $\mu = 0.2$. Simulations with considerably larger computational domains are necessary to yield synthetic intensity maps from which we can compute the rms contrast at HMI's pixel scale with statistical confidence. What we did instead was to estimate, by comparing the power spectra of the synthetic intensity maps and the test continuum filtergram, the contribution to intensity variations in the synthetic intensity maps by spatial frequencies up to the resolution limit of the test continuum filtergram.

In Fig. 13 we plot the encircled energy of the power spectrum of the 361×361 pixel crop, centred on solar disc centre, of the test continuum filtergram. There are no sunspots present in this crop. We define the cutoff spatial frequency as the spatial frequency at which the encircled energy of the power spectrum reaches 0.99, taken here as an indication of the resolution limit. The cutoff spatial frequency is 0.75 cycle/arcsec for the original test continuum filtergram (black curve), and 0.79 cycle/arcsec

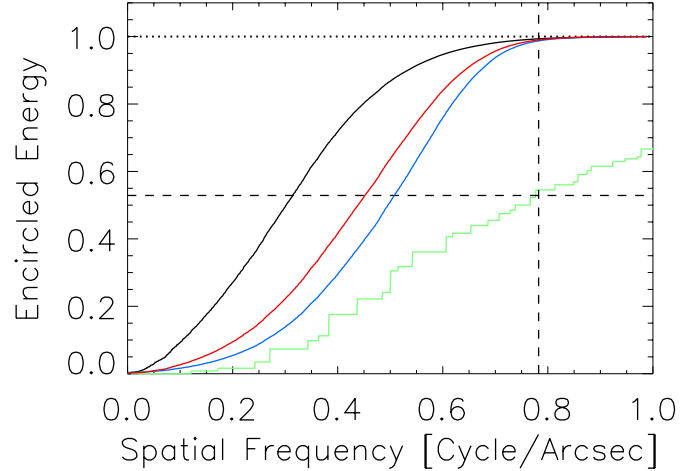


Fig. 13. Encircled energy of the power spectrum of the 361×361 pixel inset, centred on the centre of the solar disc, of the test continuum filtergram, before (black), and after image restoration with K_1 (blue) and with K_2 (red). The green series gives the encircled energy of the mean power spectrum of the synthetic intensity maps corresponding to $\mu = 1.0$. The vertical dashed line marks the cutoff spatial frequency (see text) of the restored (with K_2) test continuum filtergram and the horizontal dashed line the encircled energy of the mean power spectrum of the $\mu = 1.0$ synthetic intensity maps at this spatial frequency. The dotted line denotes encircled energy of unity.

and 0.78 cycle/arcsec for the iterations restored with K_1 (blue curve) and with K_2 (red curve).

As mentioned in Sect. 2.2, image restoration with a PSF that is the linear combination of Gaussian functions can potentially introduce aliasing artefacts from the enhancement of spatial frequencies above the Nyquist limit (0.99 cycle/arcsec for HMI). While image restoration with K_1 and K_2 enhanced image contrast, indicated here by the rightward displacement of the encircled energy profile for the restored iterations of the test continuum filtergram, it made little difference to the resolution limit which is also significantly lower than the Nyquist limit. Even after image restoration, almost all energy is confined to spatial frequencies well below the Nyquist limit. Aliasing artefacts from the restoration, if present, are likely negligible.

At each μ level for which we generated synthetic intensity maps, we computed the power spectrum of each intensity map and then the encircled energy of the mean power spectrum. Following that we estimated the encircled energy at the spatial cutoff frequency of the restored (with K_2) test continuum filtergram, illustrated in Fig. 13 for $\mu = 1.0$. The encircled energy here gives the proportion of observed intensity variation in the synthetic intensity maps arising from spatial frequencies up to the spatial cutoff frequency of the test continuum filtergram. The product of this quantity with the rms intensity contrast of the quiet Sun from the synthetic intensity maps (green circles, Fig. 12) then represents an approximation of the rms contrast if the spatial resolution of the synthetic intensity maps were similar to that of the test continuum filtergram. This treatment is very approximate, ignoring the fact that the spatial frequency response of the test continuum filtergram and synthetic intensity maps, up to the cutoff, are in all likelihood not similar.

In this analysis we had,

- defined the cutoff spatial frequency as the level where the encircled energy of the power spectrum reaches 0.99, and
- used the cutoff spatial frequency of the copy of the test continuum filtergram restored with K_2 to find the factors by

⁹ The filter transmission profiles of the HMI varies slightly with position in the CCD. The central wavelength of the main lobe, at -327 Å from line centre, differs from the bandpass position of -344 Å stated earlier. Quoted bandpass positions for HMI are theoretical figures derived assuming the filter transmission profiles are delta functions.

which to rescale the rms intensity contrast of the synthetic intensity maps (as the comparison between this restored version of the test continuum filtergram and the synthetic intensity maps is of greatest interest).

As stated above, the restoration of the test continuum filtergram made little difference to the cutoff spatial frequency. Also, the encircled energy of the power spectrum of the synthetic intensity maps does not vary strongly with spatial frequency in the regime of the cutoff spatial frequency of the test continuum filtergram, as visibly evident for the $\mu = 1.0$ example in Fig. 13. Hence, tests showed that the level of the rescaled rms contrast is not sensitive to small variations in the threshold encircled energy level chosen in the definition of the cutoff spatial frequency. The result is also not changed significantly if we employ the cutoff spatial frequency of the unrestored and restored with K_1 versions of the test continuum filtergram to derive the rescaling factors instead.

The rms intensity contrast of the quiet Sun in the restored (with K_2) test continuum filtergram (red curve, Fig. 12) and in the synthetic intensity maps, rescaled as described above (green circles), are of gratifyingly similar magnitude, less than or close to 0.01 apart at most μ , especially near disc centre. They do, however, differ in that the latter exhibits a steeper decline with distance from disc centre. The diverging trend with decreasing μ is likely, at least in part, from

- the approximate way of accounting for the influence of the Venusian atmosphere in the derivation of K_2 (Sect. 2.4),
- applying a single PSF to the entire FOV, so ignoring the variation of the PSF with position in the FOV (discussed in detail in Sect. 4.1),
- the difference in the spatial frequency response of the test continuum filtergram and the synthetic intensity maps,
- sensor noise and its centre-to-limb variation (CLV), and
- Doppler shift of the spectral line from the motion of SDO and the rotation of the Sun, which may produce small, μ -dependent effects on apparent intensity in the continuum bandpass through the line wing.

The observation that these two series are close, even with these factors present, confers confidence that image restoration with K_2 , though not exact, returns a reasonable approximation of the true aperture diffraction and stray light-free intensity contrast.

A quantitative comparison of the rms intensity contrast of the quiet Sun presented here for HMI and other measurements reported in the literature would require taking into account instrumental differences such as the spatial resolution and bandpass, which is beyond the scope of this study. Due to HMI's limited spatial resolution, the rms contrast, even after image restoration with K_2 , remains below the values returned from spaceborne and balloon-borne (i.e., similarly seeing-free) observatories at finer spatial resolutions, namely Hinode (Danilovic et al. 2008; Mathew et al. 2009; Wedemeyer-Böhm & Rouppe van der Voort 2009) and SUNRISE (Hirzberger et al. 2010). (Note though, that the divergence is also due in part to the different bandpass of the various instruments.)

3.2. Effect of image restoration on the Dopplergram, longitudinal magnetogram, continuum intensity and line depth data products

In this subsection we discuss the effect of image restoration with K_2 on the Dopplergram, longitudinal magnetogram, continuum intensity and line depth data products. We examine the influence

on the apparent continuum and line-core intensity, and magnetic field strength of small-scale magnetic concentrations, as well as sunspots and pores. We will also describe the result of image restoration on the apparent amount of magnetic flux on the solar surface and the line-of-sight velocity.

For this purpose we utilised a set of simultaneous (generated from the same sequence of filtergrams) 720 s Dopplergram, longitudinal magnetogram, continuum intensity and line depth images from the side CCD, taken shortly after this CCD resumed collection of the regular filtergram sequence, about an hour after Venus left the solar disc (at 05:35:32 UTC, June 6, 2012). Here we will refer to the result of subtracting the line depth image from the continuum intensity image, giving the intensity in the Fe I 6173 Å line, as the line-core intensity image.

As mentioned in Sect. 2.1, HMI data products cannot be corrected for stray light by the deconvolution with the PSF but instead we must correct either the Stokes parameters or the filtergrams used to compute the data products. The data set was restored for stray light by applying image restoration with K_2 to the corresponding 720 s Stokes parameters, and returning the result to the HMI data processing pipeline. A 200×200 pixel inset of the original and restored version of the data set, near disc centre ($\mu > 0.93$), featuring active region NOAA 11494, is shown in Fig. 14. The enhanced image contrast and visibility of small-scale structures is clearly evident.

The 720 s Milne-Eddington inversion data product includes the vector magnetogram. Since the inversion procedure employed to obtain this data product assumes a magnetic filling factor of unity everywhere, the process treats noise in the Stokes Q , U and V parameters as signal, creating pixel-averaged horizontal magnetic field strengths of ~ 100 G in the vector magnetogram even in the very quiet Sun. For ease of interpretation we confined ourselves to the longitudinal magnetogram data product here.

3.2.1. Intensity contrast and magnetogram signal of small-scale magnetic concentrations

Both the original and restored continuum and line-core intensity images were normalized by the fifth order polynomial in μ fit to the quiet Sun pixels. Then the intensity contrast at each image pixel was computed following the procedure applied to the test continuum filtergram in Sect. 3.1. For the line-core intensity image, the normalization not only corrects for limb darkening, but also the centre-to-limb weakening of the Fe I 6173 Å line (Norton et al. 2006; Yeo et al. 2013).

Sunspots were identified by applying a continuum intensity threshold representing the quiet Sun-to-penumbral boundary, denoted $(I/I_0)_{\text{QS,P}}$. We took the threshold value for MDI continuum intensity images, taken at 6768 Å, from Ball et al. (2012), 0.89, and estimated the equivalent level at HMI's wavelength, 6173 Å. Assuming sunspots to be perfect blackbodies and an effective temperature of 5800 K for the quiet Sun, the result is a threshold value of 0.88. This is a crude approximation, ignoring the difference in spatial resolution and variation in the continuum formation height with wavelength (Solanki & Unruh 1998; Sütterlin et al. 1999; Norton et al. 2006). Pores were also isolated by the application of this threshold. In the following we count these features to the sunspots and do not mention them separately.

We selected the image pixels where $\mu > 0.94$ (i.e., near disc centre), excluding sunspots (i.e., all points with $I/I_0 < (I/I_0)_{\text{QS,P}}$) and all points within three pixels of a sunspot. The selected points were binned by $| \langle B_l \rangle | / \mu$ such that we end up with

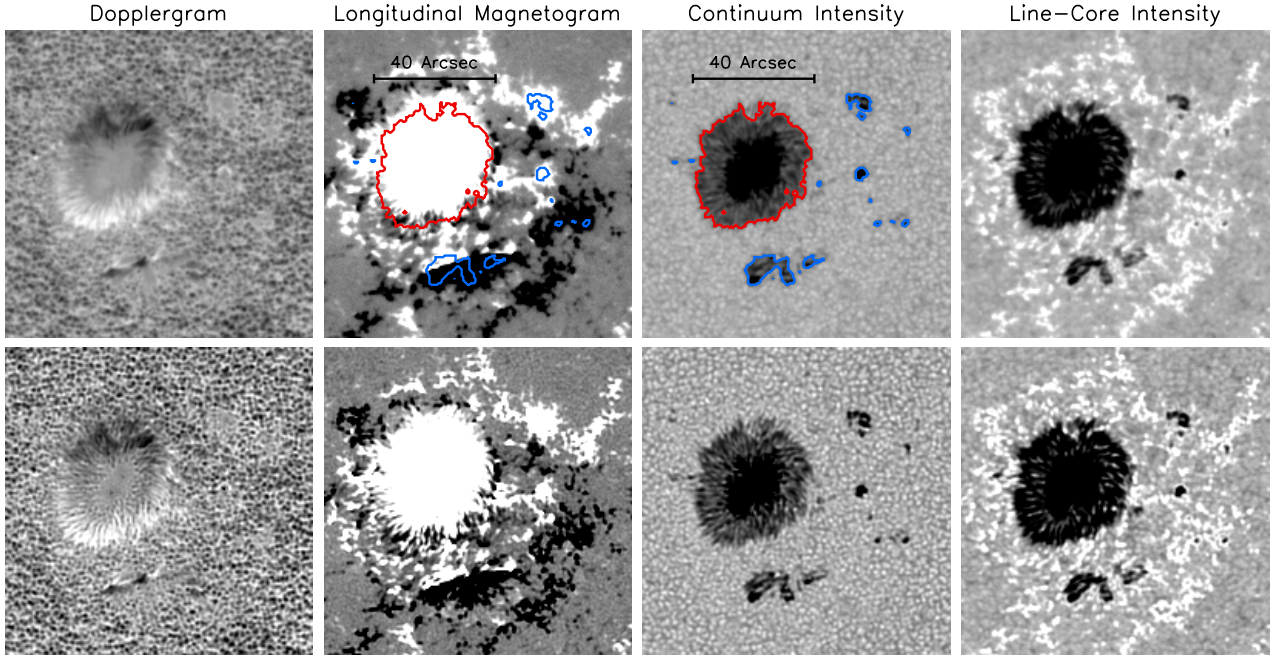


Fig. 14. 200×200 pixel (101×101 arcsec) inset, near disc centre ($\mu > 0.93$), encompassing active region NOAA 11494, of the simultaneously recorded 720 s data products examined, before (*top*) and after (*bottom*) image restoration with K_2 . The grey scale is saturated at -1200 and 1200 ms^{-1} for the Dopplergrams, at -100 and 100 G for the longitudinal magnetograms, and at 0.6 and 1.2 for the continuum and line-core intensity images. The Dopplergram was corrected for the velocity of SDO relative to the Sun and for differential rotation (Sect. 3.2.4). Both the continuum and line-core intensity images were normalized to the mean quiet-Sun level (Sect. 3.2.1). The red and blue contours in the grey scale plot of the uncorrected longitudinal magnetogram and continuum intensity image follow $I/I_0 = (I/I_0)_{\text{QS,P}}$, the quiet Sun to penumbra boundary. The colour coding is to distinguish the big sunspot feature (red) from the smaller sunspots and pores (blue), treated separately in Fig. 17.

800 bins of equal population. We then took the mean $|\langle B_1 \rangle|/\mu$, as well as the median continuum and line-core intensity contrast within each bin. The values for the uncorrected and restored copy of the data set are represented by the black and red curves respectively in Fig. 15. These profiles depict the intensity contrast of small-scale magnetic concentrations as a function of $|\langle B_1 \rangle|/\mu$, which serves as an approximate proxy of the magnetic filling factor (Ortiz et al. 2002; Yeo et al. 2013), in the continuum and core of the Fe I 6173 Å line. This is effectively a repeat of part of the analysis of Yeo et al. (2013), except now on HMI observations corrected for aperture diffraction and stray light.

Comparing the magnetogram with the continuum intensity image, we found the magnetogram signal associated with sunspots to extend beyond the continuum intensity boundary, given by the $I/I_0 = (I/I_0)_{\text{QS,P}}$ locus (for example, in Fig. 14). This was similarly noted by Yeo et al. (2013), who attributed it to the encroachment of the magnetic canopy of sunspots, and the smearing of polarized signal originating from sunspots onto its surrounds by instrumental scattered light. Hence, close to sunspots, the magnetogram signal is not entirely from local, non-sunspot magnetic features alone and would introduce a bias into the intensity contrast versus $|\langle B_1 \rangle|/\mu$ profiles (Fig. 15) if left unaccounted for. In the cited work pixels contiguous to sunspots and with $|\langle B_1 \rangle|/\mu$ above a certain threshold level were masked. Here, we excluded only all points within three pixels of each sunspot, observing that excluding pixels further than this distance made no appreciable difference to the resulting intensity contrast versus $|\langle B_1 \rangle|/\mu$ profiles. This measure is sufficient here as, unlike in the earlier study which examined almost all disc positions ($\mu > 0.1$), we are only looking at image pixels near disc centre ($\mu > 0.94$). Near disc centre, the influence of magnetic canopies, which are largely horizontal, on the longitudinal

magnetogram signal near sunspots is not as significant or extensive as at disc positions closer to the limb.

The continuum and line-core intensity contrast versus $|\langle B_1 \rangle|/\mu$ profile of small-scale magnetic concentrations near disc centre presented here for the uncorrected data set (black curves, Fig. 15) is nearly identical to that by Yeo et al. (2013; Figs. 9 and 10 in their paper), who employed similar data and method of derivation. The profiles from the restored data set (red curves) span a wider range, by a factor of about 1.3 in the continuum and line-core intensity contrast, and 1.7 in $|\langle B_1 \rangle|/\mu$, but are qualitatively similar in form.

Image restoration produced an absolute increase in the continuum and line-core intensity contrast everywhere except around the peak of the continuum contrast versus $|\langle B_1 \rangle|/\mu$ profile. The lower maximum in the profile from the restored data set, compared to the profile from the uncorrected data set (2.6×10^{-3} versus 5.7×10^{-3}), is likely from the enhanced contrast of dark intergranular lanes.

In Fig. 16 we show the uncorrected and restored continuum intensity and $|\langle B_1 \rangle|/\mu$ along a 21 pixel cut across example magnetic features near disc centre ($\mu = 0.97$). The troughs and peaks in the intensity curve (top panel) correspond to intergranular lanes and granules respectively. The magnetic features, the peaks in the $|\langle B_1 \rangle|/\mu$ curve (bottom panel), sit inside the intergranular lanes. The $|\langle B_1 \rangle|/\mu$ level at the core of these magnetic features lie in the regime of the peak of the continuum contrast versus $|\langle B_1 \rangle|/\mu$ profile. The stray light correction boosted the magnetogram signal at the core of these magnetic features but also rendered them darker here, even from positive contrast to negative, as radiation originating from nearby granulation is removed from the intergranular lanes. The spatial resolution of HMI is insufficient to resolve many of the magnetic

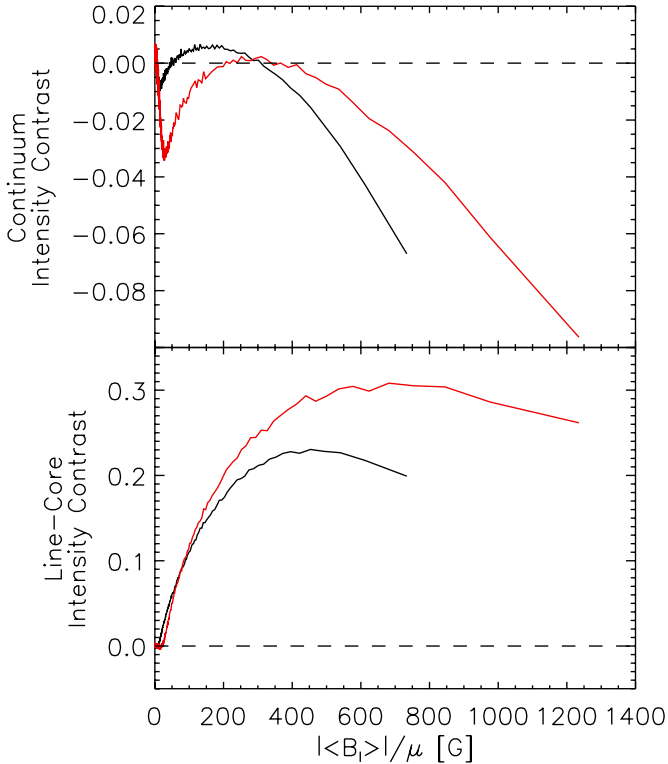


Fig. 15. Continuum (*top*) and line core (*bottom*) intensity contrast of small-scale magnetic concentrations, near disc centre ($\mu > 0.94$), as a function of $|\langle B_1 \rangle|/\mu$. The black and red curves correspond to the values from the original and restored (with K_2) data sets, respectively.

elements. Consequently, measured intensities contain contributions not only from magnetic features but also from the intergranular lanes that host them.

The intensity contrast of small-scale magnetic concentrations in both the continuum and spectral lines component of the solar spectrum, in particular the variation with position on the solar disc and magnetic field strength, is an important consideration in understanding the contribution by these features to variation in solar irradiance (Yeo et al. 2013). To the extent tested, image restoration with K_2 enhanced measured intensity contrast and $|\langle B_1 \rangle|/\mu$ significantly but made little qualitative difference to the dependence of apparent contrast on $|\langle B_1 \rangle|/\mu$. The analysis here was restricted to image pixels near disc centre ($\mu > 0.94$). To extend the analysis to other disc positions, we would need to examine multiple full-disc images from different times featuring active regions at various disc positions as done by Ortiz et al. (2002) and Yeo et al. (2013), beyond the scope of this paper.

3.2.2. Intensity and magnetogram signal of sunspots and pores

In Fig. 17 we illustrate the change introduced by image restoration with K_2 on $|\langle B_1 \rangle|$, as well as the continuum and line-core intensity of the sunspots and pores defined by the $I/I_0 = (I/I_0)_{\text{QS,P}}$ contours in Fig. 14. Signal enhancement is expressed as a function of the original level, separately for the big sunspot bounded by the red contours, and the smaller sunspots and pores bounded by the blue contours. We binned the image pixels by the uncorrected $|\langle B_1 \rangle|$ in intervals of 100 G and plotted the bin-averaged change in $|\langle B_1 \rangle|$ against the bin-averaged original

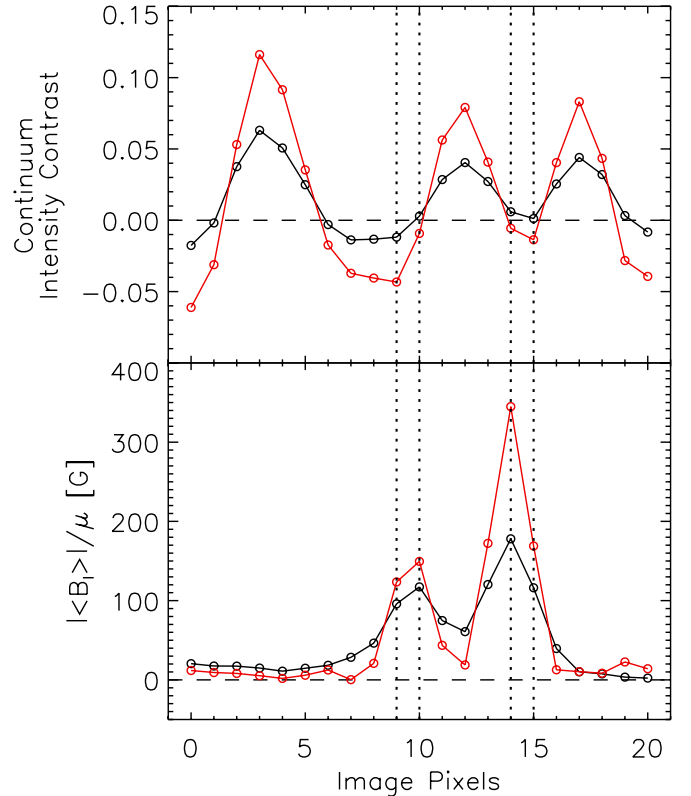


Fig. 16. Uncorrected (black circles) and restored (with K_2 , red circles) continuum intensity contrast (*top*) and $|\langle B_1 \rangle|/\mu$ (*bottom*) along a 21 pixel section across magnetic features near disc centre ($\mu = 0.97$). The plotted points represent image pixel values and are connected by straight lines to aid the eye. The dotted lines highlight the image pixels inside the magnetic features where the stray light correction effected a decrease in continuum intensity contrast accompanied by an increase in $|\langle B_1 \rangle|/\mu$. The dashed lines follow the zero level.

$|\langle B_1 \rangle|$ (Fig. 17a). This was repeated for the continuum and line-core intensity (Figs. 17b and 17c), taking a bin size of 0.05 in both instances.

Within expectation, the influence of image restoration on $|\langle B_1 \rangle|$ and intensity is highly correlated to the original values of these quantities. This comes largely from the fact that the darker regions, where $|\langle B_1 \rangle|$ is also typically higher, are more affected by stray light as scattered radiation forms a greater proportion of measured intensity, and therefore respond more strongly to image restoration. Also within expectation, the effect of restoration is more pronounced (greater absolute change) for smaller features, which are more susceptible to instrumental scattered light. An exception is the peak in the line-core intensity profile for the big sunspot feature (red curve, Fig. 17c), which arose from the enhanced brightness of the bright filaments in the penumbra from the restoration, visible in Fig. 14.

Given the variation in the response of sunspots to image restoration, it could have a profound effect on the apparent radiant and magnetic properties of these features. A full account of the effect of image restoration on sunspots, including the variation with size and disc position, would require examining a much larger sample of sunspots from multiple images taken at different times, which is outside the scope of this work (see Mathew et al. 2007 for such a study, based on MDI data).

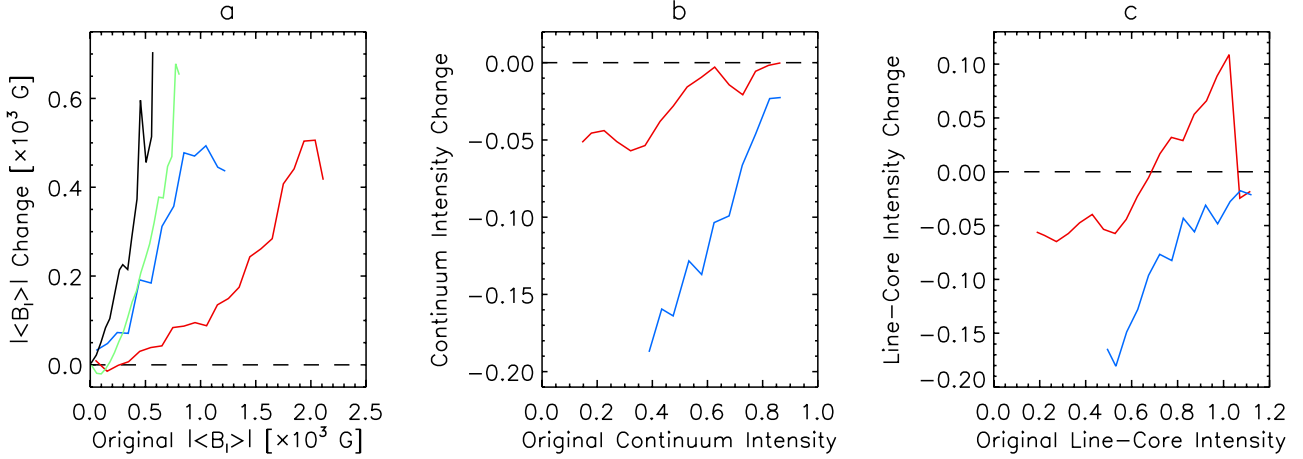


Fig. 17. Change in $|\langle B_1 \rangle|$ (left), as well as in the continuum (middle) and line-core intensity (right) introduced by image restoration with K_2 , as a function of the original value. Both the continuum and line core intensities are normalized to the quiet-Sun level. The red and blue series follow the values derived from the sunspot and pore features encircled by the similarly colour-coded contours in Fig. 14. The black and green curves (left) correspond to the change in $|\langle B_1 \rangle|$ in the quiet Sun field depicted in Fig. 19, and in a 201×201 pixel active region field near disc centre ($\mu > 0.92$), respectively. The dashed lines mark the zero level.

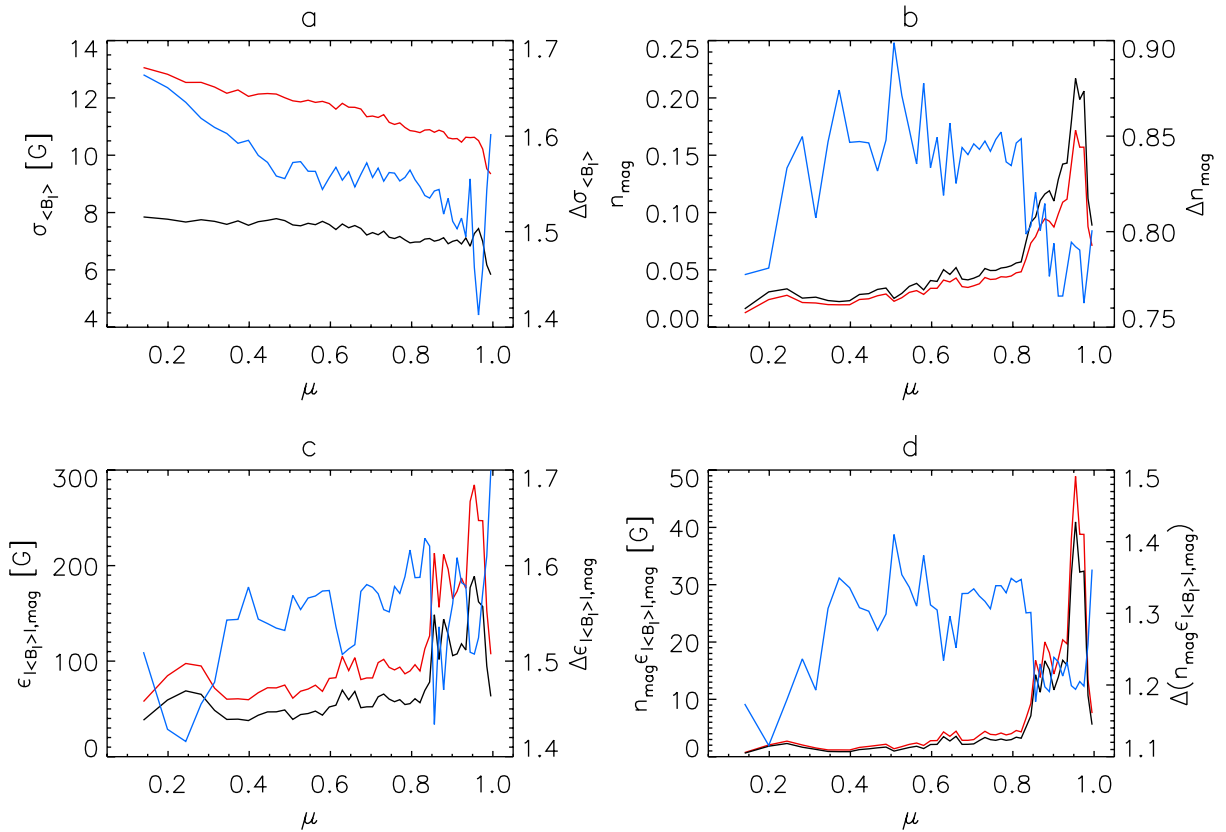


Fig. 18. Plotted as a function of μ , **a)** the noise level of the 720 s longitudinal magnetogram, $\sigma_{\langle B_1 \rangle}$, **b)** the proportion of image pixels counted as containing significant magnetic activity, n_{mag} , **c)** the mean $|\langle B_1 \rangle|$ of these points, $\epsilon_{|\langle B_1 \rangle|, \text{mag}}$, **d)** and the product of n_{mag} and $\epsilon_{|\langle B_1 \rangle|, \text{mag}}$. Left axes: the uncorrected (black series) and restored with K_2 levels (red series). Right axes: the quotient of the restored and uncorrected values (blue series).

3.2.3. Amount of magnetic flux on the solar surface

We segmented the solar disc in the 720 s longitudinal magnetogram by μ (excluding points where $\mu < 0.1$, $\sim 1\%$ of the solar disc by area) into 50 annuli of equal area. Within each annulus, we computed the quantities listed below, plotted in Fig. 18. For each quantity, we derived the level in the uncorrected and restored magnetogram (black and red series, left axes), and the

ratio of the restored and the uncorrected values (blue series, right axes), denoted by the Δ prefix.

- The noise level, $\sigma_{\langle B_1 \rangle}$ (Fig. 18a), given by the standard deviation of $\langle B_1 \rangle$. The standard deviation was computed iteratively, points more than three standard deviations from the mean were excluded from succeeding iterations till convergence, to exclude magnetic activity. The variation of the noise level of HMI longitudinal magnetograms with position

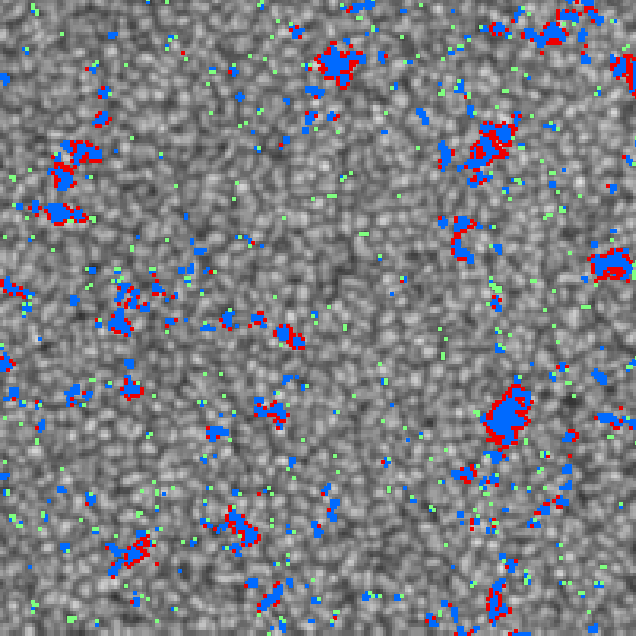


Fig. 19. 201×201 pixel inset, centred on disc centre, of the 720 s continuum intensity image, with the points displaying $|\langle B_l \rangle| > 3\sigma_{\langle B_l \rangle}$ in the 720 s longitudinal magnetogram highlighted. Blue corresponds to the points realizing this condition in both the uncorrected and restored magnetogram, red the points fulfilling it only in the uncorrected data and green the points satisfying it only in the restored data. The grey scale is saturated at 0.8 and 1.2 times the mean quiet-Sun level.

on the solar disc is dominated by a centre-to-limb increase (Liu et al. 2012; Yeo et al. 2013). It is therefore reasonable to represent the noise level within a given annulus by a single value of $\sigma_{\langle B_l \rangle}$. Image restoration increased the noise level, on average, by a factor of 1.6.

- The proportion of image pixels counted as containing significant magnetic activity, n_{mag} (Fig. 18b), taken here as the points where $|\langle B_l \rangle| > 3\sigma_{\langle B_l \rangle}$.
- The mean $|\langle B_l \rangle|$ of the image pixels counted as magnetic, $\epsilon_{\langle B_l \rangle, \text{mag}}$ (Fig. 18c).
- The product of n_{mag} and $\epsilon_{\langle B_l \rangle, \text{mag}}$ (Fig. 18d). The quantity $\Delta(n_{\text{mag}}\epsilon_{\langle B_l \rangle, \text{mag}})$ represents the factor by which the apparent amount of line-of-sight magnetic flux changed from stray light removal.

Image restoration resulted in less image pixels being counted as magnetic (around -10% to -25% , Fig. 18b), though the enhancement to the magnetogram signal (30% to 60%, Fig. 18c) meant that there is an overall increase in the apparent amount of line-of-sight magnetic flux (10% to 40%, Fig. 18d). Computing $\Delta(n_{\text{mag}}\epsilon_{\langle B_l \rangle, \text{mag}})$ taking all the annulus as a whole, the total amount of line-of-sight magnetic flux over the solar disc increased by a factor of 1.2.

In Fig. 19, we mark the location of image pixels counted as magnetic in the original and restored data, in a 201×201 pixel inset centred on the disc centre. Image restoration renders magnetic features spatially smaller as polarized radiation originating from these features, lost to the surrounding quiet Sun by aperture diffraction and stray light, is recovered (illustrated by the blue and red clusters). This change in the size of magnetic features likely depends on factors such as the surface area, and circumference to surface area ratio. The enhanced noise level also contributes to the smaller count in the restored data. Image

restoration does recover some magnetic features smeared below the magnetogram signal threshold ($|\langle B_l \rangle| = 3\sigma_{\langle B_l \rangle}$) in the original data by instrumental scattered light (green clusters). Overall, less image pixels are counted as magnetic.

The overall increase in $\sigma_{\langle B_l \rangle}$ towards the limb is partly related to the increase in low-level magnetogram signal fluctuations from the ubiquitous weak horizontal magnetic fields in the quiet Sun internetwork (Lites et al. 1996, 2008; Beck & Rezaei 2009), which obtain a line-of-sight component near the limb, and magnetic features foreshortening towards the background noise regime when approaching the limb. A probable cause of the overall centre-to-limb increase in $\Delta\sigma_{\langle B_l \rangle}$ is the enhancement of these true signal contributions to apparent noise.

In Fig. 17a we display the change in magnetogram signal as a function of the original signal, in the quiet Sun field illustrated in Fig. 19 and in a 201×201 pixel crop of an active region near the disc centre ($\mu > 0.92$), represented by the green and black curves, respectively. This was computed as done in Sect. 3.2.3 for the sunspots and pores in Fig. 14, the results of which are also plotted for comparison (blue and red curves). The only difference is here we binned the image pixels by the uncorrected $|\langle B_l \rangle|$ in intervals of 40 G instead of 100 G. As done in Sect. 3.2.1, we minimised the influence of pores present in the active region field by excluding the image pixels where $I/I_0 < (I/I_0)_{\text{QS,P}}$ and points up to three pixels away from them. (There are no image pixels where $I/I_0 < (I/I_0)_{\text{QS,P}}$ in the quiet Sun field.) The result from the quiet Sun and active region fields represent the effect of image restoration on the magnetogram signal of quiet Sun network, and active region faculae, respectively.

As noted for sunspots and pores (Sect. 3.2.2), the enhancement of the magnetogram signal of network and faculae from image restoration is highly correlated to the original level. This is possibly from the restoration enhancing the signal in the core of magnetic features, where it is also typically stronger, while depressing the signal in the fringes, from the recovery of polarized radiation scattered from the core to the fringes and surrounding quiet Sun, as discussed above and visible for the magnetic features depicted in Fig. 16.

The effect of image restoration on network and faculae is also more pronounced than in sunspots and pores, in particular for network. This is likely related to the smaller spatial scale of these features, which makes them more susceptible to stray light, and consequently they respond more acutely to restoration, than sunspots and pores. The stronger response of network compared to faculae is probably due to the fact that they appear in smaller clusters and the restoration of small-scale mixed polarities in the quiet Sun smeared out by instrumental scattered light.

As image restoration affects different magnetic features differently, the overall effect on the apparent amount of magnetic flux fluctuates with prevailing magnetic activity. This is the likely reason neither Δn_{mag} , $\Delta\epsilon_{\langle B_l \rangle, \text{mag}}$ nor $\Delta(n_{\text{mag}}\epsilon_{\langle B_l \rangle, \text{mag}})$ exhibit any obvious trend with μ , modulated by the magnetic features present within each annulus. Importantly, the relatively acute effect of image restoration on network, and the fact that the solar disc is, by area, predominantly quiet Sun means most of the increase in the measured amount of magnetic flux comes from the enhancement of these features. This is consistent with the findings of Krivova & Solanki (2004).

3.2.4. Line-of-sight velocity

Here we are interested in the part of measured line-of-sight velocities in HMI Dopplergrams arising from convective motions

on the solar surface. To this end, we corrected the 720 s Dopplergram for the contribution by the rotation of the Sun and the relative velocity of SDO to the Sun¹⁰, v_{SDO} , following the procedure of [Welsch et al. \(2013\)](#). Oscillatory motions associated with p -modes are largely undetectable in the 720 s Dopplergram data product as it is a weighted combination of filtergram observations from a 1350 s period, much longer than the period of these oscillations (~ 5 min).

The rotation rate of the Sun varies with heliographic latitude, Φ . Let v_{rot} denote the velocity of the surface of the Sun from its rotation. We first determined the Stonyhurst latitude and longitude at each image pixel within the solar disc. Then, we derived the v_{rot} at each latitude from the differential rotation profile by [Snodgrass \(1983\)](#),

$$w(\Phi) = 2.902 - 0.464 \sin^2 \Phi - 0.328 \sin^4 \Phi, \quad (3)$$

which relates angular velocity, $w = \frac{|v_{\text{rot}}|}{R_{\odot} \cos \Phi}$ (R_{\odot} being the radius of the Sun in metres) to Φ . The contribution by v_{rot} and v_{SDO} to measured velocity at a given image pixel is then given by the projection of v_{rot} and v_{SDO} onto the line-of-sight to the point, taking the small-angle approximation. The projection of v_{SDO} , in this instance, varied between 500 and 800 ms^{-1} with position on the solar disc. The significant magnitude and variation of this with disc position arises from SDO's geosynchronous orbit about Earth and Earth's orbit about the Sun.

Let $\langle v_1 \rangle$ represent the signed Dopplergram signal, the mean line-of-sight component of the vector velocity over a given image pixel.

As done in Sect. 3.2.3, we segmented the solar disc by μ , into 50 equal annuli, excluding points where $\mu < 0.1$. The image pixels where $|\langle B_1 \rangle|/\mu > 10\text{G}$ in the 720 s longitudinal magnetogram were masked, leaving quiet Sun. Within each annulus, we binned the unmasked points by the uncorrected $\langle v_1 \rangle$ in intervals of 20 ms^{-1} , and retrieved the median original and restored $\langle v_1 \rangle$ within each bin, ignoring bins with less than 100 points. The factor enhancement of $\langle v_1 \rangle$ from image restoration, $\Delta \langle v_1 \rangle_{\text{QS}}$ is then given by the slope of the linear regression fit to the restored bin-median $\langle v_1 \rangle$ against the original, illustrated for the disc centre interval of μ ($\mu > 0.99$) in Fig. 20a. By performing this computation over small intervals of μ , we avoid introducing scatter or bias in $\Delta \langle v_1 \rangle_{\text{QS}}$ from the μ dependence of the convective blueshift of the spectral line.

The enhancement of the Dopplergram signal in the quiet Sun from image restoration with K_2 is significant and exhibits an acute CLV; $\Delta \langle v_1 \rangle_{\text{QS}}$ increases monotonically with μ , from about 1.4 near the limb to 2.1 at disc centre (Fig. 20b).

In looking only at the quiet Sun, we excluded phenomena localised in active regions (for example, Evershed flow in sunspots), leaving signal largely from granulation and supergranulation. Supergranulation flows are largely horizontal. The line-of-sight velocities of supergranulation flows are thus greatest near the limb and diminishes towards disc centre from foreshortening. In contrast, the apparent line-of-sight velocities of granulation flows diminish towards the limb. Approaching the limb, granulation is more and more difficult to resolve from foreshortening and the line-of-sight increasingly crossing into multiple granulation cells. The typical diameter of granulation and supergranulation cells is about 1 Mm and 30 Mm, respectively. Granulation is therefore more affected by stray light and experiences greater signal enhancement from image restoration than supergranulation. The observed CLV of $\Delta \langle v_1 \rangle_{\text{QS}}$ is consistent

¹⁰ Given by the radial, heliographic west and north velocity of the spacecraft relative to the Sun listed in the data header.

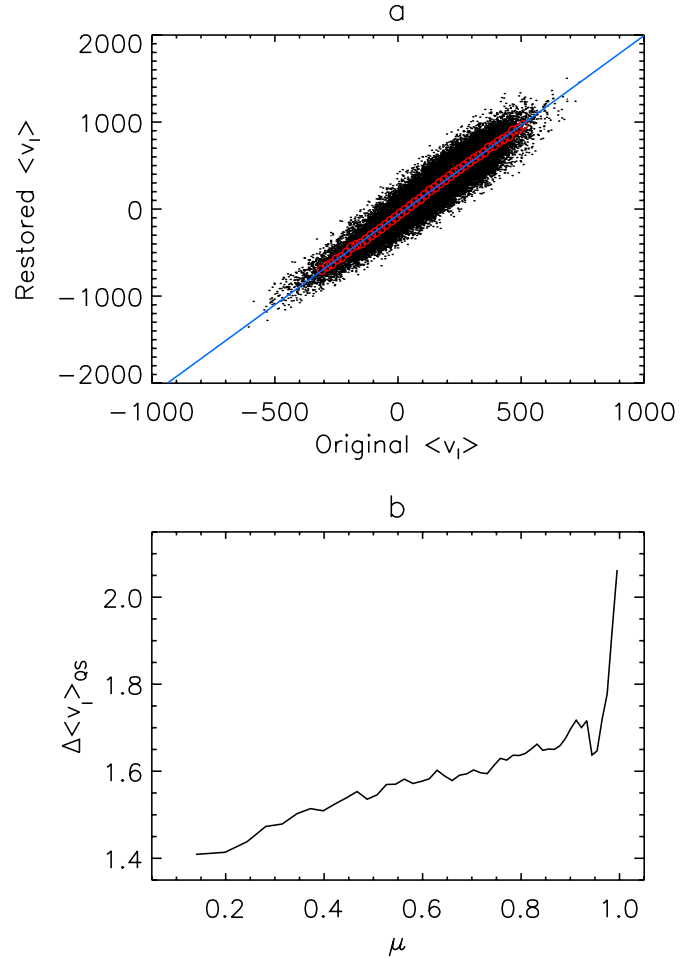


Fig. 20. a) Scatter plot of the Dopplergram signal, $\langle v_1 \rangle$ in the quiet Sun, near disc centre ($\mu > 0.99$), in the restored (with K_2) and uncorrected versions of the 720 s Dopplergram. The red circles denote the bin-median (from binning the points by the uncorrected $\langle v_1 \rangle$ in intervals of 20 ms^{-1}) and the blue line the corresponding linear regression fit. b) The factor enhancement of $\langle v_1 \rangle$ in the quiet Sun from image restoration, $\Delta \langle v_1 \rangle_{\text{QS}}$ as a function of μ .

with the converse CLV of the line-of-sight velocities of granulation and supergranulation flows, and the stronger effect of image restoration on granulation compared to supergranulation.

By correcting both the original and restored Dopplergram for differential rotation with Eq. (3), we had implicitly assumed that this component of measured line-of-sight velocity is not significantly changed by stray light or its removal. Given the line-of-sight component of v_{rot} varies gradually across the solar disc, this is true except very close to the limb. Therefore, the effect on this analysis is likely minute and confined to the annuli closest to the limb.

The pronounced Dopplergram signal enhancement effected by image restoration with K_2 could have an impact on the characterization of plasma flows in the solar surface with HMI data. In this study we will not attempt to examine the effects of image restoration on apparent Doppler shifts in active regions, p -mode oscillations (detectable in the 45 s Dopplergram data product of the front CCD) or the individual physical processes driving plasma motion on the solar surface.

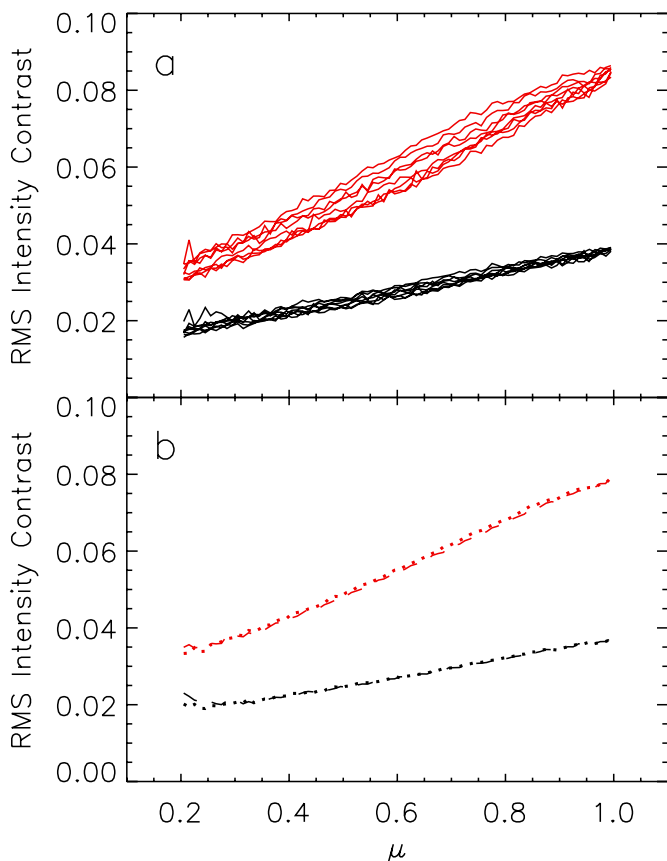


Fig. 21. RMS intensity contrast of the quiet Sun as a function of μ , before (black lines) and after (red) image restoration with K_2 . **a)** In the test continuum filtergram, the solar disc segmented into eight equal sectors. **b)** In the near-simultaneous filtergrams of similar bandpass and polarization from the side (dotted lines) and front (dashed) CCD.

4. Variation of the PSF within the FOV, between the HMI CCDs and with time

Derived from observations of Venus in transit recorded on the side CCD, K_2 characterizes the stray light in the employed data, at the position in the FOV occupied by the Venusian disc. Here we discuss the applicability of K_2 to the entire FOV, to data from the front CCD and, importantly, from other times.

4.1. Variation of the PSF with FOV position

Taking the test continuum filtergram (from Sect. 3.1), we segmented the solar disc into eight equal sectors and computed the rms intensity contrast of the quiet Sun within each sector. The level before and after image restoration with K_2 are illustrated in Fig. 21a. There is scatter in the rms contrast between the sectors which is more pronounced in the restored data. This enhanced divergence is, at least in part, caused by the fact that we restored the entire solar disc with a single PSF when the true PSF varies from sector to sector.

The scatter in rms contrast is, however, at least to the extent tested, relatively small in comparison to the absolute level. More importantly, the divergence between the sectors in the restored data (red curves) is small compared to the difference between the restored and the original data (black curves). This implies that the inhomogeneity introduced by applying a single PSF to the entire FOV is small in comparison to the contrast enhancement. Nonetheless, for sensitive measurements, care should be

taken, where possible, to average measurements from different positions in the FOV after deconvolution with the PSF deduced here.

Next, we looked at the variation, over the solar disc, of the effect of image restoration with K_2 on the 720 s longitudinal magnetogram from Sect. 3.2. Sampling the solar disc at 16 pixel intervals in both the north-south and east-west directions, we centred a 401×401 pixel window over each sampled point and took the mean $|\langle B_1 \rangle|$ of all the solar disc pixels within the window, denoted $\epsilon_{\langle B_1 \rangle}$. Let $\Delta\epsilon_{\langle B_1 \rangle}$ represent the ratio of $\epsilon_{\langle B_1 \rangle}$ in the restored and uncorrected data, representing the factor enhancement to $\epsilon_{\langle B_1 \rangle}$ from the restoration.

Expectedly, $\Delta\epsilon_{\langle B_1 \rangle}$ varied with position on the solar disc (Fig. 22b). This variation is driven by:

- differences in the magnetic activity present in the sampling window (image restoration affects different magnetic features differently, Sect. 3.2.3) and
- fluctuations in the effect of image restoration from the variation of the stray light behaviour of the instrument across the FOV.

The scatter plot of $\Delta\epsilon_{\langle B_1 \rangle}$ versus the original $\epsilon_{\langle B_1 \rangle}$ reveals an inverse relationship between the two quantities (Fig. 22c). The cause of this correlation is that the restoration enhances the magnetogram signal in the quiet Sun more strongly than in active regions (Fig. 17a). The relatively weak spread of the scatter plot suggests the variation in $\Delta\epsilon_{\langle B_1 \rangle}$ with disc position is dominantly due to the inhomogeneous distribution of magnetic activity (Fig. 22a) and the diverging effects of restoration on different magnetic features. This is further evidence that it is a reasonable approximation to restore the entire FOV of HMI for instrumental scattered light with a single PSF.

4.2. Variation of the PSF between the HMI CCDs and with time

In Fig. 21b we show the rms intensity contrast of the quiet Sun in two near-simultaneous filtergrams, one from each CCD, taken less than one minute apart. The two filtergrams were recorded about an hour after Venus left the solar disc (at around 05:36 UTC, June 6, 2012), shortly after the side CCD resumed collection of the regular filtergram sequence.

The two near-simultaneous filtergrams were taken in the same bandpass (-172 mÅ from line centre) and polarization (Stokes $I - V$). Any disparity in the rms contrast between the two would arise mainly from differences in the performance of the two CCDs, including the stray light behaviour. The rms contrast in the two filtergrams is very similar, even after image restoration with K_2 (red curves). Since we expect any disparity due to differences in the stray light behaviour of the two CCDs to be amplified by the application of the side CCD PSF to a front CCD filtergram, this agreement is encouraging.

Comparing the close similarity in the rms intensity contrast of the quiet Sun in the two near-simultaneous filtergrams to the scatter between different FOV positions in the test continuum filtergram (top panel), it appears that the difference in the stray light behaviour of the two CCDs is much smaller than the variation with position in the FOV of the side CCD. The side and front CCDs are identical and share a common optical path (Schou et al. 2012b), it is therefore within reason that the stray light behaviour, even the variation of the PSF with position in the FOV, is broadly similar.

The SDO satellite is in a geosynchronous orbit. Since the HMI commenced regular operation (May 1, 2010), the side and

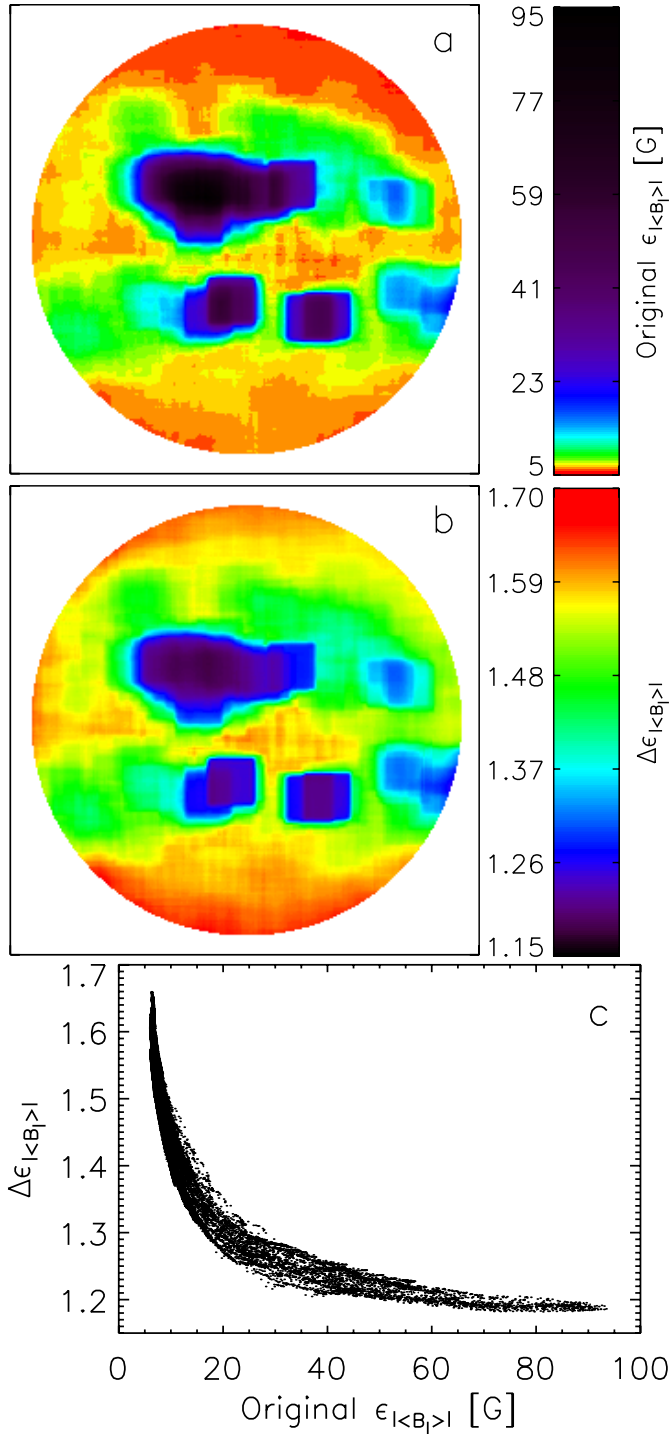


Fig. 22. **a)** Mean unsigned magnetogram signal, $\epsilon_{\langle B \rangle}$ of the original (not corrected for stray light) 720 s longitudinal magnetogram. **b)** Factor enhancement of $\epsilon_{\langle B \rangle}$ from image restoration with K_2 , $\Delta\epsilon_{\langle B \rangle}$. **c)** Scatter plot of $\Delta\epsilon_{\langle B \rangle}$ against the original $\epsilon_{\langle B \rangle}$.

front CCDs recorded a continuum filtergram each during the daily pass through orbital noon and midnight. For the purpose of investigating the stability of the stray light behaviour of the instrument over time, we examined the solar aureole, the intensity observed outside the solar disc arising from instrumental scattered light, in these daily data¹¹. We examined 2307 orbital

¹¹ The solar aureole is not to be confused with the aureole about the Venusian disc when it is in transit, discussed in Sect. 2.4.

noon and midnight continuum filtergrams from each CCD, spanning the 1157 day period of May 1, 2010 to June 30, 2013.

For each continuum filtergram, we averaged the solar aureole over all azimuths. From the resulting radial intensity profile, we determined the intensity of the solar aureole at distances of 1 and 10 arcsec from the edge of the solar disc. The derived intensities, normalized to the limb level, are expressed in Figs. 23a and 23b, respectively.

We excluded the points that are spurious or from continuum filtergrams with missing pixel values, leaving 2248 and 2288 points from the side and front CCDs respectively. To show up the broad trend with time we interpolated each time series at one day intervals and smoothed the result by means of binomial smoothing (Marchand & Marmet 1983). The time variation in the relative (to the limb level) intensity of the solar aureole at 1 and 10 arcsec from the limb reflects changes to the shape of the PSF near the core and in the wings respectively.

There is clear point-to-point fluctuation in the relative intensity of the solar aureole at 1 arcsec from the limb. This is due to the fact that near the limb, the intensity of the solar aureole decays rapidly with radial distance such that small variations in the width of the core of the PSF show up as large swings in the relative intensity at a fixed distance from and near the limb. Overall, the magnitude of the scatter, given by the standard deviation, is below 2% of the mean level. Also, the side and front CCD series are relatively stable and similar, with no overt long term trends or divergence from one another. This suggests that the width of the core of the PSFs of the two CCDs are, to the extent tested, broadly similar and constant over the period examined.

For the relative intensity of the solar aureole at 10 arcsec from the limb, there is an approximately synchronous periodic variation between the two CCDs. There is also a gradual overall drift between May 2010 and July 2011, and between August 2012 and June 2013. The fluctuation of the two time series and the divergence between them is minute, less than 5% of the overall level. The time variation of, and difference between the wings of the PSFs of the two CCDs, implied by these fluctuations, has likely little effect on image contrast. Even with the $\sim 3\%$ offset between the front and side CCD time series around the time of the Venus transit, the rms intensity contrast of the quiet Sun in the near-simultaneous filtergrams from the two CCDs (taken about an hour after the end of the transit) is practically identical (Fig. 21b).

Going from 1 to 10 arcsec from the limb, the time dependence of the relative intensity of the solar aureole changes gradually from the trend seen at 1 arcsec to that seen at 10 arcsec. Beyond 10 arcsec the variation with time does not change significantly. The relative intensity of the solar aureole at 1 and 10 arcsec from the limb therefore constitute a reasonable representation of variation in the shape of the PSFs of the two CCDs with time.

From the near identity of the rms intensity contrast of the quiet Sun in the near-simultaneous filtergrams from the two CCDs (Fig. 21b) and the minute time variation of the PSFs of the two CCDs implied by the relative stability of the shape of the solar aureole in daily data (Figs. 23a and 23b), we assert that K_2 can be applied to observations from both CCDs for the period examined (May 1, 2010 to June 30, 2013) without introducing significant error.

This assertion is consistent with the state of the focus of the instrument over the period examined. The PSF of HMI, like any optical system, is strongly modulated by the focus. The instrument is maintained in focus by varying the heating of the front window and the position of two five-element optical wheels

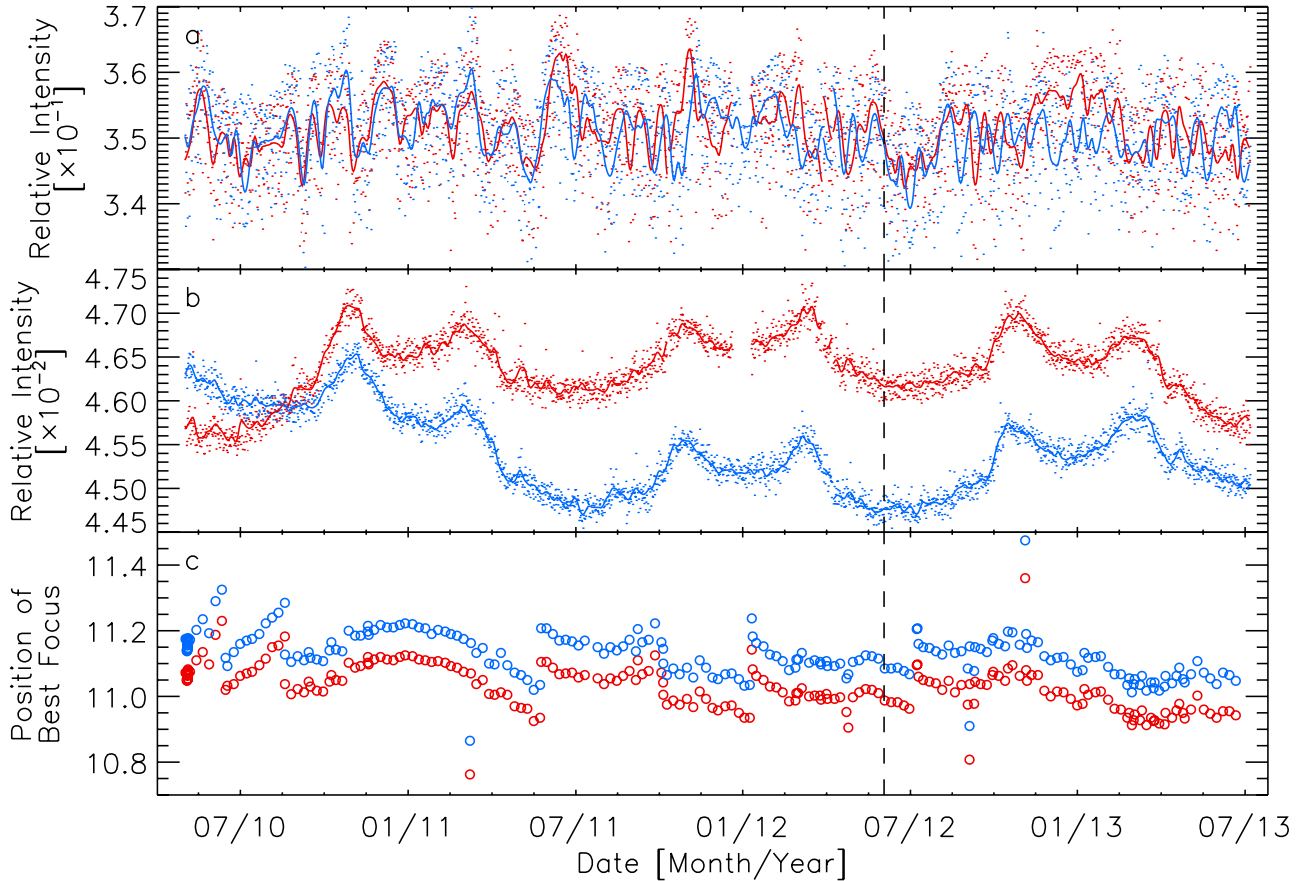


Fig. 23. Radial intensity of the solar aureole, at distances of **a)** 1 and **b)** 10 arcsec from the edge of the solar disc, in the orbital noon and midnight continuum filtergrams from the side (red) and front (blue) CCDs. The value from each filtergram is normalized to the level at the edge of the solar disc. The dots represent the measured values and the curves the smoothed time series. Segments of measured values spaced more than one day apart were treated as separate time series, giving the gaps in the curves. **c)** The position of best focus, in units of focus steps (see text), from the (approximately) weekly focus calibration of the side (red circles) and front CCDs (blue circles). The dashed line marks the time of the transit of Venus.

(Schou et al. 2012b). By varying the elements of the two optical wheels placed in the optical path, they allow the focus to be adjusted in 16 uniform, discrete steps, each corresponding to about two-thirds of a depth of focus. In Fig. 23c we plot the position of best focus, in units of the focus steps, from the regular (roughly weekly) focus calibration of the sensor, over the same period as the daily data. The focus of the two CCDs are remarkably similar and stable, differing from one another and varying over the period of interest by much less than a depth of focus. The contribution by focus to the variation of the PSF between the two CCDs and with time is most probably minute.

5. Summary

In this paper we present an estimate of the PSF of the SDO/HMI instrument. The PSF was derived from observations of Venus in transit. We convolved a simple model of the Venusian disc and solar background with a guess PSF iteratively, optimizing the agreement between the result of the convolution and observation. We modelled the PSF as the linear sum of five Gaussian functions, the amplitude of which we allowed to vary sinusoidally with azimuth. This azimuthal variation was necessary to reproduce the observations accurately. Recovering the anisotropy of the PSF was also shown to be important for the proper removal of stray light from HMI data by the deconvolution with the PSF. The interaction between solar radiation and the Venusian

atmosphere is complex and not straightforward to account for. The result is a conservative estimate of the PSF, similar in width to the ideal diffraction-limited PSF in the core but with more extended wings.

The PSF was derived with data from one of the two identical CCDs in the sensor. It therefore represents the stray light behaviour of that particular CCD, at the time of the transit of Venus, at the position in the FOV occupied by the Venusian disc in the employed observations.

Comparing the apparent granulation contrast in different parts of a single image, we showed that although the variation in the stray light behaviour of the instrument with position in the FOV introduces uncertainty to measured contrast, amplified by restoring observations with a single PSF, the scatter is relatively minute and will likely have little quantitative influence if care is taken to average measurements from multiple FOV positions. This was confirmed by an examination of the uniformity, over the FOV, of the effect of image restoration on the 720 s longitudinal magnetogram data product.

The time variation of the shape of the solar aureole in daily data was taken as an indication of PSF changes over the period examined (May 1, 2010 to June 30, 2013). Based on the relatively weak time variation of the aureole, and the similarity of the aureole and granulation contrast in data from the two CCDs, we assert that the PSF derived here can be applied to observations

from both CCDs over the period examined without introducing significant error.

Apparent granulation contrast, given here by the rms intensity contrast of the quiet Sun, in HMI continuum observations restored by the deconvolution with the PSF, exhibit reasonable agreement with that in artificial images generated from a 3D MHD simulation at equal spatial sampling. This demonstrates that the PSF, though an approximation, returns a competent estimate of the aperture diffraction and stray light-free contrast. The restoration enhanced the rms intensity contrast of the quiet Sun by a factor of about 1.9 near the limb ($\mu = 0.2$), rising up to 2.2 at disc centre.

We also illustrated the effect of image restoration with the PSF on the 720 s Dopplergram and longitudinal magnetogram data products, and the apparent intensity of magnetic features.

- For small-scale magnetic concentrations, image restoration enhanced the intensity contrast in the continuum and core of the Fe I 6173 Å line by a factor of about 1.3, and the magnetogram signal by a factor of about 1.7.
- Magnetic features in the longitudinal magnetogram are rendered smaller, as polarized radiation smeared onto surrounding quiet Sun by instrumental scattered light is recovered.
- Image restoration increased the apparent amount of magnetic flux above the noise floor by a factor of about 1.2, mainly in the quiet Sun. This may be, in part, from the recovery of magnetic flux in opposite magnetic polarities lying close to one another partially cancelled out by stray light.
- The influence of image restoration on sunspots and pores varied strongly, as expected, within a given feature and between features of different sizes.
- Line-of-sight velocity due to plasma motions on the solar atmosphere increases by a factor of about 1.4 to 2.1. The variation comes from the restoration enhancing granulation flows more strongly than larger scale supergranulation flows. Given the spatial scale dependence, the effect on Doppler shifts from large scale motions such as the meridional flow and differential rotation is probably minute.

The pronounced effect of image restoration on the apparent radiant, magnetic and motional properties of solar surface phenomena could have a significant impact on the interpretation of HMI observations. For instance, the observation that restoring HMI longitudinal magnetograms renders magnetic features smaller while boosting the magnetogram signal, and the increase in the amount of magnetic flux is dominantly in the quiet Sun, can influence models of variation in solar irradiance based on HMI data. Specifically, with models that relate the contribution by small-scale magnetic concentrations to solar irradiance variations to the number density and magnetogram signal (for example, [Wenzler et al. 2006](#); [Foukal et al. 2011](#); [Ball et al. 2012](#)).

Acknowledgements. The authors would like to express their gratitude to the SDO/HMI team, for providing the data set, and all the useful discussions and support rendered over the course of this study, with special mention to Philip Scherrer and Jesper Schou. The authors would also like to thank the members of the Solar Lower Atmosphere and Magnetism group at the Max-Planck Institut für Sonnensystemforschung, in particular Achim Gandorfer, for their interest in this work, and all the helpful advice and comments. K.L.Y. acknowledges postgraduate fellowship of the International Max Planck Research School

on Physical Processes in the Solar System and Beyond. This work has been partly supported by WCU grant No. R31-10016 funded by the Korean Ministry of Education, Science and Technology.

References

- Afram, N., Unruh, Y. C., Solanki, S. K., et al. 2011, *A&A*, 526, A120
 Albrechtsen, F., & Maltby, P. 1981, *Sol. Phys.*, 71, 269
 Archinal, B. A., A'Hearn, M. F., Bowell, E., et al. 2011, *Celest. Mech. Dyn. Astron.*, 109, 101
 Ball, W. T., Unruh, Y. C., Krivova, N. A., et al. 2012, *A&A*, 541, A27
 Beck, C., & Rezaei, R. 2009, *A&A*, 502, 969
 Borrero, J. M., Tomczyk, S., Kubo, M., et al. 2011, *Sol. Phys.*, 273, 267
 Couvidat, S., Rajaguru, S. P., Wachter, R., et al. 2012, *Sol. Phys.*, 278, 217
 Danilovic, S., Gandorfer, A., Lagg, A., et al. 2008, *A&A*, 484, L17
 Danilovic, S., Schüssler, M., & Solanki, S. K. 2010, *A&A*, 513, A1
 Danilovic, S., Röhrbein, D., Cameron, R., & Schüssler, M. 2013, *A&A*, 550, A118
 de Boer, C. R., Kneer, F., & Nesis, A. 1992, *A&A*, 257, L4
 DeForest, C. E., Martens, P. C. H., & Wills-Davey, M. J. 2009, *ApJ*, 690, 1264
 Domingo, V., Ermolli, I., Fox, P., et al. 2009, *Space Sci. Rev.*, 145, 337
 Foukal, P., Ortiz, A., & Schnerr, R. 2011, *ApJ*, 733, L38
 Frutiger, C., Solanki, S. K., Fligge, M., & Bruls, J. H. M. J. 2000, *A&A*, 358, 1109
 Gonsalves, R. A. 1982, *Opt. Eng.*, 21, 829
 Handy, B. N., Bruner, M. E., Tarbell, T. D., et al. 1998, *Sol. Phys.*, 183, 29
 Hirzberger, J., Feller, A., Riethmüller, T. L., et al. 2010, *ApJ*, 723, L154
 Kosugi, T., Matsuzaki, K., Sakao, T., et al. 2007, *Sol. Phys.*, 243, 3
 Krivova, N. A., & Solanki, S. K. 2004, *A&A*, 417, 1125
 Lites, B. W., Leka, K. D., Skumanich, A., Martínez Pillet, V., & Shimizu, T. 1996, *ApJ*, 460, 1019
 Lites, B. W., Kubo, M., Socas-Navarro, H., et al. 2008, *ApJ*, 672, 1237
 Liu, Y., Hoeksema, J. T., Scherrer, P. H., et al. 2012, *Sol. Phys.*, 279, 295
 Löfdahl, M. G., & Scharmer, G. B. 1994, *A&AS*, 107, 243
 Lucy, L. B. 1974, *AJ*, 79, 745
 Marchand, P., & Marmet, L. 1983, *Rev. Sci. Instrum.*, 54, 1034
 Martínez Pillet, V. 1992, *Sol. Phys.*, 140, 207
 Mathew, S. K., Martínez Pillet, V., Solanki, S. K., & Krivova, N. A. 2007, *A&A*, 465, 291
 Mathew, S. K., Zakharov, V., & Solanki, S. K. 2009, *A&A*, 501, L19
 Neckel, H., & Labs, D. 1994, *Sol. Phys.*, 153, 91
 Norton, A. A., Graham, J. P., Ulrich, R. K., et al. 2006, *Sol. Phys.*, 239, 69
 Ortiz, A., Solanki, S. K., Domingo, V., Fligge, M., & Sanahuja, B. 2002, *A&A*, 388, 1036
 Pasachoff, J. M., Schneider, G., & Widemann, T. 2011, *AJ*, 141, 112
 Pierce, A. K., & Slaughter, C. D. 1977, *Sol. Phys.*, 51, 25
 Richardson, W. H. 1972, *J. Opt. Soc. Am.*, 62, 55
 Sánchez Cuberes, M., Bonet, J. A., Vázquez, M., & Wittmann, A. D. 2000, *ApJ*, 538, 940
 Sánchez Cuberes, M., Vázquez, M., Bonet, J. A., & Sobotka, M. 2003, *A&A*, 397, 1075
 Scherrer, P. H., Bogart, R. S., Bush, R. I., et al. 1995, *Sol. Phys.*, 162, 129
 Schnerr, R. S., & Spruit, H. C. 2011, *A&A*, 532, A136
 Schou, J., Borrero, J. M., Norton, A. A., et al. 2012a, *Sol. Phys.*, 275, 327
 Schou, J., Scherrer, P. H., Bush, R. I., et al. 2012b, *Sol. Phys.*, 275, 229
 Shepp, L. A., & Vardi, Y. 1982, *IEEE Trans. Med. Imag.*, 1, 113
 Snodgrass, H. B. 1983, *ApJ*, 270, 288
 Solanki, S. K. 1987, Ph.D. Thesis, ETH Zürich
 Solanki, S. K., & Unruh, Y. C. 1998, *A&A*, 329, 747
 Sütterlin, P., Wiehr, E., & Stellmacher, G. 1999, *Sol. Phys.*, 189, 57
 Tanga, P., Widemann, T., Sicardy, B., et al. 2012, *Icarus*, 218, 207
 Title, A. M., & Berger, T. E. 1996, *ApJ*, 463, 797
 Vögler, A. 2003, Ph.D. Thesis, University of Göttingen
 Vögler, A., Shelyag, S., Schüssler, M., et al. 2005, *A&A*, 429, 335
 von der Lühne, O. 1993, *A&A*, 268, 374
 Wachter, R., Schou, J., Rabello-Soares, M. C., et al. 2012, *Sol. Phys.*, 275, 261
 Wedemeyer-Böhm, S. 2008, *A&A*, 487, 399
 Wedemeyer-Böhm, S., & Rouppe van der Voort, L. 2009, *A&A*, 503, 225
 Welsch, B. T., Fisher, G. H., & Sun, X. 2013, *ApJ*, 765, 98
 Wenzler, T., Solanki, S. K., Krivova, N. A., & Fröhlich, C. 2006, *A&A*, 460, 583
 Yeo, K. L., Solanki, S. K., & Krivova, N. A. 2013, *A&A*, 550, A95

A.3 Yeo, K. L., Krivova, N. A., Solanki, S. K., Glassmeier, K. H., 2014, Reconstruction of total and spectral solar irradiance from 1974 to 2013 based on KPVT, SoHO/MDI and SDO/HMI observations, *Astron. Astrophys.*, 570, A85

The contents of Chapter 5 are identical to the submitted version of Yeo, K. L., Krivova, N. A., Solanki, S. K., Glassmeier, K. H., 2014, Reconstruction of total and spectral solar irradiance from 1974 to 2013 based on KPVT, SoHO/MDI and SDO/HMI observations, *Astron. Astrophys.*, 570, A85. The printed version is reproduced here with permission from Astronomy & Astrophysics, © ESO.

Reconstruction of total and spectral solar irradiance from 1974 to 2013 based on KPVT, SoHO/MDI, and SDO/HMI observations

K. L. Yeo¹, N. A. Krivova¹, S. K. Solanki^{1,2}, and K. H. Glassmeier³

¹ Max-Planck-Institut für Sonnensystemforschung, Justus-von-Liebig-Weg 3, 37077 Göttingen, Germany
e-mail: yeo@mps.mpg.de

² School of Space Research, Kyung Hee University, Yongin, 446-701 Gyeonggi, Korea

³ Technische Universität Braunschweig, Institut für Geophysik und Extraterrestrische Physik, Mendelssohnstraße 3, 38106 Braunschweig, Germany

Received 12 February 2014 / Accepted 5 August 2014

ABSTRACT

Context. Total and spectral solar irradiance are key parameters in the assessment of solar influence on changes in the Earth's climate. **Aims.** We present a reconstruction of daily solar irradiance obtained using the SATIRE-S model spanning 1974 to 2013 based on full-disc observations from the KPVT, SoHO/MDI, and SDO/HMI.

Methods. SATIRE-S ascribes variation in solar irradiance on timescales greater than a day to photospheric magnetism. The solar spectrum is reconstructed from the apparent surface coverage of bright magnetic features and sunspots in the daily data using the modelled intensity spectra of these magnetic structures. We cross-calibrated the various data sets, harmonizing the model input so as to yield a single consistent time series as the output.

Results. The model replicates 92% ($R^2 = 0.916$) of the variability in the PMOD TSI composite including the secular decline between the 1996 and 2008 solar cycle minima. The model also reproduces most of the variability in observed Lyman- α irradiance and the Mg II index. The ultraviolet solar irradiance measurements from the UARS and SORCE missions are mutually consistent up to about 180 nm before they start to exhibit discrepant rotational and cyclical variability, indicative of unresolved instrumental effects. As a result, the agreement between model and measurement, while relatively good below 180 nm, starts to deteriorate above this wavelength. As with earlier similar investigations, the reconstruction cannot reproduce the overall trends in SORCE/SIM SSI. We argue, from the lack of clear solar cycle modulation in the SIM record and the inconsistency between the total flux recorded by the instrument and TSI, that unaccounted instrumental trends are present.

Conclusions. The daily solar irradiance time series is consistent with observations from multiple sources, demonstrating its validity and utility for climate models. It also provides further evidence that photospheric magnetism is the prime driver of variation in solar irradiance on timescales greater than a day.

Key words. Sun: activity – Sun: faculae, plages – Sun: magnetic fields – solar-terrestrial relations – sunspots

1. Introduction

Solar radiation is the principal source of energy entering the Earth system. As such, the variation in the Sun's radiative output, solar irradiance, is a prime candidate driver of externally driven changes to the Earth's climate. A significant body of publications citing correlations between solar variability and climate parameters exist in the literature and numerous mechanisms have been mooted to explain these observations (see e.g., Gray et al. 2010, for a review). The Earth's climate is believed to be modulated by variations in solar irradiance through effects related to its absorption at the Earth's surface (the so-termed "bottom-up" mechanisms) and in the atmosphere ("top-down"). An established mechanism is the interaction between ultraviolet irradiance and stratospheric ozone (see e.g., Haigh 1994; Solanki et al. 2013). As these mechanisms are wavelength dependent (Haigh 2007), both total and spectral solar irradiance (TSI and SSI) are of interest in assessing the impact of variation in solar irradiance on the Earth's climate.

TSI has been monitored since 1978 through a succession of spaceborne radiometers. The measurements from the various radiometers diverge, mainly in terms of the absolute level and long-term trends, due to instrument-related factors such as

the radiometric calibration, degradation with time and design. Accounting for these influences to combine the various data sets into a single time series is non-trivial and still a topic of debate (see e.g., Scafetta & Willson 2009; Krivova et al. 2009a; Fröhlich 2012). There are at present three composites published in the literature: ACRIM (Willson & Mordvinov 2003), IRMB (Dewitte et al. 2004b; Mekaoui & Dewitte 2008) and PMOD (Fröhlich 2000). The long-term trends in these competing series do not agree. Notably, the successive solar minima in 1986, 1996 and 2008 exhibit conflicting cycle-to-cycle variation in the three composites, encapsulating the difficulty in observing secular changes in TSI unambiguously.

As in the case of TSI, ultraviolet spectral irradiance (120 to 400 nm) has been measured from space on a regular basis since 1978. Again, the combination of the measurements from the succession of instruments into a single time series is an ongoing challenge (DeLand & Cebula 2008, 2012). In this instance, the difficulty in producing a composite is compounded by the wavelength dependence of instrumental influences.

The series of GOME instruments (the first of which was launched in 1996 onboard ERS-2, Weber et al. 1998; Munro et al. 2006) and ENVISAT/SCIAMACHY (launched in 2002; Skupin et al. 2005a) made regular measurements of the solar

spectrum in the 240 to 790 nm and 240 to 2380 nm wavelength range, respectively. As these instruments are designed for atmospheric sounding measurements which do not require absolute radiometry, they lack the capability to track instrument degradation in-flight. Consequently, long-term trends in solar irradiance cannot be recovered from these spectral observations. The spectral measurements from the Sun PhotoMeter (SPM) on the SoHO/VIRGO experiment (spanning 1996 to the present, Fröhlich et al. 1995, 1997) cover just three narrow (FWHM of 5 nm) passbands at 402, 500 and 862 nm. In the visible and the infrared, regular observation of spectral irradiance only started, in effect, with SORCE/SIM (Harder et al. 2005a,b) in 2003. The instrument, which has been surveying the wavelength range of 200 to 2416 nm ever since, provides what is effectively the only continuous and extended SSI record spanning the ultraviolet to the infrared presently available¹.

The available body of solar irradiance measurements is invaluable. However, given the limited period in time covered and uncertainties in the long-term variation, there is a need to augment observations with models. The models that ascribe variations in solar irradiance to the evolution of magnetic concentrations in the photosphere (which influences the temperature structure and therefore radiant behaviour of the solar surface and atmosphere, Spruit & Roberts 1983) have been particularly successful (Domingo et al. 2009). The recent TSI reconstructions by Ball et al. (2012) and Chapman et al. (2013) based on such models replicated 96% and 95% of the observed variation in SORCE/TIM radiometry (Kopp & Lawrence 2005; Kopp et al. 2005a,b), respectively. The model by Ball et al. (2012) also reproduced 92% of the variations in the PMOD TSI composite.

In the case of SSI, gaping disagreements between models and observations persist, exemplified in the current debate on the overall trends in the SORCE/SIM record (Harder et al. 2009; Lean & DeLand 2012; Unruh et al. 2012; Wehrli et al. 2013; Ermolli et al. 2013). SIM registered a decline in ultraviolet flux (200 to 400 nm) between 2004 to 2008 that is a factor of two to six greater than in other measurements and models. This pronounced drop in the ultraviolet, almost twice the decrease in TSI over the same period, is accompanied and so compensated by a comparable increase in visible flux (400 to 700 nm). Coming at a time where solar activity is declining, this increase in visible flux runs counter to models of solar irradiance (apart from Fontenla et al. 2011, discussed below), which point to visible solar irradiance varying in phase with the solar cycle instead.

The reconstruction of TSI and SSI by Fontenla et al. (2011) based on PSPT observations (Coulter & Kuhn 1994; Ermolli et al. 1998) and the model atmospheres of Fontenla et al. (2009) with certain adjustments does qualitatively reproduce the overall trends in early SIM visible observations. However, the reconstruction failed to reproduce the solar cycle variation in TSI. Employing PSPT images and the model atmospheres of Fontenla et al. (2009) without modification, the analogous computation by Ermolli et al. (2013) reproduced observed rotational and cyclical variation in TSI but not the long-term behaviour of SIM SSI.

Apart from the models based on the regression of indices of solar activity to measured solar irradiance, commonly referred to as proxy models (e.g., Lean et al. 1997; Lean 2000; Paganan et al. 2009; Chapman et al. 2013), present-day models of spectral solar irradiance have a similar architecture to one another (reviewed in Ermolli et al. 2013). The proportion of the

solar disc covered by magnetic features (such as faculae and sunspots) is deduced from full-disc observations. This information is converted to solar irradiance utilizing the calculated intensity spectra of said features (derived applying radiative transfer codes to semi-empirical model atmospheres). The Spectral And Total Irradiance REconstruction for the Satellite era (SATIRE-S; Fligge et al. 2000; Krivova et al. 2003, 2011b) is an established model of this type.

The SATIRE-S model has previously been applied to full-disc observations of intensity and magnetic flux from the Kitt Peak Vacuum Telescope (KPVT, Livingston et al. 1976; Jones et al. 1992) and the Michelson Doppler Imager onboard the Solar and Heliospheric Observatory (SoHO/MDI, Scherrer et al. 1995). The solar irradiance reconstructions by Krivova et al. (2003, 2006, 2009b, 2011a); Wenzler et al. (2005, 2006, 2009); Unruh et al. (2008); Ball et al. (2011, 2012, 2014), spanning various periods between 1974 to 2009, achieved considerable success in replicating observed fluctuations in TSI, SSI measurements from the missions preceding SORCE and, at rotational timescales, SORCE SSI.

The reconstruction of solar irradiance with SATIRE-S was curtailed by the deactivation of MDI in 2011. (The KPVT had ceased operation earlier in 2003.) In this study, we present a SATIRE-S reconstruction of total and spectral solar irradiance from 1974 to 2013. We update the preceding efforts with observations from the Helioseismic and Magnetic Imager onboard the Solar Dynamics Observatory (SDO/HMI, Schou et al. 2012).

The apparent surface coverage of the solar disc by magnetic features, the main input to the model, is instrument dependent. Concurrent observations from different instruments can diverge significantly from differences in spatial resolution, calibration, stray light, noise and the like. The combination of the model output based on data from multiple instruments into a single time series constitutes one of the main challenges to such a study. Apart from the extension to the present time with HMI data, this study departs from the earlier efforts with the SATIRE-S model in how this combination is done.

In the following, we describe the SATIRE-S model (Sect. 2) and the data used in the reconstruction (Sect. 3). Thereafter, we detail the reconstruction process (Sect. 4) before a discussion of the result (Sect. 5) and summary statements (Sect. 6).

2. The SATIRE-S model

SATIRE-S is presently the most precise version of the SATIRE model whose main assumption is that variations in solar irradiance on timescales of days and longer arise from photospheric magnetism alone (Foukal & Lean 1986; Fligge et al. 2000; Solanki et al. 2002; Preminger et al. 2002; Krivova et al. 2003). The solar surface is modelled as being composed of sunspot umbrae and penumbrae, faculae and quiet Sun. The different versions of the model differ by the data used to deduce the surface coverage of sunspots and faculae (see Krivova et al. 2007, 2011b; Vieira et al. 2011). SATIRE-S utilises full-disc continuum intensity images and longitudinal magnetograms.

Image pixels with intensities below threshold levels representing the umbral (umbra-to-penumbra) and the penumbral (penumbra-to-granulation) boundaries are classified as umbra and penumbra, respectively. Points with magnetogram signals exceeding a certain threshold and not already classed as umbra or penumbra are denoted as faculae. While the bright magnetic features thus isolated include both network and faculae, we refer to them collectively as faculae for the sake of brevity. The remaining image pixels are taken to correspond to quiet Sun.

¹ Due to signal-to-noise considerations, SIM measurements between 200 and 240 nm are not included in the current release of the record, version 19 (Jerry Harder, priv. comm.).

Table 1. Summary description of the daily full-disc continuum intensity images and longitudinal magnetograms selected for this study.

Instrument	No. of data days	Period [year.month.day]	Proportion of period covered	Image size [pixel]	Pixel scale [arcsec]	Spectral line
KP ₅₁₂	1371	1974.08.23 to 1993.04.04	0.20	2048 × 2048	1	Fe I 8688 Å
KP _{SPM}	2055	1992.11.21 to 2003.09.21	0.52	1788 × 1788	1.14	Fe I 8688 Å
MDI	3941	1999.02.02 to 2010.12.24	0.91	1024 × 1024	1.98	Ni I 6768 Å
HMI	1128	2010.04.30 to 2013.05.31	1.00	4096 × 4096	0.504	Fe I 6173 Å

Standalone facular pixels are reassigned to quiet Sun to minimize the misidentification of magnetogram noise fluctuations as bright magnetic features.

Let $\langle B_1 \rangle$ denote the longitudinal magnetogram signal (the pixel-averaged line-of-sight magnetic flux density) and μ the cosine of the heliocentric angle. Due to magnetic buoyancy, the kilogauss magnetic flux tubes that make up faculae are largely normal to the solar surface (Martínez Pillet et al. 1997). Therefore, the quantity $\langle B_1 \rangle / \mu$ represents a first-order approximation of the pixel-averaged magnetic flux density. This approximation breaks down very close to the limb from the combined action of foreshortening and magnetogram noise. For this reason, image pixels near the limb ($\mu < 0.1$, about 1% of the solar disc by area) are ignored. Following Ball et al. (2011, 2012), we counted facular pixels with $\langle B_1 \rangle / \mu$ above an arbitrary but conservative cutoff level denoted $(\langle B_1 \rangle / \mu)_{\text{cut}}$ as quiet Sun instead. Especially towards the limb, these points correspond mainly to the magnetic canopy of sunspots instead of legitimate faculae (Yeo et al. 2013).

The small-scale magnetic concentrations associated with bright magnetic features are largely unresolved at the spatial resolution of available full-disc magnetograms. This is approximately accounted for by scaling the filling factor of facular pixels, defined here as the effective proportion of the resolution element occupied, linearly with $\langle B_1 \rangle / \mu$ from zero at 0 G to unity at what is denoted $(\langle B_1 \rangle / \mu)_{\text{sat}}$, where after it saturates (see Fligge et al. 2000, for details). The quantity $(\langle B_1 \rangle / \mu)_{\text{sat}}$ is the sole free parameter in the model. It modulates the amplitude of the solar cycle in the reconstruction through its influence on the apparent faculae area. The appropriate value of $(\langle B_1 \rangle / \mu)_{\text{sat}}$ is recovered by comparing the reconstruction to measured TSI.

In this study, we used the same intensity spectra of umbra, penumbra, faculae and quiet Sun (at various values of μ) employed by Wenzler et al. (2006) and Ball et al. (2012) to convert the surface coverage of magnetic features to solar irradiance (the derivation of these intensity spectra is detailed in Unruh et al. 1999). The model output is the summation over the entire solar disc of the intensity spectrum assigned to each image pixel according to its filling factor. The resulting spectrum (covering the wavelength range of 115 to 160 000 nm) and the corresponding integral represent the prevailing SSI and TSI at the sampled point in time.

3. Data selection and preparation

3.1. Daily full-disc continuum intensity images and longitudinal magnetograms

In this study, we employed full-disc continuum intensity images and longitudinal magnetograms collected at the KPVT and from the first-ever spaceborne magnetographs, SoHO/MDI and its successor instrument, SDO/HMI. The NASA/NSO 512-channel diode array magnetograph (Livingston et al. 1976) installed at the KPVT started operation in 1974. In 1992, it was replaced

with the NASA/NSO spectromagnetograph (Jones et al. 1992) which was itself retired in 2003. We denote the two configurations of the KPVT as KP₅₁₂ and KP_{SPM}, respectively. We selected, for each instrument, an intensity image and a magnetogram recorded simultaneously or close in time from each observation day. The number of observation days with suitable data and the period covered are summarized in Table 1. The image size, pixel scale and spectral line surveyed by each instrument are also listed.

3.1.1. HMI

The HMI (in regular operation since 30th April 2010) captures full-disc filtergrams at six wavelength positions across the Fe I 6173 Å line almost continuously at 1.875 s intervals. The filtergram data are combined to form simultaneous continuum intensity images and longitudinal magnetograms at 45-s cadence. We took, from each observation day, the average of the intensity images and of the magnetograms collected over a 315-s period. This is to suppress intensity and magnetogram signal fluctuations from noise and p -mode oscillations. For the period of overlap with the MDI data set (30th April to 24th December 2010), we selected the 315-s intensity images and magnetograms taken closest in time to the MDI magnetograms. Thereafter, we took the first available 315-s intensity image and magnetogram from each day (up to 31st May 2013, essentially the time this work started).

3.1.2. MDI

The MDI returned observations from 19th March 1996 to 11th April 2011. The instrument recorded full-disc filtergrams at four wavelength positions across the Ni I 6768 Å line and one in the nearby continuum, from which a number of continuum intensity images and longitudinal magnetograms are produced each observation day. Unlike HMI, the two data products are recorded at different times. Following Ball et al. (2012), we selected the level 1.5 continuum intensity image and level 1.8.2 5-min longitudinal magnetogram (Liu et al. 2012) recorded closest in time to one another each observation day, excluding the observations from before 2nd February 1999. The authors presented evidence that the response of MDI to magnetic flux might have changed over the extended outages suffered by the SoHO spacecraft between June 1998 and February 1999.

The flat field of MDI continuum intensity images is severe enough to impede the reliable identification of sunspots by the method employed in SATIRE-S and varied over the lifetime of the instrument. Following Krivova et al. (2011a), we corrected the intensity images for flat field by the division with the appropriate median filter, kindly provided by the MDI team. As median filters for the intensity images from after 24th December 2010 are not available, we excluded the daily data from after this date.

March 13, 1993

March 8, 1993

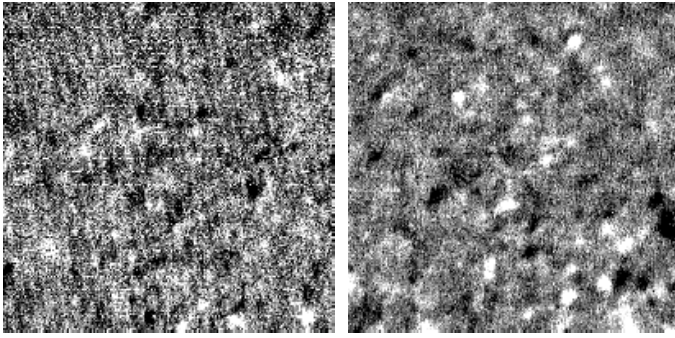


Fig. 1. 200×200 arcsec crop of one of the KP₅₁₂ magnetogram excluded from the study because of instrumental artefacts (*left*) and the similar inset of a relatively unaffected magnetogram from a nearby day. The grey scale is saturated at ±20 G.

3.1.3. KPVT

Co-temporal full-disc continuum intensity images and longitudinal magnetograms based on spectropolarimetry of the FeI8688 Å line were collected at the KPVT on a daily basis with the KP₅₁₂ between 1st February 1974 and 10th April 1993, and with the KP_{SPM} between 19th November 1992 and 21st September 2003. We considered just the 1757 KP₅₁₂ and 2055 KP_{SPM} daily continuum intensity image and longitudinal magnetogram identified by Wenzler et al. 2006 (out of the 4665 and 2894 available) to be sufficiently free of atmospheric seeing and instrumental artefacts.

On visual examination, we found instrumental artefacts in some of the KP₅₁₂ magnetograms similar to what is depicted in Fig. 1 (*left*). The magnetogram signal is spurious along rows and columns of image pixels, producing the line and cross features in the grey scale plot. Large parts of the solar disc are pervaded with this noise pattern in 386 of the 1757 KP₅₁₂ magnetograms, concentrated between 1989 and 1992, where 268 of the 321 magnetograms are so affected. We excluded the daily data from these 386 days.

From a comparison of magnetic field observations from KPVT, Mount Wilson Observatory (MWO) and Wilcox Solar Observatory (WSO), Arge et al. (2002) noted that up to 1990, the total unsigned magnetic flux in KP₅₁₂ data appear lower than in concurrent MWO and WSO observations. In response, Wenzler et al. (2006) and Ball et al. (2012) introduced various empirical corrections to pre-1990 KP₅₁₂ magnetograms. We found such measures to be unnecessary (see Appendix A), leaving the KP₅₁₂ magnetograms as they are for the succeeding analysis.

3.2. TSI measurements

For the purpose of determining the optimal value of $\langle\langle B_1 \rangle\rangle / \mu_{\text{sat}}$, we considered the daily TSI measurements from four radiometers in current operation: ACRIMSAT/ACRIM3 (version 11/13, Willson & Mordvinov 2003), the DIARAD (Crommelynck & Domingo 1984; Dewitte et al. 2004a) and PMO6V (Brusa & Fröhlich 1986) radiometers on SoHO/VIRGO (level 2, version 6_002_1302, Fröhlich et al. 1995, 1997), and SORCE/TIM (level 3, version 14, Kopp & Lawrence 2005; Kopp et al. 2005a,b). There are two calibrations of the TSI measurements from DIARAD, one by IRMB and the other by PMOD/WRC, denoted here as DIARAD_{IRMB} and DIARAD_{PMOD}, respectively. The final reconstruction was also evaluated against the three

published TSI composites: ACRIM (version 11/13), IRMB (the version dated 19th December 2013, kindly provided by Steven Dewitte) and PMOD (version d41_62_1302).

The absolute radiometric calibration of the various radiometers differ. In particular, TIM measurements were about 5 Wm^{-2} lower than the concurrent observations from preceding instruments. Tests conducted at the TSI Radiometer Facility (TRF) with ground copies of ACRIM3, TIM and VIRGO revealed stray light effects in the ACRIM3 and VIRGO instruments (Kopp & Lean 2011). Stray light correction introduced to the ACRIM3 record based on these tests brought it down to within 0.5 Wm^{-2} of TIM TSI (Kopp et al. 2012). The TSI measurements from Picard/PREMOS (launched in 2010; Schmutz et al. 2009, 2013; Fehlmann et al. 2012), the only TSI radiometer calibrated in vacuum at full solar power levels before launch at two separate facilities (the National Physical Laboratory and the TRF), agree with TIM to within a similar margin. The results of these efforts have established the lower TSI level first registered by TIM as likely the more accurate.

Taking the 2008 solar minimum as the reference, we normalized the SATIRE-S reconstruction and all the TSI measurements and composites listed in this section to the mean level in the TIM record over the period of November 2008 to January 2009².

4. Solar irradiance reconstruction

4.1. Harmonizing the model input from multiple instruments

The apparent surface coverage of magnetic features is modulated by the properties of the observing instrument. If left unaccounted for, instrumental differences can introduce inconsistencies between the segments of the reconstruction based on the various data sets. To avoid this we treat the KP₅₁₂, KP_{SPM}, MDI and HMI data sets such that the apparent surface coverage of magnetic features in the various data agrees in the periods of overlap (see Sects. 4.1.1 and 4.1.2).

4.1.1. Umbra and penumbra

The KP_{SPM}, MDI and HMI continuum intensity images were first corrected for limb darkening by the normalization to the fifth-order polynomial in μ fit (following Neckel & Labs 1994).

Granulation and fine sunspot structures are starting to be spatially resolved in HMI observations. To minimize the misclassification of darker non-sunspot and brighter sunspot features, we convolved each HMI intensity image with a 7×7 pixel (3.5×3.5 arcsec) Gaussian kernel.

We adopted the umbral and penumbral intensity thresholds determined for KP_{SPM} by Wenzler et al. (2006) and for MDI by Ball et al. (2012). Wenzler et al. (2006) set the KP_{SPM} penumbral threshold at 0.92, where the resulting sunspot area agrees with the sunspot area record by Balmaceda et al. (2009). Assuming this value for KP_{SPM}, Ball et al. (2012) found the penumbral threshold for MDI that brought the sunspot area in concurrent KP_{SPM} and MDI data into agreement to be 0.89. In both instances, the umbral threshold (0.70 for KP_{SPM} and 0.64 for MDI) was set at the level that produced an umbra to sunspot area ratio of 0.2 (a level consistent with observations, Solanki 2003; Wenzler 2005). Following the approach of Ball et al. (2012), we fixed the penumbral threshold for HMI at 0.87, the level that

² We took the epoch of solar cycle extrema from the table at www.ngdc.noaa.gov/stp/space-weather/solar-data/solar-indices/sunspot-numbers/cycle-data/

equalized the sunspot area in overlapping HMI and MDI data. An umbra to sunspot area ratio of 0.2 was achieved with an umbral threshold of 0.59. The umbral and penumbral thresholds vary between the data sets primarily from the fact that sunspot contrast is wavelength dependent.

Due to the 4-bit digitization, KP₅₁₂ continuum intensity images cannot be treated in a similar manner. For this data set, we employed the umbra and penumbra filling factors determined by Wenzler et al. (2006) from an examination of the distribution of intensities within each image. To ensure consistency with the KP_{SPM} data set, the authors brought the sunspot area to agreement with the Balmaceda et al. 2009 record and assumed an umbra to sunspot area ratio of 0.2.

4.1.2. Faculae

In the previous SATIRE-S reconstruction based on similar KP₅₁₂, KP_{SPM} and MDI data by Ball et al. (2012, 2014), the authors accounted for differences in magnetogram properties by adjusting the magnetogram signal threshold, $\langle\langle B_1 \rangle\rangle/\mu_{\text{cut}}$ and $\langle\langle B_1 \rangle\rangle/\mu_{\text{sat}}$ to each data set (in such a manner that does not introduce additional free parameters). This left weak differences in the reconstructed spectra from the various data sets which were then corrected for empirically by regression.

In this study, we took an alternative approach that allowed us to compute the faculae filling factor applying the same magnetogram signal threshold, $\langle\langle B_1 \rangle\rangle/\mu_{\text{cut}}$ and $\langle\langle B_1 \rangle\rangle/\mu_{\text{sat}}$ to all the data sets. We rescaled the magnetogram signal in the KP₅₁₂, KP_{SPM} and MDI magnetograms to the HMI-equivalent level. The relationship between the magnetogram signal in the various data sets were found comparing the daily data from the different instruments taken close in time to one another employing the histogram equalization method of Jones & Ceja (2001). We examined the KP₅₁₂ and KP_{SPM} observations from 11 days that were recorded within about three hours of one another, KP_{SPM} and MDI observations from 67 days that are less than an hour apart, and MDI and HMI observations from 187 days that are less than five minutes apart.

The histogram equalization method has been widely employed to derive the relationship between the magnetogram signal in simultaneous observations from multiple instruments, including the instruments considered in this study (see Jones & Ceja 2001; Wenzler et al. 2004, 2006; Ball et al. 2012; Liu et al. 2012). The idea is to first sort the magnetogram signal in a given magnetogram in order of strength, bin the points into N bins of equal population and take the bin-average. The N bin-average values are then matched to the similarly derived N bin-average values from the co-temporal magnetogram from a second instrument, essentially matching the distribution of magnetogram signals in the two magnetograms³. We applied the histogram equalization method to the co-temporal data from the various instruments with two major modifications relative to earlier studies.

- We masked the sunspot pixels. Our interest is the magnetogram signal of bright magnetic features. Instrumental factors such as stray light can influence the apparent magnetogram signal of faculae and of sunspots differently (see e.g., Yeo et al. 2014), making it necessary to exclude sunspots here. Another consideration is the saturation of MDI (Liu et al. 2007, 2012) and HMI (Sebastien Couvidat, pers. comm.) magnetograms in sunspot umbrae.

- Earlier studies have largely treated the solar disc as a whole, implicitly assuming that the underlying relationship between the magnetogram signal recorded by the various instruments is uniform across the solar disc. In this study, we divided the solar disc by μ into 68 partially overlapping intervals, each representing about 10% of the solar disc by area and repeated the comparison for each interval.

First, we found the relationship between the magnetogram signal registered by MDI and by HMI, denoted $\langle B_1 \rangle_{\text{MDI}}$ and $\langle B_1 \rangle_{\text{HMI}}$. For each of the 68 μ intervals, we binned the matched $\langle B_1 \rangle_{\text{MDI}}$ and $\langle B_1 \rangle_{\text{HMI}}$ values from all the data days by $\langle B_1 \rangle_{\text{MDI}}$ in intervals of 5 G and derived the median absolute $\langle B_1 \rangle_{\text{MDI}}$ and $\langle B_1 \rangle_{\text{HMI}}$ within each bin, expressed in Fig. 2a. As evident from the figure, the ratio $\langle B_1 \rangle_{\text{HMI}} / \langle B_1 \rangle_{\text{MDI}}$ varies significantly between μ intervals, demonstrating why it was necessary to segment the solar disc. The marked decline towards 0 G comes from the fact that MDI 5-min magnetograms are significantly noisier than HMI 315-s magnetograms (see the noise level estimates by Ball et al. 2012; Liu et al. 2012; Yeo et al. 2013) and so does not reflect the true relationship between $\langle B_1 \rangle_{\text{HMI}}$ and $\langle B_1 \rangle_{\text{MDI}}$ in this regime. We fitted a polynomial in $\langle B_1 \rangle_{\text{MDI}}$ and μ to $\langle B_1 \rangle_{\text{HMI}} / \langle B_1 \rangle_{\text{MDI}}$ (excluding, conservatively, the points where $\langle B_1 \rangle_{\text{MDI}} < 100$ G) and used the result to rescale the absolute magnetogram signal in the entire MDI data set to the HMI-equivalent level.

To bring the magnetogram signal in the KP₅₁₂ and KP_{SPM} data sets to the HMI-equivalent level, we repeated this process on the KP_{SPM} and rescaled MDI data sets to bring the KP_{SPM} magnetogram signal to the rescaled MDI-equivalent, and then on the KP₅₁₂ and rescaled KP_{SPM} data sets to bring the KP₅₁₂ magnetogram signal to the rescaled KP_{SPM}-equivalent. The matched KP_{SPM} and rescaled MDI magnetogram signal, and KP₅₁₂ and rescaled KP_{SPM} magnetogram signal values from the histogram equalization comparison is shown in Figs. 2b and c, respectively.

The noise level of rescaled KP₅₁₂, KP_{SPM} and MDI magnetograms over the solar disc was derived following the analysis of Ortiz et al. (2002) with HMI magnetograms. Essentially, we took sunspot-free, low-activity magnetograms and calculated the standard deviation of the magnetogram signal within a window centred on each point on the solar disc.

To calculate the faculae filling factor in a consistent manner for all the data sets, we had to take into account the fact that the MDI data set has the coarsest pixel scale and, after the rescaling of the magnetogram signal, the highest noise surface of all the data sets (Fig. 3). To this end, we took the following measures.

- The magnetogram signal threshold is set at three times the noise surface of rescaled MDI magnetograms.
- In SATIRE-S, standalone facular pixels are reclassified as quiet Sun to minimize the inclusion of magnetogram noise fluctuations as bright magnetic features at the expense of legitimate faculae that occupy just a single image pixel. To ensure that we are discriminating against similar sized faculae across all the data sets, we excluded the bright magnetic features in the KP₅₁₂, KP_{SPM} and HMI data sets that would appear standalone if we resample the magnetograms to MDI's pixel scale.

We assumed an arbitrary but conservative value of 600 G for $\langle\langle B_1 \rangle\rangle/\mu_{\text{cut}}$. The optimal value of the free parameter $\langle\langle B_1 \rangle\rangle/\mu_{\text{sat}}$ was determined to be 230 G (see Sect. 4.2).

Let n_{fac} represent the proportion of the solar disc covered by faculae. The n_{fac} in the MDI and HMI data sets over the period of overlap is drawn in Fig. 4. The red dashed curve represent the

³ We adjusted the value of N depending on the image size of the data in comparison to ensure reasonable statistics within each bin.

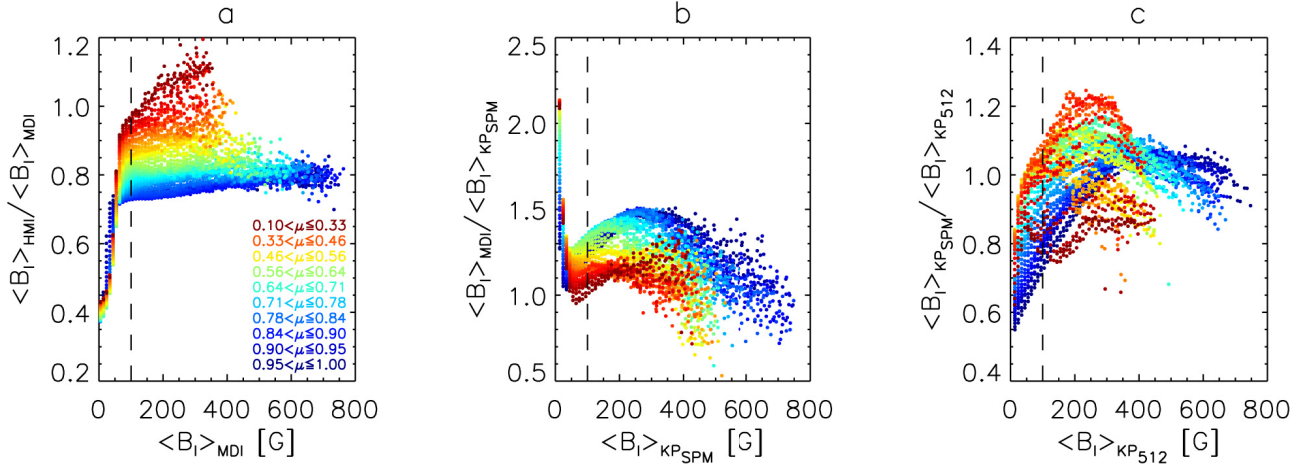


Fig. 2. a) Ratio of the magnetogram signal registered by HMI and by MDI, $\langle B_1 \rangle_{\text{HMI}} / \langle B_1 \rangle_{\text{MDI}}$ as a function of $\langle B_1 \rangle_{\text{MDI}}$ within 68 partially overlapping intervals of μ (the boundary of ten of which are annotated). Also illustrated is the same from the comparison between b) KP_{SPM} and rescaled MDI magnetograms, and c) KP_{512} and rescaled KP_{SPM} magnetograms. The vertical dashed lines at 100 G mark the threshold below which the points are excluded from the surface fitting to these data due to the influence of magnetogram noise (see text).

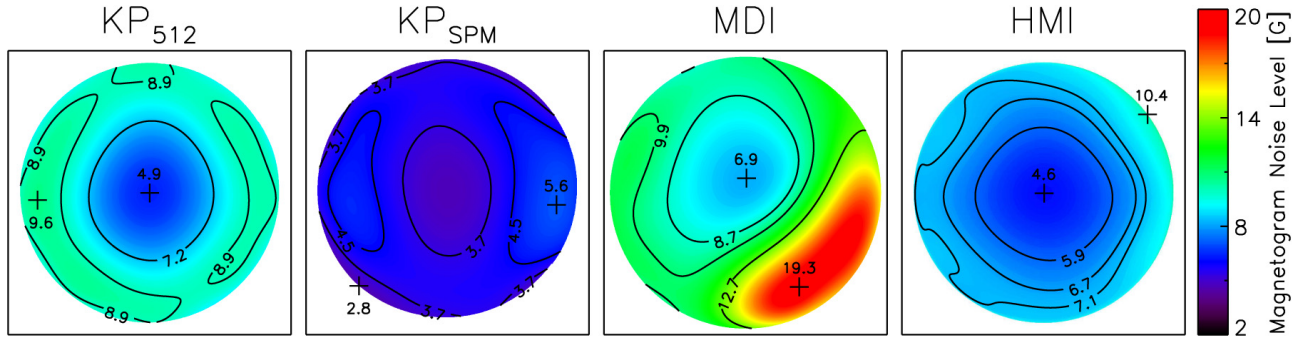


Fig. 3. Noise level of rescaled KP_{512} , KP_{SPM} and MDI 5-min magnetograms, and of HMI 315-s magnetograms (taken from Yeo et al. 2013) as a function of position on the solar disc. The circular area covered by each colour scale plot corresponds to the part of the field-of-view occupied by the solar disc and the surrounding box the boundary of the field-of-view. The contours correspond to the first, second and third quartiles, and the crosses to the minimum and maximum points. The contour and point labels are in units of Gauss. We omit the second quartile in the KP_{512} and KP_{SPM} plots to avoid cluttering. The KP_{512} , KP_{SPM} and HMI noise surfaces were resampled to MDI image size (1024×1024 pixels) to allow a direct comparison.

n_{fac} in the MDI data set if we derive the faculae filling factor as described above without first rescaling the magnetogram signal. As expected, the result departs significantly from the level in the HMI data set (black curve). Rescaling the magnetogram signal in the MDI data set to the HMI-equivalent level accounted for most of this disparity (red dotted curve). The residual discrepancy, though weak, is not negligible. The apparent facular area in the KP_{512} , KP_{SPM} and MDI data sets over where they overlap exhibit a similar response to the analysis, not shown here to avoid repetition.

The residual disparities in n_{fac} are likely due to differences in spatial resolution and the stray light properties of the various instruments. As bright magnetic features remain largely unresolved even at HMI's superior spatial resolution, they are particularly susceptible to spatial smearing effects (see e.g., Yeo et al. 2014). We accounted for this empirically by regression, rescaling the n_{fac} in the MDI data set to bring it to agreement with the HMI data set over the period of overlap (red solid curve, Fig. 4c). Again, we did not treat the solar disc as a whole, dividing it by μ in intervals of 0.01 and treating each interval separately (motivated by the observation that the required correction varied significantly from disc centre to limb). We then applied the same procedure to bring the n_{fac} in the KP_{SPM} data set to agreement

with the corrected MDI data set, and finally the n_{fac} in the KP_{512} data set to agreement with the corrected KP_{SPM} data set.

4.2. The free parameter

The appropriate value of the free parameter $(\langle B_1 \rangle / \mu)_{\text{sat}}$ was determined by optimizing the agreement between reconstructed and measured TSI. For this purpose we considered the ACRIM3, DIARAD_{IRMB}, DIARAD_{PMOD}, PMO6V and TIM records. These records exhibit discrepant overall trends, reflecting the long-term uncertainty present (Fig. 5). This long-term uncertainty is why we considered multiple records, all of which extend for at least a decade, for this part of the analysis. This is to avoid introducing bias to $(\langle B_1 \rangle / \mu)_{\text{sat}}$ by relying on just a single record or on shorter TSI records, such as that from PREMOS.

$(\langle B_1 \rangle / \mu)_{\text{sat}}$ is set at the value that minimizes the root mean square (RMS) difference between observed and reconstructed TSI, denoted k . We found the value of $(\langle B_1 \rangle / \mu)_{\text{sat}}$ that optimizes the agreement with each TSI record (summarized in Table 2), so generating five candidate reconstructions. The scatter in the estimates of $(\langle B_1 \rangle / \mu)_{\text{sat}}$ arises from the discrepant overall trends in the TSI records. The estimates from the comparison with DIARAD_{PMOD} and PMO6V TSI are identical due to the similar

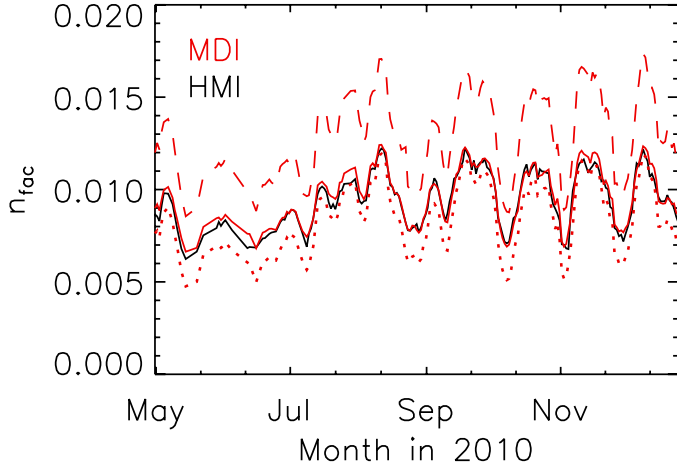


Fig. 4. Proportion of the solar disc covered by faculae, n_{fac} in the MDI (red) and HMI (black) data sets over the period of overlap. The solid red line gives the final result which incorporates the cross-calibration of the magnetogram signal and n_{fac} in the MDI data set (see text). The dotted red line shows the level if we omit the adjustment to n_{fac} and the dashed red line that from the original MDI data.

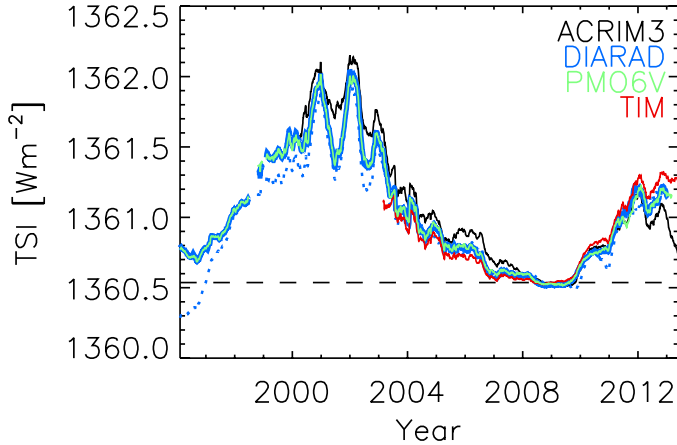


Fig. 5. 181-day moving average of the daily TSI observations from the ACRIM3 (black), DIARAD (blue), PMO6V (green) and TIM (red) radiometers. The dotted and solid blue curves correspond to the calibration of DIARAD measurements by IRMB and by PMOD/WRC, DIARAD_{IRMB} and DIARAD_{PMOD}. The DIARAD_{PMOD} series is almost completely hidden by the PMO6V series due to the close similarity. The dashed line follows the mean level in the TIM record over the period of November 2008 to January 2009. Here and in all the subsequent time series plots in this paper, segments spaced more than 27 days apart are drawn separately, giving the gaps in the plots.

overall trend exhibited by the two records (solid blue and green curves, Fig. 5).

In Fig. 6, we plot the TSI from each candidate reconstruction along with the corresponding reference TSI record (top row) and the difference between the two (middle row), smoothed with a 181-day boxcar filter to elucidate the overall trend. In the DIARAD_{PMOD} and PMO6V cases, the overall trend in modelled and measured TSI agree to within 0.05 Wm^{-2} over nearly the entire period of comparison. The alignment is significantly poorer in the other instances. The coefficient of determination, R^2 between reconstructed and observed TSI within a 361-day window centred on each data day, representing the short-term agreement, is also drawn (bottom row). The short-term agreement between modelled and measured TSI is relatively good; R^2 is

Table 2. To the nearest Gauss, the value of $\langle \langle B_1 \rangle / \mu \rangle_{\text{sat}}$ that optimizes the agreement between reconstructed and measured TSI.

TSI record	$\langle \langle B_1 \rangle / \mu \rangle_{\text{sat}}$ [G]	R^2	k [Wm^{-2}]
ACRIM3	204	0.928	0.155
DIARAD _{IRMB}	255	0.925	0.141
DIARAD _{PMOD}	230	0.940	0.131
PMO6V	230	0.959	0.107
TIM	220	0.921	0.108

Notes. Also tabulated is the coefficient of determination (R^2) and RMS difference (k) between each TSI record and the corresponding candidate reconstruction.

generally above 0.8 except around solar cycle minima where it dips as variation in solar irradiance diminishes, allowing noise a greater influence. In the ACRIM3 and DIARAD_{PMOD} cases, there are also other periods where the short-term agreement deteriorated markedly. The closest short-term agreement is seen with the TIM record.

In terms of the overall agreement, given by the R^2 and k over the entire period of comparison, the closest alignment was found between the PMO6V record and the corresponding candidate reconstruction (Table 2). Considering this and the observation that only with the PMO6V record did reconstructed TSI exhibit consistent close agreement at both rotational and cyclical timescales (Fig. 6), we retained this candidate reconstruction for the succeeding analysis. The R^2 of 0.959 between this candidate reconstruction and the PMO6V record, which spans 1996 to 2013, also suggests that at least 96% of the variability in TSI over this period can be accounted for by photospheric magnetism alone.

4.3. Ultraviolet solar irradiance

The intensity spectra of umbra, penumbra, faculae and quiet Sun currently employed in SATIRE-S were synthesized with the ATLAS9 radiative transfer code (Kurucz 1993), which assumes local thermodynamic equilibrium (LTE). As a consequence, modelled solar irradiance starts to diverge from observations below around 300 nm and progressively so with decreasing wavelength, as previously noted by Krivova et al. (2006, see their Fig. 1). This is due to the breakdown of the LTE approximation in the upper layers of the solar atmosphere.

The limitations of the model in the ultraviolet from assuming LTE in the spectral synthesis were previously accounted for by rescaling the 115 to 270 nm segment of the reconstruction to UARS/SUSIM SSI (Brueckner et al. 1993; Floyd et al. 2003), detailed in Krivova et al. (2006). The authors noted a close agreement between their SATIRE-S reconstruction and SUSIM SSI between 220 and 240 nm, which they termed the reference interval. The authors found, by regression, the relationship between each wavelength channel and the integrated flux within the reference interval in the SUSIM record. They then regenerate the 115 to 270 nm segment of the reconstruction applying these relationships to the integrated flux in the reference interval in the reconstruction. In this study, we corrected the ultraviolet segment of the reconstruction by a modified approach.

- 180 to 300 nm: we offset this segment of the reconstruction (wavelength element by wavelength element) to the Whole Heliospheric Interval (WHI) reference solar spectra (version 2, Woods et al. 2009). The aim was to bring the absolute level here to a more realistic level while retaining the variability returned by the model. This less obtrusive approach

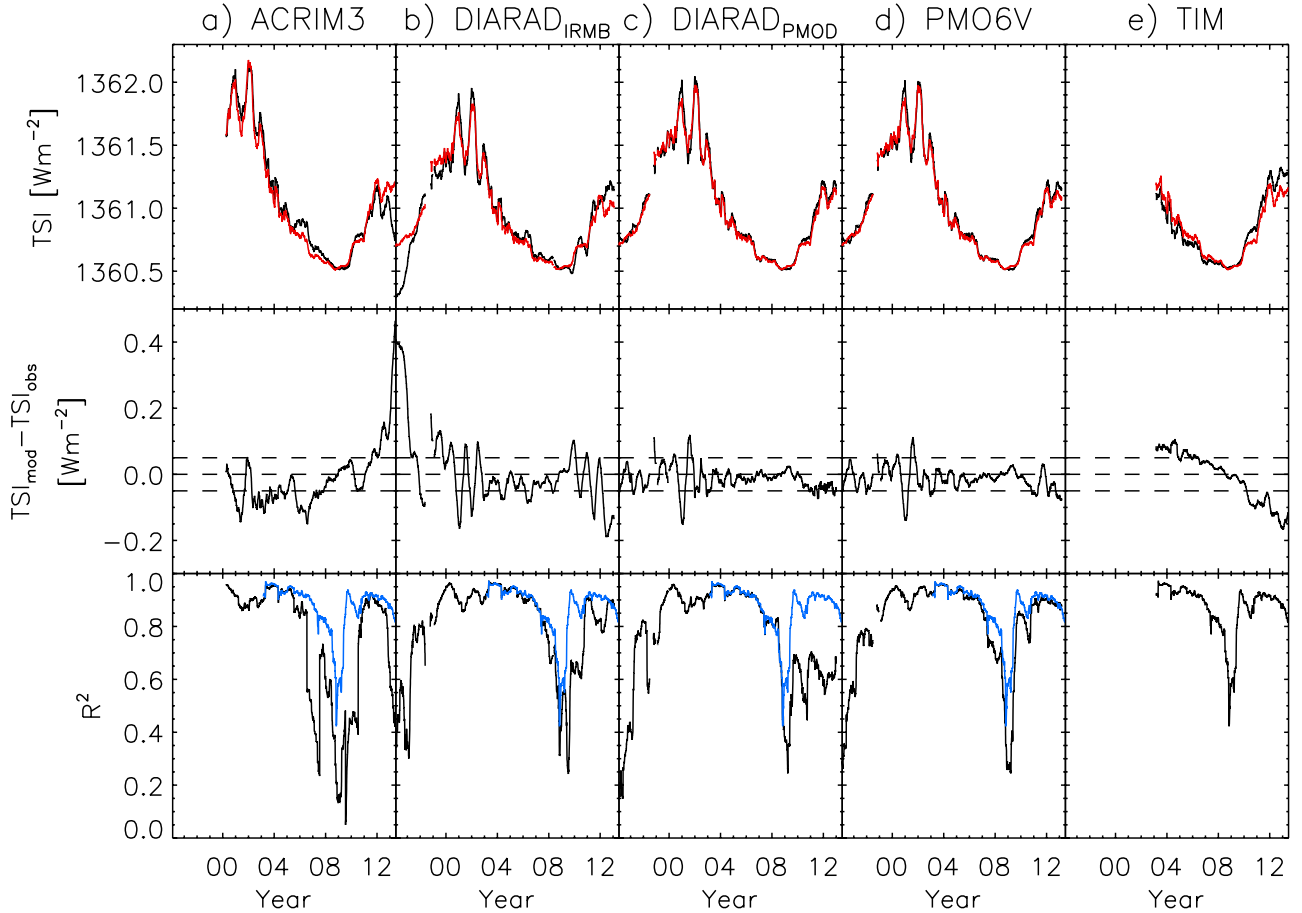


Fig. 6. *Top:* 181-day moving average of the five TSI records examined (black) and the corresponding candidate TSI reconstruction (red). *Middle:* the difference between the two, $TSI_{\text{mod}} - TSI_{\text{obs}}$. The dashed lines mark the zero level and $TSI_{\text{mod}} - TSI_{\text{obs}} = \pm 0.05 \text{ Wm}^{-2}$. *Bottom:* the R^2 between measured and modelled TSI within a 361-day window centred on each data day. The TIM series is plotted over the other series in blue for comparison.

was prompted by our observation that the reconstruction reproduces the variability in observed SSI in this wavelength range well (see Sect. 5.3). We are prohibited from extending this correction below 180 nm due to the gross disparity in the absolute level between modelled and measured solar irradiance there (see Fig. 1 in Krivova et al. 2006).

- 115 to 180 nm: we rescaled this segment of the reconstruction by an analysis similar to that of Krivova et al. (2006) except we based the correction on the observations from the FUV (115 to 180 nm) instrument on SOLARIS/SOLSTICE (level 3, version 12, McClintock et al. 2005; Snow et al. 2005a) instead of SUSIM SSI. We made this switch in the interest of consistency with the offset introduced to the 180 to 300 nm segment (this part of the WHI reference solar spectra is provided by SOLSTICE spectrometry).

The SOLSTICE FUV record extends from 14th May 2003 to 15th July 2013. We excluded the measurements from after 2008 on the observation that the agreement between model and measurement deteriorated slightly but palpably after this time. We took the wavelength range of 164 to 174 nm, where the reconstruction and SOLSTICE FUV agree best, as the reference interval. Let $SSI_{\text{obs,ref}}$ and $SSI_{\text{mod,ref}}$ denote the integrated flux within the reference interval in observed and reconstructed SSI, respectively. The linear regression of $SSI_{\text{obs,ref}}$ to $SSI_{\text{mod,ref}}$ is plotted along the scatter plot of the two in Fig. 7. Though the overall level of $SSI_{\text{obs,ref}}$ and $SSI_{\text{mod,ref}}$ differ by about a factor of three,

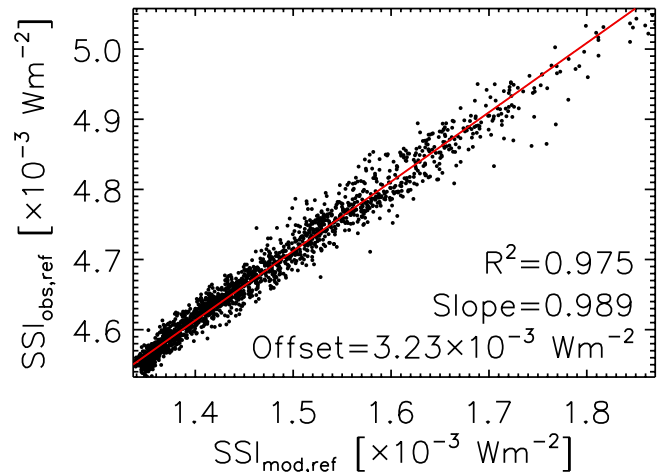


Fig. 7. Scatter plot of the integrated flux over the reference interval (164 to 174 nm) in the SOLSTICE FUV record, $SSI_{\text{obs,ref}}$ and in the reconstruction, $SSI_{\text{mod,ref}}$ (prior to the correction of the 115 to 300 nm segment, see text). The red line is the straight line fit to the scatter plot. The R^2 between the two series, and the slope and offset of the fit are indicated.

the absolute variability is remarkably similar, as indicated by the R^2 (0.975) and the slope of the fit (0.989). $SSI_{\text{obs,ref}}$ and $SSI_{\text{mod,ref}}$ differ largely only by an offset of $3.23 \times 10^{-3} \text{ Wm}^{-2}$, the vertical

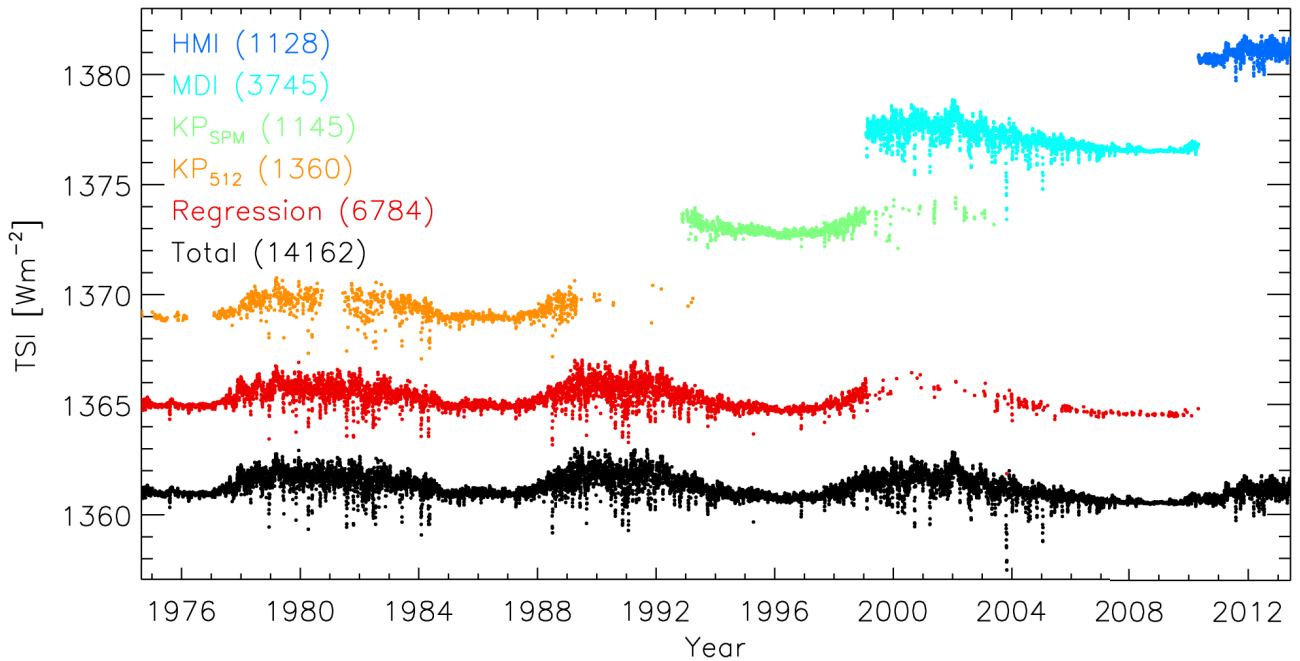


Fig. 8. Total solar irradiance from the reconstruction (black). The other time series indicate the contribution by the SATIRE-S reconstruction based on the various data sets and by the regression series (see text), progressively offset to aid visibility. The values in parentheses indicate the number of daily values.

intercept of the straight line fit. We regressed each SOLSTICE FUV wavelength channel to $SSI_{\text{obs,ref}}$ and applied the relationships derived to $(SSI_{\text{mod,ref}} + 3.23 \times 10^{-3} \text{ Wm}^{-2})$ to regenerate the 115 to 180 nm segment of the reconstruction.

4.4. Data gaps

We collated the reconstructed solar irradiance from the KP_{512} , KP_{SPM} , MDI and HMI data sets into a single time series taking, for the days where the model output from more than one data set is available, the value from the succeeding instrument (Fig. 8). The time series extends from 23rd August 1974 to 31st May 2013. Due to the limited availability of suitable magnetograms, it covers just 7378 of the 14 162 days within this period (Table 1). To yield an uninterrupted time series, we regressed indices of solar activity to the reconstruction and used the result to fill the gaps in the latter, loosely following the analysis of Ball et al. (2014).

We employed the following solar activity index records: the Ottawa and Penticton adjusted 10.7 cm radio flux (Tapping 1987, 2013), the LASP Lyman- α composite (Woods et al. 2000), the IUP Mg II index composite (version 4, Viereck & Puga 1999; Skupin et al. 2005b,c) and the projected sunspot area composite by Balmaceda et al. 2009 (version 0613). For each wavelength element in the reconstruction, we reproduced the daily solar irradiance over the entire period of the reconstruction using the index or linear combination of two indices that replicates the reconstruction best on regression. Hereafter, we refer to the result as the regression series. Minor discrepancies in the overall trend in the regression series and the reconstruction (from long-term uncertainties) were accounted for by offsetting the former to the latter.

The R^2 between the reconstruction and the regression series varies between 0.78 and 0.98 with wavelength. The R^2 between the TSI from the two series is 0.883. Within expectation, the regression series cannot reproduce all the variability in the

SATIRE-S reconstruction. The agreement is however sufficient for the intended purpose of the regression series (to fill in the gaps in the reconstruction).

4.5. Error analysis

Due to the complexity of the reconstruction procedure and limitations imposed by the full-disc observations employed, a rigorous determination of the reconstruction uncertainty is not feasible. For instance, possible variation in instrument properties with time and the amount of magnetic activity hidden by magnetogram noise and the finite spatial resolutions are neither known nor directly determinable from the various data sets. However, a reasonable estimate can be obtained by considering the uncertainty introduced by the steps taken to harmonize the model input from the various data sets and by the uncertainty in the free parameter $(\langle B_1 \rangle / \mu)_{\text{sat}}$, loosely following Ball et al. (2012, 2014).

We estimated the uncertainty for each wavelength element and the TSI from the reconstruction as follows. The uncertainty associated with the cross-calibration of the KP_{512} , KP_{SPM} , MDI and HMI data sets is given by the RMS difference between the reconstruction based on the various data sets over the periods where they overlap. For the days with no SATIRE-S reconstruction, plugged with values from the regression series, we took the RMS difference between the SATIRE-S reconstruction and the regression series over the days where the former is available as the uncertainty. Due to the long-term uncertainty of the TSI records considered to recover $(\langle B_1 \rangle / \mu)_{\text{sat}}$, we arrived at estimates ranging from 204 to 255 G (Table 2) before adopting 230 G, the value recovered with the PMO6V record as the reference, as the final value. Taking the scatter in these estimates into account, we assumed an uncertainty of ± 30 G for $(\langle B_1 \rangle / \mu)_{\text{sat}}$. The upper (lower) bound of the uncertainty range of the reconstruction is then given by the reconstruction generated with $(\langle B_1 \rangle / \mu)_{\text{sat}}$ set at 200 G (260 G) plus (minus) the cross-calibration error.

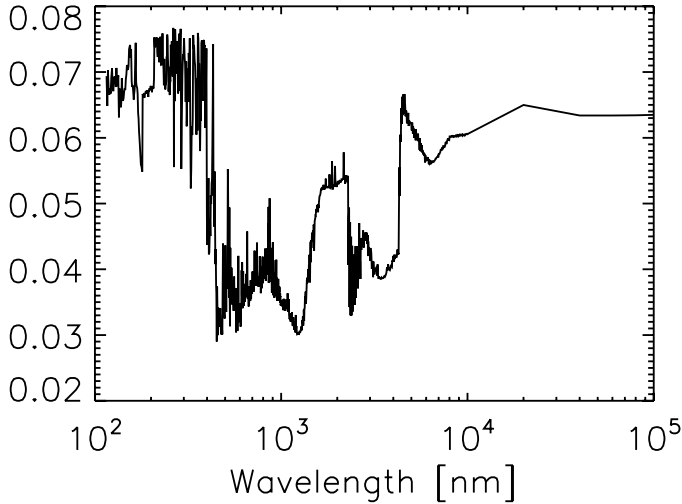


Fig. 9. Quotient of the average reconstruction uncertainty and the difference between the maximum and minimum reconstructed solar irradiance as a function of wavelength.

Table 3. The R^2 and the rms difference, k between reconstructed TSI, and the ACRIM, IRMB, and PMOD composites.

Series	R^2	k [Wm^{-2}]
ACRIM	0.747	0.301
IRMB	0.805	0.251
PMOD	0.916	0.149

Notes. Here and in the rest of the paper, these quantities are calculated excluding the part of the reconstruction provided by the regression series.

The cross-calibration error depends on the data used to reconstruct the solar spectrum for a given day and the uncertainty associated with $\langle\langle B_1 \rangle\rangle / \mu_{\text{sat}}$ on the amount of prevailing magnetism. As such, the reconstruction uncertainty varies day-to-day. The quotient of the average (over all days and between the lower and upper bounds) uncertainty and the difference between the maximum and minimum reconstructed solar irradiance, an indication of the scale of the uncertainty in relation to the range of variability, varies between about 0.03 and 0.08 with wavelength (Fig. 9). The value for the TSI from the reconstruction is about 0.04.

5. Comparison with observations

5.1. TSI composites

As with the preceding SATIRE-S reconstructions by Wenzler et al. (2006); Krivova et al. (2011a); Ball et al. (2012), of the three published composite records of TSI, the reconstruction is most consistent with the PMOD composite. The R^2 between the reconstruction and the PMOD composite (0.916) is higher and the RMS difference (0.149 Wm^{-2}) lower than with either the ACRIM or the IRMB composite by a significant margin (Table 3).

The overall trend in the PMOD composite, including the secular decline between the solar cycle minima of 1996 and 2008, is well-replicated in the reconstruction (bottom panel of Fig. 10 and Table 4) although the reconstruction is broadly higher by about 0.1 to 0.3 Wm^{-2} between 1984 and 1994 (Fig. 11). As a result, the reconstruction registers a stronger secular decline

Table 4. The difference between the TSI level at the solar cycle minima of 1976, 1986, and 1996, and the level at the 2008 minimum.

Series	1976 [Wm^{-2}]	1986 [Wm^{-2}]	1996 [Wm^{-2}]
ACRIM		-0.205	0.341
IRMB		-0.084	-0.048
PMOD		0.273	0.188
SATIRE-S	0.423	0.399	0.236

Notes. We considered the mean level over the 3 month period centred on each minimum.

between the 1986 and 1996 solar cycle minima than the PMOD composite (0.163 Wm^{-2} versus 0.085 Wm^{-2} , Table 4). To put this disparity in context, it is well within the reconstruction uncertainty and minute compared to the discrepancy between the three composites or between the TSI records depicted in Fig. 5.

The offset between the reconstruction and the PMOD composite between 1984 and 1994 is unlikely to be related to the cross-calibration of the KP_{512} and KP_{SPM} data sets. Going back in time, the reconstruction and the PMOD composite started to diverge in 1994 while the period of overlap between the KP_{512} and KP_{SPM} data sets is November 1992 to April 1993. This discrepancy could possibly be from unaccounted instrumental variation in the KPVT data sets or in the PMOD composite, especially as the period of 1984 to 1994 encompasses the ACRIM gap (Fröhlich 2006; Scafetta & Willson 2009; Krivova et al. 2009a). The higher level in reconstruction over this period suggests that a stronger correction for the ACRIM gap than already incorporated into the PMOD composite (Fröhlich 2006) might be necessary, in opposition to the claims of Scafetta & Willson (2009).

Although the PMOD composite is based on VIRGO TSI (a combination of the $\text{DIARAD}_{\text{PMOD}}$ and PMO6V records) for 1996 onwards, the fact that we had relied on the PMO6V record to fix $\langle\langle B_1 \rangle\rangle / \mu_{\text{sat}}$ is not the reason the reconstruction is more aligned towards this composite than the other two. The discrepancy in the overall trend in the five TSI records considered to retrieve $\langle\langle B_1 \rangle\rangle / \mu_{\text{sat}}$ is small compared to that between the three composites (see Figs. 5 and 10) such that fixing $\langle\langle B_1 \rangle\rangle / \mu_{\text{sat}}$ using any of the other TSI records still leads to reconstructed TSI agreeing best with the PMOD composite.

The fact that we are able to replicate the secular decline between the 1996 and 2008 solar cycle minima in the PMOD composite using a model based on photospheric magnetism alone runs counter to the claims of Fröhlich (2009, 2012, 2013) that mechanisms other than photospheric magnetism must be at play and suggested a cooling/dimming of the photosphere as an alternative.

5.2. Lyman- α irradiance and Mg II index composites

Next, we compare the reconstruction to the LASP Lyman- α composite and the Mg II index composites by IUP and by LASP (Viareck et al. 2004; Snow et al. 2005b).

In the spectral range of 115 to 290 nm, the wavelength scale of the reconstruction is 1 nm, given by the ATLAS9 code. We took the reconstructed solar irradiance in the 121 to 122 nm wavelength element, $\text{SSI}_{\text{mod},121-122\text{nm}}$ as the Lyman- α irradiance. The Mg II index of the reconstruction is given by

$$\frac{2 \times \text{SSI}_{\text{mod},279-281\text{nm}}}{\text{SSI}_{\text{mod},276-277\text{nm}} + \text{SSI}_{\text{mod},283-284\text{nm}}}, \quad (1)$$

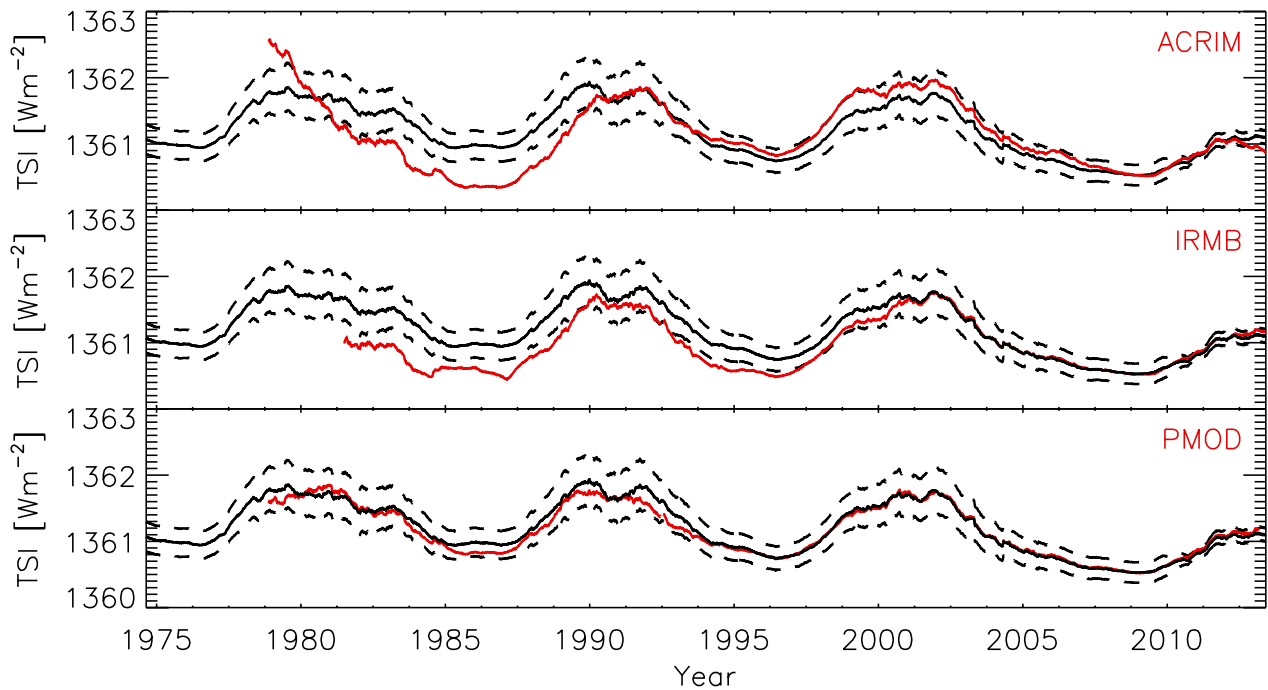


Fig. 10. 361-day moving average of the TSI from the reconstruction (black), and the ACRIM, IRMB and PMOD composite records (red). The dashed lines denote the uncertainty range of the reconstruction.

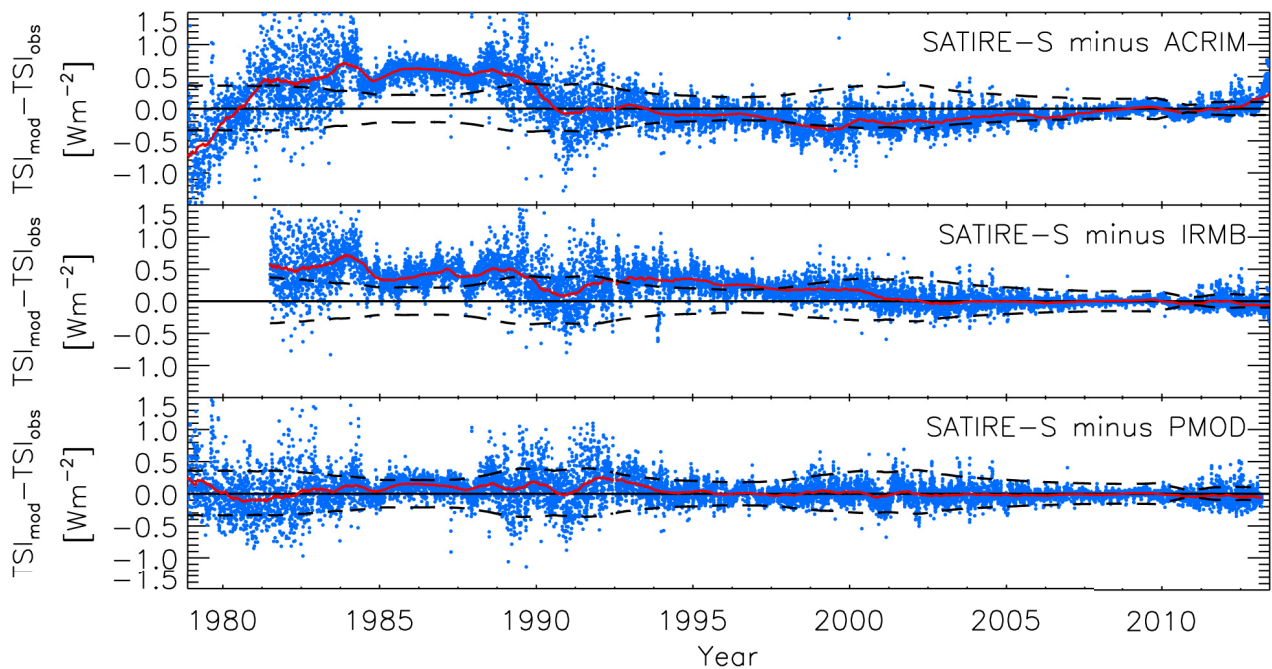


Fig. 11. Difference between reconstructed TSI, and the ACRIM, IRMB, and PMOD composite (blue dots). The red curves follow the corresponding 361-day moving average. The dashed and solid black lines represent the reconstruction uncertainty and the zero level, respectively.

crudely following the definition of the Mg II index by [Heath & Schlesinger \(1986\)](#). The Lyman- α irradiance and Mg II index so derived from the reconstruction are clearly not exactly equivalent to that in the various composites, which are computed from higher spectral resolution line profiles. However, as we are only interested in comparing the relative variability, these approximations are still appropriate. The correlation between model and measurement is excellent. The R^2 between the reconstruction and the LASP Lyman- α composite is 0.942. The R^2 with the Mg II index composites by IUP and by LASP is 0.963 and 0.899, respectively.

To compare the overall trend, we rescaled the various composites such that the rotational variability is matched to that in the reconstruction.

The overall trend in the LASP Lyman- α composite is reproduced in the reconstruction to well within the limits of uncertainty at most places (Fig. 12a). A notable exception is the higher levels in the reconstruction at the solar cycle minima of 1976, 1986 and 1996. Even with this discrepancy, the minimum-to-minimum trend in the LASP Lyman- α composite is qualitatively replicated. The observation here that the reconstruction replicates the overall trend in two independent records (the PMOD

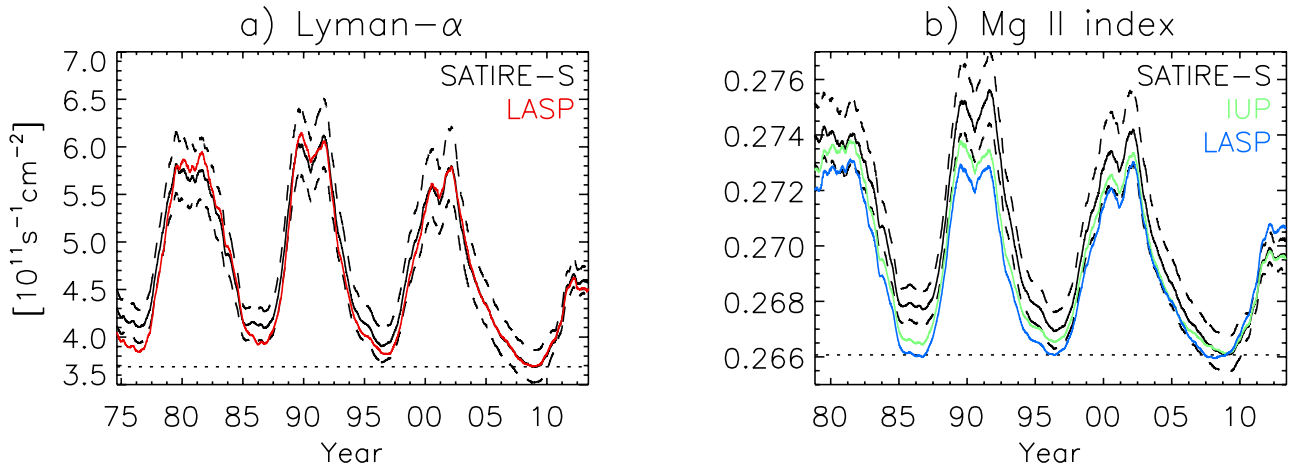


Fig. 12. 361-day moving average of the a) Lyman- α irradiance and the b) Mg II index. The various composites by IUP and by LASP were matched in terms of the rotational variability and the level at the 2008 solar cycle minimum (dotted lines) to the SATIRE-S reconstruction to allow a direct comparison of the overall trends. The dashed lines indicate the lower and upper uncertainty of the Lyman- α irradiance and Mg II index taken from the reconstruction.

TSI composite and the LASP Lyman- α composite) confers confidence on the long-term stability of the reconstruction.

The IUP Mg II index composite exhibits a secular decline between the solar cycle minima of 1996 and 2008 that is replicated in the reconstruction to within uncertainty, albeit weaker (Fig. 12b). In contrast, the LASP Mg II index composite is effectively level between the two minima. This discrepancy between the two composites suggests that the long-term uncertainty might be severe enough to obscure underlying secular variations, contributing to the failure of proxy models based on the Mg II index to replicate the secular decline in VIRGO radiometry. Foukal et al. (2011) proposed that the discrepant decadal trends in TSI and in chromospheric indices might be due to the non-linear relationship between the two (see Solanki & Krivova 2004).

5.3. UARS and *SORCE* SSI

We contrasted the reconstruction against the daily spectral measurements from the SOLSTICE⁴ (covering 119 to 420 nm, Rottman et al. 2001) and the SUSIM (version 22, 115 to 410 nm, Brueckner et al. 1993; Floyd et al. 2003) experiments onboard the UARS mission, and SOLSTICE (level 3, version 12, 114 to 310 nm, McClintock et al. 2005; Snow et al. 2005a) and SIM (level 3, version 19, 240 to 2416 nm, Harder et al. 2005a,b) onboard *SORCE*. Apart from discarding the daily spectra with missing measurements, we employed these records as they are. In the following, we discuss how the reconstruction compares to these records in the ultraviolet, where the wavelength range of the various instruments overlap (Sect. 5.3.1) and to the entire SIM record, the only to extend from the ultraviolet to the infrared (Sect. 5.3.2).

5.3.1. Ultraviolet solar irradiance

The R^2 between the reconstruction and UARS and *SORCE* SSI in the ultraviolet as a function of wavelength is given in Fig. 13. The R^2 with the observations from SUSIM and the two SOLSTICE experiments is relatively high (largely above 0.8) at lower wavelengths but starts to decrease after about 250 and

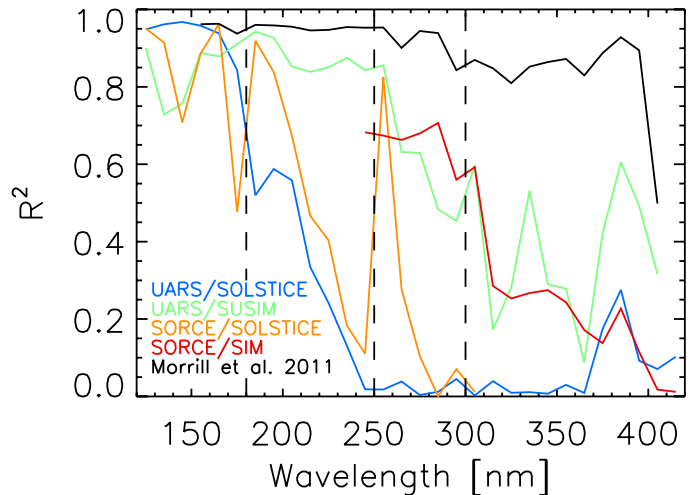


Fig. 13. R^2 between the reconstruction and UARS and *SORCE* observations in the ultraviolet as a function of wavelength in intervals of 10 nm. The dashed lines at 180, 250 and 300 nm mark approximately where there is a marked decline in the R^2 with one or more of the records (highlighted in the text).

180 nm, respectively. For SIM, the R^2 is around 0.7 up to about 300 nm before it also starts to drop. To elucidate the cause of the deteriorating agreement between the reconstruction and the various records towards longer wavelengths, we examined the integrated flux over 120 to 180 nm, 180 to 250 nm, 250 to 300 nm and 300 to 410 nm. The boundaries of these intervals correspond to where R^2 begins to decline in the various comparisons.

The overall trend in the reconstruction and in the various records is illustrated in Fig. 14. In the lowest wavelength interval (120 to 180 nm), the overall trend in the records from SUSIM and the two SOLSTICE experiments agree over the periods of overlap and are also well-replicated in the reconstruction. Both model and measurement exhibit clear solar cycle modulation. In the higher intervals (180 to 410 nm, Figs. 14b to d), the various records no longer agree over the periods of overlap or exhibit any consistent relation to the solar cycle. For example, in the 300 to 410 nm interval, SIM SSI appears to vary in phase with the solar cycle between 2005 and the 2008 solar cycle minimum, but

⁴ The version archived on lasp.colorado.edu/lisird/

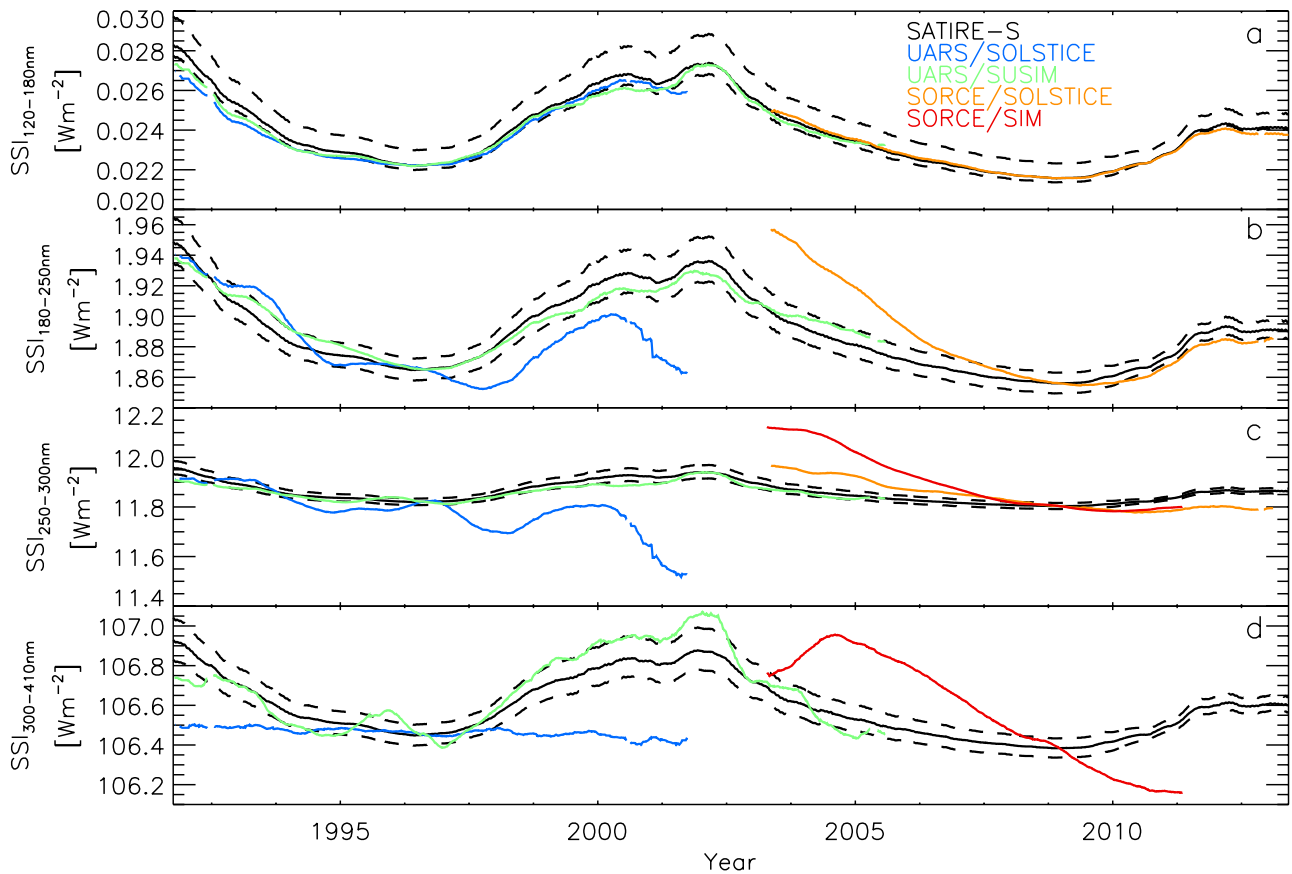


Fig. 14. 361-day moving average of the integrated flux in the reconstruction and in UARS and SORCE SSI between **a)** 120 and 180 nm, **b)** 180 and 250 nm, **c)** 250 and 300 nm, and **d)** 300 and 410 nm. The UARS and SORCE time series are normalized to the reconstruction at the 1996 and 2008 solar cycle minima, respectively. The dashed lines indicate the uncertainty range of the reconstruction.

in anti-phase before and after this period. The only exception is the SUSIM record, where the overall trend, largely reproduced in the reconstruction, remained broadly in phase with the solar cycle over the entire duration of the record. The discrepant overall trends and lack of obvious solar cycle modulation in the UARS/SOLSTICE and SORCE records after 180 nm is indicative of significant unaccounted instrumental trends above this wavelength (long-term stability issues in these records towards longer wavelengths had similarly been noted by DeLand et al. 2004; Ball et al. 2011; DeLand & Cebula 2012; Lean & DeLand 2012; Ermolli et al. 2013).

We found that the short-term uncertainty of UARS and SORCE SSI is also greater towards longer wavelengths. The rotational variability in the various records is similar and well-reproduced in the reconstruction up to around 250 nm (top row, Fig. 15) before discrepancies between the different observations start to appear (middle and bottom rows).

As an additional check, we contrasted the reconstruction against the empirical model of ultraviolet solar irradiance by Morrill et al. (2011), kindly provided by Jeff Morrill. This model, which spans 150 to 410 nm, is based on the regression of the Mg II index to SUSIM SSI. It represents an approximation of SUSIM-like spectroscopy with the stability corrected to that of the Mg II index. The R^2 between the reconstruction and the Morrill et al. (2011) model is high (>0.8) almost everywhere, even above 250 nm, where the R^2 between the reconstruction and SUSIM SSI drops (Fig. 13).

The close alignment between the reconstruction and the SUSIM-based model of Morrill et al. (2011) suggests that the

deteriorating R^2 between the reconstruction and measurements at longer wavelengths is dominantly due to the increased measurement uncertainty there (Figs. 14 and 15).

Ultraviolet solar irradiance below 242 nm and from 242 to 310 nm is responsible for the production and destruction of ozone in the stratosphere, respectively. The amplitude of the variation over the solar cycle above 240 nm is poorly constrained in available measurements and models, which differ from one another by as much as a factor of six (see Ermolli et al. 2013, and Fig. 14). Due to this spread, their application to climate models has led to qualitatively different results for the variation in mesospheric ozone (Haigh et al. 2010; Merkel et al. 2011; Ball et al. 2014). In Fig. 16, we plot the decrease in SSI over the declining phase of solar cycle 23 in the reconstruction (black) and in the Morrill et al. (2011) model (red). The solar cycle amplitude in the reconstruction is a close match to that in the Morrill et al. (2011) model, even after 240 nm, lending credence to the cyclical variability reproduced in both models.

5.3.2. SORCE/SIM SSI

Finally, we examine how the reconstruction compares to the entire SIM record. The R^2 between the reconstruction and SIM SSI remains very poor above 420 nm (0.2 at most wavelengths).

The overall trend in SIM SSI varies with wavelength. Most notably, it alternates between showing a broad increase over the duration of the record and the opposite at around 400, 700 and 1000 nm. This is illustrated in Fig. 17 where we plot the integrated flux in the reconstruction and in the SIM record over 240

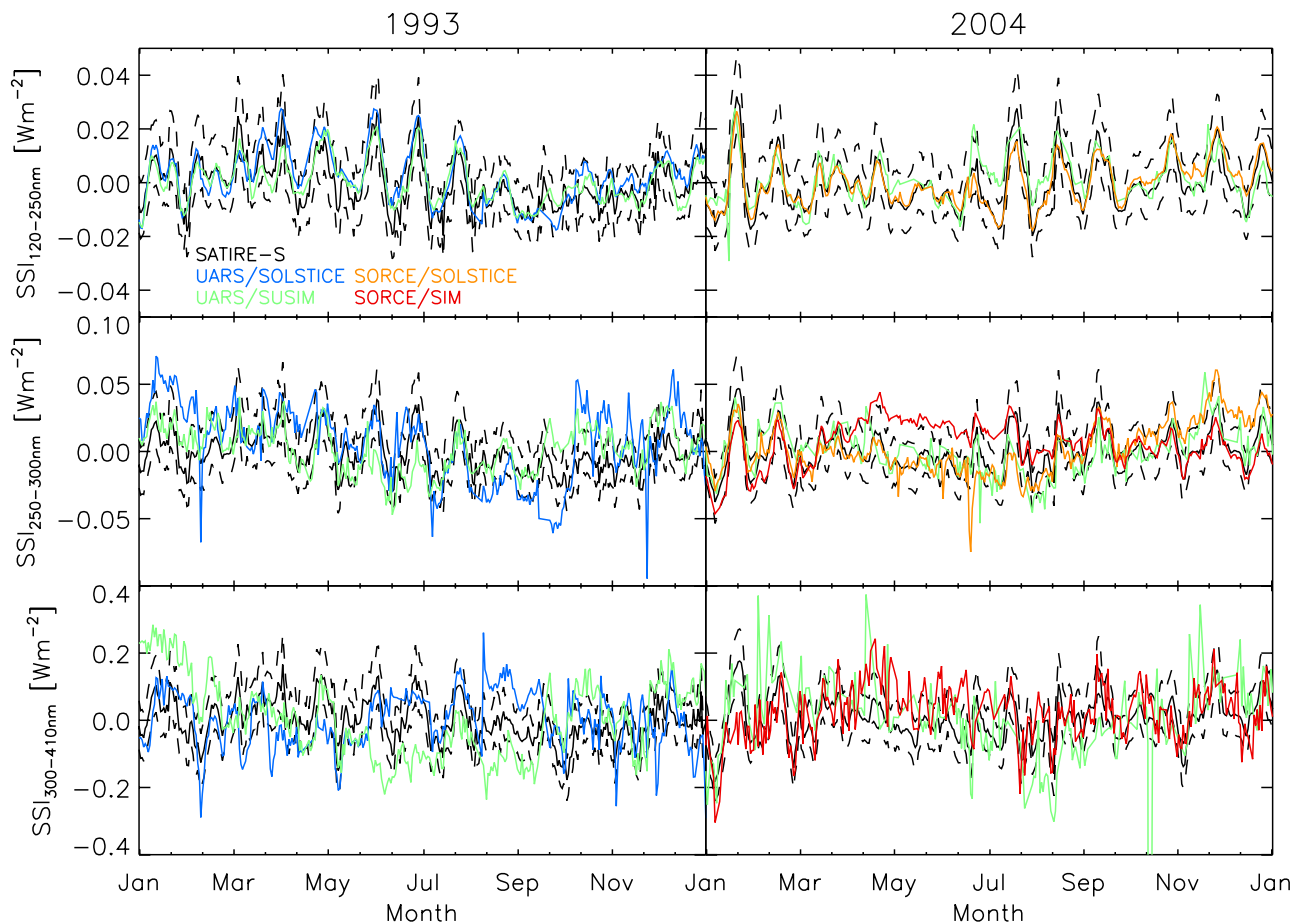


Fig. 15. Rotational variability in the reconstruction and in the spectral measurements from UARS and SORCE over the same spectral intervals as in Fig. 14 (except we combined the 120 to 180 nm and 180 to 250 nm intervals, where the relative agreement between the various time series is similar) during 1993 and 2004. The rotational variability was isolated by taking the integrated flux over each spectral interval and subtracting the corresponding 361-moving average. The dashed lines represent the reconstruction uncertainty.

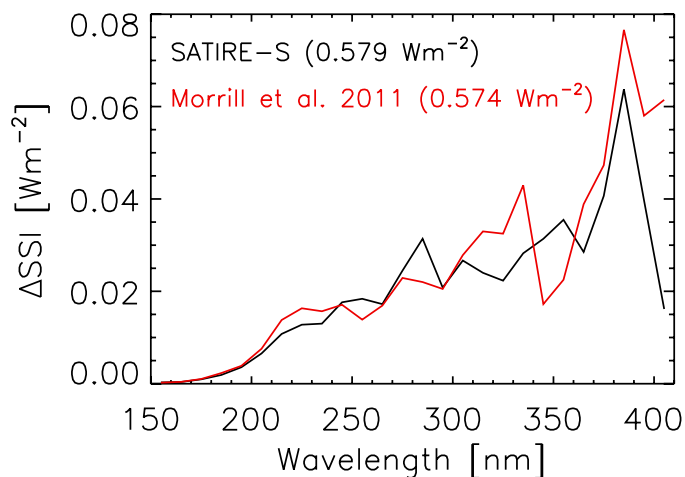


Fig. 16. Decline in SSI between the solar cycle maximum in 2000 and the minimum in 2008 in the reconstruction (black) and in the Morrill et al. (2011; red) model as a function of wavelength in intervals of 10 nm. We considered the mean spectrum over the 3 month period centred on the stated activity maximum/minimum. The integral between 240 and 410 nm is given in parentheses.

to 400 nm, 400 to 700 nm, 700 to 1000 nm and 1000 to 2416 nm. We included SIM ultraviolet solar irradiance, discussed in the

last section, for completeness and ease of comparison. As visibly evident in the figure, SIM SSI does not exhibit any consistent relation to the solar cycle in any of the wavelength intervals, in conflict with the solar cycle modulation evident in the reconstruction, certain records of ultraviolet solar irradiance (see e.g., DeLand & Cebula 2008, and Fig. 15) and VIRGO SPM photometry (Wehrli et al. 2013).

We also compared the total flux recorded by SIM with the integrated flux in the reconstruction over a similar wavelength range and PMO6V TSI (Fig. 18). With the bulk of the energy in solar radiation confined within the wavelength range surveyed by SIM (>97%), the integrated flux over this range should already replicate most of the variability in TSI (as similarly argued by Ball et al. 2011; Lean & DeLand 2012). The total flux registered by SIM, as with the integrated flux over the various wavelength intervals discussed above, lacks obvious solar cycle modulation. The R^2 with the reconstruction and the PMO6V record is very weak (0.170 and 0.183, respectively). In comparison, the integrated flux in the reconstruction over the wavelength range of SIM still replicates over 94% of the variability in PMO6V TSI ($R^2 = 0.942$).

The absence of any consistent relation to the solar cycle in the SIM record and the failure of the total flux to replicate TSI variability indicate significant unaccounted instrumental trends. It is responsible, at least in part, for the poor R^2 with the reconstruction. We are held back by the fact that there are no other

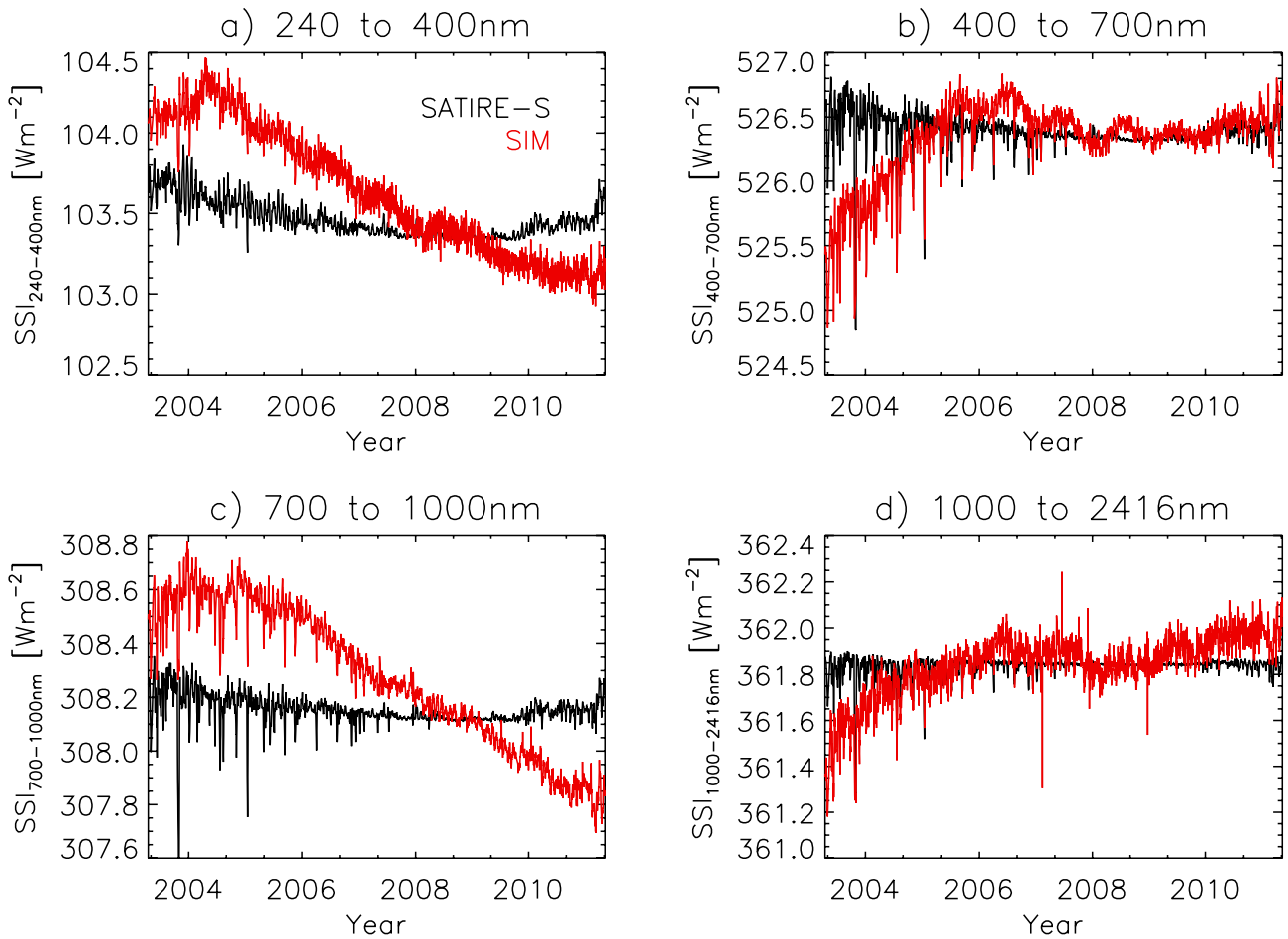


Fig. 17. Integrated flux over the wavelength intervals given at the top of each panel in the reconstruction (black) and in SIM SSI (red). The SIM time series were normalized to the reconstruction time series at the 2008 solar cycle minimum.

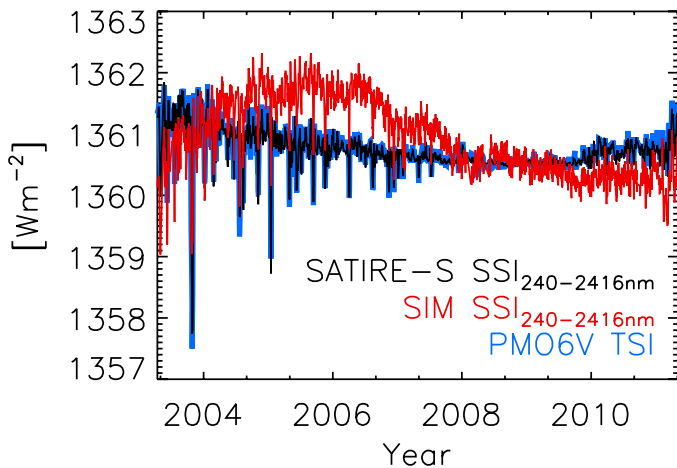


Fig. 18. Total flux recorded by SIM (red), integrated flux in the reconstruction over a similar wavelength range (black) and PMO6V TSI (blue). The SIM and SATIRE-S time series were normalized to the PMO6V series at the 2008 solar cycle minimum. The PMO6V series is largely hidden by the SATIRE-S series due to the close similarity.

continuous and extended SSI records covering a similar spectral range from a more conclusive evaluation of reconstructed visible and infrared SSI as done for the ultraviolet in Sect. 5.3.1. This highlights the need for a more accurate calibration of SIM SSI and for other measurements in the visible and infrared.

6. Summary

In this paper, we present a SATIRE-S model reconstruction of daily total and spectral solar irradiance spanning the period of 1974 to 2013. The reconstruction is based on full-disc observations of continuum intensity and line-of-sight magnetic field from the KPVT, MDI, and HMI. Gaps in the time series from the limited availability of suitable magnetograms were plugged by the regression of indices of solar activity to the reconstruction. This work extends the preceding reconstruction based on similar observations from the KPVT and MDI covering the period of 1974 to 2009 by Ball et al. (2012, 2014). Apart from the extension to 2013 with HMI data, we updated the reconstruction method.

The most significant enhancement to the reconstruction method is the procedure by which the model input from the various data sets are combined into a single solar irradiance time series. The earlier approach had been to tailor the parameters of the model to each data set. This left weak residual discrepancies between the reconstructed spectra generated from the various data sets that were then accounted for by regression. In this study, we compared the magnetogram signal and the apparent faculae area in the various data sets and brought them into agreement in the periods of overlap between them by regression. This allowed us to apply the same model parameters (apart from the umbral and penumbral intensity thresholds, which are wavelength dependent) to all the data sets. This updated procedure yielded a

consistent solar irradiance time series without the need for any additional correction of the reconstructed spectra.

The model has a single free parameter which modulates the contribution by bright magnetic features to reconstructed solar irradiance variability. The optimal value was recovered by comparing the reconstruction to TSI measurements. We considered the observations from four TSI radiometers in current operation: ACRIM3, DIARAD and PMO6V on VIRGO, and TIM. Each TSI record led to a somewhat different value for the free parameter and hence reconstructed solar irradiance. Based on the particularly close consistency between the PMO6V record and the TSI reconstruction generated using it as the reference to retrieve the free parameter, we adopted this candidate reconstruction for further study. The R^2 of 0.959 between the reconstruction and the PMO6V record, which extends 1996 to 2013, suggests that at least 96% of the variability in TSI over this period can be explained by photospheric magnetism alone.

We evaluated the reconstruction against the ACRIM, IRMB and PMOD composite records of TSI, the LASP Lyman- α composite, the Mg II index composites by IUP and by LASP, and SSI measurements from the UARS and SORCE missions.

As with previous SATIRE-S reconstructions, we found the closest match with the PMOD composite ($R^2 = 0.916$ over the span of the record, 1978 to 2013). The long-term trend in the PMOD composite is well-reproduced in the reconstruction almost everywhere except between 1984 and 1994, where the reconstruction is broadly higher by between 0.1 and 0.3 Wm^{-2} . This discrepancy is however, minute compared to the spread between the three composites, or between ACRIM, TIM and VIRGO radiometry. We attribute it to possible unresolved instrumental trends in the KPVT data sets or in the PMOD composite, especially as the period in question encompasses the ACRIM gap. In opposition to the claims of Scafetta & Willson (2009), the higher levels in the reconstruction over this period suggest that a stronger correction for the ACRIM gap than already incorporated into the PMOD composite (Fröhlich 2006) might be necessary. The reconstruction replicates the secular decline between the 1996 and 2008 solar cycle minima in the PMOD composite. This counters the suggestion by Fröhlich (2009) that a dimming of the solar photosphere, rather than photospheric magnetism, might be responsible for the secular decline registered by VIRGO.

The Lyman- α irradiance and Mg II index from the reconstruction exhibit excellent agreement with the LASP Lyman- α composite ($R^2 = 0.942$) and the IUP Mg II index composite ($R^2 = 0.963$). The overall trend in the LASP Lyman- α composite is also replicated largely to within uncertainty. The fact that the overall trend in both the PMOD TSI composite and the LASP Lyman- α composite is well-reproduced in the reconstruction is strong evidence of the long-term stability of the reconstruction. The IUP Mg II index composite exhibits a secular decline between the 1996 and 2008 solar cycle minima that is largely replicated in the reconstruction while the LASP Mg II index composite is effectively level from one minimum to the next. This implies that the long-term uncertainty in the Mg II index can possibly obscure underlying secular variation, contributing to the observation that proxy models of solar irradiance based on the Mg II index cannot replicate the secular decline between the 1996 and 2008 solar cycle minima in VIRGO radiometry.

We contrasted the reconstruction against the ultraviolet solar irradiance measurements from the SOLSTICE and SUSIM experiments onboard UARS, and SOLSTICE and SIM onboard SORCE. The agreement between reconstructed and measured solar irradiance is relatively good up to about 180 to 250 nm

(depending on the record) before it starts to deteriorate, which coincides with a marked increase in measurement uncertainty. The variability reproduced in the reconstruction is supported by the excellent agreement with the SUSIM-based empirical model by Morrill et al. (2011). Importantly, the amplitude of the variation over the solar cycle is similar, even above 240 nm. Ultraviolet solar irradiance is crucial for climate modelling but the solar cycle variation above 240 nm is poorly constrained in measurements and preceding models.

As with other similar studies, the reconstruction failed to reproduce the overall trend in the SIM record. We argue from the lack of constancy in how SIM SSI relate to the solar cycle and the disparity between the total flux recorded by the instrument and TSI that significant unaccounted instrumental trends are present. In comparison, the reconstruction exhibits clear solar cycle modulation and the integrated flux over the wavelength range of SIM still replicates at least 94% of the variability in PMO6V TSI radiometry ($R^2 = 0.942$). The present quandary between SIM SSI, and other measurements and models of solar irradiance emphasizes the need for continual calibration efforts and alternative measurements.

The results of this work strengthen support for the hypothesis that variation in solar irradiance on timescales greater than a day is driven by photospheric magnetic activity. The reconstruction is consistent with observations from multiple sources, confirming its reliability and utility for climate modeling⁵.

Acknowledgements. The authors would like to thank William Ball and Yvonne Unruh for useful discussions over the course of this study and Greg Kopp for helpful comments on the manuscript. This work is primarily based on observations recorded at the KPVT, and from SoHO/MDI and SDO/HMI. We are grateful to Thomas Wenzler, Jeneen Sommers (Stanford Solar Center) and Ray Burston (German Data Center for SDO) for their hand in preparing the KPVT, MDI and HMI data sets, respectively. Appreciation goes to the ACRIM science team, Steven Dewitte (IRMB) and Claus Fröhlich (PMOD/WRC) for their corresponding TSI composites. We thank Jeff Morrill and Judith Lean for providing their respective models. We employed data from ACRIMSAT/ACRIM3, SoHO/VIRGO, and the UARS and SORCE missions in the analysis. We also made use of the IUP Mg II index composite, the Lyman- α composite and Mg II index composite by LASP, the Ottawa/Penticton 10.7 cm solar flux record released by NOAA and the WHI solar irradiance reference spectra. K.L.Y. is a postgraduate fellow of the International Max Planck Research School for Solar System Science. This work has been partly supported by the German Federal Ministry of Education and Research under project 01LG1209A.

Appendix A: Is a correction of pre-1990 KPVT magnetograms necessary?

Arge et al. (2002) compared the Carrington rotation synoptic charts of full-disc magnetograms from KPVT, Mount Wilson Observatory (MWO) and Wilcox Solar Observatory (WSO). The data sets spanned the period of 1974 to 2002. The authors noted that the total amount of unsigned magnetic flux in the KPVT charts, up to around 1990, appear slightly lower than in the MWO and WSO charts (Fig. 1 in their paper). This was attributed to the bias in the zero level of KP₅₁₂ magnetograms, which was stated to vary with time and with position in the solar disc (from disc centre to limb and from east to west). The authors brought the magnetic flux levels in a subset of the KPVT synoptic charts from before 1990 to agreement with the MWO and WSO data by modifying the procedure by which

⁵ The SATIRE-S daily total and spectral solar irradiance time series is available for download at <http://www.mps.mpg.de/projects/sun-climate/data.html>

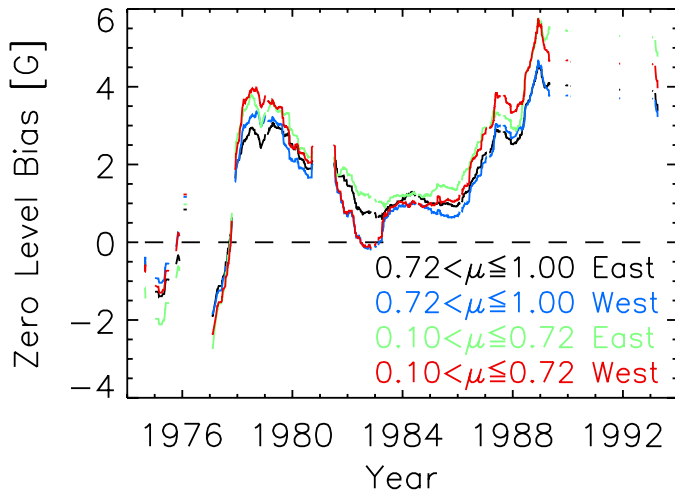


Fig. A.1. Zero level bias of KP₅₁₂ magnetograms around disc centre ($0.72 < \mu \leq 1.00$) and limb ($0.1 < \mu \leq 0.72$), and east and west of the central meridian. The dashed line indicates the null level.

KP₅₁₂ magnetograms are combined to form the synoptic charts. Wenzler et al. (2006) and Ball et al. (2012) attempted, by various approximations, to replicate the effect of this correction in KP₅₁₂ magnetograms from before 1990. Wenzler et al. (2006) multiplied the magnetogram signal by a factor of 1.242 while Ball et al. (2012) added 5.9 G to the absolute value.

We examined the zero level bias of the KP₅₁₂ magnetograms selected for the present study. Here, we term the result of calculating the mean of a sample recursively excluding points more than three standard deviations from the mean from succeeding iterations till convergence as the trimmed mean. We divided the solar disc along the central meridian and the $\mu = 0.72$ locus, yielding four segments approximately equal in area. Taking each magnetogram, we computed the trimmed mean of the signed magnetogram signal within each segment. The 361-day moving average of the time series of the trimmed mean within each segment (Fig. A.1) was taken as the zero level bias. The purpose of taking the moving average is to minimise error from the influence of magnetic activity on the trimmed mean in individual magnetograms. Consistent with the claims of Arge et al. (2002), the zero level bias is non-zero and varied with time and between the four segments. However, we found that subtracting the zero level bias from the magnetogram signal made negligible difference to the reconstruction, having little appreciable effect on the apparent surface coverage and magnetic field strength of bright magnetic features. This is likely due to the fact that the zero level bias, though non-zero, is much weaker than magnetogram noise fluctuations (the noise level of KP₅₁₂ magnetograms is around 8 G, Wenzler et al. 2006).

Arge et al. (2002) interpreted the observation that the amount of magnetic flux in the KPVT synoptic charts is slightly lower than in the MWO and WSO charts up to around 1990 and broadly similar after to indicate a problem with pre-1990 KP₅₁₂ data. Most of the KP₅₁₂ magnetograms recorded between 1989 to 1992 are pervaded by instrumental artefacts similar to what is depicted in Fig. 1 (left). The additional magnetogram signal introduced by these artefacts, which manifest as rows and columns of image pixels with spurious signals, might be responsible for the fact that the flux level in the KPVT charts from this period is no longer weaker than in the MWO and WSO charts. (The KPVT charts from after this period are based on KP_{SPM} magnetograms.) Considering this and our observations that the zero

level bias is actually rather weak, we surmise that the disparity between the KPVT charts and the MWO and WSO charts prior to 1990 might be from systematic effects not accounted for in the analysis of Arge et al. (2002) and does not constitute any conclusive indication that a correction of pre-1990 KP₅₁₂ magnetograms is necessary. This is the reason why we did not adopt either of the corrections to pre-1990 KP₅₁₂ magnetograms proposed by Wenzler et al. (2006) and Ball et al. (2012) or subtract the zero level bias determined here from the magnetogram signal, leaving the KP₅₁₂ magnetograms as they are for the solar irradiance reconstruction.

References

- Arge, C. N., Hildner, E., Pizzo, V. J., & Harvey, J. W. 2002, *J. Geophys. Res.*, 107, 1319
- Ball, W. T., Unruh, Y. C., Krivova, N. A., Solanki, S. K., & Harder, J. W. 2011, *A&A*, 530, A71
- Ball, W. T., Unruh, Y. C., Krivova, N. A., et al. 2012, *A&A*, 541, A27
- Ball, W. T., Krivova, N. A., Unruh, Y. C., Haigh, J. D., & Solanki, S. K. 2014, *J. Atmos. Sci.*, submitted [[arXiv:1408.0365](https://arxiv.org/abs/1408.0365)]
- Balmaceda, L. A., Solanki, S. K., Krivova, N. A., & Foster, S. 2009, *J. Geophys. Res.*, 114, 7104
- Brueckner, G. E., Edlow, K. L., Floyd, IV, L. E., Lean, J. L., & Vanhoosier, M. E. 1993, *J. Geophys. Res.*, 98, 10695
- Brusa, R. W., & Fröhlich, C. 1986, *Appl. Opt.*, 25, 4173
- Chapman, G. A., Cookson, A. M., & Preminger, D. G. 2013, *Sol. Phys.*, 283, 295
- Coulter, R. L., & Kuhn, J. R. 1994, in *Solar Active Region Evolution: Comparing Models with Observations*, eds. K. S. Balasubramaniam, & G. W. Simon, ASP, 68, 37
- Crommelynck, D., & Domingo, V. 1984, *Science*, 225, 180
- DeLand, M. T., & Cebula, R. P. 2008, *J. Geophys. Res.*, 113, 11103
- DeLand, M. T., & Cebula, R. P. 2012, *J. Atmos. Sol.-Terr. Phys.*, 77, 225
- DeLand, M. T., Floyd, L. E., Rottman, G. J., & Pap, J. M. 2004, *Adv. Space Res.*, 34, 243
- Dewitte, S., Crommelynck, D., & Joukoff, A. 2004a, *J. Geophys. Res.*, 109, 2102
- Dewitte, S., Crommelynck, D., Mekaoui, S., & Joukoff, A. 2004b, *Sol. Phys.*, 224, 209
- Domingo, V., Ermolli, I., Fox, P., et al. 2009, *Space Sci. Rev.*, 145, 337
- Ermolli, I., Fofi, M., Bernacchia, C., et al. 1998, *Sol. Phys.*, 177, 1
- Ermolli, I., Matthes, K., Dudok de Wit, T., et al. 2013, *Atmos. Chem. Phys.*, 13, 3945
- Fehlmann, A., Kopp, G., Schmutz, W., et al. 2012, *Metrologia*, 49, 34
- Fligge, M., Solanki, S. K., & Unruh, Y. C. 2000, *A&A*, 353, 380
- Floyd, L. E., Cook, J. W., Herring, L. C., & Crane, P. C. 2003, *Adv. Space Res.*, 31, 2111
- Fontenla, J. M., Curdt, W., Haberleiter, M., Harder, J., & Tian, H. 2009, *ApJ*, 707, 482
- Fontenla, J. M., Harder, J., Livingston, W., Snow, M., & Woods, T. 2011, *J. Geophys. Res.*, 116, 20108
- Foukal, P., & Lean, J. 1986, *ApJ*, 302, 826
- Foukal, P., Ortiz, A., & Schnerr, R. 2011, *ApJ*, 733, L38
- Fröhlich, C. 2000, *Space Sci. Rev.*, 94, 15
- Fröhlich, C. 2006, *Space Sci. Rev.*, 125, 53
- Fröhlich, C. 2009, *A&A*, 501, L27
- Fröhlich, C. 2012, *Surv. Geophys.*, 33, 453
- Fröhlich, C. 2013, *Space Sci. Rev.*, 176, 237
- Fröhlich, C., Romero, J., Roth, H., et al. 1995, *Sol. Phys.*, 162, 101
- Fröhlich, C., Crommelynck, D. A., Wehrli, C., et al. 1997, *Sol. Phys.*, 175, 267
- Gray, L. J., Beer, J., Geller, M., et al. 2010, *Rev. Geophys.*, 48, 4001
- Haigh, J. D. 1994, *Nature*, 370, 544
- Haigh, J. D. 2007, *Liv. Rev. Sol. Phys.*, 4, 2
- Haigh, J. D., Winning, A. R., Toumi, R., & Harder, J. W. 2010, *Nature*, 467, 696
- Harder, J., Lawrence, G., Fontenla, J., Rottman, G., & Woods, T. 2005a, *Sol. Phys.*, 230, 141
- Harder, J. W., Fontenla, J., Lawrence, G., Woods, T., & Rottman, G. 2005b, *Sol. Phys.*, 230, 169
- Harder, J. W., Fontenla, J. M., Pilewskie, P., Richard, E. C., & Woods, T. N. 2009, *Geophys. Res. Lett.*, 36, 7801
- Heath, D. F., & Schlesinger, B. M. 1986, *J. Geophys. Res.*, 91, 8672
- Jones, H. P., & Ceja, J. A. 2001, in *Advanced Solar Polarimetry – Theory, Observation, and Instrumentation*, ed. M. Sigwarth, ASP, 236, 87
- Jones, H. P., Duvall, Jr., T. L., Harvey, J. W., et al. 1992, *Sol. Phys.*, 139, 211
- Kopp, G., & Lawrence, G. 2005, *Sol. Phys.*, 230, 91

- Kopp, G., & Lean, J. L. 2011, *Geophys. Res. Lett.*, 38, 1706
- Kopp, G., Heurman, K., & Lawrence, G. 2005a, *Sol. Phys.*, 230, 111
- Kopp, G., Lawrence, G., & Rottman, G. 2005b, *Sol. Phys.*, 230, 129
- Kopp, G., Fehlmann, A., Finsterle, W., et al. 2012, *Metrologia*, 49, 29
- Krivova, N. A., Solanki, S. K., Fligge, M., & Unruh, Y. C. 2003, *A&A*, 399, L1
- Krivova, N. A., Solanki, S. K., & Floyd, L. 2006, *A&A*, 452, 631
- Krivova, N. A., Balmaceda, L., & Solanki, S. K. 2007, *A&A*, 467, 335
- Krivova, N. A., Solanki, S. K., & Wenzler, T. 2009a, *Geophys. Res. Lett.*, 36, 20101
- Krivova, N. A., Solanki, S. K., Wenzler, T., & Podlipnik, B. 2009b, *J. Geophys. Res.*, 114, 0
- Krivova, N. A., Solanki, S. K., & Schmutz, W. 2011a, *A&A*, 529, A81
- Krivova, N. A., Solanki, S. K., & Unruh, Y. C. 2011b, *J. Atmos. Solar-Terr. Phys.*, 73, 223
- Kurucz, R. 1993, *ATLAS9 Stellar Atmosphere Programs and 2 km s⁻¹ grid*. Kurucz CD-ROM No. 13 (Cambridge, Mass.: Smithsonian Astrophysical Observatory)
- Lean, J. 2000, *Geophys. Res. Lett.*, 27, 2425
- Lean, J. L., & DeLand, M. T. 2012, *J. Climate*, 25, 2555
- Lean, J. L., Rottman, G. J., Kyle, H. L., et al. 1997, *J. Geophys. Res.*, 102, 29939
- Liu, Y., Norton, A. A., & Scherrer, P. H. 2007, *Sol. Phys.*, 241, 185
- Liu, Y., Hoeksema, J. T., Scherrer, P. H., et al. 2012, *Sol. Phys.*, 279, 295
- Livingston, W. C., Harvey, J., Pierce, A. K., et al. 1976, *Appl. Opt.*, 15, 33
- Martínez Pillet, V., Lites, B. W., & Skumanich, A. 1997, *ApJ*, 474, 810
- McClintock, W. E., Rottman, G. J., & Woods, T. N. 2005, *Sol. Phys.*, 230, 225
- Mekaoui, S., & Dewitte, S. 2008, *Sol. Phys.*, 247, 203
- Merkel, A. W., Harder, J. W., Marsh, D. R., et al. 2011, *Geophys. Res. Lett.*, 38, 13802
- Morrill, J. S., Floyd, L., & McMullin, D. 2011, *Sol. Phys.*, 269, 253
- Munro, R., Anderson, C., Callies, J., et al. 2006, in *Atmospheric Science Conf.*, ESA SP, 628
- Neckel, H., & Labs, D. 1994, *Sol. Phys.*, 153, 91
- Ortiz, A., Solanki, S. K., Domingo, V., Fligge, M., & Sanahuja, B. 2002, *A&A*, 388, 1036
- Pagaran, J., Weber, M., & Burrows, J. 2009, *ApJ*, 700, 1884
- Preminger, D. G., Walton, S. R., & Chapman, G. A. 2002, *J. Geophys. Res.*, 107, 1354
- Rottman, G., Woods, T., Snow, M., & DeToma, G. 2001, *Adv. Space Res.*, 27, 1927
- Scafetta, N., & Willson, R. C. 2009, *Geophys. Res. Lett.*, 36, 5701
- Scherrer, P. H., Bogart, R. S., Bush, R. I., et al. 1995, *Sol. Phys.*, 162, 129
- Schmutz, W., Fehlmann, A., Hülsen, G., et al. 2009, *Metrologia*, 46, S202
- Schmutz, W., Fehlmann, A., Finsterle, W., Kopp, G., & Thuillier, G. 2013, *AIP Conf. Proc.*, 1531, 624
- Schou, J., Scherrer, P. H., Bush, R. I., et al. 2012, *Sol. Phys.*, 275, 229
- Skupin, J., Noël, S., Wuttke, M. W., et al. 2005a, *Adv. Space Res.*, 35, 370
- Skupin, J., Weber, M., Bovensmann, H., & Burrows, J. P. 2005b, in *Proc. of the 2004 Envisat & ERS Symp.*, ESA SP, 572
- Skupin, J., Weber, M., Noël, S., Bovensmann, H., & Burrows, J. P. 2005c, *Mem. Soc. Astron. It.*, 76, 1038
- Snow, M., McClintock, W. E., Rottman, G., & Woods, T. N. 2005a, *Sol. Phys.*, 230, 295
- Snow, M., McClintock, W. E., Woods, T. N., et al. 2005b, *Sol. Phys.*, 230, 325
- Solanki, S. K. 2003, *A&ARv*, 11, 153
- Solanki, S. K., & Krivova, N. A. 2004, *Sol. Phys.*, 224, 197
- Solanki, S. K., Schüssler, M., & Fligge, M. 2002, *A&A*, 383, 706
- Solanki, S. K., Krivova, N. A., & Haigh, J. D. 2013, *ARA&A*, 51, 311
- Spruit, H. C., & Roberts, B. 1983, *Nature*, 304, 401
- Tapping, K. F. 1987, *J. Geophys. Res.*, 92, 829
- Tapping, K. F. 2013, *Space Weather*, 11, 394
- Unruh, Y. C., Solanki, S. K., & Fligge, M. 1999, *A&A*, 345, 635
- Unruh, Y. C., Krivova, N. A., Solanki, S. K., Harder, J. W., & Kopp, G. 2008, *A&A*, 486, 311
- Unruh, Y. C., Ball, W. T., & Krivova, N. A. 2012, *Surv. Geophys.*, 33, 475
- Vieira, L. E. A., Solanki, S. K., Krivova, N. A., & Usoskin, I. 2011, *A&A*, 531
- Viereck, R. A., & Puga, L. C. 1999, *J. Geophys. Res.*, 104, 9995
- Viereck, R. A., Floyd, L. E., Crane, P. C., et al. 2004, *Adv. Space Res.*, 2, 5
- Weber, M., Burrows, J. P., & Cebula, R. P. 1998, *Sol. Phys.*, 177, 63
- Wehrli, C., Schmutz, W., & Shapiro, A. I. 2013, *A&A*, 556, L3
- Wenzler, T. 2005, Ph.D. Thesis, University of Göttingen
- Wenzler, T., Solanki, S. K., Krivova, N. A., & Fluri, D. M. 2004, *A&A*, 427, 1031
- Wenzler, T., Solanki, S. K., & Krivova, N. A. 2005, *A&A*, 432, 1057
- Wenzler, T., Solanki, S. K., Krivova, N. A., & Fröhlich, C. 2006, *A&A*, 460, 583
- Wenzler, T., Solanki, S. K., & Krivova, N. A. 2009, *Geophys. Res. Lett.*, 36, 11102
- Willson, R. C., & Mordvinov, A. V. 2003, *Geophys. Res. Lett.*, 30, 1199
- Woods, T. N., Tobiska, W. K., Rottman, G. J., & Worden, J. R. 2000, *J. Geophys. Res.*, 105, 27195
- Woods, T. N., Chamberlin, P. C., Harder, J. W., et al. 2009, *Geophys. Res. Lett.*, 36, 1101
- Yeo, K. L., Solanki, S. K., & Krivova, N. A. 2013, *A&A*, 550, A95
- Yeo, K. L., Feller, A., Solanki, S. K., et al. 2014, *A&A*, 561, A22

A.4 Yeo, K. L., Krivova, N. A., Solanki, S. K., 2014, Solar cycle variation in solar irradiance, Space Sci. Rev., online

The contents of Chapter 6 are identical to the submitted version of Yeo, K. L., Krivova, N. A., Solanki, S. K., 2014, Solar cycle variation in solar irradiance, Space Sci. Rev., online. The printed version is reproduced here with permission from Space Science Reviews, © Springer Science+Business Media.

Solar Cycle Variation in Solar Irradiance

K.L. Yeo · N.A. Krivova · S.K. Solanki

Received: 14 March 2014 / Accepted: 17 June 2014
© Springer Science+Business Media Dordrecht 2014

Abstract The correlation between solar irradiance and the 11-year solar activity cycle is evident in the body of measurements made from space, which extend over the past four decades. Models relating variation in solar irradiance to photospheric magnetism have made significant progress in explaining most of the apparent trends in these observations. There are, however, persistent discrepancies between different measurements and models in terms of the absolute radiometry, secular variation and the spectral dependence of the solar cycle variability. We present an overview of solar irradiance measurements and models, and discuss the key challenges in reconciling the divergence between the two.

Keywords Solar activity · Solar atmosphere · Solar cycle · Solar irradiance · Solar magnetism · Solar physics · Solar variability

1 Introduction

The 11-year solar activity cycle, the observational manifest of the solar dynamo, is apparent in indices of solar surface magnetism such as the sunspot area and number, 10.7 cm radio flux and in the topic of this paper, solar irradiance. The observational and modelling aspects of the solar cycle are reviewed in Hathaway (2010) and Charbonneau (2010), respectively. Solar irradiance is described in terms of what is referred to as the total and spectral solar irradiance, TSI and SSI. They are defined, respectively as the aggregate and spectrally resolved solar radiative flux (i.e., power per unit area and power per unit area and wavelength) above the Earth's atmosphere and normalized to one AU from the Sun. By factoring out the Earth's atmosphere and the variation in the Earth-Sun distance, TSI and SSI characterize the radiant behaviour of the Earth-facing hemisphere of the Sun.

The variation of the radiative output of the Sun with solar activity has long been suspected (Abbot et al. 1923; Smith and Gottlieb 1975; Eddy 1976). However, it was not observed di-

K.L. Yeo (✉) · N.A. Krivova · S.K. Solanki
Max-Planck-Institut für Sonnensystemforschung, 37077 Göttingen, Germany
e-mail: yeo@mps.mpg.de

S.K. Solanki
School of Space Research, Kyung Hee University, Yongin, 446-701 Gyeonggi, Korea

rectly till satellite measurements, free from atmospheric fluctuations, became available. TSI and SSI, at least in the ultraviolet, have been monitored regularly from space through a succession of satellite missions, starting with Nimbus-7 in 1978 (Hickey et al. 1980; Willson and Hudson 1988; Fröhlich 2006; DeLand and Cebula 2008; Kopp et al. 2012). A connection between variations in TSI and the passage of active regions across the solar disc was soon apparent (Willson et al. 1981; Hudson et al. 1982; Oster et al. 1982; Foukal and Lean 1986), leading to the development of models relating the variation in solar irradiance to the occurrence of bright and dark magnetic structures on the solar surface. While not the only mechanism mooted, models that ascribe variation in solar irradiance at timescales greater than a day to solar surface magnetism have been particularly successful in reproducing observations (Domingo et al. 2009). At timescales shorter than a day, excluded from this discussion, intensity fluctuations from acoustic oscillations, convection and flares begin to dominate (Hudson 1988; Woods et al. 2006; Seleznyov et al. 2011).

The measurement and modelling of the variation in solar irradiance over solar cycle timescales, a minute proportion of the overall level (about 0.1 % in the case of TSI), is a substantial achievement. Though significant progress has been made over the past four decades, considerable discrepancies remain between different measurements and models in terms of the absolute radiometry, secular variation and the spectral dependence of the cyclical variability (see the recent reviews by Ermolli et al. 2013; Solanki et al. 2013). In the following, we present a brief overview of the current state of solar irradiance observations (Sect. 2) and models (Sect. 3). We then discuss the key issues in reconciling measurements and models (Sect. 4) before giving a summary (Sect. 5). Our focus will be on the far-ultraviolet to the infrared region of the solar spectrum. This is the spectral range where the bulk of the energy in solar radiation is confined and commonly covered by present-day models aimed at returning both TSI and SSI. We refer the reader to Lilensten et al. (2008), Woods (2008) for an overview of solar cycle variability in the extreme-ultraviolet and shortwards, and Tapping (2013), Dudok de Wit et al. (2014) for radio wavelengths.

2 Measurements

2.1 Total Solar Irradiance, TSI

The measurements from the succession of TSI radiometers sent into space since 1978, collectively representing a nearly uninterrupted record, exhibit clear solar cycle modulation. This is illustrated in Fig. 1 by the comparison between the various TSI records and the monthly sunspot number. All these instruments are based on active cavity electrical substitution radiometry (Butler et al. 2008; Fröhlich 2010). Succinctly, TSI is measured by allowing solar radiation into a heated absorptive cavity intermittently and adjusting the heating power as necessary to maintain thermal equilibrium. While these observations are sufficiently stable over time to trace solar cycle variability, only about 0.1 % of the overall level, the measurements from the various instruments are offset from one another by a greater margin, reflecting the uncertainty in the absolute radiometry.

With the early instruments, specifically Nimbus-7/ERB (Hickey et al. 1980; Hoyt et al. 1992), SMM/ACRIM1 (Willson 1979) and ERBS/ERBE¹ (Lee et al. 1987), the spread in absolute radiometry arose mainly from the uncertainty in the aperture area (Fröhlich 2012;

¹Nimbus-7/ERB denotes the Earth Radiation Budget instrument onboard Nimbus-7, SMM/ACRIM1 the Active Cavity Radiometer Irradiance Monitor onboard the Solar Maximum Mission and ERBS/ERBE the Earth Radiation Budget Experiment onboard the similarly named satellite.

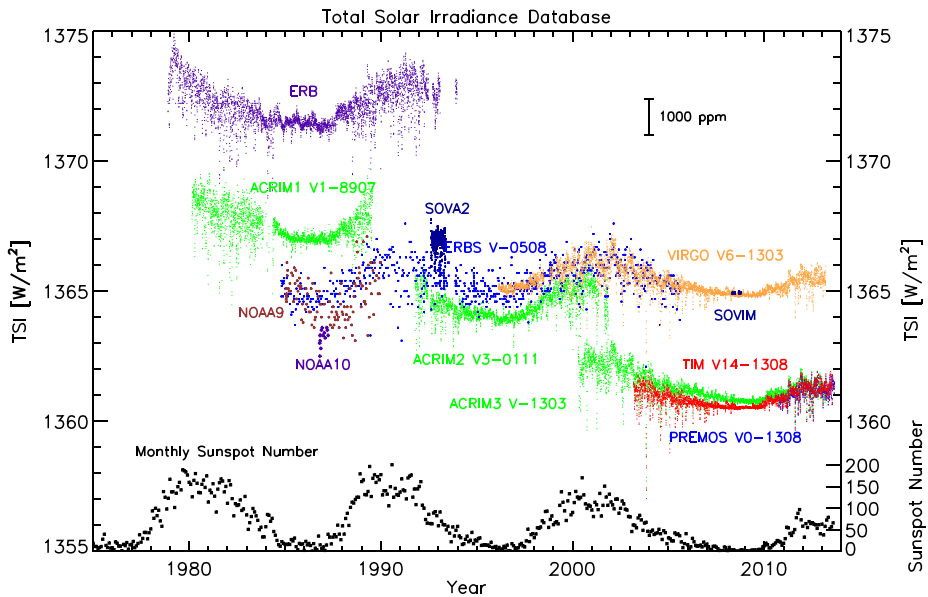


Fig. 1 The measurements from the succession of TSI radiometers sent into orbit since 1978 (colour coded) and the monthly mean of the sunspot number (black, lower right axis). Each TSI record is annotated by the name of the instrument and where applicable, the version number and/or the year and month of the version. Courtesy of G. Kopp (<http://spot.colorado.edu/~kopp/TSI/>)

Ermolli et al. 2013). As the determination of the aperture area improved, so the absolute radiometry from the succeeding missions converged. That is, up till the Total Irradiance Monitor, TIM (Kopp and Lawrence 2005; Kopp et al. 2005a,b) onboard the Solar Radiation and Climate Experiment, SORCE, launched in 2003 (Rottman 2005).

The measurements from TIM were about 5 Wm^{-2} lower than the concurrent observations from ACRIMSAT/ACRIM3² (Willson and Mordvinov 2003) and SoHO/VIRGO³ (Fröhlich et al. 1995, 1997). Tests conducted at the TSI Radiometer Facility, TRF (Kopp et al. 2007) with ground copies of ACRIM3, TIM and VIRGO revealed unaccounted stray-light effects in ACRIM3 and VIRGO (Kopp and Lean 2011; Kopp et al. 2012; Fehlmann et al. 2012). Correction for scattered light subsequently introduced to the ACRIM3 record based on the results of these tests brought it down to within 0.5 Wm^{-2} of the TIM record. The similar proximity between the measurements from the PREcision MONitor Sensor, PREMOS onboard Picard, launched in 2010 (Schmutz et al. 2009, 2013; Fehlmann et al. 2012), with TIM radiometry provided further evidence that the lower absolute level first registered by TIM is likely the more accurate. In a first, PREMOS was calibrated in vacuum at full solar power levels prior to flight at two separate facilities, the National Physical Laboratory and the TRF. As such, it is considered to be more reliably calibrated than preceding TSI radiometers.

Due to the limited lifetime of TSI radiometers, there is no single mission that covered the entire period of observation. Apart from ERBS (1984 to 2003) and VIRGO (1996 to present), there are no records that encompass a complete solar cycle minimum-to-minimum.

²The ACRIM radiometer onboard the ACRIM SATellite.

³The Variability of IRradiance and Gravity Oscillations experiment onboard the Solar and Heliospheric Observatory.

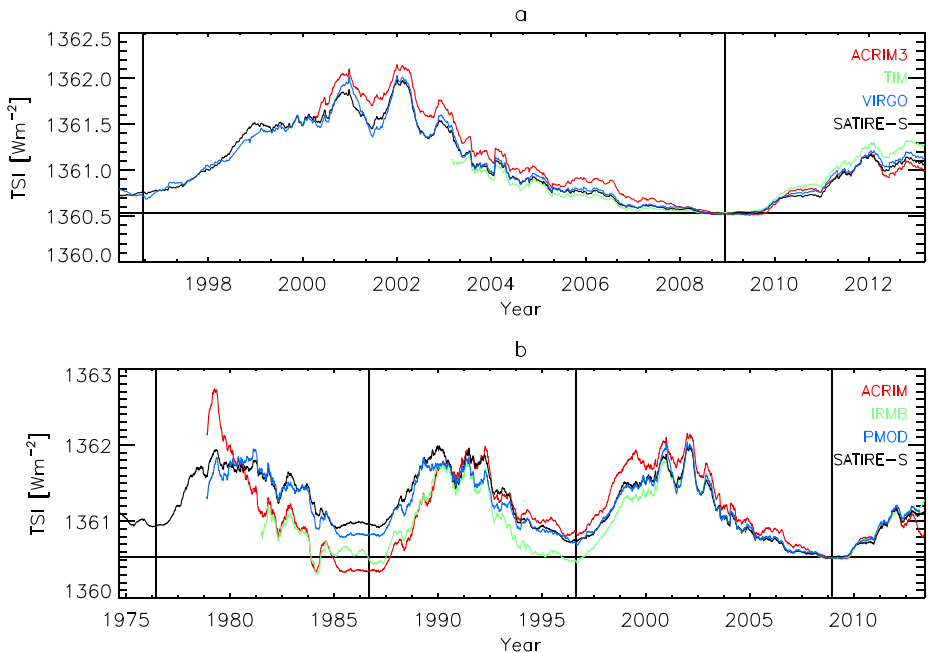


Fig. 2 (a) TSI measurements from ACRIMSAT/ACRIM3 (version 11/13), SORCE/TIM (level 3, version 14) and SoHO/VIRGO (level 2, version 6_002_1302). (b) The ACRIM (version 11/13), IRMB (version dated 19th December 2013, provided by S. Dewitte) and PMOD (version d41_62_1302) composite records of TSI. Also plotted is the SATIRE-S (Yeo et al. 2014b) reconstruction of TSI. The vertical dashed lines mark the position of solar cycle minima. All the time series were normalized to TIM at the 2008 solar cycle minimum (horizontal dashed line) and smoothed with a 181-day boxcar filter

Combining the measurements from the various missions into a single time series, obviously essential, is non-trivial due to ageing/exposure degradation, calibration uncertainty and other instrumental issues. The ACRIM, PREMOS, TIM and VIRGO instruments are designed with redundant cavities to allow in-flight degradation tracking. Even with this capability and the best efforts of the respective instrument teams, significant uncertainty persists over the long-term stability: conservatively, about 0.2 Wm^{-2} or 20 ppm per year (Solanki et al. 2013). This is visibly apparent in the discrepant amplitude of solar cycle variation in the ACRIM3, TIM and VIRGO records (Fig. 2(a)). Accounting for changes in instrument sensitivity, which are often particularly severe during early operation and can see discrete shifts such as that suffered by ERB and VIRGO, has proven to be particularly precarious (Hoyt et al. 1992; Lee et al. 1995; Dewitte et al. 2004a; Fröhlich 2006). It is worth mentioning here that the observations from the various radiometers do largely agree at solar rotational timescales, where apparent variability is much less affected by the instrumental influences discussed above.

There are, at present, three composite records of TSI, published by the ACRIM science team (Willson and Mordvinov 2003), IRMB⁴ (Dewitte et al. 2004b; Mekaoui and Dewitte 2008) and PMOD/WRC⁵ (Fröhlich 2000, 2006). These composites differ in terms of the

⁴IRMB is the francophone acronym of the Royal Meteorological Institute of Belgium. This composite is also variously referred to as the RMIB or SARR composite.

⁵The Physikalisch-Meteorologisches Observatorium Davos/World Radiation Center.

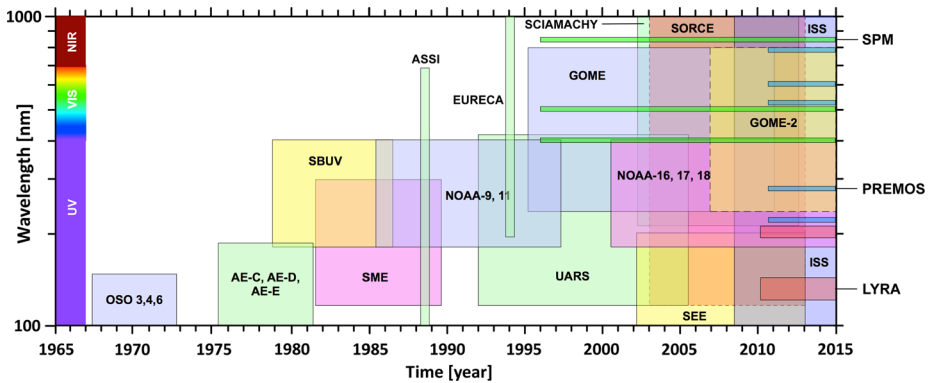


Fig. 3 Timeline and spectral range of the space missions making observations of the solar spectrum above 100 nm. Reproduced from Ermolli et al. (2013), Creative Commons Attribution 3.0 License

amplitude of solar cycle variation, most readily apparent in the conflicting secular trend of the solar cycle minima level (see Fröhlich 2006, 2012 and Fig. 2(c)). The TSI reconstructions presented by Wenzler et al. (2009), Ball et al. (2012), Yeo et al. (2014b) based on the SATIRE-S model (Fligge et al. 2000; Krivova et al. 2003, 2011) replicated, of these composites, the solar cycle and secular variation in the PMOD composite best (see Sect. 3.3.1).

2.2 Spectral Solar Irradiance, SSI

2.2.1 Ultraviolet Solar Irradiance

The solar spectrum has been probed through a miscellany of spaceborne instruments over the past five decades (Fig. 3) which differ in the regularity of measurements and the spectral range surveyed. As with TSI, SSI between around 120 and 400 nm has been monitored almost without interruption from space since 1978.

The key features of the body of ultraviolet solar irradiance measurements are similar to that of TSI, just discussed in Sect. 2.1. The observations from the various spectrometers display similar rotational variability but diverge in terms of the absolute radiometry and the amplitude of solar cycle variation, especially at wavelengths above 240 nm (see Fig. 4 and DeLand and Cebula 2012; Unruh et al. 2012; Ermolli et al. 2013; Yeo et al. 2014b). In particular, the solar cycle amplitude in the measurements from the SIM (Harder et al. 2005a,b) and SOLSTICE (McClintock et al. 2005; Snow et al. 2005a) experiments onboard SORCE is stronger than that registered by the SOLSTICE (Rottman et al. 2001) and SUSIM (Brueckner et al. 1993; Floyd et al. 2003) instruments onboard the predecessor mission, UARS⁶ by a factor of three to ten, depending on wavelength (see Fig. 7 in DeLand and Cebula 2012). This disparity, while broadly within the long-term uncertainty of said instruments, is much greater than encountered between pre-SORCE instruments (DeLand and Cebula 2012; Ermolli et al. 2013). The long-term uncertainty of available ultraviolet solar irradiance observations is of similar magnitude as the variation over the solar cycle: on the order of 0.1 to 1 % per year, varying with wavelength and between instruments (Snow et al. 2005a; Merkel et al. 2011; DeLand and Cebula 2012). The long-term uncertainty is

⁶SIM denotes the Spectral Irradiance Monitor, SOLSTICE the SOLAR STellar Irradiance Comparison Experiment, SUSIM the Solar Ultraviolet Spectral Irradiance Monitor and UARS the Upper Atmosphere Research Satellite.

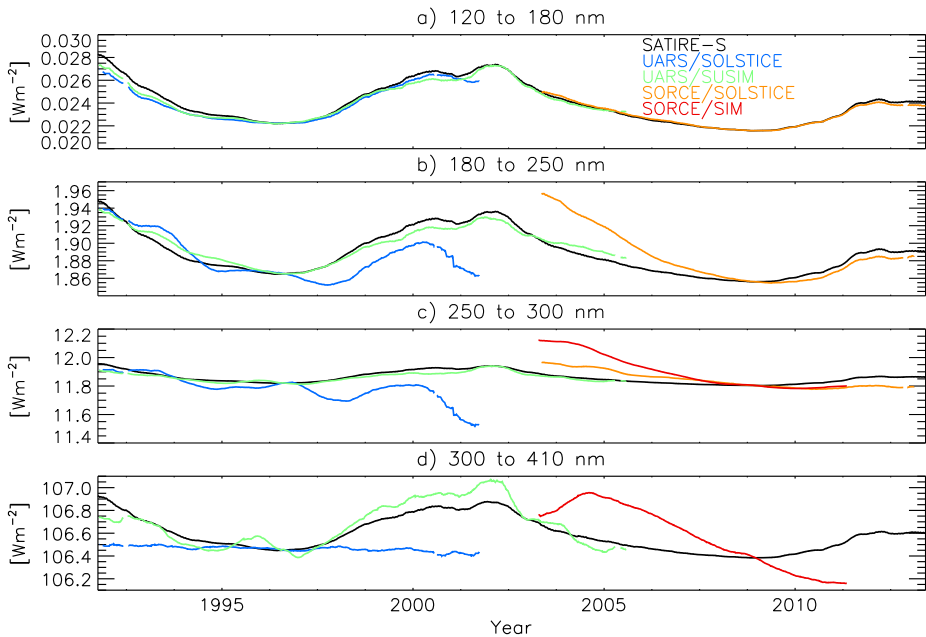


Fig. 4 Integrated solar irradiance in the annotated wavelength intervals in the SATIRE-S reconstruction of SSI (*black*). Also drawn are the measurements from the UARS and SORCE missions, rescaled to the SATIRE-S reconstruction at the 1996 and 2008 solar cycle minima, respectively. All the time series were smoothed by taking the 181-day moving average. Adapted from Yeo et al. (2014b)

also grossly greater than that afflicting TSI measurements. Again, due to the limited lifetime of spaceborne instrumentation, there is no record that extends beyond a complete solar cycle minimum-to-minimum with the exception of the observations from NOAA-9 SBUV/2⁷ (DeLand and Cebula 1998).

The solar cycle modulation in and disparity between the various pre-SORCE records is illustrated in the time series plot by DeLand and Cebula 2008 (Fig. 2 in their paper), which is qualitatively analogous to Fig. 1. The authors presented the first published effort to compose the ultraviolet solar irradiance observations from these instruments into a single time series. The result, spanning 1978 to 2005, still contains overt instrumental trends for which the appropriate correction is not known. The challenge in the account of instrumental influences is substantially greater than with TSI, exacerbated by the wavelength dependence of instrumental effects and differences in the design, operation and calibration approach.

2.2.2 SORCE/SIM SSI

The series of GOME instruments, the first of which was launched onboard ERS-2 in 1996 (Weber et al. 1998; Munro et al. 2006) and ENVISAT/SCIAMACHY,⁸ launched in 2002 (Skupin et al. 2005b) made regular measurements of the solar spectrum in the 240 to 790 nm

⁷The second generation Solar Backscatter UltraViolet spectrometer onboard the ninth National Oceanic and Atmospheric Administration satellite.

⁸GOME is short for the Global Ozone Monitoring Experiment, ERS-2 the second European Remote Sensing satellite and ENVISAT/SCIAMACHY the SCanning Imaging Absorption spectroMeter for Atmospheric CHartography onboard the ENVironmental SATellite.

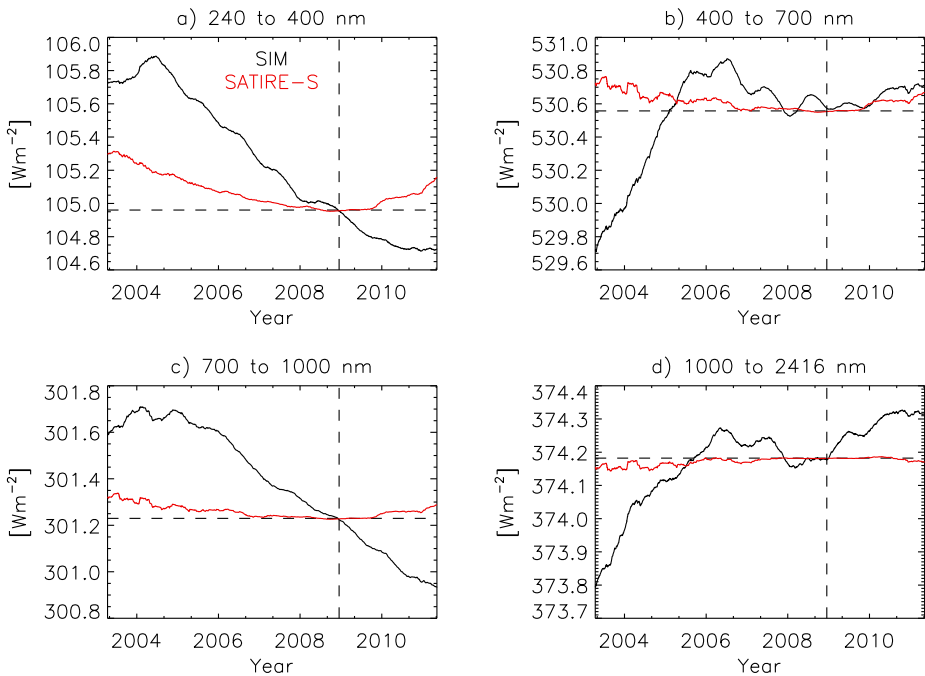


Fig. 5 181-day moving average of the integrated solar irradiance over the spectral intervals specified above each panel in the SORCE/SIM record (*red*) and in the SATIRE-S reconstruction (*black*). The SATIRE-S time series were rescaled to the corresponding SIM time series at the 2008 solar cycle minimum, the position and level at which is indicated by the dashed lines. Adapted from Yeo et al. (2014b)

and 240 to 2380 nm wavelength range, respectively. These instruments are designed primarily for atmospheric sounding measurements which do not require absolute radiometry rather than solar irradiance monitoring. As such, they lack the capability to track instrument degradation in-flight, rendering the observations unsuitable for tracing the solar cycle variation of the solar spectrum reliably. The long-term stability of the narrowband (FWHM of 5 nm) photometry at 402, 500 and 862 nm from the Sun PhotoMeter, SPM on SoHO/VIRGO (Fröhlich et al. 1995, 1997) is similarly problematic, though considerable progress has been made (Wehrli et al. 2013).

With these caveats in mind, one can say that regular monitoring of the solar spectrum longwards of the ultraviolet only started, in effect, with SIM. The instrument has been surveying the wavelength range of 200 to 2416 nm since 2003, providing the only continuous and extended record of the solar spectrum spanning the ultraviolet to the infrared presently available. The latest release (version 19, dated 23rd November 2013), covering the wavelength range of 240 to 2416 nm,⁹ is depicted in Figs. 5 and 6.

SIM returned rather unexpected results, precipitating the ensuing debate on the overall trend registered by the instrument (Harder et al. 2009; Ball et al. 2011; DeLand and Cebula 2012; Unruh et al. 2012; Ermolli et al. 2013; Yeo et al. 2014b). Between 2004 and 2008,

⁹SIM measurement from between 200 and 240 nm are not made publicly available in consideration of the fact that below about 260 nm, SIM observations start to register a lower signal-to-noise ratio than the concurrent observations from the SOLSTICE experiment onboard the same mission (J. Harder, private communication).

Fig. 6 Total flux registered by SIM (red), the integrated flux in the SATIRE-S reconstruction over a similar wavelength range (black) and VIRGO TSI (blue). The SIM and SATIRE-S time series were normalized to the VIRGO time series at the 2008 solar cycle minimum. Adapted from Yeo et al. (2014b)

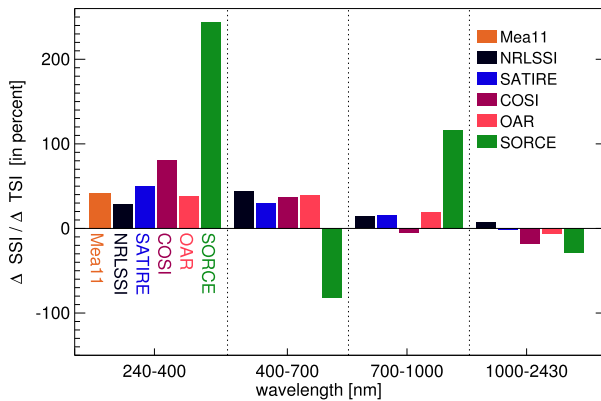
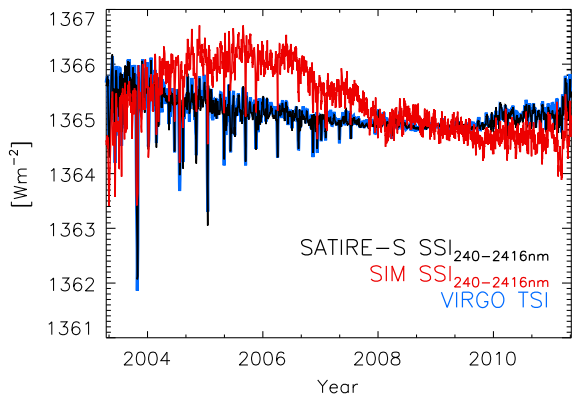


Fig. 7 Ratio of the variation in SSI over the same spectral intervals examined in Fig. 5, Δ SSI, and the corresponding variation in TSI, Δ TSI, between solar cycle maximum and minimum (2002 and 2008) in the models discussed in Sect. 3.3. For the model by Morrill et al. (2011), denoted Mea11, we took Δ TSI from the SATIRE-S model. Also depicted is the same for SORCE measurements between 2004 and 2008, with Δ SSI and Δ TSI from the SIM and TIM records, respectively. Adapted from Ermolli et al. (2013), Creative Commons Attribution 3.0 License

which is within the declining phase of solar cycle 23, SIM recorded a drop in ultraviolet flux (240 to 400 nm, Fig. 5(a)) that is almost double the decrease in TSI over the same period and multiple times greater than projections from pre-SORCE SSI measurements and models of solar irradiance (Fig. 7). Up to 2006, this pronounced downward trend in the ultraviolet is accompanied by a comparable increase in the visible (400 to 700 nm, Fig. 5(c)), in anti-phase with the solar cycle. This is in conflict with SPM photometry (see next paragraph) and present-day models, all of which (apart from Fontenla et al. 2011 see Sect. 3.3.2) point to visible solar irradiance varying in phase with the solar cycle (Fig. 7). The variation in the infrared (700 to 2416 nm, Figs. 5(c) and 5(d)) between 2004 and 2008 is also significantly stronger than in model reconstructions (Fig. 7). The investigations of Unruh et al. (2008, 2012), DeLand and Cebula (2012), Lean and DeLand (2012), Yeo et al. (2014b) did, however, note that the rotational variability in SIM SSI is similar to that in pre-SORCE measurements and models.

Looking now at the full length of the SIM record, there is no constancy in how the overall trend at a given wavelength relate to the solar cycle (Fig. 5). Measured solar irradiance is

neither in phase nor anti-phase with the solar cycle. Apart from the solar cycle modulation evident in pre-SORCE ultraviolet solar irradiance measurements, this also runs counter to the positive correlation between SPM visible (500 nm) photometry and TSI over the similar period of 2002 to 2012 reported by Wehrli et al. (2013). There being no other extended record of SSI covering a similar spectral range, it cannot be ruled out completely that segments of the solar spectrum may vary in a non-cyclic manner as apparent in SIM SSI. It is, however, almost irrefutable that the integral of the solar spectrum over all wavelengths, TSI, does exhibit solar cycle variation. As the spectral range surveyed by SIM accounts for more than 97 % of the power in solar radiation, the total flux recorded by the instrument should already replicate most of the variability in TSI but that is evidently not the case (Fig. 6). In contrast, the reconstruction of the integrated solar irradiance over the spectral range of SIM from SSI models replicates most of the variability in TSI (see Fig. 6 and Ball et al. 2011; Lean and DeLand 2012; Yeo et al. 2014b).

The discrepancies between SIM SSI and other measurements and models reported in various studies, summarized above, were taken to indicate that there are unaccounted instrumental trends in the SIM record (Ball et al. 2011; DeLand and Cebula 2012; Lean and DeLand 2012; Unruh et al. 2012; Yeo et al. 2014b). This is favoured here over alternative interpretations such as the apparent trends between 2004 and 2008 implying a change in the physics of the Sun during this period compared to earlier times or that there are gaping insufficiencies in our understanding of the physical processes driving variations in solar irradiance. As we will argue in Sect. 3.1, the decline in visible flux between 2003 and 2006 (Fig. 5(c)) is not consistent with our current understanding of solar surface magnetism and its effect on solar irradiance.

Evidently, the direct observation of the variation in SSI over solar cycle timescales is afflicted by considerable uncertainty. The situation is set to improve with the continuing efforts to calibrate SCIAMACHY and SORCE spectrometry, and spectral measurements expected from ISS/SOLSPEC (Thuillier et al. 2009, 2014a) and the upcoming JPSS¹⁰ mission (Richard et al. 2011). JPSS, set to be launched in 2017, will carry an improved version of the SIM instrument. For more extensive reviews of the measurement of solar irradiance, we refer the reader to DeLand and Cebula (2008, 2012), Domingo et al. (2009), Kopp et al. (2012), Fröhlich (2012), Ermolli et al. (2013), Solanki et al. (2013).

3 Models

The body of satellite measurements of solar irradiance, while evidently core to our understanding of the solar cycle variation in the radiative output of the Sun, cover a limited period in time and suffer significant uncertainty. Models of solar irradiance serve both to complement these observations and to advance our understanding of the physical processes driving the apparent variability.

3.1 Solar Surface Magnetism

A feature of the 11-year solar activity cycle is the cyclical emergence and evolution of kilogauss-strength magnetic concentrations in the photosphere (Solanki et al. 2006). The main properties of these magnetic concentrations can be explained by describing them as

¹⁰ISS/SOLSPEC denotes the SOLAR SPECTRUM experiment onboard the International Space Station and JPSS the Joint Polar Satellite System.

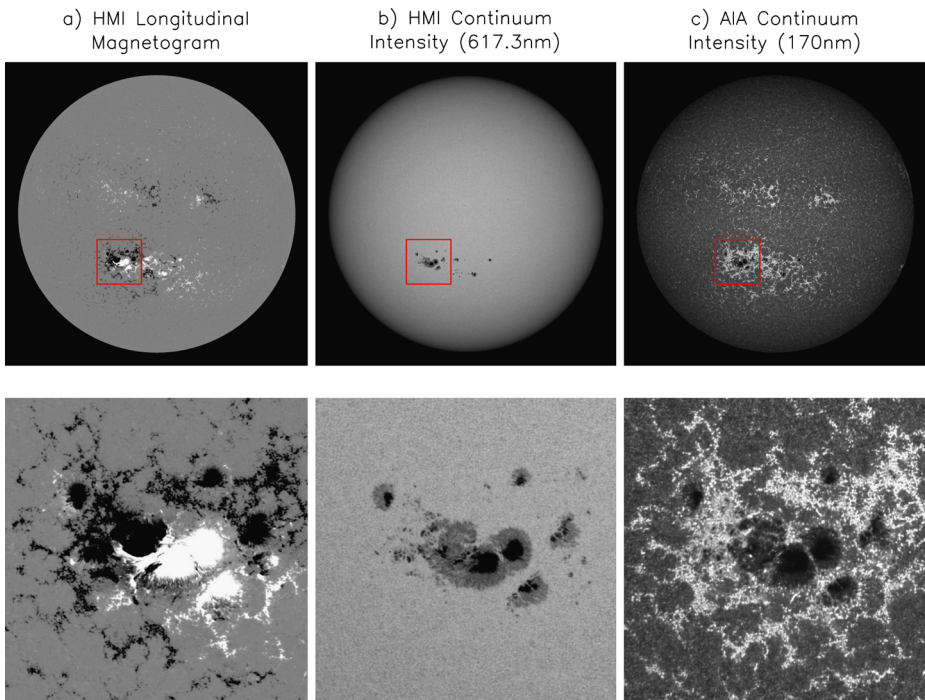


Fig. 8 *Top*: Concurrent observations, from 11th July 2012, of (a) the line-of-sight magnetic field and the continuum intensity at (b) 617.3 nm and (c) 170 nm from the Helioseismic and Magnetic Imager, HMI (Schou et al. 2012) and the Atmospheric Imaging Assembly, AIA (Lemen et al. 2012) onboard the Solar Dynamics Observatory, SDO. The AIA image has been resampled to register with the HMI images. *Bottom*: Blow up of the boxed region, featuring active region NOAA 11520. From (a) to (c), the grey scale is saturated at ± 30 G, about 60 % and 120 %, and 20 % and 300 % of the mean quiet Sun level at disc centre

magnetic flux tubes (Spruit 1976; Spruit and Roberts 1983; Solanki 1993). They range in physical extent from on the order of 10^1 to 10^5 km in cross section. The lower end corresponds to the small-scale magnetic elements which make up active region faculae and quiet Sun network/internetwork (Lagg et al. 2010; Riethmüller et al. 2014), and the upper end to sunspots and pores.

Solar irradiance is modulated by photospheric magnetic activity from its effect on the thermal/radiant property of the solar surface and atmosphere. The influence of magnetic concentrations on the local temperature structure of the solar surface and atmosphere varies strongly with the size of the magnetic feature, as described below.

As a consequence of pressure balance, the interior of magnetic concentrations is evacuated. The lower density creates a depression in the optical depth unity surface and magnetic buoyancy, the result of which is flux tubes are largely vertical. The intensity contrast in the continuum is influenced by the competing effects of magnetic suppression of convection and radiative heating from surrounding granulation through the side walls of the depression. Sunspots and pores are dark from the magnetic suppression of convection within these features (see Fig. 8 and the reviews by Solanki 2003; Rempel and Schlichenmaier 2011). For small-scale magnetic concentrations, this is overcome by the lateral heating, rendering them bright (Spruit 1976; Spruit and Zwaan 1981; Grossmann-Doerth et al. 1994; Vögler et al. 2005), especially away from the disc centre as the side walls come into greater view

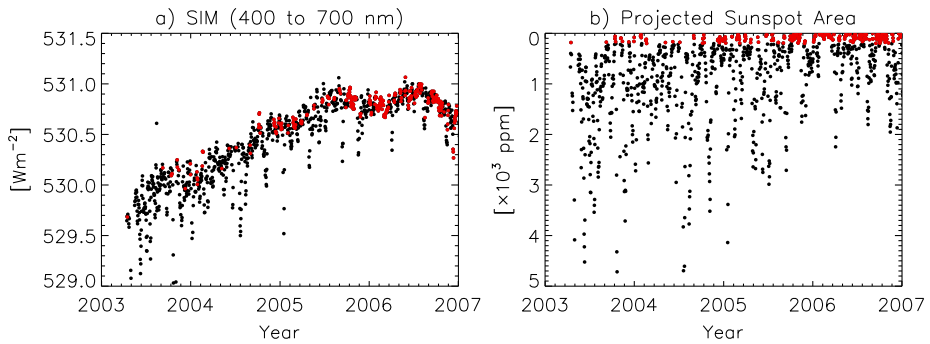


Fig. 9 (a) Integrated solar irradiance in the visible in SIM SSI and (b) the concurrent projected sunspot area from the composite record by Balmaceda et al. 2009 (version 0613). Points corresponding to days where the projected sunspot area is less than 200 ppm are highlighted in red. The vertical axis of the projected sunspot area plot is inverted to aid interpretation

(Spruit 1976; Keller et al. 2004; Carlsson et al. 2004; Steiner 2005). This feature gives rise to the bright faculae visible near the limb in white-light. The upper layers of the atmosphere enclosed within flux tubes are heated by mechanical and resistive dissipations (Musielak and Ulmschneider 2003; Moll et al. 2012), and radiation from deeper layers (Knölker et al. 1991). This enhances their intensity within spectral lines and in the ultraviolet, which are formed at greater heights than the visible continuum (see Fig. 8(c) and Frazier 1971; Mitchell and Livingston 1991; Morrill et al. 2001; Ermolli et al. 2007; Yeo et al. 2013; Riethmüller et al. 2010). A schematic of thin flux tubes and the mechanisms described above can be found in Fig. 5 of Solanki et al. (2013).

Models describing the variation in solar irradiance at timescales greater than a day by the intensity deficit and excess facilitated by photospheric magnetism have achieved substantial success in reproducing measured solar irradiance (see Sects. 3.2 and 3.3, and Domingo et al. 2009). While other plausible mechanisms have also been proposed (Wolff and Hickey 1987; Kuhn et al. 1988; Cossette et al. 2013), related to physical processes in the solar interior, supporting evidence is not straightforward to obtain and consequently still largely lacking.

The increase in visible solar irradiance registered by SIM between 2003 and 2006 (Fig. 5(c)) came at a time when solar activity was declining. For the solar cycle variation in photospheric magnetism to be compatible with this trend in visible solar irradiance, small-scale magnetic concentrations would have to be dark in the visible. The intensity deficit from sunspots and pores, while weakening over this period, is not driving the upward trend apparent in SIM visible solar irradiance. This is demonstrated in Fig. 9(a) by the variation in SIM visible flux over the days with minimal sunspot activity, highlighted in red. If the increase in SIM visible flux is indeed from sunspot darkening, then it should be absent or at least markedly weaker in the days with minimal sunspot activity. As depicted in the figure, the overall trend in the SIM visible flux time series is no less manifest in the days where the projected sunspot area is minimal, below 200 ppm.

Turning now to small-scale magnetic concentrations, various studies have noted negative contrasts in the visible continuum near disc centre at both low and high magnetogram signal levels (summarized in Table 2 of Yeo et al. 2013).

However, the results of recent investigations suggest that these apparent negative contrasts are associated with the fact that small-scale magnetic elements congregate mainly within dark intergranular lanes (Schnerr and Spruit 2011; Kobel et al. 2011) and observational effects related to the limited spatial resolutions and telescope diffraction (Röhrbein

et al. 2011) than any indication that small-scale magnetic concentrations are dark in the visible continuum near disc centre.

Taken together with the intensity enhancement towards the limb and within spectral lines (Topka et al. 1997; Ortiz et al. 2002; Yeo et al. 2013), it is highly unlikely that small-scale magnetic concentrations, at least overall, might be dark in the visible. The upward trend in SIM visible solar irradiance between 2003 and 2006 is not consistent with our current understanding of solar surface magnetism and its effect on solar irradiance.

3.2 Model Architectures

There are two broad categories of solar irradiance models, distinguished by the modelling approach, commonly referred to as ‘proxy’ and ‘semi-empirical’.

3.2.1 Proxy Models

As stated in the introduction, the measurement of solar irradiance from space quickly revealed an apparent connection between TSI and the passage of active regions across the solar disc. This was followed by the development of models aimed at reconstructing solar irradiance by the multivariate regression of indices of solar activity to measured solar irradiance. The index data serve as proxies of the effects of bright and dark magnetic structures on the radiative output of the Sun, therefore the term proxy models.

Sunspot darkening is usually represented by sunspot area or the photometric sunspot index, PSI (Hudson et al. 1982; Fröhlich et al. 1994) and facular brightening by chromospheric indices such as the Ca II K (Keil et al. 1998), Mg II (Heath and Schlesinger 1986) or F10.7 (10.7 cm radio flux, Tapping 1987, 2013) indices. In this context the term sunspot includes pores and the term faculae encompasses quiet Sun network. The Ca II K and Mg II indices are given by the ratio of the disc-integrated flux in the line core of the Ca II K line and the Mg II h and k doublet to that at nearby reference wavelengths. The line core to ‘continuum’ ratio is preferred over absolute fluxes as it is more robust to instrument degradation.

The reconstructions of TSI by the group at the San Fernando Observatory, SFO (Chapman et al. 1996, 2012, 2013; Preminger et al. 2002) employ sunspot and faculae indices derived from full-disc photometric images obtained at the observatory. These models proved to be particularly successful among proxy models. By employing full-disc imagery instead of Sun-as-a-star measures such as the indices listed above, they include the centre-to-limb variation of sunspot and faculae contrast, albeit only at the photometric bandpass. The latest iteration, based on visible red and Ca II K observations, reproduced most of the variation in TIM radiometry ($R^2 = 0.95$, Chapman et al. 2013).

Since the proxy model approach relies on reliable solar irradiance measurements, it is not straightforward to reconstruct SSI by this method due to the long-term uncertainty of available measurements and the relative paucity of observations outside the ultraviolet (Sect. 2.2). Certain proxy models make use of the fact that the effects of instrument degradation on apparent variability is relatively benign at shorter timescales to circumvent long-term stability issues. The idea is to fit index data to measured rotational variability, either by detrending the index and SSI data or confining the regression to rotational periods, and then assume the indices-to-irradiance relationships so derived to all timescales (Lean et al. 1997; Paganan et al. 2009; Thuillier et al. 2012). As we will discuss in Sect. 4.1, the assumption that the underlying relationship between indices of solar activity and solar irradiance is similar at all timescales is not likely valid.

3.2.2 Semi-empirical Models

The next level of sophistication in the modelling of solar irradiance is realized by semi-empirical models. In these models, the solar disc is segmented by surface feature type, termed ‘components’. The filling factor (proportion of the solar disc or a given area covered) and time evolution of each component is deduced from indices of solar activity or suitable full-disc observations. This information is converted to solar irradiance employing the intensity spectra of the various components. These are calculated applying spectral synthesis codes to semi-empirical model atmospheres of said feature types (Fontenla et al. 1999, 2009; Unruh et al. 1999; Shapiro et al. 2010). The reconstruction of the solar spectrum is given by the filling factor-weighted sum of the component intensity spectra. The semi-empirical model atmospheres describe the temperature and density stratification of the solar atmosphere within each component, constrained and validated by observations (therefore the term ‘semi-empirical’).

The semi-empirical approach has the advantage that it yields SSI independent of the availability of reliable measurements. Additionally, for the models that rely on full-disc observations for the filling factor of the solar surface components (i.e., when the exact disc position of magnetic features is known), the centre-to-limb variation of the radiant behaviour of each component can be taken into account by generating and applying the corresponding intensity spectra at varying heliocentric angles.

3.3 Present-Day Models

At present, there are five models aimed at reconstructing both TSI and SSI reported in the literature, reviewed in Ermolli et al. (2013). These models describe the solar spectrum over at least from the far-ultraviolet to the infrared, such that the bolometric value is a close approximation of TSI. They are,

- NRLSSI (Naval Research Laboratory Solar Spectral Irradiance, Lean et al. 1997; Lean 2000),
- SATIRE-S (Spectral And Total Irradiance REconstruction for the Satellite era, Unruh et al. 1999; Fligge et al. 2000; Krivova et al. 2003, 2006, 2011; Yeo et al. 2014b),
- SRPM (Solar Radiation Physical Modelling, Fontenla et al. 1999, 2004, 2006, 2009, 2011),
- OAR (Observatorio Astronomico di Roma, Ermolli et al. 2003, 2011, 2013; Penza et al. 2003) and
- COSI (COde for Solar Irradiance, Haberreiter et al. 2008; Shapiro et al. 2010, 2011, 2013).

Apart from the NRLSSI, these models adopt the semi-empirical approach. In the following, we discuss the recent results obtained with the SATIRE-S model by Yeo et al. 2014b (Sect. 3.3.1) before giving an overview of the other models listed (Sect. 3.3.2). For a broader review of models of solar irradiance, we refer the reader to Domingo et al. (2009), Ermolli et al. (2013), Solanki et al. (2013).

3.3.1 SATIRE-S

The SATIRE-S model (Fligge et al. 2000; Krivova et al. 2003, 2011) relies on spatially-resolved full-disc observations of magnetic field and intensity to segment the solar disc into quiet Sun, faculae, sunspot umbra and sunspot penumbra. It has been applied to longitudinal

magnetograms and continuum intensity images collected at the KPVT (in operation from 1974 to 2003, Livingston et al. 1976; Jones et al. 1992), as well as from SoHO/MDI (1996 to 2011, Scherrer et al. 1995) and SDO/HMI¹¹ (2010 to the present, Schou et al. 2012) to reconstruct total and spectral solar irradiance over various periods between 1974 and 2013 (Krivova et al. 2003; Wenzler et al. 2006; Ball et al. 2012, 2014; Yeo et al. 2014b). In the latest iteration (Yeo et al. 2014b), KPVT, MDI and HMI magnetograms were cross-calibrated in such a way that the model input from all the data sets combine to yield a single consistent TSI/SSI time series covering the entire period of 1974 to 2013 as the output. Apart from the NRLSSI, which extends back to 1950, this is the only other daily reconstruction of the solar spectrum spanning the ultraviolet to the infrared from present-day models to extend over multiple solar cycles.

At present, the model employs the intensity spectra of quiet Sun, faculae, umbra and penumbra from Unruh et al. (1999), which were generated with the ATLAS9 spectral synthesis code (Kurucz 1993). As ATLAS9 assumes local thermodynamic equilibrium (LTE), it fails in the ultraviolet below approximately 300 nm. Ultraviolet solar radiation is formed in the upper photosphere and lower chromosphere, where the plasma is increasingly less collisional. The breakdown below 300 nm is accounted for by rescaling the 115 to 180 nm segment of the reconstructed spectra to SORCE/SOLSTICE SSI¹² and offsetting the 180 to 300 nm segment to the Whole Heliospheric Interval (WHI) reference solar spectra by Woods et al. (2009), as detailed in Yeo et al. (2014b). SATIRE-S is the only semi-empirical model to include the influence of departures from LTE through such a data-driven approach. The SRPM, OAR and COSI models take a more direct approach, making use of various non-LTE spectral synthesis codes to generate the intensity spectra of solar surface components. The various non-LTE codes differ from one another by the method non-LTE effects are approximated (see Fontenla et al. 1999; Uitenbroek 2002; Shapiro et al. 2010).

Recall, due to uncertainties in the amplitude of solar cycle variation, the three published TSI composites exhibit conflicting decadal trends (Sect. 2.1). The TSI reconstructed by SATIRE-S is a significantly closer match to the PMOD composite than to the ACRIM or the IRMB composite, replicating most of the variability ($R^2 = 0.92$) over the entire length of the composites (Fig. 2(c)). Reconstructed TSI also exhibits excellent agreement with the measurements from individual instruments such as ACRIM3, TIM and VIRGO. The record from the PMO6V¹³ radiometer on VIRGO is particularly well-matched ($R^2 = 0.96$). The secular decline between the 1996 and 2008 solar cycle minima in VIRGO radiometry is reproduced to within 0.05 Wm^{-2} (Fig. 2(a)). This agreement between SATIRE-S TSI and VIRGO radiometry, which extends 1996 to the present, encompassing all of solar cycle 23, is significant. It implies that at least 96 % of the variability in solar irradiance over this period, including the secular variation between the 1996 and 2008 solar cycle minima can be explained by solar surface magnetism alone.

The bolometric facular brightening and sunspot darkening, $\Delta\text{TSI}_{\text{fac}}$ and $\Delta\text{TSI}_{\text{spt}}$ with respect to the TSI level of the magnetically quiet Sun, binned and averaged by month and

¹¹In full, the Kitt Peak Vacuum Telescope (KPVT), the Michelson Doppler Imager onboard the Solar and Heliospheric Observatory (SoHO/MDI), and the Helioseismic and Magnetic Imager onboard the Solar Dynamics Observatory (SDO/HMI).

¹²This is relatively unaffected by the long-term stability issues plaguing available SSI measurements discussed in Sect. 2.2.1 as they only emerge towards longer wavelengths (Fig. 4).

¹³VIRGO TSI is actually given by the combination of the measurements from two onboard radiometers, DIARAD and PMO6V. The solar cycle variation in the DIARAD and PMO6V records is nearly identical but they do differ at rotational timescales resulting in very different R^2 values on comparison with other measurements or models.

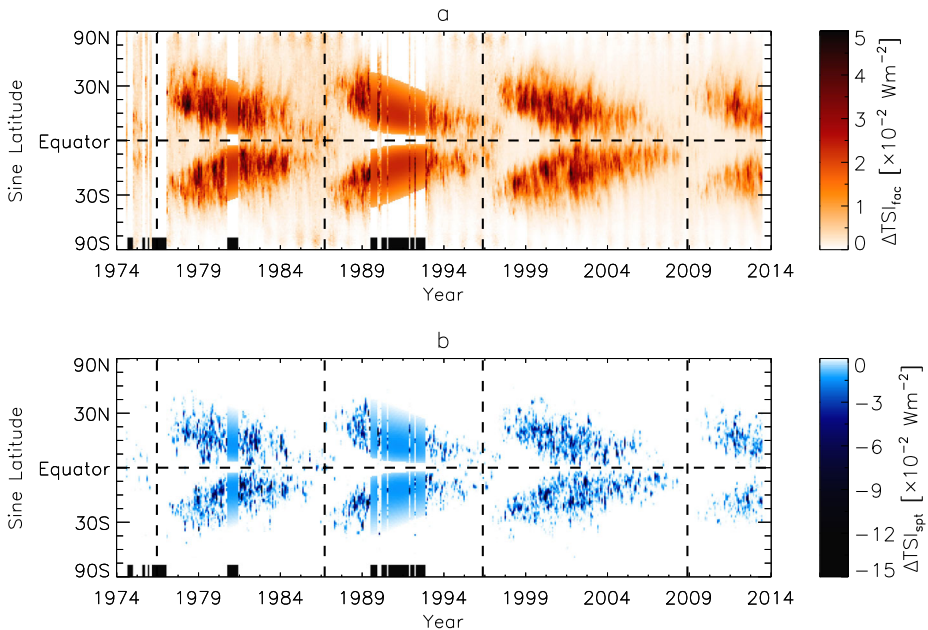


Fig. 10 Variation in TSI from (a) faculae brightening, $\Delta\text{TSI}_{\text{fac}}$ and (b) sunspot darkening, $\Delta\text{TSI}_{\text{spt}}$ in the SATIRE-S model, as a function of time and latitude (the monthly average in sine latitude intervals of 0.01). The black bars along the horizontal axes mark the months with no values from the lack of suitable magnetogram data. The gaps around the maxima of solar cycles 21 and 22 are filled by interpolation. The horizontal and vertical dashed lines denote the equator and epoch of solar cycle minima, respectively

sine latitude, is expressed in Fig. 10. This is an update of the similar figure by Wenzler (2005) based on an earlier SATIRE-S reconstruction that employed KPVT data alone. Since solar surface magnetism is concentrated in active regions, it follows then that the latitudinal distribution of the associated intensity excess/deficit demonstrate Spörer's law, resembling butterfly diagrams of sunspot area/position and magnetic flux (see e.g., Figs. 4 and 14 in Hathaway 2010). A diagram similar to Fig. 10(c), based on the PSI, was presented by Fröhlich 2013 (Fig. 5 in his paper).

Since sunspots are largely absent around solar cycle minima, the minimum-to-minimum variation in SATIRE-S TSI is dominantly from the change in facular brightening. In Fig. 11, we plot the latitudinal distribution of facular brightening at the last three solar cycle minima, taken from the butterfly diagram (Fig. 10(a)). Around the 1986 solar cycle minimum, facular brightening is elevated close to the equator, around mid-latitudes and towards high latitudes (red curve). The broad peaks near the equator and at mid-latitudes correspond to active regions associated with the preceding cycle and the succeeding cycle, respectively. The increase towards high latitudes relates to magnetic elements transported polewards by meridional circulation over the course of the previous cycle (i.e., polar flux). The differing latitudinal distribution at the three solar cycle minima illustrates how the minimum-to-minimum trend in faculae brightening and therefore TSI is modulated by the prevailing magnetic activity in the three latitude regions. The low flat profile of the blue curve, corresponding to the 2008 solar cycle minimum, reflects the near-complete absence of any form of activity during this period, which contributed significantly to the secular decline between the 1996 and 2008 solar cycle minima.

Fig. 11 Latitudinal distribution of facular brightening, $\Delta\text{TSI}_{\text{fac}}$ in SATIRE-S at the 1986, 1996 and 2008 solar cycle minima, taken from Fig. 10(a). Facular brightening is influenced by active regions in the low and mid-latitudes, associated with the preceding and succeeding solar cycles, respectively and polar flux at high latitudes

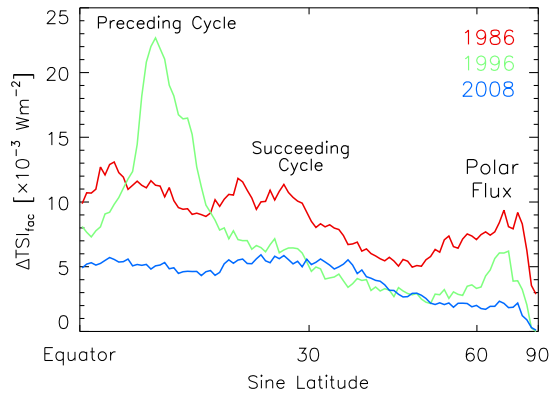
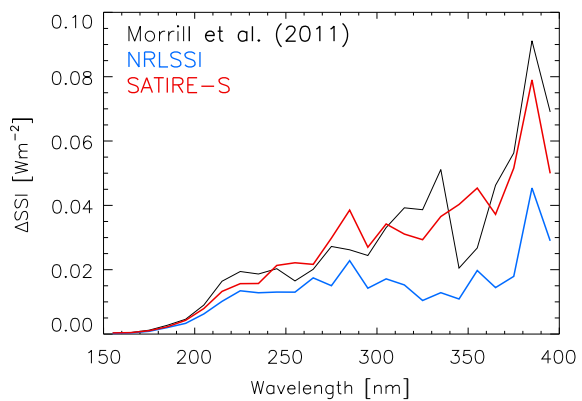


Fig. 12 The change in solar irradiance, ΔSSI , integrated over 10 nm intervals, between solar cycle maximum and minimum (as in Fig. 7), in the Morrill et al. (2011), NRLSSI and SATIRE-S models



The ultraviolet solar irradiance measurements from the various instruments sent into space diverge in terms of the amplitude of solar cycle variation, especially above 240 nm and between *SORCE* and pre-*SORCE* missions (Sect. 2.2.1). Consequently, while the SATIRE-S reconstruction reproduces the cyclical variability in the ultraviolet solar irradiance observations from the *UARS* and *SORCE* missions closely below 180 nm, above this wavelength, it replicates certain records better than others (Fig. 4). The reconstruction is a close match to the empirical model by Morrill et al. (2011). This model, based on the matching of the Mg II index to *SUSIM* SSI, represents an estimation of *SUSIM*-like spectrometry with the stability corrected to that of the Mg II index. Notably, the amplitude of solar cycle variation is similar, even above 240 nm (Figs. 7 and 12). The reconstruction does not replicate the overall trend in *SIM* SSI (Fig. 5). It is worth noting here that there is no model reported thus far that is able to reproduce the solar cycle variation in *SIM* SSI and TSI simultaneously.

The Lyman- α irradiance of the reconstruction reproduces most of the variability ($R^2 = 0.94$), including the solar cycle trend (Fig. 13(a)), in the *LASP*¹⁴ Lyman- α composite (Woods et al. 2000). The Mg II index derived from the reconstruction is highly correlated to the competing Mg II index composites by *LASP* (Viereck et al. 2004; Snow et al. 2005b) and by *IUP*¹⁵ (Viereck and Puga 1999; Skupin et al. 2005a,c), in particular with the latter

¹⁴The Laboratory for Atmospheric and Space Physics.

¹⁵*IUP* is the germanophone acronym of the Institute of Environmental Physics at the University of Bremen.

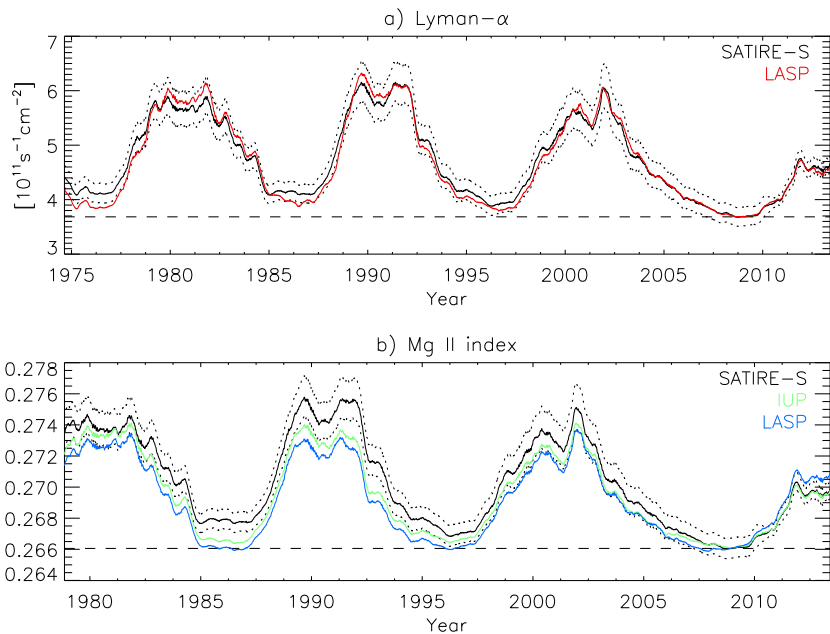


Fig. 13 (a) The Lyman- α irradiance and (b) Mg II index based on the SATIRE-S reconstruction of SSI (black solid lines). The reconstruction uncertainty is denoted by the dotted lines. Also illustrated, the LASP Lyman- α composite (red), and the IUP (green) and LASP (blue) Mg II index composites, regressed to the rotational variability and offset to the 2008 solar cycle minimum level (dashed lines) in the respective SATIRE-S time series. All the time series were smoothed with a 181-day boxcar filter. Adapted from Yeo et al. (2014b)

($R^2 = 0.96$). It was, however, less successful in replicating the decadal trend in these two composites (Fig. 13(c)). That said, it did reproduce, to within model uncertainty, the secular decline between the 1996 and 2008 solar cycle minima in the IUP Mg II index composite.

3.3.2 Other Present-Day Models

The present-day models capable of returning the solar spectrum over the ultraviolet to the infrared are, with the exception of the SRPM, broadly consistent with one another. They differ in certain aspects, most notably in terms of the spectral dependence of the cyclical variability (Fig. 7). In this section, we will give a brief description of the NRLSSI, SRPM, OAR and COSI models, and highlight the key discrepancies between these models and SATIRE-S.

The NRLSSI (Lean et al. 1997; Lean 2000) describes the effect of sunspot darkening and faculae brightening on a model spectrum of the quiet Sun. The time evolution of sunspot darkening is given by the PSI derived from sunspot area records and facular brightening by the Ca II K, Mg II and F10.7 indices. In the ultraviolet (120 to 400 nm), the variation in solar irradiance is inferred from the multivariate regression of the index data to the rotational variability in UARS/SOLSTICE SSI. This is achieved by detrending both index and SSI data prior to the regression. Above 400 nm, it is given by the sunspot and faculae contrast models from Solanki and Unruh (1998), modulated in time by the index data.

The models discussed here, apart from the SRPM, all see reconstructed SSI varying in phase with the solar cycle in the ultraviolet and visible (Fig. 7). In the infrared, facular

contrast is weak and negative at certain wavelengths, depending on the model. This allows sunspot darkening to dominate such that the overall level at activity maximum can be lower than at minimum as illustrated for SATIRE-S in Fig. 5(d). Depending on the sunspot/facular contrast adopted by the various models, they differ in the wavelength range and strength of this effect (see Fig. 7 in Ermolli et al. 2013). This effect is relatively weak in the NRLSSI such that the integrated flux over the shortwave-infrared (1000 to 2430 nm) still varies in phase with the solar cycle, contrary to the other models (Fig. 7). The variation over the solar cycle between 240 and 400 nm is also weaker, almost half of that in SATIRE-S, attributed to confining the regression to rotational variability (Ermolli et al. 2013). The consistency between SATIRE-S and the SUSIM-based model of Morrill et al. (2011) gives further support to the amplitude of solar cycle variation in the ultraviolet exhibited by these two models (Fig. 12). While SATIRE-S replicates the secular decline between the 1996 and 2008 solar cycle minima in VIRGO TSI radiometry (Fig. 2(a)), the NRLSSI does not as this minimum-to-minimum variation is absent in the Mg II index composite employed, that released by LASP (Fig. 13(c)).

The SRPM denotes the set of data and tools for semi-empirical modelling of solar irradiance, including a non-LTE spectral synthesis code, developed by Fontenla et al. (1999, 2004, 2006, 2009, 2011). Currently, the package features semi-empirical model atmospheres for nine solar surface components: quiet Sun internetwork, quiet Sun network lane, enhanced network, plage, bright plage, sunspot umbra and sunspot penumbra, presented in Fontenla et al. (2009), and dark quiet Sun internetwork and hot facula, introduced later in Fontenla et al. (2011). Fontenla et al. (2011) made various adjustments to the Fontenla et al. 2009 model atmospheres guided by SORCE SSI. The solar irradiance reconstruction presented by the authors, extending 2000 to 2009, is based on these modified model atmospheres. The filling factors of the various components were derived from full-disc images in the red part of the visible spectrum and Ca II K acquired with the Precision Solar Photometric Telescope, PSPT at OAR (Coulter and Kuhn 1994; Ermolli et al. 1998).

The modifications to the Fontenla et al. (2009) model atmospheres resulted in the reconstructed visible solar irradiance registering lower levels during periods of higher activity (Figs. 6 and 9 in Fontenla et al. 2011), qualitatively consistent with the increase in SIM visible flux between 2003 and 2006 (Fig. 5(c)). However, the solar cycle variation in the ultraviolet is still weaker than what was recorded by SORCE/SOLSTICE. The model thus failed to reproduce the solar cycle variation in measured TSI, which all the other present-day models are able to do with reasonable success. These shortcomings were taken by the authors to imply that the number of solar surface components is insufficient, which runs counter to the OAR results.

The team at OAR also employed the full-disc images recorded with the PSPT at the observatory in the series of proxy and semi-empirical reconstructions of solar irradiance reported (Penza et al. 2003; Domingo et al. 2009; Ermolli et al. 2011). Work on a new semi-empirical model is in progress (Ermolli et al. 2013). This latest effort considers the seven solar surface components defined in Fontenla et al. (2009). The filling factors were obtained from PSPT observations covering the period of 1997 to 2012 following Ermolli et al. (2010). The intensity spectra corresponding to each component were calculated with the Fontenla et al. (2009) model atmospheres, without the more recent modifications introduced by Fontenla et al. (2011), using the non-LTE spectral synthesis code RH¹⁶ (Uitenbroek 2002). The computation is therefore, apart from employing the Fontenla et al. (2009) model

¹⁶Based on the work of and abbreviated after Rybicki and Hummer (1991, 1992).

atmospheres as is, broadly analogous to the SRPM reconstruction presented by Fontenla et al. 2011.

In the ultraviolet and visible, the OAR reconstruction is roughly consistent with NRLSSI, SATIRE-S and COSI, exhibiting a similar disparity with SIM SSI (Fig. 7). Also in line with these other models, the TSI from the reconstruction replicates most of the variability in TIM radiometry and the PMOD composite. The agreement with measured TSI suggests that the seven solar surface components described in Fontenla et al. (2009) are sufficient for the semi-empirical modelling of at least TSI, in contradiction to the conclusion of Fontenla et al. (2011). The OAR results also support the conclusions of Ball et al. (2011), DeLand and Cebula (2012), Lean and DeLand (2012), Unruh et al. (2012), Yeo et al. (2014b), that the discrepancy between SIM SSI and models arise from unaccounted instrumental effects in the SIM record and does not warrant a significant rethink in how solar irradiance is modelled.

The non-LTE spectral synthesis code COSI (Haberreiter et al. 2008; Shapiro et al. 2010) has been utilised to generate intensity spectra of solar surface components for semi-empirical modelling of solar irradiance (Haberreiter et al. 2005). The current implementation utilizes intensity spectra generated with the model atmospheres by Fontenla et al. (1999). These were applied to sunspot number, ^{10}Be and neutron monitor data to reconstruct solar irradiance back to the Maunder minimum period and over the Holocene at 1-year and 22-year cadence, respectively (Shapiro et al. 2011). More recently, they were also applied to SRPM PSPT-based filling factors (Shapiro et al. 2013), and HMI full-disc longitudinal magnetograms and continuum intensity images (Thuillier et al. 2014b).

Contrary to the NRLSSI, SATIRE-S and OAR models, the Shapiro et al. (2011) reconstruction varied in anti-phase with the solar cycle in the near-infrared (700 to 1000 nm, Fig. 7), accompanied and compensated by an enhanced variability in the ultraviolet. This was attributed to the use of a single model atmosphere each for sunspots and for plage, so not distinguishing between sunspot umbra and penumbra and between plage and bright plage (Ermolli et al. 2013). To account for this simplification, Shapiro et al. (2013) reduced sunspot and plage contrast in such a manner that brought the reconstruction presented into alignment with *SORCE/SOLSTICE* measurements in the Herzberg continuum (190 to 222 nm). A more comprehensive approach is in development.

4 Reconciling Measurements and Models

4.1 Proxy Models

Solar irradiance observations, in particular SSI, suffer non-trivial long-term uncertainty (Sect. 2). As mentioned in Sect. 3.2.1, in the regression of indices of solar activity to measured SSI, certain proxy models confine the fitting to rotational variability to circumvent bias from instrumental trends. Such a step implicitly assumes that the relationship between the two is similar at all timescales.

While the rotational variability in solar irradiance is largely driven by the time evolution of active regions, the variability at longer timescales is dominated by the magnetic flux distributed in the quiet Sun (Foukal and Lean 1988; Fligge et al. 2000; Solanki et al. 2002). The response of chromospheric indices to magnetic flux in active regions and in the quiet Sun is evidently not the same (Tapping 1987; Solanki and Krivova 2004; Ermolli et al. 2010; Foukal et al. 2011). The weak solar cycle variation in the ultraviolet in the NRLSSI highlights the limitation of applying the relationship between chromospheric indices and solar irradiance at rotational timescales to longer timescales.

VIRGO registered a secular decline in TSI of over 0.2 Wm^{-2} between the 1996 and 2008 solar cycle minima, approximately 20 % of the solar cycle amplitude (Fröhlich 2009). The NRLSSI does not replicate this clear secular trend in VIRGO radiometry as it is absent in the LASP Mg II index composite. Fröhlich (2009, 2012, 2013) attributed the discrepant decadal trend in the LASP Mg II index composite and VIRGO TSI to a possible cooling/dimming of the photosphere between the two solar cycle minima. This disparity is more likely related to the non-linear relationship between chromospheric indices and solar irradiance, discussed in the previous paragraph (Foukal et al. 2011) and the long-term uncertainty of Mg II index data. While the LASP Mg II index composite is effectively level between the 1996 and 2008 solar cycle minima, the competing composite by IUP does exhibit a secular decline (Fig. 13(c)). This minimum-to-minimum drop in the IUP composite is qualitatively replicated in the Mg II index produced from the SATIRE-S reconstruction, the TSI from which reproduces the secular decline in VIRGO TSI (Sect. 3.3.1). The discrepancy between the IUP and LASP composites demonstrates how even for an activity proxy as robust to instrumental effects as the Mg II index, the long-term uncertainty can still be sufficient to obscure the underlying decadal variation.

The rigorous reconstruction of solar irradiance through proxy models would require a greater understanding of the relationship between indices of solar activity and solar irradiance, and of the long-term stability of index data, which is still largely unknown.

4.2 Semi-empirical Models

Present-day semi-empirical models, reviewed in Sect. 3.3, all employ one-dimensional or plane-parallel model atmospheres. Various studies have pointed out that the intensity spectra synthesized from one-dimensional representations of the spatially inhomogeneous solar atmosphere do not necessarily reflect the true average property (Uitenbroek and Criscuolo 2011; Holzreuter and Solanki 2013).

The intensity contrast of network and facular magnetic features varies with distance from disc centre and magnetic flux. In SATIRE-S, the magnetic flux dependence is linear with the magnetogram signal up to a saturation level, the free parameter in the model (Fligge et al. 2000). For the SRPM, OAR and COSI models, which employ full-disc Ca II K images, after identifying sunspots, the rest of the solar disc is segmented by the Ca II K intensity into multiple components. These measures are not only empirical but also do not properly account for the observation that the continuum and line core intensity contrast of small-scale magnetic concentrations scale differently with magnetogram signal (Yeo et al. 2013). As set out by Unruh et al. (2009), three-dimensional model atmospheres would allow the possibility to relate the appropriate calculated intensity spectra to the magnetogram signal or Ca II K intensity directly.

In the continuum, the intensity contrast of small-scale magnetic elements increases with distance from disc centre before declining again close to the limb while the converse is observed within spectral lines. This difference comes primarily from the differing interaction between the line-of-sight, and magnetic flux tubes and the intervening atmosphere at the continuum and spectral lines formation heights (Solanki et al. 1998; Yeo et al. 2013). In employing one-dimensional model atmospheres, present semi-empirical models do not capture these effects.

Three-dimensional model atmospheres based on observations (Socas-Navarro 2011) and magnetohydrodynamics (MHD) simulations (Vögler et al. 2005), while growing in sophistication and realism, cannot as yet reproduce observations at all heights (Afram et al. 2011). A limiting factor is our understanding of the effects of spatial resolution, that is, the point

spread function and how it is sampled by the imaging array, on observations (Danilovic et al. 2008, 2013; Röhrbein et al. 2011). This is especially severe for the small-scale magnetic concentrations which make up network and faculae as they are largely unresolved in current observations. The increasing availability of atmospheric seeing-free observations from space and balloon-borne missions, in particular high spatial resolution imagery, such as those from SUNRISE (Solanki et al. 2010; Barthol et al. 2011), will provide stringent constraints on model atmospheres. Space and balloon-borne telescopes have the advantage that the point spread function can be well-constrained (Mathew et al. 2007, 2009; Wedemeyer-Böhm 2008; Yeo et al. 2014a), rendering them particularly useful for this purpose.

Another source of uncertainty is the treatment of non-LTE effects, which are highly complex and not fully understood. The SRPM, OAR and COSI models employ various non-LTE spectral synthesis codes which differ by the approach taken to approximate non-LTE effects. In SATIRE-S, which relies on an LTE spectral synthesis code, non-LTE effects are accounted for empirically instead. While inexact, the one-dimensional model atmospheres and the various measures taken to account for non-LTE effects, direct or empirical, in present-day semi-empirical models are a practical necessity. As these simplifications are tested against and so constrained by observations, current models are found to be reasonable for the purpose of solar irradiance reconstruction. This is demonstrated by the broad consistency between reconstructed solar irradiance and measurements (Sect. 3.3).

5 Summary

The TSI observations from the succession of radiometers sent into space since 1978 readily reveal solar cycle modulation. The clear detection of such modulations, only about 0.1 % of the overall level, is a remarkable achievement. The records from the various instruments do, however, differ in terms of the absolute level and the apparent amplitude of solar cycle variation. This is chiefly from the difficulty in accounting for instrument degradation. While the absolute radiometry of present-day instruments is converging due to the collaborative efforts of various teams, significant uncertainty persists over the long-term stability. This is evident in the conflicting decadal trends exhibited by the three published TSI composites.

Like TSI, ultraviolet (120 to 400 nm) solar irradiance has been monitored from space, almost without interruption, since 1978. Spectrometry is obviously a more complicated measurement. Not surprisingly, the uncertainty in the absolute radiometry and the amplitude of solar cycle variation is more severe than with TSI. Compounded by the wavelength dependence of instrumental influences, this translates into uncertainty in the spectral dependence of the cyclical variability. The problem is particularly acute above 240 nm and between measurements from the SORCE satellite and preceding missions.

The SIM instrument onboard SORCE provides what is still the only extended (2003 to 2011) record of SSI spanning the ultraviolet to the infrared (240 to 2416 nm) available. The measurements from the first few years of operation (2003 to 2008) saw ultraviolet solar irradiance declining almost twice as rapidly as TSI and visible solar irradiance ascending, in apparent anti-phase with the solar cycle. These trends conflict with projections from other measurements and models. Looking at the full period, the overall trend shows no obvious solar cycle modulation. The total flux recorded by the instrument, which surveys a wavelength range responsible for more than 97 % of the power in solar radiative flux, also fails to replicate the solar cycle variation evident in TSI.

Satellite monitoring of solar irradiance has been accompanied by the development of models aimed at recreating the observed variability. Solar irradiance is modulated by photospheric magnetism from its effect on the thermal structure and consequently the radiant

behaviour of the solar surface and atmosphere. Models of solar irradiance based on the assumption that variations at timescales greater than a day are driven by solar surface magnetism have achieved considerable success in replicating observations.

There are two broad categories of solar irradiance models, termed proxy and semi-empirical. Proxy models are based on the regression of indices of solar activity to solar irradiance observations. Semi-empirical models employ the intensity spectra of solar surface features calculated from semi-empirical model atmospheres with spectral synthesis codes. These intensity spectra are combined with the apparent surface coverage of the various features, derived from index data or full-disc observations, to reconstruct the solar spectrum.

We discussed the present-day models capable of returning the spectrum over the ultraviolet to the infrared: NRLSSI, SATIRE-S, SRPM, OAR and COSI. Apart from the NRLSSI, these models adopt the semi-empirical approach.

In the regression of index data to solar irradiance observations, certain proxy models including the ultraviolet segment of NRLSSI restrict the fitting to the rotational variability to factor out any bias from the long-term uncertainty of the solar irradiance measurements employed. In doing so, these models implicitly assume that the relationship between chromospheric indices, utilized in these models as a proxy of facular brightening, and solar irradiance at rotational timescales is applicable to longer timescales. Likely a consequence of the fact that the relationship between chromospheric indices and solar irradiance is really non-linear, the amplitude of solar cycle variation in the ultraviolet in the NRLSSI is weaker than in other present-day models.

Another limitation of the proxy approach is the fact that the reconstructed solar irradiance adopts the variability of the index records used in the reconstruction, along with the associated uncertainty. We argued that the long-term uncertainty of Mg II index data might be the reason why the NRLSSI does not replicate the secular decline between the 1996 and 2008 solar cycle minima in VIRGO TSI radiometry.

The SRPM reconstruction of solar irradiance presented by Fontenla et al. (2011) is the only one where visible flux varied in anti-phase with the solar cycle, in qualitative agreement with early SIM observations. This was achieved with modifications to the Fontenla et al. (2009) model atmospheres. However, the TSI from the reconstruction failed to replicate the solar cycle variation in measured TSI. The other models reviewed see visible solar irradiance varying in-phase with the solar cycle and reproduced TSI variability, including the solar cycle modulation, with reasonable success. Significantly, the OAR computation is, apart from the use of the Fontenla et al. (2009) model atmospheres without any modifications, largely analogous to the Fontenla et al. (2011) study in terms of the approach.

Considering the role of photospheric magnetism in driving variations in solar irradiance, the increase in the visible registered by SIM during its early operation, coming at a time where solar activity is declining, requires that small-scale magnetic concentrations be darker than the quiet Sun in this spectral region. However, our current understanding of the radiant properties of these solar surface features point to the converse.

Apart from the NRLSSI, the semi-empirical model SATIRE-S, recently updated by Yeo et al. (2014b), gives the only other daily reconstruction of the solar spectrum spanning the ultraviolet to the infrared from present-day models to extend multiple solar cycles, covering 1974 to 2013. Of the three divergent TSI composites, the model found the greatest success in replicating the solar cycle variation in the PMOD composite. The TSI reconstruction is also a good match to present-day measurements, reproducing about 96 % of the variability in the PMO6V record and the secular decline between the 1996 and 2008 solar cycle minima in VIRGO radiometry. The SSI reconstruction replicates the solar cycle variation in the ultraviolet solar irradiance observations from the UARS and SORCE missions very closely

below 180 nm. As the amplitude of solar cycle variation is poorly constrained in available SSI measurements at longer wavelengths, particularly above 240 nm, SATIRE-S, as with all other models, cannot exactly replicate SORCE solar cycle variation very well there. The amplitude of solar cycle variation in the reconstruction does however, match closely to the empirical model of Morrill et al. (2011), which represents an approximation of SUSIM-like SSI with the stability corrected to that of the Mg II index. The model also replicates the solar cycle variation in the LASP Lyman- α composite and the secular decline between the 1996 and 2008 solar cycle minima in the IUP Mg II index composite.

The intensity spectra of solar surface features employed in present-day semi-empirical models are derived from one-dimensional model atmospheres which do not capture all the complexities of the radiant behaviour of the solar surface and atmosphere. Three-dimensional model atmospheres, though increasingly realistic, still cannot reproduce observations at all heights. Their development is impeded by the limited availability of high spatial resolution observations and the challenge in understanding instrumental influences on apparent radiance. Current semi-empirical models account for non-LTE effects either empirically by offsetting/rescaling reconstructed spectra to measured SSI or directly by employing non-LTE spectral synthesis codes, neither of which is exact. Constrained by observations, the intensity spectra of solar surface features generated from one-dimensional model atmospheres and present non-LTE schemes, are still somewhat reliable for the intended purpose. This is demonstrated by the broad consistency between the various semi-empirical models and their success in replicating measurements.

The direct observation of solar irradiance is a challenging endeavour. At present, the body of spaceborne measurements is still afflicted by uncertainties in the absolute radiometry, secular variation and spectral dependence of the cyclical variability. However, one cannot discount the considerable progress made over the past four decades with the collective effort of the community. A good example is the collaborative efforts which led to the convergence of ACRIM3, TIM and PREMOS absolute TSI radiometry. Models of solar irradiance based on solar surface magnetism have proved to be an able complement, augmenting our understanding of the observations and the physical processes underlying solar cycle variation in solar irradiance. While open questions remain, continual observational and modelling efforts will undoubtedly see the emergence of a more cohesive picture of solar cycle variation in solar irradiance.

Acknowledgements We are thankful to Yvonne Unruh for her help in preparing Fig. 7, and Ilaria Ermoli and Karl-Heinz Glassmeier for the helpful discussions. The authors are also grateful to the International Space Science Institute for their invitation to and tremendous hospitality over the ‘The Solar Activity Cycle: Physical Causes And Consequences’ workshop. Acknowledgment goes to the various individuals and teams responsible for the observations and models featured in this review. K.L.Y. is a postgraduate fellow of the International Max Planck Research School for Solar System Science. This work is partly supported by the German Federal Ministry of Education and Research under project 01LG1209A and the Ministry of Education of Korea through the BK21 plus program of the National Research Foundation, NRF.

References

- C.G. Abbot, F.E. Fowle, L.B. Aldrich, Chapter VI. *Ann. Astrophys. Obs. Smithsonian. Inst.* **4**, 177–215 (1923)
- N. Afram, Y.C. Unruh, S.K. Solanki, M. Schüssler, A. Lagg, A. Vögler, Intensity contrast from MHD simulations and HINODE observations. *Astron. Astrophys.* **526**, A120 (2011). doi:[10.1051/0004-6361/201015582](https://doi.org/10.1051/0004-6361/201015582)
- W.T. Ball, Y.C. Unruh, N.A. Krivova, S.K. Solanki, J.W. Harder, Solar irradiance variability: a six-year comparison between SORCE observations and the SATIRE model. *Astron. Astrophys.* **530**, A71 (2011). doi:[10.1051/0004-6361/201016189](https://doi.org/10.1051/0004-6361/201016189)

- W.T. Ball, Y.C. Unruh, N.A. Krivova, S.K. Solanki, T. Wenzler, D.J. Mortlock, A.H. Jaffe, Reconstruction of total solar irradiance 1974–2009. *Astron. Astrophys.* **541**, A27 (2012). doi:[10.1051/0004-6361/201118702](https://doi.org/10.1051/0004-6361/201118702)
- W.T. Ball, N.A. Krivova, Y.C. Unruh, J.D. Haigh, S.K. Solanki, A new SATIRE-S spectral solar irradiance dataset for solar cycles 21–23 and its implications for stratospheric ozone. *J. Atmos. Sci.* (2014, submitted)
- L.A. Balmaceda, S.K. Solanki, N.A. Krivova, S. Foster, A homogeneous database of sunspot areas covering more than 130 years. *J. Geophys. Res.* **114**, 7104 (2009). doi:[10.1029/2009JA014299](https://doi.org/10.1029/2009JA014299)
- P. Barthol, A. Gandorfer, S.K. Solanki, M. Schüssler, B. Chares, W. Curdt, W. Deutsch, A. Feller, D. Germerott, B. Grauf, K. Heerlein, J. Hirzberger, M. Kolleck, R. Meller, R. Müller, T.L. Riethmüller, G. Tomasch, M. Knölker, B.W. Lites, G. Card, D. Elmore, J. Fox, A. Lecinski, P. Nelson, R. Summers, A. Watt, V. Martínez Pillet, J.A. Bonet, W. Schmidt, T. Berkefeld, A.M. Title, V. Domingo, J.L. Gasent Blesa, J.C. Del Toro Iniesta, A. López Jiménez, A. Álvarez-Herrero, L. Sabau-Graziati, C. Widani, P. Haberler, K. Hárstel, D. Kampf, T. Levin, I. Pérez Grande, A. Sanz-Andrés, E. Schmidt, The SUNRISE mission. *Sol. Phys.* **268**, 1–34 (2011). doi:[10.1007/s11207-010-9662-9](https://doi.org/10.1007/s11207-010-9662-9)
- G.E. Brueckner, K.L. Edlow, L.E. Floyd IV, J.L. Lean, M.E. Vanhoosier, The Solar Ultraviolet Spectral Irradiance Monitor (SUSIM) experiment on board the Upper Atmosphere Research Satellite (UARS). *J. Geophys. Res.* **98**, 10695 (1993). doi:[10.1029/93JD00410](https://doi.org/10.1029/93JD00410)
- J.J. Butler, B.C. Johnson, J.P. Rice, E.L. Shirley, R.A. Barnes, Sources of differences in on-orbit total solar irradiance measurements and description of a proposed laboratory intercomparison. *J. Res. Natl. Inst. Stand. Technol.* **113**, 187–203 (2008)
- M. Carlsson, R.F. Stein, Å. Nordlund, G.B. Scharmer, Observational manifestations of solar magnetoconvection: center-to-limb variation. *Astrophys. J. Lett.* **610**, 137–140 (2004). doi:[10.1086/423305](https://doi.org/10.1086/423305)
- G.A. Chapman, A.M. Cookson, J.J. Dobias, Variations in total solar irradiance during solar cycle 22. *J. Geophys. Res.* **101**, 13541–13548 (1996). doi:[10.1029/96JA00683](https://doi.org/10.1029/96JA00683)
- G.A. Chapman, A.M. Cookson, D.G. Preminger, Comparison of TSI from SORCE TIM with SFO ground-based photometry. *Sol. Phys.* **276**, 35–41 (2012). doi:[10.1007/s11207-011-9867-6](https://doi.org/10.1007/s11207-011-9867-6)
- G.A. Chapman, A.M. Cookson, D.G. Preminger, Modeling total solar irradiance with San Fernando Observatory ground-based photometry: comparison with ACRIM, PMOD, and RMIB composites. *Sol. Phys.* **283**, 295–305 (2013). doi:[10.1007/s11207-013-0233-8](https://doi.org/10.1007/s11207-013-0233-8)
- P. Charbonneau, Dynamo models of the solar cycle. *Living Rev. Sol. Phys.* **7**, 3 (2010). doi:[10.12942/lrsp-2010-3](https://doi.org/10.12942/lrsp-2010-3)
- J.-F. Cossette, P. Charbonneau, P.K. Smolarkiewicz, Cyclic thermal signature in a global MHD simulation of solar convection. *Astrophys. J. Lett.* **777**, 29 (2013). doi:[10.1088/2041-8205/777/2/L29](https://doi.org/10.1088/2041-8205/777/2/L29)
- R.L. Coulter, J.R. Kuhn, RISE/PSPT as an experiment to study active region irradiance and luminosity evolution, in *Solar Active Region Evolution: Comparing Models with Observations*, ed. by K.S. Balasubramaniam, G.W. Simon. *Astr. Soc. P.*, vol. 68 (1994), p. 37
- S. Danilovic, A. Gandorfer, A. Lagg, M. Schüssler, S.K. Solanki, A. Vögler, Y. Katsukawa, S. Tsuneta, The intensity contrast of solar granulation: comparing Hinode SP results with MHD simulations. *Astron. Astrophys.* **484**, L17–L20 (2008). doi:[10.1051/0004-6361:200809857](https://doi.org/10.1051/0004-6361:200809857)
- S. Danilovic, D. Röhrbein, R.H. Cameron, M. Schüssler, On the relation between continuum brightness and magnetic field in solar active regions. *Astron. Astrophys.* **550**, A118 (2013). doi:[10.1051/0004-6361/201219726](https://doi.org/10.1051/0004-6361/201219726)
- M.T. DeLand, R.P. Cebula, Solar UV activity at solar cycle 21 and 22 minimum from NOAA-9 SBUV/2 Data. *Sol. Phys.* **177**, 105–116 (1998). doi:[10.1023/A:1004931218139](https://doi.org/10.1023/A:1004931218139)
- M.T. DeLand, R.P. Cebula, Creation of a composite solar ultraviolet irradiance data set. *J. Geophys. Res.* **113**(A12), 11103 (2008). doi:[10.1029/2008JA013401](https://doi.org/10.1029/2008JA013401)
- M.T. DeLand, R.P. Cebula, Solar UV variations during the decline of cycle 23. *J. Atmos. Sol.-Terr. Phys.* **77**, 225–234 (2012). doi:[10.1016/j.jastp.2012.01.007](https://doi.org/10.1016/j.jastp.2012.01.007)
- S. Dewitte, D. Crommelynck, A. Joukoff, Total solar irradiance observations from DIARAD/VIRGO. *J. Geophys. Res.* **109**, 2102 (2004a). doi:[10.1029/2002JA009694](https://doi.org/10.1029/2002JA009694)
- S. Dewitte, D. Crommelynck, S. Mekaoui, A. Joukoff, Measurement and uncertainty of the long-term total solar irradiance trend. *Sol. Phys.* **224**, 209–216 (2004b). doi:[10.1007/s11207-005-5698-7](https://doi.org/10.1007/s11207-005-5698-7)
- V. Domingo, I. Ermolli, P. Fox, C. Fröhlich, M. Haberleiter, N. Krivova, G. Kopp, W. Schmutz, S.K. Solanki, H.C. Spruit, Y. Unruh, A. Vögler, Solar surface magnetism and irradiance on time scales from days to the 11-year cycle. *Space Sci. Rev.* **145**, 337–380 (2009). doi:[10.1007/s11214-009-9562-1](https://doi.org/10.1007/s11214-009-9562-1)
- T. Dudok de Wit, S. Bruinisma, K. Shibasaki, Synoptic radio observations as proxies for upper atmosphere modelling. *J. Space Weather Space Clim.* **4**(26), 260000 (2014). doi:[10.1051/swsc/2014003](https://doi.org/10.1051/swsc/2014003)
- J.A. Eddy, The Maunder minimum. *Science* **192**, 1189–1202 (1976). doi:[10.1126/science.192.4245.1189](https://doi.org/10.1126/science.192.4245.1189)
- I. Ermolli, S. Criscuolo, F. Giorgi, Recent results from optical synoptic observations of the solar atmosphere with ground-based instruments. *Contrib. Astron. Obs. Skaln. Pleso* **41**, 73–84 (2011)

- I. Ermolli, M. Fofi, C. Bernacchia, F. Berrilli, B. Caccin, A. Egidi, A. Florio, The prototype RISE-PSPT instrument operating in Rome. *Sol. Phys.* **177**, 1–10 (1998). doi:[10.1023/A:1004932431519](https://doi.org/10.1023/A:1004932431519)
- I. Ermolli, B. Caccin, M. Centrone, V. Penza, Modeling solar irradiance variations through full-disk images and semi-empirical atmospheric models. *Mem. Soc. Astron. Ital.* **74**, 603 (2003)
- I. Ermolli, S. Criscuoli, M. Centrone, F. Giorgi, V. Penza, Photometric properties of facular features over the activity cycle. *Astron. Astrophys.* **465**, 305–314 (2007). doi:[10.1051/0004-6361/20065995](https://doi.org/10.1051/0004-6361/20065995)
- I. Ermolli, S. Criscuoli, H. Uitenbroek, F. Giorgi, M.P. Rast, S.K. Solanki, Radiative emission of solar features in the Ca II K line: comparison of measurements and models. *Astron. Astrophys.* **523**, A55 (2010). doi:[10.1051/0004-6361/201014762](https://doi.org/10.1051/0004-6361/201014762)
- I. Ermolli, K. Matthes, T. Dudok de Wit, N.A. Krivova, K. Tourpali, M. Weber, Y.C. Unruh, L. Gray, U. Langematz, P. Pilewskie, E. Rozanov, W. Schmutz, A. Shapiro, S.K. Solanki, T.N. Woods, Recent variability of the solar spectral irradiance and its impact on climate modelling. *Atmos. Chem. Phys.* **13**, 3945–3977 (2013). doi:[10.5194/acp-13-3945-2013](https://doi.org/10.5194/acp-13-3945-2013)
- A. Fehlmann, G. Kopp, W. Schmutz, R. Winkler, W. Finsterle, N. Fox, Fourth world radiometric reference to SI radiometric scale comparison and implications for on-orbit measurements of the total solar irradiance. *Metrologia* **49**, 34 (2012). doi:[10.1088/0026-1394/49/2/S34](https://doi.org/10.1088/0026-1394/49/2/S34)
- M. Fligge, S.K. Solanki, Y.C. Unruh, Modelling irradiance variations from the surface distribution of the solar magnetic field. *Astron. Astrophys.* **353**, 380–388 (2000)
- L.E. Floyd, J.W. Cook, L.C. Herring, P.C. Crane, SUSIM'S 11-year observational record of the solar UV irradiance. *Adv. Space Res.* **31**, 2111–2120 (2003). doi:[10.1016/S0273-1177\(03\)00148-0](https://doi.org/10.1016/S0273-1177(03)00148-0)
- J.M. Fontenla, J. Harder, G. Rottman, T.N. Woods, G.M. Lawrence, S. Davis, The signature of solar activity in the infrared spectral irradiance. *Astrophys. J. Lett.* **605**, 85–88 (2004). doi:[10.1086/386335](https://doi.org/10.1086/386335)
- J.M. Fontenla, E. Avrett, G. Thuillier, J. Harder, Semiempirical models of the solar atmosphere. I. The quiet-and active Sun photosphere at moderate resolution. *Astrophys. J.* **639**, 441–458 (2006). doi:[10.1086/499345](https://doi.org/10.1086/499345)
- J.M. Fontenla, W. Curdt, M. Haberleiter, J. Harder, H. Tian, Semiempirical models of the solar atmosphere. III. Set of non-LTE models for far-ultraviolet/extreme-ultraviolet irradiance computation. *Astrophys. J.* **707**, 482–502 (2009). doi:[10.1088/0004-637X/707/1/482](https://doi.org/10.1088/0004-637X/707/1/482)
- J.M. Fontenla, J. Harder, W. Livingston, M. Snow, T. Woods, High-resolution solar spectral irradiance from extreme ultraviolet to far infrared. *J. Geophys. Res.* **116**(D15), 20108 (2011). doi:[10.1029/2011JD016032](https://doi.org/10.1029/2011JD016032)
- J. Fontenla, O.R. White, P.A. Fox, E.H. Avrett, R.L. Kurucz, Calculation of solar irradiances. I. Synthesis of the solar spectrum. *Astrophys. J.* **518**, 480–499 (1999). doi:[10.1086/307258](https://doi.org/10.1086/307258)
- P. Foukal, J. Lean, The influence of faculae on total solar irradiance and luminosity. *Astrophys. J.* **302**, 826–835 (1986). doi:[10.1086/164043](https://doi.org/10.1086/164043)
- P. Foukal, J. Lean, Magnetic modulation of solar luminosity by photospheric activity. *Astrophys. J.* **328**, 347–357 (1988). doi:[10.1086/166297](https://doi.org/10.1086/166297)
- P. Foukal, A. Ortiz, R. Schnerr, Dimming of the 17th century Sun. *Astrophys. J. Lett.* **733**, 38 (2011). doi:[10.1088/2041-8205/733/2/L38](https://doi.org/10.1088/2041-8205/733/2/L38)
- E.N. Frazier, Multi-channel magnetograph observations. III: Faculae. *Sol. Phys.* **21**, 42–53 (1971). doi:[10.1007/BF00155772](https://doi.org/10.1007/BF00155772)
- C. Fröhlich, Observations of irradiance variations. *Space Sci. Rev.* **94**, 15–24 (2000). doi:[10.1023/A:1026765712084](https://doi.org/10.1023/A:1026765712084)
- C. Fröhlich, Solar irradiance variability since 1978. Revision of the PMOD composite during Solar Cycle 21. *Space Sci. Rev.* **125**, 53–65 (2006). doi:[10.1007/s11214-006-9046-5](https://doi.org/10.1007/s11214-006-9046-5)
- C. Fröhlich, Evidence of a long-term trend in total solar irradiance. *Astron. Astrophys.* **501**, L27–L30 (2009). doi:[10.1051/0004-6361/200912318](https://doi.org/10.1051/0004-6361/200912318)
- C. Fröhlich, Solar radiometry. *ISSI Sci. Rep. Ser.* **9**, 525–540 (2010)
- C. Fröhlich, Total solar irradiance observations. *Surv. Geophys.* **33**, 453–473 (2012). doi:[10.1007/s10712-011-9168-5](https://doi.org/10.1007/s10712-011-9168-5)
- C. Fröhlich, Total solar irradiance: what have we learned from the last three cycles and the recent minimum? *Space Sci. Rev.* **176**, 237–252 (2013). doi:[10.1007/s11214-011-9780-1](https://doi.org/10.1007/s11214-011-9780-1)
- C. Fröhlich, J.M. Pap, H.S. Hudson, Improvement of the photometric sunspot index and changes of the disk-integrated sunspot contrast with time. *Sol. Phys.* **152**, 111–118 (1994). doi:[10.1007/BF01473192](https://doi.org/10.1007/BF01473192)
- C. Fröhlich, J. Romero, H. Roth, C. Wehrli, B.N. Andersen, T. Appourchaux, V. Domingo, U. Telljohann, G. Berthomieu, P. Delache, J. Provost, T. Toutain, D.A. Crommelync, A. Chevalier, A. Fichot, W. Däppen, D. Gough, T. Hoeksema, A. Jiménez, M.F. Gómez, J.M. Herreros, T.R. Cortés, A.R. Jones, J.M. Pap, R.C. Willson, VIRGO: experiment for helioseismology and solar irradiance monitoring. *Sol. Phys.* **162**, 101–128 (1995). doi:[10.1007/BF00733428](https://doi.org/10.1007/BF00733428)

- C. Fröhlich, D.A. Crommelync, C. Wehrli, M. Anklin, S. Dewitte, A. Fichot, W. Finsterle, A. Jiménez, A. Chevalier, H. Roth, In-flight performance of the VIRGO solar irradiance instruments on SOHO. *Sol. Phys.* **175**, 267–286 (1997). doi:[10.1023/A:1004929108864](https://doi.org/10.1023/A:1004929108864)
- U. Grossmann-Doerth, M. Knölker, M. Schüssler, S.K. Solanki, The deep layers of solar magnetic elements. *Astron. Astrophys.* **285**, 648–654 (1994)
- M. Haberreiter, W. Schmutz, I. Hubeny, NLTE model calculations for the solar atmosphere with an iterative treatment of opacity distribution functions. *Astron. Astrophys.* **492**, 833–840 (2008). doi:[10.1051/0004-6361:200809503](https://doi.org/10.1051/0004-6361/200809503)
- M. Haberreiter, N.A. Krivova, W. Schmutz, T. Wenzler, Reconstruction of the solar UV irradiance back to 1974. *Adv. Space Res.* **35**, 365–369 (2005). doi:[10.1016/j.asr.2005.04.039](https://doi.org/10.1016/j.asr.2005.04.039)
- J.W. Harder, J. Fontenla, G. Lawrence, T. Woods, G. Rottman, The spectral irradiance monitor: measurement equations and calibration. *Sol. Phys.* **230**, 169–204 (2005a). doi:[10.1007/s11207-005-1528-1](https://doi.org/10.1007/s11207-005-1528-1)
- J.W. Harder, G. Lawrence, J. Fontenla, G. Rottman, T. Woods, The spectral irradiance monitor: scientific requirements, instrument design, and operation modes. *Sol. Phys.* **230**, 141–167 (2005b). doi:[10.1007/s11207-005-5007-5](https://doi.org/10.1007/s11207-005-5007-5)
- J.W. Harder, J.M. Fontenla, P. Pilewskie, E.C. Richard, T.N. Woods, Trends in solar spectral irradiance variability in the visible and infrared. *Geophys. Res. Lett.* **36**, 7801 (2009). doi:[10.1029/2008GL036797](https://doi.org/10.1029/2008GL036797)
- D.H. Hathaway, The solar cycle. *Living Rev. Sol. Phys.* **7**, 1 (2010). doi:[10.12942/lrsp-2010-1](https://doi.org/10.12942/lrsp-2010-1)
- D.F. Heath, B.M. Schlessinger, The Mg 280-nm doublet as a monitor of changes in solar ultraviolet irradiance. *J. Geophys. Res.* **91**, 8672–8682 (1986). doi:[10.1029/JD091iD08p08672](https://doi.org/10.1029/JD091iD08p08672)
- J.R. Hickey, L.L. Stowe, H. Jacobowitz, P. Pellegrino, R.H. Maschhoff, F. House, T.H. Vonder Haar, Initial solar irradiance determinations from Nimbus 7 cavity radiometer measurements. *Science* **208**, 281–283 (1980). doi:[10.1126/science.208.4441.281](https://doi.org/10.1126/science.208.4441.281)
- R. Holzreuter, S.K. Solanki, Three-dimensional non-LTE radiative transfer effects in Fe I lines. II. Line formation in 3D radiation hydrodynamic simulations. *Astron. Astrophys.* **558**, A20 (2013). doi:[10.1051/0004-6361/201322135](https://doi.org/10.1051/0004-6361/201322135)
- D.V. Hoyt, H.L. Kyle, J.R. Hickey, R.H. Maschhoff, The NIMBUS 7 solar total irradiance—a new algorithm for its derivation. *J. Geophys. Res.* **97**, 51–63 (1992). doi:[10.1029/91JA02488](https://doi.org/10.1029/91JA02488)
- H.S. Hudson, Observed variability of the solar luminosity. *Annu. Rev. Astron. Astrophys.* **26**, 473–507 (1988). doi:[10.1146/annurev.aa.26.090188.002353](https://doi.org/10.1146/annurev.aa.26.090188.002353)
- H.S. Hudson, S. Silva, M. Woodard, R.C. Willson, The effects of sunspots on solar irradiance. *Sol. Phys.* **76**, 211–219 (1982). doi:[10.1007/BF00170984](https://doi.org/10.1007/BF00170984)
- H.P. Jones, T.L. Duvall Jr., J.W. Harvey, C.T. Mahaffey, J.D. Schwitters, J.E. Simmons, The NASA/NSO spectromagnetograph. *Sol. Phys.* **139**, 211–232 (1992). doi:[10.1007/BF00159149](https://doi.org/10.1007/BF00159149)
- S.L. Keil, T.W. Henry, B. Fleck, NSO/AFRL/Sac peak K-line monitoring program, in *Synoptic Solar Physics*, ed. by K.S. Balasubramaniam, J. Harvey, D. Rabin. ASP Conf. Ser., vol. 140 (1998), p. 301
- C.U. Keller, M. Schüssler, A. Vögler, V. Zakharov, On the origin of solar faculae. *Astrophys. J. Lett.* **607**, 59–62 (2004). doi:[10.1086/421553](https://doi.org/10.1086/421553)
- M. Knölker, U. Grossmann-Doerth, M. Schüssler, E. Weisshaar, Some developments in the theory of magnetic flux concentrations in the solar atmosphere. *Adv. Space Res.* **11**, 285–295 (1991). doi:[10.1016/0273-1177\(91\)90393-X](https://doi.org/10.1016/0273-1177(91)90393-X)
- P. Kobel, S.K. Solanki, J.M. Borrero, The continuum intensity as a function of magnetic field. I. Active region and quiet Sun magnetic elements. *Astron. Astrophys.* **531**, A112 (2011). doi:[10.1051/0004-6361/201016255](https://doi.org/10.1051/0004-6361/201016255)
- G. Kopp, G. Lawrence, The Total Irradiance Monitor (TIM): instrument design. *Sol. Phys.* **230**, 91–109 (2005). doi:[10.1007/s11207-005-7446-4](https://doi.org/10.1007/s11207-005-7446-4)
- G. Kopp, J.L. Lean, A new, lower value of total solar irradiance: evidence and climate significance. *Geophys. Res. Lett.* **38**, 1706 (2011). doi:[10.1029/2010GL045777](https://doi.org/10.1029/2010GL045777)
- G. Kopp, K. Heuerman, G. Lawrence, The Total Irradiance Monitor (TIM): instrument calibration. *Sol. Phys.* **230**, 111–127 (2005a). doi:[10.1007/s11207-005-7447-3](https://doi.org/10.1007/s11207-005-7447-3)
- G. Kopp, G. Lawrence, G. Rottman, The Total Irradiance Monitor (TIM): science results. *Sol. Phys.* **230**, 129–139 (2005b). doi:[10.1007/s11207-005-7433-9](https://doi.org/10.1007/s11207-005-7433-9)
- G. Kopp, K. Heuerman, D. Harber, G. Drake, The TSI radiometer facility: absolute calibrations for total solar irradiance instruments. *Proc. SPIE* **6677**, 667709 (2007). doi:[10.1117/12.734553](https://doi.org/10.1117/12.734553), 12 pp.
- G. Kopp, A. Fehlmann, W. Finsterle, D. Harber, K. Heuerman, R. Willson, Total solar irradiance data record accuracy and consistency improvements. *Metrologia* **49**, 29 (2012). doi:[10.1088/0026-1394/49/2/S29](https://doi.org/10.1088/0026-1394/49/2/S29)
- N.A. Krivova, S.K. Solanki, L. Floyd, Reconstruction of solar UV irradiance in cycle 23. *Astron. Astrophys.* **452**, 631–639 (2006). doi:[10.1051/0004-6361:20064809](https://doi.org/10.1051/0004-6361:20064809)
- N.A. Krivova, S.K. Solanki, Y.C. Unruh, Towards a long-term record of solar total and spectral irradiance. *J. Atmos. Sol.-Terr. Phys.* **73**, 223–234 (2011). doi:[10.1016/j.jastp.2009.11.013](https://doi.org/10.1016/j.jastp.2009.11.013)

- N.A. Krivova, S.K. Solanki, M. Fligge, Y.C. Unruh, Reconstruction of solar irradiance variations in cycle 23: is solar surface magnetism the cause? *Astron. Astrophys.* **399**, 1–4 (2003). doi:[10.1051/0004-6361:20030029](https://doi.org/10.1051/0004-6361:20030029)
- J.R. Kuhn, K.G. Libbrecht, R.H. Dicke, The surface temperature of the sun and changes in the solar constant. *Science* **242**, 908–911 (1988). doi:[10.1126/science.242.4880.908](https://doi.org/10.1126/science.242.4880.908)
- R. Kurucz, ATLAS9 stellar atmosphere programs and 2 km/s grid. Kurucz CD-ROM no. 13. (Smithsonian Astrophysical Observatory, Cambridge, 1993)
- A. Lagg, S.K. Solanki, T.L. Riethmüller, V. Martínez Pillet, M. Schüssler, J. Hirzberger, A. Feller, J.M. Borrero, W. Schmidt, J.C. del Toro Iniesta, J.A. Bonet, P. Barthol, T. Berkefeld, V. Domingo, A. Gandorfer, M. Knölker, A.M. Title, Fully resolved quiet-Sun magnetic flux tube observed with the SUNRISE/IMAX instrument. *Astrophys. J. Lett.* **723**, 164–168 (2010). doi:[10.1088/2041-8205/723/2/L164](https://doi.org/10.1088/2041-8205/723/2/L164)
- J. Lean, Evolution of the Sun's spectral irradiance since the Maunder minimum. *Geophys. Res. Lett.* **27**, 2425–2428 (2000). doi:[10.1029/2000GL000043](https://doi.org/10.1029/2000GL000043)
- J.L. Lean, M.T. DeLand, How does the Sun's spectrum vary? *J. Climate* **25**, 2555–2560 (2012). doi:[10.1175/JCLI-D-11-00571.1](https://doi.org/10.1175/JCLI-D-11-00571.1)
- J.L. Lean, G.J. Rottman, H.L. Kyle, T.N. Woods, J.R. Hickey, L.C. Puga, Detection and parameterization of variations in solar mid- and near-ultraviolet radiation (200–400 nm). *J. Geophys. Res.* **102**, 29939–29956 (1997). doi:[10.1029/97JD02092](https://doi.org/10.1029/97JD02092)
- R.B. Lee III, B.R. Barkstrom, R.D. Cess, Characteristics of the Earth radiation budget experiment solar monitors. *Appl. Opt.* **26**, 3090–3096 (1987). doi:[10.1364/AO.26.003090](https://doi.org/10.1364/AO.26.003090)
- R.B. Lee III, M.A. Gibson, R.S. Wilson, S. Thomas, Long-term total solar irradiance variability during sunspot cycle 22. *J. Geophys. Res.* **100**, 1667–1675 (1995). doi:[10.1029/94JA02897](https://doi.org/10.1029/94JA02897)
- J.R. Lemen, A.M. Title, D.J. Akin, P.F. Boerner, C. Chou, J.F. Drake, D.W. Duncan, C.G. Edwards, F.M. Friedlaender, G.F. Heyman, N.E. Hurlburt, N.L. Katz, G.D. Kushner, M. Levay, R.W. Lindgren, D.P. Mathur, E.L. McFeaters, S. Mitchell, R.A. Rehse, C.J. Schrijver, L.A. Springer, R.A. Stern, T.D. Tarbell, J.-P. Wuelser, C.J. Wolfson, C. Yanari, J.A. Bookbinder, P.N. Cheimets, D. Caldwell, E.E. Deluca, R. Gates, L. Golub, S. Park, W.A. Podgorski, R.I. Bush, P.H. Scherrer, M.A. Gummmin, P. Smith, G. Auken, P. Jerram, P. Pool, R. Soufli, D.L. Windt, S. Beardsley, M. Clapp, J. Lang, N. Waltham, The Atmospheric Imaging Assembly (AIA) on the Solar Dynamics Observatory (SDO). *Sol. Phys.* **275**, 17–40 (2012). doi:[10.1007/s11207-011-9776-8](https://doi.org/10.1007/s11207-011-9776-8)
- J. Lilensten, T. Dudok de Wit, M. Kretzschmar, P.-O. Amblard, S. Moussaoui, J. Abouharham, F. Auchère, Review on the solar spectral variability in the EUV for space weather purposes. *Ann. Geophys.* **26**, 269–279 (2008). doi:[10.5194/angeo-26-269-2008](https://doi.org/10.5194/angeo-26-269-2008)
- W.C. Livingston, J. Harvey, A.K. Pierce, D. Schrage, B. Gillespie, J. Simmons, C. Slaughter, Kitt peak 60-cm vacuum telescope. *Appl. Opt.* **15**, 33–39 (1976). doi:[10.1364/AO.15.000033](https://doi.org/10.1364/AO.15.000033)
- S.K. Mathew, V. Zakharov, S.K. Solanki, Stray light correction and contrast analysis of Hinode broad-band images. *Astron. Astrophys.* **501**, L19–L22 (2009). doi:[10.1051/0004-6361/200911975](https://doi.org/10.1051/0004-6361/200911975)
- S.K. Mathew, V. Martínez Pillet, S.K. Solanki, N.A. Krivova, Properties of sunspots in cycle 23. I. Dependence of brightness on sunspot size and cycle phase. *Astron. Astrophys.* **465**, 291–304 (2007). doi:[10.1051/0004-6361:20066356](https://doi.org/10.1051/0004-6361:20066356)
- W.E. McClintock, G.J. Rottman, T.N. Woods, Solar-Stellar Irradiance Comparison Experiment II (SOLSTICE II): instrument concept and design. *Sol. Phys.* **230**, 225–258 (2005). doi:[10.1007/s11207-005-7432-x](https://doi.org/10.1007/s11207-005-7432-x)
- S. Mekaoui, S. Dewitte, Total solar irradiance measurement and modelling during cycle 23. *Sol. Phys.* **247**, 203–216 (2008). doi:[10.1007/s11207-007-9070-y](https://doi.org/10.1007/s11207-007-9070-y)
- A.W. Merkel, J.W. Harder, D.R. Marsh, A.K. Smith, J.M. Fontenla, T.N. Woods, The impact of solar spectral irradiance variability on middle atmospheric ozone. *Geophys. Res. Lett.* **38**, 13802 (2011). doi:[10.1029/2011GL047561](https://doi.org/10.1029/2011GL047561)
- W.E. Mitchell Jr., W.C. Livingston, Line-blanketing variations in the irradiance spectrum of the sun from maximum to minimum of the solar cycle. *Astrophys. J.* **372**, 336–348 (1991). doi:[10.1086/169980](https://doi.org/10.1086/169980)
- R. Moll, R.H. Cameron, M. Schüssler, Vortices, shocks, and heating in the solar photosphere: effect of a magnetic field. *Astron. Astrophys.* **541**, A68 (2011). doi:[10.1051/0004-6361/201218866](https://doi.org/10.1051/0004-6361/201218866)
- J.S. Morrill, K.P. Dere, C.M. Korendyke, The sources of solar ultraviolet variability between 2765 and 2885 Å: Mg I, Mg II, Si I, and continuum. *Astrophys. J.* **557**, 854–863 (2001). doi:[10.1086/321683](https://doi.org/10.1086/321683)
- J.S. Morrill, L. Floyd, D. McMullin, The solar ultraviolet spectrum estimated using the Mg II index and Ca II K disk activity. *Sol. Phys.* **269**, 253–267 (2011). doi:[10.1007/s11207-011-9708-7](https://doi.org/10.1007/s11207-011-9708-7)
- R. Munro, C. Anderson, J. Callies, J. Callies, E. Corpaccioli, R. Lang, A. Lefebvre, Y. Livschitz, A. Pérez Albiñana, GOME-2 on MetOp, in *Atmospheric Science Conference*. ESA Sp. Pub., vol. 628 (2006)
- Z.E. Musielak, P. Ulmschneider, Atmospheric oscillations in solar magnetic flux tubes. I. Excitation by longitudinal tube waves and random pulses. *Astron. Astrophys.* **400**, 1057–1064 (2003). doi:[10.1051/0004-6361:20030023](https://doi.org/10.1051/0004-6361:20030023)

- A. Ortiz, S.K. Solanki, V. Domingo, M. Fligge, B. Sanahuja, On the intensity contrast of solar photospheric faculae and network elements. *Astron. Astrophys.* **388**, 1036–1047 (2002). doi:[10.1051/0004-6361:20020500](https://doi.org/10.1051/0004-6361:20020500)
- L. Oster, K.H. Schatten, S. Sofia, Solar irradiance variations due to active regions. *Astrophys. J.* **256**, 768–773 (1982). doi:[10.1086/159949](https://doi.org/10.1086/159949)
- J. Paganan, M. Weber, J. Burrows, Solar variability from 240 to 1750 nm in terms of faculae brightening and sunspot darkening from SCIAMACHY. *Astrophys. J.* **700**, 1884–1895 (2009). doi:[10.1088/0004-637X/700/2/1884](https://doi.org/10.1088/0004-637X/700/2/1884)
- V. Penza, B. Caccin, I. Ermolli, M. Centrone, M.T. Gomez, Modeling solar irradiance variations through PSPT images and semiempirical models, in *Solar Variability as an Input to the Earth's Environment*, ed. by A. Wilson. ESA Sp. Pub., vol. 535 (2003), pp. 299–302
- D.G. Preminger, S.R. Walton, G.A. Chapman, Photometric quantities for solar irradiance modelling. *J. Geophys. Res.* **107**, 1354 (2002). doi:[10.1029/2001JA009169](https://doi.org/10.1029/2001JA009169)
- M. Rempel, R. Schlichenmaier, Sunspot modelling: from simplified models to radiative MHD simulations. *Living Rev. Sol. Phys.* **8**, 3 (2011). doi:[10.12942/lrsp-2011-3](https://doi.org/10.12942/lrsp-2011-3)
- E.C. Richard, D. Harber, J.W. Harder, P. Pilewskie, S. Brown, A. Smith, K. Lykke, Future long-term measurements of solar spectral irradiance by JPSS TSIS. AGU Fall Meeting Abstracts 917 (2011)
- T.L. Riethmüller, S.K. Solanki, V. Martínez Pillet, J. Hirzberger, A. Feller, J.A. Bonet, N. Bello González, M. Franz, M. Schüssler, P. Barthol, T. Berkefeld, J.C. del Toro Iniesta, V. Domingo, A. Gandorfer, M. Knölker, W. Schmidt, Bright points in the quiet Sun as observed in the visible and near-UV by the balloon-borne observatory SUNRISE. *Astrophys. J. Lett.* **723**, 169–174 (2010). doi:[10.1088/2041-8205/723/2/L169](https://doi.org/10.1088/2041-8205/723/2/L169)
- T.L. Riethmüller, S.K. Solanki, S.V. Berdyugina, M. Schüssler, V. Martínez Pillet, A. Feller, A. Gandorfer, J. Hirzberger, Comparison of solar photospheric bright points between SUNRISE observations and MHD simulations. *Astron. Astrophys.* (2014). doi:[10.1051/0004-6361/201423892](https://doi.org/10.1051/0004-6361/201423892)
- D. Röhrbein, R. Cameron, M. Schüssler, Is there a non-monotonic relation between photospheric brightness and magnetic field strength in solar plage regions? *Astron. Astrophys.* **532**, A140 (2011). doi:[10.1051/0004-6361/201117090](https://doi.org/10.1051/0004-6361/201117090)
- G. Rottman, The SORCE mission. *Sol. Phys.* **230**, 7–25 (2005). doi:[10.1007/s11207-005-8112-6](https://doi.org/10.1007/s11207-005-8112-6)
- G. Rottman, T. Woods, M. Snow, G. DeToma, The solar cycle variation in ultraviolet irradiance. *Adv. Space Res.* **27**, 1927–1932 (2001). doi:[10.1016/S0273-1177\(01\)00272-1](https://doi.org/10.1016/S0273-1177(01)00272-1)
- G.B. Rybicki, D.G. Hummer, An accelerated lambda iteration method for multilevel radiative transfer. I—Non-overlapping lines with background continuum. *Astron. Astrophys.* **245**, 171–181 (1991)
- G.B. Rybicki, D.G. Hummer, An accelerated lambda iteration method for multilevel radiative transfer. II—Overlapping transitions with full continuum. *Astron. Astrophys.* **262**, 209–215 (1992)
- P.H. Scherrer, R.S. Bogart, R.I. Bush, J.T. Hoeksema, A.G. Kosovichev, J. Schou, W. Rosenberg, L. Springer, T.D. Tarbell, A. Title, C.J. Wolfson, I. Zayer (MDI Engineering Team), The solar oscillations investigation—Michelson Doppler imager. *Sol. Phys.* **162**, 129–188 (1995). doi:[10.1007/BF00733429](https://doi.org/10.1007/BF00733429)
- W. Schmutz, A. Fehlmann, G. Hülse, P. Meindl, R. Winkler, G. Thuillier, P. Blattner, F. Buisson, T. Egorova, W. Finsterle, N. Fox, J. Gröbner, J. Hochedez, S. Koller, M. Meftah, M. Meissonnier, S. Nyeki, D. Pfiffner, H. Roth, E. Rozanov, M. Spescha, C. Wehrli, L. Werner, J.U. Wyss, The PREMOS/PICARD instrument calibration. *Metrologia* **46**(4), 202 (2009)
- W. Schmutz, A. Fehlmann, W. Finsterle, G. Kopp, G. Thuillier, Total solar irradiance measurements with PREMOS/PICARD. *AIP Conf. Proc.* **1531**(1), 624–627 (2013). doi:[10.1063/1.4804847](https://doi.org/10.1063/1.4804847)
- R.S. Schnerr, H.C. Spruit, The brightness of magnetic field concentrations in the quiet Sun. *Astron. Astrophys.* **532**, A136 (2011). doi:[10.1051/0004-6361/201015976](https://doi.org/10.1051/0004-6361/201015976)
- J. Schou, P.H. Scherrer, R.I. Bush, R. Wachter, S. Couvidat, M.C. Rabello-Soares, R.S. Bogart, J.T. Hoeksema, Y. Liu, T.L. Duvall, D.J. Akin, B.A. Allard, J.W. Miles, R. Rairden, R.A. Shine, T.D. Tarbell, A.M. Title, C.J. Wolfson, D.F. Elmore, A.A. Norton, S. Tomczyk, Design and ground calibration of the Helioseismic and Magnetic Imager (HMI) Instrument on the Solar Dynamics Observatory (SDO). *Sol. Phys.* **275**, 229–259 (2012). doi:[10.1007/s11207-011-9842-2](https://doi.org/10.1007/s11207-011-9842-2)
- A.D. Seleznyov, S.K. Solanki, N.A. Krivova, Modelling solar irradiance variability on time scales from minutes to months. *Astron. Astrophys.* **532**, A108 (2011). doi:[10.1051/0004-6361/200811138](https://doi.org/10.1051/0004-6361/200811138)
- A.I. Shapiro, W. Schmutz, M. Schoell, M. Haberreiter, E. Rozanov, NLTE solar irradiance modelling with the COSI code. *Astron. Astrophys.* **517**, A48 (2010). doi:[10.1051/0004-6361/200913987](https://doi.org/10.1051/0004-6361/200913987)
- A.I. Shapiro, W. Schmutz, E. Rozanov, M. Schoell, M. Haberreiter, A.V. Shapiro, S. Nyeki, A new approach to the long-term reconstruction of the solar irradiance leads to large historical solar forcing. *Astron. Astrophys.* **529**, A67 (2011). doi:[10.1051/0004-6361/201016173](https://doi.org/10.1051/0004-6361/201016173)
- A.V. Shapiro, A.I. Shapiro, M. Dominique, I.E. Dammasch, C. Wehrli, E. Rozanov, W. Schmutz, Detection of solar rotational variability in the Large Yield Radiometer (LYRA) 190–222 nm spectral band. *Sol. Phys.* **286**, 289–301 (2013). doi:[10.1007/s11207-012-0029-2](https://doi.org/10.1007/s11207-012-0029-2)

- J. Skupin, M. Weber, S. Noël, H. Bovensmann, J.P. Burrows, GOME and SCIAMACHY solar measurements: solar spectral irradiance and Mg II solar activity proxy indicator. *Mem. Soc. Astron. Ital.* **76**, 1038 (2005a)
- J. Skupin, S. Noël, M.W. Wuttke, M. Gottwald, H. Bovensmann, M. Weber, J.P. Burrows, SCIAMACHY solar irradiance observation in the spectral range from 240 to 2380 nm. *Adv. Space Res.* **35**, 370–375 (2005b). doi:[10.1016/j.asr.2005.03.036](https://doi.org/10.1016/j.asr.2005.03.036)
- J. Skupin, M. Weber, H. Bovensmann, J.P. Burrows, The Mg II solar activity proxy indicator derived from GOME and SCIAMACHY, in *Proceedings of the 2004 Envisat & ERS Symposium*. ESA Sp. Pub., vol. 572 (2005c)
- E.V.P. Smith, D.M. Gottlieb, Solar flux and its variations. *NASA Spec. Publ.* **366**, 97–117 (1975)
- M. Snow, W.E. McClintock, G. Rottman, T.N. Woods, Solar-Stellar Irradiance Comparison Experiment II (SOLSTICE II): examination of the solar stellar comparison technique. *Sol. Phys.* **230**, 295–324 (2005a). doi:[10.1007/s11207-005-8763-3](https://doi.org/10.1007/s11207-005-8763-3)
- M. Snow, W.E. McClintock, T.N. Woods, O.R. White, J.W. Harder, G. Rottman, The Mg II Index from SORCE. *Sol. Phys.* **230**, 325–344 (2005b). doi:[10.1007/s11207-005-6879-0](https://doi.org/10.1007/s11207-005-6879-0)
- H. Socas-Navarro, A high-resolution three-dimensional model of the solar photosphere derived from Hinode observations. *Astron. Astrophys.* **529**, A37 (2011). doi:[10.1051/0004-6361/201015805](https://doi.org/10.1051/0004-6361/201015805)
- S.K. Solanki, Smallscale solar magnetic fields—an overview. *Space Sci. Rev.* **63**, 1–188 (1993). doi:[10.1007/BF00749277](https://doi.org/10.1007/BF00749277)
- S.K. Solanki, Sunspots: an overview. *Astron. Astrophys. Rev.* **11**, 153–286 (2003). doi:[10.1007/s00159-003-0018-4](https://doi.org/10.1007/s00159-003-0018-4)
- S.K. Solanki, N.A. Krivova, Solar irradiance variations: from current measurements to long-term estimates. *Sol. Phys.* **224**, 197–208 (2004). doi:[10.1007/s11207-005-6499-8](https://doi.org/10.1007/s11207-005-6499-8)
- S.K. Solanki, Y.C. Unruh, A model of the wavelength dependence of solar irradiance variations. *Astron. Astrophys.* **329**, 747–753 (1998)
- S.K. Solanki, B. Inhester, M. Schüssler, The solar magnetic field. *Rep. Prog. Phys.* **69**, 563–668 (2006). doi:[10.1088/0034-4885/69/3/R02](https://doi.org/10.1088/0034-4885/69/3/R02)
- S.K. Solanki, N.A. Krivova, J.D. Haigh, Solar irradiance variability and climate. *Annu. Rev. Astron. Astrophys.* **51**, 311–351 (2013). doi:[10.1146/annurev-astro-082812-141007](https://doi.org/10.1146/annurev-astro-082812-141007)
- S.K. Solanki, M. Schüssler, M. Fligge, Secular variation of the Sun's magnetic flux. *Astron. Astrophys.* **383**, 706–712 (2002). doi:[10.1051/0004-6361:20011790](https://doi.org/10.1051/0004-6361:20011790)
- S.K. Solanki, O. Steiner, M. Bünte, G. Murphy, S.R.O. Ploner, On the reliability of Stokes diagnostics of magnetic elements away from solar disc centre. *Astron. Astrophys.* **333**, 721–731 (1998)
- S.K. Solanki, P. Barthol, S. Danilovic, A. Feller, A. Gandorfer, J. Hinzberger, T.L. Riethmüller, M. Schüssler, J.A. Bonet, V. Martínez Pillet, J.C. del Toro Iniesta, V. Domingo, J. Palacios, M. Knölker, N. Bello González, T. Berkefeld, M. Franz, W. Schmidt, A.M. Title, SUNRISE: Instrument, mission, data, and first results. *Astrophys. J. Lett.* **723**, 127–133 (2010). doi:[10.1088/2041-8205/723/2/L127](https://doi.org/10.1088/2041-8205/723/2/L127)
- H.C. Spruit, Pressure equilibrium and energy balance of small photospheric fluxtubes. *Sol. Phys.* **50**, 269–295 (1976). doi:[10.1007/BF00155292](https://doi.org/10.1007/BF00155292)
- H.C. Spruit, B. Roberts, Magnetic flux tubes on the sun. *Nature* **304**, 401–406 (1983). doi:[10.1038/304401a0](https://doi.org/10.1038/304401a0)
- H.C. Spruit, C. Zwaan, The size dependence of contrasts and numbers of small magnetic flux tubes in an active region. *Sol. Phys.* **70**, 207–228 (1981). doi:[10.1007/BF00151329](https://doi.org/10.1007/BF00151329)
- O. Steiner, Radiative properties of magnetic elements. II. Center to limb variation of the appearance of photospheric faculae. *Astron. Astrophys.* **430**, 691–700 (2005). doi:[10.1051/0004-6361:20041286](https://doi.org/10.1051/0004-6361:20041286)
- K.F. Tapping, Recent solar radio astronomy at centimeter wavelengths—the temporal variability of the 10.7-cm flux. *J. Geophys. Res.* **92**, 829–838 (1987). doi:[10.1029/JD092iD01p00829](https://doi.org/10.1029/JD092iD01p00829)
- K.F. Tapping, The 10.7 cm solar radio flux (F10.7). *Adv. Space Res.* **11**(7), 394–406 (2013). doi:[10.1002/swe.20064](https://doi.org/10.1002/swe.20064)
- G. Thuillier, T. Foujols, D. Bolsée, D. Gillotay, M. Hersé, W. Peetermans, W. Decuyper, H. Mandel, P. Sperfeld, S. Pape, D.R. Taubert, J. Hartmann, SOLAR/SOLSPEC: scientific objectives, instrument performance and its absolute calibration using a blackbody as primary standard source. *Sol. Phys.* **257**, 185–213 (2009). doi:[10.1007/s11207-009-9361-6](https://doi.org/10.1007/s11207-009-9361-6)
- G. Thuillier, M. Deland, A. Shapiro, W. Schmutz, D. Bolsée, S.M.L. Melo, The solar spectral irradiance as a function of the Mg II index for atmosphere and climate modelling. *Sol. Phys.* **277**, 245–266 (2012). doi:[10.1007/s11207-011-9912-5](https://doi.org/10.1007/s11207-011-9912-5)
- G. Thuillier, D. Bolsée, G. Schmidtke, T. Foujols, B. Nikutowski, A.I. Shapiro, R. Brunner, M. Weber, C. Erhardt, M. Hersé, D. Gillotay, W. Peetermans, W. Decuyper, N. Pereira, M. Haberreiter, H. Mandel, W. Schmutz, The solar irradiance spectrum at solar activity minimum between solar cycles 23 and 24. *Sol. Phys.* **289**, 1931–1958 (2014a). doi:[10.1007/s11207-013-0461-y](https://doi.org/10.1007/s11207-013-0461-y)
- G. Thuillier, G. Schmidtke, C. Erhardt, B. Nikutowski, A.I. Shapiro, C. Bolduc, J. Lean, N.A. Krivova, P. Charbonneau, G. Cessateur, M. Haberreiter, S. Melo, V. Delouille, B. Mampaey, K.L. Yeo,

- W. Schmutz, Solar spectral irradiance variability in November/December 2012: comparison of observations by instruments on the International Space Station and models. *Sol. Phys.* (2014b, submitted)
- K.P. Topka, T.D. Tarbell, A.M. Title, Properties of the smallest solar magnetic elements. II. Observations versus hot wall models of faculae. *Astrophys. J.* **484**, 479 (1997). doi:[10.1086/304295](https://doi.org/10.1086/304295)
- H. Uitenbroek, The effect of coherent scattering on radiative losses in the solar Ca II K line. *Astrophys. J.* **565**, 1312–1322 (2002). doi:[10.1086/324698](https://doi.org/10.1086/324698)
- H. Uitenbroek, S. Crisculoli, Why one-dimensional models fail in the diagnosis of average spectra from inhomogeneous stellar atmospheres. *Astrophys. J.* **736**, 69 (2011). doi:[10.1088/0004-637X/736/1/69](https://doi.org/10.1088/0004-637X/736/1/69)
- Y.C. Unruh, W.T. Ball, N.A. Krivova, Solar irradiance models and measurements: a comparison in the 220–240 nm wavelength band. *Surv. Geophys.* **33**, 475–481 (2012). doi:[10.1007/s10712-011-9166-7](https://doi.org/10.1007/s10712-011-9166-7)
- Y.C. Unruh, S.K. Solanki, M. Fligge, The spectral dependence of facular contrast and solar irradiance variations. *Astron. Astrophys.* **345**, 635–642 (1999)
- Y.C. Unruh, N.A. Krivova, S.K. Solanki, J.W. Harder, G. Kopp, Spectral irradiance variations: comparison between observations and the SATIRE model on solar rotation time scales. *Astron. Astrophys.* **486**, 311–323 (2008). doi:[10.1051/0004-6361:20078421](https://doi.org/10.1051/0004-6361:20078421)
- Y.C. Unruh, S.K. Solanki, M. Schüssler, A. Vögler, D. Garcia-Alvarez, Towards long-term solar irradiance modelling: network contrasts from magneto-convection simulations, in *15th Cambridge Workshop on Cool Stars, Stellar Systems, and the Sun*, ed. by E. Stempels. AIP Conf. Proc., vol. 1094 (2009), pp. 768–771. doi:[10.1063/1.3099228](https://doi.org/10.1063/1.3099228)
- R.A. Viereck, L.C. Puga, The NOAA Mg II core-to-wing solar index: construction of a 20-year time series of chromospheric variability from multiple satellites. *J. Geophys. Res.* **104**, 9995–10006 (1999). doi:[10.1029/1998JA900163](https://doi.org/10.1029/1998JA900163)
- R.A. Viereck, L.E. Floyd, P.C. Crane, T.N. Woods, B.G. Knapp, G. Rottman, M. Weber, L.C. Puga, M.T. DeLand, A composite Mg II index spanning from 1978 to 2003. *Adv. Space Res.* **2**, 10005 (2004). doi:[10.1029/2004SW000084](https://doi.org/10.1029/2004SW000084)
- A. Vögler, S. Shelyag, M. Schüssler, F. Cattaneo, T. Emonet, T. Linde, Simulations of magneto-convection in the solar photosphere. Equations, methods, and results of the MURaM code. *Astron. Astrophys.* **429**, 335–351 (2005). doi:[10.1051/0004-6361:20041507](https://doi.org/10.1051/0004-6361:20041507)
- M. Weber, J.P. Burrows, R.P. Cebula, GOME solar UV/VIS irradiance measurements between 1995 and 1997—first results on proxy solar activity studies. *Sol. Phys.* **177**, 63–77 (1998). doi:[10.1023/A:1005030909779](https://doi.org/10.1023/A:1005030909779)
- S. Wedemeyer-Böhm, Point spread functions for the Solar optical telescope onboard Hinode. *Astron. Astrophys.* **487**, 399–412 (2008). doi:[10.1051/0004-6361:200809819](https://doi.org/10.1051/0004-6361:200809819)
- C. Wehrli, W. Schmutz, A.I. Shapiro, Correlation of spectral solar irradiance with solar activity as measured by VIRGO. *Astron. Astrophys.* **556**, L3 (2013). doi:[10.1051/0004-6361/201220864](https://doi.org/10.1051/0004-6361/201220864)
- T. Wenzler, Reconstruction of solar irradiance variations in cycles 21–23 based on surface magnetic fields. Ph.D. Thesis (University of Göttingen, 2005)
- T. Wenzler, S.K. Solanki, N.A. Krivova, Reconstructed and measured total solar irradiance: is there a secular trend between 1978 and 2003? *Geophys. Res. Lett.* **36**, 11102 (2009). doi:[10.1029/2009GL037519](https://doi.org/10.1029/2009GL037519)
- T. Wenzler, S.K. Solanki, N.A. Krivova, C. Fröhlich, Reconstruction of solar irradiance variations in cycles 21–23 based on surface magnetic fields. *Astron. Astrophys.* **460**, 583–595 (2006). doi:[10.1051/0004-6361:20065752](https://doi.org/10.1051/0004-6361:20065752)
- R.C. Willson, Active cavity radiometer type IV. *Appl. Opt.* **18**, 179–188 (1979). doi:[10.1364/AO.18.000179](https://doi.org/10.1364/AO.18.000179)
- R.C. Willson, H.S. Hudson, Solar luminosity variations in solar cycle 21. *Nature* **332**, 810–812 (1988). doi:[10.1038/332810a0](https://doi.org/10.1038/332810a0)
- R.C. Willson, A.V. Mordvinov, Secular total solar irradiance trend during solar cycles 21–23. *Geophys. Res. Lett.* **30**, 1199 (2003). doi:[10.1029/2002GL016038](https://doi.org/10.1029/2002GL016038)
- R.C. Willson, S. Gulikis, M. Janssen, H.S. Hudson, G.A. Chapman, Observations of solar irradiance variability. *Science* **211**, 700–702 (1981). doi:[10.1126/science.211.4483.700](https://doi.org/10.1126/science.211.4483.700)
- C.L. Wolff, J.R. Hickey, Solar irradiance change and special longitudes due to r-modes. *Science* **235**, 1631–1633 (1987). doi:[10.1126/science.235.4796.1631](https://doi.org/10.1126/science.235.4796.1631)
- T.N. Woods, Recent advances in observations and modelling of the solar ultraviolet and X-ray spectral irradiance. *Adv. Space Res.* **42**, 895–902 (2008). doi:[10.1016/j.asr.2007.09.026](https://doi.org/10.1016/j.asr.2007.09.026)
- T.N. Woods, G. Kopp, P.C. Chamberlin, Contributions of the solar ultraviolet irradiance to the total solar irradiance during large flares. *J. Geophys. Res.* **111**(A10), 10 (2006). doi:[10.1029/2005JA011507](https://doi.org/10.1029/2005JA011507)
- T.N. Woods, W.K. Tobiska, G.J. Rottman, J.R. Worden, Improved solar Lyman α irradiance modelling from 1947 through 1999 based on UARS observations. *J. Geophys. Res.* **105**, 27195–27216 (2000). doi:[10.1029/2000JA000051](https://doi.org/10.1029/2000JA000051)
- T.N. Woods, P.C. Chamberlin, J.W. Harder, R.A. Hock, M. Snow, F.G. Eparvier, J. Fontenla, W.E. McClintock, E.C. Richard, Solar Irradiance Reference Spectra (SIRS) for the 2008 Whole Heliosphere Interval (WHI). *Geophys. Res. Lett.* **36**, 1101 (2009). doi:[10.1029/2008GL036373](https://doi.org/10.1029/2008GL036373)

- K.L. Yeo, S.K. Solanki, N.A. Krivova, Intensity contrast of solar network and faculae. *Astron. Astrophys.* **550**, A95 (2013). doi:[10.1051/0004-6361/201220682](https://doi.org/10.1051/0004-6361/201220682)
- K.L. Yeo, A. Feller, S.K. Solanki, S. Couvidat, S. Danilovic, N.A. Krivova, Point spread function of SDO/HMI and the effects of stray light correction on the apparent properties of solar surface phenomena. *Astron. Astrophys.* **561**, A22 (2014a). doi:[10.1051/0004-6361/201322502](https://doi.org/10.1051/0004-6361/201322502)
- K.L. Yeo, N.A. Krivova, S.K. Solanki, K.H. Glassmeier, Reconstruction of total and spectral solar irradiance since 1974 based on KPVT, SoHO/MDI and SDO/HMI observations. *Astron. Astrophys.* (2014b, submitted)

Bibliography

- Abbot, C. G., Fowle, F. E., Aldrich, L. B., 1923, Chapter VI., *Annals of the Astrophysical Observatory of the Smithsonian Institution*, 4, 177–215
- Afram, N., Unruh, Y. C., Solanki, S. K., Schüssler, M., Lagg, A., Vögler, A., 2011, Intensity contrast from MHD simulations and HINODE observations, *Astron. Astrophys.*, 526, A120
- Albregtsen, F., Maltby, P., 1981, Solar cycle variation of sunspot intensity, *Sol. Phys.*, 71, 269–283
- Archinal, B. A., A’Hearn, M. F., Bowell, E., Conrad, A., Consolmagno, G. J., Courtin, R., Fukushima, T., Hestroffer, D., Hilton, J. L., Krasinsky, G. A., Neumann, G., Oberst, J., Seidelmann, P. K., Stooke, P., Tholen, D. J., Thomas, P. C., Williams, I. P., 2011, Report of the IAU Working Group on Cartographic Coordinates and Rotational Elements: 2009, *Celest. Mech. Dyn. Astron.*, 109, 101–135
- Arge, C. N., Hildner, E., Pizzo, V. J., Harvey, J. W., 2002, Two solar cycles of nonincreasing magnetic flux, *J. Geophys. Res.*, 107, 1319
- Avrett, E. H., Loeser, R., 1992, The PANDORA Atmosphere Program (Invited Review), in *Cool Stars, Stellar Systems, and the Sun*, (Eds.) M. S. Giampapa, J. A. Bookbinder, vol. 26 of ASP Conf. Ser., p. 489
- Ball, W. T., Unruh, Y. C., Krivova, N. A., Solanki, S. K., Harder, J. W., 2011, Solar irradiance variability: a six-year comparison between SORCE observations and the SATIRE model, *Astron. Astrophys.*, 530, A71
- Ball, W. T., Unruh, Y. C., Krivova, N. A., Solanki, S. K., Wenzler, T., Mortlock, D. J., Jaffe, A. H., 2012, Reconstruction of total solar irradiance 1974-2009, *Astron. Astrophys.*, 541, A27
- Ball, W. T., Krivova, N. A., Unruh, Y. C., Haigh, J. D., Solanki, S. K., 2014, A new SATIRE-S spectral solar irradiance dataset for solar cycles 21-23 and its implications for stratospheric ozone, *J. Atmos. Sci.*, submitted
- Balmaceda, L. A., Solanki, S. K., Krivova, N. A., Foster, S., 2009, A homogeneous database of sunspot areas covering more than 130 years, *J. Geophys. Res.*, 114, A07104
- Barthol, P., Gandorfer, A., Solanki, S. K., Schüssler, M., Chares, B., Curdt, W., Deutsch, W., Feller, A., Germerott, D., Grauf, B., Heerlein, K., Hirzberger, J., Kolleck, M.,

- Meller, R., Müller, R., Riethmüller, T. L., Tomasch, G., Knölker, M., Lites, B. W., Card, G., Elmore, D., Fox, J., Lecinski, A., Nelson, P., Summers, R., Watt, A., Martínez Pillet, V., Bonet, J. A., Schmidt, W., Berkefeld, T., Title, A. M., Domingo, V., Gasent Blesa, J. L., Del Toro Iniesta, J. C., López Jiménez, A., Álvarez-Herrero, A., Sabau-Graziati, L., Widani, C., Haberler, P., Härtel, K., Kampf, D., Levin, T., Pérez Grande, I., Sanz-Andrés, A., Schmidt, E., 2011, The Sunrise Mission, *Sol. Phys.*, 268, 1–34
- Beck, C., Rezaei, R., 2009, The magnetic flux of the quiet Sun internetwork as observed with the Tenerife infrared polarimeter, *Astron. Astrophys.*, 502, 969–979
- Berger, T. E., Title, A. M., 1996, On the Dynamics of Small-Scale Solar Magnetic Elements, *ApJ*, 463, 365
- Berger, T. E., Rouppe van der Voort, L., Löfdahl, M., 2007, Contrast Analysis of Solar Faculae and Magnetic Bright Points, *ApJ*, 661, 1272–1288
- Borrero, J. M., Tomczyk, S., Kubo, M., Socas-Navarro, H., Schou, J., Couvidat, S., Bogart, R., 2011, VFISV: Very Fast Inversion of the Stokes Vector for the Helioseismic and Magnetic Imager, *Sol. Phys.*, 273, 267–293
- Brandenburg, A., Jennings, R. L., Nordlund, Å., Rieutord, M., Stein, R. F., Tuominen, I., 1996, Magnetic structures in a dynamo simulation, *Journal of Fluid Mechanics*, 306, 325–352
- Brueckner, G. E., Edlow, K. L., Floyd, IV, L. E., Lean, J. L., Vanhoosier, M. E., 1993, The solar ultraviolet spectral irradiance monitor (SUSIM) experiment on board the Upper Atmosphere Research Satellite (UARS), *J. Geophys. Res.*, 98, 10 695
- Brusa, R. W., Fröhlich, C., 1986, Absolute radiometers (PMO6) and their experimental characterization, *Appl. Opt.*, 25, 4173–4180
- Bumba, V., Howard, R., 1965, Large-Scale Distribution of Solar Magnetic Fields., *ApJ*, 141, 1502
- Bünte, M., Solanki, S. K., Steiner, O., 1993, Centre-to-limb variation of the Stokes V asymmetry in solar magnetic flux tubes, *Astron. Astrophys.*, 268, 736–748
- Butler, J. J., Johnson, B. C., Rice, J. P., Shirley, E. L., Barnes, R. A., 2008, Sources of differences in on-orbit total solar irradiance measurements and description of a proposed laboratory intercomparison, *J. Res. Natl. Inst. Stand. Technol.*, 113, 187–203
- Carbon, D. F., Barbuy, B., Kraft, R. P., Suntzeff, N. B., Friel, E. D., 1984, Carbon and nitrogen abundances in a sample of 70 metal-poor dwarfs., *PASP*, 96, 786
- Carlsson, M., Stein, R. F., Nordlund, Å., Scharmer, G. B., 2004, Observational Manifestations of Solar Magnetoconvection: Center-to-Limb Variation, *ApJ*, 610, L137–L140
- Castelli, F., 2005, ATLAS12: how to use it, *Memorie della Societa Astronomica Italiana Supplementi*, 8, 25

- Chapman, G. A., 1980, Variations in the solar constant due to solar active regions, *ApJ*, 242, L45–L48
- Chapman, G. A., Cookson, A. M., Dobias, J. J., 1994, Observations of changes in the bolometric contrast of sunspots, *ApJ*, 432, 403–408
- Chapman, G. A., Cookson, A. M., Dobias, J. J., 1996, Variations in total solar irradiance during solar cycle 22, *J. Geophys. Res.*, 101, 13 541–13 548
- Chapman, G. A., Cookson, A. M., Preminger, D. G., 2012, Comparison of TSI from SORCE TIM with SFO Ground-Based Photometry, *Sol. Phys.*, 276, 35–41
- Chapman, G. A., Cookson, A. M., Preminger, D. G., 2013, Modeling Total Solar Irradiance with San Fernando Observatory Ground-Based Photometry: Comparison with ACRIM, PMOD, and RMIB Composites, *Sol. Phys.*, 283, 295–305
- Charbonneau, P., 2010, Dynamo Models of the Solar Cycle, *Living Rev. Solar Phys.*, 7, 3
- Collados, M., Martínez Pillet, V., Ruiz Cobo, B., del Toro Iniesta, J. C., Vázquez, M., 1994, Observed differences between large and small sunspots, *Astron. Astrophys.*, 291, 622–634
- Cossette, J.-F., Charbonneau, P., Smolarkiewicz, P. K., 2013, Cyclic Thermal Signature in a Global MHD Simulation of Solar Convection, *ApJ*, 777, L29
- Coulter, R. L., Kuhn, J. R., 1994, RISE/PSPT as an Experiment to Study Active Region Irradiance and Luminosity Evolution, in *Solar Active Region Evolution: Comparing Models with Observations*, (Eds.) K. S. Balasubramanian, G. W. Simon, vol. 68 of *Astr. Soc. P.*, p. 37
- Couvidat, S., 2011, Calculation of observables from hmi data, <http://hmi.stanford.edu/doc/HMI-S031.pdf>, July 15, 2011 revision
- Couvidat, S., Rajaguru, S. P., Wachter, R., Sankarasubramanian, K., Schou, J., Scherrer, P. H., 2012, Line-of-Sight Observables Algorithms for the Helioseismic and Magnetic Imager (HMI) Instrument Tested with Interferometric Bidimensional Spectrometer (IBIS) Observations, *Sol. Phys.*, 278, 217–240
- Crommelynck, D., Domingo, V., 1984, Solar Irradiance Observations, *Science*, 225, 180–181
- Danilovic, S., Gandorfer, A., Lagg, A., Schüssler, M., Solanki, S. K., Vögler, A., Katsukawa, Y., Tsuneta, S., 2008, The intensity contrast of solar granulation: comparing Hinode SP results with MHD simulations, *Astron. Astrophys.*, 484, L17–L20
- Danilovic, S., Schüssler, M., Solanki, S. K., 2010, Probing quiet Sun magnetism using MURaM simulations and Hinode/SP results: support for a local dynamo, *Astron. Astrophys.*, 513, A1

- Danilovic, S., Röhrbein, D., Cameron, R., Schüssler, M., 2013, On the relation between continuum brightness and magnetic field in solar active regions, *Astron. Astrophys.*, 550, A118
- de Boer, C. R., Kneer, F., Nesis, A., 1992, Speckle observations of solar granulation, *Astron. Astrophys.*, 257, L4–L6
- de Toma, G., Chapman, G. A., Cookson, A. M., Preminger, D., 2013, Temporal Stability of Sunspot Umbral Intensities: 1986–2012, *ApJ*, 771, L22
- DeForest, C. E., Martens, P. C. H., Wills-Davey, M. J., 2009, Solar Coronal Structure and Stray Light in TRACE, *ApJ*, 690, 1264–1271
- Deland, M. T., Cebula, R. P., 1998, Solar UV Activity at Solar Cycle 21 and 22 Minimum from NOAA-9 SBUV/2 Data, *Sol. Phys.*, 177, 105–116
- DeLand, M. T., Cebula, R. P., 2008, Creation of a composite solar ultraviolet irradiance data set, *J. Geophys. Res.*, 113, A11103
- DeLand, M. T., Cebula, R. P., 2012, Solar UV variations during the decline of Cycle 23, *J. Atmos. Sol.-Terr. Phy.*, 77, 225–234
- DeLand, M. T., Floyd, L. E., Rottman, G. J., Pap, J. M., 2004, Status of UARS solar UV irradiance data, *Adv. Space Res.*, 34, 243–250
- Dewitte, S., Crommelynck, D., Joukoff, A., 2004a, Total solar irradiance observations from DIARAD/VIRGO, *J. Geophys. Res.*, 109, A02102
- Dewitte, S., Crommelynck, D., Mekaoui, S., Joukoff, A., 2004b, Measurement and Uncertainty of the Long-Term Total Solar Irradiance Trend, *Sol. Phys.*, 224, 209–216
- Dikpati, M., Gilman, P. A., 2009, Flux-Transport Solar Dynamos, *Space Sci. Rev.*, 144, 67–75
- Domingo, V., Ermolli, I., Fox, P., Fröhlich, C., Haberleiter, M., Krivova, N., Kopp, G., Schmutz, W., Solanki, S. K., Spruit, H. C., Unruh, Y., Vögler, A., 2009, Solar Surface Magnetism and Irradiance on Time Scales from Days to the 11-Year Cycle, *Space Sci. Rev.*, 145, 337–380
- Dorch, S. B. F., Nordlund, Å., 2001, On the transport of magnetic fields by solar-like stratified convection, *Astron. Astrophys.*, 365, 562–570
- Dudok de Wit, T., 2011, A method for filling gaps in solar irradiance and solar proxy data, *Astron. Astrophys.*, 533, A29
- Eddy, J. A., 1976, The Maunder Minimum, *Science*, 192, 1189–1202
- Eggleton, P., 2011, *Evolutionary Processes in Binary and Multiple Stars*, (Cambridge University Press)
- Ekberg, U., Eriksson, K., Gustafsson, B., 1986, Line blanketing in model atmospheres of carbon stars, *Astron. Astrophys.*, 167, 304–310

- Ermolli, I., Fofi, M., Bernacchia, C., Berrilli, F., Caccin, B., Egidi, A., Florio, A., 1998, The Prototype Rise-Pspt Instrument Operating in Rome, *Sol. Phys.*, 177, 1–10
- Ermolli, I., Criscuoli, S., Centrone, M., Giorgi, F., Penza, V., 2007, Photometric properties of facular features over the activity cycle, *Astron. Astrophys.*, 465, 305–314
- Ermolli, I., Criscuoli, S., Uitenbroek, H., Giorgi, F., Rast, M. P., Solanki, S. K., 2010, Radiative emission of solar features in the Ca II K line: comparison of measurements and models, *Astron. Astrophys.*, 523, A55
- Ermolli, I., Criscuoli, S., Giorgi, F., 2011, Recent results from optical synoptic observations of the solar atmosphere with ground-based instruments, *Cont. Astron. Obs. Skalnat' Pleso*, 41, 73–84
- Ermolli, I., Matthes, K., Dudok de Wit, T., Krivova, N. A., Tourpali, K., Weber, M., Unruh, Y. C., Gray, L., Langematz, U., Pilewskie, P., Rozanov, E., Schmutz, W., Shapiro, A., Solanki, S. K., Woods, T. N., 2013, Recent variability of the solar spectral irradiance and its impact on climate modelling, *Atmos. Chem. Phys.*, 13, 3945–3977
- Fehlmann, A., Kopp, G., Schmutz, W., Winkler, R., Finsterle, W., Fox, N., 2012, Fourth World Radiometric Reference to SI radiometric scale comparison and implications for on-orbit measurements of the total solar irradiance, *Metrologia*, 49, 34
- Fligge, M., Solanki, S. K., Unruh, Y. C., 2000, Modelling irradiance variations from the surface distribution of the solar magnetic field, *Astron. Astrophys.*, 353, 380–388
- Floyd, L. E., Cook, J. W., Herring, L. C., Crane, P. C., 2003, SUSIM'S 11-year observational record of the solar UV irradiance, *Adv. Space Res.*, 31, 2111–2120
- Fontenla, J., White, O. R., Fox, P. A., Avrett, E. H., Kurucz, R. L., 1999, Calculation of Solar Irradiances. I. Synthesis of the Solar Spectrum, *ApJ*, 518, 480–499
- Fontenla, J. M., Avrett, E. H., Loeser, R., 1993, Energy balance in the solar transition region. III - Helium emission in hydrostatic, constant-abundance models with diffusion, *ApJ*, 406, 319–345
- Fontenla, J. M., Harder, J., Rottman, G., Woods, T. N., Lawrence, G. M., Davis, S., 2004, The Signature of Solar Activity in the Infrared Spectral Irradiance, *ApJ*, 605, L85–L88
- Fontenla, J. M., Avrett, E., Thuillier, G., Harder, J., 2006, Semiempirical Models of the Solar Atmosphere. I. The Quiet- and Active Sun Photosphere at Moderate Resolution, *ApJ*, 639, 441–458
- Fontenla, J. M., Curdt, W., Haberreiter, M., Harder, J., Tian, H., 2009, Semiempirical Models of the Solar Atmosphere. III. Set of Non-LTE Models for Far-Ultraviolet/Extreme-Ultraviolet Irradiance Computation, *ApJ*, 707, 482–502
- Fontenla, J. M., Harder, J., Livingston, W., Snow, M., Woods, T., 2011, High-resolution solar spectral irradiance from extreme ultraviolet to far infrared, *J. Geophys. Res.*, 116, D20108

- Foukal, P., Lean, J., 1986, The influence of faculae on total solar irradiance and luminosity, *ApJ*, 302, 826–835
- Foukal, P., Bernasconi, P., Eaton, H., Rust, D., 2004, Broadband Measurements of Facular Photometric Contrast Using the Solar Bolometric Imager, *ApJ*, 611, L57–L60
- Foukal, P., Ortiz, A., Schnerr, R., 2011, Dimming of the 17th Century Sun, *ApJ*, 733, L38
- Frazier, E. N., 1971, Multi-Channel Magnetograph Observations. III: Faculae, *Sol. Phys.*, 21, 42–53
- Fröhlich, C., 2000, Observations of Irradiance Variations, *Space Sci. Rev.*, 94, 15–24
- Fröhlich, C., 2006, Solar Irradiance Variability Since 1978. Revision of the PMOD Composite during Solar Cycle 21, *Space Sci. Rev.*, 125, 53–65
- Fröhlich, C., 2009, Evidence of a long-term trend in total solar irradiance, *Astron. Astrophys.*, 501, L27–L30
- Fröhlich, C., 2010, Solar radiometry, *ISSI Scientific Reports Series*, 9, 525–540
- Fröhlich, C., 2012, Total Solar Irradiance Observations, *Surv. Geophys.*, 33, 453–473
- Fröhlich, C., 2013, Total Solar Irradiance: What Have We Learned from the Last Three Cycles and the Recent Minimum?, *Space Sci. Rev.*, 176, 237–252
- Fröhlich, C., Pap, J. M., Hudson, H. S., 1994, Improvement of the photometric sunspot index and changes of the disk-integrated sunspot contrast with time, *Sol. Phys.*, 152, 111–118
- Fröhlich, C., Romero, J., Roth, H., Wehrli, C., Andersen, B. N., Appourchaux, T., Domingo, V., Telljohann, U., Berthomieu, G., Delache, P., Provost, J., Toutain, T., Crommelynck, D. A., Chevalier, A., Fichot, A., Däppen, W., Gough, D., Hoeksema, T., Jiménez, A., Gómez, M. F., Herreros, J. M., Cortés, T. R., Jones, A. R., Pap, J. M., Willson, R. C., 1995, VIRGO: Experiment for Helioseismology and Solar Irradiance Monitoring, *Sol. Phys.*, 162, 101–128
- Fröhlich, C., Crommelynck, D. A., Wehrli, C., Anklin, M., Dewitte, S., Fichot, A., Finsterle, W., Jiménez, A., Chevalier, A., Roth, H., 1997, In-Flight Performance of the Virgo Solar Irradiance Instruments on SOHO, *Sol. Phys.*, 175, 267–286
- Frutiger, C., Solanki, S. K., Fligge, M., Bruls, J. H. M. J., 2000, Properties of the solar granulation obtained from the inversion of low spatial resolution spectra, *Astron. Astrophys.*, 358, 1109–1121
- Gandorfer, A., Grauf, B., Barthol, P., Riethmüller, T. L., Solanki, S. K., Chares, B., Deutsch, W., Ebert, S., Feller, A., Germerott, D., Heerlein, K., Heinrichs, J., Hirche, D., Hirzberger, J., Kolleck, M., Meller, R., Müller, R., Schäfer, R., Tomasch, G., Knölker, M., Martínez Pillet, V., Bonet, J. A., Schmidt, W., Berkefeld, T., Feger, B., Heidecke, F., Soltau, D., Tischenberg, A., Fischer, A., Title, A., Anwand, H., Schmidt, E., 2011, The

- Filter Imager SuFI and the Image Stabilization and Light Distribution System ISLiD of the Sunrise Balloon-Borne Observatory: Instrument Description, *Sol. Phys.*, 268, 35–55
- Gilman, P. A., Morrow, C. A., Deluca, E. E., 1989, Angular momentum transport and dynamo action in the sun - Implications of recent oscillation measurements, *ApJ*, 338, 528–537
- Giovanelli, R. G., 1980, An exploratory two-dimensional study of the coarse structure of network magnetic fields, *Sol. Phys.*, 68, 49–69
- Gonsalves, R. A., 1982, Phase retrieval and diversity in adaptive optics, *Opt. Eng.*, 21, 829–832
- Gray, L. J., Beer, J., Geller, M., Haigh, J. D., Lockwood, M., Matthes, K., Cubasch, U., Fleitmann, D., Harrison, G., Hood, L., Luterbacher, J., Meehl, G. A., Shindell, D., van Geel, B., White, W., 2010, Solar influences on climate, *Rev. Geophys.*, 48, RG4001, ISSN 1944-9208
- Grossmann-Doerth, U., Knölker, M., Schüssler, M., Solanki, S. K., 1994, The deep layers of solar magnetic elements, *Astron. Astrophys.*, 285, 648–654
- Haberreiter, M., Krivova, N. A., Schmutz, W., Wenzler, T., 2005, Reconstruction of the solar UV irradiance back to 1974, *Adv. Space Res.*, 35, 365–369
- Haberreiter, M., Schmutz, W., Hubeny, I., 2008, NLTE model calculations for the solar atmosphere with an iterative treatment of opacity distribution functions, *Astron. Astrophys.*, 492, 833–840
- Haigh, J. D., 1994, The role of stratospheric ozone in modulating the solar radiative forcing of climate, *Nature*, 370, 544–546
- Haigh, J. D., 2007, The Sun and the Earth's Climate, *Living Rev. Solar Phys.*, 4, 2
- Haigh, J. D., Winning, A. R., Toumi, R., Harder, J. W., 2010, An influence of solar spectral variations on radiative forcing of climate, *Nature*, 467, 696–699
- Hale, G. E., Nicholson, S. B., 1925, The Law of Sun-Spot Polarity, *ApJ*, 62, 270
- Hale, G. E., Ellerman, F., Nicholson, S. B., Joy, A. H., 1919, The Magnetic Polarity of Sun-Spots, *ApJ*, 49, 153
- Handy, B. N., Bruner, M. E., Tarbell, T. D., Title, A. M., Wolfson, C. J., Laforce, M. J., Oliver, J. J., 1998, UV Observations with the Transition Region and Coronal Explorer, *Sol. Phys.*, 183, 29–43
- Harder, J., Lawrence, G., Fontenla, J., Rottman, G., Woods, T., 2005a, The Spectral Irradiance Monitor: Scientific Requirements, Instrument Design, and Operation Modes, *Sol. Phys.*, 230, 141–167

- Harder, J. W., Fontenla, J., Lawrence, G., Woods, T., Rottman, G., 2005b, The Spectral Irradiance Monitor: Measurement Equations and Calibration, *Sol. Phys.*, 230, 169–204
- Harder, J. W., Fontenla, J. M., Pilewskie, P., Richard, E. C., Woods, T. N., 2009, Trends in solar spectral irradiance variability in the visible and infrared, *Geophys. Res. Lett.*, 36, L07801
- Hathaway, D. H., 2010, The Solar Cycle, *Living Rev. Solar Phys.*, 7, 1
- Hathaway, D. H., Wilson, R. M., Reichmann, E. J., 2002, Group Sunspot Numbers: Sunspot Cycle Characteristics, *Sol. Phys.*, 211, 357–370
- Heath, D. F., Schlesinger, B. M., 1986, The Mg 280-nm doublet as a monitor of changes in solar ultraviolet irradiance, *J. Geophys. Res.*, 91, 8672–8682
- Hickey, J. R., Stowe, L. L., Jacobowitz, H., Pellegrino, P., Maschhoff, R. H., House, F., Vonder Haar, T. H., 1980, Initial Solar Irradiance Determinations from Nimbus 7 Cavity Radiometer Measurements, *Science*, 208, 281–283
- Hirzberger, J., Wiehr, E., 2005, Solar limb faculae, *Astron. Astrophys.*, 438, 1059–1065
- Hirzberger, J., Gizon, L., Solanki, S. K., Duvall, T. L., 2008, Structure and Evolution of Supergranulation from Local Helioseismology, *Sol. Phys.*, 251, 417–437
- Hirzberger, J., Feller, A., Riethmüller, T. L., Schüssler, M., Borrero, J. M., Afram, N., Unruh, Y. C., Berdyugina, S. V., Gandorfer, A., Solanki, S. K., Barthol, P., Bonet, J. A., Martínez Pillet, V., Berkefeld, T., Knölker, M., Schmidt, W., Title, A. M., 2010, Quiet-sun Intensity Contrasts in the Near-ultraviolet as Measured from SUNRISE, *ApJ*, 723, L154–L158
- Holzreuter, R., Solanki, S. K., 2013, Three-dimensional non-LTE radiative transfer effects in Fe I lines. II. Line formation in 3D radiation hydrodynamic simulations, *Astron. Astrophys.*, 558, A20
- Hoyt, D. V., Schatten, K. H., 1997, A New Reconstruction of Solar Activity, 1610-1995, in National Aeronautics and Space Administration Report, (Ed.) J. Vallerga
- Hoyt, D. V., Kyle, H. L., Hickey, J. R., Maschhoff, R. H., 1992, The NIMBUS 7 solar total irradiance - A new algorithm for its derivation, *J. Geophys. Res.*, 97, 51–63
- Hudson, H. S., 1988, Observed variability of the solar luminosity, *ARA&A*, 26, 473–507
- Hudson, H. S., Silva, S., Woodard, M., Willson, R. C., 1982, The effects of sunspots on solar irradiance, *Sol. Phys.*, 76, 211–219
- Jafarzadeh, S., 2013, Dynamics of magnetic bright points in the lower solar atmosphere, Ph.D. thesis, University of Göttingen
- Jones, H. P., Ceja, J. A., 2001, Preliminary Comparison of Magnetograms from KPVT/SPM, SOHO/MDI and GONG⁺, in *Advanced Solar Polarimetry – Theory, Observation, and Instrumentation*, (Ed.) M. Sigwarth, vol. 236 of *Astr. Soc. P.*, p. 87

- Jones, H. P., Duvall, Jr., T. L., Harvey, J. W., Mahaffey, C. T., Schwitters, J. D., Simmons, J. E., 1992, The NASA/NSO spectromagnetograph, *Sol. Phys.*, 139, 211–232
- Jørgensen, U. G., 1992, Sampling Methods, *Rev. Mexicana Astron. Astrofis.*, 23, 195
- Keil, S. L., Henry, T. W., Fleck, B., 1998, NSO/AFRL/Sac Peak K-line Monitoring Program, in *Synoptic Solar Physics*, (Eds.) K. S. Balasubramaniam, J. Harvey, D. Rabin, vol. 140 of ASP Conf. Ser., p. 301
- Keller, C. U., Steiner, O., Stenflo, J. O., Solanki, S. K., 1990, Structure of solar magnetic fluxtubes from the inversion of Stokes spectra at disk center, *Astron. Astrophys.*, 233, 583–597
- Keller, C. U., Schüssler, M., Vögler, A., Zakharov, V., 2004, On the Origin of Solar Faculae, *ApJ*, 607, L59–L62
- Khomenko, E. V., Collados, M., Solanki, S. K., Lagg, A., Trujillo Bueno, J., 2003, Quiet-Sun inter-network magnetic fields observed in the infrared, *Astron. Astrophys.*, 408, 1115–1135
- Knölker, M., Schüssler, M., Weisshaar, E., 1988, Model calculations of magnetic flux tubes. III - Properties of solar magnetic elements, *Astron. Astrophys.*, 194, 257–267
- Knölker, M., Grossmann-Doerth, U., Schüssler, M., Weisshaar, E., 1991, Some developments in the theory of magnetic flux concentrations in the solar atmosphere, *Adv. Space Res.*, 11, 285–295
- Kobel, P., Solanki, S. K., Borrero, J. M., 2011, The continuum intensity as a function of magnetic field. I. Active region and quiet Sun magnetic elements, *Astron. Astrophys.*, 531, A112
- Kobel, P., Solanki, S. K., Borrero, J. M., 2012, The continuum intensity as a function of magnetic field. II. Local magnetic flux and convective flows, *Astron. Astrophys.*, 542, A96
- Kopp, G., Lawrence, G., 2005, The Total Irradiance Monitor (TIM): Instrument Design, *Sol. Phys.*, 230, 91–109
- Kopp, G., Lean, J. L., 2011, A new, lower value of total solar irradiance: Evidence and climate significance, *Geophys. Res. Lett.*, 38, L01706
- Kopp, G., Heuerman, K., Lawrence, G., 2005a, The Total Irradiance Monitor (TIM): Instrument Calibration, *Sol. Phys.*, 230, 111–127
- Kopp, G., Lawrence, G., Rottman, G., 2005b, The Total Irradiance Monitor (TIM): Science Results, *Sol. Phys.*, 230, 129–139
- Kopp, G., Heuerman, K., Harber, D., Drake, G., 2007, The tsi radiometer facility: absolute calibrations for total solar irradiance instruments, *Proc. SPIE*, 6677, 667 709–667 709–12

- Kopp, G., Fehlmann, A., Finsterle, W., Harber, D., Heuerman, K., Willson, R., 2012, Total solar irradiance data record accuracy and consistency improvements, *Metrologia*, 49, 29
- Kosugi, T., Matsuzaki, K., Sakao, T., Shimizu, T., Sone, Y., Tachikawa, S., Hashimoto, T., Minesugi, K., Ohnishi, A., Yamada, T., Tsuneta, S., Hara, H., Ichimoto, K., Suematsu, Y., Shimojo, M., Watanabe, T., Shimada, S., Davis, J. M., Hill, L. D., Owens, J. K., Title, A. M., Culhane, J. L., Harra, L. K., Doschek, G. A., Golub, L., 2007, The Hinode (Solar-B) Mission: An Overview, *Sol. Phys.*, 243, 3–17
- Krivova, N. A., Solanki, S. K., 2004, Effect of spatial resolution on estimating the Sun's magnetic flux, *Astron. Astrophys.*, 417, 1125–1132
- Krivova, N. A., Solanki, S. K., Fligge, M., Unruh, Y. C., 2003, Reconstruction of solar irradiance variations in cycle 23: Is solar surface magnetism the cause?, *Astron. Astrophys.*, 399, L1–L4
- Krivova, N. A., Solanki, S. K., Floyd, L., 2006, Reconstruction of solar UV irradiance in cycle 23, *Astron. Astrophys.*, 452, 631–639
- Krivova, N. A., Balmaceda, L., Solanki, S. K., 2007, Reconstruction of solar total irradiance since 1700 from the surface magnetic flux, *Astron. Astrophys.*, 467, 335–346
- Krivova, N. A., Solanki, S. K., Wenzler, T., 2009a, ACRIM-gap and total solar irradiance revisited: Is there a secular trend between 1986 and 1996?, *Geophys. Res. Lett.*, 36, L20101
- Krivova, N. A., Solanki, S. K., Wenzler, T., Podlipnik, B., 2009b, Reconstruction of solar UV irradiance since 1974, *J. Geophys. Res.*, 114, D00I04
- Krivova, N. A., Solanki, S. K., Schmutz, W., 2011a, Solar total irradiance in cycle 23, *Astron. Astrophys.*, 529, A81
- Krivova, N. A., Solanki, S. K., Unruh, Y. C., 2011b, Towards a long-term record of solar total and spectral irradiance, *J. Atmos. Solar-Terr. Phys.*, 73, 223–234
- Kuhn, J. R., Libbrecht, K. G., Dicke, R. H., 1988, The surface temperature of the sun and changes in the solar constant, *Science*, 242, 908–911
- Kurucz, R., 1993, ATLAS9 Stellar Atmosphere Programs and 2 km/s grid., ATLAS9 Stellar Atmosphere Programs and 2 km/s grid. Kurucz CD-ROM No. 13. Cambridge, Mass.: Smithsonian Astrophysical Observatory
- Lagg, A., Solanki, S. K., Riethmüller, T. L., Martínez Pillet, V., Schüssler, M., Hirzberger, J., Feller, A., Borrero, J. M., Schmidt, W., del Toro Iniesta, J. C., Bonet, J. A., Barthol, P., Berkefeld, T., Domingo, V., Gandorfer, A., Knölker, M., Title, A. M., 2010, Fully Resolved Quiet-Sun Magnetic flux Tube Observed with the SUNRISE/IMAX Instrument, *ApJ*, 723, L164–L168
- Lawrence, J. K., Chapman, G. A., Herzog, A. D., 1988, Photometric determination of facular contrasts near the solar disk center, *ApJ*, 324, 1184–1193

- Lawrence, J. K., Chapman, G. A., Walton, S. R., 1991, Weak magnetic fields and solar irradiance variations, *ApJ*, 375, 771–774
- Lawrence, J. K., Topka, K. P., Jones, H. P., 1993, Contrast of faculae near the disk center and solar variability, *J. Geophys. Res.*, 981, 18 911
- Lean, J., 2000, Evolution of the Sun's Spectral Irradiance Since the Maunder Minimum, *Geophys. Res. Lett.*, 27, 2425–2428
- Lean, J. L., DeLand, M. T., 2012, How Does the Sun's Spectrum Vary?, *J. Climate*, 25, 2555–2560
- Lean, J. L., Rottman, G. J., Kyle, H. L., Woods, T. N., Hickey, J. R., Puga, L. C., 1997, Detection and parameterization of variations in solar mid- and near-ultraviolet radiation (200–400 nm), *J. Geophys. Res.*, 102, 29 939–29 956
- Lee, III, R. B., Barkstrom, B. R., Cess, R. D., 1987, Characteristics of the earth radiation budget experiment solar monitors, *Appl. Opt.*, 26, 3090–3096
- Lee, III, R. B., Gibson, M. A., Wilson, R. S., Thomas, S., 1995, Long-term total solar irradiance variability during sunspot cycle 22, *J. Geophys. Res.*, 100, 1667–1675
- Lemen, J. R., Title, A. M., Akin, D. J., Boerner, P. F., Chou, C., Drake, J. F., Duncan, D. W., Edwards, C. G., Friedlaender, F. M., Heyman, G. F., Hurlburt, N. E., Katz, N. L., Kushner, G. D., Levay, M., Lindgren, R. W., Mathur, D. P., McFeaters, E. L., Mitchell, S., Rehse, R. A., Schrijver, C. J., Springer, L. A., Stern, R. A., Tarbell, T. D., Wuelser, J.-P., Wolfson, C. J., Yanari, C., Bookbinder, J. A., Cheimets, P. N., Caldwell, D., Deluca, E. E., Gates, R., Golub, L., Park, S., Podgorski, W. A., Bush, R. I., Scherrer, P. H., Gumm, M. A., Smith, P., Aufer, G., Jerram, P., Pool, P., Soufli, R., Windt, D. L., Beardsley, S., Clapp, M., Lang, J., Waltham, N., 2012, The Atmospheric Imaging Assembly (AIA) on the Solar Dynamics Observatory (SDO), *Sol. Phys.*, 275, 17–40
- Lites, B. W., Leka, K. D., Skumanich, A., Martínez Pillet, V., Shimizu, T., 1996, Small-Scale Horizontal Magnetic Fields in the Solar Photosphere, *ApJ*, 460, 1019
- Lites, B. W., Scharmer, G. B., Berger, T. E., Title, A. M., 2004, Three-Dimensional Structure of the Active Region Photosphere as Revealed by High Angular Resolution, *Sol. Phys.*, 221, 65–84
- Lites, B. W., Kubo, M., Socas-Navarro, H., Berger, T., Frank, Z., Shine, R., Tarbell, T., Title, A., Ichimoto, K., Katsukawa, Y., Tsuneta, S., Suematsu, Y., Shimizu, T., Nagata, S., 2008, The Horizontal Magnetic Flux of the Quiet-Sun Internetwork as Observed with the Hinode Spectro-Polarimeter, *ApJ*, 672, 1237–1253
- Liu, Y., Norton, A. A., Scherrer, P. H., 2007, A Note on Saturation Seen in the MDI/SOHO Magnetograms, *Sol. Phys.*, 241, 185–193
- Liu, Y., Hoeksema, J. T., Scherrer, P. H., Schou, J., Couvidat, S., Bush, R. I., Duvall, T. L., Hayashi, K., Sun, X., Zhao, X., 2012, Comparison of Line-of-Sight Magnetograms Taken by the Solar Dynamics Observatory/Heliioseismic and Magnetic Imager

- and Solar and Heliospheric Observatory/Michelson Doppler Imager, *Sol. Phys.*, 279, 295–316
- Livingston, W. C., Harvey, J., Pierce, A. K., Schrage, D., Gillespie, B., Simmons, J., Slaughter, C., 1976, Kitt Peak 60-cm vacuum telescope, *Appl. Opt.*, 15, 33–39
- Löfdahl, M. G., Scharmer, G. B., 1994, Wavefront sensing and image restoration from focused and defocused solar images., *A&AS*, 107, 243–264
- Lucy, L. B., 1974, , *AJ*, 79, 745
- Maltby, P., Avrett, E. H., Carlsson, M., Kjeldseth-Moe, O., Kurucz, R. L., Loeser, R., 1986, A new sunspot umbral model and its variation with the solar cycle, *ApJ*, 306, 284–303
- Marchand, P., Marmet, L., 1983, Binomial smoothing filter: A way to avoid some pitfalls of least-squares polynomial smoothing, *Rev. Sci. Instrum.*, 54, 1034–1041
- Martínez Pillet, V., 1992, Stray-light effects on the solar intensity distribution, *Sol. Phys.*, 140, 207–237
- Martínez Pillet, V., Del Toro Iniesta, J. C., Álvarez-Herrero, A., Domingo, V., Bonet, J. A., González Fernández, L., López Jiménez, A., Pastor, C., Gasent Blesa, J. L., Melado, P., Piqueras, J., Aparicio, B., Balaguer, M., Ballesteros, E., Belenguer, T., Bellot Rubio, L. R., Berkefeld, T., Collados, M., Deutsch, W., Feller, A., Girela, F., Grauf, B., Heredero, R. L., Herranz, M., Jerónimo, J. M., Laguna, H., Meller, R., Menéndez, M., Morales, R., Orozco Suárez, D., Ramos, G., Reina, M., Ramos, J. L., Rodríguez, P., Sánchez, A., Uribe-Patarroyo, N., Barthol, P., Gandorfer, A., Knoelker, M., Schmidt, W., Solanki, S. K., Vargas Domínguez, S., 2011, The Imaging Magnetograph eXperiment (IMaX) for the Sunrise Balloon-Borne Solar Observatory, *Sol. Phys.*, 268, 57–102
- Mathew, S. K., Martínez Pillet, V., Solanki, S. K., Krivova, N. A., 2007, Properties of sunspots in cycle 23. I. Dependence of brightness on sunspot size and cycle phase, *Astron. Astrophys.*, 465, 291–304
- Mathew, S. K., Zakharov, V., Solanki, S. K., 2009, Stray light correction and contrast analysis of Hinode broad-band images, *Astron. Astrophys.*, 501, L19–L22
- McClintock, W. E., Rottman, G. J., Woods, T. N., 2005, Solar-Stellar Irradiance Comparison Experiment II (Solstice II): Instrument Concept and Design, *Sol. Phys.*, 230, 225–258
- Mekaoui, S., Dewitte, S., 2008, Total Solar Irradiance Measurement and Modelling during Cycle 23, *Sol. Phys.*, 247, 203–216
- Merkel, A. W., Harder, J. W., Marsh, D. R., Smith, A. K., Fontenla, J. M., Woods, T. N., 2011, The impact of solar spectral irradiance variability on middle atmospheric ozone, *Geophys. Res. Lett.*, 38, L13802
- Mihalas, D., 1978, *Stellar atmospheres - 2nd ed.*, (San Francisco: W. H. Freeman and Co.)

- Mitalas, R., Sills, K. R., 1992, On the photon diffusion time scale for the sun, *ApJ*, 401, 759
- Mitchell, Jr., W. E., Livingston, W. C., 1991, Line-blanketing variations in the irradiance spectrum of the sun from maximum to minimum of the solar cycle, *ApJ*, 372, 336–348
- Moll, R., Cameron, R. H., Schüssler, M., 2012, Vortices, shocks, and heating in the solar photosphere: effect of a magnetic field, *Astron. Astrophys.*, 541, A68
- Morrill, J. S., Dere, K. P., Korendyke, C. M., 2001, The Sources of Solar Ultraviolet Variability between 2765 and 2885 Å: Mg I, Mg II, Si I, and Continuum, *ApJ*, 557, 854–863
- Morrill, J. S., Floyd, L., McMullin, D., 2011, The Solar Ultraviolet Spectrum Estimated Using the Mg ii Index and Ca ii K Disk Activity, *Sol. Phys.*, 269, 253–267
- Munro, R., Anderson, C., Callies, J., Callies, J., Corpaccioli, E., Lang, R., Lefebvre, A., Livschitz, Y., Pálrez AlbiÁsana, A., 2006, GOME-2 on MetOp, in *Atmospheric Science Conference*, vol. 628 of ESA Sp. Pub.
- Musielak, Z. E., Ulmschneider, P., 2003, Atmospheric oscillations in solar magnetic flux tubes. I. Excitation by longitudinal tube waves and random pulses, *Astron. Astrophys.*, 400, 1057–1064
- Narayan, G., Scharmer, G. B., 2010, Small-scale convection signatures associated with a strong plage solar magnetic field, *Astron. Astrophys.*, 524, A3
- Neckel, H., Labs, D., 1994, Solar limb darkening 1986-1990 ($\lambda\lambda$ 303 to 1099nm), *Sol. Phys.*, 153, 91–114
- Norton, A. A., Graham, J. P., Ulrich, R. K., Schou, J., Tomczyk, S., Liu, Y., Lites, B. W., López Ariste, A., Bush, R. I., Socas-Navarro, H., Scherrer, P. H., 2006, Spectral Line Selection for HMI: A Comparison of Fe I 6173 Å and Ni I 6768 Å, *Sol. Phys.*, 239, 69–91
- Norton, A. A., Jones, E. H., Liu, Y., 2013, How do the magnetic field strengths and intensities of sunspots vary over the solar cycle?, *J Phys Conf Ser.*, 440, 012038
- Ortiz, A., Solanki, S. K., Domingo, V., Fligge, M., Sanahuja, B., 2002, On the intensity contrast of solar photospheric faculae and network elements, *Astron. Astrophys.*, 388, 1036–1047
- Ortiz, A., Domingo, V., Sanahuja, B., 2006, The intensity contrast of solar photospheric faculae and network elements. II. Evolution over the rising phase of solar cycle 23, *Astron. Astrophys.*, 452, 311–319
- Oster, L., Schatten, K. H., Sofia, S., 1982, Solar irradiance variations due to active regions, *ApJ*, 256, 768–773

Bibliography

- Pagaran, J., Weber, M., Burrows, J., 2009, Solar Variability from 240 to 1750 nm in Terms of Faculae Brightening and Sunspot Darkening from SCIAMACHY, *ApJ*, 700, 1884–1895
- Parker, E. N., 1963, Kinematical Hydromagnetic Theory and its Application to the Low Solar Photosphere., *ApJ*, 138, 552
- Parnell, C. E., DeForest, C. E., Hagenaar, H. J., Johnston, B. A., Lamb, D. A., Welsch, B. T., 2009, A Power-Law Distribution of Solar Magnetic Fields Over More Than Five Decades in Flux, *ApJ*, 698, 75–82
- Pasachoff, J. M., Schneider, G., Widemann, T., 2011, High-resolution Satellite Imaging of the 2004 Transit of Venus and Asymmetries in the Cytherean Atmosphere, *AJ*, 141, 112
- Penza, V., Caccin, B., Ermolli, I., Centrone, M., Gomez, M. T., 2003, Modeling solar irradiance variations through PSPT images and semiempirical models, in *Solar Variability as an Input to the Earth's Environment*, (Ed.) A. Wilson, vol. 535 of ESA Sp. Pub., pp. 299–302
- Petrovay, K., Szakály, G., 1999, Transport Effects in the Evolution of the Global Solar Magnetic Field, *Sol. Phys.*, 185, 1–13, [astro-ph/9812464](#)
- Peytremann, E., 1974, Line-blanketing and Model Stellar Atmospheres. I. Statistical Method and Calculation of a Grid of Models, *Astron. Astrophys.*, 33, 203
- Pierce, A. K., Slaughter, C. D., 1977, Solar limb darkening. I - At wavelengths of 3033-7297, *Sol. Phys.*, 51, 25–41
- Preminger, D. G., Walton, S. R., Chapman, G. A., 2002, Photometric quantities for solar irradiance modeling, *J. Geophys. Res.*, 107, 1354
- Rabin, D., 1992, Spatially extended measurements of magnetic field strength in solar plages, *ApJ*, 391, 832–844
- Reeves, E. M., Timothy, J. G., Huber, M. C. E., 1977, Extreme UV spectroheliometer on the Apollo Telescope Mount, *Appl. Opt.*, 16, 837–848
- Rempel, M., Schlichenmaier, R., 2011, Sunspot Modeling: From Simplified Models to Radiative MHD Simulations, *Living Rev. Solar Phys.*, 8, 3
- Rezaei, R., Beck, C., Schmidt, W., 2012, Variation in sunspot properties between 1999 and 2011 as observed with the Tenerife Infrared Polarimeter, *Astron. Astrophys.*, 541, A60
- Richard, E. C., Harber, D., Harder, J. W., Pilewskie, P., Brown, S., Smith, A., Lykke, K., 2011, Future Long-term Measurements of Solar Spectral Irradiance by JPSS TSIS, *AGU Fall Meeting Abstracts*, p. A917
- Richardson, W. H., 1972, Bayesian-Based Iterative Method of Image Restoration, *J. Opt. Soc. Am.*, 62, 55

- Riethmüller, T. L., Solanki, S. K., Martínez Pillet, V., Hirzberger, J., Feller, A., Bonet, J. A., Bello González, N., Franz, M., Schüssler, M., Barthol, P., Berkefeld, T., del Toro Iniesta, J. C., Domingo, V., Gandorfer, A., Knölker, M., Schmidt, W., 2010, Bright Points in the Quiet Sun as Observed in the Visible and Near-UV by the Balloon-borne Observatory SUNRISE, *ApJ*, 723, L169–L174
- Riethmüller, T. L., Solanki, S. K., Hirzberger, J., Danilovic, S., Barthol, P., Berkefeld, T., Gandorfer, A., Gizon, L., Knölker, M., Schmidt, W., Del Toro Iniesta, J. C., 2013, First High-resolution Images of the Sun in the 2796 Å Mg II k Line, *ApJ*, 776, L13
- Röhrbein, D., Cameron, R., Schüssler, M., 2011, Is there a non-monotonic relation between photospheric brightness and magnetic field strength in solar plage regions?, *Astron. Astrophys.*, 532, A140
- Romano, P., Berrilli, F., Criscuoli, S., Del Moro, D., Ermolli, I., Giorgi, F., Viticchié, B., Zuccarello, F., 2012, A Comparative Analysis of Photospheric Bright Points in an Active Region and in the Quiet Sun, *Sol. Phys.*, 280, 407–416
- Rottman, G., 2005, The *SORCE* Mission, *Sol. Phys.*, 230, 7–25
- Rottman, G., Woods, T., Snow, M., DeToma, G., 2001, The solar cycle variation in ultraviolet irradiance, *Adv. Space Res.*, 27, 1927–1932
- Rüedi, I., Solanki, S. K., Livingston, W., Stenflo, J. O., 1992, Infrared lines as probes of solar magnetic features. III - Strong and weak magnetic fields in plages, *Astron. Astrophys.*, 263, 323–338
- Rybicki, G. B., Hummer, D. G., 1991, An accelerated lambda iteration method for multi-level radiative transfer. I - Non-overlapping lines with background continuum, *Astron. Astrophys.*, 245, 171–181
- Rybicki, G. B., Hummer, D. G., 1992, An accelerated lambda iteration method for multi-level radiative transfer. II - Overlapping transitions with full continuum, *Astron. Astrophys.*, 262, 209–215
- Sánchez Cuberes, M., Bonet, J. A., Vázquez, M., Wittmann, A. D., 2000, Center-to-Limb Variation of Solar Granulation from Partial Eclipse Observations, *ApJ*, 538, 940–959
- Sánchez Cuberes, M., Vázquez, M., Bonet, J. A., Sobotka, M., 2003, Centre-to-limb variation of solar granulation in the infrared, *Astron. Astrophys.*, 397, 1075–1081
- Scafetta, N., Willson, R. C., 2009, ACRIM-gap and TSI trend issue resolved using a surface magnetic flux TSI proxy model, *Geophys. Res. Lett.*, 36, L05701
- Scharmer, G. B., Bjelksjo, K., Korhonen, T. K., Lindberg, B., Petterson, B., 2003, The 1-meter Swedish solar telescope, in *SPIE Conf. Ser.* 4853, (Eds.) S. L. Keil, S. V. Avakyan, pp. 341–350

- Scherrer, P. H., Bogart, R. S., Bush, R. I., Hoeksema, J. T., Kosovichev, A. G., Schou, J., Rosenberg, W., Springer, L., Tarbell, T. D., Title, A., Wolfson, C. J., Zayer, I., MDI Engineering Team, 1995, The Solar Oscillations Investigation - Michelson Doppler Imager, *Sol. Phys.*, 162, 129–188
- Schmutz, W., Fehlmann, A., Højlsen, G., Meindl, P., Winkler, R., Thuillier, G., Blattner, P., Buisson, F., Egorova, T., Finsterle, W., Fox, N., Gräßner, J., Hochedez, J., Koller, S., Meftah, M., Meissonnier, M., Nyeki, S., Pfiffner, D., Roth, H., Rozanov, E., Spescha, M., Wehrli, C., Werner, L., Wyss, J. U., 2009, The PREMOS/PICARD instrument calibration, *Metrologia*, 46, S202
- Schnerr, R. S., Spruit, H. C., 2011, The brightness of magnetic field concentrations in the quiet Sun, *Astron. Astrophys.*, 532, A136
- Schou, J., Borrero, J. M., Norton, A. A., Tomczyk, S., Elmore, D., Card, G. L., 2012a, Polarization Calibration of the Helioseismic and Magnetic Imager (HMI) onboard the Solar Dynamics Observatory (SDO), *Sol. Phys.*, 275, 327–355
- Schou, J., Scherrer, P. H., Bush, R. I., Wachter, R., Couvidat, S., Rabello-Soares, M. C., Bogart, R. S., Hoeksema, J. T., Liu, Y., Duvall, T. L., Akin, D. J., Allard, B. A., Miles, J. W., Rairden, R., Shine, R. A., Tarbell, T. D., Title, A. M., Wolfson, C. J., Elmore, D. F., Norton, A. A., Tomczyk, S., 2012b, Design and Ground Calibration of the Helioseismic and Magnetic Imager (HMI) Instrument on the Solar Dynamics Observatory (SDO), *Sol. Phys.*, 275, 229–259
- Schüssler, M., Shelyag, S., Berdyugina, S., Vögler, A., Solanki, S. K., 2003, Why Solar Magnetic Flux Concentrations Are Bright in Molecular Bands, *ApJ*, 597, L173–L176
- Seleznyov, A. D., Solanki, S. K., Krivova, N. A., 2011, Modelling solar irradiance variability on time scales from minutes to months, *Astron. Astrophys.*, 532, A108
- Shapiro, A. I., Schmutz, W., Schoell, M., Haberreiter, M., Rozanov, E., 2010, NLTE solar irradiance modeling with the COSI code, *Astron. Astrophys.*, 517, A48
- Shapiro, A. I., Schmutz, W., Rozanov, E., Schoell, M., Haberreiter, M., Shapiro, A. V., Nyeki, S., 2011, A new approach to the long-term reconstruction of the solar irradiance leads to large historical solar forcing, *Astron. Astrophys.*, 529, A67
- Shapiro, A. V., Shapiro, A. I., Dominique, M., Dammasch, I. E., Wehrli, C., Rozanov, E., Schmutz, W., 2013, Detection of Solar Rotational Variability in the Large Yield Radiometer (LYRA) 190 - 222 nm Spectral Band, *Sol. Phys.*, 286, 289–301
- Shepp, L. A., Vardi, Y., 1982, Maximum Likelihood Reconstruction for Emission Tomography, *IEEE Trans. Med. Imag.*, 1, 113–122, ISSN 0278-0062
- Skupin, J., Noël, S., Wuttke, M. W., Gottwald, M., Bovensmann, H., Weber, M., Burrows, J. P., 2005a, SCIAMACHY solar irradiance observation in the spectral range from 240 to 2380 nm, *Adv. Space Res.*, 35, 370–375

- Skupin, J., Weber, M., Bovensmann, H., Burrows, J. P., 2005b, The Mg II Solar Activity Proxy Indicator Derived from GOME and SCIAMACHY, in Proceedings of the 2004 Envisat & ERS Symposium, vol. 572 of ESA Sp. Pub.
- Skupin, J., Weber, M., Noël, S., Bovensmann, H., Burrows, J. P., 2005c, GOME and SCIAMACHY solar measurements: Solar spectral irradiance and Mg II solar activity proxy indicator, *Mem. Soc. Astron. Italiana*, 76, 1038
- Smith, E. V. P., Gottlieb, D. M., 1975, Solar flux and its variations, NASA Special Publication, 366, 97–117
- Snedden, C., Johnson, H. R., Krupp, B. M., 1976, A statistical method for treating molecular line opacities, *ApJ*, 204, 281–289
- Snodgrass, H. B., 1983, Magnetic rotation of the solar photosphere, *ApJ*, 270, 288–299
- Snow, M., McClintock, W. E., Rottman, G., Woods, T. N., 2005a, Solar Stellar Irradiance Comparison Experiment II (Solstice II): Examination of the Solar Stellar Comparison Technique, *Sol. Phys.*, 230, 295–324
- Snow, M., McClintock, W. E., Woods, T. N., White, O. R., Harder, J. W., Rottman, G., 2005b, The Mg II Index from SORCE, *Sol. Phys.*, 230, 325–344
- Socas-Navarro, H., 2011, A high-resolution three-dimensional model of the solar photosphere derived from Hinode observations, *Astron. Astrophys.*, 529, A37
- Solanki, S. K., 1986, Velocities in solar magnetic fluxtubes, *Astron. Astrophys.*, 168, 311–329
- Solanki, S. K., 1987, The Photospheric Layers of Solar Magnetic Flux Tubes, Ph.D. thesis, ETH Zürich
- Solanki, S. K., 1993, Small-scale Solar Magnetic Fields - an Overview, *Space Sci. Rev.*, 63, 1–188
- Solanki, S. K., 2003, Sunspots: An overview, *A&A Rev.*, 11, 153–286
- Solanki, S. K., Krivova, N. A., 2004, Solar Irradiance Variations: From Current Measurements to Long-Term Estimates, *Sol. Phys.*, 224, 197–208
- Solanki, S. K., Schmidt, H. U., 1993, Are sunspot penumbrae deep or shallow?, *Astron. Astrophys.*, 267, 287–291
- Solanki, S. K., Stenflo, J. O., 1984, Properties of solar magnetic fluxtubes as revealed by Fe I lines, *Astron. Astrophys.*, 140, 185–198
- Solanki, S. K., Unruh, Y. C., 1998, A model of the wavelength dependence of solar irradiance variations, *Astron. Astrophys.*, 329, 747–753
- Solanki, S. K., Steiner, O., Bünte, M., Murphy, G., Ploner, S. R. O., 1998, On the reliability of Stokes diagnostics of magnetic elements away from solar disc centre, *Astron. Astrophys.*, 333, 721–731

- Solanki, S. K., Finsterle, W., Rüedi, I., Livingston, W., 1999, Expansion of solar magnetic flux tubes large and small, *Astron. Astrophys.*, 347, L27–L30
- Solanki, S. K., Schüssler, M., Fligge, M., 2002, Secular variation of the Sun's magnetic flux, *Astron. Astrophys.*, 383, 706–712
- Solanki, S. K., Barthol, P., Danilovic, S., Feller, A., Gandorfer, A., Hirzberger, J., Riethmüller, T. L., Schüssler, M., Bonet, J. A., Martínez Pillet, V., del Toro Iniesta, J. C., Domingo, V., Palacios, J., Knölker, M., Bello González, N., Berkefeld, T., Franz, M., Schmidt, W., Title, A. M., 2010, SUNRISE: Instrument, Mission, Data, and First Results, *ApJ*, 723, L127–L133
- Solanki, S. K., Krivova, N. A., Haigh, J. D., 2013, Solar Irradiance Variability and Climate, *ARA&A*, 51, 311–351
- Spruit, H. C., 1976, Pressure equilibrium and energy balance of small photospheric flux-tubes, *Sol. Phys.*, 50, 269–295
- Spruit, H. C., Roberts, B., 1983, Magnetic flux tubes on the sun, *Nature*, 304, 401–406
- Spruit, H. C., Zwaan, C., 1981, The size dependence of contrasts and numbers of small magnetic flux tubes in an active region, *Sol. Phys.*, 70, 207–228
- Steiner, O., 2005, Radiative properties of magnetic elements. II. Center to limb variation of the appearance of photospheric faculae, *Astron. Astrophys.*, 430, 691–700
- Steiner, O., Hauschildt, P. H., Bruls, J., 2001, Radiative properties of magnetic elements. I. Why are vec G-band bright points bright?, *Astron. Astrophys.*, 372, L13–L16
- Stellmacher, G., Wiehr, E., 1979, A common model for solar filigree and faculae, *Astron. Astrophys.*, 75, 263–267
- Stellmacher, G., Wiehr, E., 1991, Geometric line elevation in solar limb faculae, *Astron. Astrophys.*, 248, 227–231
- Stellmacher, G., Wiehr, E., 2001, Spatial offsets between lines and continuum in limb faculae, *Sol. Phys.*, 202, 259–268
- Stenflo, J. O., 1973, Magnetic-Field Structure of the Photospheric Network, *Sol. Phys.*, 32, 41–63
- Sütterlin, P., Wiehr, E., Stellmacher, G., 1999, Continuum photometry of solar white-light faculae, *Sol. Phys.*, 189, 57–68
- Tanga, P., Widemann, T., Sicardy, B., Pasachoff, J. M., Arnaud, J., Comolli, L., Rondi, A., Rondi, S., Sütterlin, P., 2012, Sunlight refraction in the mesosphere of Venus during the transit on June 8th, 2004, *Icarus*, 218, 207–219
- Tao, L., Proctor, M. R. E., Weiss, N. O., 1998, Flux expulsion by inhomogeneous turbulence, *MNRAS*, 300, 907–914

- Tapping, K. F., 1987, Recent solar radio astronomy at centimeter wavelengths - The temporal variability of the 10.7-cm flux, *J. Geophys. Res.*, 92, 829–838
- Tapping, K. F., 2013, The 10.7 cm solar radio flux ($F_{10.7}$), *Space Weather*, 11, 394–406
- Thuillier, G., Foujols, T., Bolsée, D., Gillotay, D., Hersé, M., Peetermans, W., Decuyper, W., Mandel, H., Sperfeld, P., Pape, S., Taubert, D. R., Hartmann, J., 2009, SOLAR/SOLSPEC: Scientific Objectives, Instrument Performance and Its Absolute Calibration Using a Blackbody as Primary Standard Source, *Sol. Phys.*, 257, 185–213
- Thuillier, G., Deland, M., Shapiro, A., Schmutz, W., Bolsée, D., Melo, S. M. L., 2012, The Solar Spectral Irradiance as a Function of the Mg ii Index for Atmosphere and Climate Modelling, *Sol. Phys.*, 277, 245–266
- Title, A. M., Berger, T. E., 1996, Double-Gaussian Models of Bright Points or Why Bright Points Are Usually Dark, *ApJ*, 463, 797
- Title, A. M., Topka, K. P., Tarbell, T. D., Schmidt, W., Balke, C., Scharmer, G., 1992, On the differences between plage and quiet sun in the solar photosphere, *ApJ*, 393, 782–794
- Tobias, S. M., Brummell, N. H., Clune, T. L., Toomre, J., 1998, Pumping of Magnetic Fields by Turbulent Penetrative Convection, *ApJ*, 502, L177
- Topka, K. P., Tarbell, T. D., Title, A. M., 1992, Properties of the smallest solar magnetic elements. I - Facular contrast near sun center, *ApJ*, 396, 351–363
- Topka, K. P., Tarbell, T. D., Title, A. M., 1997, Properties of the Smallest Solar Magnetic Elements. II. Observations versus Hot Wall Models of Faculae, *ApJ*, 484, 479
- Uitenbroek, H., 2002, The Effect of Coherent Scattering on Radiative Losses in the Solar Ca II K Line, *ApJ*, 565, 1312–1322
- Uitenbroek, H., Criscuoli, S., 2011, Why One-dimensional Models Fail in the Diagnosis of Average Spectra from Inhomogeneous Stellar Atmospheres, *ApJ*, 736, 69
- Unruh, Y. C., Solanki, S. K., Fligge, M., 1999, The spectral dependence of facular contrast and solar irradiance variations, *Astron. Astrophys.*, 345, 635–642
- Unruh, Y. C., Krivova, N. A., Solanki, S. K., Harder, J. W., Kopp, G., 2008, Spectral irradiance variations: comparison between observations and the SATIRE model on solar rotation time scales, *Astron. Astrophys.*, 486, 311–323
- Unruh, Y. C., Solanki, S. K., Schüssler, M., Vögler, A., Garcia-Alvarez, D., 2009, Towards Long-Term Solar Irradiance Modelling: Network Contrasts from Magneto-Convection Simulations, in *15th Cambridge Workshop on Cool Stars, Stellar Systems, and the Sun*, (Ed.) E. Stempels, vol. 1094 of AIP Conf. Proc., pp. 768–771
- Unruh, Y. C., Ball, W. T., Krivova, N. A., 2012, Solar Irradiance Models and Measurements: A Comparison in the 220-240 nm wavelength band, *Surv. Geophys.*, 33, 475–481

- Vernazza, J. E., Avrett, E. H., Loeser, R., 1981, Structure of the solar chromosphere. III - Models of the EUV brightness components of the quiet-sun, *ApJS*, 45, 635–725
- Vieira, L. E. A., Solanki, S. K., Krivova, N. A., Usoskin, I., 2011, Evolution of the solar irradiance during the Holocene, *Astron. Astrophys.*, 531, A6
- Viereck, R. A., Puga, L. C., 1999, The NOAA Mg II core-to-wing solar index: Construction of a 20-year time series of chromospheric variability from multiple satellites, *J. Geophys. Res.*, 104, 9995–10 006
- Viereck, R. A., Floyd, L. E., Crane, P. C., Woods, T. N., Knapp, B. G., Rottman, G., Weber, M., Puga, L. C., DeLand, M. T., 2004, A composite Mg II index spanning from 1978 to 2003, *Adv. Space Res.*, 2, S10005
- Viticchié, B., Del Moro, D., Criscuoli, S., Berrilli, F., 2010, Imaging Spectropolarimetry with IBIS. II. On the Fine Structure of G-band Bright Features, *ApJ*, 723, 787–796
- Vögler, A., 2003, Three-dimensional simulations of magneto-convection in the solar photosphere, Ph.D. thesis, University of Göttingen
- Vögler, A., 2005, On the effect of photospheric magnetic fields on solar surface brightness. Results of radiative MHD simulations, *Mem. Soc. Astron. Italiana*, 76, 842
- Vögler, A., Bruls, J. H. M. J., Schüssler, M., 2004, Approximations for non-grey radiative transfer in numerical simulations of the solar photosphere, *Astron. Astrophys.*, 421, 741–754
- Vögler, A., Shelyag, S., Schüssler, M., Cattaneo, F., Emonet, T., Linde, T., 2005, Simulations of magneto-convection in the solar photosphere. Equations, methods, and results of the MURaM code, *Astron. Astrophys.*, 429, 335–351
- von der Lühe, O., 1993, Speckle imaging of solar small scale structure. I - Methods, *Astron. Astrophys.*, 268, 374–390
- Wachter, R., Schou, J., Rabello-Soares, M. C., Miles, J. W., Duvall, T. L., Bush, R. I., 2012, Image Quality of the Helioseismic and Magnetic Imager (HMI) Onboard the Solar Dynamics Observatory (SDO), *Sol. Phys.*, 275, 261–284
- Walton, S. R., 1987, Flux tube models of solar plages, *ApJ*, 312, 909–929
- Walton, S. R., Preminger, D. G., Chapman, G. A., 2003, A Statistical Analysis of the Characteristics of Sunspots and Faculae, *Sol. Phys.*, 213, 301–317
- Weber, M., Burrows, J. P., Cebula, R. P., 1998, Gome Solar UV/VIS Irradiance Measurements between 1995 and 1997 - First Results on Proxy Solar Activity Studies, *Sol. Phys.*, 177, 63–77
- Wedemeyer-Böhm, S., 2008, Point spread functions for the Solar optical telescope onboard Hinode, *Astron. Astrophys.*, 487, 399–412

- Wedemeyer-Böhm, S., Rouppe van der Voort, L., 2009, On the continuum intensity distribution of the solar photosphere, *Astron. Astrophys.*, 503, 225–239
- Wehrli, C., Schmutz, W., Shapiro, A. I., 2013, Correlation of spectral solar irradiance with solar activity as measured by VIRGO, *Astron. Astrophys.*, 556, L3
- Weiss, N. O., 1966, The Expulsion of Magnetic Flux by Eddies, *Royal Society of London Proceedings Series A*, 293, 310–328
- Welsch, B. T., Fisher, G. H., Sun, X., 2013, A Magnetic Calibration of Photospheric Doppler Velocities, *ApJ*, 765, 98
- Wenzler, T., 2005, Reconstruction of solar irradiance variations in cycles 21-23 based on surface magnetic fields, Ph.D. thesis, University of Göttingen
- Wenzler, T., Solanki, S. K., Krivova, N. A., Fluri, D. M., 2004, Comparison between KPVT/SPM and SoHO/MDI magnetograms with an application to solar irradiance reconstructions, *Astron. Astrophys.*, 427, 1031–1043
- Wenzler, T., Solanki, S. K., Krivova, N. A., 2005, Can surface magnetic fields reproduce solar irradiance variations in cycles 22 and 23?, *Astron. Astrophys.*, 432, 1057–1061
- Wenzler, T., Solanki, S. K., Krivova, N. A., Fröhlich, C., 2006, Reconstruction of solar irradiance variations in cycles 21-23 based on surface magnetic fields, *Astron. Astrophys.*, 460, 583–595
- Wenzler, T., Solanki, S. K., Krivova, N. A., 2009, Reconstructed and measured total solar irradiance: Is there a secular trend between 1978 and 2003?, *Geophys. Res. Lett.*, 36, L11102
- Wiegelmann, T., Solanki, S. K., Borrero, J. M., Peter, H., Barthol, P., Gandorfer, A., Martínez Pillet, V., Schmidt, W., Knölker, M., 2013, Evolution of the Fine Structure of Magnetic Fields in the Quiet Sun: Observations from Sunrise/IMaX and Extrapolations, *Sol. Phys.*, 283, 253–272
- Willson, R. C., 1979, Active cavity radiometer type IV, *Appl. Opt.*, 18, 179–188
- Willson, R. C., Hudson, H. S., 1988, Solar luminosity variations in solar cycle 21, *Nature*, 332, 810–812
- Willson, R. C., Mordvinov, A. V., 2003, Secular total solar irradiance trend during solar cycles 21-23, *Geophys. Res. Lett.*, 30, 1199
- Willson, R. C., Gulkis, S., Janssen, M., Hudson, H. S., Chapman, G. A., 1981a, Observations of solar irradiance variability, *Science*, 211, 700–702
- Willson, R. C., Gulkis, S., Janssen, M., Hudson, H. S., Chapman, G. A., 1981b, Observations of solar irradiance variability, *Science*, 211, 700–702
- Wolff, C. L., Hickey, J. R., 1987, Solar irradiance change and special longitudes due to r-modes, *Science*, 235, 1631–1633

- Woods, T. N., Tobiska, W. K., Rottman, G. J., Worden, J. R., 2000, Improved solar Lyman α irradiance modeling from 1947 through 1999 based on UARS observations, *J. Geophys. Res.*, 105, 27 195–27 216
- Woods, T. N., Kopp, G., Chamberlin, P. C., 2006, Contributions of the solar ultraviolet irradiance to the total solar irradiance during large flares, *J. Geophys. Res.*, 111, A10S14
- Woods, T. N., Chamberlin, P. C., Harder, J. W., Hock, R. A., Snow, M., Eparvier, F. G., Fontenla, J., McClintock, W. E., Richard, E. C., 2009, Solar Irradiance Reference Spectra (SIRS) for the 2008 Whole Heliosphere Interval (WHI), *Geophys. Res. Lett.*, 36, L01101
- Yeo, K. L., Solanki, S. K., Krivova, N. A., 2013, Intensity contrast of solar network and faculae, *Astron. Astrophys.*, 550, A95
- Yeo, K. L., Feller, A., Solanki, S. K., Couvidat, S., Danilovic, S., Krivova, N. A., 2014a, Point spread function of SDO/HMI and the effects of stray light correction on the apparent properties of solar surface phenomena, *Astron. Astrophys.*, 561, A22
- Yeo, K. L., Krivova, N. A., Solanki, S. K., Glassmeier, K. H., 2014b, Reconstruction of total and spectral solar irradiance since 1974 based on KPVT, SoHO/MDI and SDO/HMI observations, *Astron. Astrophys.*, submitted
- Zwaan, C., 1978, On the Appearance of Magnetic Flux in the Solar Photosphere, *Sol. Phys.*, 60, 213–240

Publications

- Yeo, K. L., Krivova, N. A., Solanki, S. K., Glassmeier, K. H., 2014, Reconstruction of total and spectral solar irradiance from 1974 to 2013 based on KPVT, SoHO/MDI and SDO/HMI observations, *Astron. Astrophys.*, 570, A85
- Thuillier, G., Schmidtke, G., Erhardt, C., Nikutowski, B., Shapiro, A. I., Bolduc, C., Lean, J., Krivova, N. A., Charbonneau, P., Cessateur, G., Haberreiter, M., Melo, S., Delouille, V., Mampaey, B., Yeo, K. L., Schmutz, W., 2014, Solar spectral irradiance variability in November/December 2012: comparison of observations by instruments on the International Space Station and models, *Sol. Phys.*, online
- Yeo, K. L., Krivova, N. A., Solanki, S. K., 2014, Solar cycle variation in solar irradiance, *Space Sci. Rev.*, online
- Yeo, K. L., Feller, A., Solanki, S. K., Couvidat, S., Danilovic, S., Krivova, N. A., 2014, Point spread function of SDO/HMI and the effects of stray light correction on the apparent properties of solar surface phenomena, *Astron. Astrophys.*, 561, A22
- Yeo, K. L., Solanki, S. K., Krivova, N. A., 2013, Intensity contrast of network and faculae, *Astron. Astrophys.*, 550, A95

Acknowledgements

First off, I would like to thank my supervisors, Sami Solanki, Natalie Krivova and Karl-Heinz Glaßmeier. Coming back to science after a six-year hiatus in industry is a challenge. Thank you, for taking a gamble on me, I hope it paid off.

Sami, after every meeting with you I am left floored by the depth and width of your knowledge and understanding, and even more by how incredibly incisive you are. What really draws my admiration though, is how no matter how busy you are, you were never sloppy in your interactions with me (or as far as I can see, with anyone else), no matter how trivial the matter. You are a role model and I consider it my privilege and a great pleasure to have come under your tutelage.

Natasha, right from the beginning, you were unwavering in your belief in my capabilities. You seem more confident in me than I myself. Thank you, for taking interest not just in my work but also my personal well-being, and for going out of your way time and again to support and set up opportunities for me.

Mention goes out to my collaborators, both here at MPS and without, who had contributed their time, effort and know how to this work; William Ball, Raymond Burston, Sebastien Couvidat, Sanja Danilovic, Ilaria Ermolli, Alex Feller, Jeff Morrill, Philip Scherrer and Jesper Schou.

Appreciation goes to the co-ordinator of the International Max Planck Research School for Solar System Science, Sonja Schuh. Your door is always open, and you take such care with all our concerns and issues, well beyond the call of duty. In less than a year, you have already made an incredible impact on the school, on each and every student.

I would have never made my way back into science without the intervention of Yvonne Unruh, my tutor back in Imperial College, and Ng Teck Khim, my former lab head at DSO. To both of you, I owe a debt of gratitude.

My life here in Germany would not have been complete without all the wonderful friends I have made. What would I do without you guys? It would take another dissertation to detail our adventures and exploits together. There is, however, one name I cannot omit here, Maria Andriopoulou. Thank you, for being there, for sharing my every joy and sorrow, quite literally from day one.

Last, but certainly not the least, I would like to thank my family, who have never wavered in their support or ever once question why I would leave home and career to pursue my interests.

This thesis is dedicated, in loving memory, to the late Dieter Schmitt.

Curriculum Vitae

Name	Yeo
Vorname	Kok Leng
Geburtsdatum	02.08.1979
Geburtsort	Singapur
Staatsangehörigkeit	singapurisch
Ausbildung	1996-1997 Anglo-Chinese Junior College, Singapur 2000-2004 Imperial College London, Vereinigtes Königreich, MSci Physics 2011-2014 Doktorand am Max-Planck-Institut für Sonnensystemforschung, Göttingen und an der Technischen Universität Braunschweig
Wehrdienst	1998-2000 Singapore Armed Forces, 3rd Division Support Command, Fernmelder
Beschäftigungen	2004-2010 DSO National Laboratories, Singapur, Member of Technical Staff

Erklärung zum eigenen Beitrag

An dieser Stelle wird erklärt, welche Beiträge, die in dieser Arbeit enthaltenen wissenschaftlichen Veröffentlichungen, selbstständig verfasst wurden. Im Folgenden werden die wissenschaftlichen Arbeiten in chronologischer Reihenfolge diskutiert.

Yeo, K. L., Solanki, S. K., Krivova, N. A., 2013, Intensity contrast of network and faculae, *Astron. Astrophys.*, 550, A95

Diese Arbeit wurde komplett selbstständig verfasst und mit Hilfe der beiden Koautoren Sami K. Solanki und Natalie A. Krivova sprachlich und inhaltlich überarbeitet.

Yeo, K. L., Feller, A., Solanki, S. K., Couvidat, S., Danilovic, S., Krivova, N. A., 2014, Point spread function of SDO/HMI and the effects of stray light correction on the apparent properties of solar surface phenomena, *Astron. Astrophys.*, 561, A22

Diese Arbeit wurde komplett selbstständig verfasst und mit Hilfe der Koautoren Alex Feller, Sami K. Solanki, Sebastien Couvidat, Sanja Danilovic und Natalie A. Krivova sprachlich und inhaltlich überarbeitet.

Yeo, K. L., Krivova, N. A., Solanki, S. K., Glassmeier, K. H., 2014, Reconstruction of total and spectral solar irradiance from 1974 to 2013 based on KPVT, SoHO/MDI and SDO/HMI observations, *Astron. Astrophys.*, 570, A85

Diese Arbeit wurde komplett selbstständig verfasst und mit Hilfe der Koautoren Natalie A. Krivova, Sami K. Solanki und Karl-Heinz Glaßmeier sprachlich und inhaltlich überarbeitet.

Yeo, K. L., Krivova, N. A., Solanki, S. K., 2014, Solar cycle variation in solar irradiance, *Space Sci. Rev.*, online

Diese Arbeit wurde komplett selbstständig verfasst und mit Hilfe der beiden Koautoren Natalie A. Krivova und Sami K. Solanki sprachlich und inhaltlich überarbeitet.

Kok Leng Yeo: Analysis and modeling of solar irradiance variations

A prominent manifestation of the solar dynamo is the 11-year activity cycle, evident in indicators of solar activity, including solar irradiance. Although a relationship between solar activity and the brightness of the Sun had long been suspected, it was only directly observed after regular satellite measurements became available with the launch of Nimbus-7 in 1978. The measurement of solar irradiance from space is accompanied by the development of models aimed at describing the apparent variability by the intensity excess/deficit effected by magnetic structures in the photosphere. The more sophisticated models, termed semi-empirical, rely on the intensity spectra of photospheric magnetic structures generated with radiative transfer codes from semi-empirical model atmospheres. An established example of such models is SATIRE-S (Spectral And Total Irradiance REconstruction for the Satellite era). One key limitation of current semi-empirical models is the fact that the radiant properties of network and faculae are not adequately represented due to the use of plane-parallel model atmospheres (as opposed to three-dimensional model atmospheres). This thesis is the compilation of four publications, detailing the results of investigations aimed at setting the groundwork necessary for the eventual introduction of three-dimensional atmospheres into SATIRE-S and a review of the current state of the measurement and modelling of solar irradiance. Also presented is an update of the SATIRE-S model. We generated a daily reconstruction of total and spectral solar irradiance, covering 1974 to the present, that is more reliable and, in most cases, extended than similar reconstructions from contemporary models.